

Lecture Notes in Mechanical Engineering

G. S. V. L. Narasimham

A. Veeresh Babu

S. Sreenatha Reddy

Rajagopal Dhanasekaran *Editors*

# Recent Trends in Mechanical Engineering

Select Proceedings of ICIME 2019

 Springer

# **Lecture Notes in Mechanical Engineering**



**Lecture Notes in Mechanical Engineering (LNME)** publishes the latest developments in Mechanical Engineering - quickly, informally and with high quality. Original research reported in proceedings and post-proceedings represents the core of LNME. Volumes published in LNME embrace all aspects, subfields and new challenges of mechanical engineering. Topics in the series include:

- Engineering Design
- Machinery and Machine Elements
- Mechanical Structures and Stress Analysis
- Automotive Engineering
- Engine Technology
- Aerospace Technology and Astronautics
- Nanotechnology and Microengineering
- Control, Robotics, Mechatronics
- MEMS
- Theoretical and Applied Mechanics
- Dynamical Systems, Control
- Fluid Mechanics
- Engineering Thermodynamics, Heat and Mass Transfer
- Manufacturing
- Precision Engineering, Instrumentation, Measurement
- Materials Engineering
- Tribology and Surface Technology

To submit a proposal or request further information, please contact the Springer Editor in your country:

**China:** Li Shen at [li.shen@springer.com](mailto:li.shen@springer.com)

**India:** Dr. Akash Chakraborty at [akash.chakraborty@springernature.com](mailto:akash.chakraborty@springernature.com)

**Rest of Asia, Australia, New Zealand:** Swati Meherishi at [swati.meherishi@springer.com](mailto:swati.meherishi@springer.com)

**All other countries:** Dr. Leontina Di Cecco at [Leontina.dicecco@springer.com](mailto:Leontina.dicecco@springer.com)

To submit a proposal for a monograph, please check our Springer Tracts in Mechanical Engineering at <http://www.springer.com/series/11693> or contact [Leontina.dicecco@springer.com](mailto:Leontina.dicecco@springer.com)

**Indexed by SCOPUS. The books of the series are submitted for indexing to Web of Science.**

More information about this series at <http://www.springer.com/series/11236>

G. S. V. L. Narasimham · A. Veeresh Babu ·  
S. Sreenatha Reddy · Rajagopal Dhanasekaran  
Editors

# Recent Trends in Mechanical Engineering

Select Proceedings of ICIME 2019

 Springer

*Editors*

G. S. V. L. Narasimham  
Indian Institute of Science Bangalore  
Bangalore, Karnataka, India

A. Veeresh Babu  
National Institute of Technology Warangal  
Warangal, Telangana, India

S. Sreenatha Reddy  
Guru Nanak Institute of Technology  
Ibrahimpattanam, Telangana, India

Rajagopal Dhanasekaran  
Guru Nanak Institute of Technology  
Ibrahimpattanam, Telangana, India

ISSN 2195-4356

ISSN 2195-4364 (electronic)

Lecture Notes in Mechanical Engineering

ISBN 978-981-15-1123-3

ISBN 978-981-15-1124-0 (eBook)

<https://doi.org/10.1007/978-981-15-1124-0>

© Springer Nature Singapore Pte Ltd. 2020

This work is subject to copyright. All rights are reserved by the Publisher, whether the whole or part of the material is concerned, specifically the rights of translation, reprinting, reuse of illustrations, recitation, broadcasting, reproduction on microfilms or in any other physical way, and transmission or information storage and retrieval, electronic adaptation, computer software, or by similar or dissimilar methodology now known or hereafter developed.

The use of general descriptive names, registered names, trademarks, service marks, etc. in this publication does not imply, even in the absence of a specific statement, that such names are exempt from the relevant protective laws and regulations and therefore free for general use.

The publisher, the authors and the editors are safe to assume that the advice and information in this book are believed to be true and accurate at the date of publication. Neither the publisher nor the authors or the editors give a warranty, expressed or implied, with respect to the material contained herein or for any errors or omissions that may have been made. The publisher remains neutral with regard to jurisdictional claims in published maps and institutional affiliations.

This Springer imprint is published by the registered company Springer Nature Singapore Pte Ltd. The registered company address is: 152 Beach Road, #21-01/04 Gateway East, Singapore 189721, Singapore

# Preface

The Second International Conference on Innovations in Mechanical Engineering (ICIME 2019) by the Department of Mechanical Engineering, Guru Nanak Institutions, Telangana, India, was conducted on January 4 and 5, 2019. It includes original research and the latest advances in the field, focusing on aerospace, automobile, thermal engineering, renewable energy sources, bio-mechanics, fluid mechanics, MEMS, mechatronics, robotics, CAD/CAM, CAE, CFD, design and optimization, tribology, materials engineering and metallurgy, mimics, surface engineering, nanotechnology, polymer science, manufacturing, production and production management, industrial engineering, and rapid prototyping. The conference has grown exponentially over the years and has become a platform for scientists, researchers, academicians, and students to present their ideas and share their research in various fields of mechanical engineering. The focus for this year's conference was 'innovation,' and we had distinguished speakers from India and abroad who shared innovative solutions and technologies.

Over 212 papers were received, based on the comments of reviewers and the scientific merits of the submitted manuscripts, 100 articles were accepted for publication in the conference proceedings, of which 68 papers have been selected for Lecture Notes in Mechanical Engineering. The papers selected were presented by the authors during the conference. The presentations of ICIME 2019 were divided into four main sessions, namely (1) thermal, (2) production, (3) materials, and (4) design, and all registered authors discussed their ideas. We were happy to note that all the authors were satisfied with the arrangements and encouraged us to continue to conduct such conferences in the future as well.

We would like to thank all the participants, speakers, session chairs, committee members, reviewers, international and national board members, Guru Nanak Institutions Management, and all the people who have directly or indirectly

contributed to the success of this conference. The editors would also like to thank Springer Editorial Team for their support and for publishing the papers as part of the 'Lecture Notes in Mechanical Engineering' series.

Bangalore, India  
Warangal, India  
Ibrahimpattam, India  
brahimpattam, India

Prof. G. S. V. L. Narasimham  
Dr. A. Veeresh Babu  
Prof. S. Sreenatha Reddy  
Prof. Rajagopal Dhanasekaran

# Contents

<b>Analysis Over Trio-Tube with Dual Thermal Communication Surface Heat Exchanger [T.T.H.Xr.]</b> . . . . .	1
Devendra Yadav, Zenis Upadhyay, Akhilesh Kushwaha and Anuj Mishra	
<b>An Experimental Study of Performance and Emission Characteristics of a Diesel Engine Fueled with Palm Kernel Methyl Ester with Ethanol Additive: A Fuzzy-Based Optimization Approach</b> . . . . .	15
Siddhartha Das, Bijoy Kumar Deb and G. R. K. Sastry	
<b>Effect of Alumina Nanoparticles on Performance and Emission Study of DICl Engine Fuelled by Cymbopogon Flexuosus</b> . . . . .	29
R. Sathiyamoorthi, G. Sankaranarayanan, B. Nithin Siddharth and M. V. Natarajan	
<b>Study and Analysis of Blended Fuel on Single-Cylinder Naturally Aspirated Diesel Engine with Biofuels Coupled with EGR</b> . . . . .	43
B. Venkatesh and G. Prasanthi	
<b>Thermal Analysis of Drilled and Slotted Brake Rotors</b> . . . . .	55
Jatin Parajiya, Kaustubh Babrekar, Saurabh Bairagi and Arvind Chel	
<b>Non-premixed Combustion Analysis on Micro-Gas Turbine Combustor Using LPG and Natural Gas</b> . . . . .	65
Ch. Indira Priyadarsini, A. Akhil and V. Srilaxmi Shilpa	
<b>Life Cycle Assessment of a 100 kWp Solar PV-Based Electric Power Generation System in India</b> . . . . .	81
N. Leela Prasad, P. Usha Sri and K. Vizayakumar	
<b>Performance, Combustion, and Emission Characteristics of Diesel Engine Fuelled with Waste Cooking Oil Biodiesel/Diesel Blends with Iron Oxide Nanoparticles</b> . . . . .	95
L. Bharath and D. K. Ramesha	

<b>Effect of Multiple Injection Strategy on Combustion of Cotton Seed Oil Biodiesel in CRDI Diesel Engine</b> .....	107
Ramesh Babu Nallamothu, Nallamothu Anantha Kamal, Nallamothu Seshu Kishan, Injeti Nanaji Niranjan Kumar and Basava Venkata Appa Rao	
<b>Combustion and Emission Behaviour of Honge Biofuel in a Thermal Barrier Coated Diesel Engine Suitable for Agriculture</b> .....	121
Muralidharan Kandasamy and Duraisamy Senthilkumar	
<b>Experimental Analysis on Emission Characteristics of Palmarosa Alkyl Group Biofuel Feedstock</b> .....	129
Ganapathi Arumugam and Kandasamy Muralidharan	
<b>Development of Solar Turbine for Small-Scale Industries</b> .....	139
Anjaiah Madarapu and M. Harinatha Reddy	
<b>Performance and Emission on Raw Vegetable Oil with Hydrogen-Enriched Air for Better Combustion in a DICl Engine</b> .....	145
G. Sankaranarayanan, S. Karthikayan, R. Ganesan and T. Thirumalai	
<b>Experimental Investigation on Stir Casting Processing and Properties of Al 6082/SiC Metal Matrix Composites</b> .....	159
Debashis Mishra and Tirupati Tulasi	
<b>Effect of Change in Focal Plane Position on Hole Characteristics of Nanosecond Pulsed Laser Micro Drilled Holes</b> .....	169
Ganesh Dongre, Avadhoot Rajurkar, Ramesh Gondil, Nachiket Laddha and Jacob Philip	
<b>Production Planning of Flexible Manufacturing Systems Using an Efficient Multiobjective Function Considering Failure of Different Machines in Production Unit</b> .....	177
B. Satish Kumar, G. Janardhana Raju and G. Ranga Janardhana	
<b>Experimental Investigation of Ball Burnishing Process Parameters Optimization for Al 5083 Using Taguchi Method</b> .....	189
M. Jawahar, J. Suresh kumar, M. Sriikiran and Shiek Ismail	
<b>Experimental Investigation on Strength of Friction Stir Welded Al 6061-T6 Alloy Joints with Varying Oblique Angle</b> .....	205
D. Maneiah, K. Prahlada Rao and K. Brahma Raju	
<b>A Comparative Study on Performance of 3D-Printed EDM Electrode with Conventional EDM Electrode</b> .....	217
L. Mahipal Reddy, L. Siva Rama Krishna, S. Sharath Kumar and P. Ravinder Reddy	

<b>Effect of High-Power Intensity on Corrosion Behaviour of Aluminium—Steel Dissimilar Joints Made by Electron Beam Welding</b> .....	227
S. Sai Sravanthi and Swati Ghosh Acharyya	
<b>Evaluation and Impacts on Mechanical Behavior of Friction Stir Welded Copper 2200 Alloy</b> .....	239
L. Srinivas Naik and B. Hadya	
<b>Error Compensation Strategies for Workpiece Deflection During End Milling of Thin-Walled Straight and Curved Geometries</b> .....	249
Hareendran Manikandan, S. Sreejith, Kanjiyangat Vivek, C. Sasi Jayaram and P. A. Azeemhafiz	
<b>Effects of Micro-EDM Parameters on the Surface Integrity of the Micro-Holes Fabricated on Nickel Sheet</b> .....	259
Pankaj Kumar and Manowar Hussain	
<b>A Study on Welding of Thin Sheet of Ti6-Al-4V Alloy Using Fiber Laser and Its Characterization</b> .....	271
Manowar Hussain, Gulshad Nawaz Ahmad and Pankaj Kumar	
<b>Tool-Wear Measurement Using Parametric Optimization and Image Processing of Drilling in Al6063–Al<sub>2</sub>O<sub>3</sub> MMC</b> .....	281
Cherukupalli Sudhakar, Praveen Kumar and M. Jayaashwini	
<b>Parametric Optimization for PA2200 Quality Prototype Fabricating Process (Selective Laser Sintering) by Taguchi Method</b> .....	293
Battula Narayana and Sriram Venkatesh	
<b>Scheduling of Flexible Manufacturing System by Hybridizing Petri Net with Improved Scatter Search Algorithm</b> .....	305
T. R. Chinnusamy, Prabhakar Kammar, Fathima Praveen, T. Karthikeyan, M. Krishnan, N. Varshitha and Ashika Ananda Shetty	
<b>An Image Processing Approach for Detecting Solidification Crack in Pipeline Girth Welds</b> .....	333
Nirmala Madian, Somasundaram Devaraj, Santhi Krishnamoorthi and Rajagopal Dhanasekaran	
<b>Experimental Investigation to Optimize Process Parameters in Drilling Operation for Composite Materials</b> .....	343
K. Amarnath, P. Surendernath and V. Kumar	
<b>Hardness Characteristics of Grinding Wheel Using Al<sub>2</sub>O<sub>3</sub> with Boron Nitride</b> .....	353
Shivashankara, Rudra Naik and Mahadev Gouda Patil	



<b>Optimization of Process Parameters on EDM for Inconel 718</b> . . . . .	365
Ch. Shekar, U. Ashok Kumar, K. Kishore and P. Laxminarayana	
<b>Profile Optimization in Tooltip for FSW Process—A Numerical Investigation</b> . . . . .	373
R. Saravanan, M. S. Sreenivasa Rao, T. Malyadri and Nagasrisaihari Sunkara	
<b>Effect of Composition and Process Parameter on Mechanical Properties of Composite Coating by Laser Cladding: An Overview</b> . . . . .	387
Ranit Karmakar and Subrata Kumar Ghosh	
<b>Influence of ZrB<sub>2</sub> Particles on Dry Sliding Wear Behaviour of AA7075/ZrB<sub>2</sub> In-Situ Composites</b> . . . . .	397
M. Nallusamy, S. Sundaram and K. Kalaiselvan	
<b>Fibre Reinforced Polymer (FRP) Nanocomposites for Radar Absorption Application in the X-Band</b> . . . . .	409
Puppala Siva Nagasree, Koonam Ramji, Killi Krushna Murthy, Mantri Kannam Naidu and Tammareddy Haritha	
<b>Synthesis and Microwave Absorption Properties of MnZn Ferrite Nanocomposite</b> . . . . .	419
Tammareddy Haritha, Koonam Ramji, Killi Krushna Murthy, Puppala Siva Nagasree and Dukkupati Bala Nagesh	
<b>An Experimental Investigation of New Hybrid Composite Material Using Ramie-Flax and Its Mechanical Properties Through Finite Element Method</b> . . . . .	431
Dara Ashok, Sukumar Puhana, Raghuram Pradhan, P. Kiran Babu and Y. Srinivasa Reddy	
<b>Effect of MgO Particulates on Dry Sliding Wear of Al LM13 Metal Matrix Composite</b> . . . . .	447
C. S. Ravindra Sagar, T. K. Chandrashekar and Batluri Tilak Chandra	
<b>Flexural Fracture Analysis on 2D and 3D Weaved Carbon–Silicon Carbide Composites</b> . . . . .	455
S. Sapthagiri and S. Nagakalyan	
<b>Characterization of Aluminium Alloy 6063 Coated Over Mild Steel by Aluminization Process</b> . . . . .	469
B. Vijaya Kumar and K. John William	
<b>Investigation of Mechanical and Wear Characteristics of Aluminum Reinforced with Quartz Composites</b> . . . . .	479
T. Thirumalai, A. Harsha Vardhan Reddy, S. Nagakalyan and Rajagopal Dhanasekaran	

**Studies on Application and Mechanism of Self-Healing Polymer and Nanocomposite Materials** . . . . . 487  
 S. Sreenatha Reddy, Rajagopal Dhanasekaran, Sujeet Kumar, Shiv Shankar Kanwar, R. Shruthi and T. Navaneetha

**Comparing Fire Penetration Results of Natural Fibre Reinforced Composite Material with Plywood** . . . . . 499  
 Rajagopal Dhanasekaran, S. Sreenatha Reddy, Anwar Pasha, Akula Deep Chander, Asar Fayaz Baig and T. Thirumalai

**Microstructural Evaluation of Friction Surfaced Aluminium Alloy AA6063 Over Mild Steel** . . . . . 511  
 B. Vijaya Kumar

**Mechanical Properties of Coconut–Carbon Fiber Reinforced Hybrid Composites** . . . . . 519  
 Nampally Yadagiri, B. Naresh, B. Phanindra and P. Varalaxmi

**Frequency Analysis of Aircraft Wing Using FEM** . . . . . 527  
 Akhil Basutkar, Kunal Baruah and Shashidhar K. Kudari

**Structural and Vibrational Analysis of Femur Bone Using FEA** . . . . . 535  
 Sonu Kumar Kharatmal, Pranav Ravindrannair, Karthik Sridhar, Mir Akber Mohsin Ali and V. Rajashekhar

**CFD Analysis, Analytical Solution, and Experimental Verification for Design and Analysis of Air Intake of Formula Student Car** . . . . . 553  
 S. Vivek, Rabi Pathak and Rishabh Singh

**Noncontact Surface Roughness Assessment Using Machine Vision System** . . . . . 567  
 Dhiren Patel, Kiran Mysore and Kartikkumar Thakkar

**Optimization of Brake Pedal for FSAE Vehicle** . . . . . 579  
 Kaustubh Babrekar, Saurabh Bairagi, Jatin Parajiya and Nitin G. Phafat

**Design and Analysis of Steering Clevis Joint for Optimization and Steering Stability** . . . . . 587  
 Aniket Sawant, Dhananjay Patil, Vedashri Joshi, Amit Trisal and Arvind Chel

**Modeling and Structural Analysis of Suspension Rocker for FSAE Vehicle** . . . . . 599  
 Saurabh Bairagi, Jatin Parajiya, Kaustubh Babrekar and Nitin G. Phafat

**Control of End-Effector of a Multi-link Robot with Joint and Link Flexibility** . . . . . 611  
 E. Madhusudan Raju, L. Siva Rama Krishna and Mohamed Abbas

<b>Design of Plastic Bottle Shredding Machine and Computational Finite Element Analysis of Shaft in the Shredder</b> . . . . .	625
Aluka Dheeraj Reddy, G. V. Niharika and G. Srinivas Sharma	
<b>Effect of Temperature on Stress Concentration Factor</b> . . . . .	641
Jajula Satish, Shubhashis Sanyal and Shubhankar Bhowmick	
<b>Experimental and Finite Element Analysis of Fracture Parameters of woven Glass/Epoxy Composite</b> . . . . .	649
Venkata Sushma Chinta, P. Ravinder Reddy, Koorapati Eshwara Prasad and B. Venkata Sai Kiran	
<b>Automatic Gate System with Autofocus Camera Using Node-RED</b> . . . . .	661
Basavaraj Talikoti, Ruchira Patole, Amit Pradhan, Allen Thomas, Evin Poullose and Shubham Mane	
<b>CFD Analysis of Hydro-Dynamic Lubrication Journal Bearing Using Castor Oil</b> . . . . .	671
N. Udgire Manojkumar, H. Jagadish and B. Kirankumar	
<b>To Evaluate Chassis Frequency Harmonics of Vehicles by Modal Analysis and Measurement</b> . . . . .	685
Nilesh Ahirrao and Santosh Bhosle	
<b>Analysis of Internal Damping in Rotating Shaft</b> . . . . .	695
K. Raju, M. Ravindra Gandhi, Rajasekhar Vangala and N. Suresh	
<b>An Overview of Harmony Search Algorithm Applied in Identical Parallel Machine Scheduling</b> . . . . .	709
P. Sreenivas, Shaik Khaja Peer Saheb and M. Yohan	
<b>Computational Investigation of Stagnation-Region Gas Injection for Protection of a Locally Heated Skin</b> . . . . .	715
Tulasi Tirupati and B. S. Subhash Chandran	
<b>Techno-Economic Assessment of Wind/Photovoltaic and Conventional Generator Hybrid Off-Grid Power Systems for Rural Community in Meta Robi District</b> . . . . .	723
Kante Mallikarjuna Rao, Robera Daba Bededa, B. Somanath, L. Ranganath and Basam Koteswararao	
<b>Assessment of Unconventional and Conventional Off-Grid Power Source for Rural Areas in Ethiopia</b> . . . . .	737
Yakkala M. K. Raghunadh, M. Chakrapani, Robera Daba Bededa, P. Vijay and G. Bheemanna	
<b>A Review on Advanced Optimization Algorithms in Multidisciplinary Applications</b> . . . . .	745
M. Sreedhar, S. Akshay Navaneeth Reddy, S. Abhay Chakra, T. Sandeep Kumar, S. Sreenatha Reddy and B. Vijaya Kumar	

## About the Editors

**Dr. G. S. V. L. Narasimham** is a Chief Research Scientist in the Department of Mechanical Engineering, Indian Institute of Science (IISc), Bangalore. He received his M. Tech. from IIT Madras and his Ph.D. from IISc Bangalore, both in Mechanical Engineering. His research interests include solar thermal engineering, HVAC, refrigeration, cryogenics, heat and mass transfer, CFD, and simulation of thermal systems. He has almost three decades of experience in teaching, academic and sponsored research and guiding masters and research students. He worked as an investigator in the projects sponsored by the departments of non-conventional energy sources, atomic energy, space, power, science and technology and planning commission, as well as industrial research projects sponsored by IMI, GE, Mahindra and Mahindra. He also works as a consultant from IISc for various organizations and is a Life Member of professional bodies related to heat and mass transfer and cryogenics.

**Dr. A. Veeresh Babu** received his B.Tech in Mechanical Engineering and M.Tech. in Heat Power Refrigeration from JNTU, Andhra Pradesh in 1998 and 2000, respectively. He obtained his Ph.D. from Andhra University in 2013. He worked in refrigerator design, clean room technology, cold room/freezer room design and construction while he was associated with the Industry. He erected and commissioned clean rooms at DRDE, Gwalior, RCI, Hyderabad and CRDI, Lucknow. He has a research experience of more than 12 years since he joined NIT Warangal as an Assistant Professor in the year 2006. Currently, he is Associate Professor in the Mechanical Engineering department at NIT Warangal. He has published more than 15 papers in peer-reviewed journals. He has also presented his research in 10 international conferences. He has completed two minor research projects and two major projects are under review. He was also appointed as a course writer for certificate in Power Plant Engineering offered by IGNOU, India.

**Dr. S. Sreenatha Reddy** presently is working as Principal and Professor at Guru Nanak Institute of Technology under JNTUH, Hyderabad. He obtained his B. Tech. (Mechanical Engineering), M. Tech. and Ph.D. from JNTUA. He held various

administrative posts and developed the Institution with his projects and activities. He has received several awards like the National award for best research publication i.e. Jawaharlal Nehru memorial prize issued by Institution of Engineers on the occasion of inauguration 27th Indian Engineering Congress at New Delhi in 2012 and “Bharat Vidya Shiromani Award” and a “Certificate of Education Excellence” for Outstanding Achievements in the field of Education given by International Institute of Education & Management on 22nd December 2014 at New Delhi & Glory of Education of Excellence Award is issued by IIEEM on 4th March 2015 at New Delhi. He received the Best Academic Administrator award from Centre for Advanced Research and Design under Venus International Foundation on 5th July, 2015. He also received National Award as Eminent Educationists issued by the INDUS FOUNDATION on the occasion of Indo-American Education Summit 2016 at Hyderabad. He has an experience of almost 20 years teaching in Mechanical and Aeronautical areas and spent 3 years in the industry in thermal power plants. He has published 141 papers in reputed journals and 26 papers in international and national conferences. He also served as Expert Committee Member of AICTE for scrutinizing project reports, and as a member in the Board of Reviewers for the Institution of Engineers journal.

**Dr. Rajagopal Dhanasekaran** received his BE in Mechanical and Production Engineering from the Annamalai University in 2002, M.E, and Ph.D. from the Department of Mechanical Engineering, Anna University in 2007 and 2013, respectively. He has been working as a Professor in Mechanical Engineering, Guru Nanak Institute of Technology, Hyderabad, India since November 2015. He published more than 40 research papers and 7 patent publications. He is a member of ISTE and Tribology Society of India. His major research interests include Tribology, Engineering Failure, Wear Characterization and Production Engineering.

# Analysis Over Trio-Tube with Dual Thermal Communication Surface Heat Exchanger [T.T.H.Xr.]



Devendra Yadav, Zenis Upadhyay, Akhilesh Kushwaha and Anuj Mishra

**Abstract** The thermal performance of the trio tube with a dual thermal communication surface heat exchanger (T.T.H. Xr) is analyzed experimentally under the steady-state conditions. Water was used as a working fluid which was available at three different inlet temperatures of cold (C), hot (H), and normal (N). The performance of T.T.H. Xr was compared for the three different flow arrangements of C–H–N, C–H–C, and N–H–C at counter-current flow. The pipes were made of aluminum (inner tube 12.7 mm), copper (intermediate tube 25.4 mm), and GI tube (outer tube 38.1 mm), all pipes having a thickness of 1.5 mm. N–H–C and C–H–C flow arrangements show better heat transfer results compared to C–H–N. The results from experiments were also verified numerically by using the derived equations. A case study was also performed on the results obtained from T.T.H.Xr to compare its performance with the double-tube heat exchanger on the same parameters. It was observed that the pipe length for T.T.H.Xr reduced by ~58.39% compared to the double-tube heat exchanger to extract the same amount of heat transfer from the hot fluid.

**Keywords** Concentric tube · LMTD · Overall heat transfer coefficient · Effectiveness

---

D. Yadav (✉) · Z. Upadhyay · A. Kushwaha · A. Mishra  
Department of Mechanical Engineering, Axis Institute of Technology and Management, Kanpur,  
India  
e-mail: [ydevendra393@gmail.com](mailto:ydevendra393@gmail.com)

Z. Upadhyay  
e-mail: [zenisbharadwaj@gmail.com](mailto:zenisbharadwaj@gmail.com)

A. Kushwaha  
e-mail: [akhileshkushwahame123@gmail.com](mailto:akhileshkushwahame123@gmail.com)

A. Mishra  
e-mail: [anujmishra1098@gmail.com](mailto:anujmishra1098@gmail.com)

## List of Symbols

$C$	Cold fluid
$\rho$	Density ( $\text{kg/m}^3$ )
$d$	Diameter (m)
$\mu$	Dynamic viscosity ( $\text{N}\cdot\text{s/m}^2$ )
$Q$	Heat transfer (W)
$h$	Heat transfer coefficient ( $\text{W/m}^2\text{K}$ )
$H$	Hot fluid
$i$	Inner
$\dot{m}$	Mass flow rate (kg/s)
$N$	Normal fluid
$Nu$	Nusselt number
$o$	Outer
$U$	Overall heat transfer coefficient ( $\text{W/m}^2\text{K}$ )
$Pr$	Prandtl number
$Re$	Reynolds number
$C_p$	Specific heat ( $\text{kJ/kgK}$ )
$t$	Temperature ( $^{\circ}\text{C}$ )
$k$	Thermal conductivity ( $\text{W/mK}$ )
$v$	Velocity (m/s)
$V$	Volume flow rate ( $\text{m}^3/\text{s}$ )

## 1 Introduction

The heat exchanger is the device which facilitates the transfer of thermal energy from the fluid available at a higher temperature to the fluid at a lower temperature. It could be found in each and every field whether it is residential or industrial resources. There are many heat exchangers which are already in use for the different applications, and all perform in a similar manner. The important and useful implementations that come under the context of “heat exchanger” are the production of thermal power, waste heat recovery, air conditioning, refrigeration, and the food preserving purpose [1] by evaporation, pasteurization, etc. The trio-tube heat exchanger (TTH Xr) is insulated at the outer tube, thus, having only two thermal communicating surfaces for the analysis [2]. If it was contemplated to be uninsulated, there would be three communicating surfaces with different performances and having a surrounding air at ambient temperature as the fourth fluid. The double concentric-tube heat exchanger was the prior arrangement that did not have a complicated overall heat transfer coefficient but did not have that much of effectiveness [3], so later on introducing an intermediate tube to the former arrangement and eventually showed a better performance. Pătrășcioiu & Rădulescu [4] analyzed some model by utilizing the elaborated set of equations for different inlet temperatures and mass flow rate condition. The heat

exchangers are mainly categorized on the basis of the fluid flow direction and on the basis of their thermal contact. Heat exchangers could be multiphase; generally, they are stationary and known as “recuperators”. On the performance evaluation of different heat exchangers (direct and indirect contact), many researchers have participated in and got the results accordingly. Unal et al. [2] found that the T.T.H.Xr has a better efficiency over the double-tube heat exchanger. An active simulation and modeling of an ordered counter-flow heat exchanger over startup and frequency response was carried out by Lakshmanan and Potter [5]. The triple concentric-tube heat exchanger design and analysis with fins were studied by Rajasekar and Palanisamy [6]; in his study, milk was considered for the helical triple tube heat exchanger. It was observed that the ultrahigh temperature in sterilization process fluid being gets its temperature and raised from 90 to 150 °C and hence the minerals and proteins get accumulated on the surface of the heat exchanger, which causes the fouling in the helical triple tube heat exchanger. Due to this fouling, the conduction resistance increases and hence it prevents the heat transfer [7]. For the prognostication of the effectiveness of heat exchanger, the fluid temperature of a microchannel operating with laminar flow conditions can be predicted by some derived equations, with which, the heat transfer between fluids could be determined. The study elaborates that the effectiveness of heat exchanger for the fluids available at a different temperature always increases but the superficial heating always decreases for the specified NTU [8].

Further, the researchers have to know that for triple concentric-tube heat exchanger parameters which affect the performance must be relative in sizes, mass flow rate and material of tube [9]. The swirl generator has been used in the double concentric-tube heat exchangers for the heat transfer enhancement which was carried out by positioning the holes in different ways and later it was constituted that the heat transfer was enhanced by 130% [10]. Counterfeit was done numerically by Garcia-Valladares [11]. The numerical investigation of the performance of triple-tube heat exchanger was given by Qadir [12]. The overall calculation procedure for the transient behavior of the tubular heat exchanger was accomplished by Patankar [13]. The evaluation of transient turbulent heat transfer in an annulus was carried out by Kawamura [14].

In this experimental study, countercurrent flow and indirect contact type triple concentric heat exchanger is considered with the pipes of different materials. The outermost pipe was of GI, pipe in the middle was of copper having high thermal conductivity, and the last pipe was of aluminum (innermost). Fluids with three different temperatures of C-cold, H-hot, and N-normal were available for the thermal energy interaction. The comparative analyses between the different flow arrangements of C–H–N, N–H–C, and C–H–C were carried out. The case which found more effectiveness was N–H–C and C–H–C. Moreover, experiments that have been conducted here on trio-tube heat exchanger, have an objective to reduce surface area and material cost. For trio-tube heat exchanger, the length was reduced by 58.39% for extracting the same amount of heat transfer as from the double-pipe heat exchanger. So, the arrangement of the triple concentric-tube conquers over the double-tube heat exchanger.

J-type of thermocouples are used in order to analyze the temperature-dependent voltage and the voltage so produced elucidates the temperature at a point and the



transient retaliation is presented so that the flow rate that pertains to the internal fluid could determine the variation in temperature. The mass flow rate of the fluids was measured with the help of rotameters fitted at both the ends of an arrangement and pumps are used to move the fluid in the required direction.

## 2 Experimental Details

To appraise the performance of the dual thermal communication in the trio-tube heat exchanger, an experimental setup was invented. With the help of the setup, numerical results were acquired. In the setup, three different types of tubes were used, aluminum, copper, and galvanized iron. The inner diameter of GI shell was 38.1 mm, further, the copper pipe had 25.4 mm and Al pipe had 12.7 mm inner diameter; thickness was the same for each pipe, i.e., 15 mm; effective length of the pipe was 2.2 m. The outermost tube of galvanized iron was swathed by insulation to resist the thermal contact with the surrounding. To realize the temperature of the water in various points, J-type thermocouples were placed in different positions along the effective length. For obtaining high temperature, an immersion heater of capacity 2000 W was immersed in the water tank. In the setup, three centrifugal pumps were employed for pumping of water at a different mass flow rate. The controlling valve was located on the entry and exit of the tube for controlling the mass flow rate of fluids. This setup can be operated in different arrangement of flows, i.e. CHC, CHN, and NHC. The complete experimental setup has been shown in Fig. 1.



**Fig. 1** Experimental setup of trio-tube heat exchanger

### 3 Methodology

In order to characterize the pipe arrangement in the trio-tube heat exchanger, a solid model was designed on SOLIDWORKS 2013. This experimental setup was made on the basis of this model. Figure 2 shows only half part of the setup, and the rest of the parts will be arranged accordingly.

The theoretical analysis of the triple concentric-tube heat exchanger was carried out by Hossain et al. [15]. For insulated trio-tube heat exchanger, the heat transfer takes place among two thermal communicating surfaces as shown in Fig. 3, which then satisfies performance evaluation of the experimental setup. In this study, performance of T.T.H.Xr evaluated by the LMTD method and all parameters are given step by step (Eqs. 1–15); those are used in the triple concentric-tube heat exchanger.

For steady-state condition, the energy lost by the hot fluid (fluid 2) is the sum of energy gained by the other two fluids (fluid 1 and 3)

$$\dot{Q}_2 = \dot{Q}_1 + \dot{Q}_3 \tag{1}$$

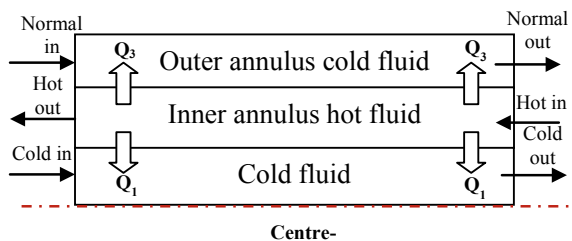
All the fluid properties were calculated at the average bulk mean temperature of the flowing liquid. The velocity was determined from the mass flow rate:

$$Re = \frac{\rho v d}{\mu} \tag{2}$$

**Fig. 2** 3D model of the trio-tube arrangement



**Fig. 3** The flow direction of the fluids in C–H–C configuration of the trio-tube heat exchanger



The Reynolds number may be different for all the fluids and Nusselt number (Nu) depend on the Re and Pr number. If the flow is laminar ( $Re < 2300$ ), then the Nusselt number is

$$Nu = 0.51 \times Re^{0.5} \times Pr^{1/3} \times \left( \frac{Pr}{Pr_s} \right)^{0.25} \quad (3)$$

If the flowing fluid is similar, then the value of  $(Pr/Pr_s)^{0.25}$  is considered as “1”.

If Reynolds number is in the range of 2300–4000, i.e., transition region, then the Nusselt number will be

$$Nu = 2.718 \times Re^{0.597} \times Pr^{1/3} \times \left( \frac{d}{1.193} \right)^{2/3} \quad (4)$$

The convective heat transfer coefficient of the heat exchanger can be obtained from Eq. (5).

For the inner cold fluid,

$$h_1 = \frac{Nu_1 k_1}{d_{in}} \quad (5)$$

For the hot fluid flowing through the intermediate region of the heat exchanger,

$$h_2 = \frac{Nu_2 k_2}{(d_{i2} - d_{o1})} \quad (6)$$

For the outer cold fluid,

$$h_3 = \frac{Nu_3 K_3}{(d_{i3} - d_{o2})} \quad (7)$$

For T.T.H.Xr, two equations for the overall heat transfer coefficient will be obtained. One equation from the inner (fluid 1) and intermediate (hot fluid 2) pipe, and another equation from the intermediate (hot fluid 2) and the outer pipe (fluid 3).

$$\frac{1}{U_{o1}} = \frac{d_{o1}}{d_{i1} h_{c1}} + \frac{d_{o1} \ln(d_{o1}/d_{i1})}{2k_{centre}} + \frac{1}{h_H} \quad (8)$$

$$\frac{1}{U_{i2}} = \frac{d_{i2}}{d_{o2} h_{c2}} + \frac{d_{i2} \ln\left(\frac{d_{o2}}{d_{i2}}\right)}{2K_{centre}} + \frac{1}{h_H} \quad (9)$$

There will be three equations in T.T.H.Xr for different fluids in a different region,

$$\dot{Q}_1 = \dot{m}_1 \times C_{p1} \times (t_{1e} - t_{1i}) \quad (10)$$

$$\dot{Q}_3 = \dot{m}_3 \times C_{p3} \times (t_{3e} - t_{3i}) \quad (11)$$

The heat transfer rate for hot fluid will be

$$\dot{Q}_2 = \dot{m}_2 \times C_{p2} \times (t_{2i} - t_{2e}) \quad (12)$$

The length of the triple tube concentric-tube heat exchanger can be obtained by Eq. (13)

$$\dot{m} \times C_{pH} \times (t_{Hi} - t_{He}) = U_{o1}A_{o1}\text{lmt}d_1 + U_{i2}A_{i2}\text{lmt}d_2 \quad (13)$$

where  $A_{o1} = \pi d_{o1}$  and  $A_{i2} = \pi d_{i2}$ .

The final equations for logarithmic mean temperature difference (LMTD) are given as

$$\text{lmt}d_1 = \frac{(t_{2i} - t_{1e}) - (t_{2e} - t_{1i})}{\ln(t_{2i} - t_{1e}/t_{2e} - t_{1i})} \quad (14)$$

$$\text{lmt}d_2 = \frac{(t_{2i} - t_{3e}) - (t_{2e} - t_{3i})}{\ln(t_{2i} - t_{3e}/t_{2e} - t_{3i})} \quad (15)$$

## 4 Result and Discussion

In this experimental analysis over the trio-tube heat exchanger, the temperature variation of the fluid along the flow direction was analyzed. The study has been carried over the various parameters (flow arrangement, volume flow rate, and inlet temperature of the fluid). Three arrangements of all three fluids have been taken for the analysis. The first arrangement was C–H–C, which means that the cold water flows through the innermost and outermost annulus, and hot water through the inner annulus. Another arrangement was the N–H–C, which means that the normal water flows through innermost tube, hot water through the inner annulus, and the cold water through the outermost annulus. The third arrangement was the C–H–N, in which the cold water is flowing through the innermost tube, hot water through the inner annulus, and normal water through the outer annulus. Hot water is always taken in the inner annulus in all arrangements. The outer pipe was insulated; therefore there was no energy interaction with the environment. Each fluid stream flows in a counter flow manner with respect to the adjacent fluid. Therefore, the result can be obtained for the maximum heat transfer for all three arrangements. It is difficult to discuss every result from the experiment, therefore, a few results from each flow arrangement have been taken for discussion.

In case of the C–H–C arrangement, if the mass flow rate of the fluid is different for different fluids, i.e.,  $M_H = 0.041$  kg/s,  $M_{c1} = 0.065$  kg/s and  $M_{c2} = 0.020$  kg/s,

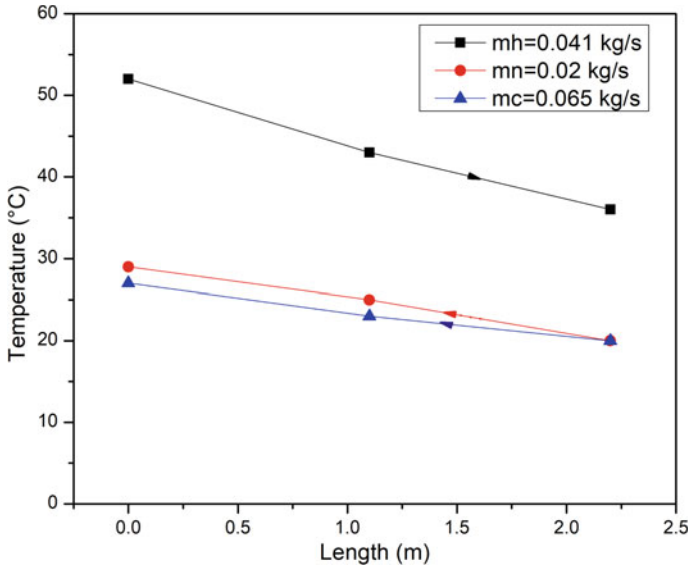


**Fig. 4** Temperature variation along the length of tube: CHC

and the inlet temperature is  $T_H = 52$  °C and  $T_{C1} = T_{C2} = 20$  °C, then the exit temperatures are  $T_H = 36$  °C and  $T_{c1} = 26$  °C and  $T_{c2} = 29$  °C, respectively, as shown in Fig. 4.

From the observation, it was found that, for different volume flow rates, the outlet temperature is different for both cold fluids due to the difference in mass flow rate and heat transfer area. When the volume low rate is same for all fluids, i.e.,  $V_{c1} = V_H = V_{c2} = 30$  l/min, the hot water temperature at the inlet is 60 °C, and cold water temperature is the same for both, i.e., 20 °C, the hot water temperature slightly decreases and cold water temperature is increased. At the exit, the temperature of hot water and cold water was 42 °C, 34 °C, and 35 °C, respectively. If the volume flow rate of the hot water is more than that of the cold water, i.e.,  $V_h = 30$  l/min. and  $V_{c1} = V_{c2} = 20$  l/min., and the temperature is 60 °C and 20 °C, then the exit temperatures were 36 °C, 38 °C, and 37 °C, respectively.

In the case of the N–H–C arrangement, when the mass flow rate of all fluids is different, i.e.,  $M_H = 0.011$  kg/s,  $M_c = 0.00575$  kg/s, and  $M_N = 0.021$  kg/s, the inlet temperature of the fluids are  $T_H = 51$  °C,  $T_N = 23$  °C, and  $T_C = 10$  °C, respectively. In this case, the temperature of the hot fluid slightly decreases to 35 °C and normal and cold water temperatures are increased to 40 °C and 25 °C respectively due to the heat exchange by the hot fluid. The difference between the hot water and cold water temperature was more as compared to that of the hot and normal water. In this case, the exit temperature of hot water is lower than the normal water temperature due to too much heat transfer between cold and the hot fluid as shown in Fig. 5.

If the volume flow rate of the hot fluid is reduced compared to the normal and cold fluids, i.e.,  $V_H = 20$  l/min. and  $V_N = V_c = 30$  l/min., then the hot fluid temperature

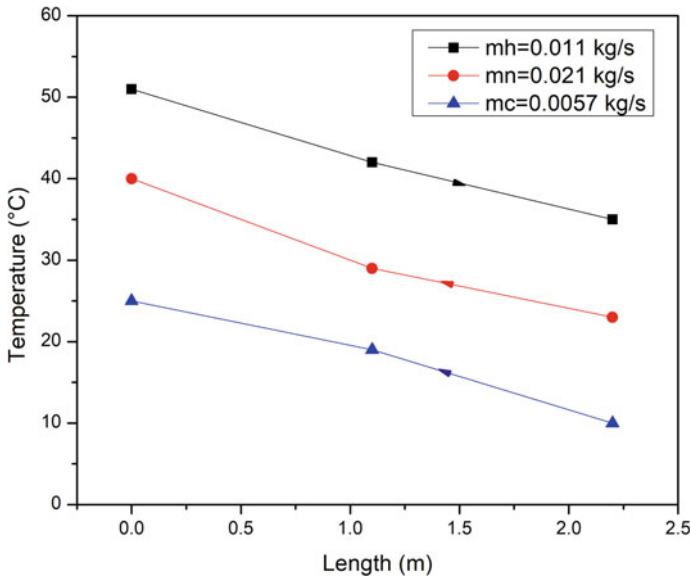


**Fig. 5** Temperature variation along the length of tube: NHC

drops from 52 °C to 39 °C, the normal water temperature increases from 28 °C to 31 °C, and the temperature of the cold water increases from 10 °C to the 28 °C, respectively. Due to the reduction in the volume flow rate of the hot water, the increment in the temperature of the normal and cold water was less compared to the case where the volume flow rate was the same for both the fluids. If the volume flow rate of all fluids is the same, i.e.,  $V_H = V_{c1} = V_{c2} = 35$  l/min. and the inlet temperature of the fluids is  $T_{ni} = 28$  °C,  $T_{hi} = 55$  °C, and  $T_{ci} = 10$  °C, respectively, the temperature of the hot fluid is slightly reduced to 30 °C. The normal and cold water temperature increased to 34 °C and 20 °C respectively due to the heat exchange by the hot fluid. On the basis of the experimental detail, temperature of the cold water increases as compared to the normal water due to the higher temperature difference between the hot water and cold water compared to that of the hot and normal water. In this condition, the exit temperature of the hot water was lower than the normal water temperature due to the very large amount of heat transfer between cold by the hot fluid.

In the case of the C–H–N arrangement, it was similar to all the above processes. When the volume flow rates for all the fluid wax are the same, i.e.,  $V_C = V_H = V_N = 30$  l/min and the inlet temperature of the hot fluid, normal fluid, and cold fluid were 52 °C, 28 °C, and 10 °C respectively, the hot water temperature dropped to 33 °C, the normal water temperature increased to 32 °C, and cold water to 17 °C, respectively. If the mass flow rate for all fluids is different, i.e.,  $M_C = 0.017$  kg/s,  $M_H = 0.028$  kg/s, and  $M_N = 0.057$  kg/s and the inlet temperature of cold, hot, and normal water temperature is 17 °C, 48 °C, and 26 °C, respectively, the exit temperature of

the cold water was 28 °C, hot water exit temperature dropped to 38 °C, and normal water temperature increased to 31 °C as shown in Fig. 6. In this case, it was analyzed that the cold temperature was far from the hot water and normal water temperatures. From this study, it was found that the heat transfer from the hot to cold water is less compared to that of the N–H–C or C–H–C flow arrangement.

In this study, fluid flow with the laminar condition was taken due to the small flow rate of the fluid, except some increase mass flow rate case of hot fluid. The Nusselt number depends upon the Reynolds number of the fluid flow. The overall heat transfer depends on the effective length of the heat exchanger. The results from all three flow arrangements which were discussed earlier were taken to calculate the effectiveness. Details of experimental results have been given in Tables 1, 2 and 3;

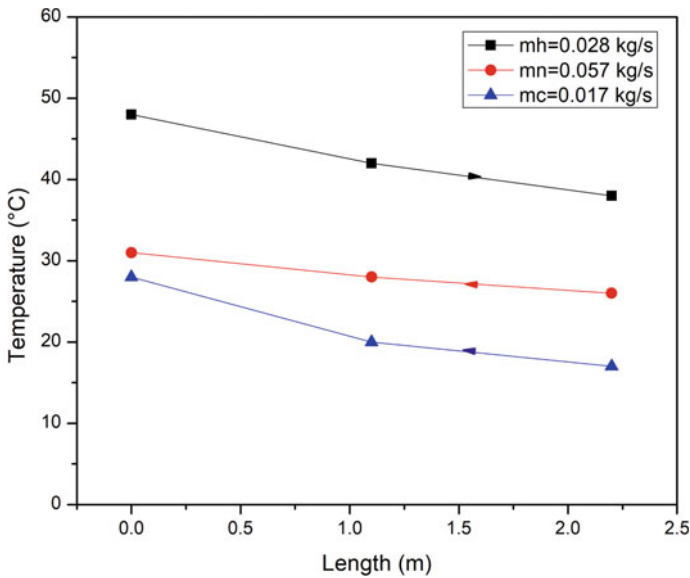


**Fig. 6** Temperature variation along the length of tube: CHN

**Table 1** Experimental results for trio-tube HXr: NHC flow arrangement

Parameters	Normal (N)	Hot (H)	Cold (C)
$\dot{m}$ (kg/s)	0.021	0.011	0.00575
$v$ (m/s)	0.067	0.021	0.045
Re	685.36	362.02	439.48
Nu	24.99	14.59	22.6
$U$	$U_{01} = 488.02$		$U_{02} = 611.99$
LMTD	LMTD ( $i - m$ ) 15.7°C		LMTD ( $m - o$ ) 15 °C
Effectiveness	0.8745		

**Table 2** Experimental results for trio-tube HXr: CHC flow arrangement

Parameters	Cold (C)	Hot (H)	Cold (C)
$\dot{m}$ (kg/s)	0.065	0.041	0.02052
$v$ (m/s)	0.5146	0.132	0.04062
Re	6503.1	2429.06	386.53
Nu	52.77	17.21	19.18
$U$	$U_{01} = 1354.4$		$U_{02} = 862.06$
LMTD	LMTD ( $i - m$ ) = 20.59 °C		LMTD ( $m - o$ ) = 19.28 °C
Effectiveness	0.3212		

**Table 3** Experimental results for trio-tube HXr: CHN flow arrangement

Parameters	Cold (C)	Hot (H)	Normal (N)
$\dot{m}$ (kg/s)	0.017	0.028	0.057
$v$ (m/s)	0.134	0.09	0.1128
Re	1589.194	1512.07	1218.85
Nu	39.87	30.64	32.88
$U$	$U_{01} = 860.58$	$U_{02} = 1072.04$	
LMTD	LMTD ( $i - m$ ) = 20.49 °C		LMTD ( $m - o$ ) = 14 °C
Effectiveness	0.2936		

for calculation of the LMTD and overall heat transfer coefficient, the trio-tube was divided into the first part from the center to the middle annular space of the hot stream and the second from the middle annular space to the outer annular. Therefore, the two LMTD and overall heat transfer coefficient.

The performance of T.T.H.Xr was compared with the theoretical performance from the double-pipe heat exchanger as shown in Fig. 7.

For the double-pipe heat exchanger, theoretical analysis was performed by considering the normal and cold fluid average temperature as the cold fluid inlet temperature, and mass flow rate as the sum of both the fluids. In order to determine the reduced length of the heat exchanger in T.T.H.Xr, a comparison was made on the basis of calculating the same amount of heat transfer from both the heat exchangers. The outcomes from the analytical study on double-pipe heat exchanger are shown in Table 4.



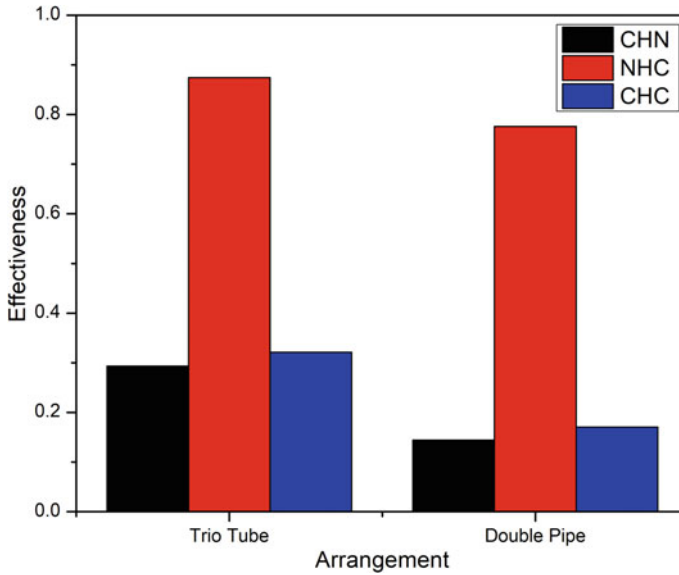


**Fig. 7** Performance comparison between trio-tube and double-pipe heat exchanger

**Table 4** Experimental results for double-pipe heat exchanger

Arrangement	NHC	CHC	CHN
LMTD (°C)	13.18	18.82	11.49
Effectiveness	0.7762	0.1706	0.1445
% save length in T.T.H.Xr (%)	58.39	58.39	58.32

## 5 Conclusion

An experimental study on the trio-tube heat exchanger was conducted with water as the working fluid available at three different temperatures. The following conclusion can be made from this study:

- Based on the arrangement of the fluid flow, NHC gives the maximum effectiveness, followed by CHC and CHN arrangements (Tables 1, 2 and 3). The CHN with the least performance was compared to the other two arrangements.
- With the increased mass flow rate, the amount of heat transfer increases.
- The experimental results manifest good agreement with the theoretical results on the same parameters with a 5% error.
- For the same amount of heat transfer rate, the length required in the trio-tube heat exchanger reduced by  $\approx 58\%$  in comparison to the double-pipe heat exchanger.
- The reduced length was independent of the fluid flow arrangement.

## References

1. Zuritz CA (1989) On the design of triple concentric-tube heat exchangers. *J Food Process Eng* 12(2):113–130
2. Unal A (2001) Theoretical analysis of triple concentric tube heat exchangers part 2. Case studies. *Int Community Heat Mass Transf* 28(2):243–256
3. Batmaz E, Sandeep KP (2005) Calculation of overall heat transfer coefficients of a triple tube heat exchanger. *Heat Mass Transf* 41:271–279
4. Pătrăşcioiu C, Rădulescu S (2015) prediction of the outlet temperatures in triple concentric-tube heat exchangers in laminar flow regime. Case study. *Heat Mass Transf* 51(1):59–66
5. Lakshmanan CC, Potter OE (1994) Dynamic simulation of a countercurrent heat exchanger modelling start up and frequency response. *Int Commun Heat Mass Transf* 21(3):421–434
6. Rajasekar K, Palanisamy S (1934) Design and analysis of triple tube heat exchangers with fins. *IOSR Journal of Mechanical and Civil Engineering*, 01–05
7. Nema PK, Datta A (2006) Improved milk fouling simulation in a helical triple tube heat exchanger. *Int J Heat Mass Transf* 49:3360–3370
8. Mathew B, Hegab H (2010) Application of effectiveness NTU relationship to parallel flow microchannel heat exchangers subjected to external heat transfer. *Int J Therm Sci* 49:76–85
9. Ghiwala TM, Matawala VK (2014) Sizing of triple concentric heat exchanger. *Int J Eng Develop Res* 2(2):1683–1692
10. Akpınar EK, Yildiz C (2004) Heat transfer enhancements in a concentric double pipe exchanger equipped with swirl elements. *Int Commun Heat Mass Transf* 31(6):857–868
11. Garcia-Valladares O (2004) Numerical simulation of triple tube heat exchanger. *Int J Therm Sci* 43(10):979–991
12. Quadir GA, Jarallah SS, Salman Ahmed NJ, Badruddin IA (2013) Experimental investigation of the performance of a triple tube concentric pipe heat exchanger. *Int J Heat Mass Transf* 62:562–566
13. Patankar SV, Spalding DB (1974) A calculation procedure for the transient and steady state behaviour of shell and tube heat exchanger. In: *Heat exchangers, design and theory sourcebook*. Scripta Book Company, Washington, DC
14. Kawamura H (1977) Experimental and analytical study of transient heat transfer for a turbulent flow in a circular tube. *Int J Heat Mass Transf* 20(5):443–450
15. Hossain A, Uddin Md., Hossen R, Afroz HMM (2017) Experimental analysis of a triple concentric tube heat exchanger. *Int J Mod Stud Mech Eng* 3(3):1–10

# An Experimental Study of Performance and Emission Characteristics of a Diesel Engine Fueled with Palm Kernel Methyl Ester with Ethanol Additive: A Fuzzy-Based Optimization Approach



Siddhartha Das, Bijoy Kumar Deb and G. R. K. Sastry

**Abstract** Researches on alternate fuels have been gaining the attention of researchers worldwide due to the energy crisis. The fossil fuel sources which are used as the most important resource of energy at present are not enough to meet the increasing energy demand. The whole world is now searching for renewable energy sources. Biodiesel reduces the emission of harmful gases to the environment. Biodiesel was produced from the palm kernel oil using transesterification process. In the present experiment, the engine was fueled with diesel and blends containing 5, 10, and 15% of palm kernel methyl ester. The developed Multi-Input Multi-Output (MIMO) fuzzy model predictions show the correlation coefficients in the range 0.908–0.998 for B15 as it has given a better performance and emission than other blends.

**Keywords** Palm kernel methyl ester · Performance · Emission · Optimization · MIMO fuzzy model

## 1 Introduction

Energy is one of the main important inputs for the development of all quarters including agricultural and industrial services and transport sectors. Energy has been at the pivotal point of national and global economic growth for several decades [1]. The

---

S. Das

Department of Automobile Engineering, Tripura Institute of Technology, Agartala, Tripura, India  
e-mail: [sidas\\_007@rediffmail.com](mailto:sidas_007@rediffmail.com)

B. K. Deb (✉)

Department of Mechanical Engineering, Tripura Institute of Technology, Agartala, Tripura, India  
e-mail: [bijoykrdb@gmail.com](mailto:bijoykrdb@gmail.com)

G. R. K. Sastry

Department of Mechanical Engineering, National Institute of Technology, Tadepalligudem, Andhra Pradesh, India  
e-mail: [grksastry@nitandra.ac.in](mailto:grksastry@nitandra.ac.in)

© Springer Nature Singapore Pte Ltd. 2020

G. S. V. L. Narasimham et al. (eds.), *Recent Trends in Mechanical Engineering*,  
Lecture Notes in Mechanical Engineering,  
[https://doi.org/10.1007/978-981-15-1124-0\\_2](https://doi.org/10.1007/978-981-15-1124-0_2)

demand for energy is rising exponentially, predominantly the demand for fossil fuel-based energy. Petroleum-derived fuels, actually, surpass the demand for any other fuels or energy resources. The world consumption for oil will increase from 85 million barrels/day in 2006 to 107 million barrels/day in 2030 [2–4]. Under these development conjectures, around half of the world's collective property would be depleted by 2030. Also, as per many studies, world oil production would hit the highest point sometime between 2007 and 2030. Therefore, future energy accessibility is a serious universal concern. One more, chief global concern is ecological degradation or climate change such as global warming. Global warming is related to greenhouse gases which are mostly emitted from the burning of petroleum fuels. In order to manage the discharge of greenhouse gases, Kyoto Protocol targets to reduce the greenhouse gas emission by a collective average of 5% below 1990 level of respective countries [5]. The Intergovernmental Panel on Climate Change (IPCC) concludes in the Climate Change 2007 that, on account of aberrant weather, change below the global surface temperatures are probably going to increase by 1.1–6.4 °C somewhere in the range of 1990–2100. Canakcia et al. [6] have looked at the significance of Counterfeit Neural Systems [ANNs] for the execution and fumes emanation estimations of a diesel motor fuelled with biodiesels from various feedstocks and oil diesel energizes. The execution and fumes emanations from a diesel motor, utilizing biodiesel mixes with No. 2 diesel fuel up to 20%, have been projected utilizing the ANN display. The real and anticipated values of SFC, CO, CO<sub>2</sub>, HC, O<sub>2</sub>, and NO<sub>x</sub> were tallied. Sahoo et al. [7] have examined the biodiesel production from polanga seed oil by transesterification process and were tested for their use as an alternate fuel of diesel in a single-cylinder diesel engine. The engine performance parameters such as fuel consumption, thermal efficiency, exhaust gas temperature and exhaust emissions fuel utilization, warm effectiveness, fumes gas temperature, and fumes discharges [CO, CO<sub>2</sub>, NO<sub>x</sub>, and O<sub>2</sub>] were observed. From release viewpoint, the unblemished POME was recorded to be the best fuel as it showed lesser smoke release when compared with HSD. Kumar et al. [8] have tested rice bran biodiesel in single cylinder, direct injection diesel engine to evaluate performance and emission results and compared with diesel fuel. The power created from the engine with biodiesel as fuel was 4% lower when contrasted with diesel, on account of lower heating value of biodiesel. BSFC and BSEC were likewise higher because of the same reason. Lin et al. [9] employed the pre-oxidation process to produce biodiesel. The experimental results have shown increase in specific fuel consumption, brake thermal efficiency, equivalence ratio, and exhaust gas temperature. The results indicate decrease in CO<sub>2</sub>, CO, and NO<sub>x</sub> emissions. Finally they concluded that pre-oxidation process effectively improves the fuel properties and reduces the emissions. The performance and emission characteristics are found out by Lapuerta et al. [10] on single cylinder and used nonedible oil. The loss of torque and power ran somewhere in the range of 5–10%, and especially at full load, the loss of intensity was nearer to 5% at low speed and 10% at high speed. Yuan et al. [11] have investigated on the combustion and emissions of engines utilizing diesel fuel and biodiesel [B10, B20, and B100] fuel. The outcomes outline that the burning occurs ahead of time and the ignition delay period is abbreviated. Rao et al. [12] have investigated the performance and emissions of

different blends [B10, B20, and B40] of PME and JME and compared with diesel fuel. A slight drop in thermal efficiency must be endorsed to the poor combustion characteristics of biodiesel due to high viscosity. Nabi et al. [13] have studied the parametric optimization of cottonseed biodiesel production and performance test of a diesel engine with neat diesel fuel and cottonseed biodiesel mixtures. The Soybean, Palm, Sunflower, Linseed B20, B40, B50, B75, B100 were tested with castor oil and its blend with diesel have been investigated [14] on a single-cylinder, 4-stroke Diesel Engine at 1500 rpm for variable loads. The emission of 25% blend of castor oil is better than that of all other blends and it is well comparable with diesel. The study was performed by Siva et al. [15] observed that with the increase in engine speed up to 850 rpm, the BTE increases. The conventional testing of the diesel engine for different fuel blends under all possible conditions of varying load and injection timings is very difficult [16]. Consequently the engine task can be displayed utilizing fake neural system (ANN) and fuzzy as a substitute technique. Fuzzy and ANN procedures are utilized to tackle the engineering issues that bargain with exceptionally nonlinear practical approximations. They vary from regular displaying approaches in their capacity to find out about the framework that can be demonstrated without earlier learning of the procedure connections. Recently, engine performance characteristics are predicted using ANN which is getting popular day by day [17–24]. Moreover, the anticipation of engine efficiency using fuzzy is also gaining popularity. The utilization of fuzzy model in engine asks about the area that has developed generously in the previous couple of decades. The fuzzy logic controller is produced to control the speed of IC engine [25]. In the literature, there is no mention of study to predict the engine performance, emission, and combustion parameters using MIMO fuzzy technique. The objectives of this study are two fold: (1) to investigate the efficiency and emission analysis of direct injection diesel engine fueled with diesel–biodiesel blends at various loads as 2 kg, 4 kg, and 6 kg and also compare this results with those operating on base diesel, (2) to build up a fuzzy model equipped for anticipating the relations between engine input and output by utilizing fuzzy interface framework for different biodiesels mixed at various loads.

## 2 Experimental Details

### 2.1 Fuel Properties

The properties of methyl ester prepared were calculated using individual regular techniques. It was found that the properties of the methyl ester suit Indian standards (IS 15607: 2005) for biodiesels. The properties of PKOME, diesel, and ethanol are outlined in Table 1.

**Table 1** Properties of fuels

Property	Diesel	PKOME	Ethanol
Density at 15 °C (kg/m <sup>3</sup> )	840	876.6	790
Cetane number	50	62	8
Kinematic Viscosity (mm <sup>2</sup> /s)	2.67	3.248	1.2
Flash point (°C)	47.5	189	40
Calorific value (MJ/kg)	44	38.53	27

**Table 2** Specifications of the diesel engine

Particulars	Specification
Make and model	Kirloskar, AV1
Method of cooling	Water cooled
Number of cylinders	One
Number of strokes	Four
Rated power output	3.7 kW (5HP)
Speed	1500 rpm
Fuel injection	Direct injection
Bore, Stroke	80 mm, 110 mm
Compression ratio	17.5:1
Fuel injection timing	23° BTDC
Loading device	Eddy current dynamometer

## 2.2 Experimental Work

For the present work, the tests were conducted on a single-cylinder, four strokes, naturally aspirated, air-cooled diesel engine coupled with electrical dynamometer test rig. The technical specifications of the test engine are given in Table 2.

Before starting the experiments, all the equipments were calibrated according to the manufacturers' guidelines. The engine was started by hand cranking and was allowed to warm up at no-load condition.

The engine was fueled with methyl ester, traditional diesel and blends containing 0, 5, 10, and 15% of palm kernel methyl ester. For every fuel change, the fuel lines were cleaned, and the engine was left to operate undisturbed for at least 30 min to stabilize the new conditions.

## 2.3 Properties of Additive

Ethanol is selected as the additive to prepare the biodiesel–diesel blends because ethanol fuels contain an oxygen component that affects the emission of engines as

discussed in the literature review; much research in the past showed that ethanol in the fuel could significantly reduce smoke and particulate matter (PM) emission from diesel engine and vehicle tests. According to previous studies on the effect of ethanol on diesel emissions [26], the result of smoke and PM reduction is unanimous, but studies of NOx and HC emission have no clear conclusion; they depend on engine configurations and operating conditions. The properties of ethanol like density and viscosity match well with that of biodiesel. Ethanol has been chosen as a cold flow improver since it has a very low solidifying temperature of the order of (-) 114 °C and is highly soluble in biodiesel. The properties of ethanol are shown in Table 1.

### 3 Fuzzy Modeling

#### 3.1 Fuzzy Logic Control

Professor. Zadeh created fuzzy logic to do away with indecision and vagueness in the decision-making process for real-world applications. The chief profits of fuzzy logic system are quicker and easier in terms of system plan, development, lower cost, and ease of continuation. Fuzzy logic does not necessitate a mathematical model. The three basics of fuzzy logic system are fuzzification, inference, and defuzzification. Here, Multi-Input Multi-Output (MIMO) fuzzy models are developed, taught, and authenticated to predict the BSFC, BTE, CO, HC, CO<sub>2</sub>, and NOx with experimental data sets.

#### 3.2 Fuzzification

The fuzzy control model is developed using the Fuzzy Logic Toolbox in MATLAB® V18. The MIMO fuzzy is a model developed for predicting the engine performance and emission characteristics as shown in Fig. 1. Two inputs are taken as load in kg and blends while BSFC, BTE, CO, HC, CO<sub>2</sub>, and NOx are considered as the

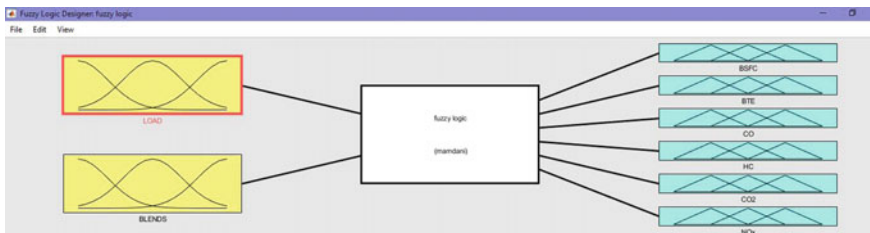


Fig. 1 MIMO fuzzy model

outputs. Load is expressed as three fuzzy sets as low, medium, and high and blends are expressed as four fuzzy sets. The output variables are expressed in seven fuzzy sets.

### 3.3 Defuzzification

Defuzzification is the process to convert fuzzy membership functions back to a crisp form and here the centroid weighted-average method is used for defuzzification.

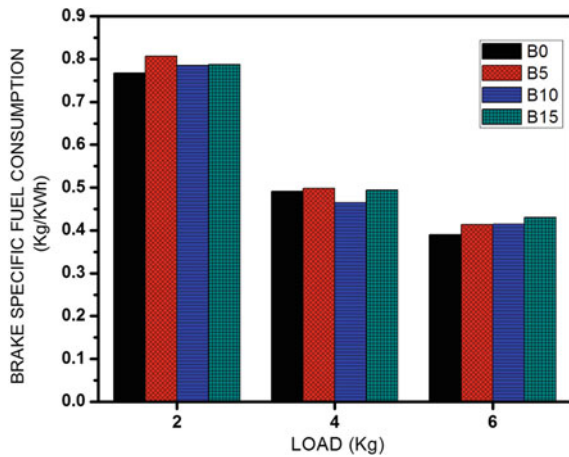
## 4 Results and Discussion

### 4.1 Performance Parameters

#### 4.1.1 Brake Specific Fuel Consumption (BSFC)

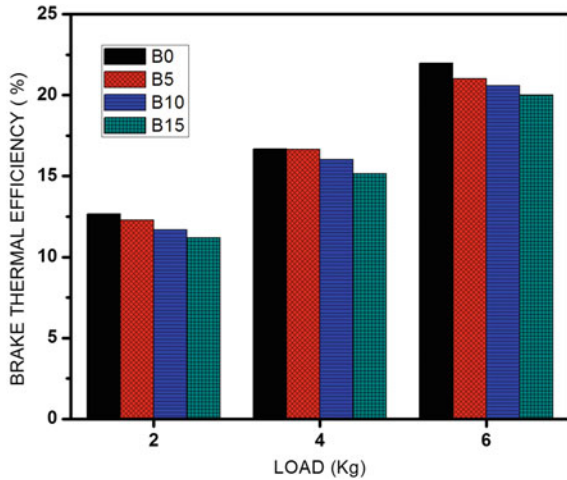
The Brake Specific Fuel Consumption acquired at various loads is shown in Fig. 2. In common, BSFC diminishes with enhancement in load and goes up with the mounting proportion of biodiesel in the fuel blends for all fuels. The chief motive for this could be that percent increase in fuel required to operate the engine is less than the percent increase in brake power due to comparatively less fraction of the heat losses at higher loads.

Fig. 2 Change of BSFC with load





**Fig. 3** Variation of BTE with load



### 4.1.2 Brake Thermal Efficiency (BTE)

The change of brake thermal efficiency with load for tested fuels is shown in Fig. 3. Based on the experiments, it is observed that the BTE of diesel varies from 10.7% at low load to 20.9% at full load and for B15 it varies from 11.2 to 21.8%.

The brake thermal efficiency of B5 and B10 are found to be similar to diesel. Hence, B15 shows better results for the BTE at 6 kg load.

## 4.2 Emission Parameters

### 4.2.1 Carbon Monoxide (CO)

The deviation of CO with load for tested fuels is shown in Fig. 4. Based on the experiments, it is observed that CO for diesel is 0.06% vol. at 2 kg load and 0.03% vol. at 4 kg and also for 6 kg load whereas for B15, it is observed that CO is 0.05% vol. at 2 kg load and 0.03% vol. for 6 kg load. Better results for CO less emission are observed for B5 that is 0.04% vol. at 2 kg load and 0.03% vol. at 6 kg load.

### 4.2.2 Hydrocarbons (HC)

The change of hydrocarbons with load for tested fuels is shown in Fig. 5. Based on the experiments, it is observed that HC for diesel is 24 ppm at 2 kg load and 28 ppm at 4 kg and 38 ppm for 6 kg load whereas for B15, it is observed that HC is 19 ppm at 2 kg load and 33 ppm for 6 kg load. Better results for HC less emission are observed for B5 that is 12 ppm at 2 kg load and 17 ppm at 6 kg load.

**Fig. 4** Change of CO with load

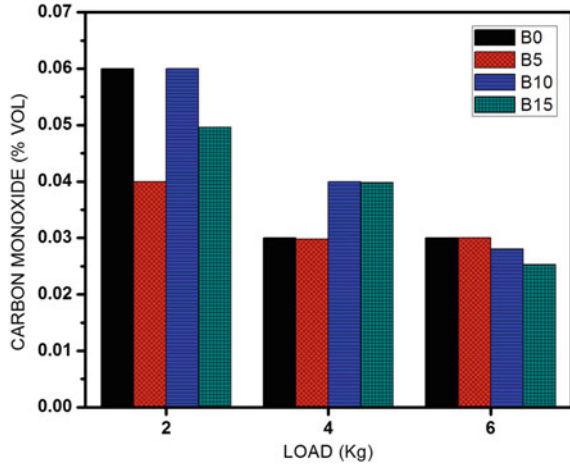
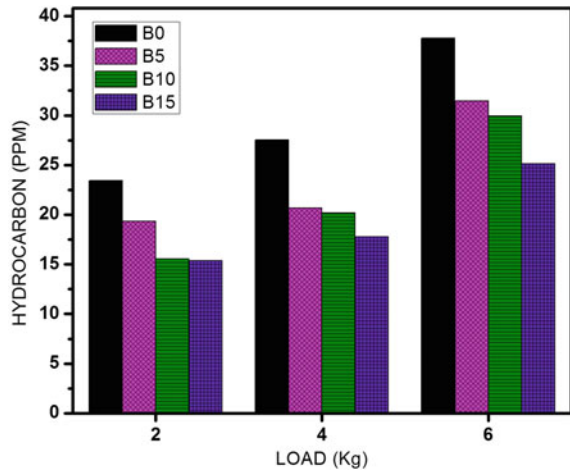


**Fig. 5** Variation of hydrocarbons with load



### 4.2.3 Carbon Dioxide (CO<sub>2</sub>)

The change of CO<sub>2</sub> with load for tested fuels is depicted in Fig. 6. Based on the experiments, it is observed that CO<sub>2</sub> for diesel is 2.4% vol. at 2 kg load, 3.4% vol. at 4 kg, and 4.4% vol. for 6 kg load whereas for B15, it is observed that CO<sub>2</sub> is 2.6% vol. at 2 kg load and 4.5% vol. for 6 kg load. Better results for CO<sub>2</sub> less emission are observed for B5 that is 1.9% vol. at 2 kg load and 4.5% vol. at 6 kg load.

### 4.2.4 Oxides of Nitrogen (NO<sub>x</sub>)

The deviation of hydrocarbons with load for tested fuels is shown in Fig. 7. Based on

**Fig. 6** Change of CO<sub>2</sub> with load

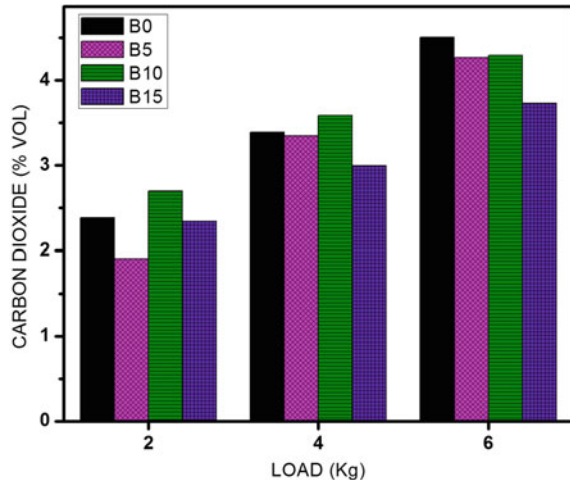
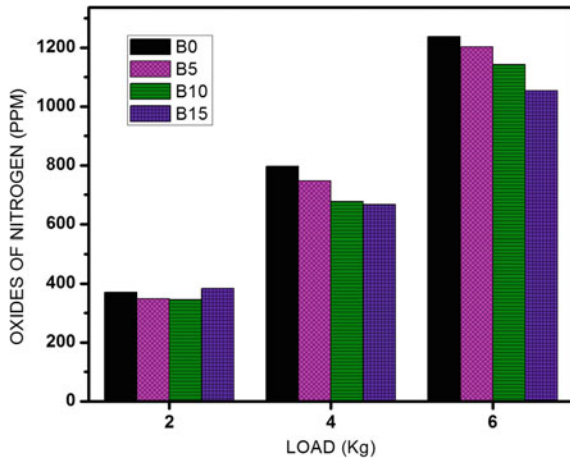


**Fig. 7** Change of NOx with load



the experiments, it is observed that NOx for diesel is 370 ppm at 2 kg load, 795 ppm at 4 kg, and 1237 ppm for 6 kg load whereas for B5, it is observed that NOx is 347 ppm at 2 kg load and 1230 ppm for 6 kg load. Better results for NOx less emission are observed for B15 that is 384 ppm at 2 kg load and 1126 ppm at 6 kg load.

### 4.3 Fuzzy Results

Graphical representations of the predicted outputs are shown in Fig. 8 for BSFC with input variables load and blends. Graphical representations of the predicted output are

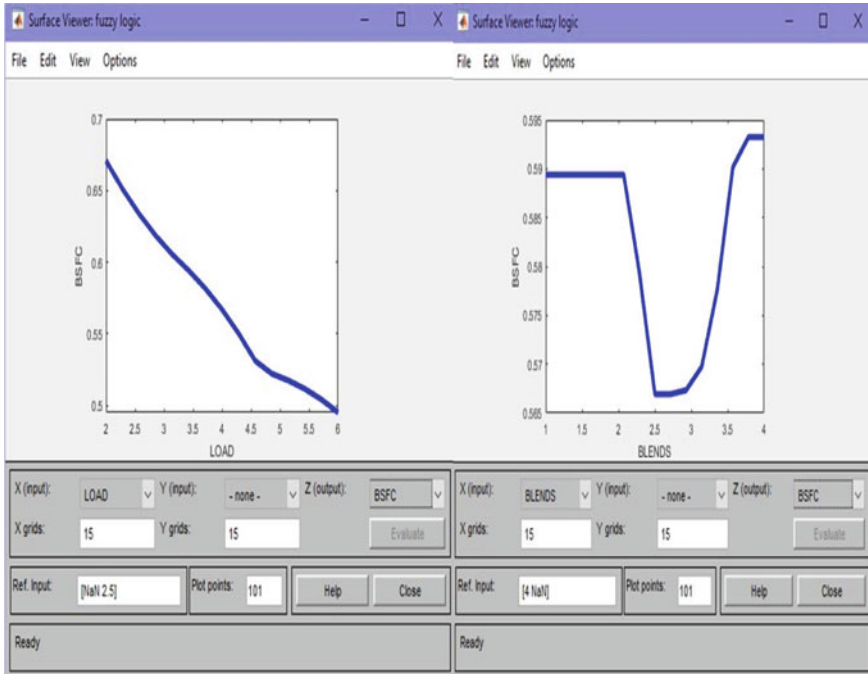


Fig. 8 Fuzzy results (BSFC)

shown in Fig. 9 for BTE with input variables load and blends. Graphical representations of the predicted output are shown in Fig. 10 for CO with input variables load and blends. Graphical representations of the predicted output are shown in Fig. 11 for HC with input variables load and blends. Graphical representations of predicted output are shown in Fig. 12 for CO<sub>2</sub> with input variables load and blends. Graphical representations of predicted output are shown in Fig. 13 for NO<sub>x</sub> with input variables load and blends.

### 5 Conclusion

The MIMO fuzzy model predictions show the correlation coefficients in the range 0.908–0.998 for B15 as it has given better performance and emission than other blends used in this paper.

The comparison of anticipated values obtained from the developed fuzzy model with experimental values showed the enhanced reliability of the fuzzy approach over theoretical and empirical methods. This method had established itself to be proficient in modeling the engine characteristics by using only a few numbers of experimental test results, thus saving both time and assets.

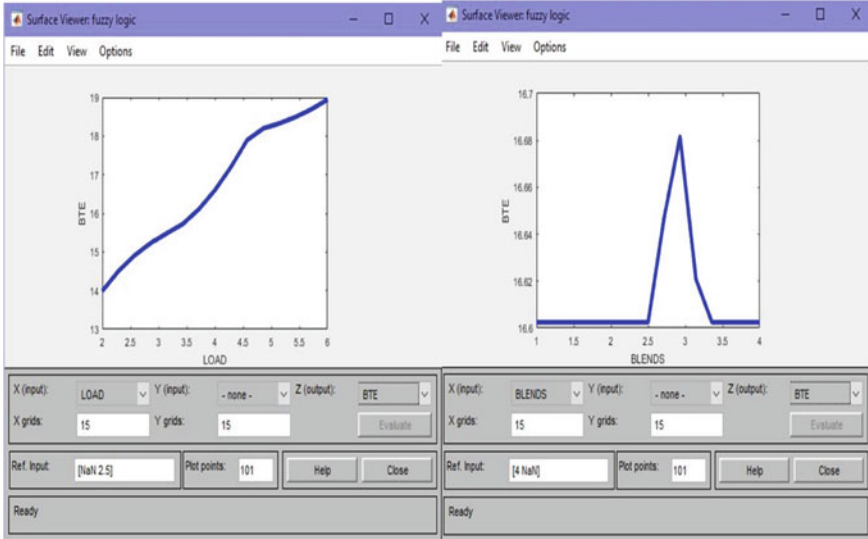


Fig. 9 Fuzzy results (BTE)

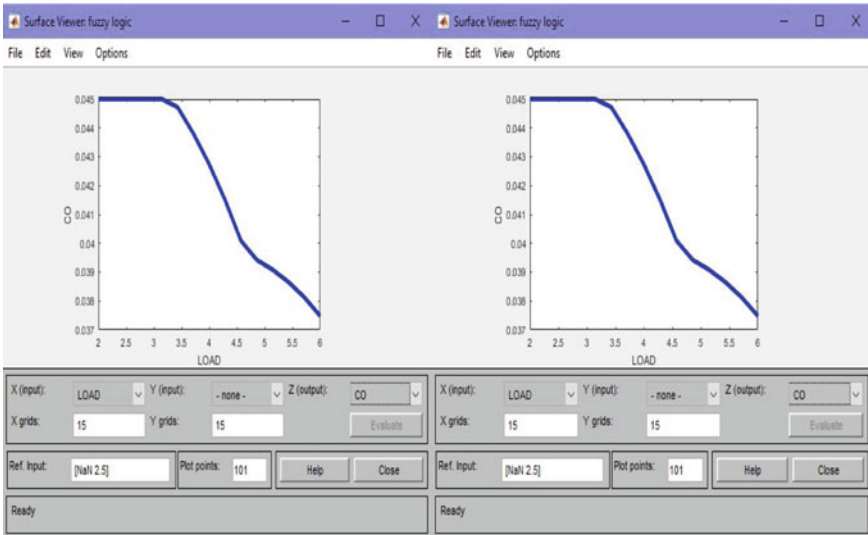


Fig. 10 Fuzzy results (CO)

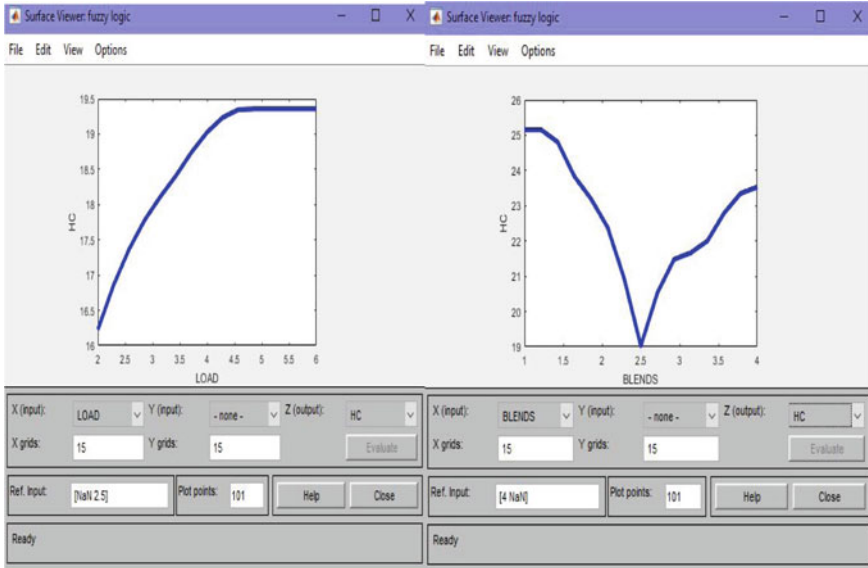


Fig. 11 Fuzzy results (HC)

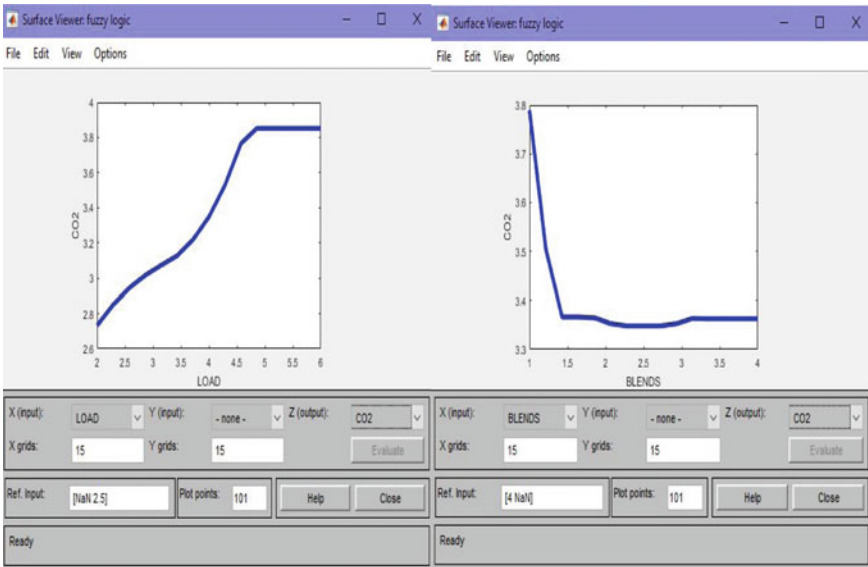


Fig. 12 Fuzzy results (CO2)

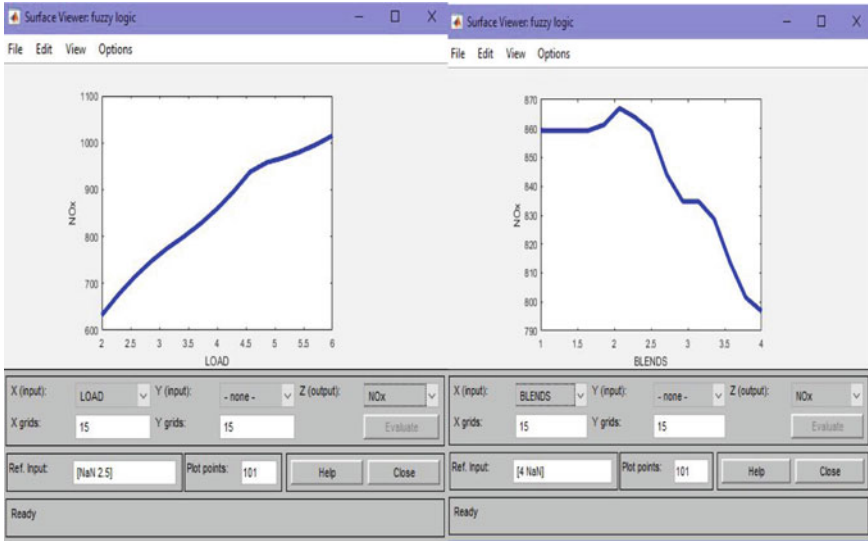


Fig. 13 Fuzzy results (NOx)

## References

1. Agarwal AK, Rajamanoharan K (2009) Experimental investigations of performance and emissions of Karanja oil and its blends in a single cylinder agricultural diesel engine. *Appl Energy* 86:106–112
2. Agarwal AK (2007) Biofuels (alcohols and biodiesel) applications as fuels for internal combustion engines. *Prog Energy Combust Sci* 33:233–271
3. Ahmad M, Rashid S, Khan M (2009) Optimization of base catalyzed transesterification of peanut oil biodiesel. *Afr J Biotech* 8(3):441–446
4. Alamu OJ, Akintola TA, Enweremadu CC (2008) Characterization of palm-kernel oil biodiesel produced through NaOH-catalysed transesterification process. *Sci Res Essay* 3(7):308–311
5. Allen C, Watts AC, Pegg MJ (1999) Predicting the viscosity of biodiesel fuels from their fatty acid ester composition. *Fuel* 78:1319–1326
6. Canakci M, Erdi A, Arcaklioglu E (2006) Performance and exhaust emissions of a biodiesel engine. *Journal of Applied Energy* 83:594–605
7. Sahoo PK, Das LM, Babu MKG, Naik SN (2007) Biodiesel development from high acid value polanga seed oil and performance evaluation in a CI engine. *Fuel* 86:448–454
8. Kumar N (2007) Production of biodiesel from high FFA rice bran oil and its utilization in a small capacity diesel engine. *J Sci Ind Res* 66:399–402
9. Lin L, Ying D, Chaitep S, Vittayapadung S (2009) Biodiesel production from crude rice bran oil and properties as fuel. *Appl Energy* 86:681–688
10. Lapuerta M, Octavio A, Rodrniguez FJ (2008) Effect of biodiesel fuels on diesel engine emissions. *Prog Energy Combust Sci* 34:198–223
11. Yuan Y, Mei D, Wang Z, Zhang T (2008) Combustion and emissions of the diesel engine using bio-diesel fuel. *Front. Mech. Eng. China* 3:189–192
12. Baiju B, Naik MK, Das LM (2009) A comparative evaluation of compression ignition engine characteristics using methyl and ethyl esters of Karanja oil. *Renewable Energy* 34:1616–1621
13. Rao TV, Rao GP, Reddy KHC (2008) Experimental investigation of methyl esters of non-edible oils as biodiesel on C.I. engine. *Int J Mat Sci* 3(2):199–209

14. Siva AK, Maheswar D, Reddy KV (2009) Comparison of diesel engine performance and emissions from neat and transesterified cotton seed oil. *Jordan J Mech Ind Eng* 3(3):190–197
15. Banapurmath NR, Tewari PG, Hosmath RS (2008) Performance and emission characteristics of a DI compression ignition engine operated on Honge, Jatropha and Sesame oil methyl esters. *Renewable Energy* 33:1982–1988
16. Bari S, Lim TH, Yu CW (2002) Effects of preheating of crude palm oil on injection system, performance and emission of a diesel engine. *Renewable Energy* 27:339–351
17. Biona JBM, Licaucou E (2009) Performance, smoke characteristics and economics of pre-heated used vegetable oil utilization in Philippine public utility jeepers. *Clean Tech. Environ Policy* 11:239–245
18. Bora DK (2009) Performance of single cylinder diesel engine with karabi seed biodiesel. *J Sci Ind Res* 68:960–963
19. Keg B (2008) Effects of biodiesel on emissions of a bus diesel engine. *Biores Technol* 99(4):863–873
20. Canoira L, Alcantara R, Carrasco J (2006) Biodiesel from Jojoba oil- wax: transesterification with methanol and properties as a fuel. *Biomass Bioenerg* 30:76–81
21. Naga Prasad S, Vijaya K, Kumar BSP, Ramjee E, Hebbel OD, Nivendgi MC (2009) Performance and emission characteristics of a diesel engine with castor oil. *Indian J Sci Technol* 2(10):25–31
22. Lin C, Lin H (2007) Engine performance and emission characteristics of a three-phase emulsion of biodiesel produced by peroxidation. *J Fuel Process Technol* 88:35–41
23. Demirbas A (2005) Biodiesel production from vegetable oils via catalytic and non-catalytic supercritical methanol transesterification methods. *Prog Energy Combust Sci* 31:466–487
24. Devan PK, Mahalakshmi NV (2009) A study of the performance, Emission and combustion characteristics of a CI engine using methyl ester of paradise oil eucalyptus oil blends. *Appl Energy* 86:675–680
25. Doradoa MP, Ballesteros E, Arnal JMI, Gomez JC, Lopez FJ (2003) Exhaust emissions from a Diesel engine fuelled with trans esterified waste olive oil. *Fuel* 82:1311–1315
26. Sathiyamoorthi R, Sankaranarayanan G (2017) The effects of using ethanol as additive on the combustion and emissions of a direct injection diesel engine fuelled with neat lemongrass oil-diesel fuel blend. *Renewable Energy* 101:747–756



# Effect of Alumina Nanoparticles on Performance and Emission Study of DICl Engine Fuelled by Cymbopogon Flexuosus



R. Sathiyamoorthi, G. Sankaranarayanan, B. Nithin Siddharth and M. V. Natarajan

**Abstract** An experimental study has been conducted on the effect of alumina nanoparticles in a DICl (Direct Injection Compression Ignition) engine using cymbopogon flexuosus (lemongrass oil) as fuel. Lemongrass oil (LGO) is extracted from the steam distillation method. This fuel may also be more suitable for diesel engines as an alternate fuel without any transesterification process and engine modification. In this study, three fuels (LGO25, LGO25+ALU50 ppm and LGO25+ALU100 ppm) were tested in a single-cylinder, four-stroke and naturally aspirated diesel engine. From the experimental analysis, it was found that BSFC decreased with an increase in BTE using alumina nanoparticles. The cylinder pressure and heat release rate are higher by 1.66% at LGO25+ALU 50 ppm and 3.7% at LGO25+ALU 100 ppm than LGO25. In the case of emission study, CO, HC and smoke emissions decreased by 16.67% and 25.79%, 5.9% and 12.83%, and 18.94% and 24.7% at LGO25+ALU50 ppm and LGO25+ALU100 ppm concentrations, respectively. NO<sub>x</sub> emission is increased by 4.95% and 8.27% for LGO25 with 50 ppm and 100 ppm respectively than LGO25.

**Keywords** Diesel · Lemongrass oil · Nanoparticles · Aluminium oxide (Alumina)

---

R. Sathiyamoorthi · B. N. Siddharth · M. V. Natarajan

Department of Mechanical Engineering, Panimalar Engineering College, Chennai, Tamil Nadu, India

e-mail: [Sathiya.ram78@gmail.com](mailto:Sathiya.ram78@gmail.com)

B. N. Siddharth

e-mail: [nitinsidharth44@gmail.com](mailto:nitinsidharth44@gmail.com)

M. V. Natarajan

e-mail: [mvnatarajan1@gmail.com](mailto:mvnatarajan1@gmail.com)

G. Sankaranarayanan (✉)

Department of Mechanical Engineering, Guru Nanak Institutions, Ibrahimpatnam, Telangana, India

e-mail: [gs2000narayanan@gmail.com](mailto:gs2000narayanan@gmail.com)

© Springer Nature Singapore Pte Ltd. 2020

G. S. V. L. Narasimham et al. (eds.), *Recent Trends in Mechanical Engineering*,

Lecture Notes in Mechanical Engineering,

[https://doi.org/10.1007/978-981-15-1124-0\\_3](https://doi.org/10.1007/978-981-15-1124-0_3)

## 1 Introduction

The world energy demand is rapidly increasing due to the growing trend in modernization and industrialization. Most of the developing countries import crude oil to meet their increasing energy demand. Most of the country's income is spent to purchase petroleum-based products only. Complying with stringent emission norms imposed by the countries poses another challenge to the transportation industry. Therefore, it is important to use alternative fuels that can be produced from natural resources available locally within the country.

Singh et al. [1] have analysed emissions and performance characteristics of a heavy-duty diesel engine fuelled with biodiesel derived from *Jatropha curcas* oil. The test results indicated the reduction in particulate matter, CO and HC emissions. But  $\text{NO}_x$  emission increased by 26% than diesel. Ali et al. [2] have conducted a detailed analysis of palm oil biodiesel in a diesel engine on engine performance. Engine tests demonstrated that engine brake power decreased with an increase in biodiesel blends up to 30%. The BSFC increased by 3% with no statistically significant difference in the brake thermal efficiency compared to standard diesel. B30 fuel blend is recommended as an optimized fuel blend to diesel for smooth engine operation.

Many techniques have been used to control the emission gases from the engine such as exhaust gas recirculation, emulsification and nanoadditives. Basha et al. [3] have used carbon nanotubes (CNT) blended *Jatropha* methyl ester emulsion on engine performance. BTE increased with a significant reduction in cylinder pressure and HRR using CNT-blended fuel. Velraj et al. [4] have investigated the influence of alumina nanoparticles; ethanol and isopropanol blend with biodiesel derived from soybean in a diesel engine. The results showed that cylinder pressure and brake-specific energy consumption increased using alumina-blended biodiesel. A considerable reduction of emission gases like CO,  $\text{CO}_2$  and UHC were observed by using nanoblended biodiesel.

Sathiyamoorthi et al. [5] have analyzed a combined effect of nano (Cerium oxide) emulsion and EGR using lemongrass oil–DEE diesel blend in a single-cylinder diesel engine. BSFC increased by 10.8% with DEE and EGR mode for nanoemulsified LGO25. HRR increased by 2.7–6.95% for nanoblended fuel. CO, HC,  $\text{NO}_x$ , and smoke emissions decreased using the combined effect of nanoemulsified blend with EGR and DEE. In this experimental study, LGO25 (25% lemongrass oil + 75% diesel on volumetric percentage) is used as biofuel and blended with alumina nanoparticles (50 and 100 ppm concentrations). The diesel engine characteristics were analysed using the obtained results with the effect of alumina nanoparticles.

**Table 1** Properties of diesel and LGO25 with alumina nanoparticles

Properties	Gross calorific value (MJ/kg)	Kinematic viscosity (Cst) at 40 °C	Density (kg m <sup>3</sup> )	Flash Point °C	Cetane Index
Diesel	43.35	3.25	840	55	40–55
LGO25	41.69	3.48	870	53	45
LGO25+ALU50 ppm	41.31	3.72	910	55	45
LGO25+ALU100 ppm	41.27	4.10	930	57	45

## 2 Test Fuel: Cymbopogon Flexuosus

Cymbopogon flexuosus (lemongrass oil) is part of an aromatic with fast-growing grass family. Its main element is citral of 65–85%. The main components of lemongrass oil are gerai, neral, limonene, terpineol, nerol, myrcene and geranyl acetate. It is found in many parts of Sikkim, Tamil Nadu, Kerala, Maharashtra and Arunachal Pradesh. The steam distillation method was used to extract citral from the fresh leaves. It is available with more than 140 species all over the world and is called Cochin grass or Malabar grass in India. The important properties of fuel blend were measured from the fuel test laboratory as per ASTM. Table 1 shows the properties of the test fuel with alumina nanoparticles which are compared with standard diesel fuels [5–7].

## 3 Synthesis and Characterization of Alumina Nanoparticles

The blended fuels are tested in a reputed test lab and properties are furnished in Table 1, which shows energy content and viscosity of the blends compared with diesel. It is seen that the viscosity increased with the addition of nanoparticles and density as well. The cetane index is not much affected by the blended fuel. Alumina nanoparticles are synthesized by sol–gen method and its Scanning Electron Microscope (SEM) image are shown in Fig. 1. SEM morphology is used to determine grain size characterization. The SEM image shows that the alumina nanoparticles have a definite crystalline nature with lower agglomeration as well as aggregate formation. Moreover, the average grain size of the alumina nanoparticles is 24 nm. Figure 2 shows the EDAX (X-ray diffraction) for alumina nanoparticles.

Nanoparticles are generally synthesized by four techniques, such as sol–gel, attrition, vapour deposition and combustion. The following steps were used to prepare alumina nanoparticles using the sol–gel technique [8, 9].

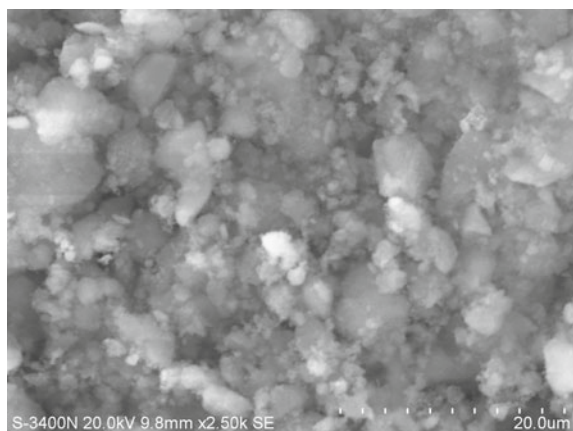


**Fig. 1** SEM image of Al<sub>2</sub>O<sub>3</sub>

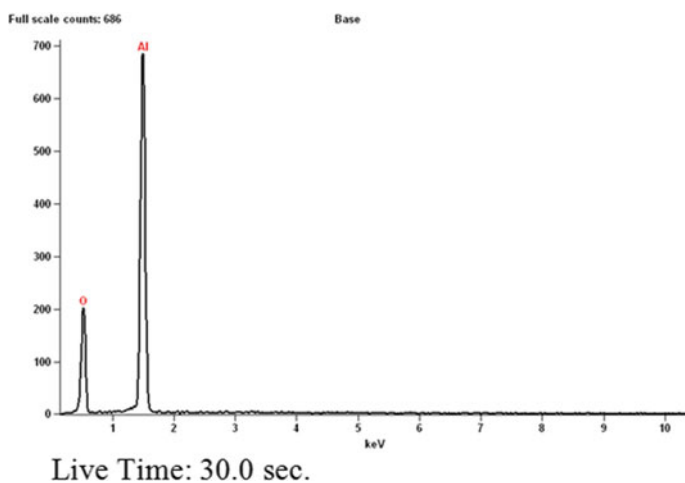


**Fig. 2** EDAX of Al<sub>2</sub>O<sub>3</sub>

- Aluminium nitrate solution of 0.5 M was dissolved in deionized water (H<sub>2</sub>O) at 22 °C and this mixture was well stirred using magnetic stirrer for thorough mixing.
- Urea of 0.05 M was dissolved with aluminium nitrate solution and this mixture was kept for 30 min till the solution reached a pH value of 2.
- The prepared base solution (Urea + aluminium nitrate solution) was titrated with a mixture of 0.1 M sodium hydroxide and 25 ml of H<sub>2</sub>O until the solution reached a pH value of 6.

- d. A cloudy gel formation ( $\text{pH} = 8$ ) was due to the excess addition of sodium hydroxide to the base solution, and then this mixture was dried and calcined at  $150\text{ }^{\circ}\text{C}$  for 12 h.
- e. The dried sample was subjected to  $300\text{ }^{\circ}\text{C}$  and 2 h in a furnace, and then the alumina nanoparticles were collected.

The alumina nanoparticles are also used in biomaterials, nanocomposites, transparent conductive coatings, wear-resistance additives and material surface coatings, etc. The nanoparticles are highly effective catalysts which improve combustion speed, combustion heat and combustion stability.

### 3.1 Test Fuels Preparation

In this research work, lemongrass oil was procured from the local agriculture oil supplier. The three types of test fuels are prepared. Table 2 shows the volumetric percentage of fuel blends used in this test. The dispersion of alumina nanoparticles with LGO25 fuel blend is prepared by an ultrasonicator (Fig. 3) for 30–45 min to get homogeneous mixture. All the prepared fuels were subjected to the stability test which is kept in a 100 ml graduated scale glass test tube at static (normal) conditions and were found to be stable for 15 h. Figure 4 shows the sample prepared after the addition of nanoparticles with the LGO25 fuel blend with stable conditions.

**Table 2** Volumetric percentage of blended fuel

Abbreviation	Percentage of fuel
LG025	75% Diesel+25% Lemongrass oil (LGO)
LG025+ALU50ppm	75% Diesel+25% LGO+50 ppm alumina nanoparticles
LG025+ALU100ppm	75% Diesel+25% LGO+100 ppm alumina nanoparticles

**Fig. 3** Ultrasonicator

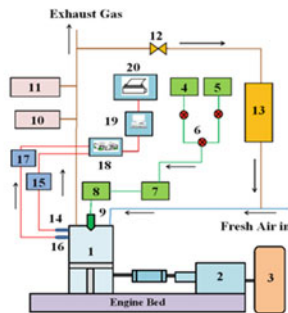


**Fig. 4** LGO25+Al<sub>2</sub>O<sub>3</sub> with 50 ppm and 100 ppm



### 4 Experimental Setup and Procedure

The experimental investigation was conducted with a naturally aspirated single-cylinder diesel engine with a compression ratio of 17.5:1. Figure 5 illustrates a detailed experimental setup with the digital data acquisition system (DDAS). The



- (1) Diesel Engine (2) Electrical Dynamometer (3) Electrical Loading Unit (4) Diesel Tank (5) LGO Tank (6) Control Valve (7) Fuel filter (8) Fuel pump (9) Fuel Injector (10) AVL Digass 444 Gas analyzer (11) AVL Smoke meter (12) EGR valve (13) Exhaust gas Storage Tank (14) TDC pickup sensor (15) Charge Amplifier (16) Pressure pickup sensor (17) TDC Amplifier (18) Digital Data Acquisition System (19) Computer (20) Printer

**Fig. 5** Schematic diagram of the experimental setup

**Table 3** Test engine specifications

Model	Kirloskar TAF1
Type	Single cylinder, 4-stroke, Direct Injection
Power	4.4 kW
Bore	87.5 mm
Stroke	110 mm
Cubic capacity	0.553 L
Compression ratio	17.5:1
Rated speed	1500 rpm
Cooling type	Air cooling
No. of holes	3
Nozzle hole diameter	0.25 mm
Fuel injection timing	23° bTDC

detailed specifications of the research engine are summarized in Table 3. The crankshaft position was measured by a crank angle encoder. The intake air was measured using an orifice metre, a manometer and an air-damping tank. An AVL Digas 444 exhaust gas analysed was used to measure the emission gases from the engine. An AVL 437 smoke meter was used to measure smoke opacity. The temperature of inlet air and exhaust gas was measured by using K-type thermocouples. The different loads to the engine were applied using an electrical loading device. The fuel consumption was calculated by measuring 10 cc of fuel consumption with a stopwatch from the burette [10].

All the experimental tests were done thrice and the results were finally calculated by taking the average values. Before taking the readings, the engine was warmed up for 20 min. All the base diesel and fuel tests were conducted at steady-state conditions only. The standard injection pressure and timing are set as 200 bar and 23bTDC respectively throughout the experiments. Piezoelectric pressure transducer is used to measure the cylinder pressures at all the engine loads. Finally, all the measured readings were stored in a personal computer which was used to plot the combustion characteristics such as HRR and cylinder pressure [11–13].

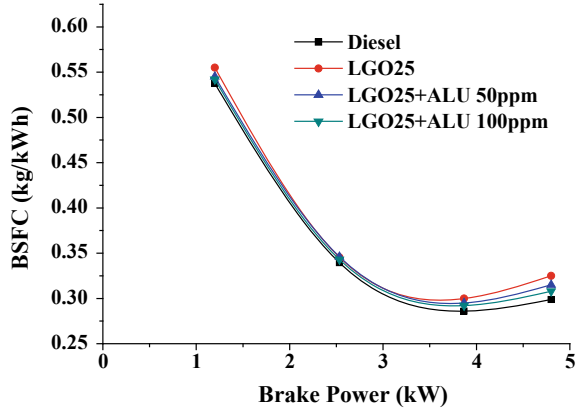
## 5 Results and Discussion

### 5.1 Performance Analysis

#### 5.1.1 Brake Specific Fuel Consumption (BSFC)

Figure 6 depicts the variation of BSFC with brake power using alumina nanoparticles in LGO25 fuel blend. BSFC is decreased by 2.97% and 5.17% for LGO25 with

**Fig. 6** Brake power versus BSFC with alumina nanoparticles



50 ppm and 100 ppm alumina nanoparticles respectively than LGO25. The ability of alumina nanoparticles is to oxidize the carbon deposits inside the combustion chamber which leads to the reduction of fuel consumption [4].

### 5.1.2 Brake Thermal Efficiency (BTE)

BTE with brake power of all the test fuels is presented in Fig. 7 using nanoparticles. BTE is increased by 1.31% and 1.93% for LGO25 with 50 ppm and 100 ppm nanoparticles respectively than LGO25. It is due to the oxygen buffer property of alumina nanoparticles which results in a complete combustion process. On the other hand, more amount of fuel can react with air because of higher surface area to volume ratio of alumina nanoparticles [14].

**Fig. 7** Brake power versus BTE with alumina nanoparticles

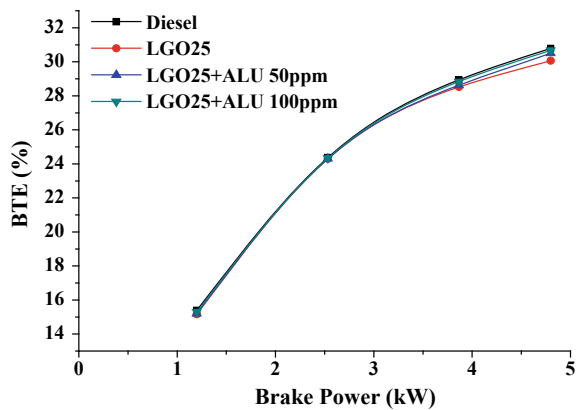
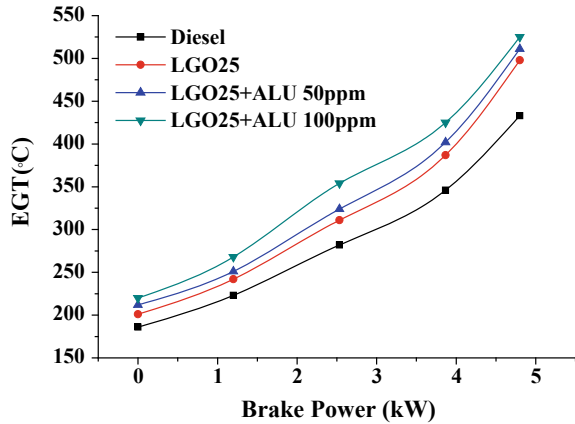




**Fig. 8** Brake power versus EGT with alumina nanoparticles



### 5.1.3 Exhaust Gas Temperature (EGT)

Figure 8 depicts the variation of EGT with brake power for alumina-blended LGO25 fuel blends. EGT is increased by 2.67% and 4.91% for LGO25 with 50 ppm and 100 ppm nanoparticles respectively than LGO25. The reason for higher EGT using alumina nanoparticles is the higher heat transfer coefficient associated with the products of the combustion process. Furthermore, the increase in exhaust gas temperature is due to the higher quantity of fuel burnt at peak engine loads which results in higher heat release rate [15].

## 5.2 Combustion Analysis

### 5.2.1 Cylinder Pressure

The cylinder pressure variation is presented in Fig. 9 with different crank angles. The cylinder pressure increased by 1.66% and 3.7% for LGO25 with 50 ppm and 100 ppm nanoparticles respectively than LGO25. The higher cylinder pressure is mainly due to the better mixing which leads to the rapid combustion process and inherent oxygen availability in the LGO25 blend. From the figure, it is noted that ignition delay decreases with an increase in the engine load. The reason for higher cylinder pressure is the higher surface area of alumina nanoparticles, resulting in better mixing at higher engine loads [14].

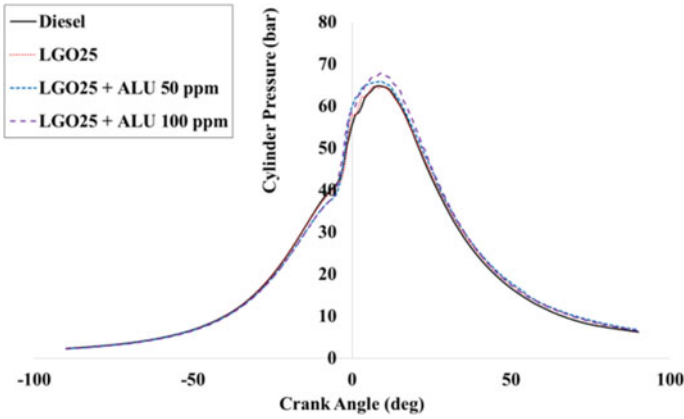


Fig. 9 Cylinder pressure versus crank angle with alumina nanoparticles blended LGO25

### 5.2.2 Heat Release Rate (HRR)

The variation of HRR is presented in Fig. 10 with various crank angles. The heat release rate increases with the addition of alumina nanoparticles than LGO25 and diesel. The alumina nanoparticles contribute to the increase in the combustion rate which produces complete combustion. This is because of its higher carbon combustion activation of alumina.

The heat release rates increased by 8.97% and 20.78% for LGO25 with 50 ppm and 100 ppm alumina nanoparticles respectively than LGO25. The maximum HRR is observed as 92.15 kJ/m<sup>3</sup>deg and 105.78 kJ/m<sup>3</sup>deg for LGO25 with 50 ppm and 100 ppm, respectively.

Fig. 10 Heat release rate versus crank angle with alumina nanoparticles

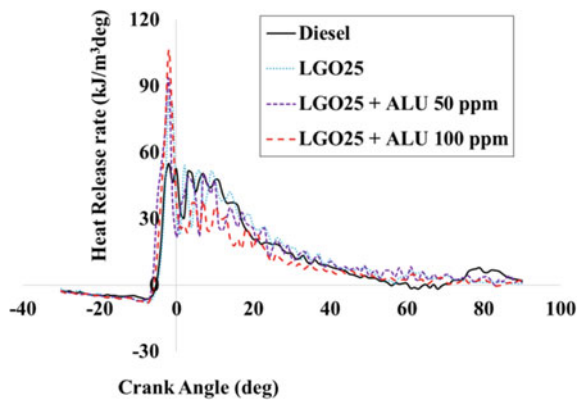
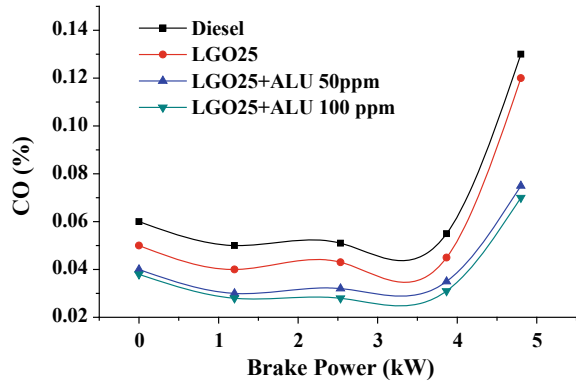


**Fig. 11** Brake power versus CO emission with alumina nanoparticles



### 5.3 Emission Analysis

#### 5.3.1 CO Emission

The variation of CO emission with brake power using nanoparticles is presented in Fig. 11. It is noted that CO emission decreases for all the fuel blends than diesel. One of the reasons for the reduction of CO emission is the availability of oxygen elements in the fuel blend. CO emission is decreased by 16.67% and 25.79% for LGO25 with 50 ppm and 100 ppm alumina nanoparticles respectively than LGO25. The nanoparticles help to increase fuel atomization rate which results in complete combustion, therefore CO emission decreases. Moreover, the conversion rate of CO to CO<sub>2</sub> alumina nanoparticles in the fuel blends influences the lower CO emission and its potent redox-active property [4].

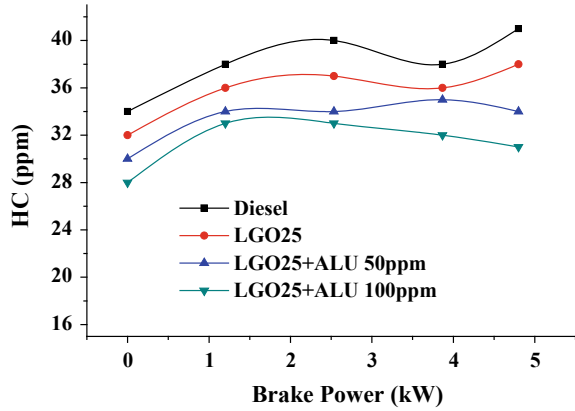
#### 5.3.2 HC Emission

From Fig. 12, it is observed that HC emission decreased for all the blends of LGO25 with alumina nanoparticles than LGO25 and diesel. HC emission is decreased by 5.95% and 12.83% for LGO25 with 50 ppm and 100 ppm respectively than LGO25. The lower HC emission is due to the influence of nanoparticles which helps to increase surface area exposure to the fuel droplets, and therefore improved the combustion process results in lower HC emission than LGO25 [14].

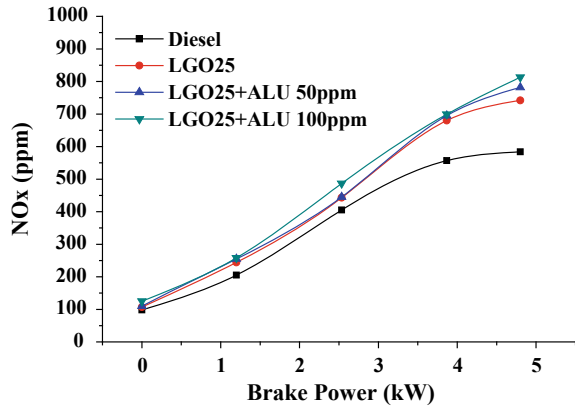
#### 5.3.3 Nitrogen Oxides (NO<sub>x</sub>) Emission

Figure 13 displays the variation of NO<sub>x</sub> emission using alumina nanoparticles blended LGO25. NO<sub>x</sub> emission increased by 4.95% and 8.27% for LGO25 with

**Fig. 12** BP versus HC emission with alumina nanoparticles



**Fig. 13** Brake power versus NO<sub>x</sub> emission with alumina nanoparticles



50 ppm and 100 ppm alumina nanoparticles respectively than LGO25. The parameters which influence the NO<sub>x</sub> emission are combustion temperature, availability of oxygen in the fuel blend and duration of combustion. Higher NO<sub>x</sub> emission is formed due to the higher diffusion-controlled combustion period using alumina-blended LGO25 fuel. On the other hand, higher heat release rate using alumina-blended LGO25 is observed with higher NO<sub>x</sub> emission at higher engine loads [15].

### 5.3.4 Smoke Emission

Figure 14 portrays the smoke emission variation with BP for alumina-blended LGO25 fuel. The smoke emission is decreased by 18.94% and 24.7% for LGO25 with 50 ppm and 100 ppm concentrations respectively than LGO25. The lower smoke emission is attributed to the better improvement in the diffusion-combustion phase and the availability of oxygen molecules in the alumina nanoparticles doped fuel.

**Fig. 14** Smoke opacity emission from engine

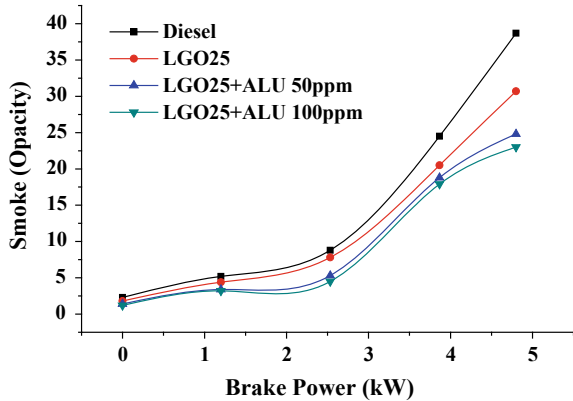


Figure 14 shows the emission pattern of Smoke Opacity in percentage is a function of brake power and other factors for the lower smoke emissions which are the reduced ignition delay, rapid evaporation and improved ignition quality of alumina nanoadditive [15].

## 6 Conclusion

The effect of alumina nanoparticles on engine performance and emission characteristics are investigated using single-cylinder diesel engine. The following conclusions were derived from the comprehensive experimental investigation.

- The addition of alumina nanoparticles resulted in higher cylinder pressure and heat release rate with a significant improvement in engine performance.
- Thus, LGO25+ALU50 ppm blend is considered as an optimized fuel blend in terms of fuel stability, high price of nanoparticles and performance parameters.
- Being an oxygenated fuel, lemongrass oil has a high oxidation rate which results in the decrease of the engine out emissions.
- Overall, the addition of alumina nanoparticles resulted in a reduction of CO, HC and smoke emission which is due to enough oxygen needed to improve the combustion of the fuel blend.

## References

1. Singh D, Subramanian KA, Singal SK (2015) Emissions and fuel consumption characteristics of a heavy duty diesel engine fueled with hydroprocessed renewable diesel and biodiesel. *Appl Energy* 155:440–446
2. Ali OM, Mamat R, Abdullah NR, Abdullah AA (2016) Analysis of blended fuel properties and engine performance with palm biodiesel-diesel blended fuel. *Renewable Energy* 86:59–67
3. Sadhik Basha J, Anand RB (2014) Performance, emission and combustion characteristics of a diesel engine using Carbon Nanotubes blended Jatropa Methyl Ester Emulsions. *Alexandria Eng J* 53:259–273
4. Shaafi T, Velraj R (2015) Influence of alumina nanoparticles, ethanol and isopropanol blend as additive with diesel-soybean biodiesel blend fuel: combustion, engine performance and emissions. *Renewable Energy* 80:655–663
5. Sathiyamoorthi R, Sankaranarayanan G, Pitchandi K (2017) Combined effect of nanoemulsion and EGR on combustion and emission characteristics of neat lemongrass oil (LGO)-DEE-diesel blend fuelled diesel engine. *Appl Therm Eng* 112:1421–1432
6. Sathiyamoorthi R, Sankaranarayanan G, Adhith Kumaar SB, Chiranjeevi T, Dilip Kumar D (2019) Experimental investigation on performance, combustion and emission characteristics of a single cylinder diesel engine fuelled by biodiesel derived from *Cymbopogon Martinii*. *Renewable Energy* 132:394–415
7. Ramalingam S, Gomathinayakam S, New alternate fuel: lemongrass oil its effect on diesel engine. Lambert Academic publishing. ISBN: 978-613-8-34241-0
8. Venu H, Madhavan V (2016) Effect of  $Al_2O_3$  nanoparticles in biodiesel-diesel-ethanol blends at various injection strategies: Performance, combustion and emission characteristics. *Fuel* 186:176–189
9. Munuswamy DB, Madhavan VR, Mohan M (2015) Comparison of the effects of  $Al_2O_3$  and CuO nanoparticles on the performance of a solar flat-plate collector. *J Non-Equilib Thermodyn* 40(4):265–273
10. Sathiyamoorthi R, Babu SC, Rajangam V, Tamizhselvan LS (2018) Evaluation of neem oil biodiesel with 2-ethyl hexyl nitrate (2-EHN) as cetane improver on performance and emission characteristics of a DI diesel engine. *Int J Eng Res* 6(2):1–4
11. Sathiyamoorthi R, Sankaranarayanan G (2015) Fuel injection timings of a direct injection diesel engine running on neat lemongrass oil-diesel blends. *Int J Automot Mech Eng* 11:2348–2363
12. Sathiyamoorthi R, Sankaranarayanan G (2016) Effect of antioxidant additives on the performance and emission characteristics of a DIC engine using neat lemongrass oil-diesel blend. *Fuel* 174:89–96
13. Sathiyamoorthi R, Sankaranarayanan G (2017) The effects of using ethanol as additive on the combustion and emissions of a direct injection diesel engine fuelled with neat lemongrass oil-diesel fuel blend. *Renewable Energy* 101:747–756
14. Gan Y, Qiao L (2010) Combustion characteristics of fuel droplets with addition of nano and micron-sized aluminium particles. *Combust Flame* 158:354–368
15. Kao MJ, Ting CC, Lin BF, Tsung TT (2018) Aqueous aluminium nanofluid combustion in diesel fuel. *J Test Eval* 36:186–190

# Study and Analysis of Blended Fuel on Single-Cylinder Naturally Aspirated Diesel Engine with Biofuels Coupled with EGR



B. Venkatesh and G. Prasanthi

**Abstract** India is the upcoming industrial revolution, wherein its economy and its fuel consumption have been rising drastically over the past two decades. Petroleum resources are depreciating rapidly in the world biofuels and its blends are the alternative sources for stabilizing demand and supply. Biofuels are eco-friendly and substitute for conventional fuels. When compared to fossil fuels except for nitrogen oxide (NO<sub>x</sub>) remains emission particles are reduced. For effective reducing, NO<sub>x</sub>, an Exhaust Gas Recirculation system (EGR) is used as exuberance for a diesel engine. The present investigation carried on Coconut oil blend (CBD20) and Cottonseed oil blend (COBD20) biofuels was prepared by the transesterification process with Al<sub>2</sub>O<sub>3</sub> as catalyst on a diesel engine with different EGR percentage ratios (10, 15, and 20%). In this analysis emission, performance parameters and exhaust gas temperature are measured and compared with two biofuels. In this study compared with neat diesel, EGR shows a better improvement on NO<sub>x</sub> level and performance levels are greasy.

**Keywords** Al<sub>2</sub>O<sub>3</sub> · Coconut oil blend · Cottonseed oil blend · Emissions · Exhaust gas recirculation · Performance parameters

## 1 Introduction

In our daily needs, transportation plays a vital role. Majority of the engines on and off road are diesel engines. Industrial and public usage engine emissions are startling the society [1]. Emissions affect the organs of the human body (asthma, eyes

---

B. Venkatesh (✉)

Research Scholar, Department of Mechanical Engineering, J.N.T.U. College of Engineering, JNTU Anantapuramu, Anantapuramu, Andhra Pradesh, India  
e-mail: [bhupalam.venkatesh2005@gmail.com](mailto:bhupalam.venkatesh2005@gmail.com)

G. Prasanthi

Professor, Department of Mechanical Engineering, J.N.T.U. College of Engineering & Director of Faculty Development & IQAC, JNTU Anantapuramu, Anantapuramu, Andhra Pradesh, India  
e-mail: [dr.smt.g.prasanthi@gmail.com](mailto:dr.smt.g.prasanthi@gmail.com)

© Springer Nature Singapore Pte Ltd. 2020

G. S. V. L. Narasimham et al. (eds.), *Recent Trends in Mechanical Engineering*, Lecture Notes in Mechanical Engineering,  
[https://doi.org/10.1007/978-981-15-1124-0\\_4](https://doi.org/10.1007/978-981-15-1124-0_4)

irritation, etc.) and cause damages to the eco-friendly animals also [2]. Biofuels are the conveniences for controlling emissions without any changes in engines [3]. But in maximum biofuels, NO<sub>x</sub> slightly increases. Exhaust gas recirculation is the solution for controlling NO<sub>x</sub>. Sakhare [4] found that the in Cotton oil (B20), BSFC increases and emissions of NO<sub>x</sub> decrease in parallel to conventional fuel, due to inadequate oxygen level and mixing of hot gases to rich mixture formation. Conversely, HC and CO slightly increase if EGR rate increases.

Attal [5] studied under oil at B20 and 10% EGR shows optimized engine performance shows bonne BSFC and brake thermal efficiency decreases matched with diesel. Emission like NO<sub>x</sub> reduced and others (HC and smoke) slightly increased.

Rajesh [6] have conducted an experiment on n-octanol for DI diesel engine and found additional solvents for mixing with conventional fuel. Due to lower cetane ignition delay slightly longer. The decrease in BSFC and BTE increases with increasing of blended ratio, but in EGR both parameters are grieved. At Oct30 blend with an increase of EGR up 30% shows NO<sub>x</sub> and Smoke opacity reduced. Hc and Co emissions gradually raised with increase in the EGR ratio.

Suresh Babu Rao [7] dopped various proportions 30, 60 and 90 ppm of Ce<sub>2</sub>O<sub>3</sub> with Calophyllum inophyllum methyl ester (CI20) with EGR 10 and 20% admitted shows better performance at EGR 10% BTE reduced at maximum loads with the increase of BSFC and emission are controlled.

Bedar [8] has conducted a test by using Simarouba glauca blends B20 and B40 which show improvement in BTE and CO; UBHC and smoke opacity are reduced. At 10–15% EGR, BTE increased and 20% slightly decrease. With the increase of EGR ratio NO<sub>x</sub> lesser and remaining increases simultaneously.

## 2 Material and Method

### Preparation of biodiesel using transesterification with Al<sub>2</sub>O<sub>3</sub>:

Oils are categories into two types: edible and nonedible oils [1]. Collect 500 g sample oil heated in a reactor at 95.7 °C. 8.5% molar ratio (methanol to sample oil) and catalysts of 0.3% to the oil used. Slowly add 0.1 g CaO–MgO (12.5 wt%) (8:2)/Al<sub>2</sub>O<sub>3</sub> to the mixture maintaining reaction temperature 95 °C during transesterification process. Figure 1 shows the SEM and TEM of Al<sub>2</sub>O<sub>3</sub> (Fig. 2).

## 3 Experimental Setup

Naturally aspirated single-cylinder diesel engine with exhaust gas recirculation setup as shown in Fig. 3. CI engine specifications are given Table 1 and exhaust emissions ranges and accuracy are listed in Table 2.



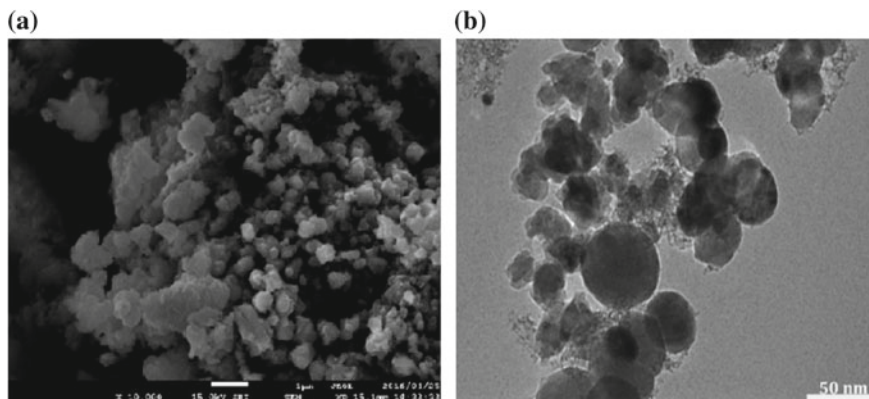


Fig. 1 Images of Al<sub>2</sub>O<sub>3</sub> SEM and TEM [9]

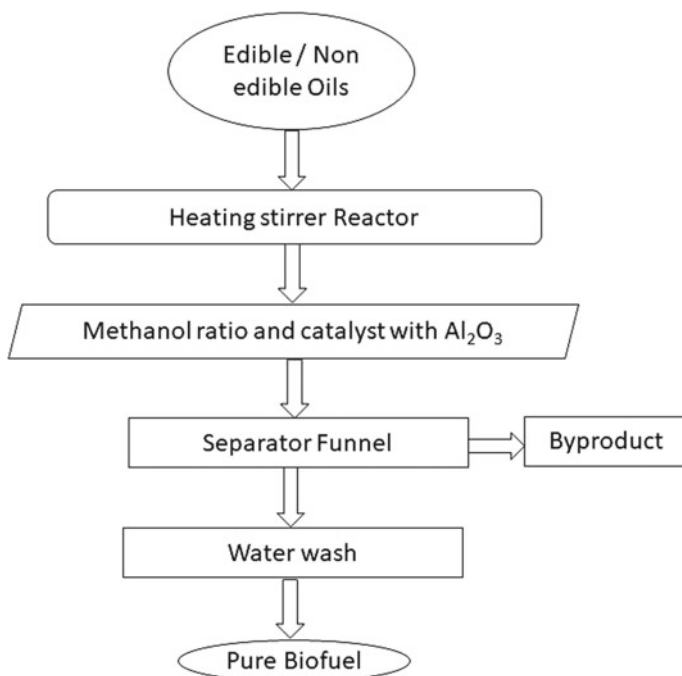
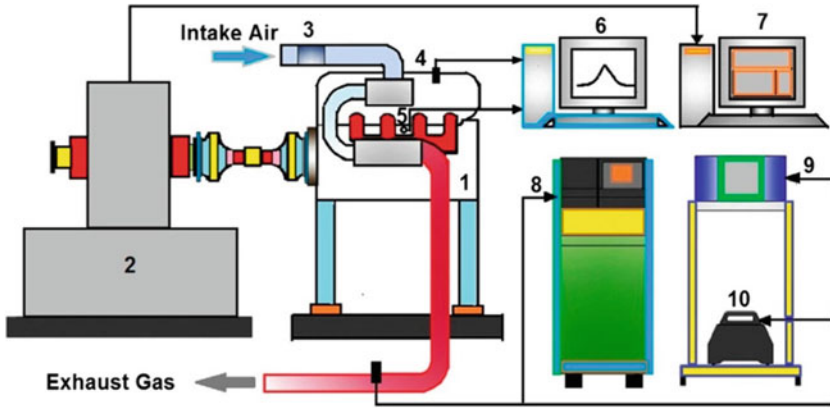


Fig. 2 Schematic sketch of biodiesel preparation [10]



- 1. Test engine
- 2. Eddy current dynamometer
- 3. Air mass sensor
- 4. Pressure sensor
- 5. Accelerometer
- 6. Data acquisition system (DAS)
- 7. Dynamometer controller
- 8. Bosch gas analyser
- 9. AVL digas analyser
- 10. Smoke opacity meter

Fig. 3 Schematic of the test engine

Table 1 Specification of the experimental setup

Make, model	TMEC-10
Stroke	2
Cylinder	1
Rated power	5.12 kW
Rated speed	1500 rpm
Number of spark plug	1
Bore dia (D)	87.5 mm
Stroke (L)	110 mm
Compression ratio	17.5:1
No. of injectors	1
Injection timing	23°BTDC
Injection pressure	200 bar

Table 2 Range and accuracy details of exhaust gas analyzer

Pollutant	Range	Accuracy
CO	0–15.0 vol. %	0.01 vol. %
HC	0–30,000 ppm vol.	±1 ppm vol.
NOx	0–5000 ppm vol.	±1 ppm vol.
Smoke metre	0–100%	±1%

## 4 Result and Discussions

The EGR is the viable technique and generally used to diminish NOx for CI engines fuel powered by diesel and biodiesels. In this method, the division of CO<sub>2</sub> gas is presented in the burning chamber so as to build the explicit warmth limit of the gas blend which thus decreases the burning temperature. The usage of EGR is the least expensive and most straightforward technique for diesel engines for a compelling decrease of NOx. Exhaust gas distribution rate can be balanced with the assistance of a control valve fitted in the admission complex. Hot EGR strategy is utilized in the present work for NOx decrease. The stream rate of EGR is assessed by assessing the CO<sub>2</sub> fixation in the admission and exhaust ventilation manifold system [7].

The EGR equation:

$$EGR (\%) = \frac{\% \text{ of } CO_2 \text{ Intake}}{\% \text{ of } CO_2 \text{ Exhaust}} \times 100$$

### 4.1 Brake Specific Fuel Consumption

For comparing both Figs. 4 and 5—Coconut and Cottonseed oil fuels—the EGR percentage increases the brake specific fuel consumption reduces due to three factors initially reduces the pumping work, loss of heat reduced in cylinder wall secondly and finally higher in dissociation degree reduction the temperature is gray gases. At initial loads, nano coconut oil shows better performance and the load increases nano cottonseed showed better improvement at 15% EGR.

**Fig. 4** Load versus BSFC (cotton oil)

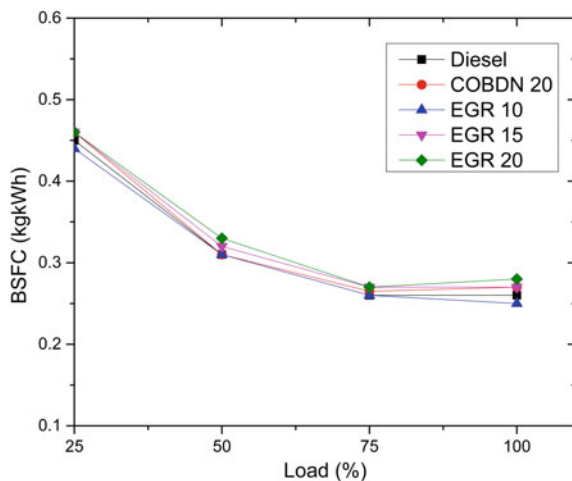
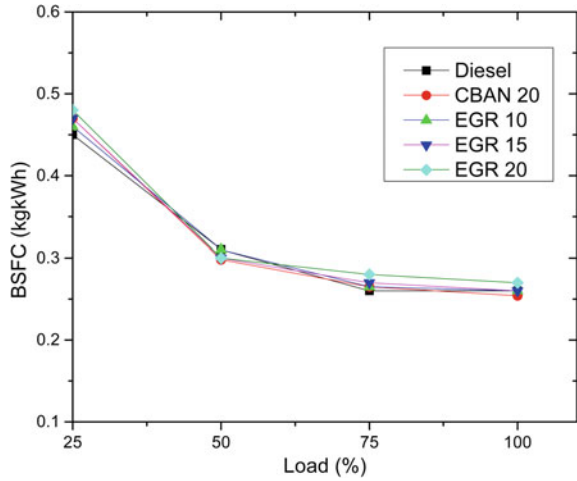


**Fig. 5** Load versus BSFC (coconut oil)



### 4.2 Brake Thermal Efficiency

Figures 6 and 7 show the load versus brake thermal efficiency. When the EGR ratio increases the unburned hydrocarbons are recharged and the fresh charge enters the manifold. The dilute gases become a homogenous mixture with intake fuel and rise the temperature of the mixture; it will increase the burning rate and better improvement in combustion and reduction in emissions. But when the dilution rate increases, the oxygen content reduces which leads to reduction in the combustion rate because at higher loads the CO<sub>2</sub> high in exhaust gases it leads to incomplete combustion. It was noted that at 15% EGR shows a better improvement when compared to 20% ration but lower than the conventional fuel due to lower calorific value.

**Fig. 6** Load versus BTHE (cotton oil)

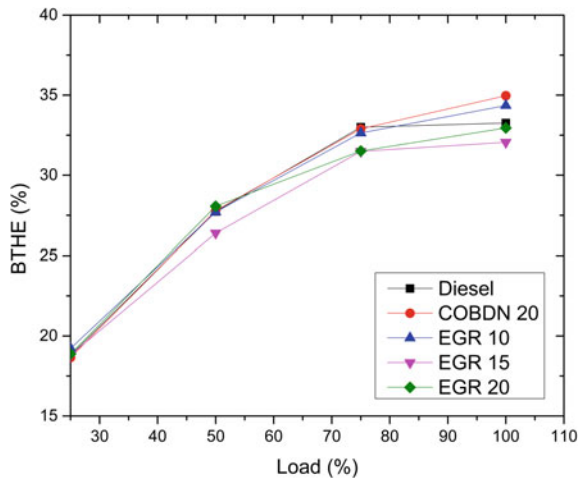
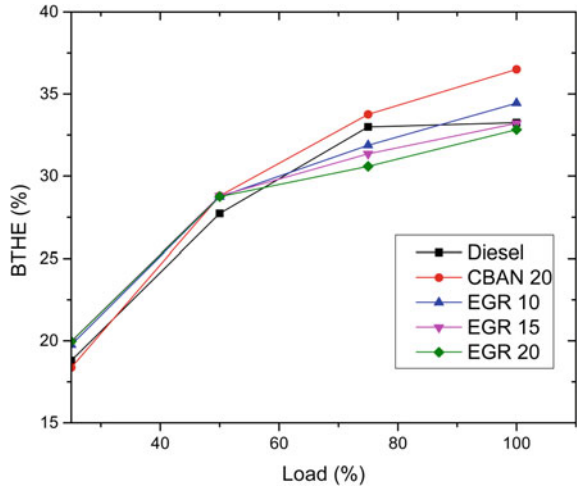


**Fig. 7** Load versus BTHE (coconut oil)



### 4.3 Emissions

In biofuels, oxygen percentage is more and the combustion rate also increases while the experimentation noticed that the combustion temperature and NO<sub>x</sub> increases. Dilution of oxygen with exhaust gases is one of the solutions for controlling NO<sub>x</sub>. Figures 8 and 9 show the percentage of EGR increase with a decrement of NO<sub>x</sub> monition. At 20% EGR, NO<sub>x</sub> will drop in an impressive way.

Oxygen status is more generally in biofuel it effuses less amount of hydrocarbons. Figures 10 and 11 show that the slightly increased when the EGR rate increases. If the percentage of dilution of fresh charge increases, it leads to nonhomogeneous mixture

**Fig. 8** Load versus NO<sub>x</sub> (cotton oil)

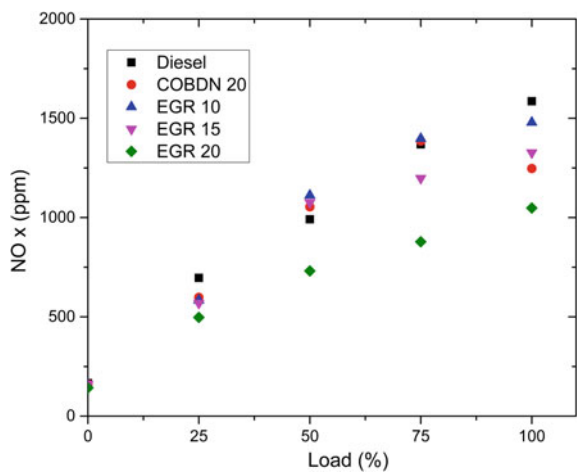


**Fig. 9** Load versus NOx (coconut oil)

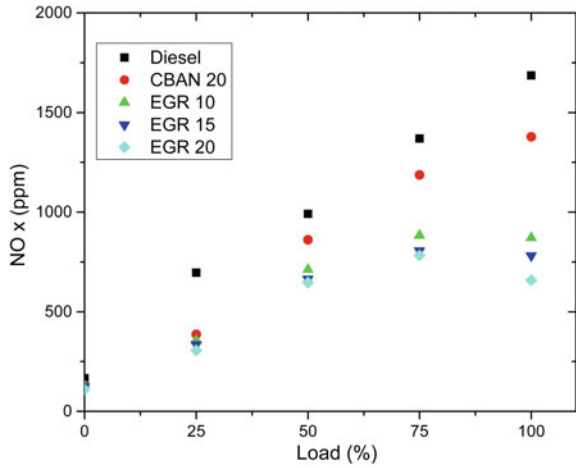
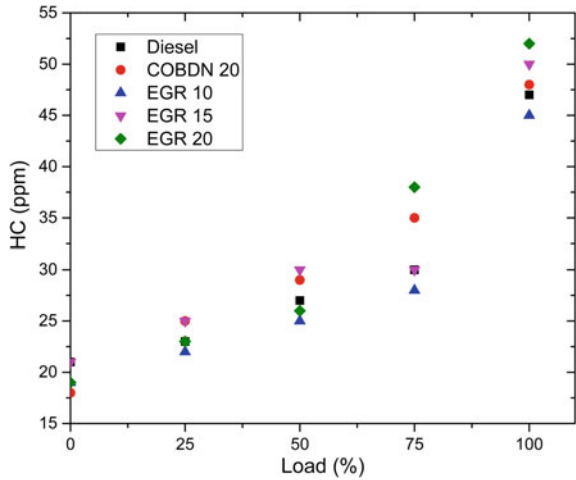


**Fig. 10** Load versus hydrocarbon (cotton oil)



and incomplete combustion may occur inside the combustion chamber. Incomplete combustion causes rise of unburnt hydrocarbon.

Generally, by using biofuels in diesel engines, the combustion rate is high where maximum amount of carbon and hydrogen molecules are converted to energy gets higher thermal efficiency and it prevents the smoke particles formation in diesel engine when compared to diesel. Due to the dilute mixture rate, the lack of oxygen inside the combustion the burning rate will reduced which primes to incomplete combustion and the combustion rate also falls down at Figs. 12 and 13 show the increase in smoke at EGR 15% more stable and show better emission rate.

**Fig. 11** Load versus hydrocarbon (coconut oil)

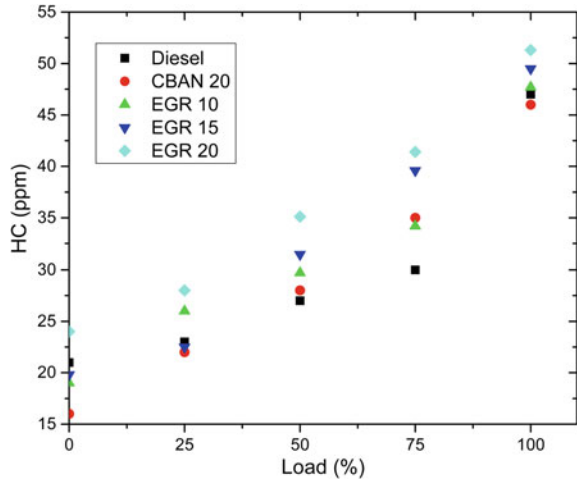
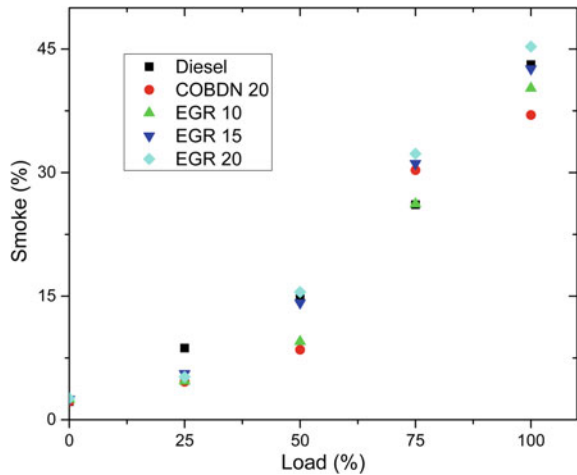


**Fig. 12** Load versus smoke (cotton oil)

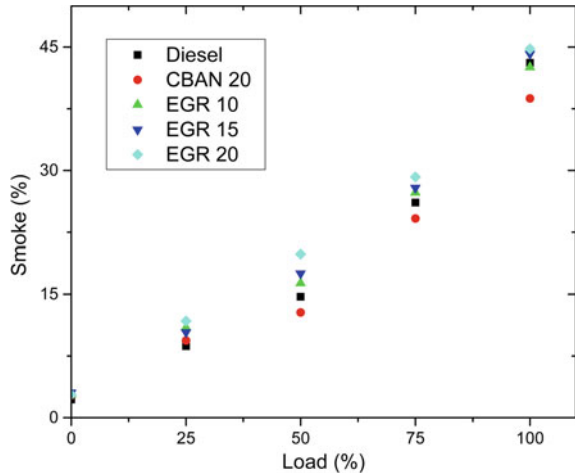


## 5 Conclusion

The negotiation drawn from the present investigation on single-cylinder CI engine with Cottonseed oil and Coconut oil with an EGR rate of 0, 10, 15, and 20% summarizes the following:

1.  $Al_2O_3$  can be used as a catalyst; it improves the properties of diesel and reduces the moisture content in biofuel when compared to KOH catalyst.
2. When compared to diesel without modification, HC and smoke are diminished and with high combustion rate, NOx increased. It may be concluded that the combination of biodiesel B20 by volume can replace the diesel, which will help

**Fig. 13** Load versus smoke (coconut oil)



control the exceptions of NO<sub>x</sub> drop in performance. Operating parameters have been changed to improve engine performance.

- At 15% EGR, BSFC and BTHE are improved and at 20% EGR showed lesser performance compared to diesel.
- NO<sub>x</sub> was reduced at 20% EGR rate and HC smoke slightly increased.

## References

- Venkatesh B, Prasanthi G (2018) Detailed analysis on emission and performance characteristics of neat biofuel-fuelled diesel engine. *International Journal of Ambient Energy*: 1–8
- Sydbom A et al (2001) Health effects of diesel exhaust emissions. *Eur Respir J* 17(4):733–746
- Rajesh Kumar B, Saravanan S (2016) Use of higher alcohol biofuels in diesel engines: a review. *Renew Sustain Energy Rev* 60:84–115
- Sakhare NM, Shelke PS, Lahane S (2016) Experimental investigation of effect of exhaust gas recirculation and cottonseed B20 biodiesel fuel on diesel engine. *Procedia Technol* 25:869–876
- Attal MH, Mahalle AM (2016) Critical analysis of performance of compression ignition engine for biodiesel with exhaust gas recirculation 6(5):1568–1572
- Rajesh Kumar B et al (2016) Effect of a sustainable biofuel–n-octanol–on the combustion, performance and emissions of a DI diesel engine under naturally aspirated and exhaust gas recirculation (EGR) modes. *Energy Convers Manage* 118:275–286
- Suresh Babu Rao H, Venkateswara Rao T, Hemachandra Reddy K (2018) Effect of exhaust gas recirculation on a nanoparticle-doped biodiesel-and diesel-blends-fuelled diesel engine. *Int J Ambient Energy* 11:1–5
- Bedar P et al (2017) Performance and emission analysis of a single cylinder CI engine using Simarouba *glauca* biodiesel. In: *Fluid mechanics and fluid power–contemporary research*. Springer, New Delhi, pp 1519–1527



9. Benjapornkulaphong S, Ngamcharussrivichai C, Bunyakiat K (2009)  $\text{Al}_2\text{O}_3$ -supported alkali and alkali earth metal oxides for transesterification of palm kernel oil and coconut oil. *Chem Eng J* 145(3):468–474
10. Mahdavi V, Monajemi A (2014) Optimization of operational conditions for biodiesel production from cottonseed oil on  $\text{CaO-MgO/Al}_2\text{O}_3$  solid base catalysts. *J Taiwan Inst Chem Eng* 45(5):2286–2292

# Thermal Analysis of Drilled and Slotted Brake Rotors



Jatin Parajiya, Kaustubh Babrekar, Saurabh Bairagi and Arvind Chel

**Abstract** Brakes are a very vital part of an automobile and with performance, safety and operational life being the most important characteristic, it becomes necessary to have a smooth braking operation throughout its life. The study is focused towards designing, analysing and comparing the result obtained using software Solidworks and ANSYS. Depending upon the usage and purpose, we compare namely two types of brake rotors, drilled and slotted, and suggest where it can be put into use for maximum output by studying its thermal analysis (heat generated) without any structural failures in both the rotors.

**Keywords** Disc brake rotors · FEA · ANSYS · Heat transfer

## 1 Introduction

The heat generated during braking should be conveyed properly to ensure the safe operation of the brakes. The coefficient of friction tends to reduce as the brake pads and liners temperatures increase and brake fade starts to occur [1]. Higher temperature of the contact surfaces may result in complete loss of braking performance, thereby increasing the stopping distance and loss of vehicle control. Therefore, it becomes a crucial task to design a proper brake rotor with high heat dissipation capacity [2].

---

J. Parajiya (✉) · K. Babrekar · S. Bairagi · A. Chel  
Department of Mechanical Engineering, MGM Jawaharlal Nehru Engineering College,  
Aurangabad, India  
e-mail: [jatinparajiya196@gmail.com](mailto:jatinparajiya196@gmail.com)

K. Babrekar  
e-mail: [kaustubh.babrekar@gmail.com](mailto:kaustubh.babrekar@gmail.com)

S. Bairagi  
e-mail: [saurabh.bairagi.434@gmail.com](mailto:saurabh.bairagi.434@gmail.com)

A. Chel  
e-mail: [dr.arvindchel@gmail.com](mailto:dr.arvindchel@gmail.com)

## 2 Literature Review

This literature is based on the examination of brake rotors under the similar braking condition and comparing the temperature distribution. The material selected for rotors is grey cast iron. The operating range of brake rotors is up to 450 °C. For better heat dissipation, more surface area is required so that brake fade would not occur and maximum cooling efficiency is achieved [3]. Material is opted considering many factors like mass of the vehicle, kinetic velocity, heat flux and cost associated with manufacturing [4, 5].

## 3 Types of Brake Rotors

### 3.1 Solid and Ventilated Rotor

The surface of the rotor is a plane without any cavities. Plane rotors are strong and hence have less deformation as compared to the other types of discs but do not support quick heat dissipation (Fig. 1). A vented rotor is two solid rotors separated by a certain space so as to allow more passage for airflow, as shown in Figs. 2 and 5. Vented rotors allow air to flow much more efficiently than the non-vented rotors due to the centrifugal action created during the rotation of the rotors.

**Fig. 1** Solid rotor



**Fig. 2** Solid ventilated rotor



**Fig. 3** Drilled rotor**Fig. 4** Slotted rotor

### ***3.2 Cross Drilled Rotor***

Holes are made on the surface of disc, as shown in Fig. 3. Holes that are provided on the surface help in removing the gases, steam, etc. developed during braking to escape through it.

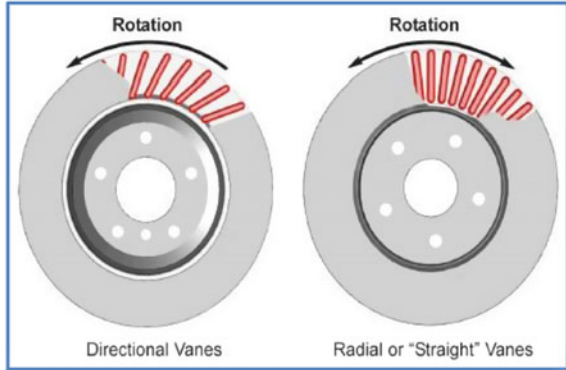
### ***3.3 Slotted Rotor***

Slotted rotors come with slots engraved on the surface of the plane disc which allow the dust and gases generated during braking to escape easily through the slots provided as shown in Fig. 4. Thus, they are mostly used for race applications [6].

### ***3.4 Geometric Cross Section of Rotors***

Vented rotors generally have straight vanes propagate from the centre to the outside of the rotor as seen in Fig. 5. Some cars come equipped with rotors that have directional vanes [7]. If the slots on the rotor are in the same direction as the cooling vanes on the inside, then the slots must bend backwards [8].

Fig. 5 Type of vanes



### 4 Design of Brake Rotor

The brake rotors seen in Fig. 6 and Fig. 7 were modelled using SOLIDWORKS. The outer and inner diameters of the brake rotor were assumed to be 280 and 150 mm, respectively. The dimension of the hub is taken accordingly. The brake pad dimensions are taken as, outer radius 121 mm, inner radius 106 mm and length 85 mm [9].

Fig. 6 Slotted rotor

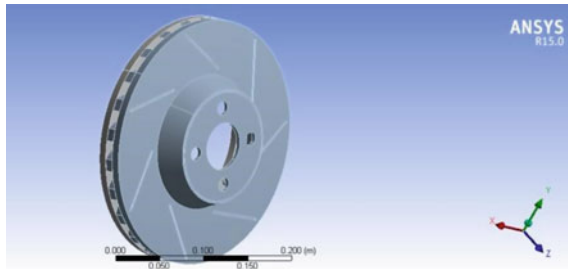
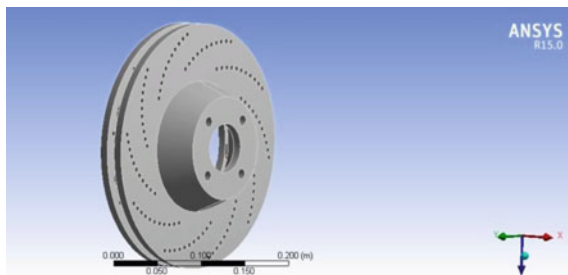


Fig. 7 Cross-drilled rotor



## 5 Heat Flux Calculations

(See Table 1)

$$\text{Total force generated during braking} = M \times a \quad (1)$$

According to Newton's first equation of motion:  $v = u + at$ ,

$$\therefore 0 = 33.33 + a(2.5); \therefore a = -13.332 \frac{\text{m}}{\text{s}^2}$$

Using Newton's second equation of motion:

$$s = (u \times t) + \frac{at^2}{2}; \therefore s = 41.6625 \text{ m} \quad (2)$$

$$F = M \times a = 1400 \times 13.332 = 18665 \text{ N}$$

$\therefore$  Torque required for stopping the vehicle:

$$T_r = \frac{F}{4} \times R_t; \therefore \frac{18665}{4} \times 0.2286 = 1066.70 \text{ Nm} \quad (3)$$

We know that

$$\text{Kinetic Energy K.E.} = 1/2 m \times u^2, \quad (4)$$

**Table 1** Input parameters

Input parameters	Values
Inner disc radius ( $R_1$ ), mm	75
Outer disc radius ( $R_2$ ), mm	140
Disc thickness ( $T_h$ ), mm	18
Vehicle mass ( $M$ ), kg	1400
Initial speed ( $u$ ), m/s	33.33
Deceleration ( $a$ ), $\frac{\text{m}}{\text{s}^2}$	13.332
Stopping time ( $t$ ), seconds	2.5
Effective rotor radius $R_{\text{rotor}}$ , mm	113.5
Torque ( $T_r$ ), N-m	2133.40
Surface of the pad ( $A_c$ ), $\text{mm}^2$	1998
Surface area of disc swept by pad ( $A_d$ ), $\text{mm}^2$	3405
Maximum temperature ( $T_{\text{max}}$ ), $^{\circ}\text{C}$	350
Maximum pressure ( $P_{\text{max}}$ ), MPa	4

$$\therefore 1/2 \times 1400 \times 33.33^2 = 777622.23 \text{ J} = \text{K.E.}$$

Also normal force for pad and rotor:

$$F_N = \left( \frac{P_{\max}}{2} \right) \times A_c \quad (5)$$

Assumed  $\mu = 0.5$ , tangential force on inner surface:

$$F_{T_I} = \mu \cdot F_N = (0.5) \times (0.5) \times \left( 4 \times \frac{10^6}{2000 \times 10^6} \right) = 2 \text{ KN}$$

Tangential force for outer face,  $F_{T_O}$  is equal to  $F_{T_I}$  because of the same normal force and the same material [10].

Total normal forces on disc brake:

$$F_T = F_{T_I} + F_{T_O} = 4000 \text{ N} \quad (6)$$

Braking torque,  $T_B = F_T \times R$ , where

$$T_B = (4000) \times (120 \times 10^{-3}) = 480 \text{ Nm}$$

Heat generated is  $Q = m \cdot Cp \cdot \Delta T$

Developed temperature difference  $\Delta T = 100^\circ \text{C}$

$$Q = m \times 460 \times 100$$

$M_s$ : Mass of slotted rotor = 1.203 kg

$M_{cd}$ : Mass of cross-drilled rotor = 1.125 kg

$$Q_s: 1.125 \times 460 \times 100 = 51,750 \text{ W}$$

$$Q_{cd}: 1.203 \times 460 \times 100 = 55,338 \text{ W}$$

$$\begin{aligned} \therefore \text{Area of generation of heat} &= 2\pi(R_2^2 - R_1^2) \\ &= 2\pi(0.140^2 - 0.075^2) = 0.08776 \text{ m}^2 \end{aligned} \quad (7)$$

For calculating heat flux ( $q$ ), we know that

$$\text{Heat flux } (q) = \frac{\text{Heat generated}}{\frac{\text{Area}}{\text{Second}}}$$

$$\therefore q = \frac{Q_{disc}}{20} \text{ KW/m}^2 \quad (8)$$

Using Eq. (8), we can calculate the heat flux for the rotors.

$$\therefore q_{\text{cross-drilled}} = \frac{51750}{\frac{0.08776}{20}} = 29.484 \text{ KW/m}^2$$

$$\therefore q_{\text{slotted}} = \frac{55338}{\frac{0.08776}{20}} = 31.528 \text{ KW/m}^2$$

The value of the heat flux obtained after calculation for the drilled rotor is 29.484 KW/m<sup>2</sup> and that of slotted rotor is 31.528 KW/m<sup>2</sup>.

## 6 Structural Analysis of Rotors

Static analysis of the brake rotor is performed and the results obtained are discussed below.

The analysis shown in Fig. 8 depicts that the equivalent stress is minimum at the hub and the value is slightly more at the surface of the disc. Figure 9 shows the total deformation which gradually decreases from the outer radius of the disc to the hub [11]. Equivalent strain and total deformation for drilled rotors are seen in Fig. 10 and Fig. 11 respectively.

**Fig. 8** Equivalent stress in drilled rotor

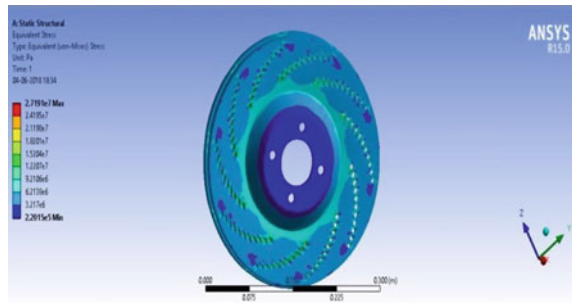


**Fig. 9** Total deformation in drilled rotor

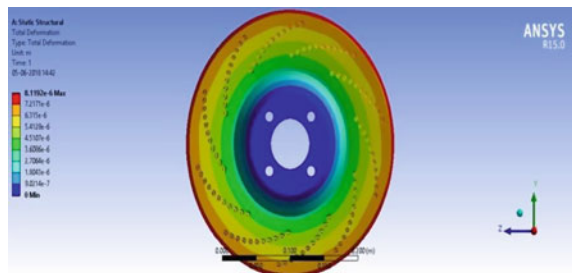




**Fig. 10** Equivalent strain in drilled rotor

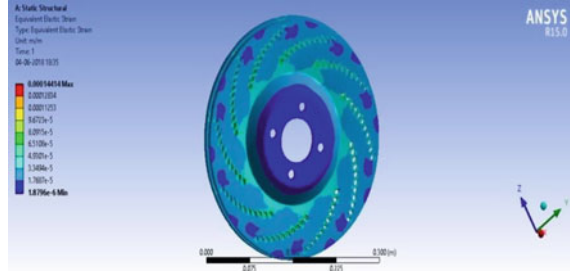
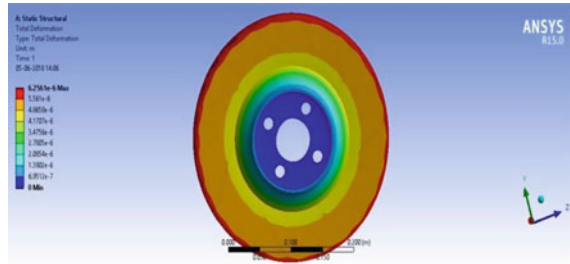


**Fig. 11** Total deformation in slotted rotor



## 7 Steady-State Thermal Analysis of Brake Rotors

### 7.1 Steady-State Thermal Analysis of Cross-Drilled Rotor

In Fig. 12, the total heat flux is minimum at the hub and outer radius of the rotor and is merely more at the surface. Figure 13 shows the different regions of temperature across cross-drilled rotor [12] and the maximum temperature obtained is 474.73 °C.

**Fig. 12** Total heat flux in drilled rotor

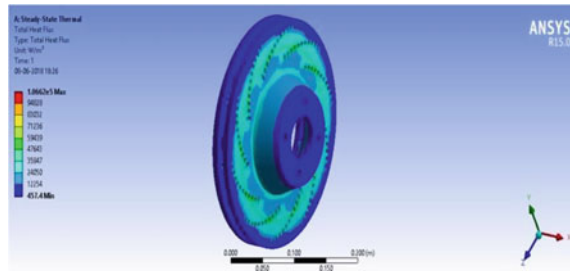
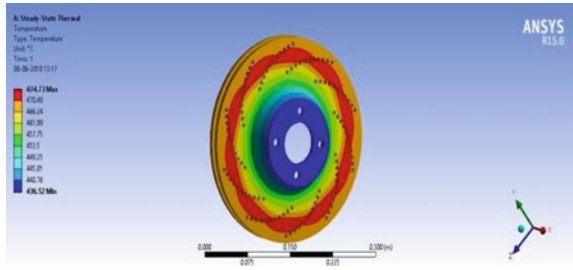


**Fig. 13** Temperature distribution in rotor



### 7.2 Steady-State Thermal Analysis of Slotted Rotor

The total heat flux is least at the outer radius of the rotor [13] which is shown in Fig. 14. Figure 15 shows the different regions of temperature across cross-drilled rotor and the maximum temperature obtained is 492.61 °C.

**Fig. 14** Total heat flux in slotted rotor

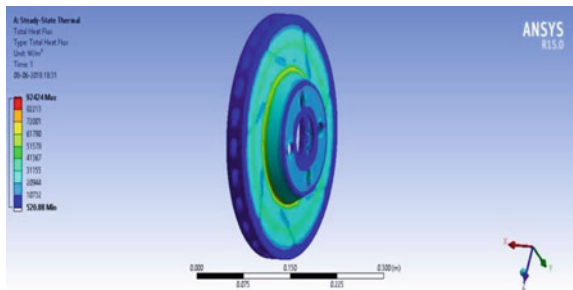
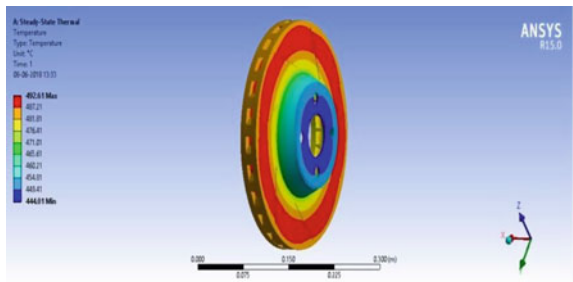


**Fig. 15** Temperature distribution in rotor



## 8 Conclusion

From the analysis reports and the results obtained, it is found that cross-drilled and slotted rotors are structurally safe as the total maximum stress is within the ultimate stress limits for the material used which is grey cast iron. According to the solutions obtained from ANSYS, it shows that the temperature range over the drilled and slotted rotor is almost the same and is the least at the centre of the rotor. The maximum temperatures produced on the rotors are 474.73 and 492.61 °C in cross-drilled and slotted rotors, respectively. The value is greater for the slotted disc because of the greater amount of frictional heat produced due to the presence of slots (more surface area under contact). The main aspect of this study was to find the temperature distribution over the disc and it is highly recommended to use slotted rotor for race applications and drilled rotor for commercial use.

## References

1. Kurkure B, Sadaphale DB (2015) *Int J Mech Ind Technol* 3(1):175–183. ISSN 2348-7593 (Online)
2. Day AJ (2014) *Braking of road vehicles*. Butterworth-Heinemann Ltd, Oxford, UK
3. Milliken WF (1995) *Race car vehicle dynamics*. SAE International, Warrendale, PA, ISBN I56091-526-9
4. Maleque M, Rahmman MM (2010) Material selection in design of brake disc. World Congress on Engineering, London
5. Saidpour H (2004) Lightweight high performance materials for car body structure. In: NTI Technology Conference, CEME, Ford Motor Company, 16 June 2004
6. Jawarikar P, Khan S, Kshirsagar B (2016) Structural optimization, thermal and vibration analysis of two wheeler disc brake rotor. *Int J Innovative Res Sci Eng* 2(8):169–186
7. Ali B, Mostefa B (2012) Simulation of fully coupled thermomechanical analysis of disc brake rotor. *WSEAS Trans Appl Theor Mech* 3(7): 169–181
8. Hwang P, Wu X, Jeion YB (2008) Repeatative temperature analysis of ventilated brake disc. SAE 2008-01-2571
9. Data records, Team VAAYU (2016) FSAE Team MGM's Jawaharlal Nehru Engineering College
10. Bhandari VB (2015) *Design of machine elements*. Tata McGraw Hill, New Delhi
11. Davis W (2012) Design and optimization of a formula SAE racecar by faculty of Worcester Polytechnic Institute. MQP-DCP2012-A11-D12
12. Choi JH, Lee I (2004) FEA of thermo elastic behaviors in disk brake. *Wear* 257(1):47–58
13. Adamowicz A, Grzes P (2011) Three-dimensional FE model of frictional heat generation and convective cooling in disc brake. *Comput Methods Mech* 9–12. Warsaw, Poland

# Non-premixed Combustion Analysis on Micro-Gas Turbine Combustor Using LPG and Natural Gas



Ch. Indira Priyadarsini, A. Akhil and V. Srilaxmi Shilpa

**Abstract** Gas turbine effectiveness is mainly having an effect on design of combustor; in this work, studies have been made on different parameters of a typical micro-gas turbine (MGT) that changes the flow inside the burning area. A combustion room is created by utilizing SOLIDWORKS modeling tool and exported to workbench design modeler where computational fluid dynamics analysis is performed by ANSYS fluent. We considered a probability density function (PDF) of LPG fuel with non-premixed combustion mode and activated in radiation model of P-1. Design criterions of chamber height and number of holes on flame tube are varied to get the optimum performance and also considered as two dead zones in between the combustion and dilution zone. The optimized design chamber resulted in a turbine inlet temperature (TIT) of 1301 °K with a velocity of 620 m/s and also is provided with low NOx emission below 54 ppm.

**Keywords** Micro-gas turbine · Radiation P-1 · CFD fluent · Non-premixed

## 1 Introduction

Energy is a crucial property in order to run any machine, one of the highest forms is an electrical mode which is easily transferred over a long stretch and can be generated almost anywhere by using proper technology. Solar PV cells or lenses, windmills, turbines, both steam and gas, nuclear and hydro are some of the mechanisms that produce energy. Out of all, gas turbine has its own merits over other types; therefore, it focuses on this aspect; it gives electrical power from the burning of inflammable fuels such as petroleum products, hydrogen gases, and air mixture; when the mixture burns, the

---

Ch. Indira Priyadarsini (✉) · A. Akhil · V. S. Shilpa  
Mechanical Engineering, C.B.I.T, Hyderabad, Telangana, India  
e-mail: [med.amere13@gmail.com](mailto:med.amere13@gmail.com)

A. Akhil  
e-mail: [ailaboinaakhil@gmail.com](mailto:ailaboinaakhil@gmail.com)

V. S. Shilpa  
e-mail: [srilaxmishilpa@gmail.com](mailto:srilaxmishilpa@gmail.com)

© Springer Nature Singapore Pte Ltd. 2020  
G. S. V. L. Narasimham et al. (eds.), *Recent Trends in Mechanical Engineering*,  
Lecture Notes in Mechanical Engineering,  
[https://doi.org/10.1007/978-981-15-1124-0\\_6](https://doi.org/10.1007/978-981-15-1124-0_6)

volume of the gas will increase which results in the expansion of gas volume, in turn, it rotates a turbine rotor in the form of mechanical energy and it may be converted to electrical energy.

Axial flow machines are used for power demand of above 500 kW, but MGT is utilized for small-scale power generation that ranging from 20 to 500 kW, having advantages of being more compact, durable, and flexible compared to other modes with the capability of handling the small flow amounts with higher efficiency. It runs at towering speeds and is suitable when combined with heat and power systems giving the overall high efficiency. In combustion chamber, two major incidents take place, fuel will mix thoroughly at the inlet to a considerable amount with air; in order to get a laminar flow, the burning fuel mixes with air just before combustion process started in some combustors; however, fuel and air should be mixed before burning. It relay on at what time fraction fuel will mixes with air in the combustor, due to the high temperature in combustion chamber the gaseous blend move on to increase the temperature this will increase volume which will drive the fluid further. The plan of a burning chamber is dependent on temperature homogeneity, and CO discharge is a basic issue in the advancement of MGT. Albeit, some normal plan and exploratory investigations on various smaller scale combustor arrangements were done before; there is requirement for further structure and advancement to enhance major issues, for example, low outlet temperature and CO discharges.

Paolo Laranci developed a new annular RQL combustion chamber of an 80kQw1 Elliott TA80R MGT by utilizing CFD techniques for combustion of natural gas and studied modified designs to control the failure of cylinder at short running hours caused by overheating [1]. Ibrahim I Enagi varied length of combustion areas by manipulating the dimensions and number of holes between each row and also analyzed experimentally the same design results which showed that CO emissions below 100 ppm at an exhaust temperature around 1123 °K when burnt with LPG as fuel [2]. The addition of H<sub>2</sub> does not improve the combustion efficiency when the gas turbine is tested with natural hydrogen gas mixtures [3]. When compared with LES and URANS approaches for modeling of turbulence, it is noted that LES-based approaches provide better accuracy than the URANS [4] and hence we carried LES approach in this current work. Under low-velocity conditions, there is a possibility of combustion instability because of the phase delay of heat release, and dynamic pressure in low-velocity conditions [5]. Natural gas, when compared to other solid, liquid or gaseous fuels, offers a cleaner and more environmentally friendly combustion. Nevertheless, it also produces unwanted pollutant species such as nitrogen oxides (NO<sub>x</sub>) and carbon monoxide (CO) when fired in combustors of industrial gas turbines under high temperature and pressure. These emissions, NO<sub>x</sub> and CO, are harmful to humans and nature and need to be kept below the regulatory limits [6].

## 2 Design of Combustion Chamber

### 2.1 Design of the Combustor Using Modeling Tool

The combustion chamber is constituted of two elements which are an air jacket and a flame tube that has fixed 100 mm height at conical exit; in order to meet the specifications of the turbocharger, inlet and outlet diameters of the chamber are decided about 50.8 mm which is shown in Fig. 1; for better combustion, the length, number of hole rows in flame tube, and diameters of holes are varied, along with changing the dead zone condition between combustion and dilution phase. Flame tube diameter is fixed to 50 mm condition while chamber length is varied from 300 to 800 mm; three zones of combustion were identified on the flame tubes that are pre-mix zones, primary combustion zone, and the dilution zone. Studies were made for different arrangements of hole diameters on flame tube: one is 6, 8, and 10 mm and the other is 8, 10, and 12 mm, where the number of holes in each row is fixed to 8 to get proper stability in simulations.

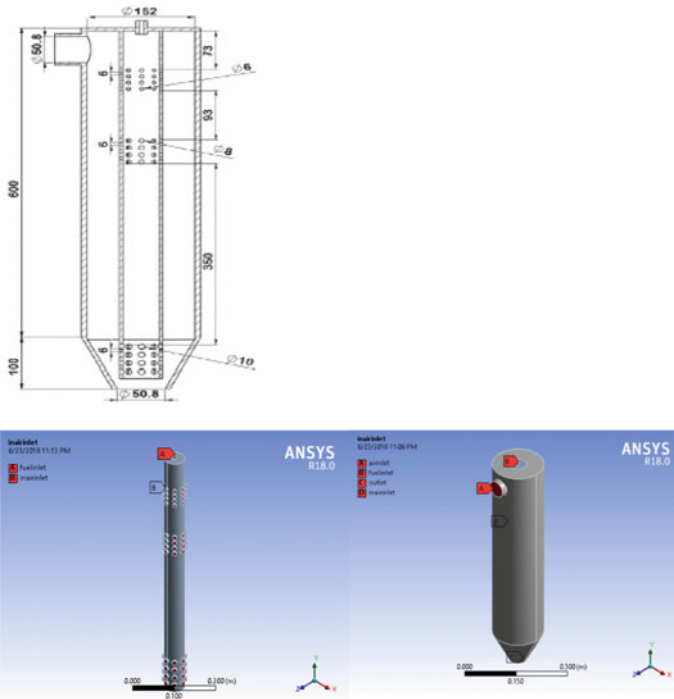


Fig. 1 Combustion chamber model with boundary names

## 2.2 Simulations Using CFD Technique

Combustion chamber design was optimized using ANSYS 18.0 CFD commercial tools in which geometry was imported to the design modeler from SOLIDWORKS in a step format. The fine-structured mesh is created that is fixed in all cases, and then three-dimensional analyses were conducted. A non-premixed combustion model was tested for two fuels of LPG (butane/propane) and natural gas; composition of working fluids is shown in Tables 1 and 2, air inlet boundaries are taken from the literature of Ibrahim [2] and the boundary conditions used for the simulations are shown in Table 3.

To get steady and stable combustion, a broad knowledge is required of the turbulent models through CFD simulation; moreover, the accuracy of this analysis is highly dependent on the turbulence and combustion modes. The non-premixed combustion was applied to predict diffusion flames as it employed assumptions of a good chemical reaction; probability density function (PDF) of LPG and natural gas fuels were assumed separately. Radiation heat transfer inside the chamber was applied by radiation P1 model which has stainless-steel wall boundary with emissivity of 0.5 as it has a positive effect on combustion through additional heat to burn the remaining unburned carbon. The PDF table was calculated with fuel and oxide temperatures as 315 and 530 °K, typical PDF table with 700 mm chamber height configuration and four rows 6, 8, 10 mm hole diameter with LPG as fuel is shown in Fig. 2.

Further NO<sub>x</sub> display is enacted with thermal and prompt NO<sub>x</sub> pathways with as species and in disturbance collaboration mode held the default choice of beta from PDF type drop-down rundown and we accepting 20 as PDF focuses to acquire progressively exact NO<sub>x</sub> expectation, and chose transported from drop-down rundown as the temperature difference and took fuel carbon number as 1 and identicalness proportion as 0.76 for brief NO<sub>x</sub>. The accompanying rundown demonstrates the arrangement techniques considered to take care of the issue:

**Table 1** Fuel composition of LPG in molar fraction

Species	Mole fraction
C <sub>3</sub> H <sub>8</sub>	0.295
C <sub>4</sub> H <sub>10</sub>	0.7
C <sub>5</sub> H <sub>12</sub>	0.005

**Table 2** Fuel composition of LPG in molar fraction

Species	Mole fraction
CH <sub>4</sub>	0.965
N <sub>2</sub>	0.013
C <sub>2</sub> H <sub>6</sub>	0.017
C <sub>3</sub> H <sub>8</sub>	0.001
C <sub>4</sub> H <sub>10</sub>	0.001

**Table 3** Parameters set out in boundary conditions

Parameters	Values
Fuel inlet temperature	300 K
Pressure	2 bar
Mass flow rate (LPG) [20–70% excess air]	0.0053–0.0075 kg/s
Mass flow rate (Natural) [20–70% excess air]	0.0056–0.0078 kg/s
Air inlet temperature	530 K
Pressure	1.4 bar
Mass flow rate	0.15 kg/s
Outlet pressure	1.4 bar
Backflow temperature	600 K
Inner walls materials	Steel
Emissivity	0.5
Outer wall material	Steel
Thickness	6 mm

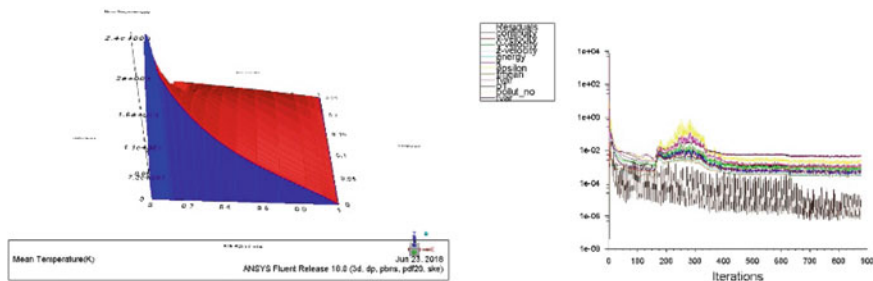


**Fig. 2** Convergence plot of nonadiabatic temperature for LPG on 700 mm 4r 6810 mm condition

Pressure–Velocity Coupling Scheme—SIMPLE  
 Gradient—Least Squares Cell Based  
 Pressure—PRESTO  
 Momentum—First-Order Upwind

The problem is initiated from the fuel inlet position and the problem is iterated till it converges.



### 3 Results and Discussions

#### 3.1 *Effect of Radiation Model*

Internal heat transfer inside the flame is mainly carried out by the forced convection by flame propagation and by natural convection causing the heat to travel vertically up to the top of the chamber. However, all air and fuel species, as well as the internal surface of the flame tube, are also heated by the radiation emitted from the flame. Radiation always has a positive effect on combustion by adding the heat to further burn the unburned CO species. Figure 3 shows the effect of radiation model on 700 mm chamber length configuration with four rows of 6, 8, and 10 mm flame tube holes diameter on LPG and Table 4 shows the turbine inlet conditions.

From the abovementioned table of results, it is clearly saying that without radiation model the results are not in acceptable limit; the emissions are high and they are reduced to more than half with radiation model with slight acceptable reduction in turbine inlet temperature for LPG, whereas for natural gas it does not show much effect in temperature and velocity but a little reduction in NO<sub>x</sub> emission levels, hence, all models are simulated with activated radiation P-1 model to get the proper results and it is easy to optimize the chamber geometry.

#### 3.2 *Effect of Dead Zone Condition*

The distance between two zones is called a dead zone, which plays a considerable role in flame stability and combustion quality. It was established earlier that four rows and 6, 8, and 10 mm has given stable combustion. Figure 4 shows the two models of the dead zone combinations, on which simulations were performed and results are compared to obtain the best optimal geometry.

Figure 5 shows the temperature contours of 700 mm four rows 6, 8, and 10 mm on LPG with two dead zone combinations.

From Fig. 5, we can clearly state that by extending the dead zone which allows most of the species to complete the reaction before it is introduced by the dilution air which will result in significant drop in CO emissions.

Also, the flame bleed in the first case is carried throughout the air jacket chamber till the end of the combustion chamber which will result in damaging the turbine blades. Hence, the second case of dead zone combination is further simulated to find the best optimal combustion chamber.

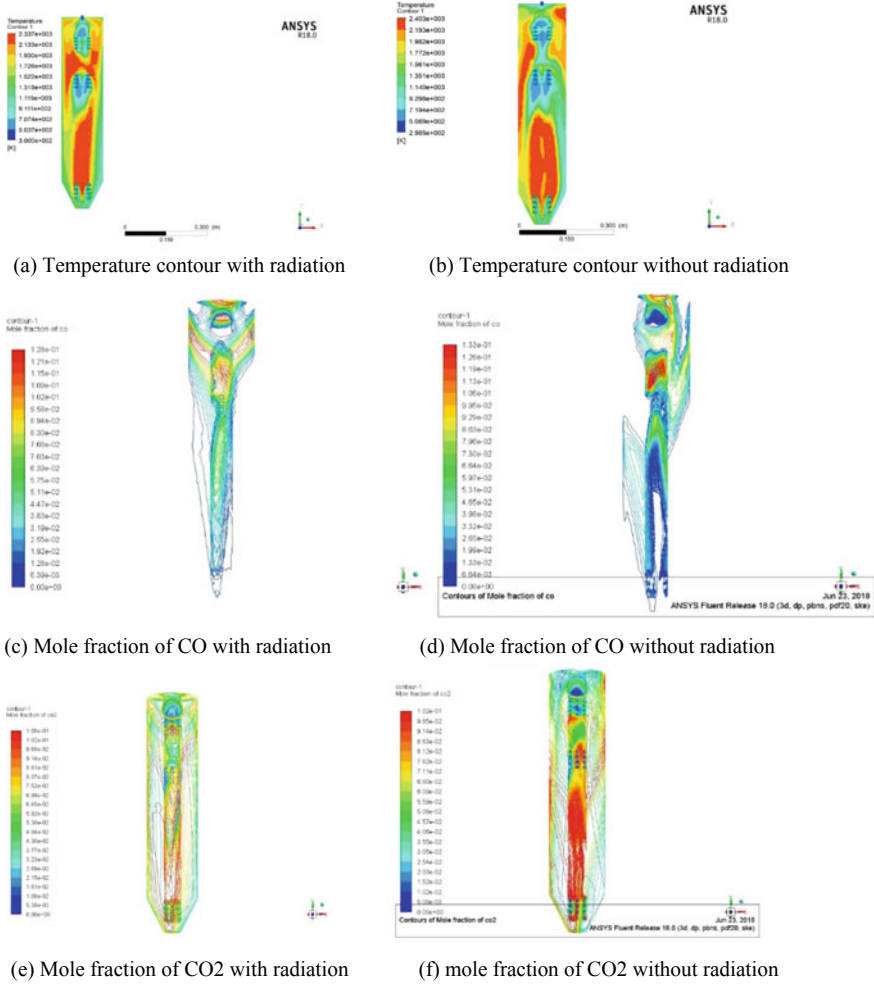


**Fig. 3** Effect of temperature, CO, and CO<sub>2</sub> species with and without radiation model

### 3.3 Effect of Number of Rows on Flame Tube

The number of rows is increased to find the optimized flame tube which is fixed with 50 mm diameter and with 6, 8, and 10 mm hole diameter for premixed, combustion, and dilution zones. The variables which are changed to optimize the flame tube are chamber length and number of rows in each zone. Figures 6 and 7 show the temperature contours of 600 mm chamber height for natural gas and LPG as fuels.

From the abovementioned results, it was noticed that increase in the number of rows increases the flame which is bleeding out to the air chamber in all cases with noticeable difference between the LPG and natural gas. From Fig. 6b, c, and d for

**Table 4** Difference of turbine inlet conditions with and without radiation model

LPG	Temperature (K)	Velocity (m/s)	NOx (PPM)
With radiation	1301.56	620.47	53.44
Without radiation	1273.54	581.321	131.30
<i>Natural gas</i>			
With radiation	1325.4	619.5	31.47
Without radiation	1354	621	46.6

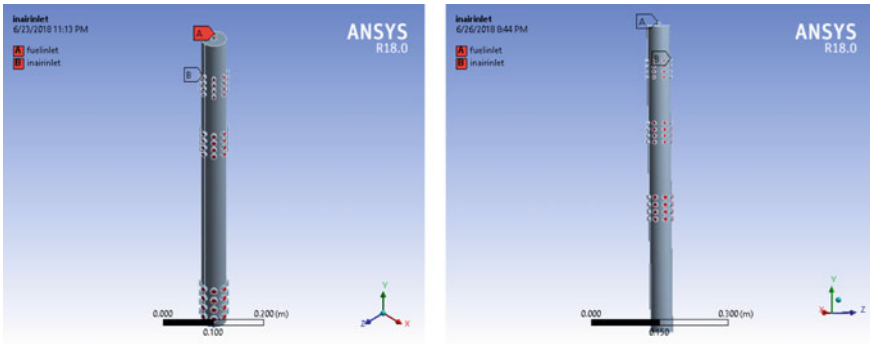


**Fig. 4** Two combinations of dead zone condition

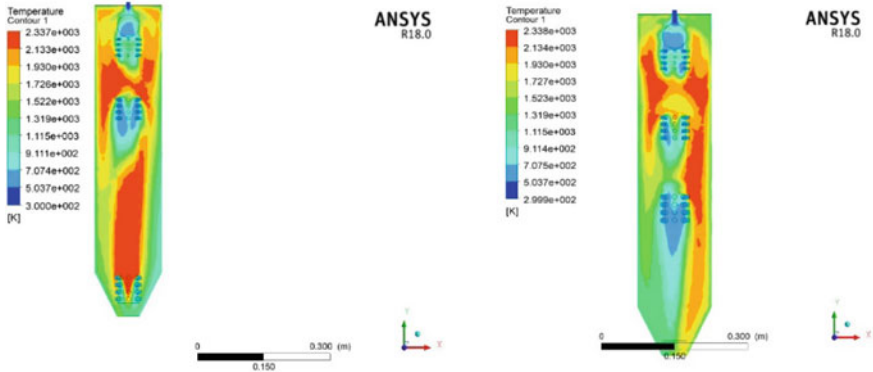


**Fig. 5** Temperature contours of 700 mm 4R 6810 mm with two dead zone conditions on LPG

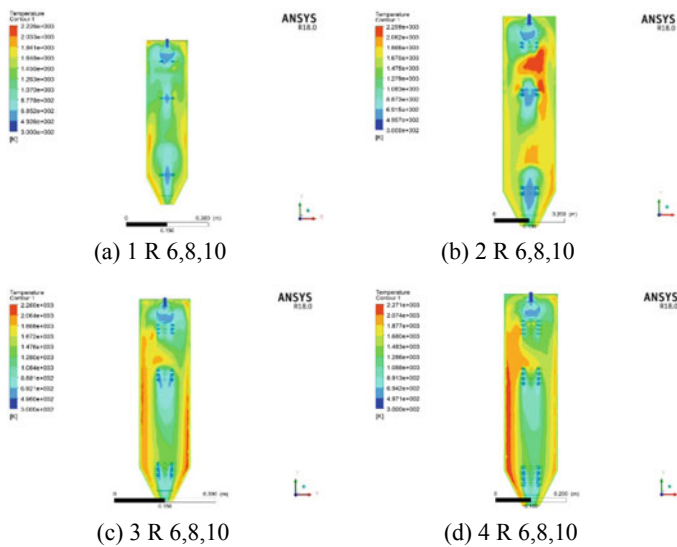


**Fig. 6** Temperature contours of 600 mm chamber height with natural gas as fuel

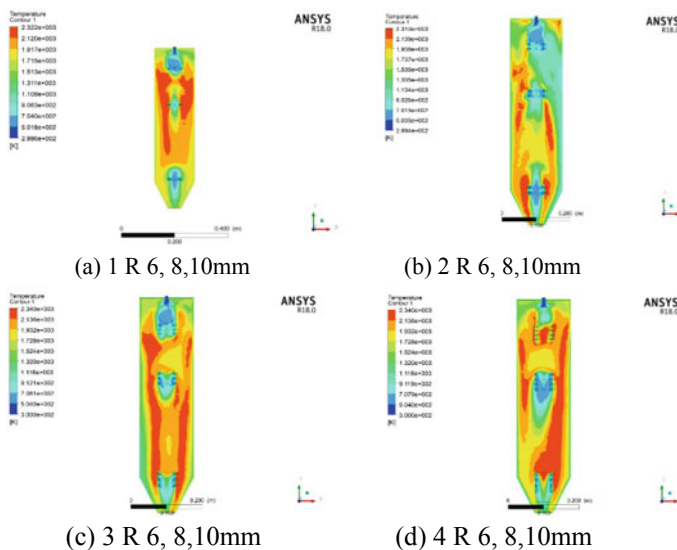


**Fig. 7** Temperature contours of 600 mm chamber height with LPG as fuel

**Table 5** Turbine inlet conditions for 600 mm chamber height geometry for natural gas

Natural Gas	TIT (K)	Velocity (m/s)	NOx (PPM)
1R6810	1616.8	746.18	12.72
2R6810	1662.5	786.1	26.7
3R6810	1658.13	783.07	33.72
4R 6810	1630	771.3	35.546

**Table 6** Turbine inlet conditions for 600 mm chamber height geometry for LPG

LPG	TIT(K)	Velocity (m/s)	NOx (PPM)
1R6810	1687	768.54	83.51
2R6810	1620.4	728.07	60.15
3R6810	1668.5	742.8	52.7
4R 6810	1644.7	709.4	47.8

natural gas, it is noticed that the flame is bleeding out of the flame tube chamber into the air jacket chamber which is allowing to react with the hot air in the air jacket which is leading to increasing the temperature of the mixed air along the corners of the chamber which can be seen clearly in Fig. 6c and d.

Whereas when considering the LPG as fuel, it is clearly visible that the flame is bleeding out to the air jacket in all conditions, which is allowing to increase the temperature of the air along with the NOx and CO emissions. Tables 5 and 6 show the temperature, velocity, and NOx emission levels entering the turbine for both the fuels.

From the above two tables, we can conclude that due to increase in the number of rows, the NOx emission levels are increasing in case of natural gas as fuel, whereas in case of LPG as fuel, the condition is vice versa, the emission levels are decreasing. However, the emissions at 4R 6810 condition is clearly stating that the NOx emission levels are less in natural gas when compared to LPG.

### 3.4 Effect of Flame Tube Holes Diameter

Further, the simulations were carried out by increasing the flame tube holes diameter from 6, 8, and 10 mm to 8, 10, and 12 mm to investigate the flame stability in the combustion chamber. This effect is investigated on 300 and 600 mm chamber length geometries and they are compared between both the flame tube hole diameter criteria. From the simulations, we came to know that for 300 mm chamber length geometry condition, the flame generation for natural gas is not proper and it is not stable, whereas for LPG fuel, the flame is stable and the results are discussed by using Fig. 8.

It is concluded by looking at Fig. 8 that by increasing the cross-flow surface area between the flame tube and air chamber is leading to bleed the flame on to the air

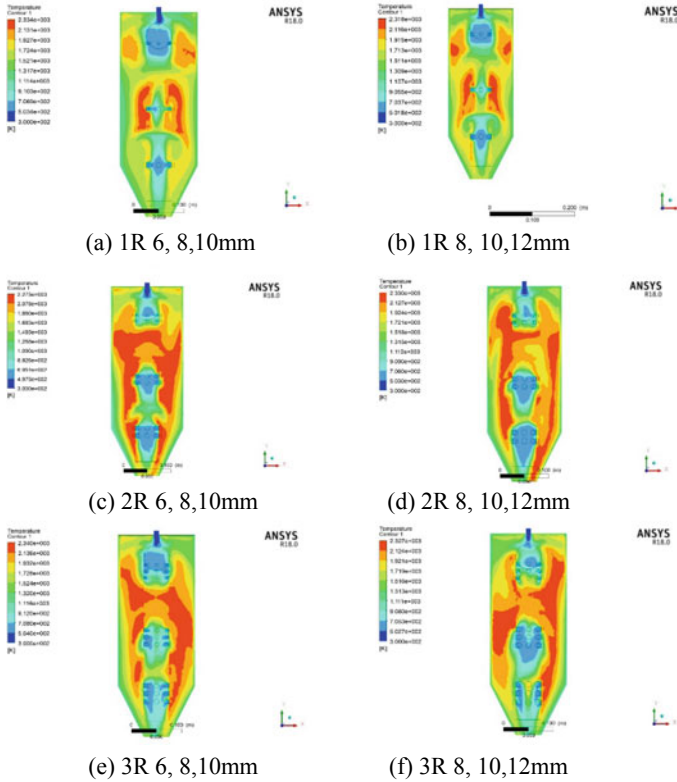


**Fig. 8** Temperature contours of 300 mm chamber height geometry with 6, 8, and 10 mm and 8, 10, and 12 mm on LPG fuel

jacket. From two-row and three-row condition, we can also conclude that the flame is bleeding toward the richer oxygen medium if the path has low cross-flow resistance which is in between the two different combustion zones. Table 7 contains the turbine inlet conditions for 300 mm chamber height geometry on LPG fuel.

**Table 7** Turbine inlet conditions for LPG on 300 mm chamber height geometry

300 mm LPG	Temperature (K)	Velocity (m/s)	NO <sub>x</sub> (PPM)
1R 6810	1628	749	29.88
2R 6810	1482	694	22.24
3R 6810	1534	670	30.7
1R 81012	1527	708	21.89
2R 81012	1458	692	33.59
3R 81012	1294	625	24.55

**Table 8** Turbine inlet NOx emission levels for various design geometries on LPG

<b>300 mm</b>	<b>NOx (PPM)</b>
1R 6810	29.88
2R 6810	22.24
3R 6810	30.7
4R 6810	23.83
<b>600 mm</b>	<b>NOx (PPM)</b>
1R 6810	83.51
2R 6810	70.82
3R 6810	60.15
4R 6810	53.06
<b>700 mm</b>	<b>NOx (PPM)</b>
1R 6810	82.9
2R 6810	62.6
4R 6810	53.44

From the above table, it is clearly stated that increasing the cross-flow surface area of the holes between the air jacket and flame tube leads to decrease the turbine inlet temperature and velocity.

Hence the combustion chamber geometry is further optimized by using the flame tube hole diameter as 6, 8, and 10 mm as the fixed parameter.

To further optimize the chamber, we need to decide the number of rows affecting emission levels. Table 8 shows the turbine inlet NOx emission levels on multiple designs; it helps to understand and conclude the best possible combination of the number of holes and its diameters on a flame tube.

From the table, we can watch the pattern in NOx discharge levels; it is diminishing and expanding in every one of the situations when contrasted and their past model for 300 mm plan criteria. In any case, for whatever is left of the structures, the NOx outflow levels are diminishing relentlessly when contrasted with the other. From the emanation levels on 4R 6810 conditions in both 600 and 700 mm load length, we can infer that the outflows are balanced out around 53 PPM for both 600 and 700 mm, the recreations are completed by utilizing the state of four columns and 6, 8, and 10 mm for premixed, burning, and weakening zones on a fire tube.

## 4 Effect of Chamber Length

Chambers with less than four rows 6, 8, and 10 mm conditions did not show a good performance in terms of turbine inlet conditions and therefore we now compare different chamber geometries, i.e., 300, 600, 700, and 800 mm with 4R 6810 condition, to find the best possible combustion chamber which suits for both fuels LPG and natural gas. Figure 9 shows the temperature contours of all four combustion chambers

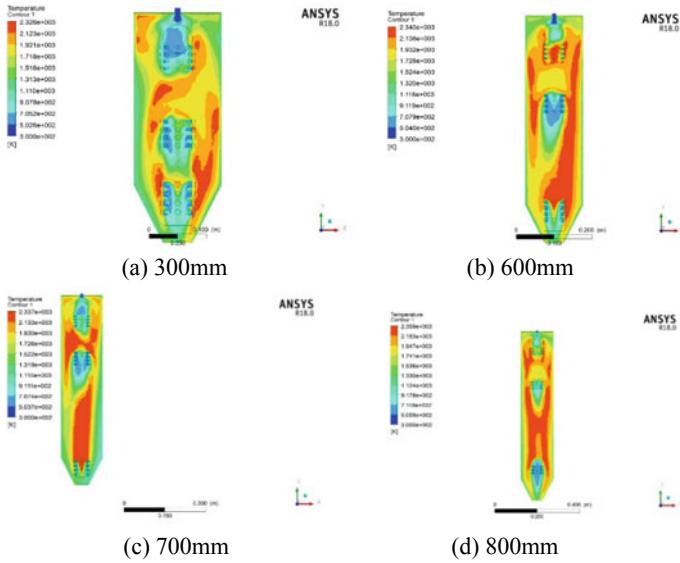


**Fig. 9** Temperature contours of various chamber designs for LPG

for LPG (Table 9).

From Fig. 10, we can plainly observe that for 300 and 600 mm chamber length geometries on LPG, the fire is seeping into the air coat with turbine gulf temperatures 1413 and 1536 K and furthermore colossal increment in NOx, and when 600 mm is contrasted and 700 mm, the temperatures are dropped to 1301.56 K and speed to 620.47 m/s; however, when we take a gander at NOx outflow it is expanded in an immaterial sum. Be that as it may, for 800 mm NOx emanations expanded radically contrasted and the past chamber show. While gaseous petrol is looked at the ignition

**Table 9** Turbine inlet conditions of all combustion chambers with 4R 6810 mm conditions

LPG	Temperature (K)	Velocity (m/s)	NOx (PPM)
300 mm	1413	655	23.83
600 mm	1536	728.07	53.06
700 mm	1301.56	620.47	53.44
800 mm	1237.98	712.72	62.65
300 mm	1413	655	23.83
<i>Natural gas</i>			
300 mm	1478	705	8.87
600 mm	1416	687	24.5
31.47	1325.4	619.5	31.47
35.5	1562	735.4	35.5



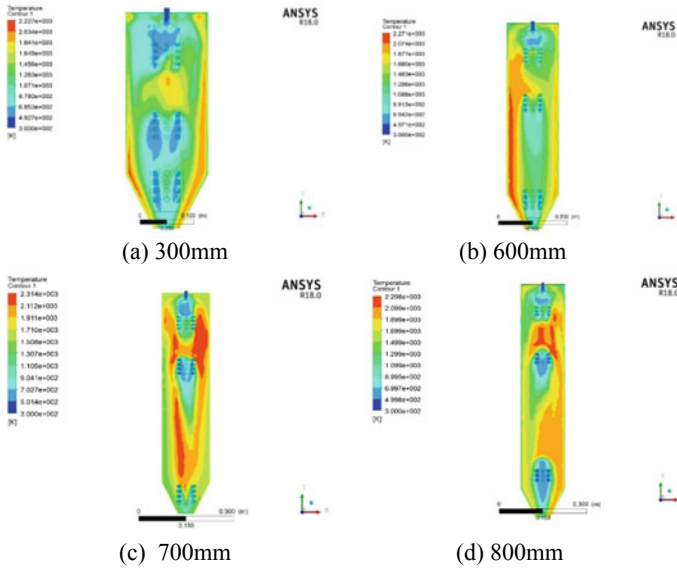


Fig. 10 Temperature contours of various chamber designs for natural gas

is brisk and it is ruled by the natural air in 300 mm chamber and in 600 mm chamber, the fire is seeping into air coat after the premixed zone and burning zone. In 700 mm, however, the temperature of turbine gulf is less contrasted and the past model, and furthermore slight increment in NOx yet it is less contrasted and LPG as fuel, the fire created in the fire tube is appropriate and the draining is less contrasted and the past model.

## 5 Conclusions

It is concluded that the suitable dimensions to burn LPG and natural gas fuels with low emissions are 700 mm chamber height, 50 mm flame tube diameter with 4 inline holes, and 6, 8, and 10 mm diameters in premixed combustion and dilution zone. It is observed with a temperature of around 1020 °C and velocity of more than 600 m/s, though size of 600 and 700 mm chamber heights did not show any considerable difference in emissions and turbine inlet temperature conditions for natural gas as fuel; but for LPG it gave better performance. Thus 600 mm height, 50 mm flame tube diameter with four rows of holes and diameters of 6, 8, and 10 mm for premixed combustion and dilution zone and extended dead zone condition between combustion and dilution zone was chosen as optimum chamber geometry and for LPG it is ideal to consider 700 mm.

## References

1. Laranci P, Fantozzi F (2017) Geometry optimization of a annular RQL combustor of a micro gas turbine for use of natural gas and vegetal oils. In: 72nd conference of the Italian Thermal Machines Engineering Association 2017, Science Direct, Energy Procedia, pp 875–882
2. Enagi II, Al-attab K, Zainal ZA (2017) Combustion chamber design and performance for micro gas turbine application. In: Fuel processing technology 2017, pp 258–268
3. De Robbio R (2017) Innovation combustion analysis of a micro-gas turbine burner supplied with hydrogen-natural gas mixtures. In: 72nd conference of the Italian Thermal Machines Engineering Association 2017. Science Direct, Energy Procedia, pp 858–866
4. Benim AC, Iqbal S, Meier W (2017) Numerical investigation of turbulent swirling flames with validation in a gas turbine model combustor. In: Applied thermal engineering 2017, Science Direct, vol 110, pp 202–212
5. De Santis A, Ingham DB, Pourkashanian M (2016) CFD analysis of exhaust gas recirculation in a micro gas turbine combustor for CO<sub>2</sub> capture. In: Fuel processing technology 2016, Science Direct. *Fuel*, vol 173, pp 146–154
6. Al-Halbouni A, Giese A, Tali E (2017) Combustor concept for industrial gas turbines with single digit NO<sub>x</sub> and CO emission values. In: INFUB—11th European conference on industrial furnaces and boilers 2017. Science Direct, Energy Procedia, vol 120, pp 134–139

# Life Cycle Assessment of a 100 kWp Solar PV-Based Electric Power Generation System in India



N. Leela Prasad, P. Usha Sri and K. Vizayakumar

**Abstract** A solar PV-based electric power generation system may be used to exploit renewable energy from the sun in order to supplement the India's growing need for electricity despite its inherent deficiencies, such as low conversion efficiencies, high capital cost, large land usage and seasonal variation in solar insolation as these techno-economic factors are expected to improve in future. This paper explores the energy performance and environmental impact assessment of a 100 kWp solar PV-based electric power generation system located in India with the help of embodied energy data available in the worldwide literature and by modeling and simulating an equivalent system on SimaPro 8.2 LCA software with ECOINVENT 3.0 as database. As part of this study, a detailed inventory analysis will be carried out on a multi-crystalline silicon (mc-Si) solar PV cell/module-based roof-top electric power generation system for the raw materials extracted, energy inputs used, energy output generated and the number of residuals consequently released to the environment. System's energy performance results are usually expressed in the form of a widely used energy metric called energy payback time (EPBT). Further, the environmental impact assessment will cover an important category such as global warming potential (GWP). These LCA results help the policy makers and energy planners to compare various power generating options available in India and justify any planned investments in renewable energy sector so that the future demand for electricity is met in a more sustainable manner.

---

N. Leela Prasad (✉)

Department of Mechanical Engineering, Vignan Institute of Technology and Science, Hyderabad, India

e-mail: [nlp123457@gmail.com](mailto:nlp123457@gmail.com)

P. Usha Sri

Department of Mechanical Engineering, Osmania University, Hyderabad, India

e-mail: [emailushasri@yahoo.com](mailto:emailushasri@yahoo.com)

K. Vizayakumar

Mechanical Engineering, Bapatla Engineering College, Bapatla, India

e-mail: [vizaya@gmail.com](mailto:vizaya@gmail.com)

© Springer Nature Singapore Pte Ltd. 2020

G. S. V. L. Narasimham et al. (eds.), *Recent Trends in Mechanical Engineering*,

Lecture Notes in Mechanical Engineering,

[https://doi.org/10.1007/978-981-15-1124-0\\_7](https://doi.org/10.1007/978-981-15-1124-0_7)

**Keywords** Life cycle assessment (LCA) · Net energy analysis (NEA) · Embodied energy · Global warming potential (GWP) · Energy payback time (EPBT) · Balance of system (BOS)

## 1 Introduction

The growing population with better life styles is pushing up the energy demand, especially in the form of electricity, and the retirement of old generating plants based on conventional fuels necessitates the investment in new electric power generation options. In future, stringent environmental regulations and uncertain fuel prices may complicate the choice of fuels and generation technologies in power sector. Generation of electricity based on conventional fossil fuels is the major source of CO<sub>2</sub>, SO<sub>x</sub>, NO<sub>x</sub> emissions and suspended particles; it also produces large quantities of solid waste and contributes to the water pollution. To refurbish old plants or to invest on new ones based on alternatives, policy makers should have enough information on the environmental implications of every fuel and generation technology. One such alternative is photovoltaic technology which converts the sun's rays directly into electrical energy. India is so fortunate enough to have a rich solar energy resource as it is in the equatorial sun belt of the earth by receiving solar power of about 5000 trillion kWh with 300 clear and sunny days around the year. The daily average of solar energy falling over India ranges from 4 to 7 kWh/m<sup>2</sup>, with about 2300–3200 sunshine hours per annum, depending upon geographical location.

## 2 Methodology

The impact on environment due to various products, services and processes has become one of the much-discussed issues in today's world and it is imperative to assess their detrimental effects on our environment. One such analytical tool that can be adapted for this purpose is life cycle assessment (LCA). The definitions of LCA and its fundamental concepts, methodology and applications are described in the ISO 14040–14049 series of standards. Net energy analysis (NEA) of a system in conjunction with the evaluation of its environmental impacts is commonly referred as LCA.

The objective of any LCA study is to estimate the total environmental impacts of a product or a process or a system by analyzing all the stages of its life cycle from raw materials extraction, transport, production and up to recycling and disposal, in other words “from birth to death”. The LCA methodology is a systematic approach that consists of four steps: goal and scoping, inventory analysis, impact assessment and interpretation of results (Fig. 1).

The results from an LCA study will help the decision makers to identify a product or a process or a system that has minimal effect on our environment and has better

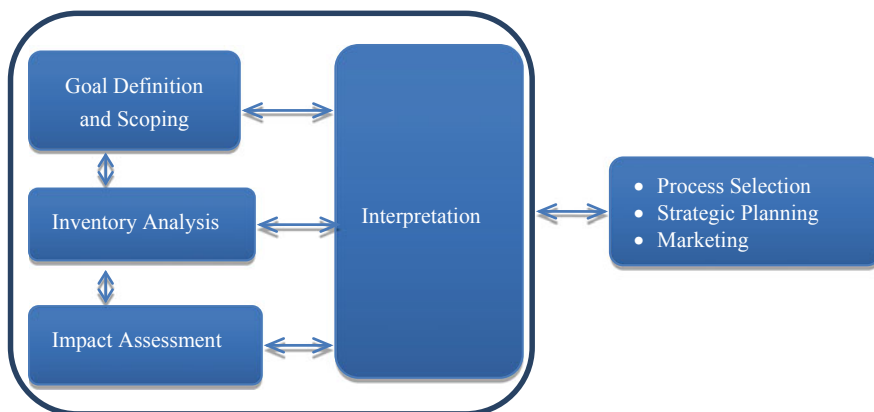


**Fig. 1** ISO 14040:1997—stages of life cycle assessment [1]

energy performance. Some important applications of LCA are environmental labeling of products, identification of improvements in a method of electric power generation process and comparative assessment of various electric power generation options. According to Meier [2], the LCA methodology can also be applied to evaluate the fuel substitution strategies aimed at reducing the greenhouse gas emissions in the power generation sector. With the growing popularity of renewable energy systems, it is crucial that the policy makers are provided with accurate information describing the quality and quantity of benefits that are offered by the diversity of energy alternatives. In order to do so, many of the research groups involved in such practices are turning to the life cycle assessment (LCA) methodology. There are some issues which may limit the applicability of LCA, and they are:

- Performing an LCA study can be resource-intensive and time-consuming;
- Uncertainty in the results due to uncertainty in the quality of data available; incomplete scope (some impacts are not covered, and boundary is not broad enough);
- Static analysis in nature (technological progress is not reflected); and
- Site-specific nature of the method.

### **3 LCA of Solar PV-Based Electric Power Generation System: A Case Study**

#### **3.1 Goal and Scope of the Study**

The present LCA study evaluates the complete life cycle of solar PV-based electric power generation system for the energy requirements, useful energy output and GWP.

However, analyzing energy balance between inputs and outputs is too complex as the inputs are so diverse, and it is not always clear how far they should be taken into our analysis. Also, data related to inputs vary with capacity of plant and type of solar PV cells installed at that plant location. The task of collecting data related to solar PV electric power generation system is even more difficult in countries like India because of poor record keeping and scarce research outputs in this area. So, this study uses data available in the worldwide literature and real-time data available for a grid connected 100 kWp roof-top poly-Si PV system installed at KITS, Warangal, Telangana State, India (latitude: 18.1 °N, longitude: 79.5 °E), for analysis with 1 kWh as functional unit. The scope of this study also covers a well-defined disposal scenario when the system is modeled and run on a SimaPro 8.2 LCA software, due to the convenience of data availability in ECOINVENT 3.0 database.

### 3.2 Inventory Analysis

The most important phase of any LCA study is the inventory analysis, which includes the data collection and compilation about material and energy inputs, emission and product outputs for the complete life cycle of system under consideration. So, the basic step in the inventory analysis is the creation of a process-flow diagram as shown in Fig. 2, which will serve as the blue print for the inventory data to be collected.

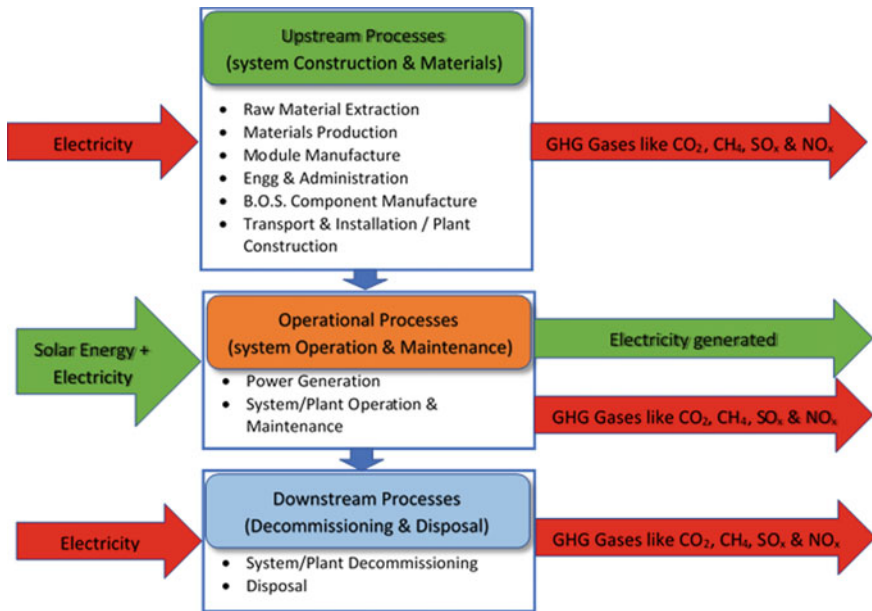


Fig. 2 Main steps in LCA chain for solar PV electric power generation

**Net Energy Analysis (NEA).** One of the performance evaluation techniques usually applied for energy systems is the net energy analysis, which seeks to compare the amount of energy delivered in the readily usable form by a technology to the total energy required to discover, extract, process, deliver, or otherwise to upgrade that energy into a socially useful form. The two types of energy inputs that were accounted for are the energy used directly in each process block and the energy contained in the materials used in that process block. The latter type of energy is the sum of combustion and process energies which is sometimes referred to as the embodied energy of the material. To determine the net energy output in this LCA, the total energy used directly in all process blocks plus the embodied energy of all materials consumed by the system were subtracted from the energy produced by the system.

*Indirect Life Cycle Energy Inputs.*

1. Construction and material energy inputs of 100 kWp poly-Si PV system.

The energy inputs associated with the system include embodied energies of main components and BOS and the energy expended on installation and transportation as detailed in Table 1.

**Table 1** Construction and material energy inputs of a 100 kWp poly-Si PV system

Process/Material	Description/specifications	Embodied energy	Energy input (GJ)
Solar panels/modules	In series 20 modules In parallel 20 strings Total 400 modules of 250 Wp rating each Module Area = 648 m <sup>2</sup>	4070 MJ/m <sup>2</sup>	2637.36
Inverters	5 Inverters of 20 kW capacity Or 40 inverters of 2.5 kW	1930 MJ/kWp	193
Array support + cabling	4000 feet DC wire and 9300 feet AC wire 0.009 kg copper per foot of AC wire and 0.0575 kg copper per foot of DC wire	100 MJ/m <sup>2</sup>	64.8
Installation	AC power required	500 kWh @ 16.7 MJ/kWh	8.35
Transport	Solar panels from Mumbai to Warangal, inverters from Pune to Warangal and remaining materials from Hyderabad to Warangal	Trucks 3.58 MJ/km-ton LCVs 4.66 MJ/km-ton	31.36
Total construction and material energy			2934.87

2. PV System Operation and Maintenance.

The reliability of power conditioning equipment, that is, inverter is the primary consideration for determining operation and maintenance energy requirements. This study assumes a 15-year inverter lifetime with one replacement during system’s life.

3. Decommissioning and Disposal.

Input energy requirements for disposal of PV modules as a land fill are considered in this analysis. Decommissioning energy and emissions are estimated as 20% of installation energy and emissions.

*Lifetime Electric Output (LEO)<sup>1,2</sup>*

$$\begin{aligned} \text{Energy output of a 100 kWp rated poly-Si PV system (for 25 years lifetime)} \\ &= 90.3 \times 25 \times 365 \times 5.5 \times 3600 \\ &= 16,315 \text{ GJe} \end{aligned}$$

*Direct Lifetime Renewable Energy Input (DLREI)*

$$\begin{aligned} \text{Renewable Energy Input} &= 582 \times 5.5 \times 25 \times 365 \times 3600/1000000 \\ &= 105,153 \text{ GJ} \end{aligned}$$

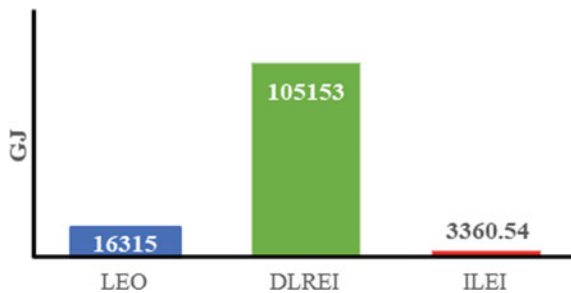
(with cell area of 582 m<sup>2</sup> for a grid connected 100 kWp rated poly-Si PV system and with a daily average of 5.5 kWh/m<sup>2</sup>/day solar insolation over India [9]).

*Conversion Efficiency of the System/Plant.*

$$= \text{LEO} \times 100/\text{DLREI} = 15.5\%$$

ILEI in Fig. 3 is the total indirect lifetime energy input in GJ from Table 2.

**Fig. 3** NEA summary of a grid connected 100 kWp rated poly-Si PV system



<sup>1</sup>The average rating of a 100 kWp rated poly-Si PV system at operating conditions will be 90.3 kWp only. The average rating is taken at the lowest possible value in view of PV array loss factors like thermal loss factor, wiring Ohmic loss, module quality loss, module mismatch loss, and DC to AC conversion losses @ 98.2% and incidence effect.

<sup>2</sup>Average sunshine is taken as 5.5 h/day throughout the year.



**Table 2** Summary of primary energy inputs to a 100 kWp poly-Si PV system over a 25-year lifetime

S. no.	Life cycle stage	Energy input (GJ)	References
i.	System construction and materials (Table 1)	2934.87	[3–8]
ii.	System operation and maintenance	193 <sup>a</sup> + 231 <sup>b</sup>	[2]
iii.	System decommission	1.673 <sup>c</sup>	[2]
Total indirect life cycle energy input		3,360.54	

<sup>a</sup>Replacement of inverters nearly at half-way point of the system life

<sup>b</sup>Electricity requirement for water cleaning of panels @ 50 kWh/month

<sup>c</sup>Decommissioning energy and emissions are estimated as 20% of installation energy and emissions

**Table 3** Construction and Material-related GHG Emissions of a grid connected 100 kWp poly-Si PV System

Process/material	Embodied carbon in kg CO <sub>2</sub>	Total emissions in kg CO <sub>2</sub> e
Materials and manufacturing	208 kg CO <sub>2</sub> /m <sup>2</sup>	142,871
Inverters	125 kg CO <sub>2</sub> e/kWp	12,500
Array support + cabling	6.1 kg CO <sub>2</sub> e/m <sup>2</sup>	3952.8
Installation	500 kWh @ 1.52 kg CO <sub>2</sub> e/kWh	760
Transport	Trucks 0.22 kg CO <sub>2</sub> e/km-ton LCVs 1.96 kg CO <sub>2</sub> e/km-ton	2824.16
Total emissions		162,908

*Note* Refer Table 2 for description/specifications of process/material

### 3.3 Environmental Impact Assessment

PV systems generate electricity using the photoelectric effect, which itself has no associated emissions. However, due to overdependence on fossil fuel infrastructure, many phases of the system's life cycle have corresponding greenhouse gas emissions. The method used to estimate the emissions is by multiplying material mass with material embodied emission factor.

The life cycle greenhouse gas emission factor (GWP) of Indian Electricity Mix is 1.52 kg CO<sub>2</sub>—equivalent/kWh as per ECOINVENT database [8] for low-voltage supply. By assuming 100% of ILEI in electric energy terms is supplied by Indian Electricity Mix, the calculations are done and accordingly results are presented in Table 4.

**Table 4** Life cycle GHG emissions of a grid connected 100 kWp poly-Si PV system

S. no.	Life cycle stage	Tons of CO <sub>2</sub> —equivalent	References
1	System construction and Materials (Table 3)	162.90	[3–8]
2	System operation and maintenance	33.5	[2]
3	System decommission	0.1523	[2]
Total life cycle emissions (TLE)		196.552	

The total emissions for a grid connected 100 kWp roof-top poly-Si PV system is 196.552 tons of CO<sub>2</sub>—equivalent (referred later as CO<sub>2</sub>e) over a 25 years lifetime from Table 4.

### 3.4 Results/Metrics

The metric widely used within the existing literature to summarize the results of NEA are energy payback time (EPBT), which is the time needed for a system to generate useful energy output equal to its life cycle energy input. Most LCA studies on electricity generation systems also include estimates of greenhouse gas emissions. The metric accounting for greenhouse gas emissions is usually expressed as mass of carbon dioxide equivalents emitted per unit of electricity produced by the system in kg—CO<sub>2</sub>e per kWh.

$$\begin{aligned} \text{Total Energy Input} &= \text{DLREI} + \text{ILEI} \\ &= 1,05,153 + 3360.54 = 1,08,513.54 \text{ GJ} \end{aligned}$$

$$\text{Lifetime Electric Output (LEO)} = 16,315 \text{ GJe} = 45,31,944.4 \text{ kWh}$$

$$\text{Annual Energy output (AEO)} = \text{TLE}/25 = 652.6 \text{ GJe}$$

#### Energy Pay Back Time (EPBT)

The EPBT is the time required to recover the indirect lifetime energy inputs in primary energy terms in all life cycle stages of the system including embodied energies and AC power. This term “EPBT” is generally used by energy policy makers.

$$\begin{aligned} \text{Energy Payback Time} &= \text{ILEI}/\text{AEO} \\ &= 3360.54/652.6 = 5.15 \text{ Years} \end{aligned} \quad (1)$$

$$\begin{aligned} \text{GWP (Global Warming Potential)} &= \text{TLE}/\text{LEO in kWh} \\ &= 196.552 \times 1000 \times 1000/4531944.4 \\ &= 43.37 \text{ grams of CO}_2\text{e/kWh} \end{aligned} \quad (2)$$

### 3.5 Modeling and Simulation Results

Life cycle assessment of a 100 kWp, roof-top, solar PV-based electric power generation system located in India is also conducted by modeling and simulation on SimaPro 8.2 LCA software [10] with ECOINVENT 3.0 [8] as database.

Figure 4 is the network representation of same 100 kWp roof-top, solar PV-based electric power generation system with disposal scenario<sup>3</sup> generated after it is modeled and run on SimaPro software by using cumulative energy demand (CED) method and Figs. 5, 6 and 7 are the graphical representations of impact of this system on energy resources.

$$\text{Energy Payback Time} = \text{LEI or CED/AEO} = 2650/652.6 = 4.06 \text{ Years}$$

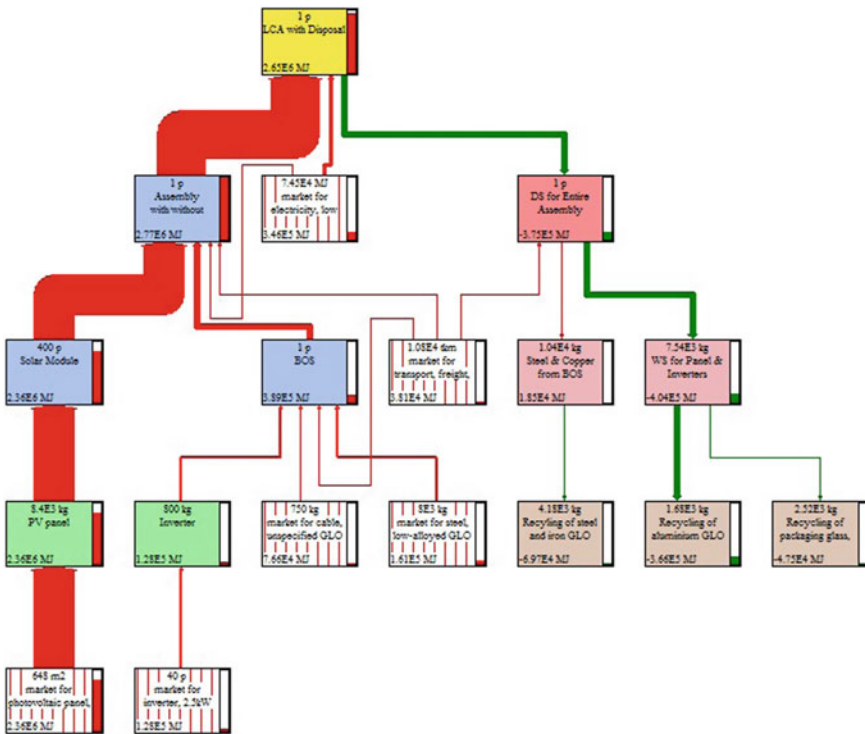


**Fig. 4** Model flowchart for a 100 kWp roof-top solar PV system in SimaPro with cut-off value of 1%/CED method

<sup>3</sup>Disposal Scenario: PV Modules/100% Land Fill as Electronic Scrap, Steel and Iron/90% Recycling, Energy Intensive materials like Copper and Aluminum/95% Recycling, Plastics/100% Incineration.

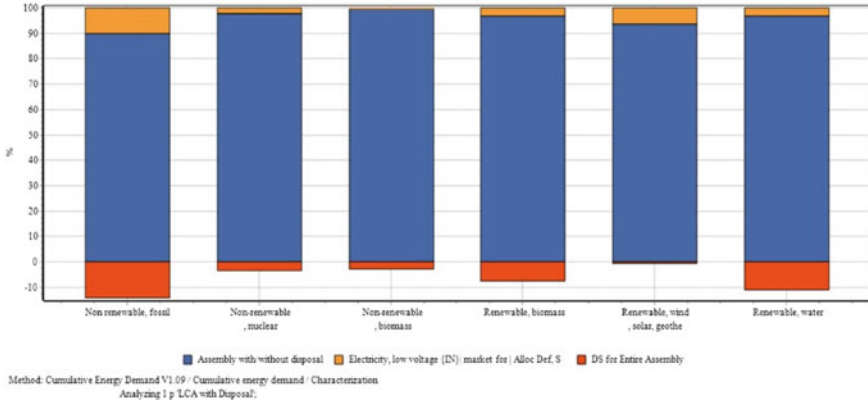


Fig. 5 Impact assessment on energy resources/characterization results

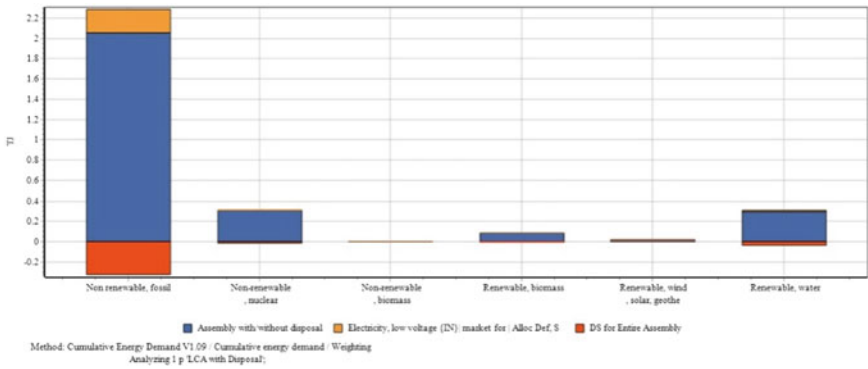


Fig. 6 Impact assessment on energy resources/weighting results

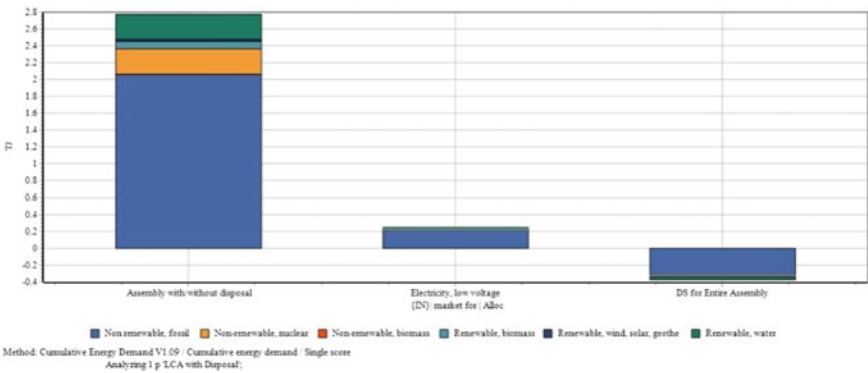
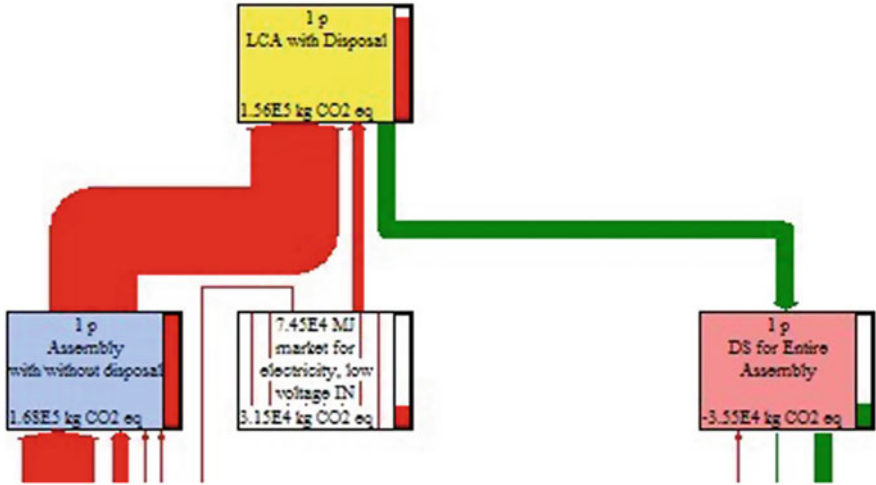
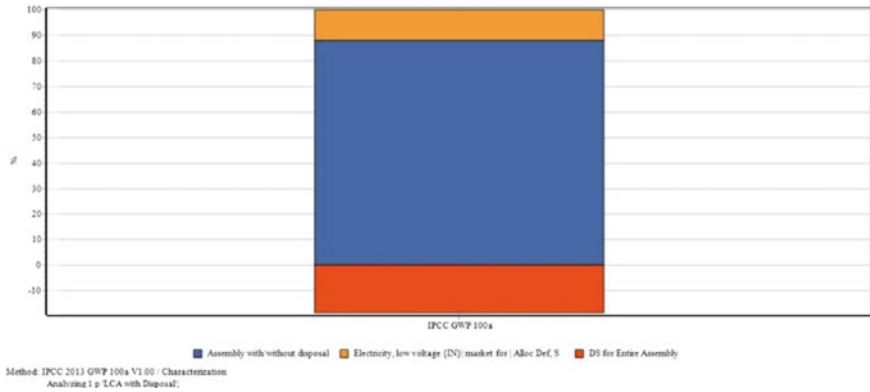


Fig. 7 Impact assessment on energy resources/single score results

Figure 8 is the network representation of the same 100 kWp roof-top, solar PV-based electric power generation system with disposal scenario, generated after it is modeled and run on SimaPro software by using IPCC 2013 GWP 100a V1.00 method and Fig. 9 is the graphical representation of GWP during various phases.<sup>4</sup>



**Fig. 8** Model flowchart (up to Level 1) for a 100 kWp roof-top solar PV system in SimaPro with cut-off value of 1%/IPCC 2013 GWP 100a V1.00 method



**Fig. 9** Global warming potential/characterization results

<sup>4</sup>Obtained value from simulation

$$\begin{aligned}
 \text{GWP (Global Warming Potential)} &= \text{TLE/AC output in kWh} \\
 &= 156 \times 1000 \times 1000/4531944.4 \\
 &= 34.42 \text{ grams of CO}_2\text{e/kWh}
 \end{aligned}$$

### 3.6 Comparative Results and Analysis

Results of net energy analysis, modeling and simulation on SimaPro with/without disposal scenarios are tabulated in Table 5 and possible reasons for the deviation in EPBT and GWP values are analyzed in this section.

Based on the results tabulated in Table 5, one can conclude that EPBT appears to be around 4–5 years and GWP appears to be around 35–40 g of CO<sub>2</sub>e for the above SPV system at the given location. Irrespective of location, scope and scale, SPV system appears to be capable of paying back energy nearly five to six times and GWP appears to be very low in comparison to the conventional systems. Owing to poor data availability, transport and disposal phases after decommissioning are not added in NEA analysis. The above results emphasize the importance of a well-defined end of the life disposal scenario, which can be conveniently added in SimaPro software while modeling and its positive influence on system’s energy and environmental performance.

**Table 5** Comparative results on energy and environmental performance of the system

Case	Analysis scope	EPBT in years	GWP in grams of CO <sub>2</sub> e/kWh
NEA based on embodied energy	With decommissioning alone	5.15	43.37
Modeling and simulation on SimaPro 8.2 LCA software with ECOINVENT 3.0 as database	Without disposal scenario	4.63	42.14
Modeling and simulation on SimaPro 8.2 LCA software with ECOINVENT 3.0 as database	With disposal scenario	4.06	34.42

### 3.7 *Improvement Analysis*

This life cycle assessment study can be used to identify the opportunities in reducing the environmental burden of the system through process design improvements or by alternative process designs that may result in more environment-friendly systems. Around 90% of system's indirect lifecycle energy inputs and 88% of green house gas emissions are during system construction and materials phase of the life cycle. So, our focus must be on those stages for overall improvement in environmental performance and for a reduced EPBT. Even better disposal scenarios with recycling make the difference in the energy and environmental performance of the system. Further improvements are expected in future as PV cell technology is set to upgrade in terms of conversion efficiency. Use of judicious energy mix as input to the system is also expected to improve the system's performance.

## 4 **Summary and Conclusions**

The results of LCA analysis presented in this paper are based on Indian specific data collected and data taken from literature and a reputed inventory database. These results are sensitive to country-specific energy mix as input to the system. Scope of the study may vary from one study to another study and because of site-specific character of the methodology adopted; results of two LCA studies will never match with each other. But the results arrived in this LCA study are handy in the comprehensive decision-making process by policy makers and energy planners while selecting right options among various electricity generating technologies and fuel choices available, for a secure and sustainable future in the energy front.

## References

1. International Organization for Standardization (ISO) series: ISO14040: 1997 Environmental Management—Life Cycle Assessment—Principles and Framework
2. Meier PJ (2002) Life-cycle assessment of electricity generation systems and applications for climate change policy analysis, PhD Dissertation, University of Wisconsin–Madison
3. Marimuthu C, Kirubakaran V (2013) Carbon payback period for solar and wind energy project installed in India: a critical review. *Renew Sustain Energy Rev* 23:80–90
4. Hammond G, Jones C (2011) Inventory of Carbon and Energy (ICE), Ver 2.0. Sustainable Energy Team, University of Bath, UK
5. du Can SR, Letschert V, McNeil M, Zhou N, Sathaye J (2009) Residential and Transport Energy Use in India: Past Trend and Future Outlook. Environmental Energy Technologies Division, Ernest Orlando Lawrence Berkeley National Laboratory
6. System Construction and Materials Data, Novus Green Energy Systems, Hyderabad (2015)

7. Alsema EA, de Wild-Scholten MJ (2006) Environmental impacts of crystalline silicon photovoltaic module production. In: 13th CIRP International Conference on Life Cycle Engineering, Leuven
8. ECOINVENT 3.0 Database. The Ecoinvent Centre, Swiss Centre for Life Cycle Inventories: Duebendorf, Switzerland (2015)
9. Muneer T, Asif M, Munawwar S (2005) Sustainable production of solar electricity with particular reference to the Indian economy. *Renew Sustain Energy Rev* 9:444–473
10. Software SimaPro 8.2., PRé Consultants, Amersfoort, NL (2016)



# Performance, Combustion, and Emission Characteristics of Diesel Engine Fuelled with Waste Cooking Oil Biodiesel/Diesel Blends with Iron Oxide Nanoparticles



L. Bharath and D. K. Ramesha

**Abstract** In the present research work, WCO biodiesel with iron oxide nanoparticle samples was considered for DI diesel engine, and its impacts on engine efficiency, combustion, and exhaust gas (emission) characteristics were studied. In this investigation the biodiesel is obtained from WCO by transesterification procedure. The experimental tests were conducted in a CI engine using WCO biodiesel with iron oxide nanoparticles. Engine trials were conducted for all the blends (B20WCOME and B20WCOMEINP75) and the obtained results were compared with diesel. All the tests regarding this work are carried out in a CI engine (diesel engine) at (1500 RPM) constant speed. The biofuel is obtained from WCO and commercially available iron oxide nanoparticles (INP) is used in the present experimental work. INP is added to biodiesel in proportions of 50, 75, and 100 ppm using an Ultrasonicator. The results obtained upon experimentation clearly show that the BTE increases marginally (14.285%) for iron oxide nanoparticles (for 75 ppm) blended WCOME while BSEC decreases (26%) when compared to other blends. The emission levels of oxides of nitrogen (4.87%), carbon oxide (16%), and unburnt hydrocarbons (10%) are marginally decreased as compared to diesel for 75 ppm concentration. From the present experimental work, the blending of iron oxide nanoparticles in WCOME produces most promising results in the CI engine performance with marginal drop in the harmful exhaust gases from CI engines.

**Keywords** CI engine · Waste cooking oil · Transesterification · Iron oxide · Engine parameters

---

L. Bharath (✉) · D. K. Ramesha  
Department of Mechanical Engineering, University Visvesvaraya College of Engineering,  
Bangalore University, Bengaluru 560001, India  
e-mail: [bharathsmg@yahoo.co.in](mailto:bharathsmg@yahoo.co.in)

D. K. Ramesha  
e-mail: [rameshdkuvce@gmail.com](mailto:rameshdkuvce@gmail.com)

© Springer Nature Singapore Pte Ltd. 2020  
G. S. V. L. Narasimham et al. (eds.), *Recent Trends in Mechanical Engineering*,  
Lecture Notes in Mechanical Engineering,  
[https://doi.org/10.1007/978-981-15-1124-0\\_8](https://doi.org/10.1007/978-981-15-1124-0_8)

## 1 Introduction

Due to remarkable progress in industrial development, transportation sector and modernization in lifestyle have led to substantial increase in fuel demand (petroleum-based). Some features of petroleum resources are its limited availability, utility, and potential for depletion [1]. At present, biofuel is stated as “fuel for future” due to being recyclable and environmentally friendly and biodiesel is possessing characteristics almost the same as diesel fuel. Biodiesel resulting from renewable resources is further used by means of fuels in the transportation sector. The production of biofuels is significant for declining exhaust emissions and dependency on fossil fuels [1, 2]. Biofuels are obtained by combining the methyl esters of fatty acids, by responding diverse oils with methanol after removal of glycerol and this process is called as transesterification process [4]. Based on existing feedstocks obtainable for biodiesel making, WCO is under the foremost potential for extensive biodiesel making as it can reduce the fuel prices than other alternative feedstocks. Huge volume of WCO can be composed from hotels, cafeterias, and hostels. Certainly, a single outlet of fast-food center can produce 15 L of WCO per day [5]. The methodology for the usage of biodiesels in the range of 20% as alternative fuel in CI engine is a well-known and recognized technique. With respect to this methodology, some appropriate variation of biofuels by means of suitable nanoparticles could be of benefit. To estimate the impacts of iron oxide nanoparticles (INP) mixed WCO on the performance and combustible products of CI engine, a test was carried out in a single-cylinder diesel engine. The addition of iron oxide nanoparticles with biodiesel will result in better performance with reduced emission characteristics [6]. CI engines generally used in the field of automobiles. And these engines release harmful emission gases. The emission distresses humans, animals, and plants. Chiranjeeva Rao Seela et al. conducted a test to assess the impacts of nanoparticles by considering CeO<sub>2</sub> in CI engines. The investigational results designated improved BTE and better pollutant controls of CI engine [7]. At present, many researchers are doing research by using the metal-based and oxygenated additives aimed to enhance the CI engine performance and emission parameters. The impact of zinc oxide nanoparticles with a variety of biofuel engine characteristics can be analyzed. Calophyllum inophyllum methyl ester with zinc oxide nanoparticles as performance enhancer can be used in a CI engine in the absence of geometric changes [8].

BTE	Brake thermal efficiency
HRR	Heat release rate
B20	20% biodiesel and 80% diesel
NOx	Oxides of nitrogen
UBHC	Unburnt hydrocarbons
WCO	Waste cooking oil
INP	Iron oxide nanoparticle

(continued)

(continued)

WCOME	Waste cooking oil methyl ester
B20WCOME	20% WCOME + 80% diesel
B20WCOME + INP75	B20WCOME + INP75 ppm

## 2 Experimental Setup

In the current experimental investigation, all tests were conducted in a computerized diesel engine test rig as shown in Fig. 1. Dynamometer and engine are coupled to a regulator board, which was associated to a processor. The test rig is entirely instrumented; OROTECH exhaust gas analyser is used to obtain the emission of the engine. The AVL 437C instrument (smoke meter) is considered toward obtaining the opaqueness (opacity) of the drain (exhaust) smokes. The complete engine specification is recorded in Table 1.

**Fig. 1** Schematic of experimental setup

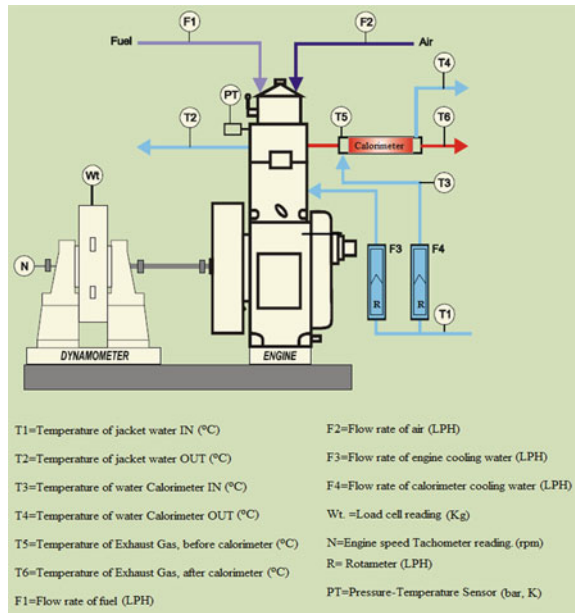


**Table 1** Description of engine

Four-stroke single-cylinder diesel engine test rig	
Make	Kirloskar
Capacity	3.5 KW
Compression ratio	17.5:1
Cylinder bore	80 mm
Stroke	110 mm
Cylinder capacity	661 cc
Cooling	Water cooling
Loading	Eddy current dynamometer
Speed	1500 rpm

### 3 Methodology

#### 3.1 Production of Biodiesel from Waste Cooking Oil (WCO)

Current experimentation work considered transesterification process to obtain biodiesel [4]. Transesterification process consists of acid transesterification and base transesterification. In acid transesterification WCO is heated up to 500 °C. Then methanol is added to preheat the WCO. After this reaction, the bottom deposit is detached for other reactions (base transesterification). The obtained mixture is heated for 45–55 min in the presence of potassium hydroxide and methanol. When the reaction is completed, the reactants are permitted to dispel into dual deposits. The bottom deposit, which is having glycerol, is removed. The ester leftovers are in the upper deposit. Figure 2 demonstrates the complete operation of the transesterification method.

#### 3.2 Determination of Fuel Properties

Fuel properties of diesel, WCO with iron oxide nanoparticles, and without iron oxide nanoparticles were determined and tested to meet the ASTM standard requirement. Heat value of the fuel is measured by using Bomb calorimeter, Kinematic viscosity is measured by using Capillary Tube Viscometer Test Method, flash point is marked by using open-loop method, and measurement of density is carried out by using two separate measurements of mass and volume. All the properties of verified biofuels are tabulated in Table 4.

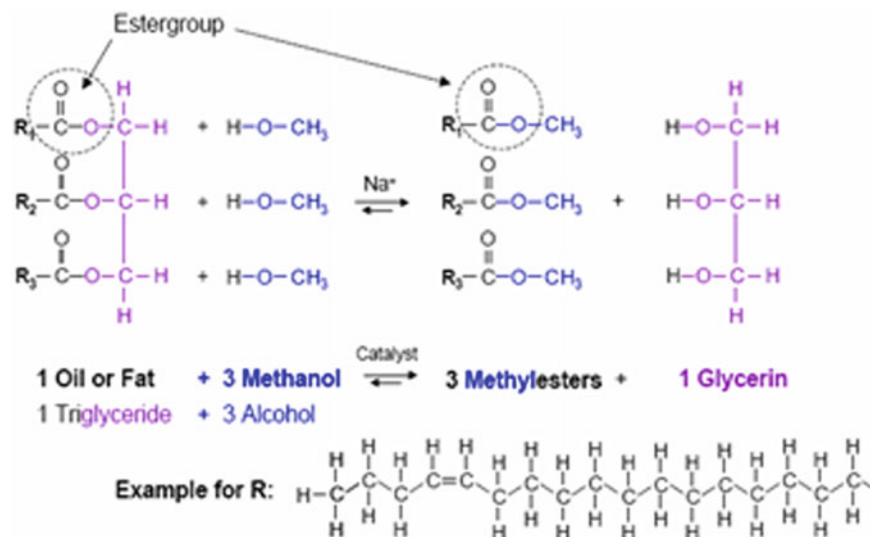


Fig. 2 Schematic demonstration of transesterification method

### 3.3 Preparation of Nanofluids

B20WCOME is obtained by adding 20% of biodiesel to 80% of diesel. B20WCOMEINP75 is prepared by adding 75 ppm iron oxide nanoparticles to B20WCOME biodiesel blend. The INP are mixed to B20WCOME with the help of an ultrasonicator at 22 kHz for 35 mi. This method is well suited to disperse iron oxide nanoparticles. The detailed specification of iron oxide nanoparticles is listed in Tables 2, 3, and 4.

**Table 2** Iron oxide nanoparticles properties

Formula	Fe <sub>2</sub> O <sub>3</sub>
Purity	>99%
Color	Red brown
Melting point	1566 °C
Density	5.24 g/cm <sup>3</sup>
Morphology	Spherical
APS	30–50 nm

**Table 3** Uncertainties percentage

Parameters	Average uncertainties (%)
Airflow rate	1.2
LCV of fuel	1.0
Engine speed	1.3
Gas flow rate	2.1
Engine load	0.2
Liquid fuel flow rate	0.15
Temperature	1.0
Cylinder pressure	0.8

## 4 Results and Discussion

### 4.1 Performance Parameter

**Brake Thermal Efficiency.** The variation of BTE with load for all the tested fuels is shown in Fig. 3. Here the BTE increases by increasing load for all the tested fuels. Because of the rise in brake power with a reduction in heat losses, B20WCOME + INP75 shows better BTE compared to B20WCOME and diesel. Because of high surface area to volume proportion of iron oxide nanoparticles ensuring good atomization and quick evaporation of fuel causes better BTE.

**Brake Specific Energy Consumption.** The variation in BSEC with load is shown in Fig. 4. Brake-specific energy consumption is a level of energy consumption of the engine to generate power. From Fig. 4, it is observed that the BSEC continuously reduces for higher loading, indicating efficient use of fuel. The impact of iron oxide nanoparticles reduces the BSEC at peak load conditions. High range Cv value blends with iron oxide nanoparticles causing similar range of power along minimum utilization of fuel compared to diesel.

**Table 4** Properties of fuels

Properties	Diesel	WCO	WCOME	B20WCOME
Kinematic viscosity (40 °C, Cst)	3.05	43	5.83	4.01
Heat value (MJ/kg)	42.6	29	37.2	39.2
Density (Kg/m <sup>3</sup> )	828	914	874	826
Flash point °C	60	307	150	98
Cetane number	40	53	51.48	51.48

**Fig. 3** Distinction of BTE with load

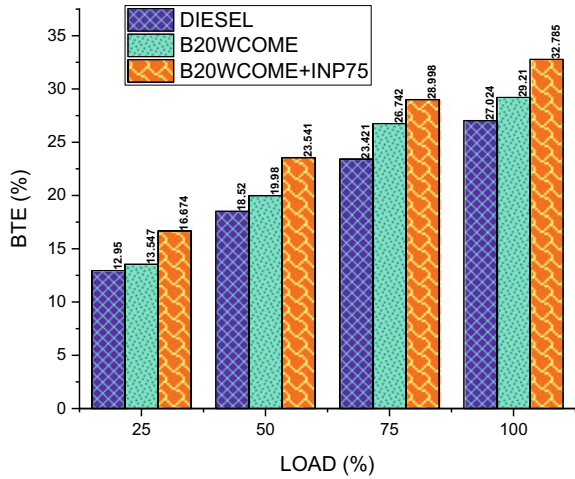
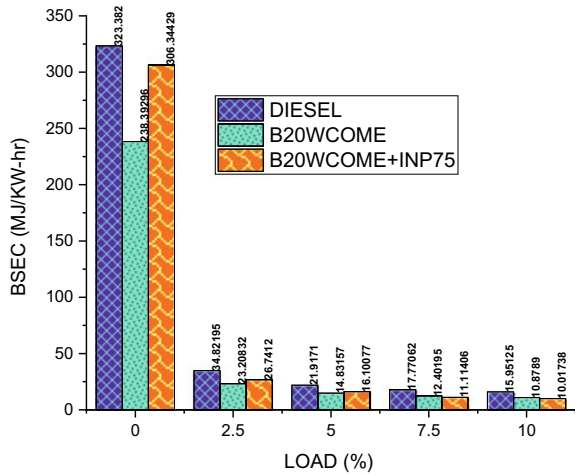


**Fig. 4** Distinction of BSEC with load



### 4.2 Combustion Parameters

**HRR.** Variation in HRR with the crank angle is shown in Fig. 5. It is observed that higher HRR reduced for B20WCOME B20WCOME + INP75 samples, when measured with diesel. For diesel, maximum HRR may be credited to its maximum Cv. A decrease in maximum HRR for biofuels is due to its lesser Cv.

**Peak Pressure.** Variation in peak pressure with a crank angle for all the tested fuels is shown in Fig. 6. It is noticed that B20WCOME shows higher pressure compared to diesel. More oxygen and inferior ignition delay consequently illustrate developed peak pressure. Adding iron oxide nanoparticles to B20WCOME maximizes the Cv of the fuel samples, leading to better combustion which leads to higher peak pressure.

**Fig. 5** Distinction of HRR with crank angle

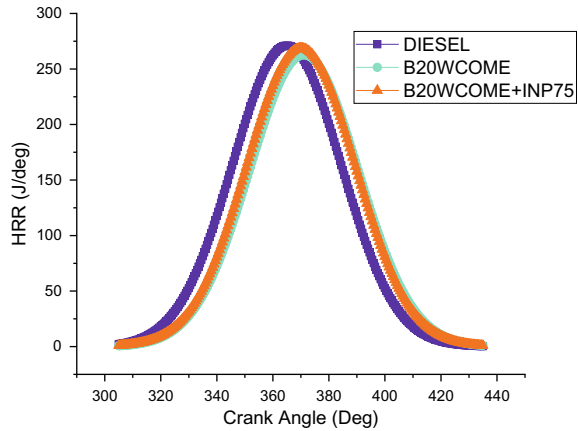
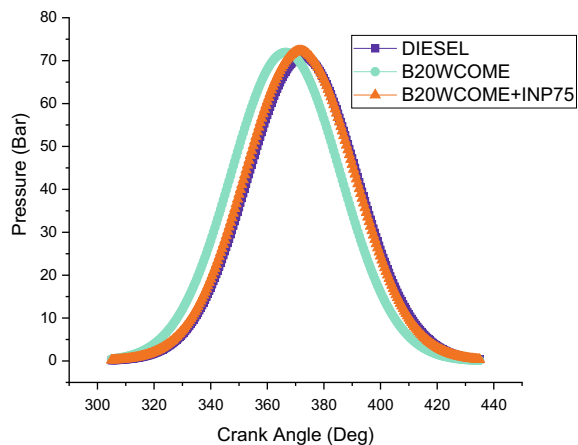


**Fig. 6** Distinction of peak pressure with crank angle



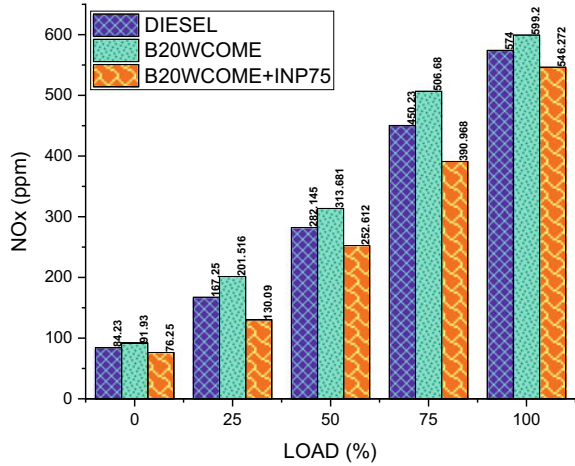
## 5 Emission Parameter

### 5.1 Oxides of Nitrogen (NOx)

The variation of NO<sub>x</sub> with load for all the tested fuels is shown in Fig. 7. Here, the NO<sub>x</sub> rises for the higher load for all the tested fuels. Increase in load or when there is a increase in load there is increase in combustion chamber temperature as NO<sub>x</sub> is a temperature-dependent phenomenon. For B20WCOME (biodiesel blend), NO<sub>x</sub> emission is high compared to diesel and B20WCOME + INP75 is due to more oxygen content. At higher load condition, B20WCOME + INP75 shows lower NO<sub>x</sub> emission compared to diesel and B20WCOME. This is due to iron oxide nanoparticles promoting improved homogenization and maximizing the chemical reactivity of the fuel samples by maximizing the surface.



**Fig. 7** Distinction of NO<sub>x</sub> with load



### 5.2 Carbon Monoxide (CO)

The variation of CO with load for all the tested fuels is shown in Fig. 8. Biodiesel always leads to a reduction in CO. At lower or part load, the CO emission is more compared to full load condition, this is due to lean mixture. At higher load B20WCOME + INP75 shows lower CO emission compared to diesel and B20WCOME. This is due to more oxygen content and catalytic behavior of nanoparticles.

**Fig. 8** Distinction of CO with load

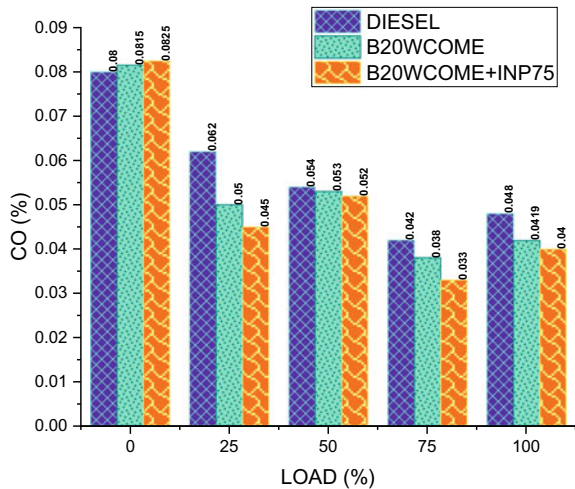
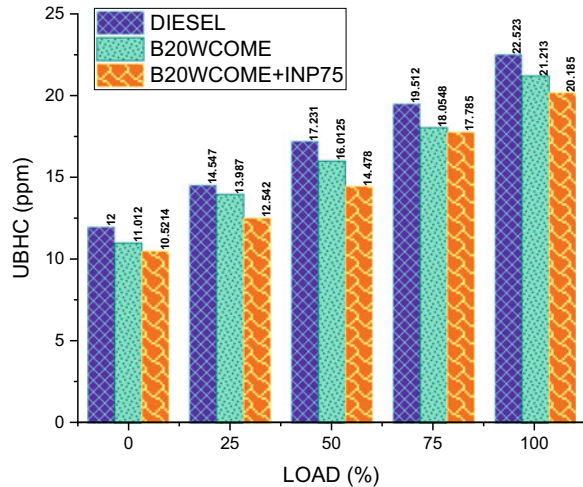


**Fig. 9** Distinction of UBHC with load



### 5.3 Unburnt Hydrocarbon (UBHC)

Figure 9 shows that UBHC emission of B20WCOME and B20WCOME + INP75 is less than diesel. Hydrocarbons present in the biodiesel contain more oxygen content. Due to catalytic behavior of iron oxide nanoparticles at higher load, B20WCOME + INP75 shows lesser UBHC emission than the diesel and B20WCOME.

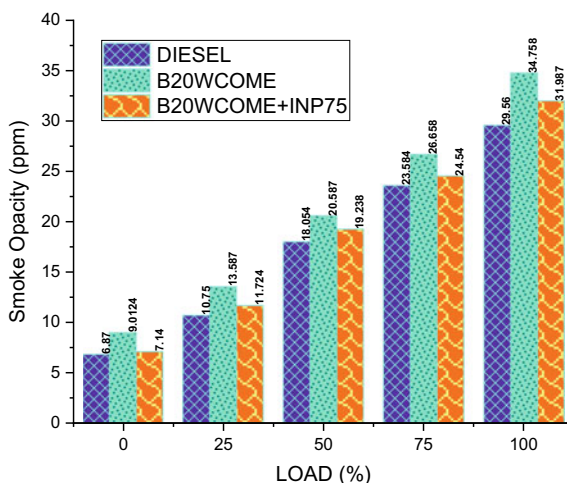
### 5.4 Smoke Opacity

The variation in smoke opacity with load is shown in Fig. 10. The smoke opacity increases for maximum load due to additional SFC. The smoke opacity of B20WCOME and B20WCOME + INP75 is more compared to diesel. Because of low volatility and higher viscosity, the B20WCOME and B20WCOME + INP75 samples. The particles of B20WCOME and B20WCOME + INP75 also one of the reasons to increase the smoke emission.

## 6 Conclusion

The performance, combustion, and emission (combustible products) characteristics of a CI engine fueled with biofuel with iron oxide and without iron oxide additives are experimentally investigated. Due to the acid and base esterification process, the kinematic viscosity and density of the WCO are reduced with increase in Cv of the fuel. B20WCOME with 75 ppm iron oxide nanoparticles (B20WCOME + INP75)

**Fig. 10** Distinction of smoke opacity with load



shows better brake thermal efficiency compared to B20WCOME and diesel. BSFC decreases significantly due to its catalyst effect by adding the iron oxide nanoparticles. At maximum load condition, HRR of the blends is lesser compared to diesel. The addition of iron oxide nanoparticles (INP 75PPM) to the B20WCOME, the emissions of NO<sub>x</sub>, CO, and UBHC decrease with slight increase in smoke opacity. A small amount of iron oxide in the variety of 75 ppm is used to achieve better engine performance through lower emissions, mainly to eliminate the drawbacks related to the use of biodiesel samples into diesel. By using WCO biodiesel with iron oxide nanoparticles, a significant percentage of the limited diesel can thus be eradicated.

## References

1. Ramesha D, Prema Kumara K, Abhishek Jain C, Akash N, BabuReddy B, Kallappa R, Kammara M (2015) Experimental investigation on combustion, performance and emission characteristics of plastic oil and biodiesel as a substitute fuel in diesel engine. IRJET 02
2. Mani M, Nagarajan G, Sampath S (2013) Characteristic and effect of using waste plastic oil and diesel fuel blends in compression ignition engine. Energy 36:212–219
3. Ramesh DK, Dhananjaya Kumar JL, Hemanth Kumar SG, Namith V, Jambagi PB, Sharath S (2016) Study on effects of Alumina nanoparticles as additive with Poultry litter biodiesel on Performance, Combustion and Emission characteristic of Diesel engine. Mater Today Proc PMME EMT 338:2214–7853
4. Madheshiyaa AK, Vedrtnamea A (2018) Energy-energy analysis of biodiesel fuels produced from waste cooking oil and mustard oil. Fuel 214:386–408
5. Avinash A, Sasikumarp, Murugesan A (2018) Understanding the interaction among the barriers of biodiesel production from waste cooking oil in India: an interpretive structural modeling approach. Renew Energy
6. Debbarma S, Misra RD (2017) Effects of iron nanoparticles blended biodiesel on the performance and emission characteristics of a diesel engine. J Energy Res Technol ASME 139

7. Seela CR, Ravi Sankar B, Kishore D, Babu MVS (2019) Experimental analysis on a DI diesel engine with cerium oxide added Mahua Methyl Ester blends. *Int J Ambient Energy*. <https://doi.org/10.1080/01430750.2017.1360203>
8. Ashok B, Nanthagopal K, Aravind M, Ajith J, Tamilarasu A (2017) Comparative analysis on the effect of zinc oxide and Ethanox as additives with biodiesel in CI engine. *Energy* (2017)
9. Jiaqiang E, Minhieu P (2017) Effect of different technologies on combustion and emissions of the diesel engine fueled with biodiesel. *Renew Sustain Energy Rev* 80:620–647
10. Sadafb S, Iqbala J, Ullahd I (2018) Biodiesel production from waste cooking oil: an efficient technique to convert waste into biodiesel. *Sustain Cities Soc* 41:220–226
11. Musthafa MM, Kumar TA, Mohanraj T, Chandramouli R (2018) A comparative study on performance, combustion and emission characteristics of diesel engine fuelled by biodiesel blends with and without an additive. *Fuel* 225:343–348
12. Knoth G, Steidley KR (2018) The effect of metals and metal oxides on biodiesel oxidative stability from promotion to inhibition. *Fuel Process Technol* 177:75–80
13. Attia AMA, Hassaneen AE (2016) Influence of diesel fuel blended with biodiesel produced from waste cooking oil on diesel engine performance. *Fuel* 167:316–328
14. Hwang J, Bae C, Gupta T (2016) Application of waste cooking oil (WCO) biodiesel in a compression ignition engine. *Fuel* 176:20–31
15. Vairamuthu G, Sundarapandian S, Kailasanathan C, Thangagiri B (2015) Experimental investigation on the effects of cerium oxide nanoparticle on calophyllum inophyllum (Punnai) biodiesel blended with diesel fuel in di diesel engine modified by nozzle geometry. *J Energy Inst* 89(4):668–682
16. D Silva R, Binu KG, Thirumaleshwara B (2015) Performance and Emission characteristics of a C.I. Engine fuelled with diesel and TiO<sub>2</sub> nanoparticles as fuel additive. *Mater Today Proceed* 2:728–3735
17. Man XJ, Cheung CS, Ning Z (2015) Effect of diesel engine operating conditions on the particulate size, nanostructure and oxidation properties when using wasting cooking oil biodiesel. *Energy Procedia Energy* 66:37–40
18. Cheung CS, Man XJ, Fong KW, Tsang OK (2015) Effect of waste cooking oil biodiesel on the emissions of a diesel engine. *Energy Procedia Energy* 66:93–96
19. Nanthagopal K, Ashok B, Tamilarasu A, Ajith J, Aravind M (2017) Influence on the effect of zinc oxide and titanium dioxide nanoparticles as an additive with Calophyllum inophyllum methyl ester in a CI engine. *Energy Convers Manage* 146:8–19

# Effect of Multiple Injection Strategy on Combustion of Cotton Seed Oil Biodiesel in CRDI Diesel Engine



**Ramesh Babu Nallamothe, Nallamothe Anantha Kamal, Nallamothe Seshu Kishan, Injeti Nanaji Niranjana Kumar and Basava Venkata Appa Rao**

**Abstract** Owing to their higher thermal efficiency, fuel economy and power, diesel engines are found to be a successful option in commercial vehicles, either on road or off road. But in diesel engines NO<sub>x</sub> and smoke emissions are high due to heterogeneous combustion. There is immediate need to exert effort in reducing these harmful emissions and to comply with the stringent emission regulations imposed. It is observed that the requirements in order to reduce NO<sub>x</sub> and smoke are contradicting. Adaptation of better injection strategy helps in having better tradeoff between NO and smoke. For smoke reduction advancing injection is favorable, and for reducing NO<sub>x</sub> emission, retardation of injection timing is required. Biodiesel which is eco-friendly is a good renewable alternative fuel to petro-diesel. Various methods are tried for reducing NO<sub>x</sub>, like retardation of injection, water injection, EGR and so on. In this work multiple injection strategy is used for improving combustion process in CRDI diesel engine for having better compromise in the requirements for the reduction of NO<sub>x</sub> and smoke emission. Biodiesel blend B20 is prepared from nonedible cotton seed oil using transesterification process. Combustion characteristics are analyzed with a selected multiple injection strategy while retarding injection timings. The strategy consists of three fuel pulses: pilot, main and post. The fuel

---

R. B. Nallamothe (✉)

Mechanical Systems and Vehicle Engineering Department, SoMCME, Adama Science and Technology University, 1888 Adama, Ethiopia  
e-mail: [ramesh.babu@astu.edu.et](mailto:ramesh.babu@astu.edu.et)

R. B. Nallamothe · I. N. Niranjana Kumar · B. V. Appa Rao

Marine Engineering Department, Andhra University, Visakhapatnam, India  
e-mail: [neeru9@yahoo.com](mailto:neeru9@yahoo.com)

B. V. Appa Rao

e-mail: [rao.basava@gmail.com](mailto:rao.basava@gmail.com)

N. Anantha Kamal

Department of Mechanical Engineering, Politecnico Di Milano, Lecco, Milan, Italy  
e-mail: [ananthakamal@gmail.com](mailto:ananthakamal@gmail.com)

N. Seshu Kishan

Department of Mechanical Engineering, Politecnico Di Milano, Bovisa, Milan, Italy  
e-mail: [seshukishan1997@gmail.com](mailto:seshukishan1997@gmail.com)

© Springer Nature Singapore Pte Ltd. 2020

G. S. V. L. Narasimham et al. (eds.), *Recent Trends in Mechanical Engineering*,  
Lecture Notes in Mechanical Engineering,  
[https://doi.org/10.1007/978-981-15-1124-0\\_9](https://doi.org/10.1007/978-981-15-1124-0_9)

quantity in pilot is fixed at 10% and that in post is fixed as 0.5 mg per cycle. The pilot pulse is at 10° crank angle before main injection pulse and post is closely coupled with CAD of 3 from main injection. The timing of the main injection along with pilot and post was retarded from the recommended 23° bTDC in intervals of 3°. The parameters related to combustion, like temperature, in-cylinder pressure, rate of pressure rise, cumulative heat release, net heat release and mass fraction of fuel burned, are compared with the baseline data obtained with diesel single injection at 23° bTDC.

**Keywords** Biodiesel · Dwell · Pilot injection · Post injection · Retardation

## 1 Introduction

Most of the commercial vehicles on and off road are powered by diesel engines. Thermal efficiency as well as fuel economy of diesel engines is superior to gasoline engines. Owing to their higher smoke and NO<sub>x</sub> emissions and related negative consequences on environment and human health, stringent emission regulations are imposed by the countries world over. Another pressurizing problem is fast depletion of nonrenewable petroleum fuels as their usage is growing at a higher rate to meet the growing energy demand of the world. The emissions from diesel engines are environmentally unfriendly and have an adverse effect on human health. It became inevitable for automotive industries and researchers in the field to work and find renewable fuel replacement to the conventional petroleum fuels to reduce emissions.

Fuels of bio-origin, like biodiesel, bioethanol, are found to be promising alternative fuels in terms of renewability and nonpolluting characteristics. It is imperative to work on engine design and optimization of combustion process to adopt biofuels and to reduce harmful emissions from the engines. With the implementation of the CRDI fuel system, fuel injection system became flexible with which one can vary injection parameters like injection pressure, number of injection pulses, injection timing, quantity of fuel injection and the like. Tradeoff between smoke and NO<sub>x</sub> emission is possible with optimization of multiple injection strategy.

Vegetable oils, having features of renewability, biodegradability, eco-friendly and so on, are promising replacement for conventional petroleum diesel. Higher viscosity is the major drawback of straight vegetable oils that hinder its usage directly in unmodified diesel engines. Direct usage of vegetable oils may cause deposits in combustion chamber and may damage the engine. Transesterification process is a well-established procedure that can be used to produce biodiesel by bringing down the viscosity. Triglycerides present in vegetable oil get converted into mono alkyl esters of long chain fatty acids (biodiesel) when vegetable oil reacts with alcohol in the presence of catalyst. Glycerin comes out as a byproduct [1]. Usage of biodiesels in compression ignition engines does not need any modification to the engine, and

with multiple environmental benefits, biodiesel is found to be one of the most promising alternative fuels to petro-diesel. Biodiesel is nonexclusive, biodegradable, non-flammable, renewable, nontoxic, environment-friendly and similar to diesel fuel [2]. Biodiesel has the advantages, such as it is miscible in diesel at any proportion; diesel engine does not need any modifications for usage of it as a fuel; it does not contain any harmful substances; and emissions from it are less harmful to environment than diesel. Biodiesel popularly known as mono alkyl esters is derived from triglycerides (animal fats or vegetable oils). Transesterification is mostly used for converting triglycerides to biodiesel. In transesterification process mono alkyl esters are produced by reacting light alcohol with triglycerides (existing in the oil) in the presence of base catalyst. Currently, potassium and sodium hydroxides are being used as catalysts in industrial scale for biodiesel production [3].

The engine development in the last few decades was mostly focused on the fuel economy improvement and reducing harmful emissions. Vehicle owners are more interested in fuel economy because it minimizes the expenses. The second is to comply with the regulations imposed by legislation, sometimes also supported by excise reductions or customers' demands for clean engines.

The NO<sub>x</sub> emission is detrimental to environment. It plays a role in causing global warming, acid rain and ozone depletion [4]. NO<sub>x</sub> emission is also one of the main causes of formation of the photochemical smog. Smog, which is dangerous, decreases visibility, damages materials, harms plants, irritates eyes and throat, and causes asthmatic attacks as well. NO<sub>x</sub> becomes acid when it mixes with moisture which leads to acid rain, harming the plants and human beings. Urea solution with high potential for the reduction of NO<sub>x</sub> is used as a reducing agent in a famous after-treatment system called selective catalytic reduction (SCR) [5]. SCR system with urea solution for reducing NO<sub>x</sub> emission is an established old idea. From then, many of the applications developed and some of them reached commercialization [6]. But, still it remains one of the challenging tasks for the researchers. With the recent development of common rail direct injection system, it became possible to reduce smoke, nitrogen oxides and other emissions by adopting multiple injection strategy [7, 8].

Split fuel injection involves reducing splitting the injection into multiple injection pulses, which leads to reduction of ignition delay of the first fuel injection. It leads to reduction in premixed combustion, and combustion extends toward the expansion stroke. Majority of NO<sub>x</sub> occur during premixed stage, due to the existence of peak temperature. The split injection helps in reducing NO<sub>x</sub> emission [9]. Multiple injection strategy is observed to be more effective in reducing PM emission at higher loads. Combined technique of multiple injections with EGR is effective at intermediate and light loads. However, increased particulate emissions due to EGR lead to degradation of lubrication oils which increases the engine wear. Brake specific fuel consumption (BSFC) increases with EGR. Split injection up to five splits is experimented in combination with EGR [10]. It is crucial to maintain optimum dwell period between injections. With very short dwell period, multiple injections become like a single injection, while long dwell period reduces the effect of premixed combustion. In case of pilot injection dwell period around 10 CAD reduces emission



efficiently. The first injection injected at around 21 CAD bTDC was found to be optimum for simultaneous reduction of soot and NOx [11]. The depletion of petroleum fuels and increasing price of petroleum led to an intensive search for alternative fuels. Biofuels are bio-based, biodegradable, environment-friendly, renewable, and are attracting growing interest around the world [12]. It is found that the emissions from the selected vehicles are very high and may continue to grow, if the problem is not unsolved. Exhaust emission findings estimated the highest level of NOx emissions at 3.44 g/km, HC emissions at 6.53 g/km, PM2.5 at 1.3 g/km, CO at 13.9 g/km and 35.96 g/km of CO<sub>2</sub>. These emissions are high and exceeding the proposed draft NEMA ambient air quality emission data and the ambient air quality guidelines of World Bank. Humans exposed to such a high level of emissions develop various ailments over a period of time. Several mitigation methods like reducing fossil fuel consumption and increasing the efficiency of energy usage in transportation can reduce harmful emissions [13].

Multiple injection strategy and addition of nanoparticles are used for improving combustion process in CRDI diesel engine for having better compromise in the requirements for the reduction of NOx and smoke emissions [14]. It is observed that the requirements in order to reduce NOx and smoke are contradicting. Adaptation of better injection strategy helps in having better tradeoff between NO and smoke [15]. Biodiesel which is eco-friendly is a good renewable alternative fuel to petrodiesel. Various methods are tried for reducing NOx, like retardation of injection, water injection and EGR [16].

## 2 Methodology

Multiple injection strategy is applied on CRDI diesel engine fueled with B20, which is a blend of 80% of diesel and 20% of biodiesel for the comparative analysis of combustion characteristics. Diesel injected at recommended injection timing of 23° bTDC is used to obtain baseline data. Biodiesel is produced from cotton seed oil using transesterification process.

The injection was split into three pulses: pilot, main and post. The pilot fuel quantity is fixed at 10% and post fuel quantity is fixed as 0.5 mg/cycle. The crank angle difference (dwell) between the main and pilot injection is 10° CAD and the main and post pulse is 3° CAD. The following are the steps followed in this work:

- Oil was extracted from cotton seeds using mechanical press.
- Transesterification process was used for preparing biodiesel using standard method. Phase separation is shown in Fig. 1. Washing of biodiesel is shown in Fig. 2.
- Produced biodiesel was characterized using standard procedure.
- 200 ml of biodiesel was mixed in 800 ml of diesel for preparing B20 blend. Prepared blend is shown in Fig. 3.



- Experiments were conducted with single injection diesel injected at  $23^\circ$  bTDC and the baseline data were obtained.
- The combustion performance testing of CRDI diesel engine was conducted with B20 using multiple injection strategy with varying injection timing at 75% load and constant speed of 1500 rpm and injection pressure of 300 bar.
- Combustion characteristics obtained from the selected multiple injection strategy were compared with that of single injection.

## 2.1 Engine Setup

The engine setup consists of four-stroke, single-cylinder and CRDI variable compression ratio (VCR) engine with eddy current dynamometer (Fig. 4). The necessary instruments for measuring cylinder combustion pressure, crank angle, load, temperature, airflow and fuel flow are provided. High-speed data-acquisition device is provided for interfacing the signals to the computer. The setup includes standalone panel box, which includes piezo powering unit twin fuel tank, air box, manometer, fuel flow measurements, fuel measuring unit process indicator and transmitters for air. For measuring engine

**Fig. 1** Preparation of biodiesel



**Fig. 2** Washing of biodiesel



**Fig. 3** Cotton seed oil, Biodiesel, B20, Diesel



**Fig. 4** Experimental setup



cooling water rotameter is provided. High pressure fuel pump is given in Fig. 5. In this CRDI VCR engine diesel injection is controlled with programmable open ECU, common rail with rail pressure sensor and pressure regulating valve, fuel

**Fig. 5** High pressure pump injection system



**Fig. 6** Open ECU**Fig. 7** Emission measuring instruments (AVL 437C Smoke Meter, AVL DIGAS 444 N)

injector, fuel pump, crank position sensor and wiring harness. Open ECU is shown in Fig. 6. The emission measuring instruments used are given in Fig. 7.

It is possible to measure the performance of CRDI VCR engine using programmable ECU with different EGR and at different compression ratios. It is possible to measure the engine performance parameters like indicated power, brake power, frictional power, IMEP, BMEP, indicated thermal efficiency, brake thermal efficiency, volumetric efficiency, mechanical efficiency, combustion analysis and heat balance. Figure 8 shows the schematics of engine setup. The detailed specifications are listed in Table 1.

### 3 Results and Discussions

#### 3.1 Biodiesel Characteristics

The measured properties of biodiesel prepared from cotton seed oil are given in Table 2. The properties are found to be in conformity with the standards.

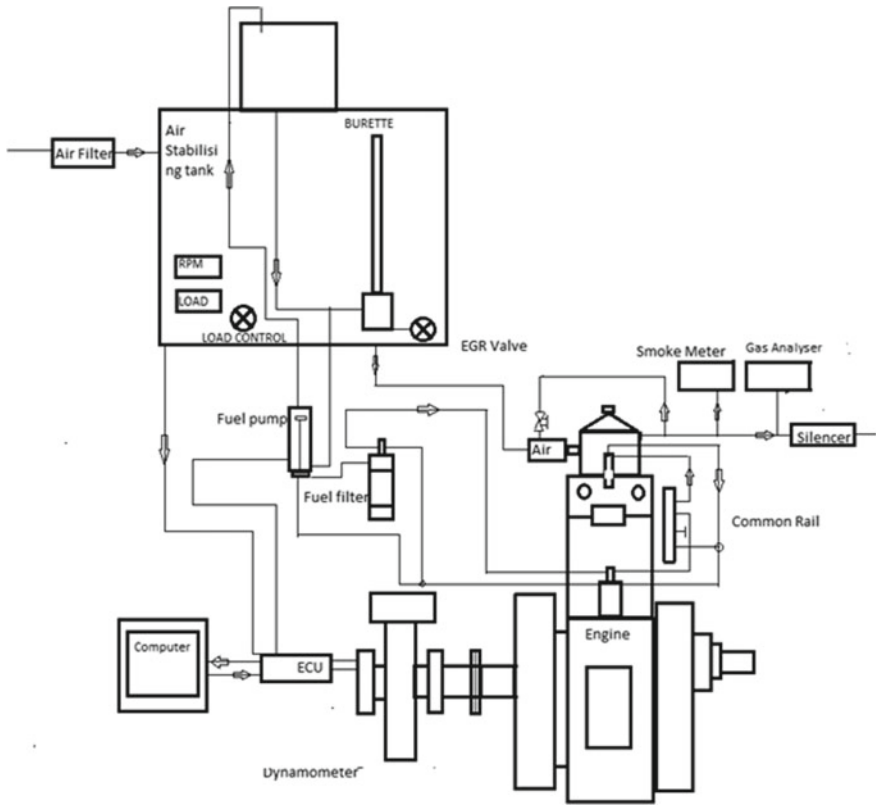


**Fig. 8** Schematics of engine setup

**Table 1** Specification of the CRDI engine

Engine	Kirloskar, four-stroke water cooled, single-cylinder, VCR
Stroke	110 mm
Bore	87.5 mm
Capacity	661 cc
Power	3.5 kW
Speed	1500 rpm
Compression ratio	12–18
Injection system	Common rail direct injection with open ECU
Injection pressure	300 bar
Dynamometer	Eddy current dynamometer
Dynamometer arm	185 mm

**Table 2** Properties of biodiesel (Eta Laboratories)

Properties	B100
Density @ 15 °C (g/cm <sup>3</sup> )	0.8865
Kinematics viscosity @ 40 °C	4.85
Flash point, °C	149
Fire point, °C	160
Cloud point, °C	+1
Gross calorific value, kJ/kg	40,695
Cetane number	50.8
Copper strip corrosion @ 50 °C for 3 h	Not worse than no 1
Acid value as mg of KOH/g	0.063
Carbon residue	0.041%
Sulfur	0.0043%

### Combustion Characteristics

Combustion characteristics like in-cylinder rate of pressure rise, pressure, in-cylinder temperature, heat release rate, cumulative heat release, mass fraction fuel burned and so on are depicted in the following graphs.

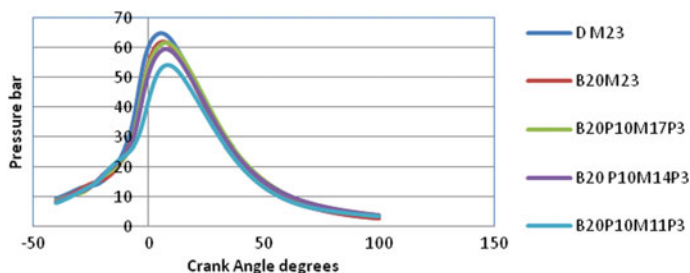
Combustion process analysis is very much required to understand the complex and intervening influence of many parameters on performance and emission of the engine.

### In-Cylinder Pressure

The in-cylinder pressure variation can be seen in Fig. 9. It is seen that the peak pressure of biodiesel blend with multiple injections is less than diesel. Also it is observed that the peak pressure continues to reduce as the multiple injection scheme is retarded. In case of retardation, due to reduction of ignition delay, the mass of fuel burned in premixed stage reduces, thus reducing the peak pressure.

### Rate of Pressure Rise

Rate of pressure rise is highest in diesel injected at recommended crank angle of 23°bTDC as shown in Fig. 10. For B20 at 23°bTDC is almost equal to diesel. In

**Fig. 9** Variation of in-cylinder pressure

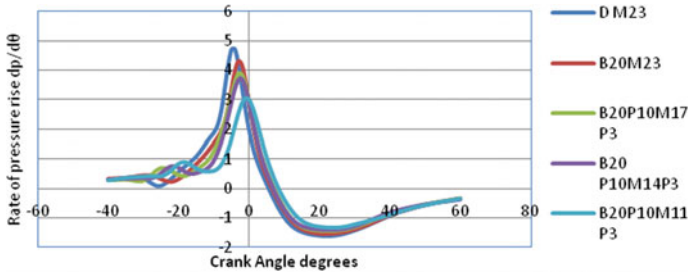


Fig. 10 Rate of pressure rise

other cases with B20 and multiple injection strategy as injection, retarding the rate of pressure rise observed to be reducing continuously. The position of peak pressure also moves closer to TDC as injection is retarded. Lower rate of pressure rise leads to smooth running of the engine, which improves the durability of the engine.

### In-Cylinder Temperature

In-cylinder temperature shown in Fig. 11 also observed to be following the similar pattern. The temperature for B20 is almost the same as that of diesel. It is slightly less because of higher cetane number, ignition delay reduces and peak temperature may reduce somewhat. Splitting the injection and retarding causes reduction in the cylinder temperature. In case of multiple injections, it is observed that the temperatures are maintained little less than diesel at recommended injection timing. Splitting and retarding injection causes further reduction in peak temperature. This helps in reduction of NOx emission. Here a very specific feature is observed in case of multiple injections, that the temperature in later stages of combustion is higher than diesel and B20 single injection. Maintenance of higher temperature in later stages of combustion helps in oxidation of soot, which helps in reduction of smoke somewhat. B20 P10M11P3 maintained higher temperature.

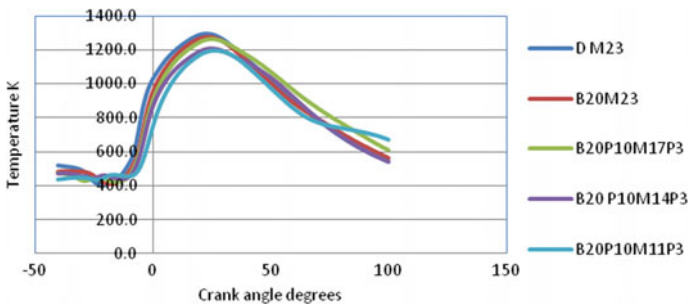
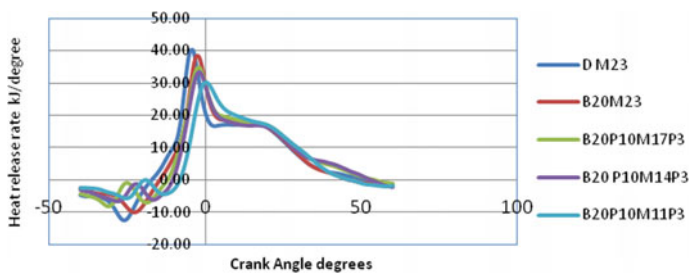


Fig. 11 In-cylinder temperature



**Fig. 12** Heat release rate

### Heat Release Rate

Figure 12 shows the heat release rate for diesel, B20, and B20 with multiple injections at different injection timings of retarded injection at 75% load. Two distinct zones in heat release rate are observed clearly from the graph. The first zone of combustion is premixed combustion and second zone is controlled combustion zone. Premixed combustion zone starts from start of injection and extends up to the point where heat release rate drops deeply. After the first zone, controlled combustion zone of longer duration starts and extends up to the end of combustion. Somewhat lower heat release rate exists in this zone and spreads over longer combustion duration. In second zone heat release rate mostly depends upon the rate at which fuel is injected and mixing rate of air and fuel in the combustion chamber. In the first zone the rate of heat release is higher for diesel due to longer ignition delay and accumulation of more fuel. The heat release rate in multiple injections is less in the first zone and the peak heat release rate is also less than single injection diesel due to shorter ignition delay, causing smooth combustion. Heat release rate is higher for multiple injections in second zone.

### Cumulative Heat Release

Figure 13 shows the variation existing in cumulative heat release. Higher cumulative heat release is observed for B20P10M17P3 than others. This is because of appropriate mixing of air and fuel and higher thermal efficiency. Variation of mass fraction of fuel burned is shown in Fig. 14.

## 4 Conclusions

- Multiple injections lead to smooth combustion which may reduce the noise and improve the durability of the engine.
- The peak in-cylinder pressure is higher for diesel whereas for biodiesel blend with multiple injections the peak pressure reduced and peak point moves away from TDC.

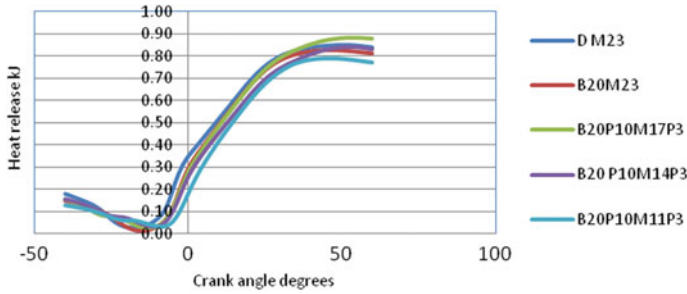


**Fig. 13** Cumulative heat release

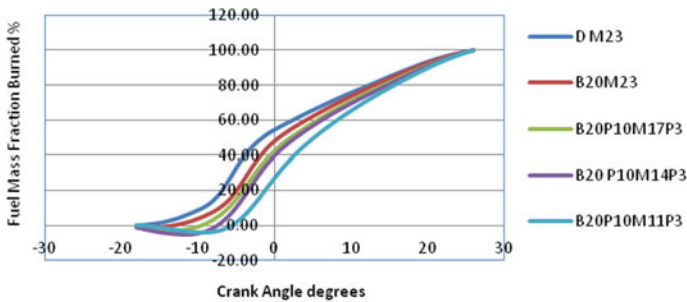


**Fig. 14** Mass fraction of fuel burned

- Owing to higher ignition delay, the pressure rises with higher rate in case of diesel and accumulation of the fuel. For multiple injections the rate of pressure rise is less. With retardation the rate at which pressure is rising is observed to be reducing.
- In-cylinder temperature is higher for diesel single injection. For multiple injections the peak temperature is less. In later part of the combustion process slightly higher temperature is maintained in case of multiple injection strategy. This helps in oxidation of soot formed during premixed combustion phase. Owing to lower peak temperatures, the NO<sub>x</sub> emission is less in multiple injection strategy. Retardation further reduces the NO<sub>x</sub> emissions.
- Multiple injection strategy helped in reducing heat release rate, due to shorter ignition delay. Heat release rate is higher for the multiple injections in second zone.
- In case of B20P10M17P3 cumulative heat release is observed higher than others. This is because of appropriate mixing of air and fuel and higher thermal efficiency.

**Acknowledgements** The authors express their heartfelt gratitude to Marine engineering Department, Andhra University and Adama Science and Technology University, Ethiopia for giving this opportunity to work on biodiesel applications in diesel engines. They are thankful to Sri Venkateswara Research Center, Kanchipuram for providing necessary research facilities.



## References

1. Pankaj Shelke S, Nitin Sakharea M, Lahanea S (2016) Investigation of Combustion Characteristics of a Cottonseed Biodiesel Fuelled Diesel Engine. *Global Colloquium in Recent Advancement and Effectual Researches in Engineering, Science and Technology (RAEREST 2016)*, Procedia Technology 25
2. Putrasari Y, Nur A, Muharam A (2013) Performance and emission characteristic on a two cylinder DI diesel engine fuelled with ethanol-diesel blends. In: *International Conference on Sustainable Energy Engineering and Application [ICSEEA]* Energy Procedia 32
3. Atabani AE, Silitonga AS, Ong HC, Mahlia TMI, Masjuki HH, Badruddin IA, Fayaz H (2013) Non-edible vegetable oils: a critical evaluation of oil extraction, fatty acid compositions, biodiesel production, characteristics, engine performance and emissions production. *Renew Sustain Energy Rev J* 18:211–245
4. Pushparaj T, Ramabalan S (2013) Green fuel design for diesel engine combustion, performance and emission analysis. In: *International Conference on Design and Manufacturing IConDM*. Research Scholar, Tamil Nadu, India
5. Busca G, Lietti L, Ramis G, Berti F (1998) Chemical and mechanistic aspects of the selective catalytic reduction of NO<sub>x</sub> by ammonia over oxide catalysts: a review. *Appl catal B. Environ* 18(1–2):1–36
6. Bosch H, Janssen FJJG (1988) Catalytic reduction of nitrogen oxides: a review on the fundamentals and technology. *Catal Today* 2(369)
7. Perry RA, Siebers DL (1986) Rapid reduction of nitrogen oxides in exhaust gas streams. *Nature* 324:657–658
8. Imarisio R, Ricco M, Rossi Sebastiano GH (2000) Multiple injection, a cost effective solution for emission reduction of common-rail DI diesel engines. *Aachener Kolloquium Fahrzeug-und Motorentechnik* 9:1047–1062
9. Badami M, Millo F, Mallamo F, Rossi EE (2002) Influence of multiple injection strategies on emissions, combustion noise and BSFC of a DI common rail diesel engine. *SAE Tech Ser*, No. 2002-01-0503
10. Gao Z, Schreiber W (2001) The effects of EGR and split fuel injection on diesel engine emission. *Int J Automot Technol* 2(4):123–133
11. Nallamothu RB, Anantha Kamal N, Seshu Kishan N, Niranjan Kumar IN, Appa Rao BV (2018) Emission analysis of CRDI diesel engine fueled with cotton seed oil biodiesel with multiple injection strategy. *Int J Emerg Technol Innovative Res* 5(9):707–712
12. Nallamothu RB, Fekadu G, Appa Rao BV (2013) Comparative performance evaluation of gasoline and its blends with ethanol in gasoline engine. *G.J.B.A.H.S* 2(4):100–106
13. Neway S, Nallamothu RB, Seshu Kishan N, Anantha Kamal N (2016) Investigation on pollution caused by gasoline and diesel fuelled vehicles. *Int J Eng Trends Technol (IJETT)* 36(7):376–381
14. Nallamothu RB, Niranjan Kumar IN, Appa Rao BV, Anantha Kamal N, Seshu Kishan N (2018) Emission analysis of CRDI diesel engine fueled with cotton seed oil biodiesel with multiple injection strategy. *Int J Emerg Technol Innovative Res* 5(9):707–712
15. Nallamothu RB, Birbirs G, Niranjan Kumar IN, Appa Rao BV, Seshu Kishan N (2019) A review on performance of biodiesel in engines with and without addition of nanoparticles. *Int J Manag Technol Eng IJMTE/1592 IX(I)*, January
16. Nallamothu RB, Lemma M, Niranjan Kumar IN, Appa Rao BV, Anantha Kamal N, Seshu Kishan N (2019) Performance of cotton seed biodiesel with nano additives in diesel engines: a review. *J Appl Sci Comput VI(II):142–147*

# Combustion and Emission Behaviour of Honge Biofuel in a Thermal Barrier Coated Diesel Engine Suitable for Agriculture



Muralidharan Kandasamy and Duraisamy Senthilkumar

**Abstract** Vehicular air pollution causes a huge threat to mankind, especially diesel engines. This study focuses on estimating the pollutant levels of Honge biodiesel in a single-cylinder IC engine which would be ideally suitable for agricultural field. The engine combustion chamber was coated with thin film ceramic material YSZ of 150  $\mu\text{m}$  thickness using plasma spray technique and fuel injection pressure was varied. Honge blend B15 at 230 bar exhibited earlier heat release rate at 4°CA BTDC than diesel in coated engine. Emission reduction of CO, HC and smoke of about 50, 26.5 and 20% was attained for blend B15 compared with diesel and other biodiesel blends at 230 bar. NO<sub>x</sub> and CO<sub>2</sub> emissions were high for Honge biodiesel fuels.

**Keywords** Honge biofuel · Injection Pressure · Thermal Barrier Coating

## Abbreviation

TBC	Thermal Barrier Coating
CA	Crank angle
BTDC	Bottom dead center
DI	Direct injection
D	Diesel
B5	5% Biodiesel + 95% Diesel
B10	10% Biodiesel + 90 % Diesel
B15	15% Biodiesel + 85 % Diesel
B20	20% Biodiesel + 80% Diesel
B25	25% Biodiesel + 75% Diesel
B30	30% Biodiesel + 70% Diesel

---

M. Kandasamy (✉) · D. Senthilkumar  
Department of Mechanical Engineering, Sona College of Technology, Salem, Tamil Nadu, India  
e-mail: [Muralidharan\\_dr@Sonatech.ac.in](mailto:Muralidharan_dr@Sonatech.ac.in)

D. Senthilkumar  
e-mail: [mech@sonatech.ac.in](mailto:mech@sonatech.ac.in)

CO	Carbon monoxide
HC	Hydrocarbon
CO <sub>2</sub>	Carbon dioxide
NO <sub>x</sub>	Oxides of nitrogen
HRR	Heat release rate
YSZ	yttria-stabilized zirconia
CI	Compression Ignition
IC	Internal Combustion

## 1 Introduction

The usage of fossil fuels for transportation poses environmental pollution in India. Owing to high farming cost of Jatropha oil, it was replaced by Honge and castor oils in India which can be grown in arid and wastelands. Honge oil seeds are widely available and its oil content was around 35% [1, 2].

Several studies have exposed the consequence of injection pressure in fuel consumption rate, which tends to increase fuel and air mixing causing better atomization and enhanced combustion process at high injection pressures [3, 4]. The effective use of sunflower biodiesel in CI engine was investigated using thermal barrier coating technique. Performance factors are examined by running the engine at various speeds in full load condition and the values are compared with uncoated engine. Scientists suggested thin film coating of thickness less than 500  $\mu\text{m}$  of YSZ over bond coat for better improvement of engine performance and emission features [5, 6].

Thermal coating enables use of lower heating value fuels effectively in diesel engine since it allows using of higher combustion temperatures that improve engine performance and emission characters. The engine output power and efficiency has improved in coated engines. Biodiesels possess lesser heating value compared with diesel which resulted in rise of specific fuel consumption with the increase of blend percentage in diesel. Coated engine uses higher combustion temperatures which increases the overall engine performance [7].

## 2 Materials and Methods

### 2.1 Fuel Preparation

The most suitable method of producing biodiesel is transesterification process where raw Honge oil is reacted with methanol in the existence of alkyl catalyst sodium hydroxide to form methyl ester and glycerol [1].

## 2.2 Engine Operating Conditions

The tests were done on a single-cylinder CI engine connected with dynamometer to regulate engine speed and load. The fuel injection rate was varied from 210 bar in terms of 10 bar pressure by adjusting fuel injector. For each injection pressure, the engine performance evaluation parameters are measured at varying engine load. The total uncertainty for the entire experiment was calculated to be  $\pm 2.28\%$  [8].

In this experimental work, the cylinder head, inlet valve, piston top and exhaust valve of direct injection IC engine were covered with ceramic material of low thermal conductivity of thickness 100  $\mu\text{m}$  above the nickel chromium aluminium alloy (NiCrAl) coating, with a total thickness of 150  $\mu\text{m}$ .

## 3 Results and Discussion

### 3.1 Carbon Monoxide Emission (CO)

Carbon monoxide emission reduces in part loads and rises in higher loads, as shown in Fig. 1, for all the fuels investigated, which might be due to high viscosity values and specific gravity during the entire combustion process [9]. Lower blends B10 and B15 emitted lesser CO at all loads due to their oxygen content, which enhances the combustion process. The coated engine resulted in significant reduction of CO emission in percentage of 25 for diesel, 26.67 for B5, 36.36 for B10, 40 for B15, 28.57 for B20, 30.77 for B25 and 33.33 for B30 than that of conventional diesel engine due to the high cylinder wall temperature [10].

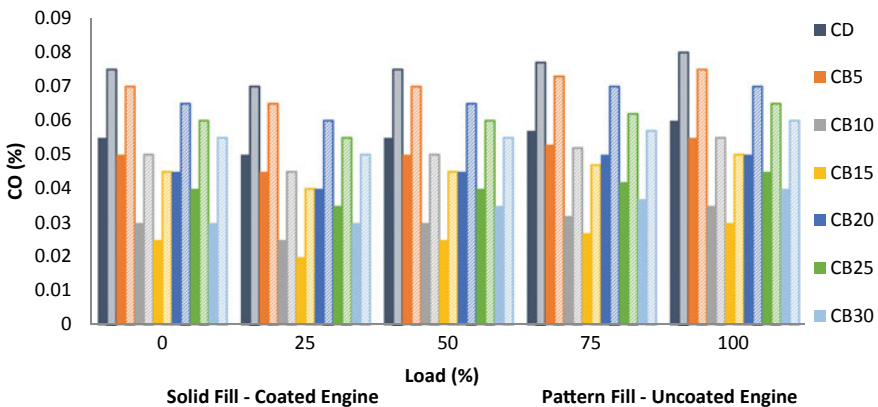


Fig. 1 Variation in CO emission versus engine load at 230 bar pressure

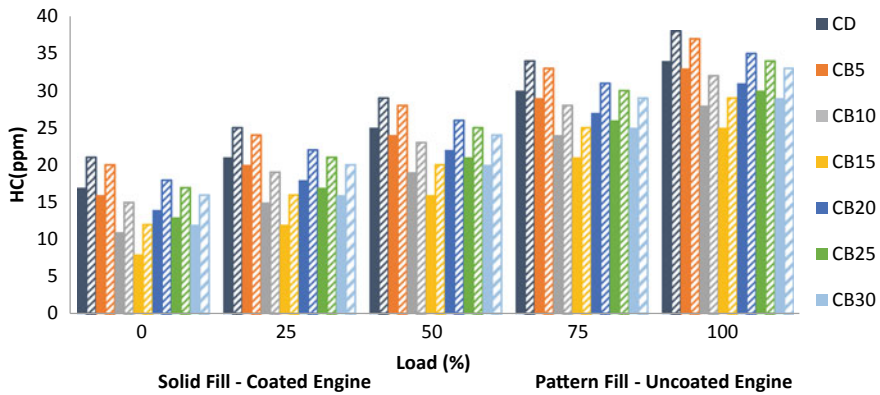


Fig. 2 Variation in HC emission versus engine load at 230 bar pressure

### 3.2 Unburnt Hydrocarbon Emission (HC)

The unburnt HC emission increases with engine load, as indicated in Fig. 2. Coated engine produces significant reduction in unburnt HC level due to its high operating temperature for all the fuels examined at the rate of 10.53%, 10.81%, 12.5%, 13.8%, 11.43%, 11.76% and 12.12% for fuels D, B5, B10, B15, B20, B25 and B30, respectively, at full load. Blend B15 exhibits lower HC emission than other fuels at all loads, since slightly higher viscosity and intrinsic oxygen content in biodiesel along with high working temperature in coated engine is responsible for the reduction of HC at 230 bar.

### 3.3 Oxides of Nitrogen ( $NO_x$ )

Coated engine resulted in higher levels of  $NO_x$  emissions at the rate of 5.82% for diesel, 5.08% for B5, 5.56% for B10, 5.69% for B15, 5.56% for B20, 5.31% for B25 and 5.19% for B30 due to its higher operating temperature and oxygen content of fuel, as represented in Fig. 3 [10]. Diesel and biodiesel blends in coated engine produced higher emission of  $NO_x$  in percentage of 5.5 for diesel, 5.43 for B5, 5.64 for B10, 5.85 for B15, 5.71 for B20, 5.45 for B25 and 5.33 for B30 than that of conventional diesel due to better fuel spray characteristics produced at 230 bar pressure.

### 3.4 Smoke Emission

Smoke emission increases with increase of engine load, as indicated in Fig. 4. The coated engine exhibits lesser smoke emission than uncoated engine in percentage of

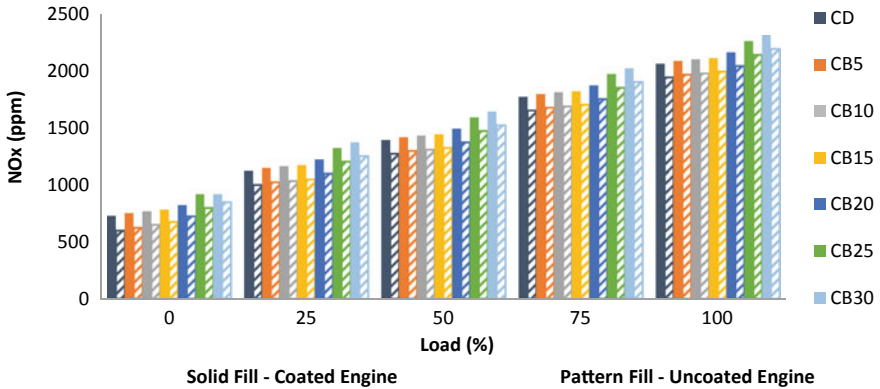


Fig. 3 Variation in NO<sub>x</sub> emission versus engine load at 230 bar Pressure

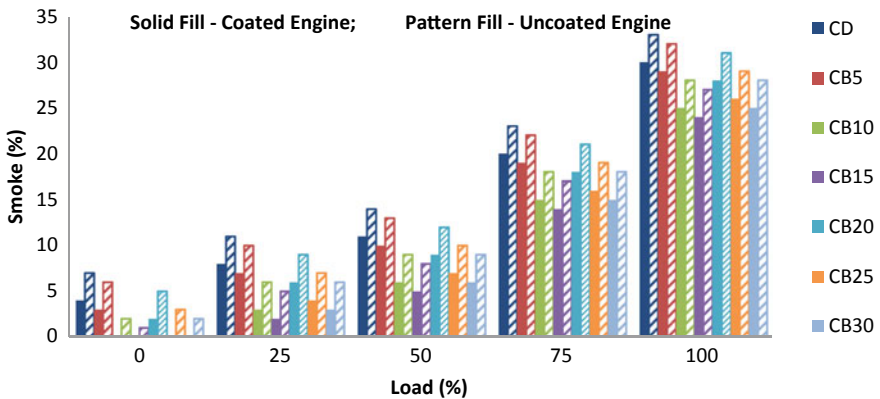


Fig. 4 Variation in smoke emission versus engine load at 230 bar pressure

9.09 for diesel, 9.38 for B5, 10.71 for B10, 11.11 for B15, 9.68 for B20, 10.35 for B25 and 10.71 for B30 due to its high working temperature.

### 3.5 Cylinder Peak Pressure

It was noticed from Fig. 5 that the coated engine exhibits higher peak cylinder pressure for diesel and biodiesel blend B15 at full load at the rate of 5.37% for diesel, 5.62%, 5.83%, 5.74% and 5.85% for B15 at 210 bar, 220 bar, 230 bar and 240 bar, respectively. It was observed that biodiesel blend B15 up to 230 bar produced higher heat release rates.

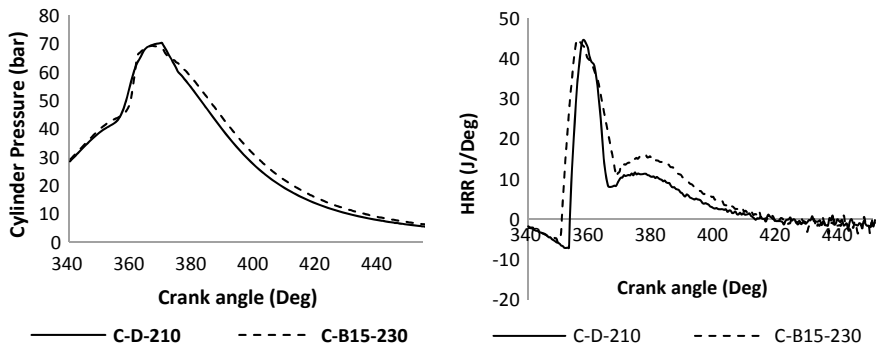


Fig. 5 Variation in cylinder pressure and HRR versus crank angle

Biodiesel blend B15 at 230 bar pressure exhibits slightly lower peak cylinder pressure of about 1.41% than diesel fuel at 210 bar pressure in coated engine due to its calorific value. The occurrence of peak cylinder pressure rise is slightly earlier to blend B15 than diesel due to its shorter ignition delay [10].

### 3.6 Heat Release Rate (HRR)

In coated engine, diesel exhibits higher HRR of about 6.76% than uncoated diesel, and biodiesel blend B15 shows higher HRR of 7.55% at 210 bar, 6.83% at 220 bar, 10.26% at 230 bar and 9.8% at 240 bar when compared with uncoated engine, as indicated in Fig. 5. The occurrence of maximum heat release rate was about 2.5°CA BTDC for diesel at 210 bar, and blend B15 at 230 bar experiences earlier heat release at 4°CA BTDC due to its rapid combustion process in coated engine.

## 4 Conclusion

Experimental results confirmed that biodiesel blend B15 derived from Honge oil feedstock shows better emission and combustion levels at fuel pump pressure of 230 bar and can be recommended as a fuel substitute to diesel which could be suitable for farmers. The influence of YSZ coating of 150  $\mu\text{m}$  on engine combustion chamber revealed 40% CO emission reduction, HC emission of 17.14%, smoke emission of 7.69% in full load with slightly higher  $\text{NO}_x$  levels of 2.84%. The increase in fuel injection pressure of about 20 bar (230 bar) gives 5.21% maximum heat release rate for diesel and 4.655 for B15 fuel in coated engine. The occurrence of maximum HRR for B15 was earlier around 2°CA before diesel fuel.

**Acknowledgements** The authors would like to acknowledge the Management, Secretary, Principal and Head of Department of Mechanical Engineering in Sona College of Technology, Salem-636 005 for providing all the institutional help and support for this research work.

## References

1. Murugesan A, Umarani C, Chinnusamy TR, Krishnan M, Subramanian R, Neduzchezhain N (2009) Production and analysis of bio-diesel from non-edible oils-A review. *Renew Sustain Energy Rev* 13:825–834
2. Ghassan Tashtoush M, Al-Widyan Mohamad I, Albatayneh Aiman M (2007) Factorial analysis of diesel engine performance using different types of biofuels. *J Environ Manage* 84:401–411
3. Purushothaman K, Nagarajan G (2009) Effect of injection pressure on heat release rate and emissions in CI engine using orange skin powder diesel solution. *Energy Convers Manag* 50:962–969
4. Hazar H, Ozturk U (2010) The effects of  $\text{Al}_2\text{O}_3$ - $\text{TiO}_2$  coating in a diesel engine on performance and emission of corn oil methyl ester. *Renew Energy* 35–10:2211–2216
5. Hejwowski T, Weronki A (2002) The effects of thermal barrier coatings on diesel engine performance. *J Vac* 65:427–432
6. Hasimoglu C, Ciniviz M, Ozsert I, Icingur Y, Parlaand A, Sahir Salman M (2008) Performance characteristics of a low heat rejection diesel engine operating with biodiesel. *Renew Energy* 33:1709–1715
7. Haldar SK, Ghosh BB, Nag A (2009) Utilization of unattended Putranjivaroxburghii non-edible oil as fuel in diesel engine. *Renew Energy* 34:343–347
8. Holman JP (2001) *Experimental methods for engineers*, 7th edn. McGraw-Hill International Edition, New York
9. Hazar H (2009) Effects of biodiesel on a low heat loss diesel engine. *Renew Energy* 34:1533–1537
10. Hazar H (2010) Cotton methyl ester usage in a diesel engine equipped with insulated combustion chamber. *Appl Energy* 87(1):134–140



# Experimental Analysis on Emission Characteristics of Palmarosa Alkyl Group Biofuel Feedstock



Ganapathi Arumugam and Kandasamy Muralidharan

**Abstract** This work proposes palmarosa methyl ester (PME) as a potential alternative energy source as the above species is widely grown in wetland provinces of India, Bhutan, Afghanistan, including Nepal and China. PME was emulsified with oil fuel at varied volume magnitudes of PME10, PME20, PME30, PME40 and PME100 and their properties were analyzed as per ASTM standards in a single-cylinder ICE at continuous swiftness (1500 rev/min) for its regulated emissions. Test results foretold that the characteristics of PME20 resulted in marginally more elevated amounts of THC (2%), carbon-dioxide (4.1%) and carbon monoxide (3.86%) emissions when equated with diesel.

**Keywords** Palmarosa methyl ester · Combustion · Biofuel · Regulated emission

## 1 Introduction

Diesel engines (compression ignition) were widely preferred in industrial, automotive sector and in agricultural applications because of its enhanced thermal efficiency, sturdiness and persistence than SI engines. This addiction is increasing with rapid exhaustion property of fossil ferrous fuel, escalating fuel prices, and raising concerns of environmental pollution by combustion of hydrocarbon fuel. This scenario has accelerated the emphasis on emerging an energy-efficient biofuel for CI engine and reducing the habituation of fossil assets. Abu-Zaid et al. [1], Bilgin and Sezer [11], Cheung et al. [14], Zhao et al. [40] and Zhu et al. [41] found that the alcohols were operative in depressing the exhaust emissions. Importing fossil fuels for the economic advancement and development in some countries has also been an uncertainty in the last few decades, since they could not root their own alternative

---

G. Arumugam (✉)

Mechanical Engineering, AVS College of Technology, Salem, Tamil Nadu, India

e-mail: [ganomec@gmail.com](mailto:ganomec@gmail.com)

K. Muralidharan

Mechanical Engineering, Sona College of Technology, Salem, Tamil Nadu, India

e-mail: [Muralidharan\\_dr@sonatech.ac.in](mailto:Muralidharan_dr@sonatech.ac.in)

© Springer Nature Singapore Pte Ltd. 2020

G. S. V. L. Narasimham et al. (eds.), *Recent Trends in Mechanical Engineering*,

Lecture Notes in Mechanical Engineering,

[https://doi.org/10.1007/978-981-15-1124-0\\_11](https://doi.org/10.1007/978-981-15-1124-0_11)

fuel source [24]. Higher alcohol fuels, like propanol and n-octanol, give variation in performance than the lower alcohol fuels, like methyl and ethyl alcohol [38, 12, 16]) in rapport with upgraded knock resistance, higher performance and curtailed hydrocarbon and carbon mono-oxide emissions. In recent years, alcohols like isomers of propanol and butanol attain attractions owing to its striking physio-chemical properties as they are easily renewable [15, 23, 36].

## 2 Experimental Materials and Methods

### 2.1 Test Fuel Preparation

Cymbopogon martini methyl ester (PME) was produced using a 2L batch reactor, a magnetic stirrer, a condenser, a sampling outlet unit and a thermometer. Biodiesel was prepared by means of acid–base catalyst procedure. Initially before starting esterification, the palmarosa oil stays heated up to 65 °C with the help of a rotary evaporator in vacuum for moisture removal. For esterification, a molar mixture of methanol in the ratio of 6:1 with preheated raw oil and 1.5% (v/v) sulfuric acid ( $H_2SO_4$ ) were stirred for 1 h at 65 °C at 600 rpm. Then, using a funnel separator the esterified oil was separated from sulfuric acid and other impurities. The separated esterified oil was heated at 65 °C for 1 h in an evaporator of rotary type for removing water and methanol. After esterification, transesterification is further conducted to minimize the viscosity as the raw oil is very viscous. For transesterification, a molar mixture of ratio 6:1 of methanol to raw oil and 0.9 (wt%) of KOH (potassium hydroxide) were added to the esterified oil and stirred for 1 h at 65 °C at 600 rpm (Tables 1, 2).

**Table 1** Properties of palmarosa

S. no	Properties	Parameter
1	Color	Pale yellow
2	Odor	Pleasing
3	Flash point, °F	116
4	Cetane number	54
5	Viscosity @40 °C, mm <sup>2</sup> /s	3.67
6	Calorific value (kJ/kg)	42,440
7	Density @20 °C (kg/m <sup>3</sup> )	869

**Table 2** Main properties of blending stocks

Properties	DIESEL	PME10	PME20	PME40	PME100
Density at 20 °C, kg/m <sup>3</sup>	840	834	841	851	869
Kinematic viscosity at 40 °C, mm <sup>2</sup> /s	3.246	3.302	3.392	3.592	3.67
Calorific value, kJ/kg	44,780	42,340	41,820	40,910	40,220

## 2.2 Engine Tests

A fixed diesel Kirloskar engine (model: TAF-1 make: Kirloskar) was engaged for investigation. Tests were performed at five load intervals of 0, 25, 50, 75 and 100 percentages that measure tantamount with various brake power ranges. Initially, the engine was run with diesel for 20 min to heat it up before the testing of different blends. Similarly, between one and different fuel, engine was allowed to run for 10 min to make sure complete combustion of the residual fuel and in cylinder homogeneity. The schematic layout of installation is forecasted in Fig. 1.

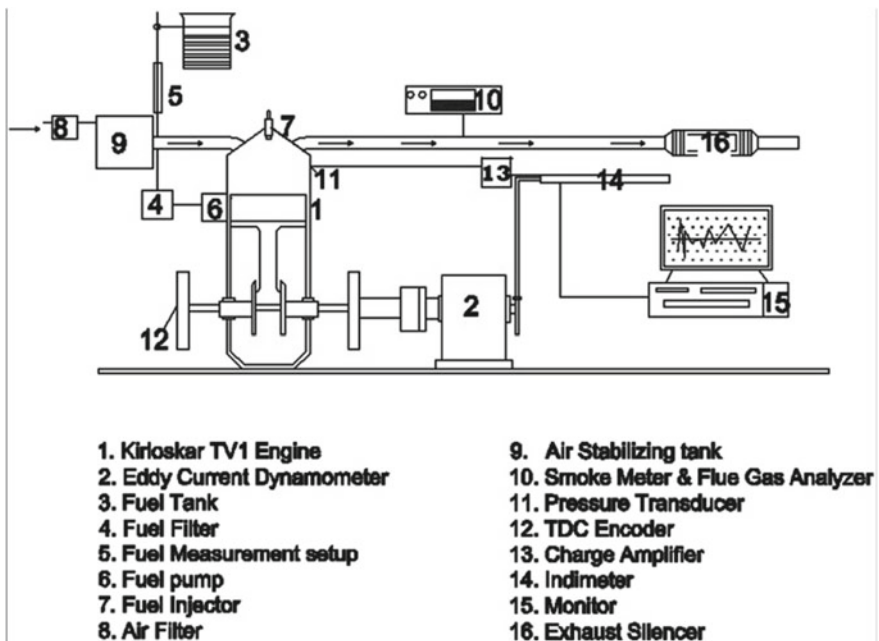


**Fig. 1** Schematic layout of test installation

### 2.3 Test Fuel Preparation

## 3 Results and Discourse

### 3.1 Total Unburned Hydrocarbon (THC)

There are numerous possible sources for unburned organic compound formation in CI engines. HC are incompletely burnt fuel particles either in volatile state (organic compounds) or in solid state (particulate matter) which are shaped in CI engines as a result of fuel being stuck in nozzle, crevice areas, piston boundary, incomplete evaporation of fuel mixture, elevated rich/lean mixture and liquid wall film edge with additional spray impingement [17] and accounts for majority of HC emission. HC emissions inferred from Fig. 2 of biofuel blends compared to diesel at part load 25% are increased by 35.16% for PME10, 2% for PME20, 138% for PME30, 108% for PME40 and 240% for PME100. This might be attributed to the concentration of alcohol that could probably end in cooling effect of blends and showcases reduced cylinder temperatures and imperfect combustion followed by elevated THC [39]. Additionally, quenching within the lean mixture zones and drop in cetane range results in Campos-Fernandez et al. [12] depressed self-ignition characteristics of PME-diesel blends that causes dejected evaporation rate, poor blending rate and partial combustion. Along with depressed density and viciousness of PME-diesel

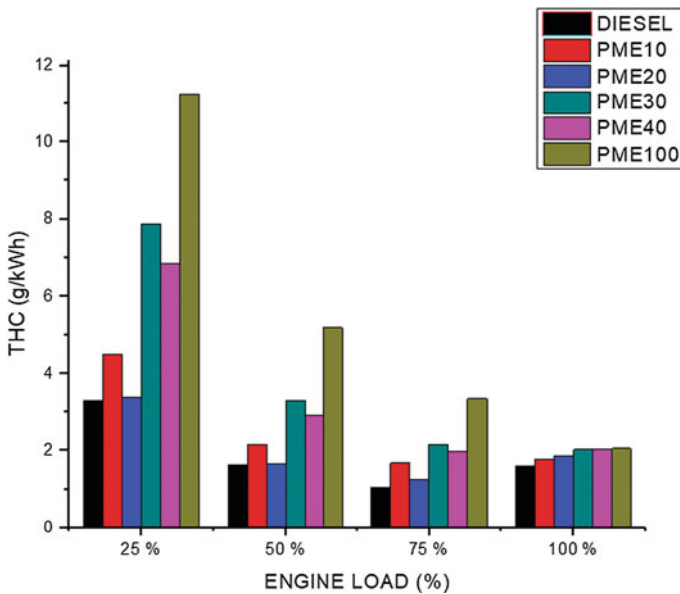


Fig. 2 Variation of THC with respect to engine load

blends, fine fuel droplets development adherent to the cylinder walls vaporizes late throughout the expansion stroke. THC emission was almost similar at full load compared to diesel (0.69% for PME10, 1.2% for PME20, 1.8% for PME30, 1.9% for PME40 and 2.3% for PME100).

### 3.2 Carbon Dioxide (CO<sub>2</sub>)

CO<sub>2</sub> formation depends on elemental carbon, C/H ratio, mixture density and total offered gas throughout combustion. For any fuel, there is a well-defined trade-off between CO and CO<sub>2</sub>, stated whenever there is an increase in CO for a specific fuel, and there will be even dwell period in CO<sub>2</sub> formation. We tend to infer from Fig. 3 that during the 25% load condition PME-blends with base fuel possess slightly higher levels of CO<sub>2</sub> emission (7.577% PME10, 4.118% PME20, 8.126% PME30, 11.504% PME40 and 6.277% PME100) signifying the presence of O<sub>2</sub> content in biodiesel, and thus promoting complete combustion. Additionally, there is a clear call that the CO<sub>2</sub> emission for PME100 as compared with different blends like PME30 and PME40 may well be explained on the idea of lowered calorific value and better fuel density poignant the entire combustion of fuel molecule followed by lowered greenhouse gas (CO<sub>2</sub>) formation.

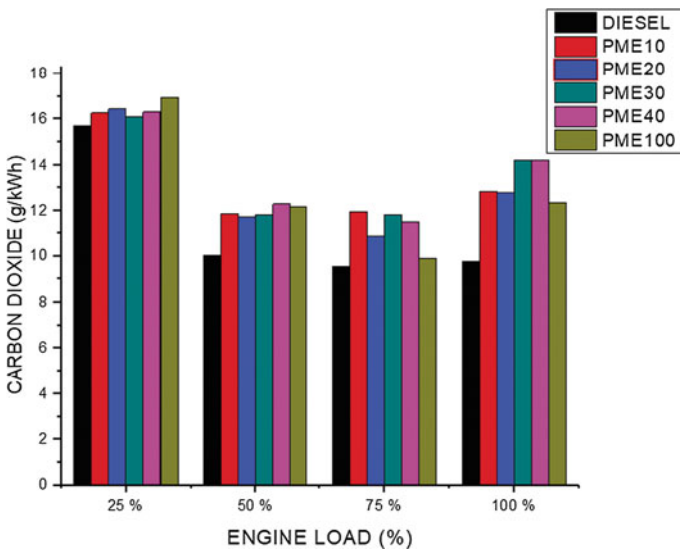


Fig. 3 Variation of CO<sub>2</sub> to engine load

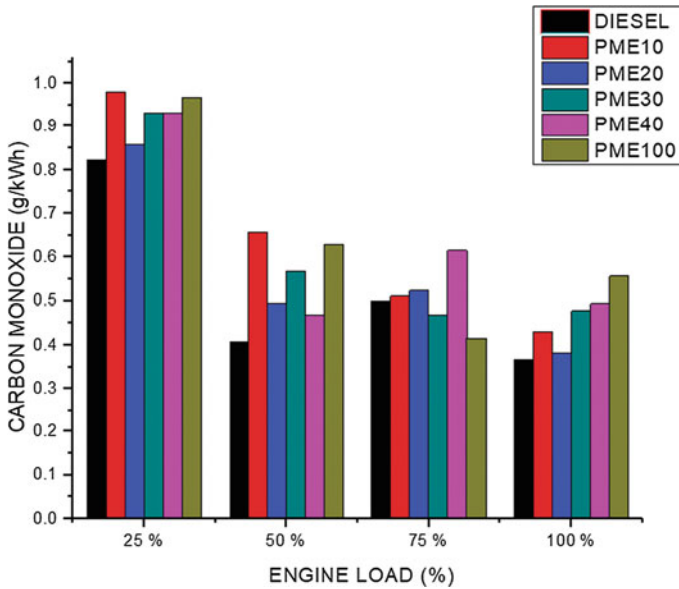


Fig. 4 Variation of CO compared to engine load

### 3.3 Carbon Monoxide (CO)

In general, diesel engines' functions overrun the lean mixture zone; therefore, CO liberated from a diesel motor is significantly inferior to be unimportant [18]. However, CO emission should be controlled owing its toxicity. But the impact of alcohol and ignition agitator vagaries the fuel spray physiognomies, O<sub>2</sub> content, reaction rate, temperatures, low/high equivalence ratios and ignition center formation that influences the conception of CO [37]. Figure 4 illustrates that the lowest CO formation is determined for diesel. At 100% load condition, additional fuel enters the cylinder for maintaining continuous engine swiftness and once additional fuel with lesser energy takes part in combustion, it ends up in higher CO emission. At 100% load, the CO emission emitted by PME-diesel blends is above diesel by 16.27% (PME10), 3.86% (PME20), 23.4% (PME30) and 26.46% (PME40), while the concerns is for vegetable oil (PME100) which is 34.54%.

## 4 Conclusion

In the present experimental study, engine performance and emission properties of 10, 20, 30, 40 and 100% blends of palmarosa methyl ester were investigated and equated with diesel fuel. On the basis of experimental results, the subsequent conclusions were drawn:

- Biofuel blends exhibit higher THC emissions compared to diesel at part (25%) load and are increased by 35.16% for PME10, 2% for PME20, 138% for PME30, 108% for PME40 and 240% for PME100 but similarity is found at 100% load conditions (0.69% for PME 10, 1.2% for PME20, 1.8% for PME30, 1.9% for PME40 and 2.3% for PME100).
- It has been inferred from the analysis that at the 25% load condition, PME-blends with base fuel possess slightly higher levels of CO<sub>2</sub> emission (7.577% PME10, 4.118% PME20, 8.126% PME30, 11.504% PME40 and 6.277% PME100).
- The CO emission emitted by PME-diesel blends is above diesel by 16.27% (PME10), 3.86% (PME20), 23.4% (PME30), 26.46% (PME40) and 34.54% (PME100) as a result of enriched fuel supply at 100% load conditions.

In relation to regulated emissions, palmarosa methyl ester and its blends showcase negligible increase in HC, CO and CO<sub>2</sub> compared to diesel fuel except PME20 which is slightly similar to diesel. Grounded on the overhead inferences, it is concluded that this mix is a potential alternative feed stock without engine alteration and by means of minimal emissions.

## References

1. Abu-Zaid M, Badran OY, Yamin J (2004) Effect of methanol addition on the performance of spark ignition engines. *Energy Fuels* 18(2):312–315
2. Alriksson M (2005) Rente T and Denbratt I. Low soot, low NO<sub>x</sub> in a heavy-duty diesel engine using high levels of of EGR. Technical Paper 2005-01-3836
3. An H, Yang WM, Maghbouli A, Li J, Chou SC, Chua KJ (2013) Performance, combustion and emission characteristics of biodiesel derived from waste cooking oils. *Appl Energy* 112:493–499
4. Anand K, Sharma RM, Mehta PS (2011) Experimental investigations on combustion, performance and emissions characteristics of neat karanji biodiesel and its methanol blend in a diesel engine. *Biomass Bioenergy* 35(1):533–541
5. Atabani AE, Mahlia TMI, Badruddin IA, Masjuki HH, Chong WL, Lee KT (2013) Investigation of physical and chemical properties of potential edible and non-edible feedstocks for biodiesel production, a comparative analysis. *Renew Sustain Energy Rev* 21:749–755
6. Atabani AE, Silitonga AS, Ong HC, Mahlia TMI, Masjuki HH, Badruddin IF, Fayaz H (2013) Non-edible vegetable oils: a critical evaluation of oil extraction, fatty acid compositions, biodiesel production, characteristics, engine performance and emissions production. *Renew Sustain Energy Rev* 18:211–245
7. Atadashi IM, Aroua MA, Aziz AA (2010) High quality biodiesel and its diesel engine application: a review. *Renew Sustain Energy Rev* 14(7):1999–2008
8. Balat M (2008) Progress in biogas production processes. *Energy Educ Sci Technol* 22:15–36
9. Benjumea P, Agudelo JA, Agudelo A (2009) Effect of altitude and palm oil biodiesel fuelling on the performance and combustion characteristics of a HSDI diesel engine. *Fuel* 88(4):725–731
10. Bhaskar K, Nagarajan GS, Sampath S (2013) Optimization of FOME (fish oil methyl esters) blend and EGR (exhaust gas recirculation) for simultaneous control of NO<sub>x</sub> and particulate matter emissions in diesel engines. *Energy* 62:224–234
11. Bilgin AS, Sezer I (2008) Effects of methanol addition to gasoline on the performance and fuel cost of a spark ignition engine. *Energy Fuels* 22(4):2782–2788. Bio: fuels need of hour. *Energy Fuel Users J* January–March 2007, 18–20

12. Campos-Fernandez J, Arnal JM, Gómez J, Dorado MP (2012) A comparison of performance of higher alcohols/diesel fuel blends in a diesel engine. *Appl Energy* 95, 267–275
13. Chauhan BS, Kumar N, Cho HL, Lim HC (2013) A study on the performance and emission of a diesel engine fueled with Karanja biodiesel and its blends. *Energy* 56:1
14. Cheung CS, Zhu LH, Huang Z (2009) Regulated and unregulated emissions from a diesel engine fueled with biodiesel and biodiesel blended with methanol. *Atmos Environ* 43(32):4865–4872
15. Esarte C, Abián M, Millera A, Alzueta MU (2012) Gas and soot products formed in the pyrolysis of acetylene mixed with methanol, ethanol, isopropanol or n-butanol. *Energy* 43(1):37–46
16. Gravalos I (2013) Emissions characteristics of spark ignition engine operating on lower-higher molecular mass alcohol blended gasoline fuels. *Renew Energy* 50:27–32
17. Heywood JB (1988) *Internal combustion engine fundamentals*, vol 930. McGraw-Hill, New York
18. Holman JB (1988) *Experimental techniques for engineers*. McGraw Hill Publications, New York
19. Huang G, Chen F, Wei D, Zhang XC, Chen G (2010) Biodiesel production by microalgal biotechnology. *Appl Energy* 87(1):38–46
20. International conference on bio-fuels 2012 vision to reality. *Energy Fuel Users J* January–March 2006, 6–8
21. Kakati JG, Gogoi TK (2016) Biodiesel production from Kutkura (*Meynaspinosaroxb*. Ex.) Fruit seed oil: its characterization and engine performance evaluation with 10% and 20% blends. *Energy Convers Manag* 121:152–161
22. Kim ML, Lee CS (2007) Effect of a narrow fuel spray angle and a dual injection configuration on the improvement of exhaust emissions in a HCCI diesel engine. *Fuel* 86(17):2871–2880
23. Kohse-Höinghaus K, Oßwald P, Cool T, Kasper T, Hansen N, Qi F (2010) Biofuel combustion chemistry: from ethanol to biodiesel. *Angew Chem Int Ed* 49(21):3572–3597
24. Konwar LJ, Boro JD, Deka D (2014) Review on latest developments in biodiesel production using carbon-based catalysts. *Renew Sustain Energy Rev* 29:546–564
25. Koç M, Sekmen Y, Topgül TY, Yücesu HS (2009) The effects of ethanol–unleaded gasoline blends on engine performance and exhaust emissions in a spark ignition engine. *Renew Energy* 34(10):2101–2106
26. Kumar MS, Ramesh AN, Nagalingam B (2003) An experimental comparison of methods to use methanol and Jatrophia oil in a compression ignition engine. *Biomass Bioenergy* 25(3):309–318
27. Ladommatos N, Abdelhalim S, Zhao H (1998) Control of oxides of nitrogen from diesel engines using diluents while minimizing the impact on particulate pollutants. *Appl Therm Eng* 18:963–980
28. Ladommatos N, Abdelhalim SM, Zhao HH, Hu Z (1997) The dilution, chemical, and thermal effects of exhaust gas recirculation on diesel engine emissions—part 4: effects of carbon dioxide and water vapour. *SAE Technical Paper* 971660
29. Larsen C, Oey F, Levendis YA (1996) An optimization study on the control of NO and particulate emissions from diesel engines
30. Liaquat AM, Masjuki HH, Kalam MA, Fattah IR, Hazrat MA, Varman M, Mofijur MS, Shahabuddin M (2013) Effect of coconut biodiesel blended fuels on engine performance and emission characteristics. *Procedia Eng* 56:583–590
31. Maheshwari P, Tandon S (1959) Agriculture and economic development in India. *Econ Bot* 13(3):205–242
32. Mazumdar BA, Agarwal AK (2008) Performance, emission and combustion characteristics of biodiesel (waste cooking oil methyl ester) fueled IDI diesel engine. *SAE Technical Paper* 2008-01-1384
33. Moreno F, Munoz MMR, Morea-Roy J (1999) Sunflower methyl ester as a fuel for automobile diesel engines. *Trans ASAE* 42(5):1181
34. Murugan S, Ramaswamy MN, Nagarajan G (2008) Performance, emission and combustion studies of a DI diesel engine using distilled tyre pyrolysis oil-diesel blends. *Fuel Process Technol* 89(2):152–159



35. Nabi MN, Rahman MA, Akhter MS (2009) Biodiesel from cotton seed oil and its effect on engine performance and exhaust emissions. *Appl Therm Eng* 29(11):2265–2270
36. Nigam PS, Singh A (2011) Production of liquid biofuels from renewable resources. *Prog Energy Combust Scivol* 37:52–68
37. Sudheesh K, Mallikarjuna JM (2010) Diethyl ether as an ignition improver for biogas homogeneous charge compression ignition (HCCI) operation-an experimental investigation. *Energy* 35(9):3614–3622
38. Yacoub Y, Bata R, Gautam, M (1998) The performance and emission characteristics of C1-C5 alcohol-gasoline blends with matched oxygen content in a single-cylinder spark ignition engine. *Proceedings of the Institution of Mechanical Engineers, Part A: J Power Energy*, 212(5):363–379
39. Yilmaz N (2012) Comparative analysis of biodiesel–ethanol–diesel and biodiesel–methanol–diesel blends in a diesel engine. *Energy*, 40(1):210–213
40. Zhao H, Ge Y, Hao C, Han X, Fu M, Yu L, et al (2010) Carbonyl compound emissions from passenger cars fueled with methanol/gasoline blends. *Sci Total Environ* 408(17):3607–3613
41. Zhu L, Cheung CS, Zhang WG, Huang Z (2010) Emissions characteristics of a diesel engine operating on biodiesel and biodiesel blended with ethanol and methanol. *Sci Total Environ* 408(4):914–921

# Development of Solar Turbine for Small-Scale Industries



Anjaiah Madarapu and M. Harinatha Reddy

**Abstract** Owing to power shortage problems, especially in summer, industries are not able to meet their production goals. The concept of deriving electrical power from solar radiation started in early 1990s to get rid of these problems. This concept did not see much of light as water is being used as primary working fluid in all solar devices. Water is considered to be less reactive fluid as it takes more time to get transformed into vapor phase. Because of this reason utilization of solar power is limited to the extent of deriving hot water only instead of steam. Reason for this can also be attributed to certain design deficiencies associated with various inversions of solar devices that are being in use till today. The idea adopted in this work is to evolve an efficient design configuration of solar turbine which converts heat energy that is being extracted from solar energy to mechanical energy. The superiority in this design is utilization of smart fluid in substitute of water. The advantage of using smart fluid is that it vaporizes at relatively low temperature compared to water which needs high temperature to vaporize. Design and development of such device is taken up as research work. This paper brings out the design configuration details along with the principle of operation.

**Keywords** Solar energy · Solar turbine · Smart fluid · Heat capacity-reservoir

## 1 Introduction

The global scarcity of conventional energy resources is unable to meet the existing demand, which in turn needs alternate energy resources for sustainable development [1, 2]. Hence much focus is being placed on the usage of nonconventional energy resources like solar energy. Solar radiation represents a large energy source. The earth

---

A. Madarapu · M. Harinatha Reddy (✉)  
Department of Mechanical Engineering, Guru Nanak Institutions Technical Campus,  
Hyderabad, India  
e-mail: [Harinathareddy.maddika@gmail.com](mailto:Harinathareddy.maddika@gmail.com)

A. Madarapu  
e-mail: [anjaiahm19@gmail.com](mailto:anjaiahm19@gmail.com)

© Springer Nature Singapore Pte Ltd. 2020  
G. S. V. L. Narasimham et al. (eds.), *Recent Trends in Mechanical Engineering*,  
Lecture Notes in Mechanical Engineering,  
[https://doi.org/10.1007/978-981-15-1124-0\\_12](https://doi.org/10.1007/978-981-15-1124-0_12)

receives energy from the sun at the rate which, expressed in terms of heat energy according to the solar constant, is  $1356 \text{ Joules/m}^2/\text{second}$  [3, 4]. It is projected that the amount of solar energy directed by the sun upon the earth in just three days and is equivalent to the earth's total supply of all fossil fuels [5, 6]. This work relates to a solar energy device conceptualized as a solar turbine, which consumes power by using a working medium which can be vaporized at relatively low temperatures and further condensed by temperature variations to enable the device to operate. This device consists of rotary mounted frame which in turn supports number of heat exchangers, which will be alternately coming in contact with hot and cold fluids. The hot fluid is nothing but conventional water, which gets heated up by solar energy. This device is basically a two-stage fluid system. Primary fluid is the smart fluid that will be enclosed in the above said expansion chambers and secondary fluid is the water. This device is simple in construction and uses a temperature differential to convert heat energy to mechanical energy.

## 2 Solar Power Systems

Attention is limited to solar power systems for small-scale industries in the present work. Solar power systems generally operate with maximum efficiency [7, 8] during summer season and it reduces in remaining seasons. Availability of solar radiation energy in summer season is to be properly assessed as the present system is aimed for use in summer. However, to have an idea, variation of solar radiation from sun in two different seasons [9] is represented in Fig. 1.

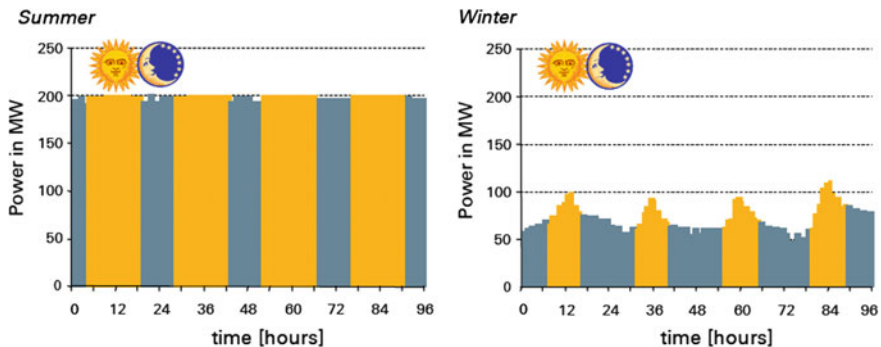


Fig. 1 Variation of solar radiation in summer and winter seasons

### 3 Design of Solar Turbine

Design of solar turbine for small-scale industries is taken up in this work. The intended device is divided into two portions, one of which is evaporator side and the other is condenser side. The evaporator portion consists of a reservoir which contains secondary fluid that is water. The heat energy available in secondary fluid serves as a source of energy for the device. This secondary fluid will be heated by means of solar panel. The solar panel will be having light transparent surface exposed to solar radiation. Solar energy passes through the panel and the ultraviolet energy will be converted to heat energy and retained within the panel. Secondary fluid that is to be heated will be passed through the heat exchanger within the panel. The heated secondary fluid from the solar panel will be delivered to the reservoir. The secondary fluid to be heated will be extracted from the reservoir and introduced into the solar panel.

The design configuration of the intended device is shown in Fig. 2.

Turbine rotor is mounted for rotation above the reservoir. Reservoir will be supported on either ends of the turbine rotor shaft, which will be hollow through bearings to enable free rotation of rotor shaft while keeping the reservoir stationary. Turbine rotor consists of number of steam generators, which are nothing but tubes disposed about rotor shaft. The opposite ends of steam generators are connected to a hollow rotor shaft. Nonreturn valves are provided in these passages in such a way that flow takes place in one direction only; that is, in any given orientation flow takes place from top steam generators to the rotor shaft and from rotor shaft to the bottom steam generators. There is no restriction for number of steam generators; however, in the present scheme designed four such steam generators are considered.

The condenser portion consists of a suitable liquid to promote extraction of heat from working fluid flowing through the heat exchanger.

### 4 Design Philosophy

The power output of the intended device is a function of amount of incident solar radiation, efficiency of solar panel and efficiency of turbine, and it can be expressed as follows:

$$P = Q_{\text{solar}} \times \eta_{\text{solar panel}} \times \eta_{\text{turbine}}$$

Amount of incident solar radiation in turn can be expressed as follows [10]:

$$Q_{\text{solar}} = G_h \times A_{\text{solar panel}}$$

where  $G_h$  is the global horizontal radiation and  $A_{\text{solar panel}}$  is the area of solar panel.

The overall efficiency of the system can be expressed as follows:

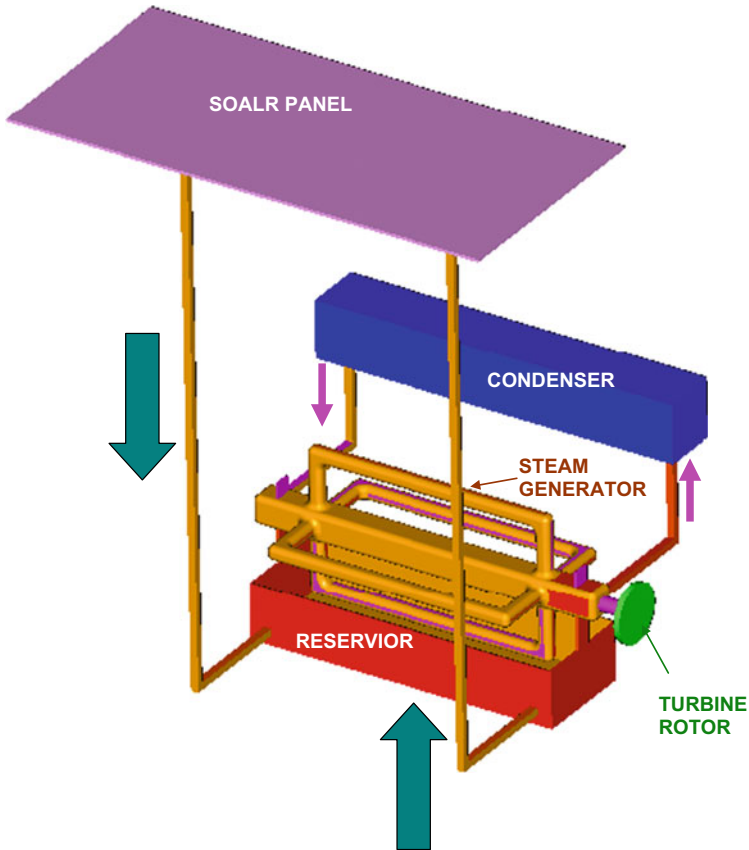


Fig. 2 Design configuration of solar turbine

$$\eta = \frac{P}{Q_{solar}}$$

## 5 Principle of Operation

The basic working scheme of the intended device is represented in Fig. 3.

As discussed earlier, this device consists of a turbine rotor having oppositely oriented steam generators arranged about the shaft for rotation with the shaft. Steam generators consist of primary fluid. During a portion of the rotary cycle, the steam generators will be exposed to the heat source, that is, secondary fluid. The primary fluid will be heated due to heat exchange between secondary and primary fluids due to their temperature difference. The primary fluid will be chosen such that it

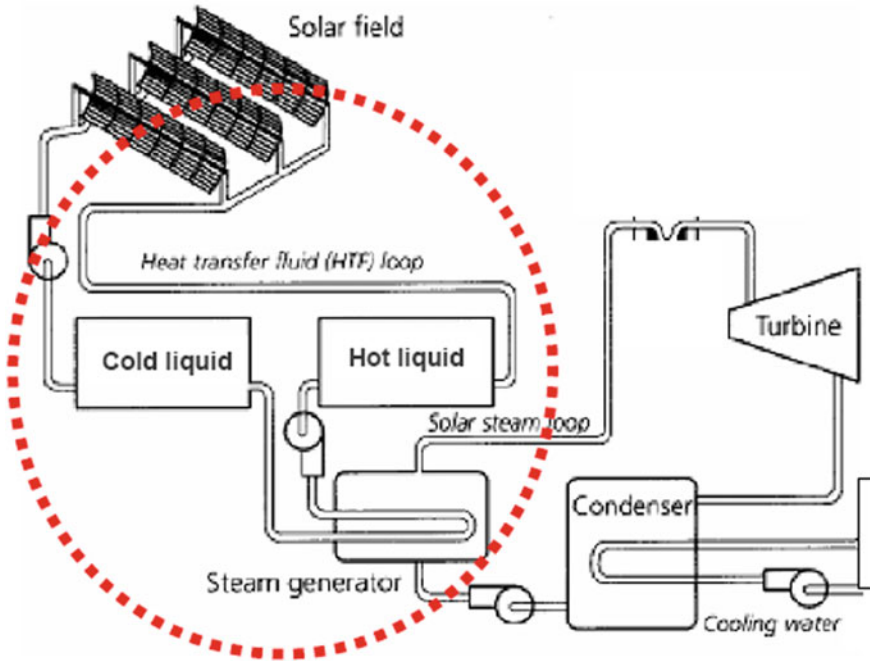


**Fig. 3** Basic working scheme

will have low boiling point. The secondary fluid gets vaporized and this results in increase in pressure in the steam generator, causing the appropriate nonreturn valve to open and the vapor will be discharged from steam generator and across a first rotary valve associated with the turbine rotor shaft. The evacuation of steam generator will cause an imbalance imparting rotation to the rotor and shaft. The vapor is removed and is condensed to a liquid and returned to the steam generator across the second rotary valve. Condensation will take place by extracting heat from the primary fluid to a cold fluid. Cooled primary fluid returns back to steam generator, thus enabling for closed-loop operation. The advantage with closed-loop operation is that the system pressure builds and promotes flow with the operation of the nonreturn valves preventing the system from stabilizing at an equilibrium condition.

As the rotor shaft is caused to rotate, power extraction unit like a gearbox will be energized. This power extraction unit will be coupled to the rotor shaft.

## 6 Conclusion

It is concluded that the device developed in this work is simple construction and can be utilized with functional materials to effectively increase the efficiency.

## 7 Future Work

As a part of research work, evolution of design configuration is completed. Reliability of the system will be established after realizing the hardware and experimentation. It is also planned to add second phase of steam generators in condenser to improve the system, which will be Mark-II of the proposed design.

## References

1. Zang C, Li B, Li X, Zheng F, Li A (2004) Structural design and analysis of the dish solar thermal power system. American Institute of Aeronautics and Astronautics (AIAA) vol 5645, pp 1–4. In 2nd International Energy Conversion Engineering Conference, Providence, Rhode Island, 16–19 August 2004
2. Arasu AV, Sornakumar ST (2006) Performance characteristics of the solar parabolic trough collector with hot water generation system. *Therm sci* 10(2):167–174
3. Yao Z, Wang Z, Lu Z, Wei X (2009) Modeling and simulation of the pioneer 1 MW solar thermal central receiver system in China. *Renew Energ* 34:2437–2446
4. Zahedi A (2006, August) Design, size optimization, performance prediction of a solar PV / hydrogen system supplying electricity for a remote located community. *J ISESCO Sci Technol Vision* 2(1):5–9
5. Li W, Zhu XJ, Cao GY (2007, April) Modeling and control of a small solar fuel cell hybrid energy system. *J Zhejiang Univ SC A* 8(5):734–740
6. Gannon AJ, von Backström TW (2000, August) Solar chimney cycle analysis with system loss and solar collector performance. *J Sol Energy Eng* 122:133–137
7. Davidson J, Mantell S, Liu W (2000 May) Thermal analysis of polymer heat exchangers for solar water heating: a case study. *J Sol Energy Eng, Trans ASME* 122:84–91
8. Duffie JA, Beckman WA (1991) *Solar engineering of thermal processes*, 2nd edn. Wiley Interscience, New York
9. Do Sacramento EM, Sales AD, De Lima LC, Veziroglu TN (2008) A solar–wind hydrogen energy system for the Ceará state–Brazil. *Int J Hydrogen Energ* 33:5304–5311
10. Price H, Lu¨pfert E, Kearney D, Zarza E, Cohen G, Gee R, Mahoney R (2002, May) Advances in parabolic trough solar power technology. *J Sol Energy Eng* 124:109–125

# Performance and Emission on Raw Vegetable Oil with Hydrogen-Enriched Air for Better Combustion in a DIC Engine



G. Sankaranarayanan, S. Karthikayan, R. Ganesan and T. Thirumalai

**Abstract** The rapid growth of the society is based on transportation. The global economy hugely depends on surface transports, such as road transport, rail and marine. Diesel engines are the main power source for the transport. There is a huge demand for fossil fuel and strict norms on pollution also compel the researchers to probe in for discovering alternate fuels. Present work investigates the use of high viscous raw vegetable oil, Simarouba glauca (SG oil) oil, in a DIC engine with hydrogen as combustion enhancer. The hydrogen gas is generated by hydrolysis of water and stored in a cylinder. The hydrogen gas is passed by inducting into inlet manifold. Neat vegetable oil was added through high-pressure fuel injection pump and hydrogen was inducted through inlet manifold. The inducted high-energy gaseous fuel was flashed by the intermediate breakdown products of neat oil. It creates a higher temperature ambience to complete the combustion of bulky molecules of high viscous non-edible oil within a short span of time. The result of the experimentation reveals that the use of  $H_2$  certainly enhanced the combustion behavior of neat vegetable oil. In addition, 5% higher brake thermal efficiency, 6% higher EGT, 17% lower smoke, 5% lower CO can be observed from the result. The  $NO_x$  emission was higher by 17% due to hydrogen inclusion, and 33% reduction in HC emission than diesel. The significance of the investigation reveals that a notable development has been achieved in combustion performance and emission.

---

G. Sankaranarayanan (✉)

Guru Nanak Institutions Technical Campus, Khanapur, Ibrahimpatnam, Hyderabad, India  
e-mail: [gs2000narayanan@gmail.com](mailto:gs2000narayanan@gmail.com)

S. Karthikayan

Professor & Head, Department of Mechanical Engineering, CK College of Engineering, Cuddalore 607003, Tamilnadu, India  
e-mail: [sskksmit@gmail.com](mailto:sskksmit@gmail.com)

R. Ganesan

Sathyabama Institute of Science and Technology, Chennai 600119, India

T. Thirumalai

Department of Mechanical Engineering, Guru Nanak Institutions Technical Campus, Khanapur, Ibrahimpatnam, Hyderabad, India  
e-mail: [tmala@rediffmail.com](mailto:tmala@rediffmail.com)

© Springer Nature Singapore Pte Ltd. 2020

G. S. V. L. Narasimham et al. (eds.), *Recent Trends in Mechanical Engineering*,  
Lecture Notes in Mechanical Engineering,  
[https://doi.org/10.1007/978-981-15-1124-0\\_13](https://doi.org/10.1007/978-981-15-1124-0_13)



**Keywords** Hydrogen · Direct injection · Simarouba glauca oil · Raw vegetable oil · Combustion and emission

## 1 Introduction

Most of the vegetable oils are more suitable to run a regular diesel cycle engine without any engine alteration [1, 2]. But the use of raw oil poses many engine problems, like smoky exhaust, high level of carbon deposit and engine lubricant dilution [3].

This work used the above suggestion with some modification to apply high viscous oil in engine. This paper introduces combustion improving technique for injecting high viscous oil in DIC engine. Hydrogen gas was introduced as a combustion enhancer in the present work. The high calorific value, higher flame speed and simpler molecular structure make the fuel to combust at very high temperature. By introducing high temperature ambience with hydrogen enhances the combustion behavior of vegetable oil. Hence, the neat vegetable oil combusts completely without any traces of smoky exhaust. The consequences of the engine trial show a notable progress [4–18] in fuel combustion and exhaust emission of high viscous oil.

### A. *Simarouba glauca oil*

Simarouba grow up well under any environmental circumstances. Simarouba were harvested every year in the month of April. The seed contains 58–69% of oil.

### B. *Literature review*

Sankaranarayanan et al. [19] carry out research using Mahua oil with hydrogen. The trial provides evidence that the gaseous hydrogen enhanced the BTE and reduced the smoke emission. Hydrogen gas enhancement improved the Mahua combustion rate and NO emission increased.

Senthil Kumar et al. [20] carry out a complete trial to estimate the CI engine performance with jatropha biofuel along with little amount of gaseous  $H_2$ . The experiment proved an increase in the efficacy at 7% of  $H_2$  mass. Smoke, HC and CO emission was reduced (Table 1).

Karthikayan and Sankaranarayanan [2] studied the performance and combustion analysis of duel-fuelled DIC engine. The engine controlling variables were suitably optimized, and the duel-fuel blend prepared in mid range by volume basis. 40, 50 and 60% of neat non-edible oil blended with low sulfur diesel (LSD). Measurements on BTE, EGT, peak pressure and heat release were recorded. The 50% blend performed better 29.6% BTE, and 68 bar peak pressure at 7°bTDC for full load condition was observed.

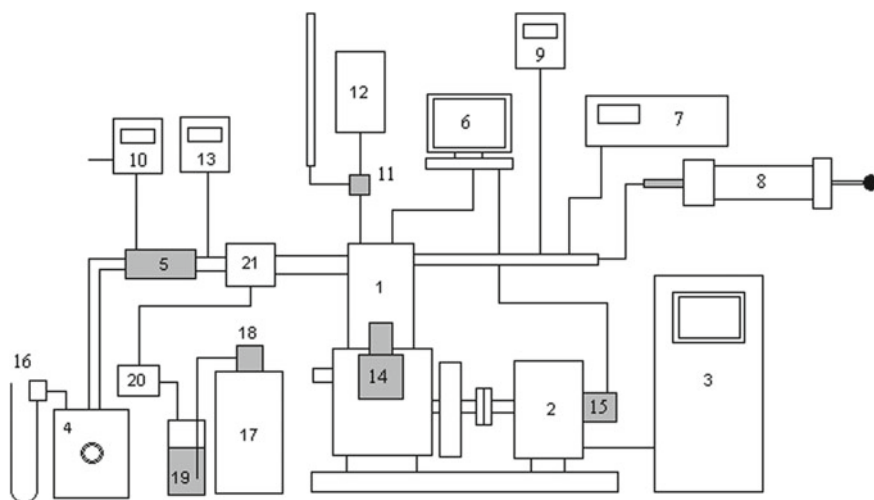
**Table 1** Properties of SG oil

S. No.	Properties of vegetable oil		
	Properties	Vegetable oil	Diesel
1	Molecular weight	435	200
2	Mass density at 20 °C, kg/m <sup>3</sup>	906	820
3	Specific gravity @ 20 °C	0.910	0.820
4	Vaporization point, K	523–533	453–613
5	Viscosity at 20 °C, cSt	17.3	3–4
6	Lower calorific value kJ/kg	38,090	42,720
7	Fuel flash point, K	503	348
8	Cetane number	45–48	45–50

## 2 Experimental Setup

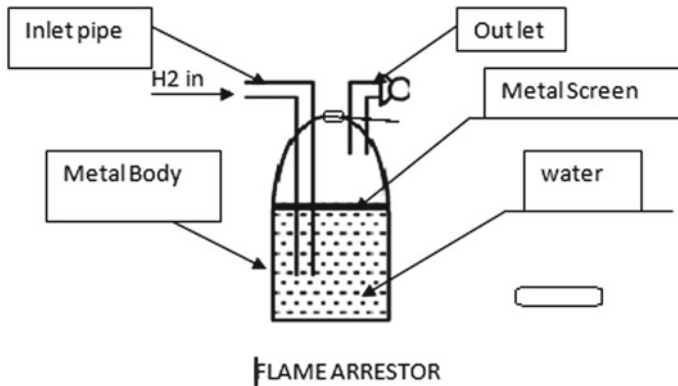
1. Compression ignition engine, 2. Electric-type loading, 3. Loading control, 4. Air anti-pulsating chamber, 5. Intake air pre-heater, 6. Laptop + DAQ, 7. Five gas analyzers, 8. Engine smoke sampling pump, 9. EGT indicator, 10. Electrical energy meter, 11. Two-way valve, 12. LSD, 13. Intake air inlet temperature, 14. FIP, 15. Crank angle encoder, 16. Manometer, 17. H<sub>2</sub> storage, 18. Pressure controller, 19. Flame return arrester kit, 20. H<sub>2</sub> gas flow meter, 21. Hydrogen nozzle (NRV).

NI-LABVIEW calculates combustion performance. The engine test setup is published in Fig. 1 and the engine specification in Table 2.

**Fig. 1** Experimental setup

**Table 2** Specifications of the engine

S. No.	Specifications of the engine	
1	Manufacturer name	Kirloskar-TAF1
2	Basic details	Direct injection compression ignition, vertical, air-cooled
3	Number of cylinders	1
4	Cylinder bore and piston stroke	0.0875 and 0.11 m
5	Cylinder volume	0.661 L
6	Engine compression ratio	17.5:1
7	Rated output and speed	6 HP at 25 rps
8	Fuel entry pressure and crank angle	180 bar @ 23° before top dead center
9	Number of nozzle hole and diameter	3 and 0.23 mm

**Fig. 2** Flame Arrester

The hydrogen pressure regulator helps to allow the gas flow from cylinder, then gas is allowed to pass through a flame arrester kit and then through flow meter. The gas enters into intake manifold through a non-return valve and a nozzle is mounted to admit the  $H_2$  gas in the engine manifold.

Flame arrester kit is a unit which contains a metallic cylinder, half filled with water, and an inlet pipe is inserted through a metallic gauze and immersed into water. Hence the flame at any time cannot enter into hydrogen attachment (Fig. 2).

### 3 Experimental Method

#### A. Testing process

- Engine was initially started with petroleum diesel and then changed to the raw oil mode.

**Table 3** Optimum values of engine operating parameters

S. No.	Optimum values of engine operating parameters	
	Parameters	Optimum level
1	Inlet air temperature (IAT) (°C)	65
2	Engine compression ratio	19.5
3	Fuel entry crank angle (°b TDC)	27
4	Fuel entry pressure (bar)	275

- The required quantity of gaseous hydrogen was passed into the engine intake manifold.
- Observations are made only after the stabilization of engine operation at that load.
- Combustion performance parameters and emissions were noted at various loads.

#### B. *Engine modifications*

The engine modifications were attained in the test setup before the trials.

1. The engine control variables are reset according to the optimum values (given in Table 3).
2. The intake side of the engine was equipped with gaseous fuel admission device.
3. The standard piston of engine was replaced with a newer one to increase the engine compression ratio.
4. The hydrogen gas is fed into the inlet manifold.

## 4 Results and Discussion

The optimized variables were implemented and the engine trial has been carried out with the help of hydrogen. From the engine trials 15% of hydrogen + raw oil was chosen to compare with the only raw oil and diesel.

1. *Exhaust gas temperature:* The comparison of EGT of 15% H<sub>2</sub> + neat vegetable oil with neat vegetable oil and diesel is shown in Fig. 3. The peak EGT is attained with 15% H<sub>2</sub> + neat vegetable oil than that of raw oil and diesel. The introduction of H<sub>2</sub> increases ignition temperature and combusts heavy fuel molecules in a shorter time. It offers elevated burning ambiance and hence, it offers the peak EGT than that of raw oil and diesel fuel.

The highest EGT produced by 15% H<sub>2</sub> neat vegetable oil is 447 °C, for diesel 422 °C and for neat oil 360 °C. There is 6% increase than diesel fuel and 21% increase than neat oil. The introduction of H<sub>2</sub> increases EGT of neat oil performance from 360 °C to 447 °C.

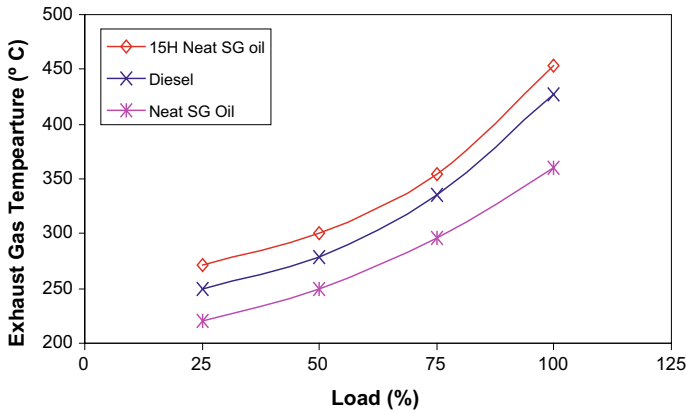


**Fig. 3** Exhaust gas temperature

2. *Break thermal efficiency:* Fig. 4 compares BTE of 15% H<sub>2</sub> + neat vegetable oil with neat vegetable oil and diesel. The maximum BTE attained is with 15% H<sub>2</sub> + neat vegetable oil than that of neat oil and diesel.
3. *Heat release rate:* The comparison of HRR of 15% H<sub>2</sub> + neat vegetable oil with diesel and neat oil is shown in Fig. 5. The peak HRR is obtained with 15% H<sub>2</sub> + raw vegetable oil than that of neat oil and diesel. As hydrogen has poor auto ignition property the ignition of the mixture was initiated by the breakdown particles of neat oil. The neat oils have considerable quantity of unsaturation in it. They deteriorate and crack the free fatty acids chain of neat oil due to the high temperature ambience and higher pressure presence. These breakdown particles start the burning of the fuel mixture in the combustion chamber.

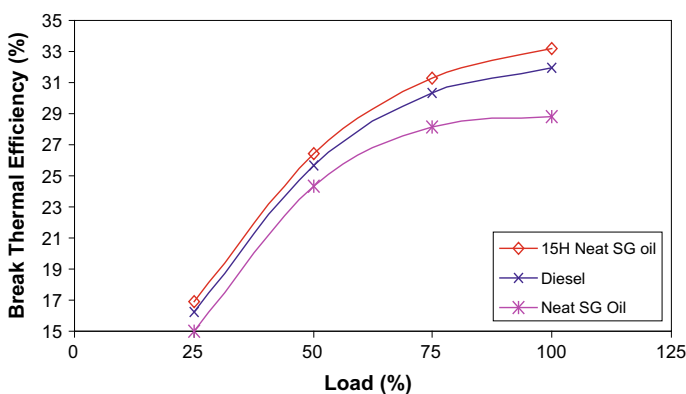


**Fig. 4** Brake thermal efficiency

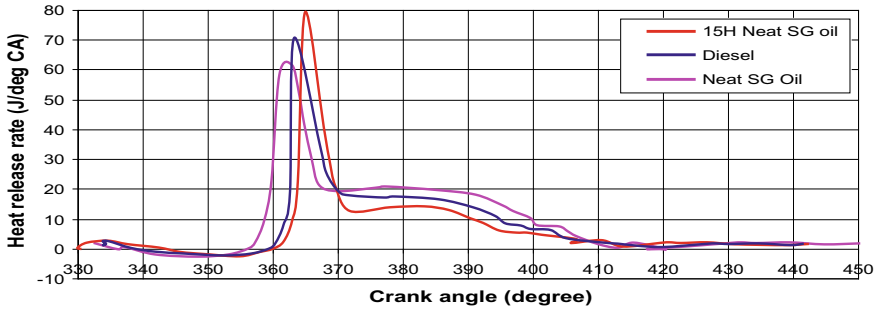


Fig. 5 Heat release rate

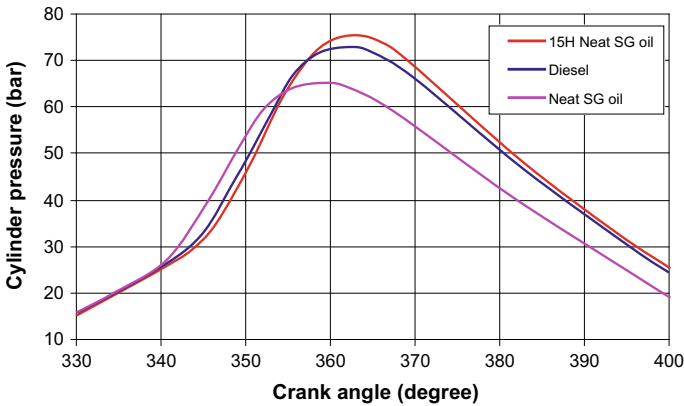
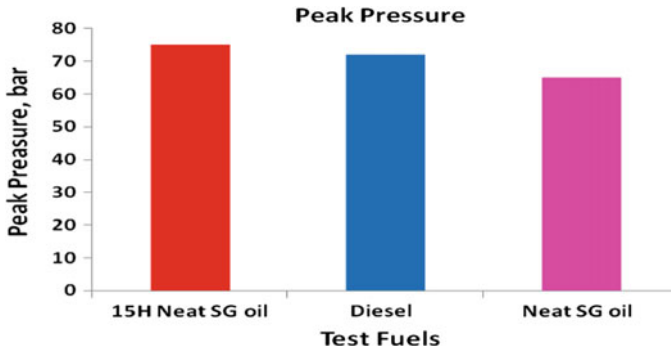


Fig. 6 Pressure—Crank angle diagram

In general, neat oils produce breakdown particles immediately after the injection and then helps to initiate combustion relatively prior than other fuels. The application of hydrogen changes the phenomenon and combusts the neat oil with sufficient ignition delay.

This delay accumulates fuel vapor and starts combustion little later than raw oil combustion. This is the prime cause for the high HRR in the prephase of combustion. The excessive peak temperature offered by hydrogen reduces the length of combustion. Consequently, the postphase of combustion of 15% H<sub>2</sub> neat vegetable oil is shorter than neat oil and diesel during combustion.

The highest heat liberation rate produced by 15% H<sub>2</sub> neat vegetable oil is 80 J/°CA. This is 20% higher than neat vegetable oil and 12.5% higher than diesel fuel. The role of hydrogen increases heat release rate of raw vegetable oil from 63 to 80 J/°CA. However, the diesel shows 71 J/°CA.



**Fig. 7** Peak pressure for tested fuels

4. *In-cylinder pressure:* Fig. 6 matches up to in-cylinder pressure of 15% H<sub>2</sub> + neat vegetable oil with neat vegetable oil and diesel. The maximum in-cylinder pressure is attained with 15% H<sub>2</sub> + neat vegetable oil than that of neat oil and diesel. The co-firing of gaseous hydrogen rose the cylinder gas temperature extremely high and hence it offers higher peak pressure. Besides, the elevated combustion temperature of hydrogen stimulates the neat oil to release more breakdown particles in rapid manner. This is the prime for the production of higher peak pressure. The higher flame speed and its high calorific value of hydrogen are also other causes for the progress of good combustion.
5. *Peak combustion pressure:* At full load operation of the engine, the in-cylinder peak combustion pressure developed is 76 bar at 2°ATDC for 15% H<sub>2</sub> neat SG oil, 72 bar in case of diesel operation and 63 bar was observed for raw SG oil. The reduction in peak pressure is coherently observed on par with energy content of the fuel used. These small differences in the change of peak pressure do not affect the engine performance, wear and knock (Fig. 7).

The highest cylinder peak pressure produced by 15% H<sub>2</sub> neat vegetable oil is 76 bar at 2°ATDC. This is 11 bar higher than the raw vegetable oil and 5 bar higher than the diesel fuel. The adding up of hydrogen increases peak pressure of neat vegetable oil from 65 bar at 1°BTDC to 76 bar.

6. *Smoke:* A good diesel engine produces no visible black smoke during operation. The black smoke is high carbon which is objectionable. The black smoke indicates the lube oil is being burnt due to sticky valve, worn-out rings, thin lubricating oil and oil dilution in fuel. At present, the CRDI engine not at all emitting visible smoke. White smoke occurs due to faulty injectors, incorrect injection timing and lower compression. Figure 8 evaluates the smoke of 15% H<sub>2</sub> + raw vegetable oil with neat vegetable oil and diesel. The maximum smoke is attained with 15% H<sub>2</sub> + neat vegetable oil than that of neat oil and diesel. The combustion improvement was achieved by gaseous fuel enhancer that resulted in low smoke emission. The H<sub>2</sub> gas increases the intermediate compounds production rate and helps the vegetable oil to combust with no evidence of visible smoke.

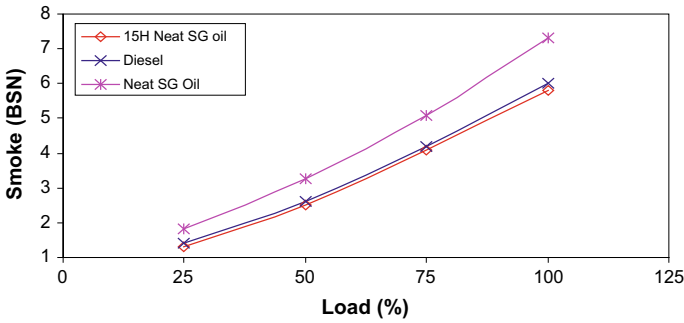


Fig. 8 Smoke emission

The lowest smoke emission produced by 15% H<sub>2</sub> + raw vegetable oil is 5.8 BSN and for diesel is 6 BSN. This is closer to diesel and 1.50 smoke index number is inferior than neat vegetable oil. The inclusion of H<sub>2</sub> decreases smoke of neat vegetable oil from 7.3 to 5.8 index.

*Oxides of Nitrogen:* NO<sub>x</sub> emission of 15% H<sub>2</sub> + raw vegetable oil with raw vegetable oil and diesel are compared in Fig. 9. At 100% load the maximum NO<sub>x</sub> is obtained with 15% H<sub>2</sub> + neat vegetable oil than that of raw oil and diesel. Fundamentally, H<sub>2</sub> has poor self-ignition. It was ignited by the raw oil injection. At 15% H<sub>2</sub> mode, combustion was glowing, consequently, higher efficacy and higher gas exit temperature and causes more NO<sub>x</sub> emission.

At full load the highest oxides of nitrogen produced by 15% H<sub>2</sub> + raw vegetable oil is 10.60 g/kW h. This is 17% greater than diesel and 33% greater than neat vegetable oil. The inclusion of hydrogen increases NO<sub>x</sub> of neat vegetable oil from 7.1 to 10.6 g/kW h.

7. *HC and CO Emission:* Figs. 10 and 11 compared HC and CO emission of 15% H<sub>2</sub> + raw vegetable oil with diesel and neat vegetable oil. From the figure, it is seen

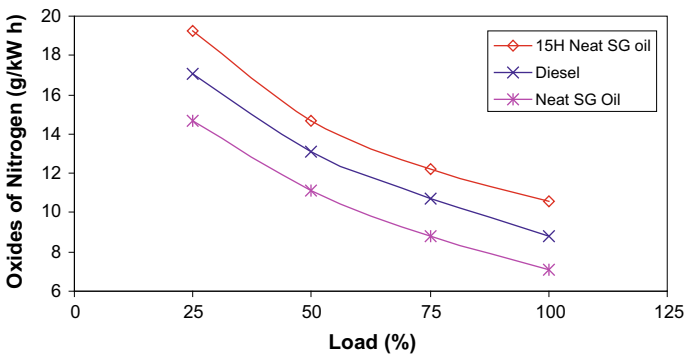


Fig. 9 Oxides of Nitrogen



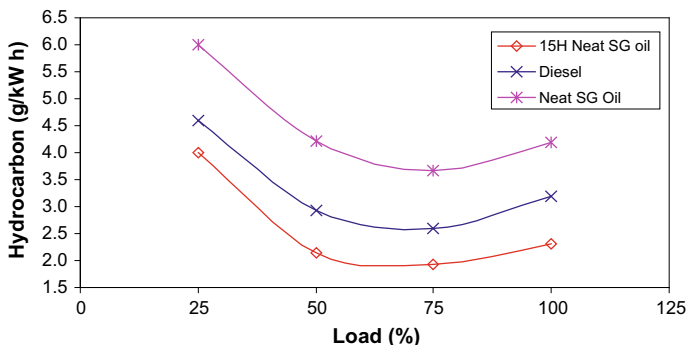


Fig. 10 Hydrocarbon emission

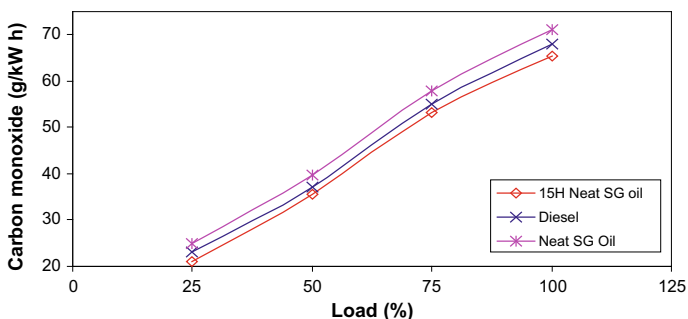


Fig. 11 Carbon monoxide emission

that the lowest HC and CO are obtained with 15% H<sub>2</sub> + raw vegetable oil than that of neat oil and diesel. The creation of higher temperature during combustion is due to H<sub>2</sub> assistance; hence the HC and CO emissions were decreased. Since the flame velocity is high, uniform temperature was created in entire combustion chamber, and hence the HC and CO emission levels are lower.

At full load the lowest HC emission produced by 15% H<sub>2</sub> + raw vegetable oil is 2.3 g/kW h, which is 38% lower than diesel and 80% lower than neat vegetable oil. The addition of hydrogen decreases HC emission of neat vegetable oil from 4.2 to 2.3 g/kW h.

The lowest CO exhausted by 15% H<sub>2</sub> + raw vegetable oil is 65.30 g/kW h which is 5% lower than diesel and 6% lower than raw vegetable oil. The addition of hydrogen decreases CO emission of neat vegetable oil from 71 to 67 g/kW h.

## 5 Conclusion

- The effect of combustion enhancer on neat oil combustion in a DI diesel engine using neat vegetable oil and H<sub>2</sub> was producing appreciably more noise.
- The hydrogen enhanced operation also exhibited more temperature.
- The inherent qualities of H<sub>2</sub> such as high flame speed, calorific value and gaseous state assist to combust vegetable oil with reduced emission and higher efficacy.
- The introduction of 15% H<sub>2</sub> combustion with vegetable oil is evaluated with diesel, and it reveals that 5% higher BTE, 6% higher EGT, 5% lower CO, 17% lower smoke, 17% higher NO<sub>x</sub>, and 38% lower HC than that of diesel mode.
- The enhancement attained by 15% H<sub>2</sub> with vegetable oil is 25% in heat release rate, 15% in efficacy, 20% in smoke, 40% in NO<sub>x</sub>, 5% in CO, 45% in HC, 17% in cylinder pressure and than that of vegetable oil (without H<sub>2</sub>).

## References

1. Karthikayan S, Sankaranarayanan G, Karthikayan R (2015) Green technology effect of injection pressure, timing and compression ratio in constant pressure heat addition cycle by an eco-friendly material. *Int J Ecotoxicol Environ Saf* 121:63–66
2. Karthikayan S, Sankaranarayanan G (2014) Influence of engine parameters optimization in the neat non-edible oil + LSD fuel combustion analysis: measurement of cylinder pressure and heat release at various loads. *Int J Appl Eng Res* 9(22):12741–12756
3. Agarwal D, Agarwal AK (2007) Performance and emission characteristics of jatropha oil (preheated and blends) in a direct injection compression ignition. *Appl Therm Eng* 27:2314–2323
4. Deepanraj B, Lawrence P, Sankaranarayanan G (July 2012) Performance and emission characteristics of diesel engine fuelled with rice bran oil methyl ester blends. *Daffodil Univ J Sci Technol* 7(2):51–55.
5. Sankaranarayanan G, Jayaraj J, Saravanan N, Jeyachandran K (2005) Performance and emission studies on DI diesel engine using mahuca indica oil and hydrogen as dual fuel. In: *Proceedings of the 19th national conference on I.C. engines and combustion*, Annamalai University, Chidambaram, pp 83–86
6. Ganesan S, Elango A (2013) Influence of nanocatalyst in the performance of Direct injection CI Engine using blends of castor oil. *ICANMEET 2013, IEEE Xplore*, pp 645–647
7. Karthikayan S, Vasanthakumar P, Krishnaraj J, Madhankumar D, Kalaiyarasan K (2016) A performance, combustion and emission study on HCCI engine: trends and innovations. *SAE Technical Paper*, 2016-28-0013
8. Sathiyamoorthi R, Sankaranarayanan G (April 2014) Experimental investigation of performance, combustion and emission characteristics of neat lemongrass oil in DI diesel engine. *Int J Curr Eng Technol, Special Issue* 3, pp 25–30
9. Ganesan S, Elango A, Krishna EV, Balaji A (2014) Influence of nano catalyst on emission characteristics of DI diesel engine with blends of lemon grass oil using Taguchi approach. *Int J Appl Eng Res* 9:9941–9945
10. Karthikayan S, Sankaranarayanan G (2014) Experimental investigation on higher proportion esters of Simarouba glauca in DI diesel engine. *Int J Design Manufact Technol* 8(1):27–35
11. Karthikayan S, Sankaranarayanan G (2010) Study of air intake system of turbo charged diesel engines. *IEEE Trans* 978-1-4244-9082-0/10©2010

12. Prakash R, Singh RK, Murugan S (2015) Studies on behaviour of a DI diesel engine fuelled with bio oil biodiesel emulsions. *Int J Oil, Gas Coal Technol* 9(1):89–108
13. Murugan S, Ramaswamy MC, Nagarajan G (2009) Assessment of pyrolysis oil as an energy source for diesel engines. *J Fuel Process Technol* 90(1):67–74
14. Prakash R, Singh RK, Murugan S (2015) An experimental investigation on diesel engine fueled by biodiesel and its emulsions with wood pyrolysis oil. *Int J Oil, Gas Coal Technol* 9(1):89–108
15. Karthikayan S, Ganesan S, Sankaranarayanan G (2016) Emission estimation of neat paradise tree oil combustion assisted with superheated hydrogen in a 4-stroke natural aspirated DIC1 engine. *Therm Sci: Year 20(Suppl. 4):s1137–s1144*
16. Karthikayan S, Ganesan S, Vasanthakumar P, Sankaranarayan G, Dinakar M (2017) Innovative research trends in the application of thermal barrier metal coating in internal combustion engines. *Mater Today: Proc* 4(8):9004–9012. ISSN: 2214-7853
17. Ganesan S, Karthikayan S, Krishna GS, Reddy GVR (2018) Investigation on performance and emission characteristics of diesel engine with the blends of rosemary oil with magnesium oxide. *ARPJ Eng Appl Sci* 13(1):386–390
18. Karthikayan S, Sankaranarayanan G (2013) Optimisation of engine performance variables using Taguchi and Grey Relational Analysis. *Natl J Adv Build Sci Mech* 4(2):11–19. ISSN-0975-7317
19. Sankaranarayanan G, Pugazhvidivu M (2012) Effect of hydrogen enriched air on the performance and emissions of mahua oil fuelled diesel engine. *Int J Renew Energy Technol* 3(1):94–106
20. Senthil Kumar M, Ramesh A, Nagalingam B (2003) Use of hydrogen to enhance the performance of a vegetable oil fuelled compression ignition engine. *Int J Hydrogen Energy* 28:1143–1154
21. Krishnaraj J, Vasanthakumar P, Hariharana J, Vinoth T, Karthikayan S (2017) Combustion simulation and emission prediction of different combustion chamber geometries using finite element method. *Mater Today: Proc* 4(8):7903–7910



#### **Dr. G. Sankaranarayanan**

Professor & Dean, Department of Mechanical Engineering, GNITC, Khanapur, Ibrahimpatnam. INDIA. He is an automobile engineer and has more than 5 years of industry and 26 years of teaching experience.

He has supervised 4 scholars and 4 more are doing research under him. He has 102 publications and filed 5 patents. He has given lectures in many FDP, seminars and in workshops. He has authored 2 text books. He is an FIE, life member of Combustion Institute, ISTE and member of SAE.

**S. Karthikayan**

Professor, Department of Mechanical Engineering, MLR Institute of Technology, Hyderabad-500043, India, passionate in IC Engine Research. He has 17 years of experience in industry and teaching.

He has published 26 papers in various journals and conferences in national and international level and a text book for Anna University engineering students. He received DRDO grant twice. He has received “Best Faculty Advisor Award” for the year of 2010–2011, from SAE India. He led the team for Supra, BAJA, effi-cycle and Tractor Design Competition.

He is a management committee member of SAE India Southern Section, Chennai. He is also an active member of Combustion Institute (Indian Chapter), ISTE & NIQR

Contact Details: [sskksmit@gmail.com](mailto:sskksmit@gmail.com), +91-8838918273.

# Experimental Investigation on Stir Casting Processing and Properties of Al 6082/SiC Metal Matrix Composites



Debashis Mishra and Tirupati Tulasi

**Abstract** Ceramic particles are submerged into the metal to enhance the mechanical properties and also the tear and wear resistance properties and it is named as metal matrix composites (MMCs). MMCs find wide applications in the most advanced high-end engineering industries for structural applications, including aerospace and automobiles. The most easy and economical technique to produce MMCs is by dispersing solid ceramic particulates in a molten metal matrix by means of a stirrer and is named as stir casting method. The resulting mechanical properties are influenced by the uniform combination of ceramic particulates in the molten metal. The Al/SiC MMC is prepared by the mechanical stir casting technique in different compositions by varying the percentage of SiC with 0, 8, 9 and 10. The mechanical properties are evaluated by carrying the tensile and hardness testing of the standard samples as per the ASTM E8/E8 M-08. The strength under tension is maximum for the 10% SiC MMC with the value of 169.94 MPa is achieved. The hardness test results reveal that the 0% SiC has highest hardness number of 57.8 HRB. From the microstructural investigation, it is observed that clustering of the particulates occurs in the 8% SiC and gradual scattering in 9% and 10% SiC.

**Keywords** Metal matrix composites (MMCs) · Stir casting · Mechanical properties · Ceramic materials · Aluminium 6082 alloy

## 1 Introduction

The unique material properties like strength, durability in harsh environmental conditions, that is, resistance to wear and tear, light weight and economy are of great demand in the present world of manufacturing. Manufacturing of such a product that

---

D. Mishra (✉) · T. Tulasi  
Department of Mechanical Engineering, CMR Technical Campus, Kandlakoya, Medchal,  
Hyderabad, India  
e-mail: [debashis171@gmail.com](mailto:debashis171@gmail.com)

T. Tulasi  
e-mail: [tirupatitulasi@gmail.com](mailto:tirupatitulasi@gmail.com)

© Springer Nature Singapore Pte Ltd. 2020  
G. S. V. L. Narasimham et al. (eds.), *Recent Trends in Mechanical Engineering*,  
Lecture Notes in Mechanical Engineering,  
[https://doi.org/10.1007/978-981-15-1124-0\\_14](https://doi.org/10.1007/978-981-15-1124-0_14)

has technological adoptability and sustainability is an essential factor in the recent engineering as well as non-engineering applications. Currently, fuel economy, strong and light weight featured structures with enhanced engine execution are the interested area of research. To achieve the desired and customized combinations of various properties for engineering, applications-reinforced MMCs are widely accepted over other engineering materials. They possess properties such as high specific strength, extreme corrosion resistance, ductility, high thermal resistance and specific stiffness [1]. MMCs are succeeded by conventional metallic metals and their alloys in the high-end manufacturing and research areas like aerospace, automotive, defence, marine, sports and so on. In general, MMCs are metallic alloys (Al, Mg, Zn, Cu, SS and Ti) reinforced with ceramic materials (SiC, TiC, TiB<sub>2</sub>, AlN, Si<sub>3</sub>N<sub>4</sub>, Al<sub>2</sub>O<sub>3</sub>, SiO<sub>2</sub> and ZrB<sub>2</sub>) [2]. Aluminium-based particulate-reinforced metal matrix composites (AMCs) evolved as finest choice over regularly used metallic materials for its tailored mechanical, physical and thermal properties for the intended and suitable performance as structural and functional applications in high-tech manufacturing industries. AMCs are manufactured following the different techniques such as liquid state, semisolid and powder metallurgy methods. Mechanical stir casting is the commonly used liquid-state technique for the manufacturing of metal matrix composites by means of a mechanical stirrer. In this technique a desired percentage of ceramic material is mixed with a molten metal matrix to produce an MMC, followed by casting [3]. The widely used and the most economic, suitable technique to manufacture AMCs is mechanical stir casting for its unique stirring action. Reinforcement of ceramics up to 30% with the large variety of molten metal matrix can be mixed to achieve superior bonding between them [4, 5]. The stir casting process can be effectively used for the mass production of MMCs and AMCs [6–8].

Aluminium 6082 is a medium strength alloy having exceptional corrosion resistivity and is widely used for structural applications. The density of Al 6082 alloy is reported as 2.70 g/cm<sup>3</sup> and melting point is 555 °C. Workability, machinability, weldability, brazability of Al 6082 alloy are found to be good. The tensile strength of Al 6082 alloy is reported as 140–330 MPa and the Brinell hardness value is 91 HB. Al 6082 alloy is typically used in high-stress applications, trusses, bridges, cranes and transport vehicles.

Reinforcing hard ceramic materials into soft Al alloys improves the mechanical properties such as strength, hardness and wear-resistance. Stiffness of the Al alloy can be improved by the addition of SiC. Carbide is used to restrict the enlargements of grains [9]. SiC is a refractory material having 70% silicon and 30% carbon contents. The density of SiC is 2.22 g/cm<sup>3</sup> and melting point is 2700 °C. It possesses excellent thermal conductivity and low thermal expansion. The high hardness and tremendous corrosion resistance and stiffness makes SiC a useful ceramic material for the manufacturing of rubber tyres, grinding wheels and sealing valves to withstand at high temperature [10].

In this investigation the reinforcement of SiC as 8, 9, 10% with aluminium 6082 alloy and pure aluminium round bar specimens are prepared by the mechanical stir casting process. The tensile properties, hardness and microstructures of Al 6082/SiC metal matrix composites specimens are analyzed and reported.

## 2 Experimental Details

- The base metal is chosen as aluminium 6082 alloy.
- The reinforcement ceramic material is chosen as silicon carbide particulates.
- Al 6082/SiC metal matrix composites specimens of desired size are manufactured by mechanical stir casting process.
- The chemical compositions of Al 6082 alloy are given in Table 1.

### 2.1 Mechanical Stir Casting Process

A graphite crucible furnace is used for the melting of Al 6082 alloy at well maintained temperature of 700 °C. The furnace has an in-built frequency-based mechanical stirrer continuously rotated at 500 rpm for a homogeneous mixture of Al and SiC particulates. The SiC particulates are added manually into the vortex of furnace by varying its percentage as 0, 8, 9 and 10. The mixture is discharged into the mould cavity and left to solidify at room temperature. The mechanical stir casting process followed in manufacturing of composite specimens is shown in Fig. 1.

### 2.2 Manufactured Al 6082/SiC MMCs Specimen Information

Approximately 2 kg of Al 6082 alloy are melted without the addition of SiC particulates. Cylindrical rod samples are prepared of size 200 mm length and 21 mm diameter. Then the specimens are extracted following the standard ASTM E8/8 M-08. Composite metal sheets of Al 6082/SiC are prepared of size 120 × 120 mm with thickness 18 mm. The cylindrical rods and sheets are given in Fig. 2. Further, the Al 6082/SiC composite specimens are prepared with the SiC addition with the percentage of 8, 9 and 10. The composite specimens for different percentage 8, 9 and 10 of SiC added with Al 6082 alloy are shown in Figs. 3, 4 and 5.

## 3 Results and Discussion

### 3.1 Hardness Observations

The Rockwell hardness assessment is conducted using an auto digital hardness tester. The diamond cone indenter is used to produce an indentation mark on the metal surface of the Al 6082/SiC composite metal sheets and the hardness values are obtained, as shown in Table 2. Pure aluminium composite having more hardness value

**Table 1** Chemical compositions of Al 6082 alloy

Elements	Si	Fe	Cu	Mn	Mg	Zn	Ti	Cr	Al
% Present	0.7-1.3	0.0-0.5	0.0-0.1	0.4-1.0	0.6-1.2	0.0-0.2	0.0-0.1	0.0-0.25	Balance



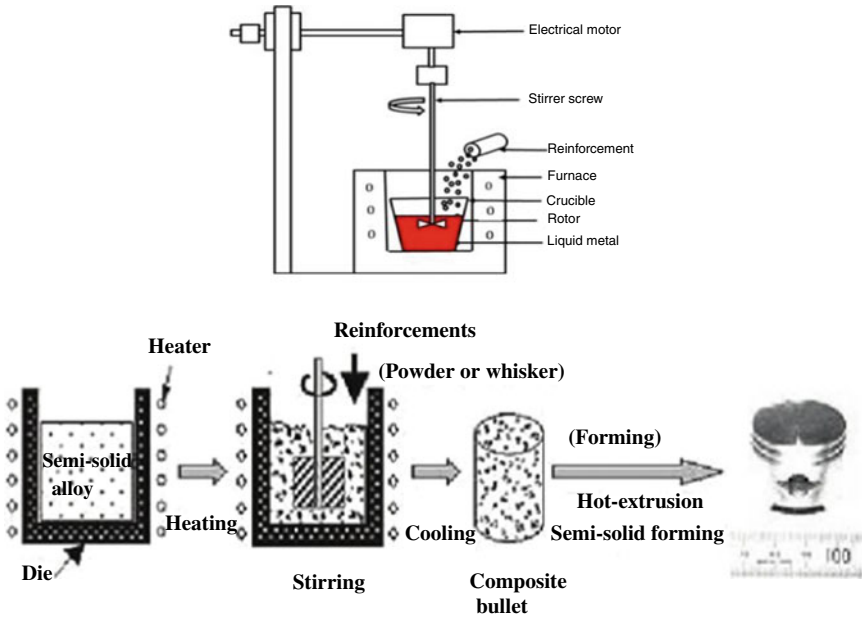


Fig. 1 Mechanical stir casting process



Fig. 2 Al 6082 specimen without the addition of SiC particulates



Fig. 3 Al 6082/SiC MMCs specimen with the addition of 8% SiC particulates

than the addition of SiC is identified. The obtained hardness values of manufactured composite material are described in Fig. 6.

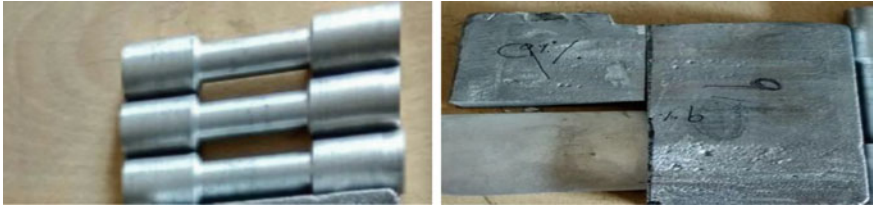


Fig. 4 Al 6082/SiC MMCs specimen with the addition of 9% SiC particulates



Fig. 5 Al 6082/SiC MMCs specimen with the addition of 10% SiC particulates

Table 2 Rockwell hardness analysis of composite

Al 6082-weight % of SiC	Hardness value
0	57.8
8	42.2
9	37.1
10	47.2

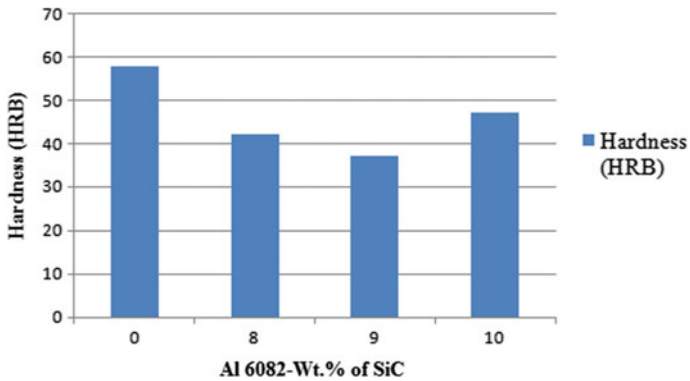
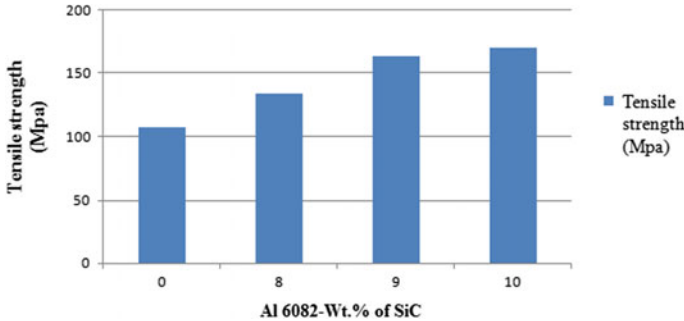


Fig. 6 Hardness values of Al 6082/SiC MMCs

**Table 3** Tensile strength of Al 6082/SiC MMCs

Al 6082-weight % of SiC	Tensile strength (Mpa)
0	106.98
8	133.5
9	163.31
10	169.94



**Fig. 7** Value of tensile strength of Al 6082/SiC MMCs

### 3.2 Tensile Strength Observations

The tensile test using 250 kN Instron UTM is performed. The obtained tensile strength of the composite specimens is tabulated in Table 3. Figure 3 describes the strength of composites in which it is observed that the strength is rising with varying percentage of SiC. The 10% SiC addition into the Al 6082 alloy gives the maximum strength of 169.94 MPa (Fig. 7).

### 3.3 Microstructural Observations

The microstructures of Al 6082/SiC MMCs are obtained with the help of BX51 M microscope. The test specimens are properly polished and mounted. Then with the application of Keller’s reagent the microstructures are observed. The microstructures are collected in 200 × and 500 × magnifications. The dendrite structure is observed in pure Al 6082 composite with 0% addition of SiC. Blocky morphology of SiC (gray) in the matrix of dendrite structure is observed in Al 6082/SiC MMCs with the 8, 9 and 10% addition of SiC. The microstructures shown in Figs. 8, 9, 10 and 11 are with the 0, 8, 9 and 10% addition of SiC in the MMC composites.

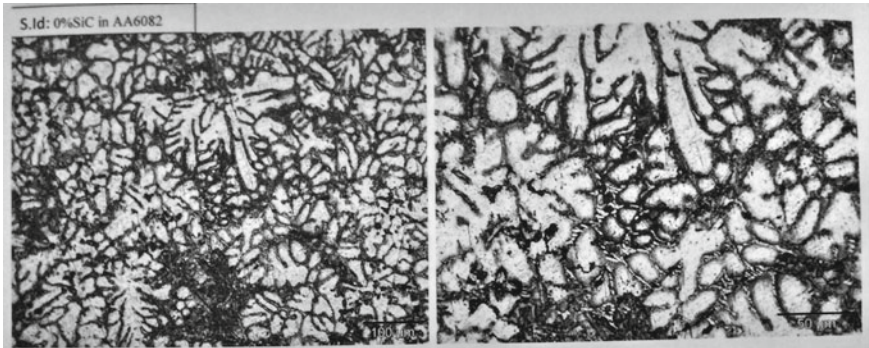


**Fig. 8** Microstructure of Al 6082 MMCs without the addition of SiC

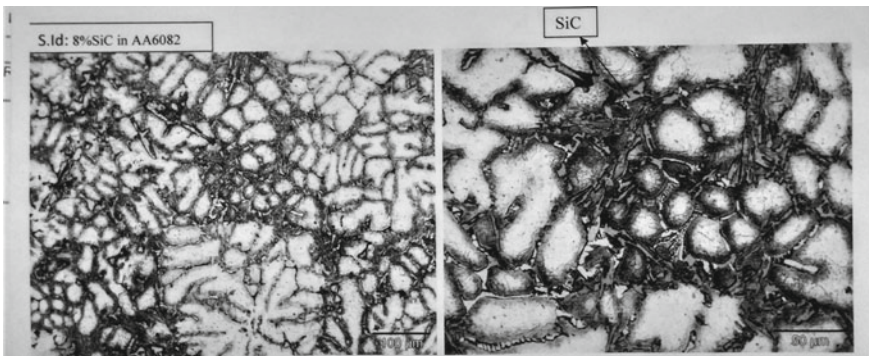


**Fig. 9** Microstructure of Al 6082 MMCs with 8% addition of SiC

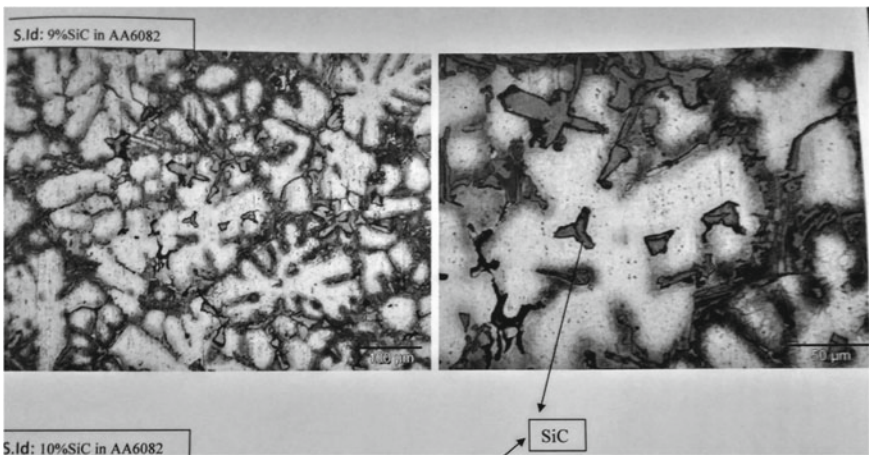


**Fig. 10** Microstructure of Al 6082 MMCs with 9% addition of SiC

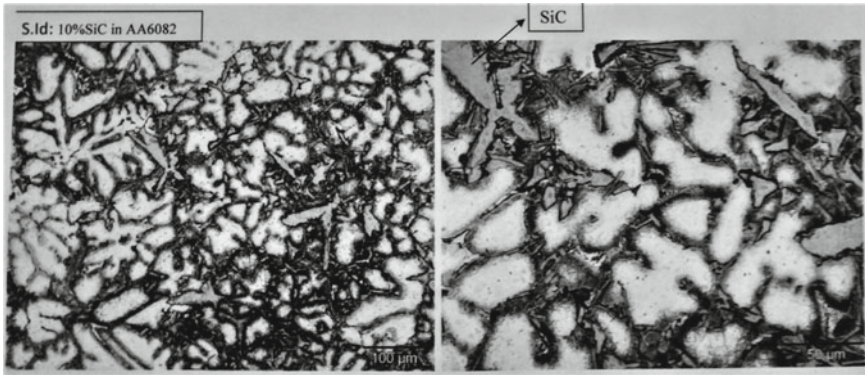


**Fig. 11** Microstructure of Al 6082 MMCs with 10% addition of SiC

## 4 Conclusion

The mechanical stir casting process is successfully used to manufacture Al 6082/SiC MMCs and is found to be an easy, economical technique. The Al 6082/SiC MMCs are manufactured with the addition of SiC percentage of 0, 8, 9 and 10. The hardness value is found maximum 57.8 HRB with the Al 6082 composite without the addition of SiC. With the addition of 10% SiC the hardness achieved is 47.2 HRB. Tensile strength is enhanced with the change in addition of SiC from 0% to 8, 9 and 10%. The 10% SiC particulates into the Al 6082 alloy giving the maximum strength of 169.94 MPa. The microstructure reveals the bonding strength is attained to be good with the mechanical stirring action. The dendrite structures in Al 6082 alloy composite and clustered SiC in the addition of SiC are observed in microstructures.

## References

1. Bodunrin OM, Alaneme KK, Chown HL (2015) Aluminium matrix hybrid composites: a review of reinforcement philosophies; mechanical, corrosion and tribological characteristics. *J Mater Res Technol, Elsevier* 4(4):434–445
2. Suresh S, Moorthi SVN (2013) Process development in stir casting and investigation on microstructure and wear behavior of  $TiB_2$  on Al6061 MMC. *Procedia Eng, Elsevier* 64:1183–1190
3. Raviraj MS, Sharanprabhu CM, Mohankumar GC (2014) Experimental analysis on processing and properties of Al-TiC metal matrix composites. *Procedia Mater Sci, Elsevier* 5:2032–2038
4. Sharma P, Sharma S, Khanduja D (2015) A study on microstructure of aluminium matrix composites. *J Asian Ceram Soc, Elsevier* 3:240–244
5. Johny JS, Venkatesh K, Kuppan P, Ramanujan R (2014) Hybrid aluminium metal matrix composite reinforced with SiC and  $TiB_2$ . *Procedia Eng, Elsevier* 97:1018–1026
6. Kala H, Mer KKS, Kumar S (2014) A review on mechanical and tribological behaviors of stir cast aluminium matrix composites. *Procedia Mater Sci, Elsevier* 6:1951–1960

7. Pradhan KS, Chatterjee S, Mallick BA, Das D (2016) A simple stir casting technique for the preparation of in situ Fe-aluminides reinforced Al-matrix composites. *Perspect Sci*, Elsevier 8:529–532
8. Kandpal CB, Kumar J, Singh H (2018) Manufacturing and technological challenges in stir casting of metal matrix composites: a review. *Mater Today: Proc*, Elsevier 5:5–10
9. Ramnath VB, Elanchezhian C, Annamalai RM, Aravind S, Atreya AST, Vignesh V, Subramanian C (2014) Aluminum metal matrix composites: a review. *Rev Adv Mater Sci* 38:55–60
10. Pawar PB, Utpat AA (2014) Development of Al based SiC particulates metal matrix composite for spur gear. *Procedia Mater Sci*, Elsevier 6:1150–1156



# Effect of Change in Focal Plane Position on Hole Characteristics of Nanosecond Pulsed Laser Micro Drilled Holes



Ganesh Dongre, Avadhoot Rajurkar, Ramesh Gondil, Nachiket Laddha and Jacob Philip

**Abstract** In laser micro drilling, on changing the focal plane position of the workpiece, there is a significant change in the hole characteristics. This change can be used as an application in some of the industries. In this experiment, the effect of change in focal plane position in the positive, that is upward, direction on the hole parameters is studied and explained. A stainless steel 316 plate is used as the workpiece and a diode-pumped nanosecond pulsed laser is used for micro drilling because of its accuracy and comparatively low cost than picosecond or femtosecond pulsed lasers. It is seen that a significant change in the entry diameter, exit diameter and taper of the hole takes place when the focal plane position is changed. Also, this is carried out at different laser powers.

**Keywords** Laser · Focal plane · Micro drilling · Taper

## 1 Introduction

Laser micro drilling process involves focusing a high-intensity coherent light beam onto the workpiece surface to produce sufficient power densities to melt or even vaporize the surface material [1]. Laser micro drilling is one of the most used processes in aerospace industries and slowly it is expanding its range in other industries like automobile, electronics and telecommunication, because of its vast applications and high accuracy. It is used for various applications which include production of lubrication holes in turbine blades and engine parts, production of cooling channels in various components, circuit boards, and so on. The four most used processes for laser drilling are single pulse, percussion drilling (using multiple pulses in same

---

G. Dongre (✉) · A. Rajurkar · R. Gondil · N. Laddha  
Department of Industrial and Production Engineering, Vishwakarma Institute of Technology,  
Maharashtra, India  
e-mail: [ganesh.dongre@vit.edu](mailto:ganesh.dongre@vit.edu)

J. Philip  
Vikram Sarabhai Space Centre, Trivandrum, Kerala, India

© Springer Nature Singapore Pte Ltd. 2020  
G. S. V. L. Narasimham et al. (eds.), *Recent Trends in Mechanical Engineering*,  
Lecture Notes in Mechanical Engineering,  
[https://doi.org/10.1007/978-981-15-1124-0\\_15](https://doi.org/10.1007/978-981-15-1124-0_15)

spot), trepanning (moving the laser beam along the circumference of hole) and helical drilling (trepanning while simultaneously adjusting the focal plane) [2]. After studying further the above applications, it is seen that the main requirement of these applications is high aspect ratio holes. Aspect ratios  $>50$  have been produced with high quality, mainly by employing helical or trepanning drilling [3–5].

Resolidified material, taper, barrelling, inlet cone, exit cone, surface debris and mean hole diameter are other hole characteristics which are taken into account for most of the applications [6]. Although there are many non-traditional machining processes by which we can get good hole characteristics, but laser micro drilling happens to be the most economical and accurate as compared to other processes. All the above characteristics can be optimized by optimizing process parameters such as peak power, pulse duration, pulse frequency, pulse width, repetition rate, focal plane position and assist gas pressure [7].

Gas-assisted percussion drilling using Nd:YAG pulsed laser for 2 mm thick Ti plate was conducted by Avvari et al. It was revealed that hole taper increases with increase in gas pressure. However, this trend continues till a certain hole depth and then hole taper reduces. Further, MRR and hole taper increases with the increase in laser cutting speed [8]. Yvonne et al. used nanosecond pulsed laser on a 1 mm thick aluminium plate. Percussion drilling technique was used in the presence of inert gas. It was found that minimum redeposited material on surface with smallest hole diameter was drilled. At the same time, use of compressed gas was found to be efficient for other materials like SS and Al [9]. Liquid-assisted laser percussion drilling was performed by authors Jiao et al. on 0.3 mm silicon wafer. They used ethanol as liquid assist during laser drilling. Ethanol exhibited high material removal rate which causes increase in exit hole diameter. Further, their study concludes that liquids with higher boiling point tends to decrease exit hole diameter. Liquid with low boiling point is most effective parameter in reducing the debris formation as well as taper angle [10]. Manninen et al. studied the effect of pulse width on hole diameter and hole taper. It was observed that increase in pulse width increases hole diameter and reduces hole taper. This may be due to the fact that the high pulse energy and longer interaction with the material leads to more molten material being ejected by vapour pressure [2]. Fornaroli et al. adopted helical laser drilling approach for microholes. They studied the effect of pulse energy on the entry and exit hole diameters. Moderate increase in entry and exit diameters was observed in their study. However, hole diameters can also be increased using pulse energies  $>0.75$  mJ [5]. Li et al. found through statistical modelling that hole taper is most sensitive to focal plane position variations followed by pulse width, peak power and number of pulses [11]. Effect of laser energy, pulse width and gas pressure on heat affected zone (HAZ) and spatter area was studied by Chatterjee et al. HAZ and spatter area increases with the increase in pulse energy and pulse width, whereas it decreases with increase in gas pressure [12].

In the recent past, literatures reveal that optimization of micro hole drilling using various laser drilling techniques and assisted mediums, however, very few literature were available on analysis of change in focal plane position. Therefore, the aim of the presented work is to study the effect of change in focal plane position on the entry and exit diameter of the hole as well as hole taper variation.



**Table 1** Machine specification

NUQA-1064-NA-0030-YZ	
Output power	30.0 W
Mode of operation	Pulsed
Peak power	10.0 kW
Pulse energy	1.0 mJ
Pulse width	100 ± 20 ns
Pulse repetition rate (PRR)	30–100 kHz

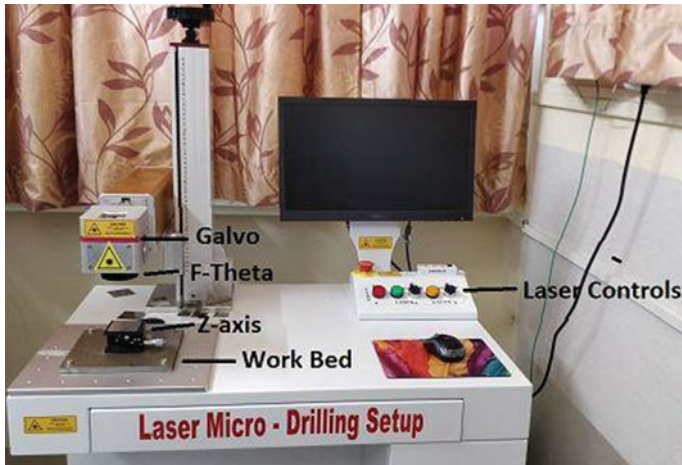


**Fig. 1** Nanosecond pulsed laser setup

## 2 Experimentation Details

A NUQA 30-W fibre marking laser machine manufactured by COHERENT was used for producing diode-pumped Nd:YAG laser for experimentation. Machine specifications are mentioned in Table 1. The machine has a two-axis Galvo named basiCube10, which is manufactured by Scanlab. Figure 1 shows the machine setup that was used for the experiment.

## 3 Methodology

The experiment was performed on a stainless steel 316 plate. The plate thickness was 0.8 mm. The sample size was 30 mm × 30 mm. The experiment was done to study the effect of variation in focal plane position on the entry diameter, exit diameter and taper of the hole. The focal plane position can be changed by two ways: (1) Using a 3

axis Galvo or (2) by changing the table position in the Z-axis direction. The changing of the table position in the Z-direction is more economical as compared to the other way. So, in this experiment we used a Z-axis linear stage which is manually operated. Figure 2 shows the Z-axis linear stage which was used. The movement of the stage is controlled manually by micrometer-like scale which is visible in the figure. By rotating the scale by ten divisions in the anti-clockwise direction, the stage moves by 0.1 mm in downward direction, which ultimately moves the focal plane position in the upward direction by 0.1 mm.

At each power, total nine holes are micro drilled by varying the focal plane position. Starting from the focal point, that is on the scale, we will name it as 0 mm. Further by moving the focal plane position in the positive direction by 0.1 mm distance, micro holes are drilled. To move the focal plane position in the positive direction, the Z-axis stage is moved in the downward direction by 0.1 mm after each hole.

As the thickness of the workpiece is 0.8 mm, the focal plane position is shifted in the positive direction till 0.8 mm. In short, micro holes are drilled by keeping focal plane position on 0, 0.1, 0.2, 0.3, 0.4, 0.5, 0.6, 0.7, 0.8 mm in the positive direction. Now this whole cycle is carried out at five different laser powers (12, 15, 18, 21 and 24 W) to see the effect of change in laser power. While drilling of each micro hole, roughing, finishing and cleaning passes are given. The parameters of finishing and cleaning passes are the same. The difference is, in finishing pass, hatch pattern is given while in cleaning pass, no hatch pattern is given. The parameters of roughing, finishing and cleaning passes are shown in Table 2. To see the effect of change in power, only the power of roughing pass is changed and finishing and cleaning pass power are constant for all the experiments.

Figure 3 shows the laser beam profile. It is seen that till a particular point, the laser beam converges and after that point, the laser beam diverges further. The point at which the beam converges and then diverges is called the focal point of the laser

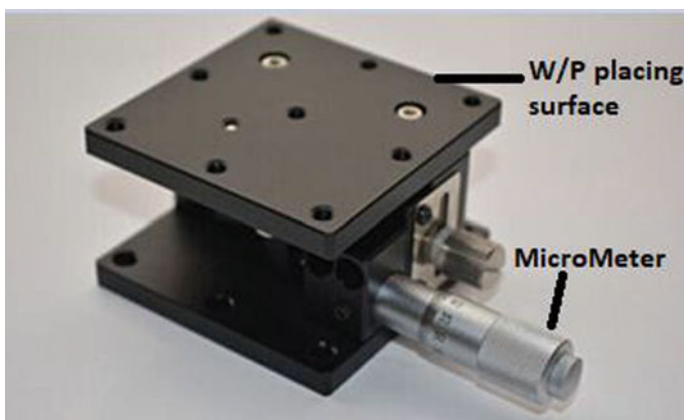


**Fig. 2** Z-axis linear stage used in the experiment

**Table 2** Laser parameters

Parameter	Roughing pass	Finishing pass	Cleaning pass
Loop count (passes)	250	500	500
Speed (mm/sec)	150	500	500
Power (W)	12, 15, 18, 21, 24	12	12
Pulse repetition rate (kHz)	60	60	60

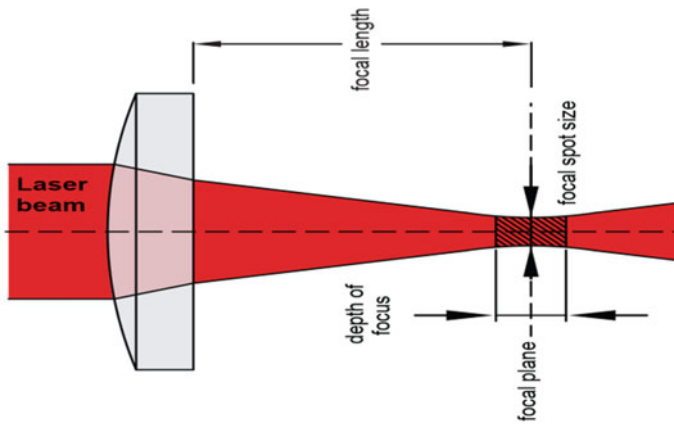


**Fig. 3** Laser beam profile

beam. The maximum amount of beam energy is seen when the workpiece is at the focal point of the laser beam. By moving the workpiece away from the focal point, the amount of beam energy goes on decreasing.

## 4 Results and Discussion

### 4.1 Effect of Change in Focal Plane Position on the Entry Diameter of the Hole at Various Laser Powers

Figure 4 shows the effect of change in focal plane position on the entry diameter of the hole at various laser powers. It is clearly seen from the graph that as the focal plane position increases, the entry diameter increases at all laser powers. This trend is explained by the laser beam profile, as shown in Fig. 3. On moving the focal plane

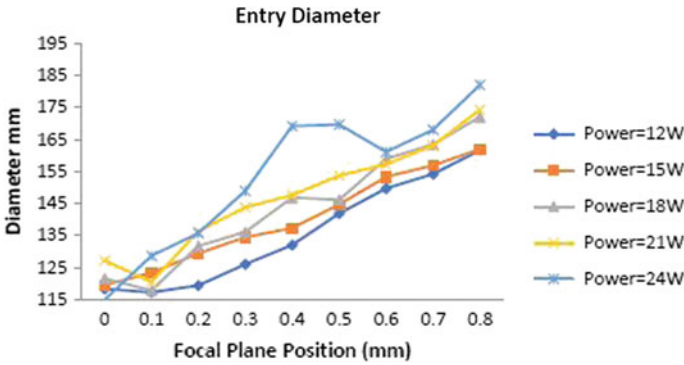


Fig. 4 Effect of focal plane position on the entry diameter of hole at different laser powers

position, the beam diverges, so the entry diameter increases. After comparing the entry diameter for different power, it is seen that as the power increases the entry diameter at each focal plane position increases; that is, for a specific focal plane position, highest power hole will have highest entry diameter. This is because the increase in power increases the amount of pulse energy due to which there is more melting and vaporization, resulting in enlarged hole.

#### 4.2 Effect of Change in Focal Plane Position on the Entry Diameter of the Hole at Various Laser Powers

Figure 5 shows the effect of change in focal plane position on the exit diameter of the hole at various laser powers. It is seen from the graph that as the focal plane position increases, there is a decrease in the exit diameter of the hole. Theoretically,

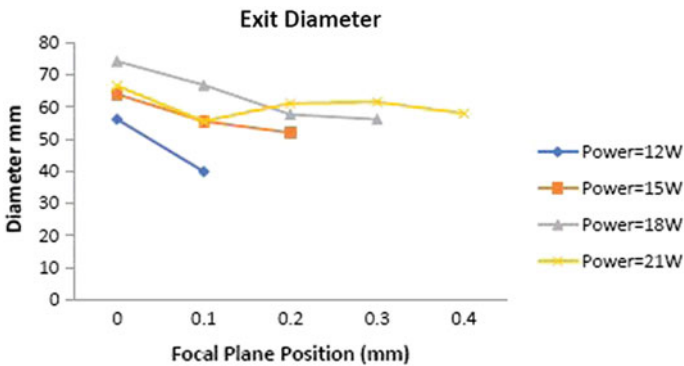
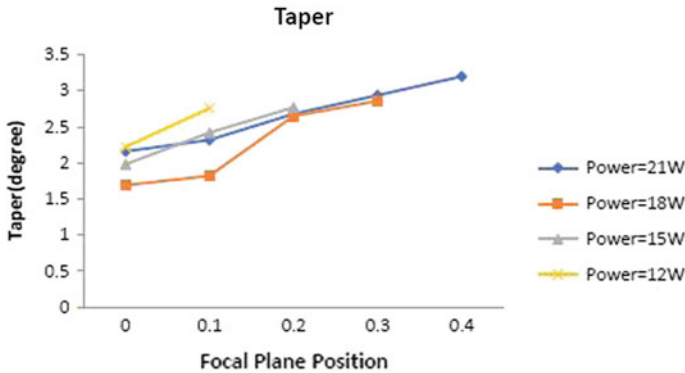


Fig. 5 Effect of focal plane position on the exit diameter of hole at different laser powers



**Fig. 6** Effect of focal plane position on the taper angle of the hole at various laser powers

as explained in Fig. 3, due to the laser beam divergence, the exit diameter should increase. But it decreases, because the amount of energy left till the beam reaches the exit side is very low. Also, the comparison of the exit diameter at different laser powers is shown in the graph (Fig. 5). At a particular focal plane position, the hole with highest power has the highest exit diameter. This is because as the power increases, the pulse energy increases and more removal of material takes place. Also, it is seen that for least power, only two through holes are obtained out of nine and for the highest power, five through holes are obtained. As the power increases, the number of through holes increases which is again because of more pulse energy.

#### ***4.3 Effect of Change in Focal Plane Position on the Taper Angle of the Hole at Various Laser Powers***

The effect of change in focal plane position on the taper angle of the hole at different laser powers is shown in Fig. 6. It is observed that as the focal plane position increases, the taper angle increases. This is because with increase in focal plane position, the entry diameter increases and exit diameter decreases which ultimately increases the taper. No specific relation can be found on comparing the taper angle at different powers.

### **5 Conclusions**

After doing various experiments to find the effect of change in the focal plane position in the positive direction (i.e. towards the laser) on SS316 plate of 0.8 mm thickness at various powers by percussion drilling by using nanosecond pulsed laser, the following conclusions were made:

- As the focal plane position is increased in the positive direction, the entry diameter increases and the exit diameter decreases.
- With the increase in the laser power, the entry diameter as well as the exit diameter at a particular focal plane position increases.
- With the increase in the focal plane position in the positive direction, the taper angle increases.

**Acknowledgements** This work has been supported under ISRO RESPOND project grant. The authors are grateful to VSSC, Trivandrum and the management of Vishwakarma Institute of Technology, Pune, India.

## References

1. Tam SC, Yeo CY, Lau MWS, Lim EN, Yang LJ, Noor Y (1993) Optimization of laser deep-hole drilling of Inconel 718 using Taguchi method. *J Mater Process Technol* 37:741–757
2. Manninen M, Hirvimäki M, Matilainen VP, Salminen A (2017) Comparison of laser-engraved hole properties between cold-rolled and laser additive manufactured stainless steel sheets. *Appl Sci* 7:913
3. Weck A, Wilkinson DS, Preston JS (2008) Laser drilling of high aspect ratio holes in copper with femtosecond, picosecond and nanosecond pulses. *Appl Phys A* 90:537–543
4. Patwa R, Herfurth H, Christophersen M, Philips BF (2014) Laser drilling for high aspect ratio holes and a high open area fraction for space applications. *Taper* 200(10):0–05
5. Fornaroli C, Holtkamp J, Gillner A (2013) Laser-beam helical drilling of high quality micro holes. *Phys. Procedia* 41:661–669
6. Ghoreishi M, Low DKY, Li L (2002) Comparative statistical analysis of hole taper and circularity in laser percussion drilling. *Int J Mach Tools Manuf* 42(9):985–995
7. Ghoreishi M (2006) Statistical analysis of repeatability in laser percussion drilling. *Int J Adv Manuf Technol* 29:70–78
8. Avvari M, Manjaiah M, Able M, Laubscher RF, Raghavendra K (2017) Optimization of hole characteristics during pulse Nd:YAG laser drilling of commercially pure titanium alloy. *Laser Manuf Mater Process* 4:76–91
9. Reg Y, Leitz KH, Schimdt M (2011) Influence of processing gas on the ablation quality at ns-laser beam ablation. *Phys Procedia* 12-B:182–187
10. Jiao LS, Ng EYK, Wee LM, Zheng HY (2011) The effect of assist liquid on the hole taper improvement in femtosecond laser percussion drilling. *Phys Procedia* 19:426–430
11. Li L, Low DKY, Ghoreishi M, Crookall JR (2002) Hole taper characterization and control in laser percussion drilling. *CIRP Ann* 51(1):153–156
12. Chatterjee S, Mahapatra SS, Sahu AK, Bhardwaj VK, Choubey A, Upadhyay, BM, Bindra KS (2017) Experimental investigation of quality characteristics in Nd:YAG Laser drilling of SS316. In: International conference on materials manufacturing and modelling. ICMMM 2017. VIT, Vellore

# Production Planning of Flexible Manufacturing Systems Using an Efficient Multiobjective Function Considering Failure of Different Machines in Production Unit



B. Satish Kumar, G. Janardhana Raju and G. Ranga Janardhana

**Abstract** In modern-day manufacturing process, flexible manufacturing system (FMS) is used for efficient production of parts. In FMS, processing times are important while preparing the production schedule. The manufacturing cost will vary from part to part depending on the processing time and type of machine used. In this paper a case study is considered in which three machines produce three different parts by doing different operations. Each machine can perform all the different operations to produce all the three parts. All the operations can be done in all the three machines. The production timings and corresponding costs vary from machine to machine. The operations sequences for different parts are different. The objective functions considered are minimization of the total flow time, machine workload balancing, maximum workload on machine and minimization of total tool cost. In the first step, we have considered randomly different sequence of operations on different machines, that is, operation index and machine index, and the objective function values are calculated. In the second step, the values of objective function are calculated if a particular machine is not working for manufacturing the three parts, and hence those operations are processed on alternate machines. The observations after calculations are that the total flow time, machine workload, maximum workload on machine and total cost are found to be different for different sequences and due to machine failure these values increased and better operation index and machine index are identified to meet the objective functions.

---

B. Satish Kumar (✉)

Department of Mechanical Engineering, S.R. Engineering College, Warangal, Telangana, India  
e-mail: [satishbk91@gmail.com](mailto:satishbk91@gmail.com)

G. Janardhana Raju

Dean School of Engineering, Nalla Narsimha Reddy Group of Institutions, Hyderabad, Telangana, India  
e-mail: [gjraju\\_06@rediffmail.com](mailto:gjraju_06@rediffmail.com)

G. Ranga Janardhana

Department of Mechanical Engineering, University College of Engineering, JNTU, Anathapur, Andhra Pradesh, India  
e-mail: [ranga.janardhana@gmail.com](mailto:ranga.janardhana@gmail.com)

© Springer Nature Singapore Pte Ltd. 2020

G. S. V. L. Narasimham et al. (eds.), *Recent Trends in Mechanical Engineering*,  
Lecture Notes in Mechanical Engineering,  
[https://doi.org/10.1007/978-981-15-1124-0\\_16](https://doi.org/10.1007/978-981-15-1124-0_16)

**Keywords** Production planning · Manufacturing costs · Flexible manufacturing system · Idle time · Failure of machines

## 1 Introduction

Flexible manufacturing systems (FMSs) are a group of machines, most preferably CNC, which are coordinated by a common control centre that has the ability and flexibility to deal with the variety of products. Although the flexibility in the manufacturing systems is an advantage, it proves to be a very complicated task when it comes to scheduling of parts in a changing environment.

The FMS was introduced around 1960s and used by Robos, programmable controllers (PCs) and computerized numerical control machines, and used in automated guided vehicles (AGVs) and so on, as shown in Fig. 1. In the current business scenario the competitiveness of any manufacturing industry is determined by its ability to respond quickly to the rapidly changing market and to produce high-quality products at low costs. These capabilities can be achieved by FMS. FMS is called flexible because of its capability to process various part style.

The beauty of FMS is that a component can be processed on many machines; a machine can process various operations of variety of products. The scope of work, the number of objects, use of machines and the sequence of operations are unlimited.

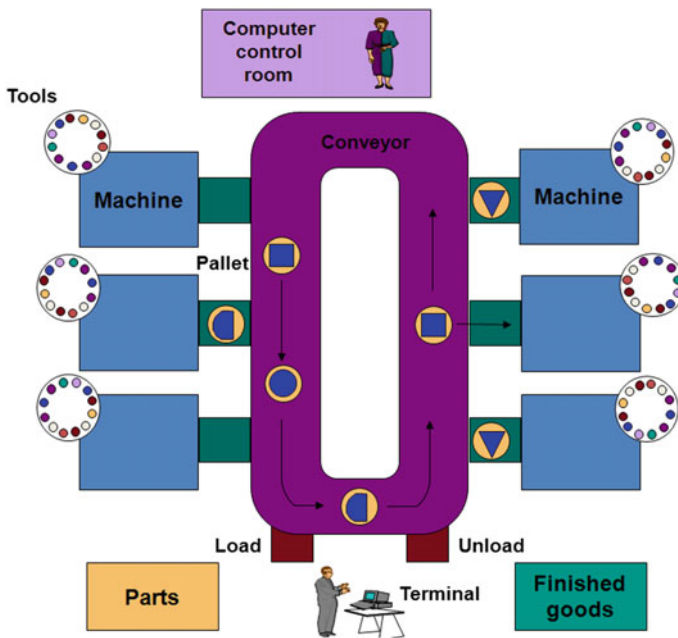


**Fig. 1** Typical View of FMS



The only task of the manufacturing engineers is to select the best possible ways of production. Sometimes it is complex and complicated.

Theoretical knowledge of manufacturing process and practical experience in production activity mixed with automated machines is the main heart of the FMS. To find the feasible solutions, the engineers use the mathematical formula, programming with feasible functions, objective function, constrained by some constraints and achieve a solution. The FMS can be mathematically modeled and visualized with simulation and that's the wonderfulness of the FMS. The FMS may need high initial investment but it can be operated with low maintenance and minimum use of energy in the manufacturing activity.

## 2 Literature Review

J. Jerald et al. used C language for writing the algorithms of optimization of scheduling of FMS. The performance is analyzed for multiobjective function of minimum total penalty costs and machine idleness. They found that particle swarm algorithm gives the best results [1].

Vahid Roshanaei noted that MILPs are unable to solve industrial-scale problems, and proposed an enhanced meta-heuristic algorithm AIA and simulated annealing. Of the mathematical models and meta-heuristics, the meta-heuristics is found to be superior in applications, since infeasible solutions are avoided and complete search space is exposed in a specified time [2].

Stephen F. Smith concluded that practical scheduling problems can be effectively solved by developing transition techniques with better solutions. Using this, major technical problems can be easily solved. Still there is a lot to be explored in the field of sequencing and scheduling [3].

In a FMS problem, multiple constraints and objectives exist. Genetic algorithms are used for solving the problems. Akhilesh Kumar proposed a FMS program and tested to get feasible solutions [4].

A.V S. Sreedhar kumar tried to optimize the FMS problem using DE and BFOA. Bacterial foraging optimization algorithm (BFOA) showed better results. Validation of the results plays a crucial role in taking the decision [5].

Sunil Kumar and Sanjay Jain studied the various techniques of dynamic scheduling of FMS. They explained various techniques to study the FMS, like dispatching rule, heuristics, GA and artificial intelligence. They suggested to combine the various techniques and get more effective solution [6].

Production planning is an important item for a manufacturing plant. The parts to be machined, use of tools should be minimum, allocation of pallet fixtures, assignment of operations are the things to be decided while planning production [7].

Jian-Hung Chen and Shinn-Ying Ho proposed EMOGA for planning flexible manufacturing system. Minimization of total flow time, machine workload unbalance, greatest machine workload and total tool cost are the four objectives they considered while problem formulation. The main feature of their program is that it can optimize

the objective function without decomposing the problem into small subset problem [8].

FMS is a complex system and has elements like workstation, ASRS, material handling. It can plan machine and vehicle scheduling problems simultaneously. Anshuman Mishra concluded that for an objective function particle swarm optimization (PSO) can give optimization better than GA for a CPU run time. PSO does not need iterations [9].

Manufacturing process is a mixture of most unexpected uncertainties, such as unexpected events, sudden or unindicated machine breakdowns, sudden surplus orders, order cancellations. In spite of this complex nature, the FMS can be planned efficiently with program formulations [10].

Rishu Sharma et al. concluded that the manufacturing industry is becoming a complex issue in view of the maintaining of demand and supply. It is important to accommodate the changes that take place in manufacturing processes [11].

K. Mallikarjuna et al. studied the machines arranged in single row assisted by AVG. The programming is composed of simulated annealing (SA) and genetic algorithm. The results obtained by GA are superior to SA [12].

Satish Kumar et al. concluded that suitable material handling system is proposed for a layout at different speeds of material handling system [13].

Srinivas et al. concluded that L2R protocol is initiated to generate an alternate path for link failures in backbone networks. To ensure link failure recovery, L2R is implemented [14].

Srinivas et al. proposed an efficient backbone-based quick link failure recovery multicast routing protocol in order to overcome the limitations of existing protocols [15].

### 3 Problem Statement

A sample problem is considered from the literature of Jian-Hung Chen and Shinn-Ying Ho for minimizing total flow time, machine workload unbalance, maximum machine workload and total tool cost [9] shown in Tables 1 and 2.

#### 3.1 Nomenclature

$f_1$  = Total processing time of three parts in required production quantity.

$f_2$  = Total transportation time in between machines.

$F_1 = f_1 + f_2$  = Total machining and transportation time.

$F_2$  = Workload balancing

$F_3$  = Minimization of maximum workload

$F_4$  = Minimization of total tool cost

**Table 1** Processing time and operation indexes for producing three parts on three machines

		Part 1			Part 2			Part 3			
Operation index		1	2	3	4	1	2	3	1	2	3
Processing time	Machine-1	1	3	3	5	9	2	9	7	8	7
	Machine-2	7	5	4	6	4	1	4	1	6	2
	Machine-3	6	9	5	1	2	5	1	3	3	5
Tool cost	Machine-1	1	2	1	6	1	8	4	8	3	6
	Machine-2	2	3	7	5	9	2	5	9	8	5
	Machine-3	4	5	4	2	8	7	8	9	6	2
Production volume		51				39			23		

**Table 2** Traveling times between the machines

	Machine-1	Machine-2	Machine-3
Machine-1	4	11	17
Machine-2	11	3	9
Machine-3	7	18	5

### 3.2 Sample Calculations

For operation index shown in Table 3, sample calculations were done:

Step I: To find F1

$$f_1 = 51 \times (7 + 5 + 5 + 5) + 39 \times (2 + 2 + 1) + 23 (7 + 8 + 2)$$

$$= 51 \times 22 + 39 \times 5 + 23 \times 17 = 1122 + 195 + 391 = 1708$$

$$f_2 = 51/10(3 + 9 + 7) + 39/10(4 + 5) + 23/10(4 + 3) = 148.1$$

$$F_1 = f_1 + f_2 = 1708 + 148.1 = 1856.1$$

Step II: To find F2

$$F_2 = (rtw1 - ew)^2 + (rtw2 - ew)^2 + (rtw3 - ew)^2 = (0.678 - 0.569)^2 + (0.658 - 0.569)^2 + (0.372 - 0.569)^2 = 0.0586$$

Step III: To find F3

$$F_3 = \text{Max}\{0.678, 0.658, 0.372\} = 0.678$$

Step IV: To find F4

$$= (2 + 3 + 4 + 6) + (8 + 8+8) + (8 + 3 + 5) = 55$$

## 4 Results and Discussions

The performance of the production process by using flexible manufacturing system using three different machines with different timings, different costs is studied by using new numerical calculations. The study was done by assuming all three machines are working properly, and then some of the machines stopped working. All these calculations are done by randomly taking different machine indices. Large calculations are done. The proposed approach can be used to study the optimization in case of failure of few machines. Results of randomly selected operations index when all machines working, machine-1 fails, machine-2 fails and machine-3 fails are tabulated in Table 4.

**Table 3** Part index, operation index and machine index for sample calculations

Part index	1	2	3
Operation index	1 2 3 4	1 2 3	1 2 3
Machine index	2 2 3 1	3 1 2	1 1 2

**Table 4** Details of best F<sub>1</sub>, F<sub>2</sub>, F<sub>3</sub> and F<sub>4</sub> values for different machine indexes

Sl. No.	Part 1			Part 2			Part 3			F <sub>1</sub>	F <sub>2</sub>	F <sub>3</sub>	F <sub>4</sub>			
	OP-1	OP-2	OP-3	OP-4	OP-1	OP-2	OP-3	OP-1	OP-2					OP-3		
When all machines are working																
1	1	1	1	3	2	2	2	2	2	2	3	2	1048	0.096	0.558	42
2	1	1	1	3	2	2	2	2	2	2	2	2	1131	0.130	0.558	44
3	1	1	1	3	2	3	3	2	3	2	3	3	1187	0.043	0.469	47
4	1	1	1	3	2	3	2	2	3	2	3	2	1348	0.002	0.381	47
5	1	1	1	3	2	3	2	2	3	2	3	3	1355	0.005	0.43	44
When machine-1 fails																
6	3	3	3	3	2	2	3	2	2	2	2	3	1732	0.831	1.225	53
7	3	3	3	3	2	2	2	2	2	2	2	2	1743	0.574	1.071	53
8	2	3	3	3	2	2	3	2	2	3	3	3	1803	0.465	0.919	51
9	2	2	3	3	2	3	3	3	2	3	2	3	1804	0.438	0.906	57
10	2	2	3	3	2	3	3	3	2	3	2	3	1833	0.459	0.906	54
When machine-2 fails																
11	1	1	1	3	3	3	1	3	3	1	3	3	1533	0.378	0.869	46
12	1	1	1	3	1	3	3	1	3	1	1	3	1602	0.378	0.869	38
13	1	1	1	3	1	3	3	1	3	1	3	3	1602	0.381	0.869	41
14	1	1	1	3	1	3	3	1	3	1	1	3	1715	0.56	1.053	38
15	1	1	3	3	1	3	3	1	3	1	1	3	1822	0.445	0.9	41

(continued)

**Table 4** (continued)

Sl. No.	Part 1			Part 2			Part 3			F <sub>1</sub>	F <sub>2</sub>	F <sub>3</sub>	F <sub>4</sub>	
	OP-1	OP-2	OP-3	OP-4	OP-1	OP-2	OP-3	OP-1	OP-2					OP-3
When machine-3 fails														
16	1	1	1	2	1	2	2	2	1	2	1664	0.408	0.892	34
17	1	1	2	2	1	2	2	2	1	2	1710	0.382	0.774	40
18	1	2	2	2	1	2	2	2	1	2	1807	0.533	1.029	41
19	1	1	1	2	1	1	2	1	1	2	1829	0.642	1.131	39
20	1	1	2	2	1	1	2	1	1	2	1875	0.511	0.978	45

### ***4.1 Selection of Problem***

A problem is selected from the work of Jian-Hung Chen and Shinn-Ying Ho, that is from the paper titled: “A novel approach to production planning of flexible manufacturing systems using an efficient multiobjective genetic algorithm” [8]. These authors studied the manufacturing of three parts with various operations using three machines. They minimized the objective function for a feasible manufacturing. They defined the objective function in four parts: first part— $F_1$ : minimization of flow time, second part— $F_2$ : minimization of unbalanced workload, in other words, the balancing of the workload, third part— $F_3$ : minimization of maximum machine workload and the fourth— $F_4$ : minimization of tool cost.

### ***4.2 Problem Formulation***

In the present paper, we have made an attempt by considering some additional constraints, like all machines are working, first machine not working, second machine not working, third machine not working, only first machine working, only second machine working, and only third machine working. These working conditions are considered by taking the various operational indexes on different machines by random selection. By considering all these constraints corresponding objective function values, that is  $F_1$ ,  $F_2$ ,  $F_3$  and  $F_4$ , are calculated. Another important constraint we have taken is a machine does not work while manufacturing a particular product, like Machine 1 does not work while product one is manufactured, but works while manufacturing product two and three. We have also considered other conditions, like machine 1 completely fails, machine 2 completely fails and machine 3 fails completely. We have studied the effect of failure of machines on objective functions while production is going on and products are manufactured with the use of available working machines.

### ***4.3 When All the Machines Are Working***

Results shows that operation index 1113,222,232 gives the least manufacturing time for manufacturing of three products: operation index 1113,232,232 gives the workload balancing, operation index 1113,232,232 gives the minimization of workload and operation index 1113,122,233 gives the total tool cost minimum. To meet all the objectives, operation index 1113,232,232 appears to be better.

#### ***4.4 When Machine-1 Fails***

Results show that operation index 3333,223,223 gives the least manufacturing time for manufacturing of three types of products: operation index 3232,231,321 gives the workload balancing, operation index 3232,231,231 gives the minimization of workload and operation index 2333,223,223 gives the total tool cost minimum. To meet all the objectives, operation index 3232,231,231 appears to be better.

#### ***4.5 When Machine-2 Fails***

Results show that operation index 1113,331,331 gives the least manufacturing time for manufacturing of three types of products: operation index 1133,131,131 gives the workload balancing, operation index 1113,331,331 gives the minimization of workload and operation index 1113,133,133 gives the total tool cost minimum.

#### ***4.6 When Machine-3 Fails***

Results show that operation index 1112,122,212 gives the least manufacturing time for manufacturing of three types of products: operation index 1122,122,212 gives the workload balancing, operation index 1122,122,212 gives the minimization of workload and operation index 1112,122,212 gives the total tool cost minimum. To meet all the objectives, operation index 1122,122,212 appears to be better.

#### ***4.7 Only One Machine Working***

As the calculated results show while only one machine out of the three machines works, M2 shows least value for F1; M3 shows least value for F2 and F3; and the M1 shows the least value for F4. No machine shows all the objective functions F1, F2, F3 and F4 least values. This is the complexity nature of the defined problem. Working with only M1 is preferred when the tool cost minimization is given importance; M2 is preferred when the flow time is preferred; M3 is preferred when workload is to be minimized. Because no single machine can minimize all the objective constraints, it is suggested to use all the three M1, M2 and M3 machines. Working with all the three machines is preferred for the on time completion of manufacturing is preferred so that the products are delivered on time to the customer.



## 5 Conclusions

In this paper the different operations index on machines by considering the objective functions is identified, minimizing the total flow time, machine workload balancing, maximum workload on machine and minimization of total tool cost. The objective functions values calculated for randomly selected operation index sequence when all the three machines are working, when machine-1 fails, machine-2 fails, machine-3 fails, machines 2 and 3 fail, machines 3 and 1 fail and machines 1 and 2 fail are reported. The results show that when all the machines are working the objective function values are better for operations indexes 1113,222,232 for manufacturing of three parts, that is part A, B and C. From the tabulated results, it is observed that when machine-2 fails, F1—total flow time and F2—machine workload balancing are better than when machines 3 or 1 fail, which means it is advisable to maintain machine-2 properly to avoid failures. F3 value that is maximum workload on machine and F4 value that is minimization of total tool cost are better when machine-3 fails than when machines 1 or 2 are failed. It is observed from the results that any one single operation index is not satisfying all the four objectives, however, for two objective functions we can suggest better operation indexes. Depending upon the objective functions we can select the operation index while doing the production planning. In future, we are planning to develop an algorithm for identifying the better operation index depending upon the objective function to be achieved when all machines are working, any one machine fails and any two machines fail.

## References

1. Jerald J, Asokan P, Prabakaran G, Saravanan R (2005) Scheduling optimization of flexible manufacturing systems using particle swarm optimization algorithm. *Int J Adv Manuf Technol* 2(5):964–971
2. Roshanaei V (2012) Mathematical modeling and optimization of flexible job shops scheduling problem. Electronic theses and dissertations. University of Windsor
3. Smith SF (2003) Is scheduling a solved problem. In: 1st international conference on multidisciplinary scheduling theory and applications, August 2003, 13–15, Nottingham, UK
4. Kumar A, Prakash, Tiwari MK, Shankar R, Baveja A (2006) Solving machine-loading problem of a flexible manufacturing system with constraint-based genetic algorithm. *Eur J Oper Res* 17(5):1043–1069
5. Sreedhar Kumar AVS, Veeranna V, Durgaprasad B (2015) Multi objective scheduling of jobs in flexible manufacturing system using meta heuristic approaches with inclusion of simulation modeling. *Int J Comput Eng Res Trends* 2(4):264–269
6. Sunil Kumar SJ (2015) Comparison of dynamic scheduling techniques in flexible manufacturing system. *Int J Eng Res Appl* 5(7):143–146
7. Zaied AHR (2008) Quantitative models for planning and scheduling of flexible manufacturing system. *Emirates J Eng Res* 13(2):11–19
8. Chen J-H, Ho S-Y (2005) A novel approach to production planning of flexible manufacturing systems using an efficient multi-objective genetic algorithm. *Int J Mach Tools Manuf* 45(7–8):949–957

9. Mishra A, Dash A, Bishoyee N, Mahapatra SS (2009) Simultaneous scheduling of machines and Agvs in FMS environment using swarm optimization and comparison with Genetic algorithm. In: POMS 20th annual conference, Abstract no: 011-0631, Orlando, Florida, U.S.A.
10. Entezari S, Saeedeh Gholami L (2015) Multi-objective flexible flow shop scheduling with unexpected arrivals of new jobs. *Appl Math Eng Manage Technol* 3(3):172–181
11. Sharma R, Jain P, Sharma G (2013) Implementation issues in FMS: a literature review. *Int J Innovations Eng Technol* 2(2):190–197
12. Mallikarjuna K, Veeranna V, Hemachandra Reddy K (2013) Multi-objective optimization for design of single row layout in flexible manufacturing system with scheduling constraint: an approach of nontraditional optimization techniques. *Int J Appl Res Mech Eng* 3(2):41–51
13. Santhosh Kumar M, Satish Kumar B (2018) Performance analysis of material handling systems for a layout with different speeds. *Int J Mech Prod Eng Res Develop* 8(5):1–16
14. Deepika, Phani Kumar S, Srinivas A (2016) L2R: multicast routing protocol for effective localized route recovery in backbone networks. *Int J Control Theory Appl* 33(9):79–87
15. Deepika, Phani Kumar S, Srinivas A (2016) An efficient backbone based quick link failure recovery multicast routing protocol. *Elsevier Perspect Sci* 8(1):135–137

# Experimental Investigation of Ball Burnishing Process Parameters Optimization for Al 5083 Using Taguchi Method



M. Jawahar, J. Suresh kumar, M. Srikirana and Shiek Ismail

**Abstract** The present work focuses on optimizing the newly designed ball burning tool using Taguchi analysis method experiment on traditional lathe machine with process parameters for burning. The test piece and ball materials used are Aluminum Alloy 5083 with different percentages of zirconium and high carbon chromium with 6 mm diameter. The levels of parameters of the input process parameters are selected on the basis of one element at a time of the experiment: burning feed, burning rate, and material composition. The response parameters are hardness and roughness of the surface. The main objective of this study is to compare surface roughness and surface hardness values on a workpiece of 100% aluminum alloy and aluminum (99%, 98%) with zirconium (+1%, +2%).

**Keywords** Ball burning tool parameters for burning · Hardness · Optimization of surface roughness · Taguchi technique

## 1 Introduction

The ball burning (BB) process is a surface finishing method at room temperature that consists of creating minor plastic deformations on the surface of a workpiece by moving and compressing a hardball on the surface which leads to an improvement in the physical and mechanical properties of this workpiece. As a deforming component, this process uses a high-hardness ball to induce material from peaks to valleys of superficial irregularities with a normal and uniform load [1, 2], as shown in Fig. 1. The ball burning process is already well known and has recently been commonly used as improved in the surface finishing of mechanical parts. This is because it is a

---

M. Jawahar (✉) · M. Srikirana  
Mechanical Engineering, Jayamukhi Institute of Technological Sciences, Warangal, India  
e-mail: [jawahar.mamidala123@gmail.com](mailto:jawahar.mamidala123@gmail.com)

J. Suresh kumar  
Mechanical Engineering, JNTUH, Hyderabad, India

S. Ismail  
Mechanical Engineering, Vidya Jyothi Institute of Technology, Hyderabad, India

© Springer Nature Singapore Pte Ltd. 2020

G. S. V. L. Narasimham et al. (eds.), *Recent Trends in Mechanical Engineering*,  
Lecture Notes in Mechanical Engineering,  
[https://doi.org/10.1007/978-981-15-1124-0\\_17](https://doi.org/10.1007/978-981-15-1124-0_17)

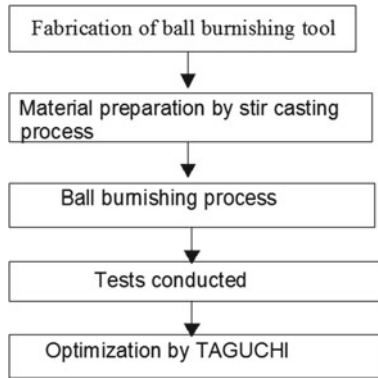


**Fig. 1** Shows the methodology of ball burning process

simple, quick, and low-cost process that makes high-quality surface finish with low energy and little contamination of the environment. Compared to traditional methods such as grinding and thermal treatment, this results in a promising alternative. The most popular applications of the BB process are, among other items, the manufacture of polymer injection molds, metal forming devices and various components for industries such as automobile, aeronautical, railway, and aerospace. This method induces compressive residual stress on the surface of a workpiece and thus increases wear and tiredness resistance is shown in Fig. 2. Certain benefits provided by this method are the high dimensional precision of the product, avoiding secondary and costly processes (i.e., grinding, super-finishing, etc.), increasing corrosion resistance, mending manufacturing defects and since this process does not produce metal chips, it is known to be a safe process for the environment.

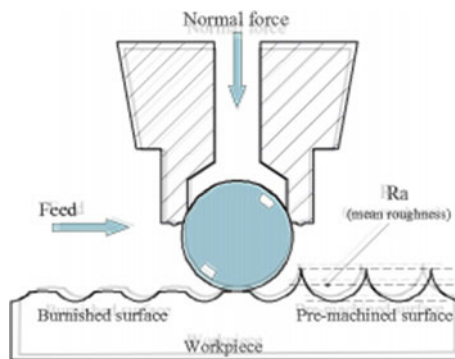


**Fig. 2** Process of ball burning

## ***1.1 The Work Objectives***

In this study, experiments will be performed to improve surface finish quality, aluminum alloy product removal rate 5083 with zirconium compositions' (+1%, 2%) low chromium and high carbon work part. The type is the tip of the ball's nose. A series of experiments will be carried out by varying the frequency, feed rate, and composition of the spindle parameters. The speed of the spindle is 97, 192, and 256 rpm. Feed concentrations were 0.44, 0.48, and 0.56 mm/min, as well as compositions (aluminum alloy 5083, Al 5083+Zr 1%, and Al 5083+Zr 2%).

## ***1.2 Methodology***

See Fig. 1.

## **2 Review of the Literature**

Roller Burnishing is a process used to superfinish different components. The type of contact between the workpiece and the tool in this technique is a line. The workpiece rotates on the chuck, keeping the tool parallel to the workpiece's length. Plastic deformation of the surface of the workpiece results in a new topography. The effect of different operating parameters such as burning power, speed, feed, roller length, and number of passes will be investigated for better surface finish [2]. The Zirconium Dioxide Particles Are Synthesized By Solution Combustion Method. The Nan composite Materials Are Prepared By Mechanical Stir Casting Method Effect Of Burnishing Process Parameters On Surface Quality—A Review [3] Banerjee Andrei (2004) Mechanical Engineering Institute proceedings, part J: Journal of Engineering Tribology. In the present age of globalization, surface performance of machined components is of utmost importance for every industry. The usability and durability of the service depend on the quality of the layer [4]. Whatever the manufacturing process used may be, perfectly smooth surface development is impossible. The imperfections and irregularities are bond that occurs on the machined components in some type of peaks and valleys. A solid, highly polished ball or roller is used in burning to flatten this rough peak by plastic deformation into the valleys. Burnishing is a method of production that is very simple, inexpensive, and less chip-based.

### 3 Design of Burnishing Tool in 2D Model

The decision was made to carry out the ball burnishing process in the present work between two burning processes, the first and foremost work being to design and develop the ball burnishing tool by selecting the appropriate materials, dimensions, and design so that the process and tool is simpler, cheaper, and requires minimum time consumption at minimum cost [5]. It is possible to use the method built in this work on convection machine tools such as lathe. Figure 3 shows the tool built in this research with interchangeable roller burning tool assembly to perform ball burnishing operation. This method improves the tool's versatility and allows all processes to be carried out. The burning tool built in the above way consists of ball holder, square case, lock pins and threaded lock aid, and spring components. Taking into account the parameters to be selected and managed in the project, the tool design is made is shown in Fig. 4.

#### 3.1 Fabrication of Ball Burnishing Tool

HCHCR-D2 steel is High Carbon High Chromium Cold Work Steel. Performance with high wear-resistant properties and durability is due to 0.90% vanadium addition. It is normally an annealed supply state and will provide hardness to achieve 57–59 HRC. In the annealed condition, it can be machinable. D2 is inferior to D3 steels due to the high properties of alloys.

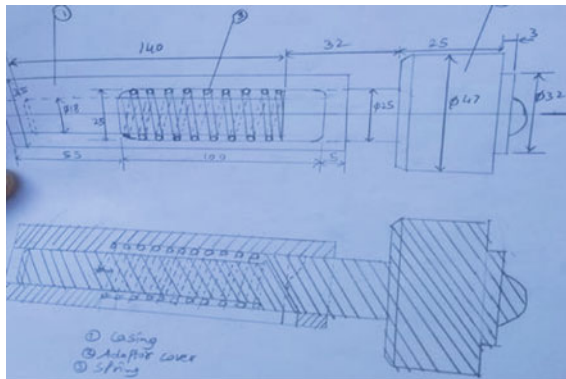


**Fig. 3** Interchangeable roller burning tool assembly

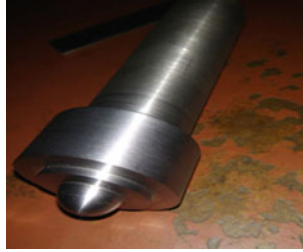


**Fig. 4** Fabrication of work piece

### **3.2 Fabrication of Work Piece**

5083 Aluminum Alloy is an aluminum alloy, in which the main alloy being zirconium. It is solid, with comparable strength to many steels, and has good strength of fatigue and average machinability [6].

## **4 Stir Casting Process**

Stir casting process is a quick and cost-effective liquid state manufacturing method of metal matrix composites; in this process, aluminum alloy has been overheated to 800 °C (Fig. 5) and then the temperature is slowly lowered below the liquid temperature to hold the matrix content in semi-solid condition is shown in Fig. 6. The preheated zirconium particles are with different volume proportions at this temperature.



**Fig. 5** Placing aluminum material in sand mould and heated the material up to 760 °C



**Fig. 6** Stir casting machine

## **5 Experimental Investigation**

The experiments are done on the Lathe machine (turning) with the following parameters:

Cutting tool—Ball burnishing tool

Workpiece material—aluminum compositions (Fig. 7)

Feed—0.56, 0.48, 0.44 mm/min

Cutting speed—97, 192, 256 rpm,

Aluminum composition—Al, Al+1%, Al+2% zirconium.





**Fig. 7** Casting component

## **6 Aluminum Composition**

### ***6.1 Preparation of Workpiece for Burnishing Process on Lathe Machine***

Choose the perfect tool to conduct workpiece turning process is shown in Fig. 8. Turning operations are conducted to decrease rod diameter and increase workpiece surface finish. The cross slide crank now advances about 10 divisions or .010" (ten one-thousandths or one-hundredth of an inch). Turn the handwheel of the wagon counterclockwise to drive the wagon gradually toward the headstock. Keep a steady cranking motion as the tool starts to slice into the metal to get a good even break. It is difficult to get a smooth turn and even slice by hand. Continue to move the tool toward the headstock until it is about 1/4" away from the chuck jaws. Clearly, you want to be cautious not to let the tool reach the chuck jaws. Mark the parameters chosen on the workpiece using marker. Nine divisions are made on each line. On each part number of the ball burning tool passes are set as 3 passes (Table 1).



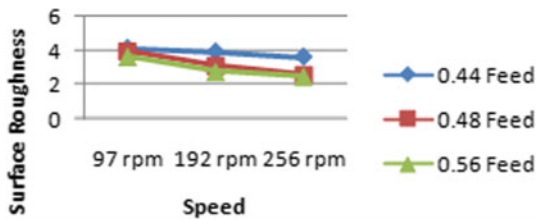
**Fig. 8** Turning process

**Table 1** Constant parameters chosen for experiment

Feed rate mm/min		Spindle speed rpm		
0.44		97		
0.44		192		
0.44		256		
0.48		97		
0.48		192		
0.48		256		
0.56		97		
0.56		192		
0.56		256		

Factors	Process parameters	Level 1	Level 2	Level 3
A	Cutting speed	97	192	256
B	Feed rate	0.56	0.48	0.44
C	Al composition	Al	Al+Zr 1%	Al+Zr 2%



**Fig. 9** Surface roughness versus speed by means of keeping pressure and range of passes steady of 100% aluminum

Feed at 0.40: surface roughness decreases with speed boom as shown in Fig. 9. At 0.48 of feed: surface roughness decreases until medium speed 192 rpm and remains

consistent for good speed of 256 rpm. At zero56 of feed: surface roughness decreases as speed increases. Feed at 0.44: surface roughness decreases as rate increases as shown in Fig. 10. At 0.48 of feed: surface roughness decreases to a medium speed of 192 rpm and remains steady for a good speed of 256 rpm. At 0.56 of feed: surface roughness decreases with increased speed is shown in Fig. 11.

**Hardness test results**

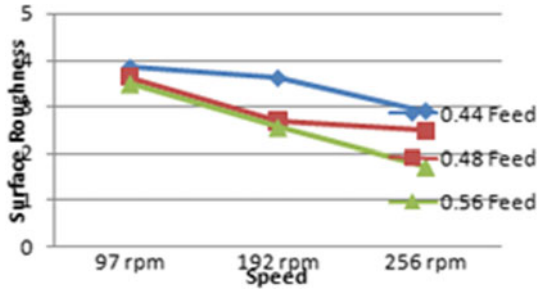


**Fig. 10** Surface roughness versus speed by keeping force, number of passes constant of 99% Al+1% Zr

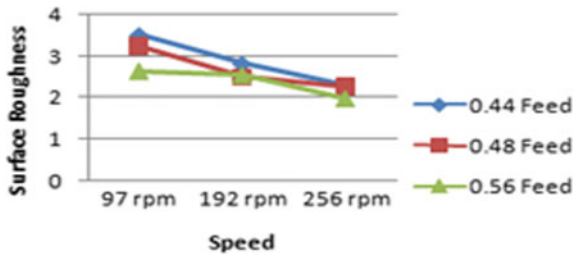


**Fig. 11** Surface roughness versus speed by way of maintaining force, quantity of passes constant of 98% aluminium+2% zirconium

**Table 2** Speed vs surface roughness

0.44	97	3.85
0.44	192	3.62
0.44	256	2.9
0.48	97	3.64
0.48	192	2.70
0.48	256	2.49
0.56	97	3.50
0.56	192	2.56
0.56	256	1.72

Hardness is a fabric feature, not an integral physical component anymore. It is defined because the resistance to indentation is determined by measuring the indentation’s permanent strength. Typically it is commonly used to check materials that have a form that is too coarse or have a ground that is too rough to look at the use of some other solution, castings, and forgings. As defined in ASTME-18, the Rockwell hardness test method is the most widely used technique for hardness testing (Table 2).

**Table 3** Surface roughness versus speed by way of maintaining force, quantity of passes constant of 98% aluminium+2% zirconium

0.44	192	2.82
0.44	256	2.31
0.48	97	3.24
0.48	192	2.50
0.48	256	2.27
0.56	97	2.63
0.56	192	2.53
0.56	256	1.98

**Table 4** Surface hardness values for 100% Al

Feed rate (mm/min)	Spindle speed (rpm)	Rockwell	Brinell (BHN)
0.44	97	29	65
0.44	192	31	66
0.44	256	33	67
0.48	97	37	70
0.48	192	41	71
0.48	256	44	72
0.56	97	34	67
0.56	192	40	68
0.56	256	42	70

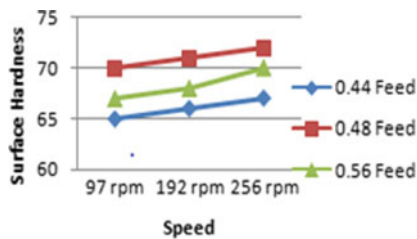


**Fig. 12** Speed versus Surface Hardness

At 0.44 of Feed: surface hardness can increase by increasing speed. At 0.48 of Feed: surface hardness should increase by increasing speed as shown in Fig. 12. It will increase periodically up to a medium speed of 192 rpm and increase to extinction at a speed of 256 rpm. Feed at 0.56: surface hardness increases with the aid of increasing speed. The cloth's hardness increases by increasing pace from 97 to 256 rpm, step by step (Tables 3 and 4).

Feed at 0.44: surface hardness increases with increasing speed. It gradually increases from a frequency of 97 to 256 rpm. At 0.48 feed: the hardness of the surface increases by increasing speed as shown in Fig. 13. It will rise periodically to a moderate velocity of 192 rpm and will increase to 256 rpm to extinction. Feed at 0.56: surface hardness will increase as speed increases is shown in Fig. 14. The material's hardness would gradually increase by increasing the speed from ninety seven to 256 rpm (Tables 5 and 6).

**Table 5** Surface hardness values for 99%Al+1%Zr

Feed rate (mm/min)	Spindle speed (rpm)	Rockwell	Brlnell (BHN)
0.44	97	29	66
0.44	192	31	68
0.44	256	33	69
0.48	97	36	70
0.48	192	41	71
0.48	256	42	72
0.56	97	35	73
0.56	192	36	74
0.56	256	38	75

**Table 6** Surface hardness values for 98% Al+2% Zr

Feed rate (mm/min)	Spindle speed (rpm)	Rockwell	Brinell (bhn)
0.44	97	36	68
0.44	192	37	69
0.44	256	38	70
0.48	97	39	71
0.48	192	40	75
0.48	256	44	76
0.56	97	39	71
0.56	192	43	74
0.56	256	44	76

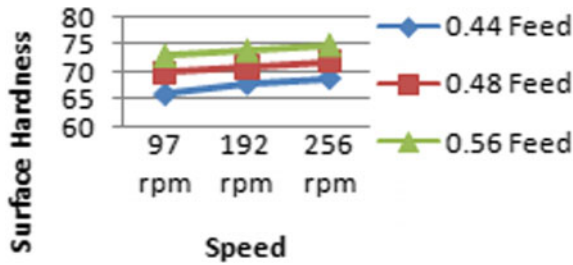


Fig. 13 Surface hardness versus speed by preserving pressure, number of passes regular of 99% aluminium+1% zirconium

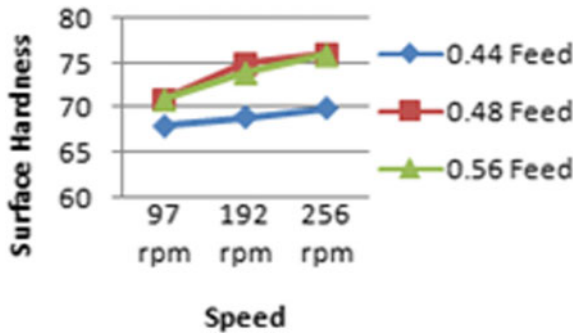


Fig. 14 Surface hardness versus speed by keeping force, number of passes constant of 98% aluminium+2% zirconium

## 7 Results and Discussions

**Comparison of surface roughness:** The surface roughness of a hundred percent wire are measured with different speeds and feeds. Rate growth is observed to decrease the workpiece’s roughness until excessive 256 rpm speed and 0.56 feed cost. The surface roughness values are calculated with 2% zirconium and 98% aluminum by changing the speed and feed. It is found that the surface roughness is lower at a frequency of 97 rpm and a feed rate of 0.44. Surface roughness values at 256 rpm and 0.56 feed are higher.

### Comparison of Surface Roughness with different compositions

The surface roughness of the entire experiment is higher for 100% aluminum at 0.44 feed rate and 97 rpm feed rate and the surface roughness is reduced for composite cloth with 98% aluminum with 2% zirconium at 0.56 feed charge and 256 rpm level. Generally, an increase in the percentage of zirconium in the roughness of the aluminum floor can be calculated (Table 7).

**Table 7** Comparison of surface hardness with different compositions

S. no	Speed	Feed	100% Al	99%Al+1% Zr	98% Al+2% Zr
1	97	0.44	65	66	68
2	192	0.48	71	71	75
3	256	0.56	70	75	76

**Comparison of surface Hardness**

The surface hardness is measured with varying speed and feed for 100% of the aluminum wire. It is situated that the speed increases the hardness of the surface. The surface roughness is measured using different speeds and feeds of zirconium as 1% and aluminum as 99%. It is found that the change in velocity raises the stiffness of the ground to a high speed of 256 rpm and a cost of 0.56

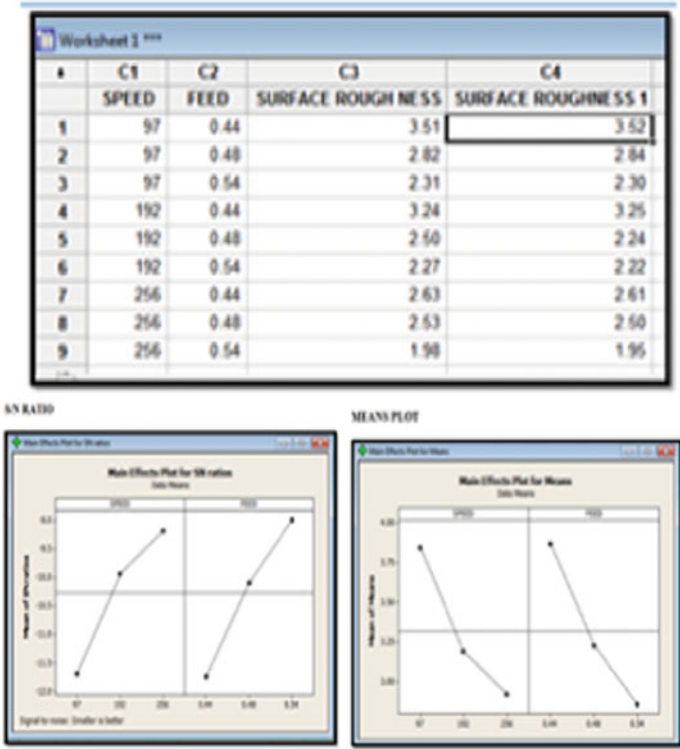
**Taguchi technique**

Taguchi describes a product’s quality level as the total loss suffered by society as a result of a product’s failure to perform as desired when deviating from the overall performance degrees of the added target. It includes expenses attributable to poor performance, operating expenses (which change as a product ages), and any costs incurred due to the harmful aspect of the product being used; It aid’s the performance repair teams to succeed. Noise is any unnecessary effect that will increase due to noises in the material or procedure system [7].

**Optimization of surface roughness using minitab software material–aluminum alloy**

	C1	C2	C3	C4	C5	C6
	SPEED	FEED	SURFACE ROUGHNESS	SURFACE ROUGHNESS 1	SNR1	MEANT
1	97	0.44	4.10	4.00	-12.1498	4.050
2	97	0.48	3.90	3.85	-11.7656	3.875
3	97	0.54	3.60	3.61	-11.1381	3.605
4	192	0.44	3.96	3.92	-11.9100	3.940
5	192	0.48	3.09	3.11	-9.8273	3.100
6	192	0.54	2.53	2.54	-8.0796	2.535
7	256	0.44	3.62	3.61	-11.1622	3.615
8	256	0.48	2.72	2.70	-8.6594	2.710
9	256	0.54	2.45	2.43	-7.7479	2.440

**Fig. 15** Material–aluminum alloy with zirconium 2%



The force values measured from the experiments and their corresponding S/N ratio values are shown in Figs. 15, 16 and 17.

#	C1	C2	C3	C4	C5	C6
	SPEED	FEED	SURFACE ROUGHNESS	SURFACE ROUGHNESS 1	SNRA3	MEAN3
1	97	0.44	3.51	3.52	-10.9185	3.515
2	97	0.48	2.82	2.84	-9.0358	2.830
3	97	0.54	2.31	2.30	-7.2534	2.305
4	192	0.44	3.24	3.25	-10.2243	3.245
5	192	0.48	2.50	2.24	-7.5080	2.370
6	192	0.54	2.27	2.22	-7.0249	2.245
7	256	0.44	2.63	2.61	-8.3661	2.620
8	256	0.48	2.53	2.50	-8.0109	2.515
9	256	0.54	1.98	1.95	-5.8675	1.965

Fig. 16 Optimization of hardness using minitab software Material–aluminum alloy



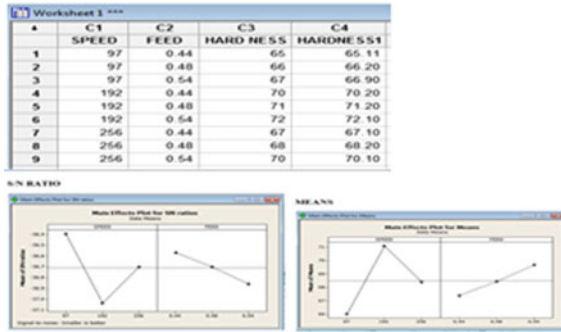


Fig. 17 Aluminum alloy with zirconium+2%

### 8 Conclusion

Using CREO, the ball burnishing method was effectively modeled. Prototype model is used in early stage and the workpiece is also made using similar types of fabric. For experimental analysis, the ball burnishing tool manufactured here is performed using lathe device by different compositions of zirconium in aluminum to examine surface roughness and surface hardness on distinctive pieces of paintings. The results obtained from the experimental analysis really suggest that there is a boom inside the workpiece hardness for the same values of different materials with growth within the composition of zirconium in aluminum. From the consequences, it can be said that the surface hardness values are better at a velocity of 256 rpm and feed price of 0.56. From complete experimentation the surface hardness is lower for 100% aluminum at 0.44 feed charge and 97 rpm velocity and surface hardness is higher for composite material having 98% aluminum with 2% of zirconium at feed rate of 0.56 and velocity of 256 rpm. Overall it can be observed that growth in percentage of zirconium in aluminum floor hardness values is improved. From whole experimentation the floor roughness is higher for a 100% aluminum at 0.44 feed price and 97 rpm velocity and surface roughness is decreased for composite having 98% aluminum with 2% of zirconium at feed price of 0.56 and pace of 256 rpm. Overall it may be determined that growth in percent of zirconium in aluminum surface roughness values is decreased.

### References

1. Jayakrishnan J, Suraj R Effect of roller burnishing process on tool steel material using Cnc lathe. J Des Manufact Technol 5:155–159
2. Rakic R, Rakic Z (2002) The Influence of the metal working fluids on machine tool failures, vol 252(5–6), pp 438–444
3. Banerjee S, Mithra S, Panja B Using Taguchi method. J Mech Civ Eng 13:46–50
4. Solanki RG, Patel KA, Dhruv RB Effect of burnishing system parameters on surface quality. IJEDR 4. ISSN: 2321-9939

5. Kumar P, Purohit GK Design and development of ball burnishing tool. J Eng Res Technol 6:733–738
6. Stalin B, Murugan C Evaluation of mechanical behavior of aluminium alloy boron carbide MMC. In: International conference on emerging engineering trends and science (ICEETS – 2016). ISSN: 2348-8360
7. Tripathi H, Pungotra H, Gandotra S, Beri N (2013) Experimental investigation into ball burnishing process of brass using Taguchi approach. J Sci Eng Res 4(8)

# Experimental Investigation on Strength of Friction Stir Welded Al 6061-T6 Alloy Joints with Varying Oblique Angle



D. Maneiah, K. Prahlada Rao and K. Brahma Raju

**Abstract** The friction stir welding, abbreviated as FSW, is an innovative solid-state welding process widely used for welding of different metals and their alloys, particularly aluminum and its alloys, in various industries including aerospace and automotive. The tensile properties such as strength under tension of friction stir butt welded joints of Al 6061-T6 alloy sheets under the variable welding (oblique) angle  $0^\circ$ ,  $30^\circ$  and  $60^\circ$  are experimentally investigated. The Taguchi L9 experimental method is chosen to construct the numbers of welding experiment. The friction stir welding is performed by considering the process parameters such as rotational speed, tilt angle and feed. The probe is chosen as circular. The operating ranges of process parameters are rotational speed 560, 900 and 1400 rpm, tilt angle  $0^\circ$ ,  $0.5^\circ$  and  $1^\circ$  and feed rate 20, 63 and 100 mm/min. The highest strength under tension is obtained as 316 MPa, when the rotational speed is 560 rpm, tilt angle  $0.5^\circ$  and feed rate 63 mm/min. An empirical relationship is generated between the obtained weld joint strength and chosen process parameters. The most effective process parameter is suggested as rotational speed by conducting the regression and ANOVA analysis.

**Keywords** Friction stir welding · Tensile strength · Dye penetrant inspection · Rotational speed · Tilt angle · Feed

---

D. Maneiah (✉)

Department of Mechanical Engineering, CMR Technical Campus, JNTU, Hyderabad, India  
e-mail: [manidakkiliphd2012@gmail.com](mailto:manidakkiliphd2012@gmail.com)

K. Prahlada Rao

Department of Mechanical Engineering, JNTU, Ananthpur, India  
e-mail: [drkpro1@yahoo.com](mailto:drkpro1@yahoo.com)

K. Brahma Raju

Department of Mechanical Engineering, SRKR Engineering College, JNTU, Ananthpur, India  
e-mail: [brahmaraju@yahoo.com](mailto:brahmaraju@yahoo.com)

© Springer Nature Singapore Pte Ltd. 2020

G. S. V. L. Narasimham et al. (eds.), *Recent Trends in Mechanical Engineering*,  
Lecture Notes in Mechanical Engineering,  
[https://doi.org/10.1007/978-981-15-1124-0\\_18](https://doi.org/10.1007/978-981-15-1124-0_18)

205

# 1 Introduction

In friction stir welding the joining action is performed by rubbing of two metal sheets together. Owing to the rubbing of two surfaces, frictional heat is generated, which is accountable for the joining of two sheets. This welding technique is a well-organized and controllable method used for welding Al alloys, and is also environment-friendly. In addition, flux, filler metal and inert gas are not needed. This welding technique is an accepted and widely used technique nowadays for the joining action in various manufacturing industries; it may be marine, aviation or other structural industrial applications. The welding process and its process parameters have number of different impacts on the properties of base metal. For example, large heat input may have direct impact upon mechanical properties of unwelded metal. High heat input will lead to wider bead formation on the weld. Owing to various stress involved in welding, solid-state cracks may occur when a material is unable to bear the stresses developed by the welding process, which is explained by Liu et al. [1]. Ma et al. [2] explored the severity of applied stress which varies with the change of welding technique. The mechanical properties of the unwelded metal may change due to heat produced during the welding. The impact of the individual process parameters on the mechanical properties varies with their functions. In the friction stir welding, the observations made are that with the high rotational speed and low rate of feed, the heat input will increase, leading to the formation of groove, wider bead. With high feed rate and high rotational speed, internal cracks may occur due to improper joining, as described by Yan et al. [3]. Welding speed shows direct effect on the strength of weld joint. Therefore, the strength of the weld joint is not only dependent on the action and effect of individual factors but also simultaneous action and effects of all the factors. There are various factors in the FS welding technique in which some can be kept constant and some can vary, to produce a desired quality of weld joint, as explained by Aliha et al. [4]. Optimization of the process parameters during welding process is needed to check the suitability of chosen process parameters for the FS welding of particular material of particular thickness and size. It also gives an operating range in which the action can be performed to get the desired quality and properties of the material. Therefore, optimization of the process and its parameters can be performed to make the system robust, as explained by Sahu et al. [5] and Kim et al. [6]. Padhy et al. [7] mentioned in their review paper that the important process parameters in the FS-based welding and processing technologies are the tool rotation speed, tool traverse speed, feed rate or plunge speed, tool geometry and tool tilt angle. These process parameters are responsible for the generation of heat and plasticization of material, and subsequent material transfer from the starting to the end point of welding of two sheets. Therefore, attentive optimization of these process parameters is mostly desirable to produce a quality weld. Rodriguez et al. [8] explained the microstructure of the FS-welded zones that mainly constitutes re-crystallized and rectified areas and the fine micro-structural and mechanical properties. The friction stir technique is widely used for the metal working techniques and to a various range of ferrous and non-ferrous materials for its welding benefits, as explained by Panda

et al. [9]. Antony et al. [10] mentioned that the FS welding technique developed by The Welding Institute (TWI), England, UK in 1991, is an advanced form of welding technique. It is mostly used for the manufacturing of light weight structures. This technique can drastically decrease the grain size, conferring tremendous super plastic behavior of the particular Al alloys.

Nourani et al. [11] published case studies on Taguchi optimization of welding factors using FS welding technique for the welding of Al 6061 alloy in which it is mentioned that the welding technique which they used is easy, where a non-consumable rotating tool with a critically prepared pin and shoulder is pushed into the adjoined edges of the two parts to be welded and moved along the line of joint.

Ilangovan et al. [12] mention that the FS welding tool mainly performs two jobs, that is, heating of the metal sheets and the movement of material to form the joint. The FS welding process parameters that can be studied and optimized to enhance the quality of the weld joint are: rotational speed (rpm), welding speed (mm/s), axial force (KN) and tool geometry—pin length (mm); tool shoulder diameter,  $D$  (mm); pin diameter,  $d$  (mm); tool tilt angle ( $^\circ$ ); and  $D/d$  ratio of the tool.

Elatharasan et al. [13] performed a research work on welding AA 6061-T6 alloy sheets of thickness 6 mm. The FS welding process parameters selected are: tool rotational speed, welding speed and axial force. The optimization of process parameters is carried with the help of response surface methodology central composite design method. Axial force is varied as 6, 8, 10 kN, welding speed 800, 1000, 1200 rpm and traverse speed 30, 60, 90 mm/min. The mathematical model is developed and produced with a valid regression expression for the maximum tensile strength.

The process is used successfully for the welding of the two rolled metal sheets of Al 6061-T6 alloy of size  $400 \times 200 \times 3$  (mm). The shape of the probe which is considered as an important factor for the research is chosen as circular. The effect of the shape of probe on the strength of the welded joints is experimentally investigated. The process parameters considered are: rotational speed, feed and tilt angle for the experimental investigation. The process is optimized by following Taguchi L9 design of experiment approach. The mechanical properties like strength under tension of weld joint are measured. The welding is carried out by varying the weld angle at  $0^\circ$ ,  $30^\circ$  and  $60^\circ$  to identify the effect of weld angles on the strength of the weld joint. The concept of change of welding angle is to measure the differences in strength of the weld joint if welded in different welding angle. Oblique position means neither parallel nor at right angle to the line or plane, that is, slanting, slopping or at an angle [14].

If some load is applied on a welded structure which is in different angled position, like  $0^\circ$ ,  $30^\circ$  and  $60^\circ$ , then in such cases the variation in the strength of weld is the main focus of this research. The oblique angle is shown in Fig. 1. A detailed and thorough analysis is performed and based on the result the best welding condition and tool profile to get defect-free weld is recommended through this research. The obtained results will be useful for the welding of other Al alloys by varying the weld angle apart from the present Al alloy under investigation. The strength of the Al weld joint can also be predicted following the present investigation. Further research can

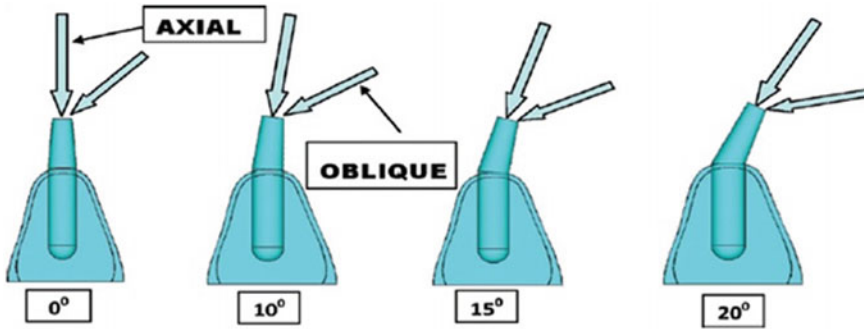


**Fig. 1** Oblique angle

be carried out for the micro-structural evolution of the material under the different variability of process and its parameters.

## 2 Experimental Details

The Al 6061-T6 alloy metal sheets of size  $400 \times 3$  (mm) are received for welding. Before welding the aluminum metal sheets are cut into the desired length by the shearing machine to the size of  $200 \times 200 \times 3$  (mm). The chemical compositions and mechanical properties of Al 6061-T6 alloy as per the literature are given in Tables 1 and 2 simultaneously. The friction stir welding setup and circular profiled pin is shown in Fig. 2. The Al 6061-T6 alloy friction-welded sheets at different weld angles  $0^\circ$ ,  $30^\circ$  and  $60^\circ$  are presented in Fig. 3. As per the Taguchi L9 experimental design, nine friction-welded joints of Al 6061-T6 alloy are produced in each experiment for the three numbers of experiments and their tensile results are shown in Table 3. In all the experiments, three FS welding process parameters such as rotational speed, tilt angle and feed at three levels are taken for the welding of Al 6061-T6 alloy sheets. Statistical software named Minitab is used to draw a valid and meaningful conclusion by optimizing the FS welding process parameters. The acceptability of the achieved

**Table 1** Chemical compositions of aluminum 6061-T6 (wt%)

Al	Mg	Si	Cr	Cu	Fe	Mn	Ti	Zn
95.8–98.6	0.8–1.2	0.4–0.8	0.04–0.35	0.15–0.4	$\leq 0.7$	$\leq 0.15$	$\leq 0.15$	$\leq 0.25$

**Table 2** Mechanical properties of Al 6061-T6

Yield strength	Ultimate strength	Modulus of elasticity	Poisson's ratio	Elongation	Hardness (HB)
276 MPa	310 MPa	68.9 GPa	0.33	17%	95



**Fig. 2** Friction stir welding setup and circular profiled pin



**Fig. 3** Friction stir welding at weld angle 0°, 30° and 60°

relationship is evaluated using the analysis of variance technique (ANOVA). ANOVA assists in determining the impact of each factor versus the objective function and it also determines the total variation present in the model. In this technique F ratio obtained using Fisher’s test is used to identify the fit of the experimental data to the 95% confidence interval statistically. The signal-to-noise ratio (S/N) determines the robustness by identifying the control factors which can decrease the impact of noise on the responses. Minitab determines the S/N ratio for each combination of control factor and their levels present in the experimental design. For static experimental design there are different S/N ratios which are termed as: larger is better, smaller is better and nominal is the best. The formula for the larger is better S/N ratio using base 10 log is

$$S/N = -10 \times \log(\Sigma(1/Y^2)/n) \tag{1}$$

**Table 3** Process parameters and response values

Friction stir welding process parameters				Experiment 1	Experiment 2	Experiment 3
				Welding angle—0°	Welding angle—30°	Welding angle—60°
S. No.	Rotational speed (rpm)	Tilt angle (degree)	Feed (mm/min)	Tensile strength (MPa)	Tensile strength (MPa)	Tensile strength (MPa)
1	560	0	20	213	256	200
2	560	0.5	63	171	316	167
3	560	1	100	212	243	191
4	900	0	63	140	239	92
5	900	0.5	100	161	255	105
6	900	1	20	204	220	108
7	1400	0	100	160	201	157
8	1400	0.5	20	188	111	188
9	1400	1	63	211	173	191

### 3 Results and Discussions

The observations made from the experiment 1, tabulated in Table 3, are when rotational speed is kept constant at 560 rpm, tilt angle is changed as 0°, 0.5°, 1° and feed is varied as 20, 63, 100 mm/min. The weld strength obtained is 213, 171 and 212 MPa. When the rotational speed increased to 900 rpm and kept constant with varying tilt angle and feed, the tensile strength of the weld joint obtained is 140, 161 and 204 MPa. Further increase in rotational speed to 1400 rpm and with the change in tilt angle and feed, the strength of the weld joint obtained is 160, 188 and 211 MPa. Signal-to-noise ratio for each process parameters is calculated using the condition larger is better and the mean value of the obtained tensile strength is tabulated in Table 4. Delta is the variability between the maximum and minimum average response (signal-to-noise ratio and mean) for the individual factors. Ranking

**Table 4** Process parameters, their S/N ratio and mean values

Level	Rotational speed (rpm)		Tilt angle (degree)		Feed (mm/min)	
	S/N ratio	Mean values	S/N ratio	Mean values	S/N ratio	Mean values
1	45.92	198.7	44.52	171.0	46.08	201.7
2	44.42	168.3	44.76	173.3	44.69	174.0
3	45.35	186.3	46.40	209.0	44.92	177.7
Delta	1.50	30.3	1.88	38.0	1.39	27.7
Rank	2		1		3	



of each delta value is defined in terms of largest delta value (tilt angle) is rank 1 and smallest delta value (feed) is rank 3.

From Table 5, the regression analysis symbolizes the relationship between the variables, that is, process parameters and responses, to predict the significant effect of process parameters on the response. The F value explains the significance of the process parameters on the tensile strength, such as rotational speed (0.23) represents to be more significant than feed (1.66) and tilt angle (3.92). The ‘P’ value is the probability of getting the obtained results. Rotational speed 65.2% (0.652) illustrates the high impact on the tensile strength than by other parameters, tilt angle 10% and feed 25%. The response surface plots is a three-dimensional image of acquired strength of the weld joint and preferred process parameters such as rotational speed, tilt angle, feed, as shown in Fig. 4. The regression expression shown in Eq. 2 can be used to predict the tensile strength (TS) of friction stir Al 6061-T6 alloy joints and is given by:

$$TS = 194.7 - 0.0109 \times \text{Rotational speed} + 38.0 \times \text{Tilt angle} - 0.309 \times \text{Feed} \quad (2)$$

The observations made from the experiment 2, tabulated in Table 3, are that when the rotational speed is maintained constant at 560 rpm, tilt angle is varied as 0°, 0.5°,

**Table 5** Regression Analysis: tensile strength versus rotational speed, tilt angle, feed

Sources	Degrees of freedom	Adjusted sum of square	Adjusted mean square	F-value	P-value
Regression	3	3212.8	1070.9	1.94	0.242
Rotational speed	1	127.2	127.2	0.23	0.652
Tilt angle	1	2166.0	2166.0	3.92	0.105
Feed	1	919.6	919.6	1.66	0.254
Error	5	2765.4	553.1		
Total	8	5978.2			

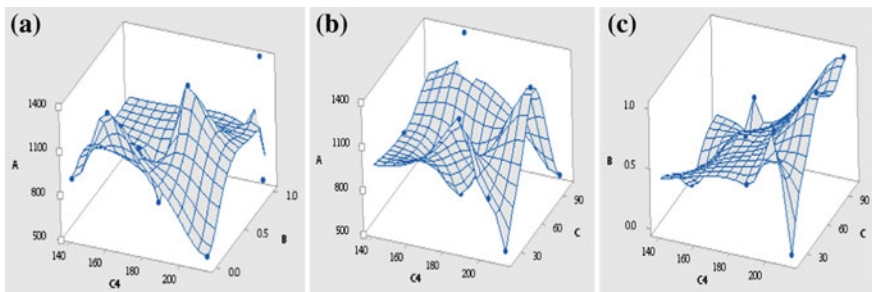


**Fig. 4** Response surface plot between rotational speed (a), tilt angle (b) and feed (c) versus obtained tensile strength of weld joints (C4)

1° and feed is varied as 20, 63, 100 mm/min, the weld strength obtained is 256, 316 and 243 MPa. When the rotational speed changed to 900 rpm and kept constant with varying tilt angle and feed, the tensile strength of the weld joint gained is 239, 255 and 220 MPa. Further increase in rotational speed to 1400 rpm and with the change in tilt angle and feed, the strength of the weld joint achieved is 201, 111 and 173 MPa. Signal-to-noise ratio of each factor is calculated using the condition larger is better, and the mean value of the obtained tensile strength is tabulated in Table 6. Ranking of each delta value is defined in terms of largest delta value (rotational speed) is rank 1 and smallest delta value (tilt angle) is rank 3.

The F value in the regression analysis Table 7 expresses the significance of the process parameters on the tensile strength, such as tilt angle (0.57) represents to be more significant than feed (2.13) and rotational speed (17.85). The ‘P’ value is the probability of getting the achieved results. The rotational speed 48.5% (0.485) explains the high impact on the tensile strength than by other parameters, tilt angle 0.8% and feed 20%. The response surface plots, which are three-dimensional images of obtained strength of the weld joint and selected process parameters such as rotational speed, tilt angle and feed, are revealed in Fig. 5. The regression expression revealed in Eq. 3 can be used to guess the tensile strength (TS) of friction stir Al 6061-T6 alloy joints, and is given by:

**Table 6** Process parameters, their S/N ratio and mean values

Level	Rotational speed (rpm)		Tilt angle (degree)		Feed (mm/min)	
	S/N ratio	Mean values	S/N ratio	Mean values	S/N ratio	Mean values
1	48.62	271.7	47.27	232.0	45.31	195.7
2	47.52	238.0	46.34	227.3	47.44	242.7
3	43.91	161.7	46.44	212.0	47.30	233.0
Delta	4.71	110.0	0.92	20.0	2.13	47.0
Rank	1		3		2	

**Table 7** Regression Analysis: tensile strength versus rotational speed, tilt angle, feed

Sources	Degrees of freedom	Adjusted sum of square	Adjusted mean square	F-value	P-value
Regression	3	21,675.4	7225.1	6.85	0.032
Rotational speed	1	18,827.3	18,827.3	17.85	0.008
Tilt angle	1	600.0	600.0	0.57	0.485
Feed	1	2248.1	2248.1	2.13	0.204
Error	5	5274.1	1054.8		
Total	8	26,949.6			

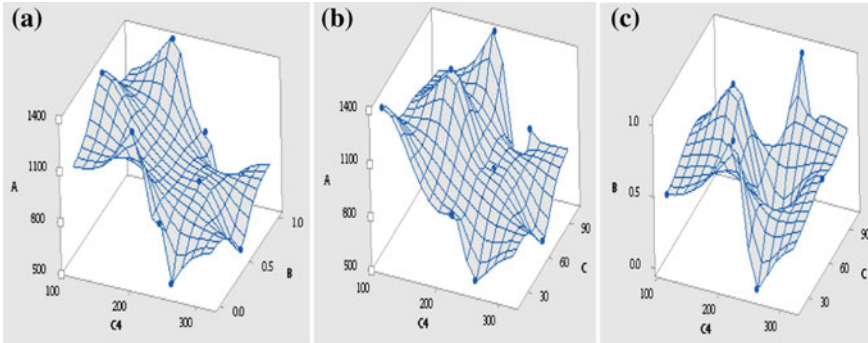


**Fig. 5** Response surface plot between rotational speed (a), tilt angle (b) and feed (c) versus obtained tensile strength of weld joints (C4)

$$TS = 330.7 - 0.1326 \times \text{Rotational speed} - 20.0 \times \text{Tilt angle} + 0.483 \times \text{Feed} \tag{3}$$

The observations made from the experiment 3, tabulated in Table 3, are when rotational speed remained constant at 560 rpm, tilt angle is altered as 0°, 0.5°, 1° and feed is varied as 20, 63, 100 mm/min, the weld strength gained is 200, 167 and 191 MPa. When the rotational speed is increased to 900 rpm and remained invariable with varying tilt angle and feed, the tensile strength of the weld joint achieved is 92, 105 and 108 MPa. Further increase in rotational speed to 1400 rpm and with the altering tilt angle and feed, the strength of the weld joint gained is 157, 188 and 191 MPa. Signal-to-noise ratio for each process parameters is determined using the condition larger is better and the mean value of the obtained tensile strength is tabulated in Table 8. Ranking of each delta value is defined in terms of largest delta value (rotational speed) is rank 1 and smallest delta value (tilt angle) is rank 3. The F value in Table 9 illustrates the significance of the process parameters on the tensile strength, such as rotational speed (0.00) symbolizes to be more significant than feed (0.12) and tilt angle (0.10). The ‘P’ value is probability of receiving the gained results. The rotational speed 94.9% (0.00) shows the high impact on the tensile strength than by other parameters, tilt angle 76% and feed 74%.

**Table 8** Process parameters, their S/N ratio and mean values

Level	Rotational speed (rpm)		Tilt angle (degree)		Feed (mm/min)	
	S/N ratio	Mean values	S/N ratio	Mean values	S/N ratio	Mean values
1	45.37	186.0	43.07	149.7	44.06	165.3
2	40.12	101.7	43.45	153.3	43.12	150.0
3	45.01	178.7	43.97	163.3	43.32	151.0
Delta	5.24	84.3	0.90	13.7	0.94	15.3
Rank	1		3		2	

**Table 9** Regression analysis: tensile strength versus rotational speed, tilt angle, feed

Sources	Degrees of freedom	Adjusted sum of square	Adjusted mean square	F-value	P-value
Regression	3	618.1	206.03	0.07	0.971
Rotational speed	1	12.6	12.55	0.00	0.949
Tilt angle	1	280.2	280.17	0.10	0.764
Feed	1	325.4	325.37	0.12	0.746
Error	5	13,912.1	2782.43		
Total	8	14,530.2			

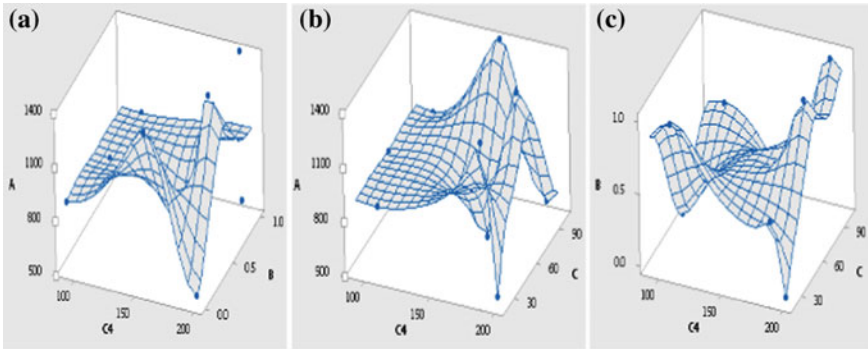


**Fig. 6** Response surface plot between rotational speed (a), tilt angle (b) and feed (c) versus obtained tensile strength of weld joints (C4)

The response surface plots are three-dimensional images of acquired strength of the weld joint and selected factors such as rotational speed, tilt angle, feed, which are shown in Fig. 6. The regression expression shown in Eq. 4 can be used to forecast the tensile strength (TS) of friction stir Al 6061-T6 alloy joints, and is given by:

$$TS = 156.6 - 0.0034 \times \text{Rotational speed} + 13.7 \times \text{Tilt angle} - 0.184 \times \text{Feed} \tag{4}$$

### 4 Conclusion

In the case of experiment one, the highest tensile strength of 213 MPa was obtained when the rotational speed is 560 rpm, tilt angle 0° and feed 20 mm/min. In the case of experiment two, the highest tensile strength of 316 MPa was obtained when the

rotational speed is 560 rpm, tilt angle  $0.5^\circ$  and feed 63 mm/min. In the case of experiment three, the highest tensile strength of 200 MPa is obtained when the rotational speed is 560 rpm, tilt angle  $0^\circ$  and feed 20 mm/min. An empirical relationship is formed to predict the tensile strength of friction stir welding of Al 6061-T6 alloy joints using Taguchi L9 experimental approach. The developed relationship is used to forecast the strength of friction stir welding of Al 6061-T6 alloy. The process parameter rotational speed has more effect than tilt angle and feed on the strength of the weld joint.

## References

1. Liu XC, Sun YF, Morisada Y, Fujii H (2018) Dynamics of rotational flow in friction stir welding of Al alloys. *J Mater Process Technol* 252(1):643–651
2. Ma ZY, Feng AH, Chen DL, Shen J (2017) Recent advances in friction stir welding/processing of Al alloys: micro-structural evolution and mechanical properties. *Crit Rev Solid State Mater Sci* 43(4):269–333
3. Yan Z, Liu X, Fang H (2017) Mechanical properties of friction stir welding and metal inert gas welding of Al-Zn Al alloy joints. *Int J Adv Manuf Technol* 91(9–12):3025–3031
4. Aliha MRM, Shahheidari M, Bisadi M (2016) Mechanical and metallurgical properties of dissimilar AA6061-T6 and AA7277-T6 joint made by FSW technique. *Int J Adv Manuf Technol* 86(9–12):2551–2565
5. Sahu PK, Pal S, Pal SK, Jain R (2016) Influence of plate position, tool offset and tool rotational speed on mechanical properties and microstructures of dissimilar Al/Cu friction stir welding joints. *J Mater Process Technol* 235(1):55–67
6. Kim YG, Kim JS, Kim IJ (2014) Effect of process parameters on optimum welding condition of dp590 steel by friction stir welding. *J Mech Sci Technol* 28(12):5143–5148
7. Padhy GK, Wu CS, Gao S (2018) Friction stir based welding and processing technologies—processes, parameters, microstructures and applications: A review. *J Mater Sci Technol* 34(1):1–38
8. Rodriguez RI, Jordon JB, Allison PG, Rushing T, Garcia L (2015) Microstructure and mechanical properties of dissimilar friction stir welding of 6061-to-7050 Al alloys. *Mater & Des* 86(1):60–65
9. Panda B, Garg A, Jian Z, Heidrzadeh A, Gao L (2016) Characterization of the tensile properties of friction stir welded Al alloy joints based on axial force, traverse speed, and rotational speed. *Front Mech Eng* 11(3):289–298
10. Antony M, Pavithran BT, Thamban I (2013) Friction stir processing of AA6061—a study. *Int J Emerg Technol Adv Eng* 3:589–595
11. Nourani M, Milani AS, Spiro Y (2011) Taguchi optimization of process parameters in friction stir welding of 6061 Al alloy: a review and case study. *Sci Res* 3:144–155
12. Ilangovan M, Boopathy SR, Balasubramanian V (2015) Effect of tool pin profile on microstructure and tensile properties of friction stir welded dissimilar AA 6061-AA 5086 Al alloy joints. *Defence Technol* 11(2):174–184
13. Elatharasan G, Senthil Kumar VS (2013) An experimental analysis and optimization of process parameter on friction stir welding of AA 6061-T6 aluminium alloys using RSM. *Procedia Eng* 64:1227–1234 Elsevier
14. Jen YM, Chang LY, Fang CF (2008) Assessing the fatigue life of butt-welded joints under oblique loading by using local approaches. *Int J Fatigue* 30:603–613

# A Comparative Study on Performance of 3D-Printed EDM Electrode with Conventional EDM Electrode



L. Mahipal Reddy, L. Siva Rama Krishna, S. Sharath Kumar  
and P. Ravinder Reddy

**Abstract** Electro Discharge Machining (EDM) is an unconventional machining process used to make hard metal tools and complex shapes, which are difficult to machine by the conventional machining process. Additive manufacturing is the process of creating a 3D object from a CAD Model by adding one layer over another layer. In this work, it is proposed to fabricate an EDM electrode using Direct Metal Laser Sintering (DMLS) 3D printing process and compare its performance with conventional EDM electrodes in terms of Material Removal Rate (MRR), Tool Wear Rate (TWR), and surface finish. The material used for printing the EDM electrode is aluminum AlSi10 Mg and it is proposed to print it on the Direct Metal Laser Sintering 3D Printing machine. The workpiece material used for the EDM process is steel alloy 681-08 of grade D3. The experiment is conducted on EDM with the DMLS electrode and conventional electrode by varying the peak Current (I), Pulse on time ( $T_{on}$ ), and Pulse off time ( $T_{off}$ ). A comparison of MRR, TWR, and surface roughness is made varying the above-mentioned parameters.

**Keywords** EDM · 3D Printing · DMLS · MRR · TWR

---

L. Mahipal Reddy (✉) · L. Siva Rama Krishna · S. Sharath Kumar  
Department of Mechanical Engineering, UCE (A), Osmania University, Hyderabad, India  
e-mail: [l.mahipal@gmail.com](mailto:l.mahipal@gmail.com)

L. Siva Rama Krishna  
e-mail: [lsrkou@gmail.com](mailto:lsrkou@gmail.com)

S. Sharath Kumar  
e-mail: [sankasharath@gmail.com](mailto:sankasharath@gmail.com)

P. Ravinder Reddy  
Chaitanya Bharathi Institute of Technology, Hyderabad, India  
e-mail: [reddy.prr@gmail.com](mailto:reddy.prr@gmail.com)

## 1 Introduction

EDM is the best unconventional machining process by generating spark with the help of electrical energy and removal of material is due to thermal energy. The tool and workpiece material should consist of electrically conductive materials in order to machine on EDM.

Direct Metal Laser Sintering (DMLS) is used to melt and fuse the metallic powder by using high-intensity laser. The process starts by designing a 3D CAD model that is converted into.stl format, which converts the data into 2D layers, i.e., 20 to 100  $\mu\text{m}$  micrometers. The DMLS machine uses Yb-fiber optic laser by 200 watts power. To machine on DMLS, the material must be in the form of fine powder (atomized form). The synthesized materials presently used for DMLS are AlSi10 Mg, Ti6Al4 V, Inconel 625 and 718 and various grades of stainless steel.

## 2 Literature Review

L. Mahipal Reddy et al. [1] made an attempt to estimate the electrical conductivity of ABS and PLA Based EDM Electrode Fabricated by using FDM 3D printing process. ABS and PLA are the most popular materials used in the FDM process. Azhar Equbal [2] explains the electroless coating of ABS (acrylonitrile–butadiene–styrene) parts on surfaces. Cu deposition technique by two acidic containers is done and compared with their electrical performance. D. Fefar Savan [3] explained the FDM-based ABS electrode metallization by electroless copper coating to get conductivity. Fred L. Amorim et al. [4] focused on the investigation of direct production of EDM electrodes through selective laser sintering process using a new metal matrix composite material made of molybdenum and a copper–nickel alloy. The optimization of the main SLS parameters on the densification behavior and porosity is experimentally studied. Fred L. Amorim et al. [5] conducted the experiments on the performance of EDM electrodes made by SLS using the materials pure copper, bronze–nickel alloy, copper/bronze–nickel alloy, and steel alloy powders. Vijay Kumar Meena and Naganumaiah [6] have investigated DMLS electrode feasibility and also optimized the parameters of EDM. The experimental results show that the gray relational approach can be quantified and controlled effectively of the performance characteristics of the DMLS EDM electrode. Brent E. Stucker [7] explained the production of electrical discharge machining electrodes using SLS: Preliminary results have been obtained John kechagias et al. [8] gave a review of the EDM electrodes manufacturing using the rapid tooling techniques and also explained that Rapid Tooling (RT) is a new technology which uses rapid prototyping models to reduce the time and cost of tool manufacturing. Nayan Patel [9] reviewed and explained the performance improvement of EDM by alternate electrode materials like copper, tungsten, brass and composite electrodes. Azhar Equbal et al. [10] explained the possibilities of making of EDM electrodes by using RP techniques with complex shapes in less time and low-cost

high potential. Those materials can be conductive or nonconductive. Saumya Darsan Mohanty and Ramesh Chandra Mohanty [11] studied the highlights of multiobjective optimization problem by using utility concepts coupled with Taguchi method through a case study in EDM of D2 steel by using electrode manufactured by DMLS process. The Taguchi method is useful and efficient to solve a multi-response optimization problem. C. Mathalai Sundaram [12] focused on the fabrication of metal matrix composite electrode by mixing the powder with TiC and WC. The optimization of parameters is done on EDM. Samuel M. Allen and Emanuel M. Sachs [13] investigated the manufacturing of the EDM electrode using the RP technique based on electroless plating and electroforming.

### 3 Problem Statement

The aim of this work is to compare the performance of 3D-Printed EDM Electrode with the Conventional EDM Electrode in terms of the MRR, TWR, and Surface Roughness of Electrode by varying the parameters like Current, Pulse on time, and Pulse off time. It is proposed to fabricate the conductive material EDM electrode by using the DMLS process by EOS aluminium material. It is an aluminum alloy in fine powder form, which has been specially optimized for processing on EOSINT M systems and then compared with the conventional aluminum electrode.

## 4 Research Methodology

### 4.1 Modeling of EDM Electrode

The dimensions of the tool are length 50 mm and diameter 10 mm, which were taken based on the literature. The EDM electrode is modeled using Creo Parametric Design software as per the dimensions, then the file is exported into.stl format. Figure 1 shows the EDM electrode modeled in Creo software.

### 4.2 Fabrication of EDM Electrode

The metal-based electrode is manufactured using DMLS 3D printing process by EOSINT M280 which shown in Fig. 2. The material used to fabricate the EDM electrode is AlSi10 Mg, which is specially optimized for EOSINT M280 Machine. Figure 3 represents the EDM electrode fabricated by DMLS.



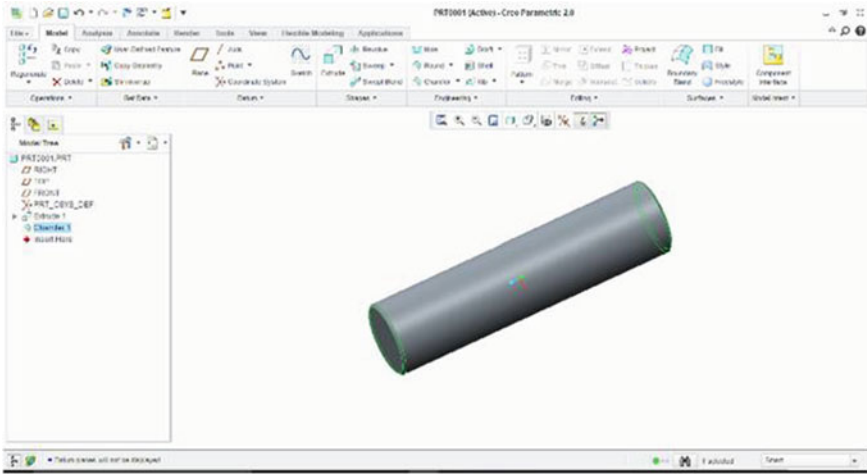
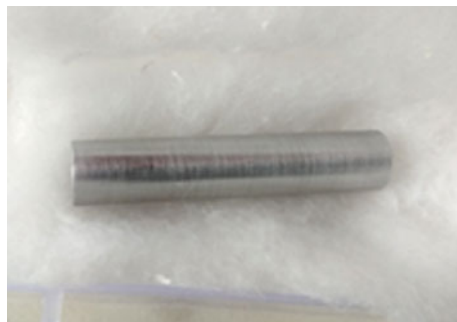


Fig. 1 3D CAD Model of EDM electrode

Fig. 2 EOSINT M280



Fig. 3 EDM electrode by DMLS



**Table 1** Input parameters

Current (Amps)	$T_{on}$ ( $\mu s$ )	$T_{off}$ ( $\mu s$ )
3	100	50
6	200	100
9	500	200

### 4.3 Experimental Investigation

The experiments were conducted on the EDM machine using 3D-printed EDM electrode and a conventional EDM electrode. The EDM tests were carried out by varying the three parameters for machining time of 10 min i.e., input current, pulse on time ( $T_{on}$ ), and pulse off time ( $T_{off}$ ). Table 1 shows the input parameters.

The tool materials used for EDM machining are AlSi10 Mg as DMLS electrode and Al HE30 as the conventional electrode. The workpiece material used is steel alloy 681-08 of grade D3, which are cold work tool steels characterized by high carbon and high chromium content, which exhibits high resistance to abrasion. The applications for D3 steel are blanking and forming dies, press tools, punches, and bushes.

### 4.4 Measurements of Responses

Digital balance with a precision of 0.01 gm is used to weigh electrodes and workpiece before and after EDM machining. The material removal rate and surface roughness are calculated using Eqs. 1 and 2, respectively.

$$MRR = \frac{W_{bm} - W_{am}}{t} \text{ gm/min} \tag{1}$$

$$TWR = \frac{W_{bm} - W_{am}}{t} \text{ gm/min} \tag{2}$$

where  $W_{bm}$  = weight of tool/material before machining

$W_{am}$  = weight of tool/material after machining

$T$  = machining time (10 min).

The surface roughness is measured on the workpiece machined with DMLS aluminum electrode and conventional aluminum electrode with the help of Taylor Hobson Precision Surtronic 3+ surface roughness tester.

## 5 Results and Discussions

Electrical Discharge Machining is done on steel alloy 681-08 according to the experimental setup. By varying process parameters current, pulse on, and pulse off time on performance measures the material removal rate and tool wear rate using DMLS 3D-printed Al electrode and conventional Al electrode are tabulated. Table 2 represents the material removal rate and tool wear rate.

**Table 2** MRR and TWR values for various levels

Sl. No.	Current (I) amps	$T_{ON}$ $\mu$ S	$T_{OFF}$ $\mu$ S	MRR (gm/min)		TWR (gm/min)	
				DMLS	C-Al	DMLS	C-Al
1	3	100	50	0.001	0.001	0.001	0.002
2	3	100	100	0.003	0.002	0.002	0.001
3	3	100	200	0.002	0.005	0.001	0.001
4	3	200	50	0.003	0.006	0.001	0.001
5	3	200	100	0.001	0.006	0	0.003
6	3	200	200	0.004	0.007	0.001	0.002
7	3	500	50	0.012	0.007	0.001	0.001
8	3	500	100	0.01	0.005	0.003	0.002
9	3	500	200	0.006	0.007	0.001	0.001
10	6	100	50	0.028	0.011	0.002	0.004
11	6	100	100	0.009	0.006	0.006	0.002
12	6	100	200	0.014	0.032	0.004	0.001
13	6	200	50	0.02	0.027	0.005	0.003
14	6	200	100	0.01	0.002	0.005	0.003
15	6	200	200	0.014	0.011	0.001	0.002
16	6	500	50	0.037	0.037	0.006	0.005
17	6	500	100	0.068	0.049	0.012	0.005
18	6	500	200	0.060	0.048	0.012	0.003
19	9	100	50	0.055	0.011	0.011	0.004
20	9	100	100	0.042	0.035	0.01	0.008
21	9	100	200	0.016	0.025	0.002	0.005
22	9	200	50	0.043	0.037	0.011	0.007
23	9	200	100	0.013	0.008	0.007	0.003
24	9	200	200	0.038	0.023	0.005	0.004
25	9	500	50	0.088	0.089	0.012	0.011
26	9	500	100	0.092	0.089	0.014	0.012
27	9	500	200	0.085	0.015	0.011	0.01

The comparison graphs are plotted for maximum MRR and TWR obtained from Table 2. The graphs are plotted MRR versus Current and TWR versus Current (Figs. 4 and 5).

From the above graphs, it is observed that as the current increases material removal rate and tool wear rate is increased. The Maximum Material Removal (MRR) rate for DMLS and conventional electrodes is found to be 0.092 gm/min and 0.089 gm/min, respectively, at 9 amps current, pulse on time ( $T_{on}$ ) 500  $\mu$ s, pulse off time ( $T_{off}$ ) 100  $\mu$ s. Similarly, the maximum Tool Wear Rate (TWR) for DMLS tool and conventional electrodes is found to be 0.014 gm/min and 0.012 gm/min, respectively, at 9 amps of current, pulse on time ( $T_{on}$ ) 500  $\mu$ s, pulse off time ( $T_{off}$ ) 100  $\mu$ s.

The surface roughness values are measured by using Taylor Hobson precision Surtronic 3+ profilometer. The surface roughness is measured for the maximum material removal rate obtained at the different parameters of current, i.e., are 3, 6, and 9 amps. Table 3 shows the surface roughness ( $R_a$ ) measurements.

**Fig. 4** Comparison graph of MRR

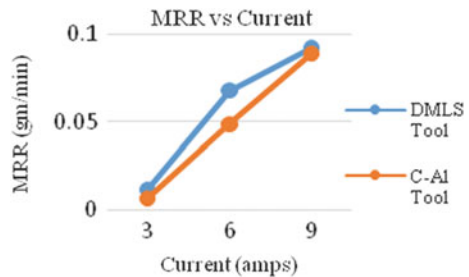


**Fig. 5** Comparison graph of TWR

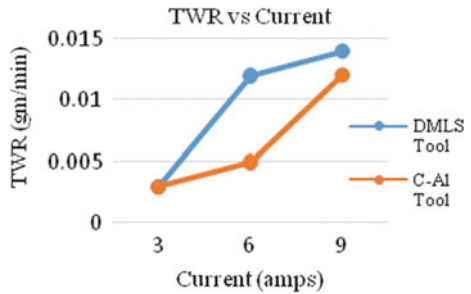


**Table 3** Surface roughness measurements

Sl. No.	DMLS tool electrode in $\mu$ m	C-Al tool electrode in $\mu$ m
1	2.5	2.3
2	4.2	4.4
3	6.2	5.0

**Fig. 6** Comparison of surface roughness measurements

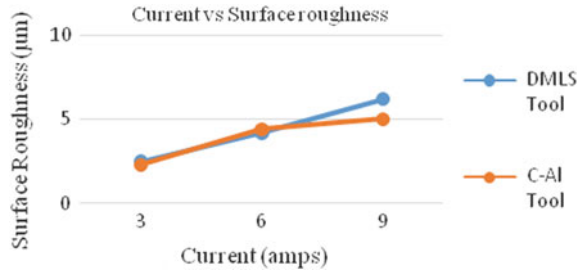


Figure 6 above shows the comparison graph of surface roughness measurements for both the electrodes. It is observed that as current increases surface roughness increases linearly.

## 6 Conclusions

The aim of this paper is to compare the performance of a 3D-printed EDM electrode with the conventional EDM electrode in terms of MRR, TWR and Surface Roughness. The following conclusions can be made from the results.

- For the metal-based 3D printed EDM electrode, it has been observed that the Maximum Material Removal (MRR) rate for DMLS and conventional electrodes are found to be 0.092 gm/min and 0.089 gm/min respectively at 9 amps Current, Pulse on time ( $T_{on}$ ) 500  $\mu$ s, Pulse off time ( $T_{off}$ ) 100  $\mu$ s. Similarly, the maximum Tool Wear Rate (TWR) for DMLS tool and conventional electrodes is found to be 0.014gm/min and 0.012gm/min, respectively, at 9 amps of current, pulse on time ( $T_{on}$ ) 500  $\mu$ s, pulse off time ( $T_{off}$ ) 100  $\mu$ s.
- It has been observed that the DMLS electrode has a more average Material Removal Rate (MRR), i.e., 0.0277 gm/min than the conventional electrode which is 0.0255 gm/min. The average Tool Wear Rate (TWR) of DMLS tool electrode is 0.0577 gm/min while for conventional electrode it is found to be 0.0037 gm/min.
- The maximum surface roughness of DMLS and conventional electrode is found to be 6.2  $\mu$ m and 5.0  $\mu$ m, respectively, at 9 amps of current. The average surface roughness obtained for the DMLS electrode (4.2  $\mu$ m) is more when compared to the conventional electrode (3.9  $\mu$ m).

## References

1. Mahipal Reddy L, Siva Rama Krishna L, Sharath Kumar S, Ravinder Reddy, P (2018) Estimation of electrical conductivity of ABS and PLA based EDM electrode fabricated by using FDM 3D printing process. *IJMERT* 5(Special Issue):332–338
2. Eqbal A, Sood AP (2014) Metallization on FDM parts using chemical deposition technique. *Coatings* 4:574–586
3. Fefar Savan D, Karajagikar JS (2014) Study and analysis of metallized electrode fabricated with FDM rapid prototyping technique for electro discharge machining. In: IITGuwahati—conference AIMTDRC-2014, vol 15(3), pp 171–176
4. Amorim FL et al (2014) Selective laser sintering of Mo-CuNi composite to be used as EDM electrode. *Rapid Prototyp J* 59–68 (Emerald publications)
5. Amorim FL et al (2013) Performance of sinking EDM electrodes made by selective laser sintering technique. *Int J Adv Manuf Technol* 65:1423–1428
6. Meena VK, Nagahanumaiah (2006) Optimization of EDM machining parameters using DMLS electrodes. *Rapid Prototyp J* 12(4):222–228
7. Stucker BE, Bradley WL (1995) The production of electrical discharge machining electrodes using SLS: preliminary results. *Research gate Article*, pp 278–286
8. Kechagias J et al (2008) EDM electrode manufacture using rapid tooling: a review. *J Mater Sci* 43:2522–2535 (Springer)
9. Patel N (2015) Review on importance of electrodes in electrical discharge machining process. *Int J Res Aeronaut Mech Eng* 3:36–41
10. Eqbal A, Dixit NK, Sood AK (2013) Rapid prototyping application in manufacturing of EDM electrode. *Int J Sci Eng Res* 4(8):1–4
11. Mohanty SD, Mohanty RC (2017) Study on performance of EDM electrodes produced through rapid tooling route. *J Adv Manuf Syst* 16(4):357–374
12. Mathalai Sundaram C, Sivasubramanian R, Chandrasekaran K (2016) Experimental investigations of new powder metallurgy electrode in electrical discharge machining of OHNS using Taguchi method. *Int J Adv Engg Technol* VII(1):559–564
13. Allen SM, Sachs EM (2000) Three-dimensional printing of metal parts for tooling and other applications. *Met Mater* 6(6):589–594

# Effect of High-Power Intensity on Corrosion Behaviour of Aluminium—Steel Dissimilar Joints Made by Electron Beam Welding



S. Sai Sravanthi and Swati Ghosh Acharyya

**Abstract** The automotive sector is keen on using lightweight components with aluminium–steel joints since it leads to reduced fuel consumption and lowered CO<sub>2</sub> emission. However, huge variations in the metallurgical properties of aluminium and steel and the use of high energy beam processes such as electron beam welding for fabrication challenge the durability of the resultant joints obtained. The present work establishes the effect of high heat input applied during electron beam welding on the corrosion resistance of 5052 Al–galvanized mild steel lap joints. The study includes microstructural characterization of the weld interfaces using scanning electron microscope (SEM), hardness measurement near the interfacial regions using Vickers’s hardness tester. Results indicated the generation of Al–Fe intermetallic layer at the weld bead–mild steel interface whose width ranged between 2.8 and 10.5  $\mu\text{m}$  from head to foot regions. The composition of the layer was confirmed by the elemental analysis that was done on the layer by Energy Dispersion Spectroscopy which was attached to SEM. The layer had shown a severe impact on the corrosion resistance of the joints when exposed to nitric acid for 24 h following ASTM G 67-04. The joints experienced de-bonding at the interface and have undergone a huge weight loss of 38.9 mg.

**Keywords** Corrosion · Dissimilar welds · Electron beam · Hardness · Interface

## 1 Introduction

The concept of light-weighting the automotive components has become a great deal of interest in the present times since it plays a key role in fuel conservation. Hence, automotive manufacturers have started to replace the steel parts with lightweight alloys of

---

S. Sai Sravanthi (✉) · S. G. Acharyya  
School of Engineering Sciences and Technology, University of Hyderabad, Hyderabad 500046,  
India  
e-mail: [s.sravanthisagar@gmail.com](mailto:s.sravanthisagar@gmail.com)

S. G. Acharyya  
e-mail: [swati364@gmail.com](mailto:swati364@gmail.com)

© Springer Nature Singapore Pte Ltd. 2020  
G. S. V. L. Narasimham et al. (eds.), *Recent Trends in Mechanical Engineering*,  
Lecture Notes in Mechanical Engineering,  
[https://doi.org/10.1007/978-981-15-1124-0\\_20](https://doi.org/10.1007/978-981-15-1124-0_20)

227

Aluminium and Magnesium. For this purpose, fusion hybrid blanks of Aluminium-steel are being fabricated. However, Aluminium-steel joining is a challenging job due to the huge variation in their metallurgical properties.

### **1.1 Literature Review**

According to the literature reports, dissimilar weld fabrication was previously attempted by using various joining technologies such as Gas Metal Arc Welding (GMAW), Tungsten Inert Gas Welding (TIG), Laser Beam Welding (LBW), etc. [1–7]. Milani et al. analyzed the influence of filler wire feed rate on the properties of Al-steel MIG-braze joints [4]. Similarly, Taban et al. made a comparative study of Al-steel joints fabricated by various arc welding processes [5]. Aluminium-steel joining results in the formation of several Al-Fe intermetallic compounds (IMCs) due to the difference in their solid solubilities. In addition to the variation in their properties, use of high energy beam processes such as electron beam welding results in the involvement of high power density during welding, which results in severe deterioration of mechanical properties and corrosion resistance of the fabricated welds. However, very limited research is available on aluminium-steel dissimilar joints fabricated using electron beam welding [8–11]. Wang et al. studied the effect of beam deflection on electron beam welds of Aluminium and steel [9]. Whereas; T. Wang et al studied the influence of varied beam current on the integrity of Aluminium-Steel welds [10].

The authors had previously reported the corrosion behaviour of Aluminium-mild steel dissimilar welds joined by GMAW-brazing and Cold Metal Transfer processes [12, 13]. In the present work, the authors have explained the result of using high voltage, current and welding speed on the corrosion behaviour of 5052 Aluminium-galvanized mild steel electron beam welds.

## **2 Materials and Methodology**

The electron beam welds of 5052 Aluminium-galvanized mild steel were prepared in lap joint configuration and the schematic is shown in Fig. 1. The base metal plates of Aluminium alloy and steel were thoroughly machined and each plate was sectioned to  $100 \times 75 \times 1.5$  mm dimensions, followed by thorough surface cleaning with acetone to get rid of the impurities. A support plate was clamped in butt configuration in right angles with the mild steel plate that was already placed on the welding table. Aluminium plate was positioned above the support plate and was tightly clamped by means of the equipment's vision system to maintain regular lap distance throughout the joint length. The processing parameters applied for welding of these joints were carefully chosen from the literature [14–16] and are given in Table 1.



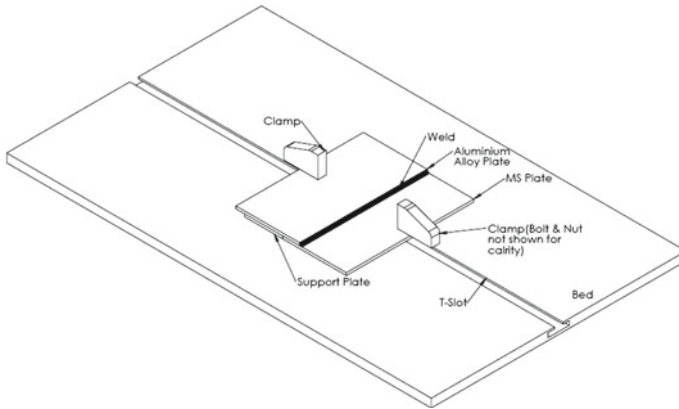


**Fig. 1** Schematic of the electron beam welding setup of 5052 Aluminium-Galvanized mild steel lap joint

**Table 1** Processing parameters used for electron beam welding

Sample ID	Welding parameters			
	Weld current (mA)	Voltage (kV)	Weld speed (mm/min)	Heat input (J/mm)
Sample A	23	60	1000	82.799

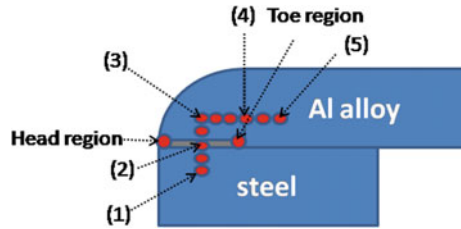
### 2.1 Sample Preparation

Prior to the microstructural characterization, the weld sample was cut to 25 mm × 3.5 mm dimensions along the cross section of the weld plate and was subjected to the metallographic polishing by means of emery papers of grades 320, 550, 700, and 1000 which was followed by fine polishing with Alumina powder of grades A and B. Later, the weld sample was etched with Keller’s reagent at the interfacial regions of weld bead–mild steel and weld bead–5052 Aluminium, respectively, to observe the microstructure.

### 2.2 SEM and EDX

The microstructural characterization of the sample was done along the cross section at the weld interfaces using Scanning Electron Microscope (SEM) with Energy Dispersion Spectroscopy (EDS) attached to it. The EDS equipment was used for the elemental composition evaluation at the weld bead–5052 Al and weld bead–steel interfaces.

**Fig. 2** Schematic of the cross section of weld sample showing the head and foot regions of the weld bead—mild steel interface and the hardness profile taken



### 2.3 Hardness Measurement

Vickers's microhardness tester was used to take the hardness profile near the weld interfacial regions as shown in Fig. 2. A dwell time of 15 s was maintained with a load of 100 gm applied on the weld sample.

- \*(1): weld bead—mild steel interface
- (2): intermetallic layer region
- (3): weld bead region
- (4): weld bead—Al alloy interface
- (5) Al alloy.

### 2.4 Corrosion Testing

The weld sample was exposed to nitric acid as part of the nitric acid mass loss test, which is generally conducted to evaluate the intergranular corrosion behaviour of Aluminium alloys. The test was done as per ASTM G 67-04 [17]. The authors have performed this test on GMAW-braze joints of 6061 Al—mild steel to observe the intergranular corrosion behaviour at the joint interfaces. As per the test, microstructural features and weight loss of the weld sample were recorded every time after exposing the weld sample in 5 wt% caustic soda for 60 s at 80 °C exposing to nitric acid for 30 s and 24 h, respectively.

## 3 Results and Discussion

### 3.1 Microstructural Evaluation

The fabrication of dissimilar joints of mild steel and 5052 Aluminium resulted in the generation of two interfaces, viz., (1) weld bead—mild steel interface and (2) weld bead—5052 Al interface. The weld bead—mild steel interface is further classified into

head and toe regions as we proceed from the initial point to the final point of the IMC layer along the cross section as shown in Fig. 2.

### 3.1.1 Weld Bead–Mild Steel Interface

The cross-sectional micrographs of the weld sample in as-received condition are given in Fig. 3. The micrograph had shown the IMC layer formation with a thickness ranging between 2.85 and 10.5  $\mu\text{m}$  from head to toe region. The layer thickness was found to be higher in the toe region because of greater heat intensity. At higher heat intensities, more amount of Aluminium is diffused from 5052 Al alloy to Fe of galvanized mild steel, leading to the generation of more number of intermetallic layers. As a result, the thickness increased. Crack formation was evident near the intermetallic layer region of the weld bead–mild steel interface because of tensile residual stresses that are generated due to heat intensity variation from head to toe region. This leads to distortion of weld and as a result, cracks were evidenced in the interfacial regions.

#### (a) EDX Analysis

The chemical composition was analyzed in the IMC layer area of weld bead–mild steel interface at both head and toe regions as indicated in Fig. 3. The EDX spectra confirmed the composition of the IMC layer in both the regions of the weld sample as shown in Fig. 4. Zinc entrapment was evident in the foot region of the weld sample as shown in Fig. 4(b). When a high-energy beam such as an electron beam is incident on the weld sample, the surface temperature of the steel is instantly increased which results in Zinc coating evaporation. When Zinc vapors lack time to escape they get settled either at head or toe regions of the weld bead, finally leading to porosity [12, 13].

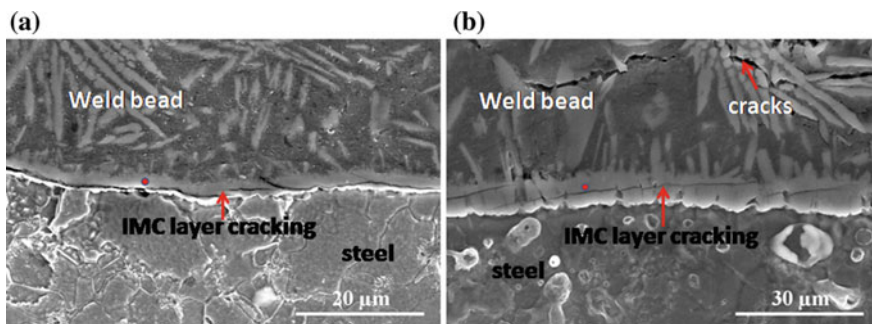


**Fig. 3** As-received micrographs of 5052 Al–mild steel weld sample showing cracks in the weld bead–mild steel interface at **a** head region and **b** foot region of the IMC layer

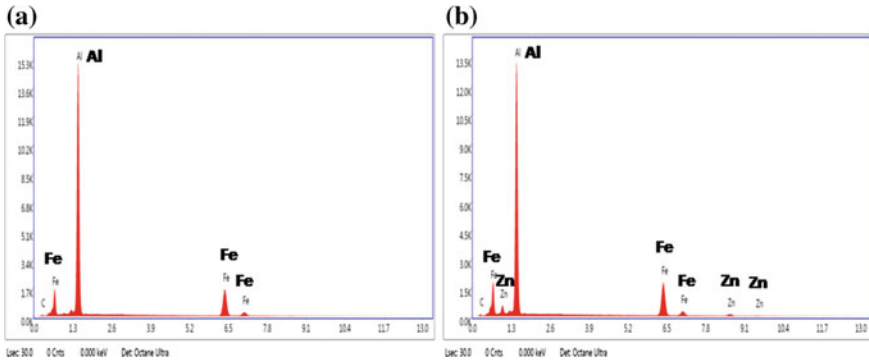


Fig. 4 EDX spectra at a head region and b foot region of the weld bead-mild steel interface

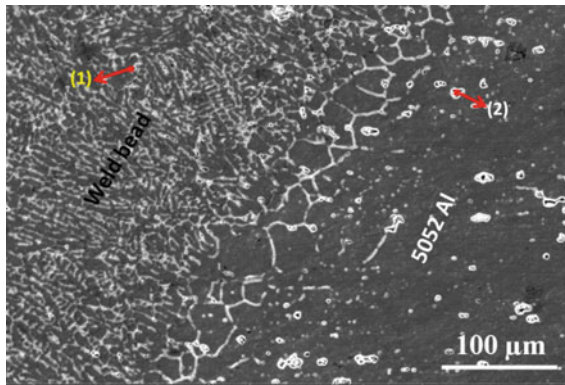


Fig. 5 Micrograph of weld bead–aluminium interface in the as-received condition

### 3.1.2 Weld Bead–5052 Al Interface

The weld bead had shown the formation of long, needle-shaped Al–Fe particles randomly distributed throughout the matrix. Whereas 5052 Al alloy region near the weld bead–Aluminium interface was characterized by the formation of Al–Mg precipitates. Grain coarsening was observed in the weld zone of 5052 Al near the interface. High heat input can cause the expansion of grains in the weld zone [18].

#### (a) EDX Analysis

The EDX analysis at the regions (1) and (2) indicated in Fig. 5 confirmed the formation of Al–Fe particles in the weld bead and Al–Mg precipitates in 5052 Al near the interface. Figure 6 gives the EDX spectra at the weld bead–Aluminium interface in the regions indicated in Fig. 5.

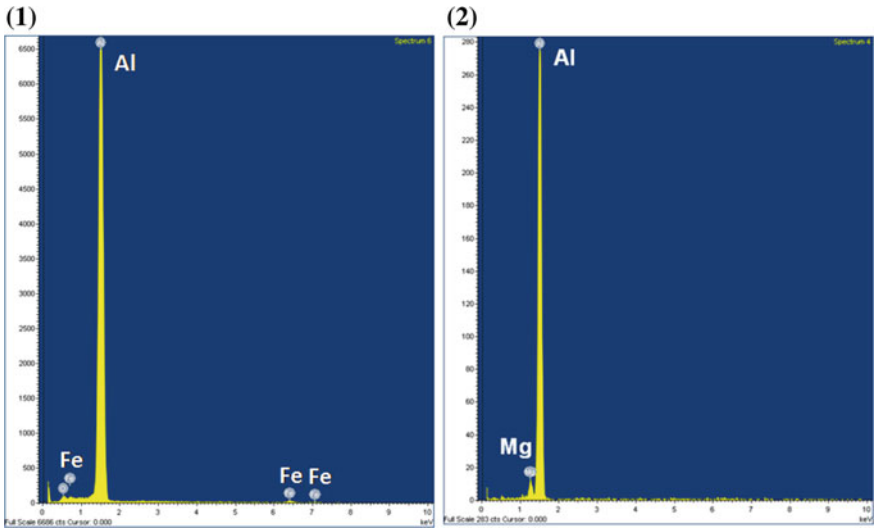


Fig. 6 The EDX spectra of regions (1) and (2) of weld bead–5052 Al interface of the weld sample

### 3.2 Hardness Measurement

As shown in Fig. 7, the weld sample was evidenced by high hardness in the interfacial areas of weld bead–mild steel and weld bead–Aluminium alloy which confirms the formation of a higher volume fraction of intermetallics when compared to the

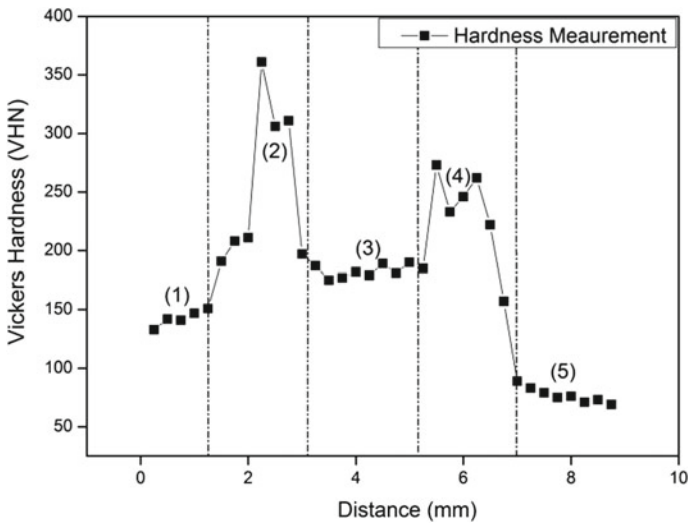
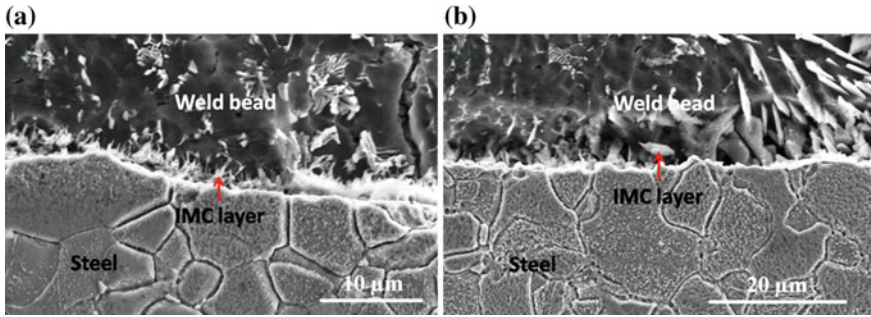


Fig. 7 Plot showing the Vickers’s hardness profile along the cross section of the weld sample



**Fig. 8** Micrographs of the weld sample at **a** head region and **b** toe region after exposing to nitric acid for 30 s

respective base metal regions of steel and 5052 Al. The average hardness at the weld bead–mild steel interface (IMC layer region) was 264 VHN and at weld bead–Aluminium interface was 232 VHN respectively. As shown in the figure, the weld bead region had also shown high hardness because of the presence of Al–Fe particles and Al–Mg precipitates.

### 3.3 Corrosion Testing

#### 3.3.1 Weld Bead–Steel Interface

When the weld sample was exposed to 5 wt% caustic soda for 60 s, no microstructural changes were observed at the weld bead–mild steel interface but a weight loss of 14.3 mg was recorded. The micrographs at the head and toe regions of the weld sample after exposing to nitric acid for 30 s are given in Fig. 8. The micrographs have shown a gradual dissolution of the IMC layer in both regions thereby, initiating a gap at the interface. The layer dissolution was more in the toe region and hence the gap was also found to be high. Higher is the thickness of the IMC layer, greater will be the corrosion attack since IMC area is highly anodic in nature.

When the sample was exposed to nitric acid for 24 h, a complete dissolution of IMC layer had taken place at weld bead–mild steel interface, which finally resulted in the interfacial de-bonding as shown in Fig. 9.

#### 3.3.2 Weld Bead–5052 Al Interface

Exposing the weld sample to caustic soda resulted in the generation of spherical voids near the weld bead–5052 Al interface. This is because of the damage of the oxide layer on the surface of Al alloy on its reaction to caustic soda. The authors have explained about this reaction in detail while evaluating the corrosion resistance

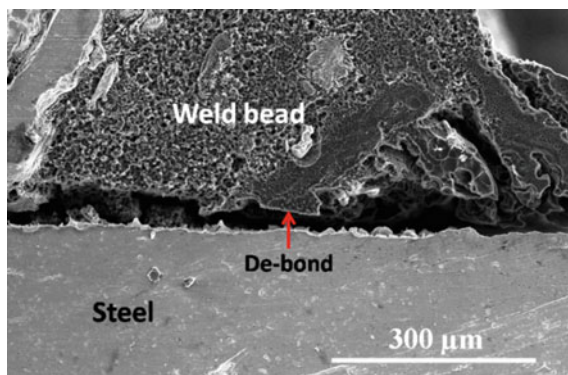


**Fig. 9** Micrograph showing de-bonding at the weld bead-mild steel interface on exposing the sample to nitric acid for 24 h

of MIG-braze joints of 6061 Al–mild steel [12]. The voids remained on the interface after exposing the sample to nitric acid for 30 s as shown in Fig. 10(a). The voids were found to contribute to the initiation of intergranular corrosion at the weld bead–5052 Al interface. Similarly, immersion of the weld specimen in nitric acid for 24 h resulted in intergranular corrosion at the interface as shown in Fig. 10(b).

The weight loss experienced by the weld sample after each test is given in Table 2. The weight loss after exposing the sample to caustic soda occurred in the sample

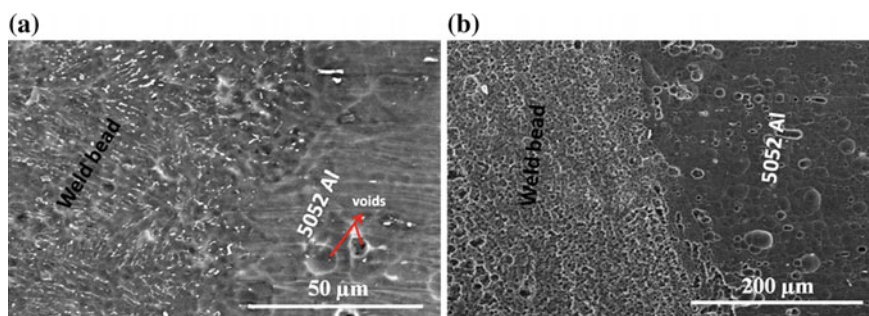


**Fig. 10** Micrographs of the weld sample after immersing in nitric acid for **a** 30 s and after **b** 24 h exposure at weld bead–5052 Al interface

**Table 2** Weight loss details of the weld sample during nitric acid mass loss test

Weight loss in the weld sample			
Weight loss after NaOH test (mg)	Weight loss after HNO <sub>3</sub> (30 s) test (mg)	Weight loss after HNO <sub>3</sub> (24 h) test (mg)	Total weight loss (mg)
14.3 ± 0.3	9.5 ± 0.6	15.1 ± 0.9	38.9

due to the damage of protective oxide film on the aluminium alloy surface. The reaction between nitric acid and Fe of steel leads to the formation of iron nitrate, which contributed to a faster dissolution of steel. Hence, weight loss was high in the weld sample when exposed to nitric acid. As shown in Table 2, the weld sample had experienced an overall weight loss of 38.9 mg after nitric acid mass loss test.

## 4 Conclusions

Fabrication of Aluminium alloy–mild steel dissimilar joints is a challenging task unless the weld processing parameters are carefully optimized. The following conclusions can be made out of this study.

1. The IMC layer thickness had increased from head to toe region in the weld specimen due to a gradual increase in the heat intensity.
2. High hardness was observed at the weld interfaces which confirmed the formation of several Al–Fe intermetallics at weld bead–mild steel interface and Al–Mg precipitates at weld bead–5052 Al interface.
3. Higher hardness results in a greater corrosive attack. This resulted in high corrosion at weld interfaces.

**Acknowledgements** The authors are thankful to Mr. V.N.S.K. Chaitanya, Scientific officer, Nuclear Fuel Complex for his support in weld fabrication. The authors are also thankful to the School of Engineering Sciences and Technology, University of Hyderabad for supporting the work.

## References

1. Sakihama H, Tokisue H, Katoh K (2003) Mechanical properties of friction surfaced 5052 aluminum alloy. *J Mater Trans* 44(12):2688–2694
2. Oikawa H, Saito T, Yoshimura T, Nagase T, Kiriyaama T (1996) Spot welding of aluminium clad steel to steel or aluminium: joining steel to aluminium with an intermediate layer. *Jpn Weld Soc* 14:69–80
3. Kikuchi M, Takeda H, Morozumi SJ (1984) Friction welding of aluminium and aluminium alloys with steel. *J Jpn Inst Light Met* 34:165–173
4. Milani A, Paidar M, Khodabandeh A, Nategh S (2016) Influence of filler wire and wire feed speed on metallurgical and mechanical properties of MIG welding–brazing of automotive galvanized steel/5754 aluminum alloy in a lap joint configuration. *Int J Adv Manuf Technol* 82:1495–1506
5. Taban E, Kaluc E (2007) Comparison between microstructure characteristics and joint performance of 5086-H32 aluminium alloy welded by MIG, TIG and friction stir welding processes. *Kov Mater* 45(5):241
6. Zhang HT, Feng JC, He P (2008) Interfacial phenomena of cold metal transfer (CMT) welding of zinc coated steel and wrought aluminium. *J Mater Sci Technol* 24:1346–1349



7. Cornacchia G, Cecchel S, Panvini A (2017) A comparative study of mechanical properties of metal inert gas (MIG)-cold metal transfer (CMT) and fiber laser-MIG hybrid welds for 6005A T6 extruded sheet. *Int J Adv Manuf Technol* 94:2017–2030
8. Cam G, Ventzke V, Jorge F, Gonthier-Maurin P (1999) Characterization of electron beam welded aluminium alloys. *Sci Technol Weld Joining* 4(5):317–323
9. Wang T, Zhang B, Feng J, Zhong S (2014) Experimental study of electron beam welded pure aluminum to Q235 steel joint with beam deflection. *Trans China Weld Inst* 35(6):69–72
10. Wang T, Zhang Y, Li X, Zhang B, Feng J (2017) Influence of beam current on microstructures and mechanical properties of electron beam welding-brazed aluminium—steel joints with an Al<sub>5</sub>Si filler wire. *Vacuum* 141:281–287. <https://doi.org/10.1016/j.vacuum.2017.04.029>
11. Dinda SK, Sk MB, Roy GG (2016) Microstructure and mechanical properties of electron beam welded dissimilar steel to Fe-Al alloy joints. *Mater Sci Eng: A*. <https://doi.org/10.1016/j.msea.2016.09.050>
12. Sravanthi SS, Acharyya SG, Phani Prabhakar KV, Padmanabham G (2018) Effect of welding parameters on the corrosion behaviour of dissimilar alloy welds of T6 AA6061 Al-galvanized mild steel. *Mater Eng Perform* 27(10):5518–5531. <https://doi.org/10.1007/s11665-018-3596-z>
13. Sravanthi SS, Acharyya SG, Phani Prabhakar KV, Padmanabham G (2019) Integrity of 5052 Al-mild steel dissimilar welds fabricated using MIG-brazing and cold metal transfer in nitric acid medium. *J Mater Process Technol* 268:97–106. <https://doi.org/10.1016/j.jmatprotec.2019.01.010>
14. Çam G, Santos JF, Koçak M (1997) Laser and EB weldability of Al-alloys: literature review. GKSS 97/E/25, GKSS Research Center, Geesthacht, Germany, IIW Doc. IX-:1896–98
15. Bakish R, White S (1964) *Handbook of Electron Beam Welding*. Wiley, New York
16. Tonpe S, Saibaba N, Jayaraj RN, Ravi Shankar A, Kamachi Mudali U, Raj B (2011) Process development for fabrication of Zircaloy–4 dissolver assembly for reprocessing of spent nuclear fuel. *Energy Procedia* 7:459–467
17. Standard test method for determining the susceptibility to Intergranular Corrosion of 5XXX series Aluminium alloys by mass loss after exposure to Nitric Acid (NAMLT Test), G 67 – 04. American Society for Testing and Materials (2004)
18. Wan S, Muda HW, Nurul S, Nasir M (2016) Effect of welding heat input on microstructure and mechanical properties at coarse grain heat affected zone of ABS grade a steel. *ARPN J Eng Appl Sci* 10(15). ISSN 1819-6608

# Evaluation and Impacts on Mechanical Behavior of Friction Stir Welded Copper 2200 Alloy



L. Srinivas Naik and B. Hadya

**Abstract** In the recent years, friction stir welding (FSW) is playing vital role in automobile and aerodynamic industrial applications. Butt joint configuration is the mainstream of FS welding. In this research work, copper alloys are used for analysis and evaluation by FS welding. The endeavor of this work is to find out the achievability of FS welding process by welding pair of copper plates and study the consequences on the physical properties and mechanical characteristics of welded joints. These geometries are used comprehensively in aerodynamic vehicles, in naval vessels, marines. Since of its weak weldability, it is not comprehensively used in automobile industries. To conquer this barrier, weldability analysis is carried out with Cu 2200 copper alloys using a high-speed steel H13 tool. On further attempts, investigations conceded an influence of elevated revolving speed of tools 900 rpm, axial force 5KN, and welding feed 31.25 mm/sec on tensile strength of 254.25 N/mm<sup>2</sup>, hardness of 451HRB, and impact test of 34 J of copper alloys joint. Vertical milling machine (VMM) is used for conducting experiments. Determining the good tensile strength is main aim of investigation. The end results show that axial load and tensile strength are inversely related, whereas if tool rotating speed and welding velocity increase, the tensile strength increases.

**Keywords** Friction stir welding (FSW) · Copper alloy · Tensile strength · Mechanical properties · Rotational speed

---

L. Srinivas Naik (✉) · B. Hadya  
Department of Mechanical Engineering, Osmania University, Hyderabad, Telengana, India  
e-mail: [naiks.phd@gmail.com](mailto:naiks.phd@gmail.com)

B. Hadya  
e-mail: [hadyaou@gmail.com](mailto:hadyaou@gmail.com)

© Springer Nature Singapore Pte Ltd. 2020  
G. S. V. L. Narasimham et al. (eds.), *Recent Trends in Mechanical Engineering*,  
Lecture Notes in Mechanical Engineering,  
[https://doi.org/10.1007/978-981-15-1124-0\\_21](https://doi.org/10.1007/978-981-15-1124-0_21)

## 1 Introduction

At present days, researches are focusing on development of rapid and eco-friendly, pleasant processes in manufacturing industries and in this view FS welding processing has become prominent. FSW is a solid-state welding process which was originated and developed by The Welding Institute (Cambridge, UK) in 1991 [1–3]. The FSW technology is creature beleaguered by contemporary aircraft fabrication for high execution configurationally applications. FS welding strongly diminishes residual stresses and also dwindles the occurrence of distortions correlated to conventional welding techniques [4]. FSW technology requires rigorous understanding procedure and subsequent mechanical properties of welds that can be used in the fabrication of components for aerodynamic applications [5]. In this process, a revolving tool drives into the plate material and translated along coalition of pair welded plates. The material gets heated by abrasion and extruded around tool and tool shoulder produces large pressure which forges the material. FSW has several advantages, for instance, esteemed repeatability, quality joints, minimum energy process essentials, precise external control, and no need for extraordinary preparation of samples, low formation of solid waste or air pollution, and eco-friendly [6, 7]. Moreover, this mechanization is ideal for copper metal alloys which are contemplated arduous to be welded by traditional welding technology or even for contradictory alloys. Moreover, weld joint is acquired by the distortion of material at below melting point temperatures, thereby reducing the troubles correlated to residual stresses and distortions. For the reasons explained above, this FSW technique has become significant in applications of aerospace, naval industries, and transportation industries [8]. In FS welding process, weld joint is created by pervasive a particularly premeditated nonconsumable rotating tool shouldered probe into the edge of pair of plates and stirring the length of weld path to stir and heat the thin plate materials by generating friction among the slim plates surface and shoulder the material motion engendered by the probe movement. As weld tool moves the length of weld path, the heat-affected material produced from the two plates flow and mix together below the recrystallization temperature and makes the welded joint [9–11]. Impact of process specifications on the weld order and the weld properties like feed rate, spindle speed, travel tool geometry, tool tilt angle, orientation of probe axes, axle force, probe length and diameter, and shoulder diameter were investigated to achieve high eminence welds [12–17]. In this research work, welding parameter effects on mechanical properties of Copper 2200 joints were studied and show an impact of welding feed on fatigue behavior. FSW joints usually consist of four special zones, and they are publicized in Fig. 1, such as Heat-affected zone (HAZ), unaffected parent metal (UAZ), thermo-mechanically affected zone (TMAZ), and FS processed zone or friction nugget zone (FNZ) [18–21]. The material flow behavior by action of revolving tool will show its impact on formation zones.

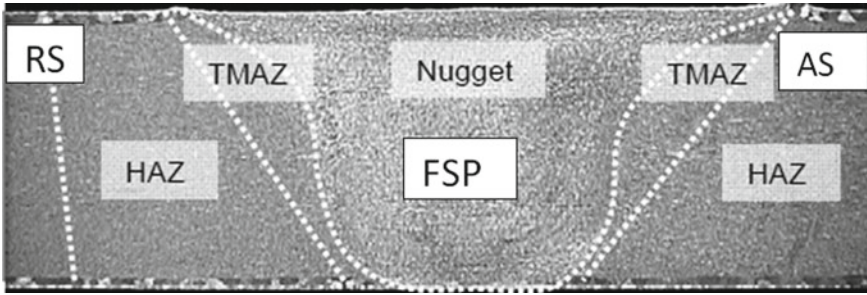


**Fig. 1** Various types of weld rezone

**Table 1** Chemical composition of copper 2200

Material	Cu	Fe	Pb	Zn
Copper C2200	94–96%	0.05%	0.05%	Remaining

**Table 2** Chemical composition of H13 tool

Material	Cu	Cr	Fe	Mo	Si	V
Copper 2200	0.4%	5.25%	95%	1.33%	1	1

## 2 Material and Methodology

In this work, study of copper alloy material sheet used the chemical composition constituted in Tables 1 and 2 represents H13 composition.

## 3 Experimental Method

Plates of Cu alloys, Cu 2200 of size  $200 \times 75 \times 5$  mm, were chosen for butt joint welding. Vertical milling machine of capacity 10hp with maximum revolving speed of spindle of 1800 rpm is manufactured by HMT used for welding. The weld tool used in this process quenched H13 and tempered steel with tool shoulder and probe diameter is 20 mm and 6 mm, respectively, with probe pin 4.5 mm long. Exposed in Fig. 2 and tilted angle by  $1^\circ$  provides compressive pressure to SWZ. As tool shoulder diameter increases, sticking torque increases, reaches maximum then decreases (Figs. 3 and 4).

Initially, the sheets to be welded are held in reserve on backing plate and tightly fixed to machine table among facilitate of fixtures, because throughout welding process the plates may perhaps get separated appropriate to force arising. Before welding process, a hole of 6 mm diameter on interface of the working plates was drilled by

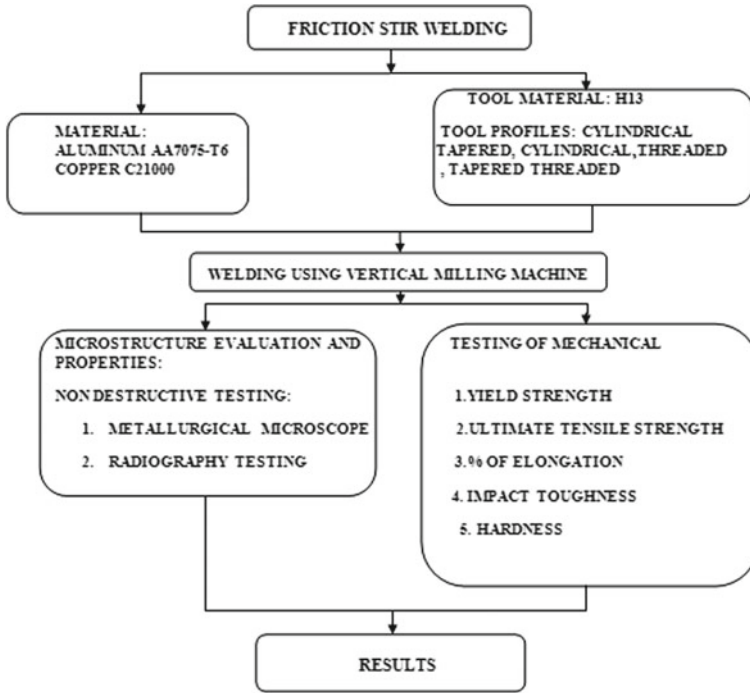
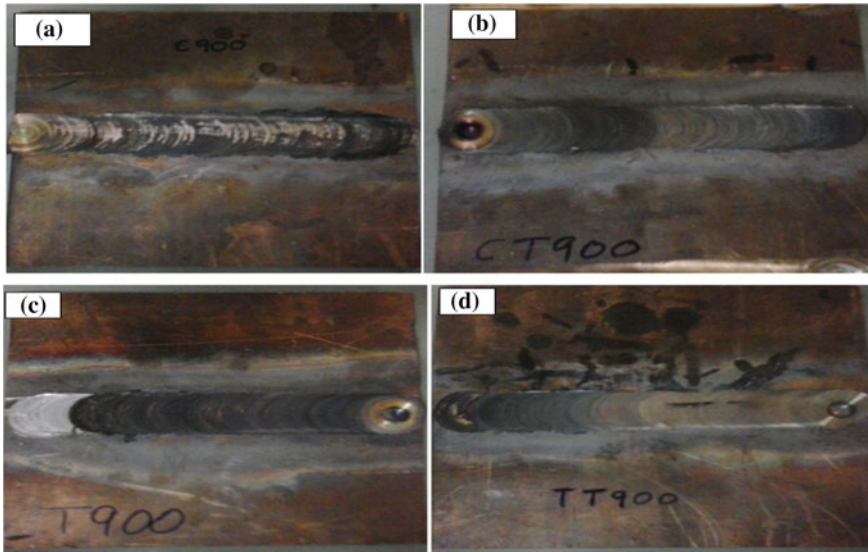


Fig. 2 Flowchart of methodology



Fig. 3 Experimental FS welding setup

which plunging pressure on the tool probe gets eliminated in this manner increasing life of tool probe. Welding tool injected into the spindle shaft and the spindle is rotated at preferred welding speed. Now the probe of welding tool is gradually penetrated into pre-drilled hole and the weld tool is kept revolving in the pre-drilled hole for few minutes without applying movement so that an adequate quantity of heat is generated among tool and base material because of friction. The temperature of welded joints is such that the plastic flow of material is possible during welding period. Weld joint is formed at the interface of two places on giving movement to tool and owing to plastic flow of material. To interpret the consequence of tool probe profile and spindle revolving speed on mechanical properties of FS welded joint,



**Fig. 4** FSW on copper plates (a) cylindrical, (b) cylindrical threaded, (c) taper, (d) taper threaded

the welding travel speed is constant at 31.25 mm/sec. After welding is finished, the weld tool is pulled out the joint after stopping the feed. The experiment is repeated by altering weld tool geometry and spindle rotational speed and the welding was executed on copper work plates.

Frictional heat energy is engendered among material of plates and connects the wear-resistant welding tool pin probe and shoulder by moving tool probe in opposition to workpiece, and vice versa. This heat and heat produced by mechanical action mixing development and adiabatic heat generated within material cause the stimulated materials to become softer without attainment of recrystallization temperature. As pin probe rotates in path of welding, the most important face of probe, abet by particular pin shape, forces plasticized material back of probe at the few minute as applying generous forging load to unite weld metal.

## 4 Result and Discussions

### 4.1 Tensile Testing

Tensile properties of analogous copper alloys FS weldments were determined by conducting tensile tests in universal testing machine (UTM) at tool spindle rotational speed (900 rpm) according to ASTM standards. It is observed that tensile strength of FSW welds is directly associated to the travel welding speed. Hardness fall was

noticed in stir region leading to softening of material and this softening in HAZ on advancing side of the weld joint corresponds to failure region in tensile tests.

The FS welding copper joints are produced at invariable forwarding tool feed of 31.25 mm/min., and invariable tool spindle rotation speed of 900 rpm and it was observed that ultimate tensile strength is maximum and same for both cylindrical and taper tool joints. A yield strength of cylindrical tool and taper tool is lower than the weld joint prepared by cylindrical threaded tool. It is furthermore observed that % elongation is more for taper tool joint. The cylindrical threaded joint gives 10.56% elongation and the cylindrical tool joint gives 16.46% elongation, whereas the % of elongation in taper tool joint is 26.98%.

## ***4.2 Hardness Testing***

Hardness of FS weldments was determined by conducting Rockwell hardness tests of similar copper alloys at constant rotational speed of 900 rpm. Hardness changes in weld material with effect of heat during weld process. The hardness profiles obtained at weld center at nugget area were lower than thermo-heat-affected area and heat-affected area. It is observed that maximum hardness is obtained with cylindrical tool and minimum hardness with cylindrical thread tool.

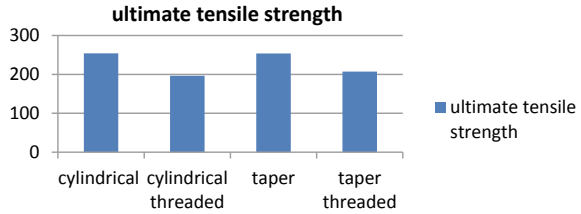
## ***4.3 Impact Testing***

An impact test energy of copper plates FS welding was determined by conducting Charpy impact test at spindle speed of 900 rpm which is constant and tool feed speed is 31.25 mm/min in accordance with ASTM standards. It is distinguished that impact strength is least at tapered threaded tool joint compared to all other joints. This least strength is due to inappropriate fusion and porosity. As there is no much variation in strength of joints, it may be concluded that type of tool shape has no effect on the impact strength.

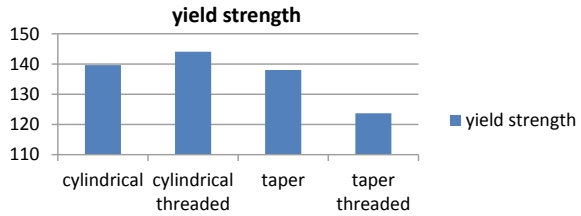
## ***4.4 Ultimate Tensile Strength (UTS)***

Figure 5 is bar chart showing the UTS (N/mm<sup>2</sup>) of FSW copper (Cu) joints with dissimilar tool probe profiles at persistent tool spindle rotation speed and tool forwarding speed of 900 rpm and 31.25 mm/min, respectively. It is observed that UT strength is least at cylindrical threaded tool joint and topmost at cylindrical and tapered tool joints. This least UT strength is due to inappropriate fusion and porosity.

**Fig. 5** UTS of FSW copper joints



**Fig. 6** Yield strength of FSW copper joints



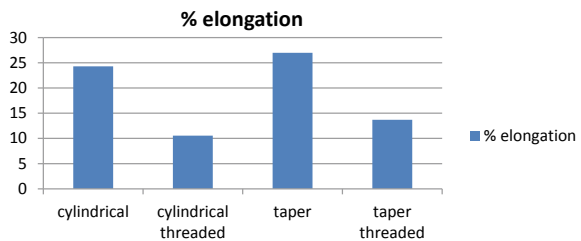
### 4.5 Yield Strength

Figure 6 is bar chart showing the acquiesce strength (N/mm<sup>2</sup>) of FS weld copper joints among dissimilar tool probe shapes prepared at constant tool spindle rotation alacrity and tool forwarding speed is 900 rpm, 31.25 mm/min, respectively. It is pragmatic that acquiesce strength is extreme at cylindrical threaded tool joint of 143 N/mm<sup>2</sup> and lowest at taper threaded tool joint of 130 N/mm<sup>2</sup>. This least acquiesce strength is due to inappropriate fusion and porosity and tool wear.

### 4.6 Percentage Elongation

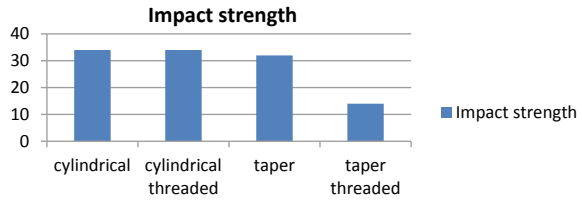
Figure 7 is bar chart showing the rate elongation of FS welding copper welded joints with diverse tool probe profiles processed at invariable tool spindle rotation speed of 900 rpm and tool feed of 31.25 mm/min. It is evident that rate elongation is tremendous in joint framed by taper tool. The maximum elongation is 26.98% in

**Fig. 7** % Elongation on FSW copper welded joints





**Fig. 8** Impact strength of weld joints



taper tool and minimum at cylindrical threaded tool joints during the tensile test (Fig. 8).

#### 4.7 Analysis of Impact Strength

Impact strength (J) of FS welded copper joints through special tool shapes equipped at stable tool rotary motion speed 900 rpm and tool forward feed 31.25 mm/min. It is recorded that impact strength is almost similar, minimum on tapered threaded tool and maximum on cylindrical and cylindrical threaded tool. The cause of minimum strength in taper threaded tool joint is due to improper fusion and porosity.

### 5 Conclusion

Experimental considerations on FS welding of Cu 2200 are conducted to optimize the FSW parameters. The welding was effectively executed with four separate types of tools cognate as cylindrical tool, cylindrical threaded tool, taper tool, tapered threaded tool by constant rotational tool speed, and tool feed is 31.25 mm/min. During welding, weld speed and tool feed are constant for all tool profiles.

The repercussions show that for copper, the extremity yield strength is observed in cylindrical threaded tool scheduled 900 rpm followed by cylindrical tool and taper tool. The minimum yield strength is found in taper threaded joint. During welding process, well stirring of plasticized metal was achieved due to the appearance of threads on the tool. Hence, it is completed that copper welding obtained by cylindrical threaded tool prob at 900 rpm is best suited for welding.

### References

1. Mahoney MW, Rhodes CG (1998) Properties of friction welded 7075 T651 aluminum. *Metall Mater Trans A* 29:1955–1964
2. Khorrami MS, Kazeminezhad M, Miyashita Y, Kokabi AH (2017) Improvement in the mechanical properties of Al/SiC nanocomposites fabricated by severe plastic deformation and FSW.

- Int J Miner Metall Mater 24:297
3. Longo M, D'Urso G, Giardini C, Ceretti E (2012) Process parameters effect on mechanical properties and fatigue behavior of friction stir weld AA6060 joints. *J Eng Mater Technol* 134(2):021006 (March 27)
  4. Adamowski J, Szkodo M (2007) Friction Stir Welds (FSW) of aluminum alloy AW6082-T6. *J Achiev Mater Manuf Eng* 20(1–2):403–406 (February)
  5. Aziziech M, Kokabi AH, Abachi P (2011) Effect of rotational speed and probe profile on microstructure and hardness of AZ31/Al<sub>2</sub>O<sub>3</sub>, nanocomposites fabricated by FSWP. *Mater Des* 32(2):2034–2044
  6. Nandan R, DebRoy T, Bhadeshia HKDH (2008) Recent advances in friction stir welding-process, weldment structure and properties. *Prog Mater Sci* 53:980–1023
  7. Mishra RS, Ma ZY (2002) Friction stir processing a novel technique for fabrication of surface composite. *Mater Sci Eng* 341(2):307–310
  8. Nagamalleswara Rao A, Srinivas Naik L, Srinivas C (2017) Evaluation and impacts of tool profile and rotational speed on mechanical properties of friction stir welded copper 2200 alloy. *Mater Today Proceeding* 4(2017):1225–1229
  9. Srinivas Naik L, Jush Kumar S, Murahari K (2016) Tool design and analysis of friction stir welding process by using FEA. *JMER* 6(9):7–16
  10. Zhang Z, Zhang HW (2007) Material behaviors and mechanical features in FSW process. *Int Jr Adv Manuf Technol* 35:86–100
  11. Kulekci MK, Sik A, Kaluc E (2008) Effects of tool rotation and pin diameter on fatigue properties of stir weld lap joints. *Int Jr Adv Manuf Technol* 36:877–882
  12. Arora A, Mehta M, De A, DebRoy T (2012) Load bearing capacity of tool pin during friction stir welding. *Int J Adv Manuf Technol* 61:911–920
  13. Emamikhah A, Abbasi A, Atefat A, Givi MB (2014) Effect of tool pin profile on FS butt welding of high zinc brass. *Int J Adv Manuf Technol* 71:81–90
  14. Zhao Y, Huang X, Li Q, Huang J (2015) Effect of FSP with B<sub>4</sub>C particles on the microstructure and mechanical properties of 6061 Al alloy. *Int J Adv Manuf Technol* 78:1437–1443
  15. Zahmatkesh B, Enayati MH (2010) A novel approach for development of surface nano composite by FSP. *Mater Sci Eng A* 527:6734–6740
  16. Aziziech M, Kokabi AH, Abachi P (2011) Effect of rotational speed and probe profile on microstructure and hardness of AZ 31/Al<sub>2</sub>O<sub>3</sub> nano composites fabricated by FSW. *Mater Des* 32:2014–2041
  17. Suvama Raju L, Kumar A (2014) A novel approach for fabrication of Cu-Al<sub>2</sub>O<sub>3</sub> surface composites by FSP. *Procedia Mater Sci* 5:434–443
  18. Li S, Chen Y, Zhou X (2019) High strength titanium alloy/steel butt joint produced via FSW. *Mater Lett* 234:155–158 (Elsevier)
  19. Kumar R, Pancholi V, Bharti RP (2018) Material flow visualization and determination of strain rate FSW. *J Mater Process* 255:470–476 (Elsevier)
  20. Liu CY, Jiang HJ, Zhang B (2018) High damping capacity of Al alloy produced by FSW. *Mater Charact* 136:382–387 (Elsevier)
  21. Shah LH, Guo S, Walbridge S, Gerlich A (2018) Effect of tool eccentricity on the properties of FSW AA 6061 alloy. *Manuf Lett* 15:14–17 (Elsevier)

# Error Compensation Strategies for Workpiece Deflection During End Milling of Thin-Walled Straight and Curved Geometries



Hareendran Manikandan, S. Sreejith, Kanjiyangat Vivek, C. Sasi Jayaram and P. A. Azeemhafiz

**Abstract** Thin-walled parts and their precision manufacturing is finding importance in the field of aerospace as well as automobile component manufacturing industries. The value of machining of thin walls like honeycomb structures increases because of the efficiency of such parts in any assembly as robust members which results in reducing the fuel usage and increasing strength of the system. In this part of research work, characterization of surface errors and compensation of errors by offline toolpath modification techniques is discussed. Major concerns of machining in end milling and cutting conditions variables include axial as well as radial depths of cut. After validation of errors by some results of cutting experiments toward predicted using a model, compensation strategies negating the errors are proposed. The results are directly applicable to similar manufacturing of various complex parts.

**Keywords** Thin-walled part · Workpiece and tool deflection · Surface error · Error compensation · Offline toolpath compensation method

---

H. Manikandan (✉)  
National Institute of Technology, Calicut, Kerala, India  
e-mail: [manikandan.h@pilani.bits-pilani.ac.in](mailto:manikandan.h@pilani.bits-pilani.ac.in)

S. Sreejith  
Gurudeva Institute of Science and Technology, Kottayam, Kerala, India  
e-mail: [sreejith.astro@gmail.com](mailto:sreejith.astro@gmail.com)

K. Vivek  
College of Engineering, Eranad Knowledge City, Manjeri, Malappuram, Kerala, India  
e-mail: [iamvivekka@gmail.com](mailto:iamvivekka@gmail.com)

C. S. Jayaram  
Ilahiya College of Engineering and Technology, Muvattupuzha, Kerala, India  
e-mail: [jayaramcs007@gmail.com](mailto:jayaramcs007@gmail.com)

P. A. Azeemhafiz  
College of Engineering, Prince Sattam Bin Abdulaziz Univeristy, Al Kharj, Saudi Arabia

## 1 Introduction

Precision contour machining is a crucial important operation in engineering of today's world. The quality of parts is inspected for dimensional specifications, geometric accurateness, component surface quality finish, and physical and mechanical properties. Machining of flexible parts is most wanted process in part manufacturing industry. Obtaining the exact shape in such components is contingent on the use of computer aid for describing accurate cutting tool trails. Program preparation for intricate geometries is done by toolpath alteration and validation methods.

Peripheral machining of thin workings is a largely practiced production process in industries. Thin components are having very high aspect ratio. The wall thickness of the part is stepped down again by exterior milling using a protracted, multi-fluted helical end mills. The peripheral milling of works is complex, where intermittently fluctuating cutting forces affect the flexible tool and cut plate both at static status and dynamic status. Dimensional and geometrical errors are the result of static tool and workpiece deflections, and poor surface finish is caused by dynamic displacements produced in milling. The surface errors between the tool and the workpiece are function of interval and rigidity of tool, workpiece, and machine tool.

Exterior error is caused mostly by the rebound phenomena of workpiece and tool due to normal component of cutting force of the tool and the workpiece for the duration of machining, which does not get rid of the substance as per design. If the mill and cut workpiece are rigid and are firm, the rebound that happened on the end mill and workpiece is lower and can be ignored. In the peripheral milling of a very flexible component using multi-fluted end mill, the deflection is visibly high and not negligible. There are several workpiece-tool mathematical models which consider the elements such as part-tool rebound and agreement in machining. The errors are usually dealt with a trial-and-error NC program authentication procedure which is time-consuming and expensive. Motivated by the necessity to simplify interval and price, manufacturers are vigilant to find out lateral techniques for NC reprogramming methods centered on offline error forecasting and tool-trail recompense in tooling.

Error avoidance and error reparation are the major two techniques to deal with the inaccuracies in the parts. The machine tool is fine-tuned to avoid the errors and there is a practical limit for this process anyhow. The other technique of error recompense derives to operate since industries demand more versatile and error-proof machining at lower economic rates. Dissimilar to the case of error evasion, no fine-tuning of machine tool is made to evade the error. Rather, no matter what the error is, how much is the error considered or forecasted, it will be recompensed or negated with some undercut or overcut by manipulating the cutting strategy. Error compensation is considered as a more important method for error elimination when compared to error avoidance. Figure 1 demonstrates the nature of occurrence of positive surface error during end milling.

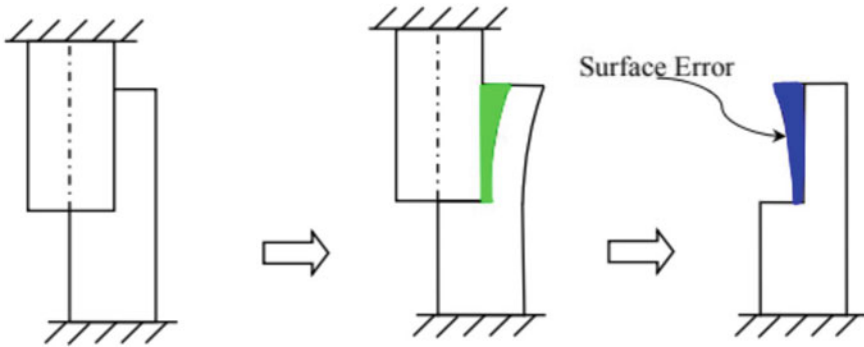


**Fig. 1** Positive surface error due to work specimen deflection in end milling

## 2 Literature Review

Berend Denkena et al. [1] studied about tool deflection and its effect on workpiece and its geometry. The study gives the glimpses of currently available practices of compensation for tool deflection errors. In the work, they used strain sensors. A formulation based on rapid prototyping is also accompanied by the method. Finally, two compensation strategies for tool deflection with the help of feed control and position control are discussed and experimentally validated.

Gururaj Bolar et al. [2] suggested that due to the sensitivity of stressed working parts, enhancing component accuracy and value for the duration of machining of high aspect ratio walled components has constantly stayed as a tough issue. Therefore, process parameters are to be selected cautiously to obtain the adequate quality. Experimentations were performed on end milling of aluminum alloy AL 2024-T351 by means of a repository of determined critical constraints. Regression analysis and variance analysis were operated on the trial data repositories to learn the impact of cutting constraints in attaining proper cutting force and third-order deviations. Three-dimensional surface topographical study of machined parts made it visible that variation due to deflection and chatter is more at the free end of the thin-walled components. Experimental research derived solid mathematical models for exact forecast of the cutting force and energy and surface roughness for given cutting environments.

S. Ratchev et al. [3] announced a multiple-stage machining error recompense method concentrated on errors caused by forces in machining of high aspect ratio components. The forecast method incorporates the deflection error of the machined component in entire horizon of the tool trail. The environments for machining or cutting environments are updated at each feed interval when the cutting force, energy, and rebound are coming in balance. The deviation and errors are forecasted by means of a mathematical flexible force-deflection model using software. The error

recompense and negation techniques are virtually visualized using numerical simulation application and are experimentally tested by cutting experiments. The error reparation and correction are centered on altering the tool trail taking the projected machining error into account.

Weifang Chen et al. [4] studied that deflection prediction and error negation by compensation are absolutely proper methods to develop machining precision in machining of high aspect ratio components. In this work, it is found that the distortion due to machining of the last cut stratum will affect the desired depth of cut of the present stratum. Therefore, a dynamic model is prepared to forecast the multistrata variations such as deformations in machining a high aspect ratio part. The model is endorsed by investigating the virtual realization outcome with the trial cutting results. An innovative method of dynamic error reparation is projected, in which the machining error is recompensed at each level.

L. Feng et al. [5] developed a firm and precise modeling for the flatness faults of machine tools which were significantly vital for the process of error recompensing. The reparation experimentations are focused to substantiate the accurateness of the spatial straightness error model and the efficiency of the error recompense scheme.

Jie Gu et al. [6] studied that currently, the claim of highly geometrically accurate parts requires more perfect and adaptable machine tools with recompensing system. Chuxiong Hu et al. [7] led a key investigation theme for multiple axis CNC systems. In this work, the challenges of correct contouring error assessment as well as extraordinary-routine contouring regulation are dealt with. Dissimilar to any prevailing regular geometric guesstimating approaches, the projected outline computes the contouring error over a mathematical design algorithm. The proposed contour recompense plan will be able to be apprehended iteratively for additional progress of contouring routine. The results reveal that the projected system can accomplish not only closely faultless contouring error appraisal but also understandable elevation of contouring routine precision.

Zhou-Long-Li et al. [8] studied about dimensional precision of flexible high aspect ratio space and automobile components which can be can be debased by the extreme deflections for the duration of cut. The work projected a technique to forestall the geometric exterior deviation errors instigated by movement and rebounds of both workpiece and end mill of high aspect ratio components. The end mill is considered as a free cantilevered beam. The overall rigidity index of the high aspect ratio component varies as the aluminum is detached in the form of chips step by step and the tool interaction locus proceeds from one point to another. The cutting energy and forces are spread above together at the cutting tool and the component in the meeting area, and the consequence of rebounds on the tooth engagement is formulated. The result of radial run out and total run out of the tool is reflected in chip width, which in turn regulates the cutting force forecast.

S. Ratchev et al. [9] account on progressive error estimation and recompense plan precisely on energy-prompted errors in machining of high aspect ratio thin-walled monolithics. The surface error is forecasted using a conjectural flexible energy-deflection model and recompensed by optimizing the tool trail preceding to machining. The error recompense design is virtually generated using NC confirmation tools and practically endorsed. The trial results reveal the complete error in the flexible machining can be apprehended and forecasted with identical extraordinary accuracy using the projected flexible force-deflection model and a huge proportion of it will be able to be excluded through the suggested error recompensing strategy.

### **3 Experimental and Computational Work**

#### ***3.1 Error Prediction Using Model (MATLAB)***

A MATLAB program takes the input cuttings conditions and calculates the force by applying convolution conditions to cantilever beam theory and the forces are used to predict the surface error and the same amount of error will be used to recalculate the toolpath so that the material removal is complete as per the design. The detailed algorithm is given below (Fig. 2).

#### ***3.2 Offline Toolpath Error Compensation***

In this method, toolpath will be corrected by deflection model until the desired contour is obtained. Since error compensation is done offline, it will not hamper productivity. Once a cutting program is generated using the software according to the original design of the part then it is revised using the deflection model so that toolpath is modified by modifying the CNC program itself. Uniqueness of current work is increase in multiple iterations for the compensation process so that the surface error is almost eliminated by instantaneous change of the tool position and improvising the entire path. Figure explains this process well. As the milling cutter moves on the periphery, it covers the entire spring back volume and when it completes the cut the product results as per the primary design which is not materialized during cuts without the deflection models (Fig. 3).

Fig. 2 Flowchart for error compensation algorithm

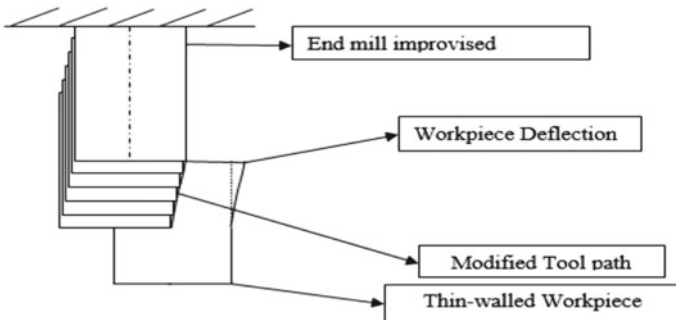
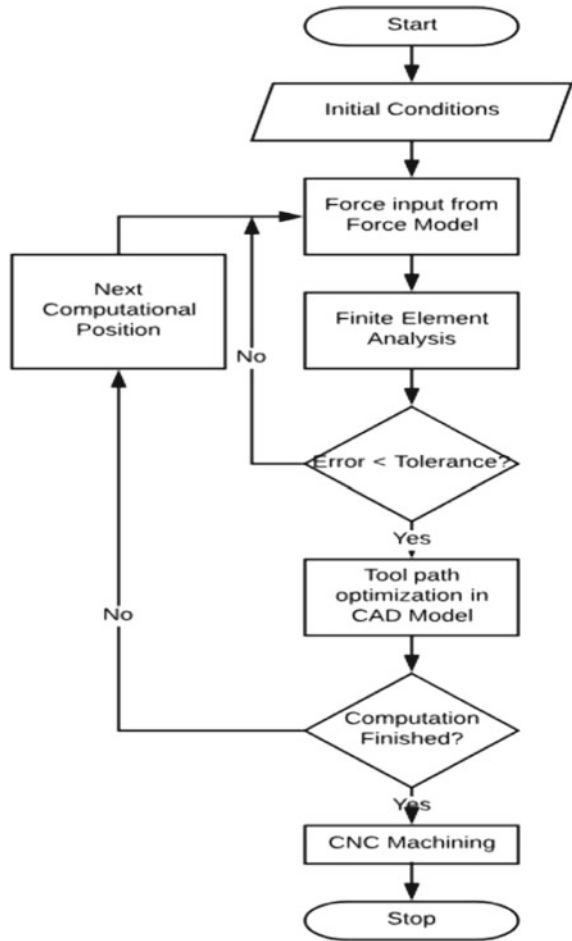


Fig. 3 Error compensation by toolpath modification



**Table 1** Cutting conditions for validating experiments

Workpiece type	Tool overhang (mm)	Thickness of workpiece (mm)	Height of workpiece (mm)
Straight wall	70	5	60
Elliptical wall	70	10	60
Circular Wall(Inner)	70	6	85
Circular Wall(Outer)	70	6	85
ADOC	RDOC	Feed(dry cutting)	Cutting speed
20	3	102	1020
20	3	102	1020
45	2	102	1020
45	2	102	1020

NB. Tool used is 16 mm 4 fluted HSS end mill (30° helix)

### 3.3 *Experimental Procedure for Error Characterization, Compensation, and Validation*

See Table 1.

### 3.4 *Error Recompense Authentication on a CNC Machine Center*

Figures 4, 5, 6, and 7.

## 4 Results and Discussion

The initial and final programs for elliptical cut as per design and the program as per modified toolpath algorithm are different as the deflection values are incorporated in the modified one. The parts during validation cuts are measured with CNC Touch Trigger Probe (Renishaw OMP) before and after cuts and surface error are measured by subtracting initial touch point from final touch point using distance formula and then one more subtraction with radial depth of cut at that position of Z. This should give a value tending to zero which is happening in real case and thus the model can be declared as effective and working for production environments.

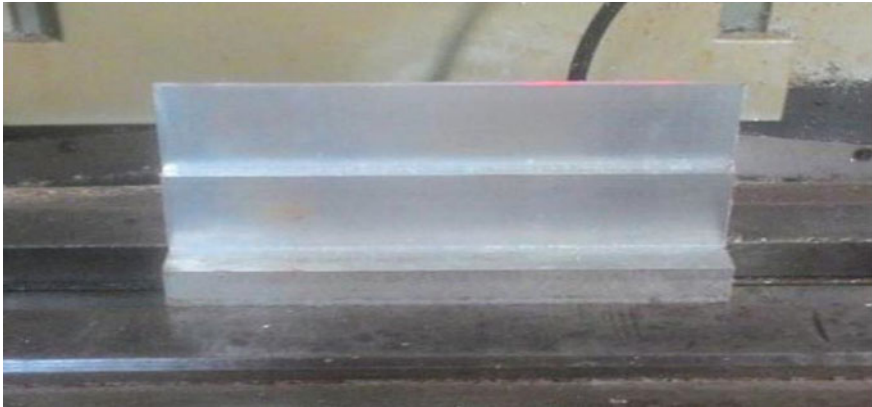


**Fig. 4** Straight-walled part after experimental cut

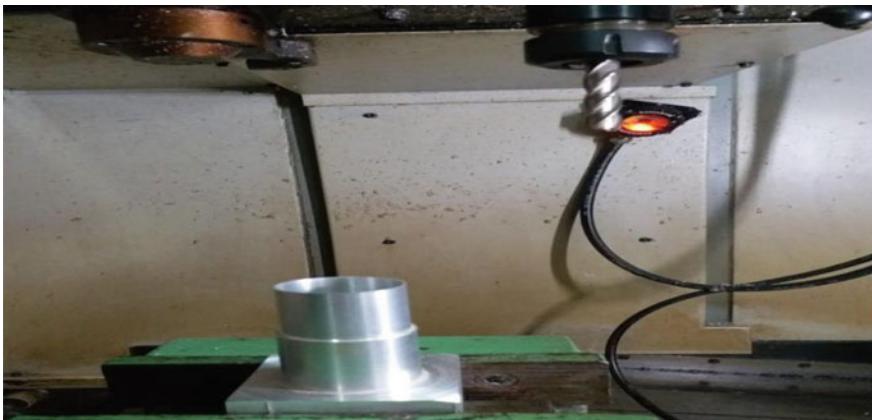


**Fig. 5** Circular-walled part after experimental cut

## **5 Concluding Remarks**

Important observation is relationship between iteration density and the surface error values direct proportion. Earlier methods which gave compensation results using similar algorithms were having less reduction due to less number of iterations. So this gives offline tool path compensation as a powerful method to reduce the surface error and its use is recommended as repeatedly iterative and intense in order to reach almost elimination of error in cutting programs.



Fig. 6 Elliptical-walled part experimental setup

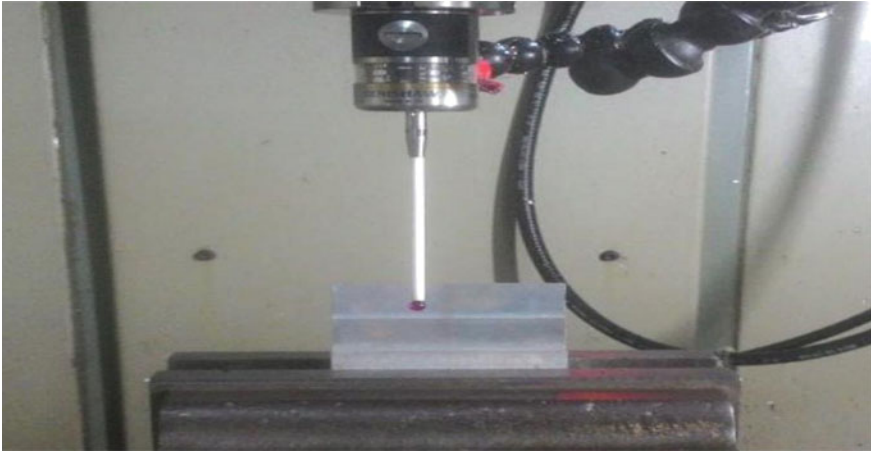


Fig. 7 Measurement using Renishaw touch trigger probe

## References

1. Denkena B, Boujnah H (2018) Feeling machines for online detection and compensation of tool deflection in milling. *CIRP Ann—Manuf Technol* 67:4
2. Bolar G, Das A, Joshi SN (2018) Measurement and analysis of cutting force and product surface quality during end-milling of thin-wall components. *Measurement* 121:190–204
3. Ratchev S, Liu S, Huang W, Becker AA (2006) An advanced FEA based force induced error compensation strategy in milling. *Int J Mach Tools Manuf* 46:542–551
4. Chen W, Xue J, Tang D, Chen H, Qu S (2009) Deformation prediction and error compensation in multilayer milling processes for thin-walled parts. *Int J Mach Tools Manuf* 49:859–864

5. Feng WL, Yao XD, Azamat A, Yang JG (2015) Straightness error compensation for large CNC gantry type milling centers based on B-spline curves modeling. *Int J Mach Tools Manuf* 88:165–174
6. Gu J, Agapiou JS (2016) Assessment and implementation of Global offset compensation method. *J Manuf Syst* 48:7
7. Hu C, Wang Z, Zhu Y, Zhang M (2018) Accurate three-dimensional contouring error estimation and compensation scheme with zero-phase filter. *Int J Mach Tool Manuf* 128:33–40, May
8. Li ZL, Tuysuz O, Zhu LM, Altintas Y (2018) Surface form error prediction in five-axis flank milling of thin-walled parts. *Int J Mach Tools Manuf* 128:21–32
9. Ratchev S, Liu S, Becker AA (2005) Error compensation strategy in milling flexible thin-wall parts. *J Mater Process Technol* 162–163:673–681

# Effects of Micro-EDM Parameters on the Surface Integrity of the Micro-Holes Fabricated on Nickel Sheet



Pankaj Kumar and Manowar Hussain

**Abstract** This paper presents the machining of the nickel sheet using The micro-EDM process. The effect of machining parameters such as pulse on time and gap voltage on the surface integrity parameters such as recast layer thickness, heat affected zone, change in micro-hardness of the workpiece surface and metallurgical transformation in the machined samples has been reported. It is found that ultrasonic vibration given to the workpiece, results in a reduction in the thickness of the recast layer and varies from 7 to 22  $\mu\text{m}$ . The hardness of the fabricated micro-holes improves significantly on the introduction of ultrasonic vibration to the workpiece and was in the range of 116–141HV. In this study, heat-affected zone was not observed in optical as well as in SEM images. The result of the EDS analysis shows that less amount of the residuals of the carbon and oxygen were present over the fabricated holes.

**Keywords** Micro-hole · Micro-EDM · Nickel sheet · Ultrasonic vibration · Surface topography · Micro-hardness

## 1 Introduction

In recent years, the needs for the development of products containing micron-size features are growing very rapidly. Some of the application areas of these products include missiles, space vehicles, micro-electromechanical systems (MEMS) and communication systems. The micro-holes are used in various components for different applications such as in fuel injection nozzles, inkjet printer nozzles, spinner holes, drug delivery orifices, and cooling channels of the turbine blades [1]. At present, the micro-holes in different materials are manufactured by different machining processes

---

P. Kumar

Department of Mechanical Engineering, S R Engineering College, Warangal 506001, Telangana, India

e-mail: [pikupankaj82@gmail.com](mailto:pikupankaj82@gmail.com)

M. Hussain (✉)

Department of Mechanical Engineering, Chaitanya Bharathi Institute of Technology, Hyderabad 500075, Telangana, India

e-mail: [manowar.bit07@gmail.com](mailto:manowar.bit07@gmail.com)

© Springer Nature Singapore Pte Ltd. 2020

G. S. V. L. Narasimham et al. (eds.), *Recent Trends in Mechanical Engineering*,

Lecture Notes in Mechanical Engineering,

[https://doi.org/10.1007/978-981-15-1124-0\\_23](https://doi.org/10.1007/978-981-15-1124-0_23)

like laser beam machining, micro-electro-discharge machining, and electrochemical machining processes [2–5]. Among these processes, micro-EDM has become a well-accepted nontraditional micromachining process in terms of cost of machining, fabrication of 3D shapes, and high aspect ratio features. Moreover, this process can produce burr-free surfaces with minimum distortions in the feature size due to non-contact machining process [6]. In micro-EDM process, there are many factors that affect the process performance such as inter-electrode voltage, pulse duration, maximum current, machining gap, flushing conditions, nature of dielectrics, physical and chemical properties of workpiece and tool material. The flushing condition in the inter-electrode gap is one of the most important aspects which influence the process performance greatly. In this process, the machining time can be reduced significantly with considerably better surface quality by the introduction of workpiece vibration of constant amplitude and high frequency [7–9]. The experiments with workpiece vibration have been conducted and reported that the machining time reduces significantly and the stability of the process improves in comparison to normal micro-EDM process [10]. For the machining of micro-holes on Ti-6Al-4 V alloy with different dielectric fluids were investigated by Kibria et al. [11]. They observed that the use of a suitable dielectric improves process performance. Kansal et al. [12] have reported that the powder mixed dielectric gives a better quality of machined surfaces. Masaki et al. [13] carried out experiments on the applied and fundamental issues of the micro-EDM process and reported that the fabricated micro-holes with a high aspect ratio of 10, roughness of 0.1  $\mu\text{m}$  and roundness of 0.5  $\mu\text{m}$  can be achieved. The comparison of the performances of different electrode materials of micro-electrode with positive polarity was reported by Her et al. [14]. It has been reported that with Cu electrode, better surface roughness and lower electrode wear can be achieved. On-machine fabrication of micro-electrodes and their uses for micro-fabrication has been reported by Lim et al. [15]. They found that the depth of machining was directly proportional to the feed rate of the tool electrode. Blind holes with high aspect ratio have been presented by Z.

Y. Yu et al. [16]. Due to rapid growth in the demand for miniature products, a large number of components are to be accommodated in a device, which needs new machines and processes to be explored. Due to the compactness of the devices, the magnetic interference between these components becomes more severe. To overcome these issues, a material having shielding properties to prevent any magnetic interference becomes important. The Nickel has outstanding properties of soft magnetic materials such as high magnetic permeability, high saturation temperature with a small change in permeability, low hysteresis, and low eddy current loss. Due to these properties, it is an excellent material for shielding the magnetic interferences and is used in all most all MEMS devices. Due to the high toughness of the nickel sheet, it becomes difficult to drill micro-holes in it through the conventional machining process. As it causes high tool wear, the formation of burrs on the machined surfaces and induction of high residual stresses in the workpiece. From the previous literature, it has been found that very few works has been done on the surface integrity of the fabricated micro-holes in pure nickel. In this study, nickel sheet having high magnetic permeability has been used as work material. The effect of input parameters on

the thickness of recast layer, change in micro-hardness of the machined holes and metallurgical changes on the machined holes reported.

## 2 Experimentation

### 2.1 Machine Tools

A micro-EDM setup has been developed in-house to carry out all the experiments. The machine has a maximum travel range of 25 mm × 25 mm × 50 mm in X, Y, and Z axis, with a resolution of 5 μm in each direction. Figure 1 represents the micro-EDM experimental setup.

### 2.2 Workpiece, Tool, and Dielectric

In this study, the nickel sheet was used as workpiece material which has dimensions of 60 mm × 50 mm × 0.3 mm. The composition of the nickel sheet was verified through the EDS test and results are presented in Table 1. Pure tungsten rod of

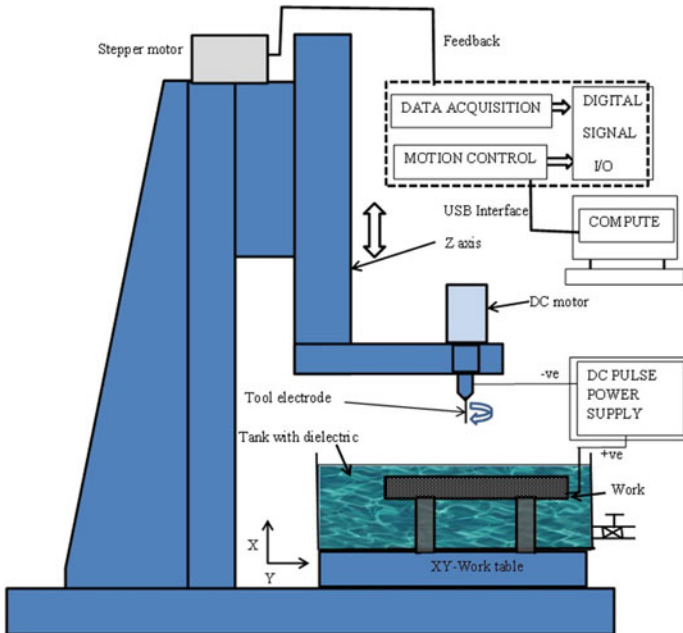


Fig. 1 Schematic diagram of the developed setup for performing micro-EDM experiments

1 mm diameter was reduced to a diameter of 0.5 mm by reverse polarity micro-EDM process and using EDM oil a dielectric fluid. The chemical composition and mechanical properties of the tool have been presented in Table 2.

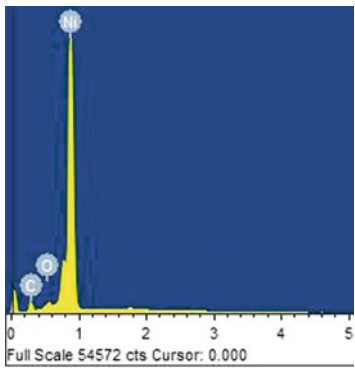
### 2.3 Experimental Procedure

All the experiments were performed in the developed setup. In this investigation, the tool electrode was given negative polarity to get low tool wear and better material removal rate. Before conducting final experiments, trial runs were performed to select a suitable range of parameters. The Micro-EDM process parameter has been shown in Table 3. All the final experiments were performed as per the parameter settings presented in Table 4.

### 2.4 Instruments Used for Measurements and Analysis

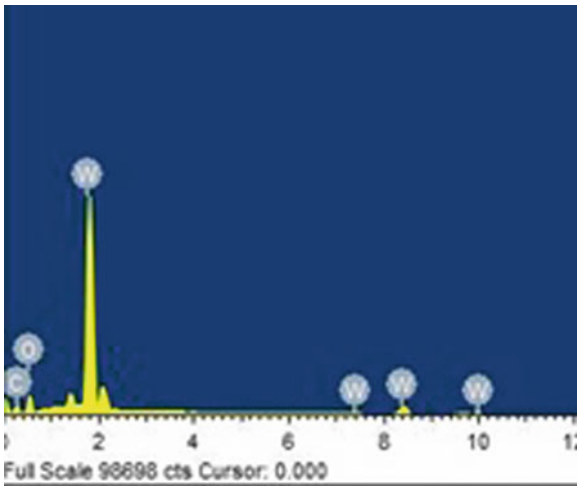
After machining of all the micro-holes in the nickel sheet, the workpiece surface was etched with the Marble's reagent (Composition: 2 ml HCl, 10 ml CuSO<sub>4</sub> and 88 ml distilled water) for 1 min. Then the EDMed samples were cleaned using acetone. For measuring and analysis of quality and size of micro-holes, Olympus metallurgical microscope and FESEM was used. EDS analysis of the edges of micro-holes was carried out for evaluation of the material composition of the machined surfaces. The change in the microhardness of the work surface after the machining operation was measured by Vickers micro-hardness tester.

**Table 1** Chemical composition and mechanical properties of the work piece material

Workpiece material	Nickel sheet	
Material composition (wt%)	Ni-96.97 O-0.6 C-2.35	
Density (g/cm <sup>3</sup> )	8.47	
Vickers hardness (HV)	106	
Melting point (°C)	1455	
Thermal conductivity (W/m - K)	90.9	



**Table 2** Chemical composition and mechanical properties of the electrode material

Tool material	Tungsten	
Material composition (wt%)	W-96.02, C-1.08, O-2.89	
Density (g/cm <sup>3</sup> )	19.3	
Relative conductive	14.0	
Thermal expansion coefficient (K <sup>-1</sup> )	4.6 × 10 <sup>-6</sup>	
Specific resistance (μΩ)	56	

**Table 3** Micro-EDM process parameters

Workpiece material	Nickel Sheet
Tool material	Tungsten (W): φ 500 μm
Dielectric liquid	EDM oil
Gap voltage (V)	30, 40, 50, 60
Pulse on time (μs)	30, 40, 50, 60
Pulse frequency	10 kHz

### 3 Results and Discussion

In this investigation, the effects of the input parameters on the thickness of the recast layer, micro-hardness and metallurgical transformation of the workpiece surface reported [17]. The variation of output parameters of the machined holes with the variation in experimental parameters is described in the following sections.

#### 3.1 Investigation on Recast Layer Thickness (RLT)

During the micro-EDM process, the material is melted and evaporated from the workpiece surface by the spark generated. Some of the molten materials are carried away by re-circulating dielectric fluid and the remaining part is re-solidified and

**Table 4** Layout for experimentation

Experiment no.	Frequency (kHz)	Gap voltage (V)	Pulse on time ( $\mu$ s)	Ultrasonic vibration
1	10	40	30	Without vibration
2			40	
3			50	
4			60	
5	10	40	30	With vibration
6			40	
7			50	
8			60	
9	10	30	40	Without vibration
10		40		
11		50		
12		60		
13	10	30	40	With vibration
14		40		
15		50		
16		60		

sticks to the crater surface. This re-solidified layer is known as the white layer or recast layer [18]. From the captured FESEM images, the RLT was measured using image processing software. Figures 2b, d have low RLT as compared to Figs. 2a, c, due to ultrasonic vibration given to the workpiece. Application of ultrasonic vibration results in the reduction of re-solidification of the molten materials over the existing recast layer (Figs. 3 and 4).

### 3.2 Investigation on Micro-Hardness of the Machined Holes

Change in the micro-hardness of the fabricated micro-holes is tested using a Vickers micro-hardness tester. The micro-hardness was measured from the periphery of the machined holes at a regular distance gap of 20  $\mu$ m. This procedure was repeated at least four times for each hole at different locations. Figure 5a represents the sample image of indentation which was obtained during the micro-hardness testing.

It is found that the micro-hardness of the fabricated holes decreases from the edge of the holes towards the parent materials. The micro-hardness is highest in the recast layer and it gradually reduces and becomes constant in the parent material zone in each sample which is in line with the results published by Imran et al. [19]. Figures 5b,c indicate the variation of micro-hardness of the machined hole at different pulse on duration without and with ultrasonic vibration given to the workpiece. It is

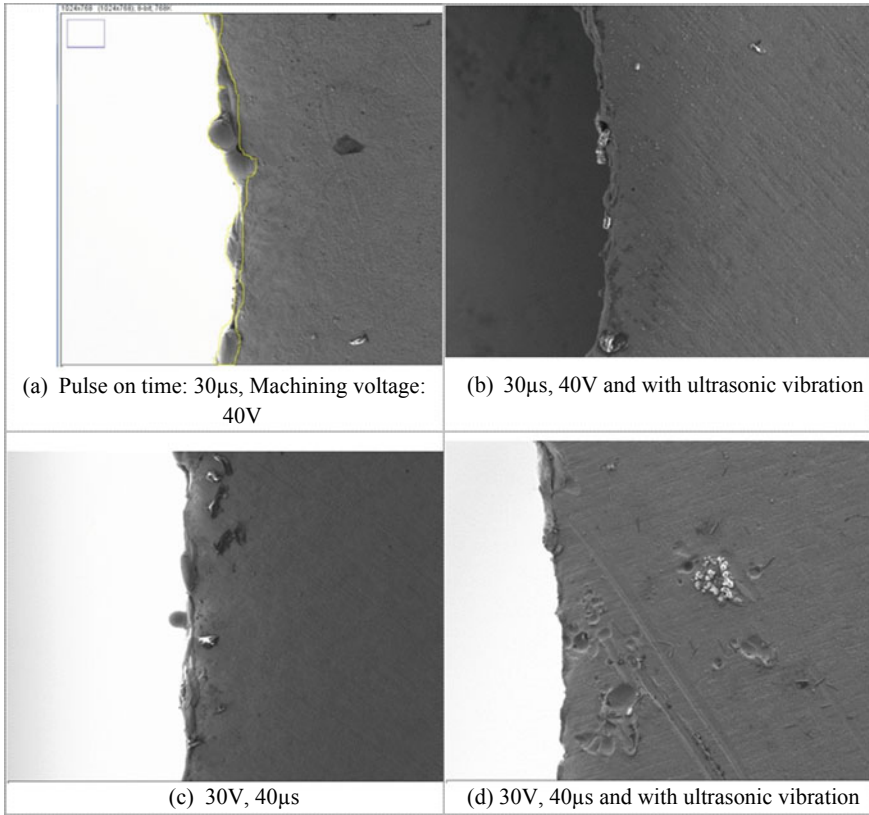


Fig. 2 FESEM images of the periphery of the machined holes at different machining parameters

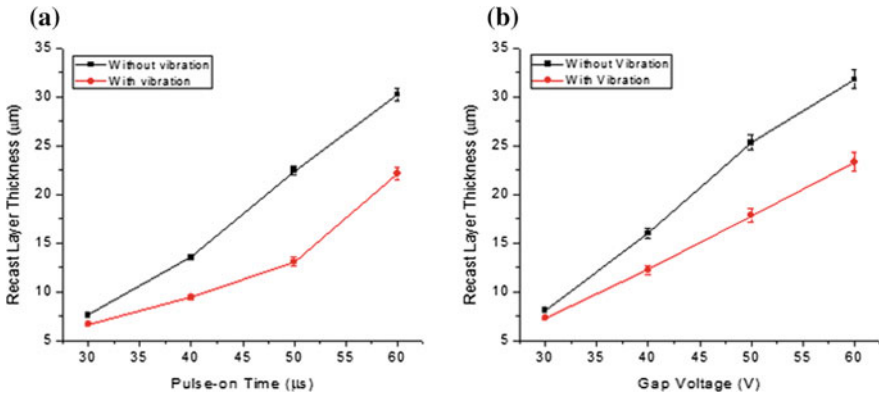
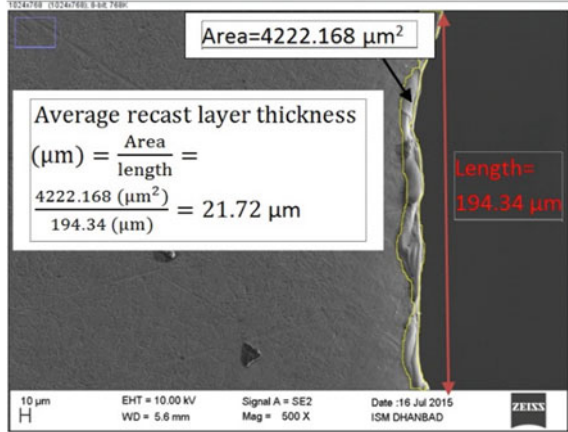


Fig. 3 Variation in thickness of recast layer with a pulse on time duration and b gap voltage

**Fig. 4** Measurement procedure of average thickness of recast layer



observed that the micro-hardness increases on increasing the pulse on time duration [20–22] for Fig. 5b, c. Similar results for micro-hardness are also obtained at different gap voltages which are shown in Fig. 5d, e.

### 3.3 Investigation on Metallurgical Changes at the Machined Holes

It is observed from the EDS test that the residuals of foreign elements such as oxygen and carbon were present in the machined sample. In Figs. 6a, b, the percentage composition of both carbon and oxygen was different which may be due to the fact that both samples were machined at different parameter settings. In Figs. 6c, d, the percentage composition of both carbon and oxygen reduces significantly on the introduction of vibration given to the workpiece.

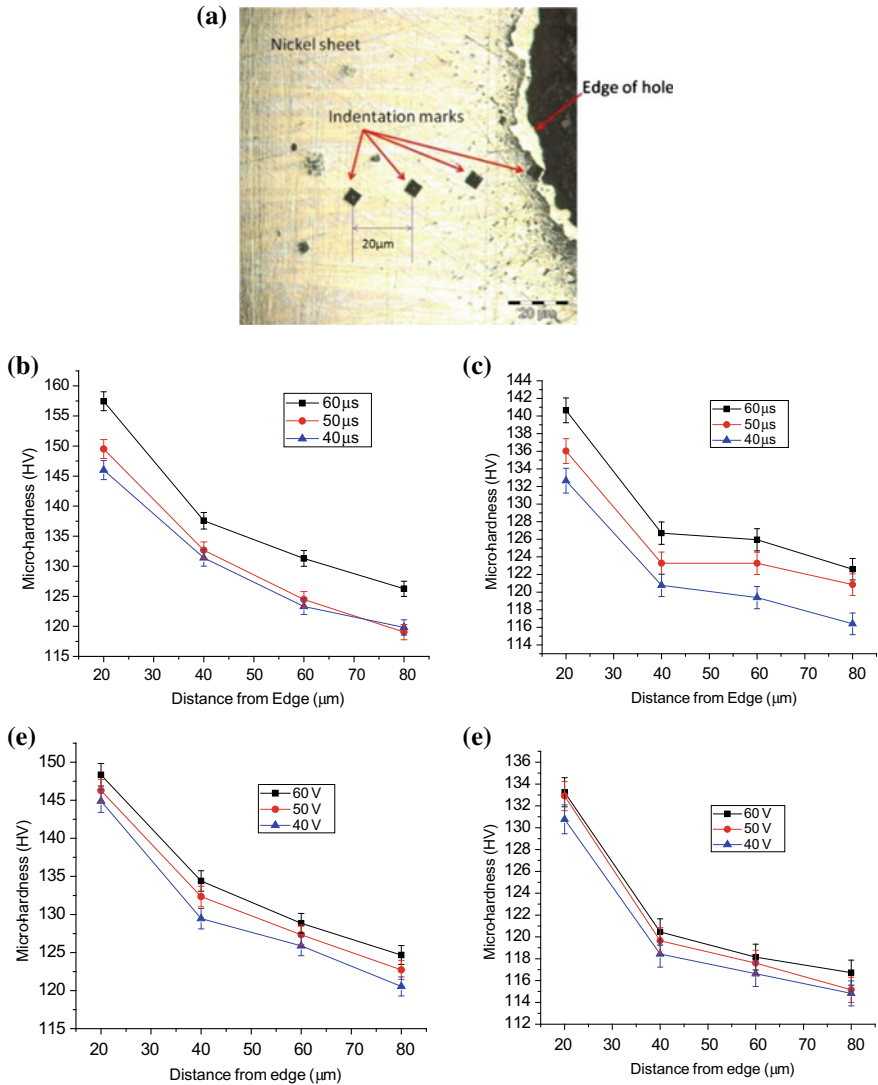


**Fig. 5** Variation in micro-hardness from edge of the hole **a** optical micrograph indicating the penetration of the tip of diamond indenter; **b** effects of pulse on time; **c** effects of pulse on time with vibration of the workpiece; **d** effects of gap voltage and **e** effects of gap voltage with vibration of the workpiece

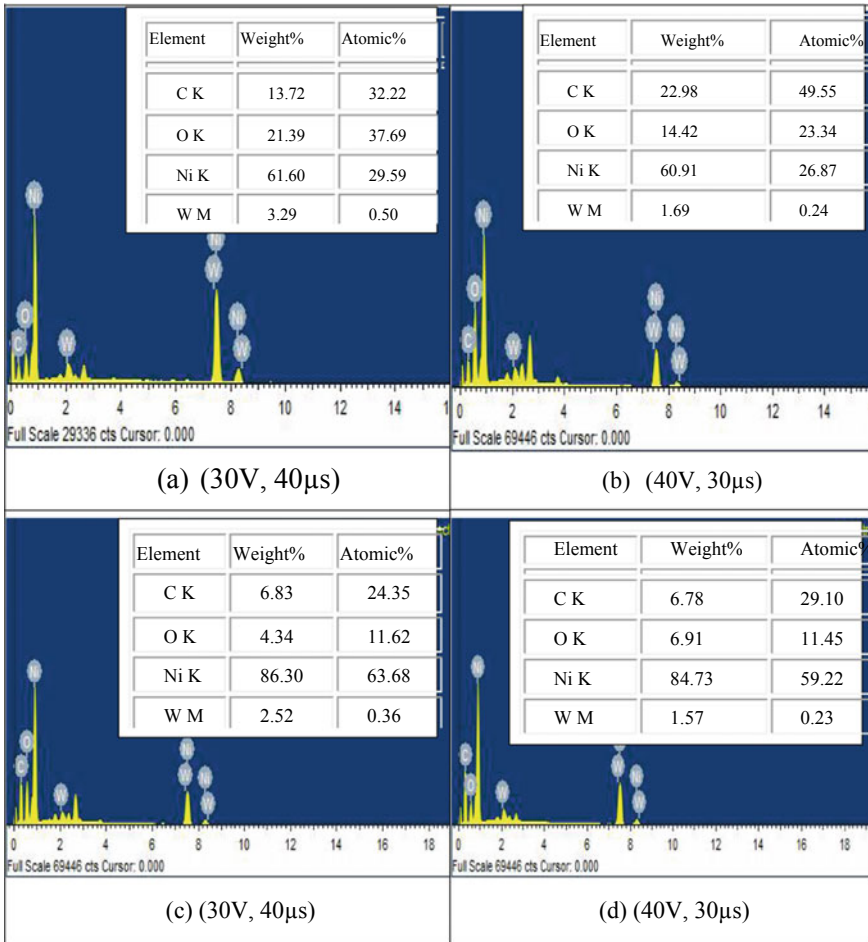


**Fig. 6** EDS plot and their chemical composition at different parameters **a** and **b** without vibration and **c** and **d** with vibration

### 4 Conclusions

In this investigation, analysis of the influence of different input parameters on recast layer thickness, heat micro-hardness and metallurgical changes in the fabricated micro-holes performed. From the obtained results the following points are listed as follow:

- The average thicknesses of the recast layer obtained were in the range of 8–32  $\mu$ m for change of pulse duration from 30 to 60  $\mu$ s and 9–35  $\mu$ m with machining voltage variation (machining without vibration). Comparatively less recast layer thick was

obtained by use of the ultrasonic vibration. and was 6–21  $\mu\text{m}$  on the variation of pulse on time duration and 7–22 with the variation of machining voltage.

- The micro-hardness near to machining zone was measured for all three layers, i.e., recast layer, HAZ and parent materials. It was found between 119–160 HV without workpiece vibration and 116–141 HV with vibration.
- In this study, heat affected zone was not observed in optical as well as in SEM images.
- From EDS images, some percentage of carbon and oxygen can be easily seen on the machined hole surface. It was also observed that the percentage of both carbon and oxygen were less with assisted vibration compared to the without vibration work piece.

## References

1. Diver C, Atkinson J, Helml HJ, Li L (2004) Micro-EDM drilling of tapered holes for industrial applications. *J Mater Process Technol* 149(1–3):296–303
2. Yan BH, Huang FY, Chow HM, Tsai JY (1999) Micro-hole machining of carbide by electric discharge machining. *J Mater Process Technol* 87(1–3):139–145
3. Das AK, Kumar P, Sethi A, Singh PK, Hussain M (2016) Influence of process parameters on the surface integrity of micro-holes of SS304 obtained by micro-EDM. *J Braz Soc Mech Sci Eng* 38(7):2029–2037
4. Zheng HY, Huang H (2007) Ultrasonic vibration-assisted femtosecond laser machining of microholes. *J Micromech Microeng* 17(8):N58
5. Bhattacharyya B, Munda J, Malapati M (2004) Advancement in electrochemical micro-machining. *Int J Mach Tools Manuf* 44(15):1577–1589
6. Fleischer J, Schmidt J, Haupt S (2006) Combination of electric discharge machining and laser ablation in microstructuring of hardened steels. *Microsyst Technol* 12(7):697–701
7. Garn R, Schubert A, Zeidler H (2011) Analysis of the effect of vibrations on the micro-EDM process at the workpiece surface. *Precis Eng* 35(2):364–368
8. Prakash V, Shubham, Kumar P, Singh PK, Das AK, Chattopadhyaya S, Dixit AR (2018) Surface alloying of miniature components by micro-electrical discharge process. *Mater Manuf Process* 33(10):1051–1061
9. Huang H, Zhang H, Zhou L, Zheng HY (2003) Ultrasonic vibration assisted electro-discharge machining of microholes in Nitinol. *J Micromech Microeng* 13(5):693
10. Endo T, Tsujimoto T, Mitsui K (2008) Study of vibration-assisted micro-EDM—the effect of vibration on machining time and stability of discharge. *Precis Eng* 32(4):269–277
11. Kibria G, Sarkar BR, Pradhan BB, Bhattacharyya B (2010) Comparative study of different dielectrics for micro-EDM performance during microhole machining of Ti-6Al-4 V alloy. *Int J Adv Manuf Technol* 48(5–8):557–570
12. Kansal HK, Singh S, Kumar P (2007) Technology and research developments in powder mixed electric discharge machining (PMEDM). *J Mater Process Technol* 184(1–3):32–41
13. Masaki T, Kawata K, Masuzawa T (1990) Micro electro-discharge machining and its applications. In: *Micro Electro Mechanical Systems, 1990. Proceedings, An Investigation of Micro Structures, Sensors, Actuators, Machines and Robots*. IEEE, pp 21–26
14. Her MG, Weng FT (2001) Micro-hole machining of copper using the electro-discharge machining process with a tungsten carbide electrode compared with a copper electrode. *Int J Adv Manuf Technol* 17(10):715–719
15. Lim HS, Wong YS, Rahman M, Lee ME (2003) A study on the machining of high-aspect ratio micro-structures using micro-EDM. *J Mater Process Technol* 140(1–3):318–325

16. Prakash V, Kumar P, Singh PK, Hussain M, Das AK and Chattopadhyaya S (2019) Micro-electrical discharge machining of difficult-to-machine materials: a review. Proceedings of the Institution of Mechanical Engineers, Part B: J of Eng Manuf 233(2) 339-370
17. Jabbaripour B, Sadeghi MH, Faridvand S, Shabgard MR (2012) Investigating the effects of EDM parameters on surface integrity, MRR and TWR in machining of Ti-6Al-4V. Mach Sci Technol 16(3):419-444
18. Ekmekci B (2009) White layer composition, heat treatment, and crack formation in electric discharge machining process. Metall Mater Trans B 40(1):70-81
19. Imran M, Mativenga PT, Gholinia A, Withers PJ (2015) Assessment of surface integrity of Ni superalloy after electrical-discharge, laser and mechanical micro-drilling processes. Int J Adv Manuf Technol 79(5-8):1303-1311
20. Shabgard M, Oliaei SNB, Seyedzavvar M, Najadebrahimi A (2011) Experimental investigation and 3D finite element prediction of the white layer thickness, heat affected zone, and surface roughness in EDM process. J Mech Sci Technol 25(12):3173-3183
21. Kumar P, Hussain M, Das AK. Effect of process parameters on the surface integrity of micro-holes of Ti6Al4V obtained by micro-edm
22. Kumar P, Hussain M, Singh PK, Das AK (2015) A new method for modeling of cathode and anode erosion in micro-EDM Process. Int J Appl Eng Res 10(24)



# A Study on Welding of Thin Sheet of Ti6-Al-4V Alloy Using Fiber Laser and Its Characterization



Manowar Hussain, Gulshad Nawaz Ahmad and Pankaj Kumar

**Abstract** In the present research work, an attempt has been made to study and investigate the weldability of 1.2-mm-thick Ti6-Al-4V alloy sheet using CW (continuous wave) fiber laser. The influences of the variable process parameters such as laser power, weld scanning speed and laser beam diameter on the microstructure, heat-affected zone (HAZ) and mechanical properties of the final butt-welded joints of Ti6-Al-4V sheets have been investigated. All the experiments were performed by using a CW fiber laser having a laser power capacity of 400 W. At different parameter setting conditions such as laser power varying from 200 to 350 W, weld scanning speed from 120 to 200 mm/min and laser beam diameter (0.4 mm) were considered for the experimentation. Based on the experiments weld quality was investigated and characterized in terms of the surface microstructure, micro-hardness, and tensile strength of the welded samples. Morphological studies at different processing conditions were carried out to study their effects on the HAZ (Heat-affected zone) and weld bead geometry. Microscopic images of welded samples clearly show a decrease in weld width of the welded sample with an increase in weld scanning speed and with increasing laser power increase in width was observed. At a scanning speed of 120 mm/min with varying power from 200 to 350 W the size of heat-affected zone (HAZ) are 3.55, 3.70, 3.84, 4.8 mm, and the corresponding size of fusion zones is 1.751 mm, 1.83 mm, 1.921 mm, 2.032 mm, respectively. The trend in micro-hardness variation was observed and it depends on grain size in laser welding. At 350 W laser power with varying speed from 120 to 300 mm/min, the micro-hardness values of the welded sample were found as 387.1, 395, and 403 HV. The tensile strength of the

---

M. Hussain

Department of Mechanical Engineering, Chaitanya Bharathi Institute of Technology, Hyderabad 500075, Telangana, India

G. N. Ahmad

Department of Mechanical Engineering, Indian Institute of Technology (ISM) Dhanbad, Dhanbad 826004, Jharkhand, India

P. Kumar (✉)

Department of Mechanical Engineering, S R Engineering College, Warangal 506371, Telangana, India

e-mail: [pikupankaj82@gmail.com](mailto:pikupankaj82@gmail.com)

© Springer Nature Singapore Pte Ltd. 2020

G. S. V. L. Narasimham et al. (eds.), *Recent Trends in Mechanical Engineering*,

Lecture Notes in Mechanical Engineering,

[https://doi.org/10.1007/978-981-15-1124-0\\_24](https://doi.org/10.1007/978-981-15-1124-0_24)

original sample was found to be  $940 \text{ N/mm}^2$ . The testing results of the welded sample have a maximum failure strength of  $507 \text{ N/mm}^2$  at 350 W and 200 mm/min scanning speed. FESEM images of the welded sample at different processing conditions were used for the study of microstructural changes in the welded zone and the presence of defects at the micro level.

**Keywords** Fiber laser · Ti6Al4V · Microstructure · Vickers hardness · FESEM

## 1 Introduction

In the past few years, with the increasing demand for lightweight materials by the industries where fuel consumption and resistance to adverse effects on the environmental conditions are the prime aspects. Titanium alloys are known for their high specific strength (strength to weight ratio), high toughness, good corrosion resistance, high stiffness, and hot hardness. These remarkable properties of Ti6Al4V make titanium (Ti-6Al-4V) useful for many industrial as well as in biomedical applications, for example, it is widely used in making human body implant, biomedical devices, nuclear, aerospace, and automotive industries. One of the important applications of the Ti-6Al-4V has been found in the static and moving parts of the turbine engines [1]. For welding of titanium sheet fusion welding is the most preferred technique. Welding variable process parameters such as weld scanning speed, laser power and workpiece thickness have a great effect on dimensions of fusion zone as well as on joining or melting efficiency [2, 3]. Macroscopic geometry, microstructure, fatigue and tensile properties of the welded samples were greatly influenced by weld scanning speed and laser power [4] and as a result, there was a slight decrease in the tensile strength after laser welding due to brittle intermetallic compounds formed in the weld zone [5]. Fiber laser is being used due to its high efficiency as compared to other lasers [6]. The main limitation of the conventional fusion welding is the large heat input that results in decreasing the mechanical properties as it persuades heat-affected zone of larger dimensions, broader weld seam, greater distortion and formation of residual stress [7, 8]. In order to get a better mechanical property, fatigue strength [9]; a small HAZ, less distortion, and narrower bead width are required. Phase transformation also reported in the weld pool [10] during the welding process and it extends up to its heat-affected zone. Laser welding is one of the most precision welding techniques suitable for joining similar and dissimilar materials. LBW is used for joining intricate geometries and configurations with a smaller weld pool than conventional arc welding because of the small and high-intensity focusing laser diameter [11]. LBW has been used for high productivity and high welding efficiency. Previously, many research work has been done by different researchers and analysts using different types of lasers and their mechanical and morphological characterizations were carried out. However, very little work has been reported on thin sheet welding of Ti6Al4V using fiber laser. So the present work is aimed at welding of Ti64 sheets of 1.2 mm thickness using a CW 400 W fiber laser.

The ideas of the present study are as follows: (1) Laser Beam Welding (LBW) of Ti-6AL-4V alloy sheets at different process parameter—laser power varying from 200 to 350 W and welding speed from 120 to 200 mm/min. (2) To evaluate the influence of welding process parameters on weld bead morphology, metallurgical and mechanical properties particularly tensile strength and micro-hardness. (3) The different analyses such as morphology study, micro-hardness, tensile tests and SEM image analysis have been carried out to evaluate welding quality, which is described elaborately in the results and discussion section.

## **2 Materials and Experimental Procedure**

### **2.1 Material Selection**

Among the commonly utilized metallic materials in the aerospace and medical industry are titanium and its alloys, as their mechanical properties are particularly suitable for the service. Titanium alloys offer various advantages to be used in the aerospace and medical industry due to its high specific strength, excellent corrosion resistance, thermal and electrochemical compatibility with advanced component materials [12].

### **2.2 Experimental Setup**

A 400 W continuous wave (CW) fiber laser, Model: HS Laser Systems, Make: SPI Lasers, UK with output Laser power range of 50–400 W has been used for the experimentation. The laser welding setup is provided with an automatic gas purging arrangement to shield the welding and prevent the welding pool from oxidation. The laser head is fixed to the Z-axis of the CNC stage that moves up-down to control the laser beam spot diameter required for welding. The welding is carried out in a closed cuboid shape chamber made up of perspex material. High-intensity laser resistant quartz plate of dimension 50 mm × 50 mm is fixed at the top center position of the cuboid chamber. During the laser welding operation, the chamber is filled with the desired gas and laser is scanned on the samples through the quartz windows.

### **2.3 Sample Preparation**

A block of Ti-6Al-4V of (30 mm × 75 mm × 75 mm) dimension was taken. The composition of the received material (Ti6Al4V) is shown in Table 1. Twelve specimens of size (30 mm × 15 mm × 1.2 mm) were cut on the Wire-EDM machine. The

**Table 1** Composition of the Ti-6Al-4V (Grade 5) (wt. %)

Al	V	Fe	O	C	H	Ti
6.6	4	<0.4	<0.3	<0.003	<0.002	89.9

specimen obtained after cutting has a very fine finished edge and of exact dimensions. The surfaces of the samples were then polished with emery paper to remove oxides formed during Wire-EDM cutting and then cleaned using acetone to remove dirt and loose particles from the surface before clamping to produce defect-free weld joint. The specimen after cleaning is properly dried slowly.

## 2.4 Experimental Parameters and Processing Conditions

All the laser welding experiments were conducted by considering different input parameters and different parameter settings as shown in Tables 2 and 3, respectively.

**Table 2** Input parameters

Input system parameters	Value
Power (in Watt)	200, 250, 300, 350
Scanning speed (in mm/min)	120, 160, 200
Spot diameter (in mm)	0.4
Wavelength (in nm)	1070
Operation mode	CW mode

**Table 3** Different parameter setting for the experiment

Sl. No	Power (Watt)	Scanning speed (mm/min)	Sl. No	Power (Watt)	Scanning speed (mm/min)
1	200	120	7	300	160
2	250	120	8	350	160
3	300	120	9	200	200
4	350	120	10	250	200
5	200	160	11	300	200
6	250	160	12	350	200

## 2.5 *Experiment Procedure*

Before butt welding operation the specimens were properly clamped at the base with minimum or no gap between the finished edges of the joints, also to avoid the development of crack due to rapid cooling of the welded joint. Titanium is considered as a reactive material at elevated temperature with the atmospheric gases. Due to this reason the weld pool is shielded during the welding operation using shielding gas like argon. The use of shielding gas also protects the oxidation of heat-affected zone when it gets heated during the welding till cooling has occurred. In this study, argon was used as a shielding gas with supply of 15 l/min at 1 bar to avoid reactions between the molten weld pool and the atmospheric gases [13]. Welding operations of the specimen were carried out with 50–400 W CW/Modulated fiber laser machine. Welding operation was performed at different process parameters. In this operation, autogenous laser welding of Ti-6Al-4V is carried out.

## 2.6 *Output Parameters*

Output parameters to be discussed in the result and discussion part are: (1) Optical Microscope Image Analysis (2) Micro-hardness (3) Tensile Testing (4) SEM Image analysis

# 3 **Results and Discussion**

## 3.1 *Morphological Study*

The microscopic images of the welded sample were taken at different welding processing conditions using Olympus microscope to study the weld bead geometry and heat-affected zone (HAZ). Images of the welded sample are shown in Fig. 1(a) and (b). The figure shows that the weld width of the sample decreases with an increase in welding speed and an increase in weld width with an increase in laser power [14].

It was observed that as the laser power is increased, a wider molten metal pool is formed due to high-intensity laser heat input. A higher weld scanning speed results in low interaction of the material with a laser beam which decreases the size of the weld pool. Higher the beam diameter, the wider the weld pool is expected. It is also found that the microstructure gradient in the fusion zone of laser-welded Ti alloy sheet promotes crack initiation and fatigue damage [15]. From Fig. 2(a) and (b) it is clear that at constant scanning speed with an increase of power from 200 to 350 W size of heat-affected and fusion zone increases. At constant scanning speed, with the increase of laser power, a wider weld pool is observed due to high heat input. For example, at a scanning speed of 120 mm/min with varying power from 200 to

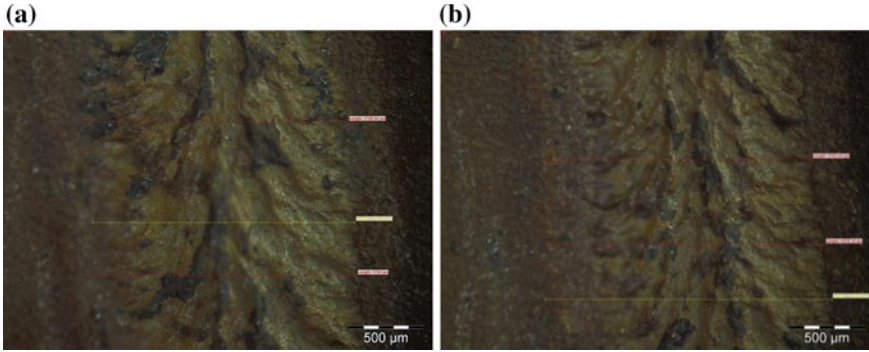


Fig. 1 Weld bead at (a) 200 W (b) 250 W laser power and 120 mm/min welding speed

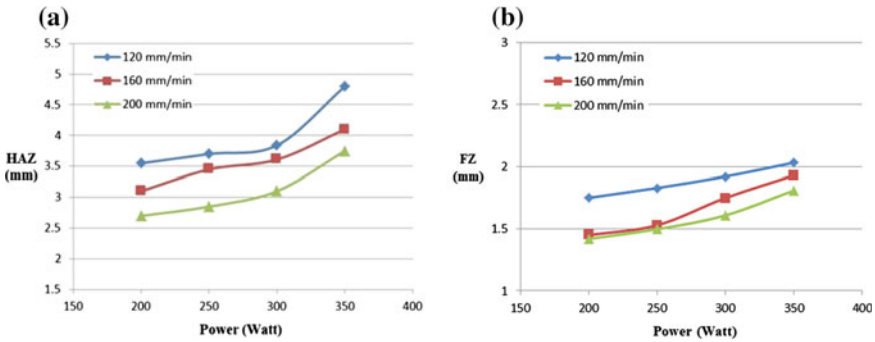


Fig. 2 a Laser power versus heat-affected zone, b plot of laser power versus fusion zone

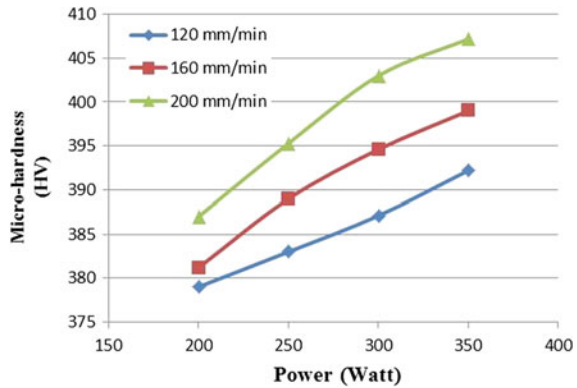
350 W, the size of heat-affected zones (HAZ) are 3.55, 3.70, 3.84, 4.8 mm and the corresponding size of fusion zone are 1.751, 1.83, 1.921, 2.032 mm. Similarly for other scanning speed with varying laser power in the given range size of HAZ & FZ increases. Figure 2 shows the variation of the HAZ with the laser power of the welded sample as per the input process parameter given in Table 2.

### 3.2 Micro-Hardness

The micro-hardness was examined by Economet micro-hardness testing machine, using 100 gf load and a dwell time of 10 s. The micro-hardness variation of welded joints not only depends on grain size but it is affected by the flow of molten metal in the weld pools i.e. the flow velocity, welding time, density of fluid, etc. High welding speed leads to the formation of more residual stress in the material as a resultant micro-hardness of material increases.

Figure 3 shows that the micro-hardness of the welded sample increases with the

**Fig. 3** Plot of laser power versus micro hardness



increase in scanning speed at constant laser power due to the high cooling rate at high speed [16, 17]. For example, at a laser power of 350 W and scanning speed varying from 120 to 300 mm/min, micro-hardness or Vicker hardness value of welded sample are found to be 387.1, 395, and 403 HV. Micro-hardness versus laser Power graph of welded sample is shown in Fig. 3 as per the input process parameter given in Table 3.

### 3.3 Tensile Test

Tensile testing has been done using a Zwick Roell tensile test machine operating with a crosshead speed of 10 mm/min with the load cell of 50 KN. The tensile strength of the parent material was found to be 940 N/mm<sup>2</sup>. Testing results of the welded sample has a maximum failure strength of 507 N/mm<sup>2</sup> at 350 W and 200 mm/min scanning speed, which is not good in comparison of the parent material.

Results have not come good may be due to improper shielding, as shielding has been done only from the top side not on the bottom side of the welding zone and it results in the formation of porosity and intermetallic compound weak in tension [18–22]. Tensile test of the welded sample as per process parameter shown in Table 3 has been performed and graph between laser power versus tensile strength plotted in Fig. 4.

### 3.4 FESEM

The SEM images of the welded sample at different processing conditions were taken for the study of microstructural change in the welded zone and the heat-affected zone of the welded sample. Images in Fig. 5(a) and (b) show the microstructural changes in the welded zone of Ti-6Al-4V alloy at different operating parameters. SEM images

**Fig. 4** Plot of laser power vs. tensile strength

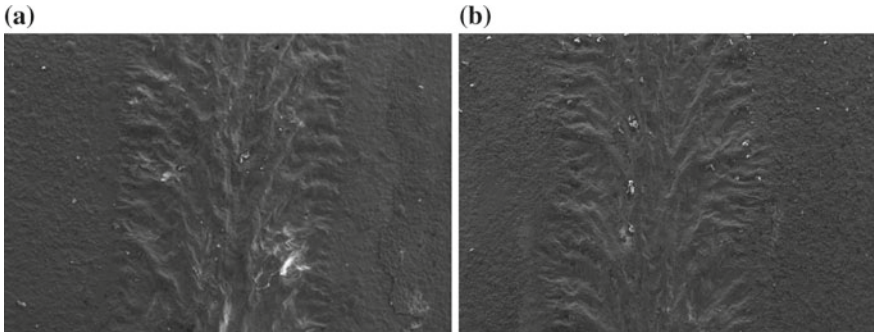
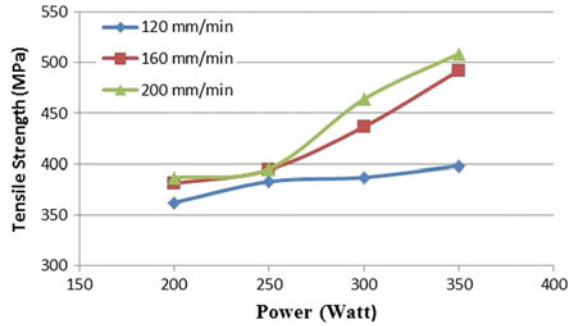


**Fig. 5** **a** SEM images of weld zone at 200 W and 120 mm/min speed, **b** SEM images of weld zone at 250 W and 160 mm/min speed

of the welded sample as per the input process parameter in Table 3 has been taken and shown in Fig. 5a, b.

## 4 Conclusions

LBW of Ti-6Al-4V (Titanium Grade-5) sheets of 1.2 mm thickness was carried out to evaluate the influence of laser welding parameters on the output process parameters such as macroscopic geometry, microstructure, micro-hardness and tensile strength of laser butt weld joints in Ti6-Al-4V were investigated.

- It was observed that the size of weld bead is significantly influenced by changing the input laser power, welding or scanning speed and laser beam diameter. It was also seen that the width of weld beads and HAZ decreases on increasing the scanning speed and an increase in width was observed with an increase in laser power.
- Micro-hardness at the weld bead is higher as compared to both, welding interface and the parent material. At constant laser power, Micro-hardness value increased



with increasing weld scanning speed as a result of high cooling rate and phase transformation.

- During the tensile test, all prepared specimens failed at a strength lower than the strength of the base material with reduced ductility in the welded sample.

## References

1. Boyer RR (1996) An overview on the use of titanium in the aerospace industry. *Mater Sci Eng, A* 213(1–2):103–114
2. Mazumder J, Steen WM (1982) Microstructure and mechanical properties of laser welded titanium 6Al-4V. *Metall Trans A* 13(5):865–871
3. Kumar V, Hussain M, Raza MS, Das AK, Singh NK (2017) Fiber laser welding of thin nickel sheets in air and water medium. *Arab J Sci Eng* 42(5):1765–1773
4. Squillace A, Prisco U, Ciliberto S, Astarita A (2012) Effect of welding parameters on morphology and mechanical properties of Ti–6Al–4V laser beam welded butt joints. *J Mater Process Technol* 212(2):427–436
5. Mirshekari GR, Saatchi A, Kermanpur A, Sadmezhaad SK (2013) Laser welding of NiTi shape memory alloy: comparison of the similar and dissimilar joints to AISI 304 stainless steel. *Opt Laser Technol* 54:151–158
6. Quintino L, Costa A, Miranda R, Yapp D, Kumar V, Kong CJ (2007) Welding with high power fiber lasers—a preliminary study. *Mater Des* 28(4):1231–1237
7. Sathiya P, Panneerselvam K, Soundararajan R (2012) Optimal design for laser beam butt welding process parameter using artificial neural networks and genetic algorithm for super austenitic stainless steel. *Opt Laser Technol* 44(6):1905–1914
8. Dawes C. (1992) *Laser welding*. McGraw-Hill, New York, USA, 73 pp
9. Fricke W (2003) Fatigue analysis of welded joints: state of development. *Mar Struct* 16(3):185–200
10. Elmer JW, Palmer TA, Babu SS, Zhang W, DebRoy T (2004) Phase transformation dynamics during welding of Ti–6Al–4V. *J Appl Phys* 95(12):8327–8339
11. Kabir ASH, Cao X, Medraj M, Wanjara P, Cuddy J, Birur A (2010) Effect of welding speed and defocusing distance on the quality of laser welded Ti–6Al–4V. In: *Proceedings of the Materials Science and Technology (MS&T) 2010 Conference*. Houston, TX, pp 2787–2797
12. Chen HC, Pinkerton AJ, Li L (2011) Fibre laser welding of dissimilar alloys of Ti-6Al-4V and Inconel 718 for aerospace applications. *Int J Adv Manuf Technol* 52(9–12):977–987
13. Zhang LJ, Zhang JX, Gumenyuk A, Rethmeier M, Na SJ (2014) Numerical simulation of full penetration laser welding of thick steel plate with high power high brightness laser. *J Mater Process Technol* 214(8):1710–1720
14. Cao X, Jahazi M (2009) Effect of welding speed on butt joint quality of Ti–6Al–4V alloy welded using a high-power Nd: YAG laser. *Opt Lasers Eng* 47(11):1231–1241
15. Liu J, Gao XL, Zhang LJ, Zhang JX (2014) A study of fatigue damage evolution on pulsed Nd: YAG Ti6Al4V laser welded joints. *Eng Fract Mech* 117:84–93
16. Dhanasekaran R, Sathish Kumar K (2015) Microstructure, mechanical properties of A356/Li aluminum alloy fabrication by stir casting method. *Int J Appl Eng Res* 10(50):416–419
17. Hussain M, Mandal V, Kumar V, Das AK, Ghosh SK (2017) Development of TiN particulates reinforced SS316 based metal matrix composite by direct metal laser sintering technique and its characterization. *Opt Laser Technol* 97:46–59
18. Hussain M, Mandal V, Singh PK, Kumar P, Kumar V, Das AK (2017) Experimental study of microstructure, mechanical and tribological properties of cBN particulates SS316 alloy based MMCs fabricated by DMLS technique. *J Mech Sci Technol* 31(6):2729–2737

19. Gao XL, Zhang LJ, Liu J, Zhang JX (2014) Porosity and microstructure in pulsed Nd: YAG laser welded Ti6Al4V sheet. *J Mater Process Technol* 214(7):1316–1325
20. Hussain M, Kumar V, Mandal V, Singh PK, Kumar P, Das AK (2017) Development of cBN reinforced Ti6Al4V MMCs through laser sintering and process optimization. *Mater Manuf Processes* 32(14):1667–1677
21. Mandal V, Hussain M, Kumar V, Das AK and Singh NK (2017) Development of reinforced TiN-SS316 metal matrix composite (MMC) using direct Metal laser sintering (DMLS) and its characterization. *Materials Today: Proceedings* 4(9):9982–9986
22. Gupta A, Hussain M, Misra S, Das AK and Mandal A (2018) Processing and characterization of laser sintered hybrid B4C/cBN reinforced Ti-based metal matrix composite. *Opt Lasers Eng* 105:159–172

# Tool-Wear Measurement Using Parametric Optimization and Image Processing of Drilling in Al6063–Al<sub>2</sub>O<sub>3</sub> MMC



**Cherukupalli Sudhakar, Praveen Kumar and M. Jayaashwini**

**Abstract** The present work undergoes drill tool wear in drilling of aluminum metal matrix composite materials Al6063/Al<sub>2</sub>O<sub>3</sub> with different drill bits like tin-coated HSS, and TiAlN-coated HSS. HSS tool image is captured before and after drilling by using high-resolution camera when it is fixed in a fabricated setup. Camera solution drill bit image is processed using MATLAB image processing technique and the drill tool wear before machining process and after machining process is obtained drilling processed using MATLAB image processing technique and the drill tool wear before drilling process and after drilling process is obtained drilling experiments are conducted according to Taguchi OA9 design for different parameter combination and tool wear is measured and parameter levels are identified for minimum tool wear by analyzed using Taguchi technique.

**Keywords** Al6063 · SiC · Al<sub>2</sub>O<sub>3</sub>

## 1 Introduction

General conditions of a cutting tool have the main role in the optimization of metal removal processes since the accurate prediction of the exact moment for tool change to keep tolerances under control and defect of pieces by the deterioration of the tool conditions can be prevented. Metal cutting, tool wear on the tool–chip and tool–workpiece interfaces are strongly influenced by the cutting tool temperature, contact stresses, and relative sliding velocity at the interface. Wear detection is basics aspect in the Verification of production techniques as the quality of the cutting tool is directly related to the quality of the product, the level of tool wear should be kept

---

C. Sudhakar (✉) · Praveen Kumar · M. Jayaashwini  
Siddhartha Institute of Engineering and Technology, Hyderabad, Telangana, India  
e-mail: [Saisudha343@gmail.com](mailto:Saisudha343@gmail.com)

Praveen Kumar  
e-mail: [Praveen92reddy@gmail.com](mailto:Praveen92reddy@gmail.com)

M. Jayaashwini  
e-mail: [mukkerajayaashwini@gmail.com](mailto:mukkerajayaashwini@gmail.com)

© Springer Nature Singapore Pte Ltd. 2020  
G. S. V. L. Narasimham et al. (eds.), *Recent Trends in Mechanical Engineering*,  
Lecture Notes in Mechanical Engineering,  
[https://doi.org/10.1007/978-981-15-1124-0\\_25](https://doi.org/10.1007/978-981-15-1124-0_25)

under control during machining operations. These process variables depend on tool and workpiece materials, tool geometry, cutting conditions. The conventional way to characterize tool wear for a cutting operation is to perform cutting tests at constant cutting conditions and then analyse the tool wear using indirect methods such as empirical formulae, and direct method such as toolmaker microscope and a microscope or graduated magnifying lens. The disadvantage of using such an empirical approach is that in order to achieve acceptable accuracy, this procedure requires a large number of experimental tests and hence it is cumbersome and time-consuming. Sortino et al. [1] described the application of a series of filters a statistical filter to detect edges, and a high pass filter to reduce low values and a final filter to reconstruct the sliding wear land and measure the amount of tool wear. Bradley et al. [2] experiment using a machine based on the sensor system. The degree of tool wear was estimated by extracting three parameters (intensity histogram, image frequency domain content, and spatial domain surface texture). It was shown that tool wear can be characterized by a feature. Yongjin et al. [3] analyzed wear surface areas and material loss from the tool using micro-optics CCD monochrome camera and image processing algorithms. Andrew Otieno et al. [4] investigated and developed machine vision application for micromachining tool location and tool wear monitoring Zhou and Xu et al. [5] developed the idea of reinforcing metals with ceramics to produce materials with high-strength to weight ratios is an attractive one, the development of metal matrix composites (MMCs) has been one of the major innovations in the materials in the past two decades. To sun, Mehtap Muratoglu et al. [6] investigated the effect of the various cutting parameters on the surface quality and microstructure on drilling of Al/17% SiC particulate MMC by using various drills. They have suggested that TiN-coated HSS drills can be used for drilling Al/SiC-MMC rather than solid carbide tools. Pardeep Sharma [7]. The result of this microstructural investigation revealed that a nonuniform distribution of graphite particles takes place at all weight percentages of graphite reinforcement. The result of this microstructural investigation revealed that a nonuniform distribution of graphite particles takes place at all weight percentages of graphite reinforcement. Abdul Raheem K. Abid Ali [8] Metal matrix composites have attracted a lot of attention in recent years due to their excellent properties in different applications. In this study, aluminum metal matrix composites reinforced with different weight percentages (1, 2, 3, 5, 7, 10%) from alumina and silicon carbide have been preparing by using stir casting. A finite element modeling using ANSYS software is used to model aluminum metal matrix composites. Sudhakar et al. [9] work undergoes drill tool wear in drilling of aluminum metal matrix composite materials Al6061/SiCP with different drill bits the tool image are captured before And after drilling by using high-resolution camera when is fixed in fabricated setup. The tool wear image processing. Raviraj Shetty et al. [10] described the Taguchi's optimization methodology, which is applied to optimize cutting parameters in turning of age-hardened Al6061–15% vol. SiC 25  $\mu\text{m}$  particle size metal matrix composites with Cubic boron nitride inserts (CBN) KB-90 grade using steam as cutting fluid. Analysis of variance (ANOVA) is used to study the effect of process parameters on the machining process. This procedure eliminates the need for

**Table 1** Process parameters and their levels for the tool wear

Factors	Levels		
	Level 1	Level 2	Level 3
%PRM	10	15	20
Speed in rpm	450	560	630
Feed (mm/rev)	0.15	0.2	0.3
Tool materials	HSS	TiN	TiAlN

**Table 2** Experimental layout using L9 Taguchi orthogonal array

%PRM	Speed	Feed	Tool type
10	450	0.15	HSS
10	560	0.2	TiN
10	630	0.3	TiAlN
15	450	0.2	TiAlN
15	560	0.3	HSS
15	630	0.15	TiN
20	450	0.3	TiN
20	560	0.15	TiAlN
20	630	0.2	HSS

repeated experiments, time and conserves the material by the conventional procedure. The turning parameters evaluated are speed, feed, depth of cut, nozzle diameter and steam pressure. In this work, a simple method using image processing measures the drill tool wear, and Taguchi technique is used for drill bit wear optimization.

## 2 Methodology

### 2.1 Experimental Design and Fabrication

The parameters which influence tool wear are identified (Table 1). Based on the number of factors and levels OA9, OA27, OA81, we consider minimum levels, i.e., OA9 experimental design is chosen (Table 2).

## 3 Drilling Operation Process and Measurement of Tool Wear

Drilling operation is performed at Al6063 metal matrix composite material  $Al_2O_3$  at different conditions as (Fig. 1).



**Fig. 1** Experimental setup

Shown in Table 2 as per Taguchi experimental Design (OA9) and tool wear is measured through image processing. The drill tool images are captured before and after the drilling machining process. This is done for all mine experimental runs as in the following section (Fig. 2 and Table 3).



**Fig. 2** Al6063–Al<sub>2</sub>O<sub>3</sub> MMC with 10, 15, and 20%

**Table 3** Requirements of the drilling operation

Sl. No	Tool	Description
1	Work material	Al6063–Al <sub>2</sub> O <sub>3</sub> MMC with 10, 15, and 20% of reinforcement
2	Cutting tool	HSS, TiN-coated HSS, TiAlN coated HSS
3	Drill tool image	Flexible height and distance
		Digital Camera
4	Software's	Photoshop, MATLAB image processing
5	Machine	Radial drilling machine

### 4 Image Processing and Capturing of Images

Setup is fabricated for capturing drill bit images before and after the drilling process of holes. It has the flexibility to change the focal length as well as the height of the camera. In this arrangement, the camera is fixed in front of the tool holder which holds the tool in a fixed position for capturing the image of the tool. In this work, before starting drilling, the drill tool is fixed in the tool holder and an image is captured. After drilling of holes on Al6063–Al<sub>2</sub>O<sub>3</sub> MMC 10, 15, and 20% of reinforcement plate, the drill tool is removed from the drilling machine and fixed in the tool holder for capturing the image (Fig. 3).

#### Part A: Processing of before machining process for drill too

Step-I: Before drilling capture image (Fig. 4)

Step 2: Tools Select the white color and fill in the background (Fig. 5)

Step 3: Create a binary version of the image and invert the colors of this binary

After the formation of binary image, cutting edge portion of drill tool has been Fig. 6 shown in pixel region Fig. 7.

#### Part B: Processing of after machining process for drill tool

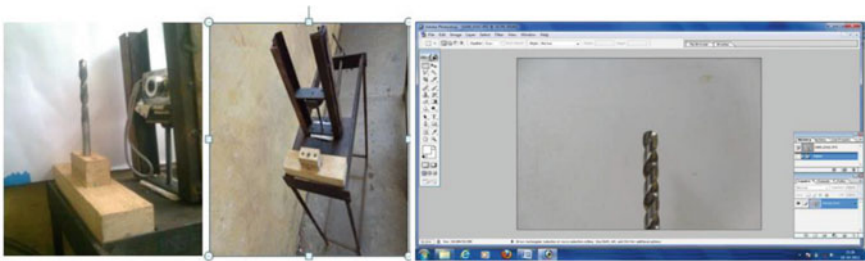


Fig. 3 Views of camera holder for capturing images

Fig. 4 Unmachined drill tool





Fig. 5 The image in image processing

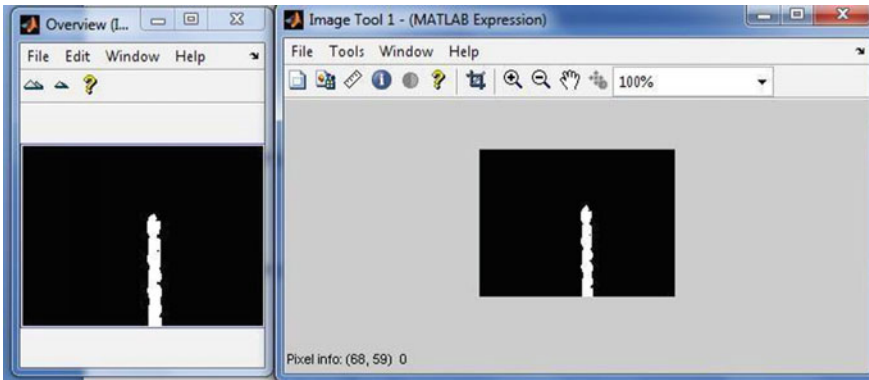


Fig. 6 Binary image and image after changing the display color

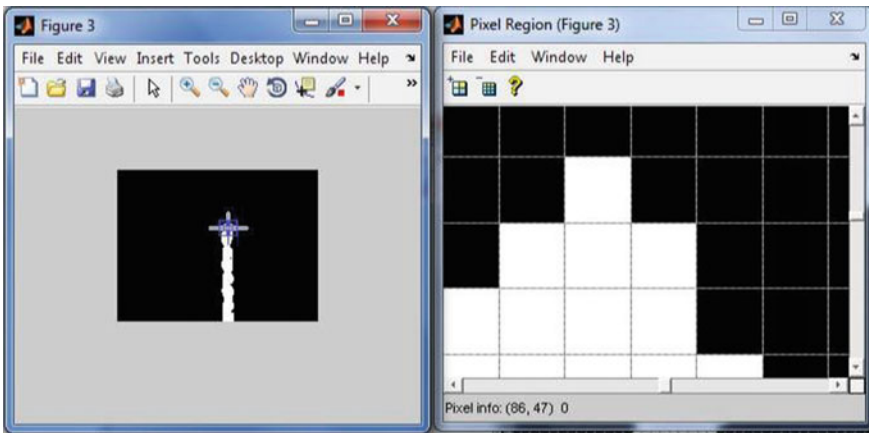


Fig. 7 Shown in the pixel region



Fig. 8 Machined drill bit

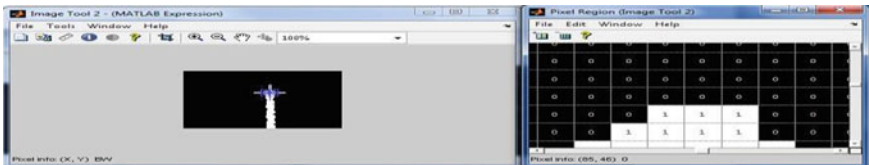


Fig. 9 Pixel region for a machined drill bit

Step-I: After drilling capture image (Fig. 8)

Step 2: After the formation of binary image, cutting edge portion of drill tool has shown in pixel region Fig. 9

**Part C: The difference between before and after machining process**

Binary images of the tool before and after drilling are machine processed using logical exclusive-XOR. The result of logical exclusive-OR is shown in Figs. 10 and 11.

Finally, the position of distance tool wear and measurement from the pixel region is specified (Fig. 12).

Aluminum metal matrix plates are drilled with an HSS drill bit, TiN and TiAlN at different workpiece speed-feed conditions and drill tool wear is measured as shown in Table 4. Tool wear while drilling Aluminum metal matrix composite 6063 with 20% Al<sub>2</sub>O<sub>3</sub> material is more when compared with the drilling of other workpiece.

## 5 Parametric Optimization

### Taguchi method

Tool wear values (Table 4) are analyzed using Taguchi S/N ratio analysis by applying lower is the better quality character. The S/N ratios are calculated using

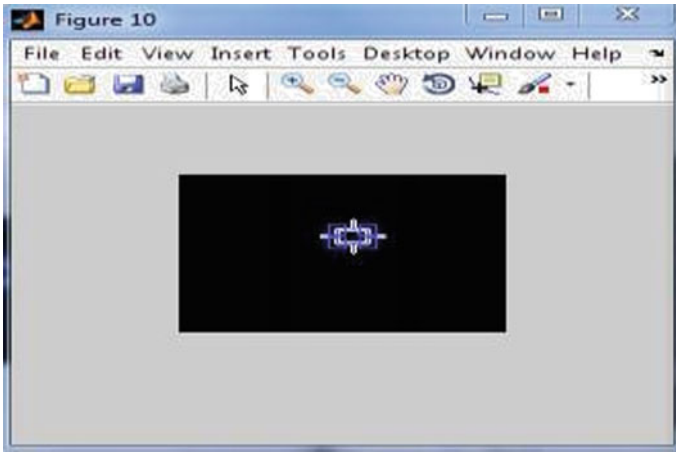


Fig. 10 Tool wear image

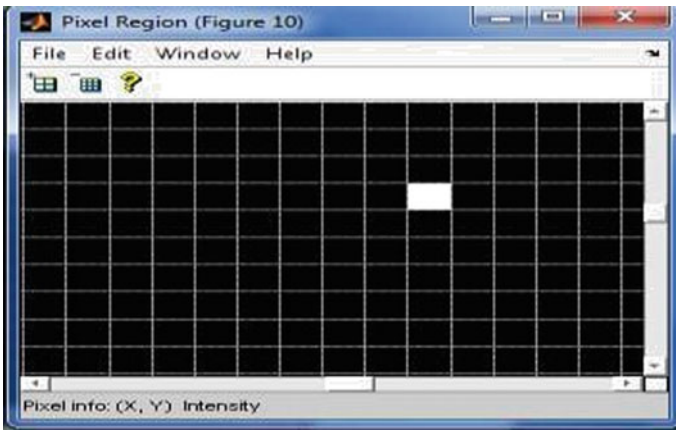


Fig. 11 Image pixel region



Fig. 12 Image showing drill tool wear

**Table 4** Tool wears from image processing

S.NO	Work piece Al6063 and Al <sub>2</sub> O <sub>3</sub> MMC	Speed in rpm	Feed-in mm/rev	Tool materials	Tool wear-in mm
1	10	450	0.15	HSS	0.708
2	10	560	0.2	TiN	0.752
3	10	630	0.3	TiAlN	0.958
4	15	450	0.2	TiAlN	0.858
5	15	560	0.3	HSS	1.015
6	15	630	0.15	TiN	0.884
7	20	450	0.3	TiN	0.925
8	20	560	0.15	TiAlN	0.8703
9	20	630	0.2	HSS	1.878

the Eq. (1) and shown in Table 5. S/N ratio for smaller the better type response is  $S/N = -10 * \log (\text{Mean Square Deviation})$ .

$$S/N = -10 \log \left( \frac{1}{r} \sum_{i=1}^r y^2_i \right) \dots \dots \dots (1)$$

where  $r = (1)$  Number of tests in a trail (no. of repetitions)  
 $y =$  response for tool wear (0.708)

$$S/N = -10 \log \left( \frac{1}{r} \sum_{i=1}^r 0.708^2_i \right) = 2.6954$$

**Table 5** S/N ratio values for tool wear

Experimental run	Tool wear in mm	S/N ratio for tool wear
1	0.708	2.6954
2	0.754	2.3456
3	0.958	0.37269
4	0.858	1.33024
5	1.015	-0.12932
6	0.884	1.07095
7	0.925	0.67717
8	0.8703	1.130111
9	1.878	-5.47392

**Table 6** Mean S/N response table for tool wear

Level	Percentage of reinforcement material (PRM)	Speed (S)	Feed (F)	Tool Material (TM)
1	1.8685	1.58826	1.65281	-0.94862
2	0.75730	1.15881	-0.55600	1.40792
3	-1.22221	-1.3434	0.30684	0.94435
Delta	3.09078	2.93169	2.20882	2.35654
Rank	1	2	4	3

**Table 7** Difference between the initial and optimal combination of parameters

Combination	Combination of controllable parameters	Tool wear (mm)
Initial combination	PRM2, S2, F2, TM2	0.824
Optimal combination	PRM1, S1, F1, TM2	0.522
Gain	N/A	0.302
Percentage of gain	N/A	36.6%

**Evaluation of optimal levels of process parameters for responses:**

In Table 6, the optimum combination of parameters is identified. For this combination PRM(1) S(1) F(1) TM(2), confirmation experiment is conducted and obtained tool wear is compared with results of initial combination and optimal combination of controllable parameters in Table 7.

**6 Conclusions**

Results are depicted that in PRM(1) S(1) F(1) TM(2), the percentage of reinforcement material is mainly influencing the drill tool wear, the second influencing factor is spindle speed follows the tool material and feed rate. Now this work, image processing technique has been used for determining drill tool wear. By using this method, the value and also the image of tool wear can be observed, directly, it can economically measure the tool wear more accurately without contacting the tool. It is also useful in preventing damage to the surface quality, surface roughness, and dimensional accuracy of the product. This method can be also extended for other operations like turning-milling, etc.

## References

1. Sortino M (2003) Application of statistical filtering for optical detection of wear. *Int J Mach Tools Manuf* 43(5): 493–497
2. Bradley C, Wong YS (2001) Surface texture indicators of tool wear—a machine vision approach. *Int J Adv Manuf Technol* 17:435–443
3. Yongjin K, Fischer GW (2003) A novel approach to quantifying tool wear and tool life measurement for optimal tool management. *Int J Mach Tools Manuf* 43:359–368
4. Otieno A Vision proceedings of the 2006 IJME-INTERTECH conferences, vol 4.5
5. Zhou W, Xu ZM (1997) Casting of SiC Reinforced metal matrix composites. *J Mater Process Technol* 24
6. Tosun G, Muratoglu M (2004) The drilling of Al/SiCp metalmatrix composites. Part II: work piece surface integrity. *Compos Sci Technol* 64:1413–1418
7. Sharmaa P, Sharma S, Khanduj D (2015) A study on microstructure of aluminium matrix composites. *J Asian Ceram Soc* 3: 240–244
8. Ali ARKA (2018) Finite element analysis of metal matrix composite materials. *J Univ Babylon, Eng Sci* 26(5):166–175
9. Sudhakar C, Jayashwini M, Swapana D (July 2017) Tool-wear measurement in drilling of Al6063-Al<sub>2</sub>O<sub>3</sub> MMC using parametric optimization & image processing. *Int J Sci Eng* 6(24):4798–4802
10. Shetty R, Pai RB, Nati, Nayak R (2006) Taguchi's technique in machining of metal matrix composites, vol 2.3

# Parametric Optimization for PA2200 Quality Prototype Fabricating Process (Selective Laser Sintering) by Taguchi Method



Battula Narayana and Sriram Venkatesh

**Abstract** This research study presents the development of the quality prototype is critical in any additive manufacturing process as it directly relates to its strength and accuracy. The process of Selective Laser Sintering (SLS) is a versatile and proven process to build quality prototypes. This paper attempts to study the influence of build factors such as part orientation, part bed temperature, and refresh rate (one time used and virgin material by percentage of volume) on the part quality. Taguchi design technique L9 (3 × 3) array settings used. Aimed at the required process factors with least number of experimental runs, the L9 orthogonal array method of experiments prepared using the analysis tools S/N ratio, and Analysis of variance, (ANOVA). The significant control factors are identified for surface roughness, which is necessary for designers and Rapid Prototype machine users.

**Keywords** Selective Laser Sintering (SLS) · Analysis of variance (ANOVA) · Rapid Prototype · S/N ratio

## 1 Introduction

In this study, a model design technic will be introduced to determine the optimal surface finish, based on changing the orientation of the structure, chamber temperature, refresh rate and other parameters using a selective laser-firing process (SLS) [1]. The design studies these parameters effect on the surface. The experiments were passed out by means of the Taguchi L9 3 × 3 arrays with three levels for build Orientation, Temperature, and refresh rate, presented in Table 1. The results are analyzed statistically to determine the essential factors and their interactions. The essential

---

B. Narayana (✉) · S. Venkatesh  
Department of Mechanical Engineering, Osmania University College of Engineering, Hyderabad  
500007, India  
e-mail: [bnarayan@gmail.com](mailto:bnarayan@gmail.com)

S. Venkatesh  
e-mail: [venkatmech@yahoo.com](mailto:venkatmech@yahoo.com)

© Springer Nature Singapore Pte Ltd. 2020  
G. S. V. L. Narasimham et al. (eds.), *Recent Trends in Mechanical Engineering*,  
Lecture Notes in Mechanical Engineering,  
[https://doi.org/10.1007/978-981-15-1124-0\\_26](https://doi.org/10.1007/978-981-15-1124-0_26)

**Table 1** Report on experimental control factors and levels

Symbol(i)	Factors	Level-1	Level-2	Level-3
A	Orientation	0°	45°	90°
B	Temperature (°C)	173	170	167
C	Refresh rate (%)	0	30	60

factors, their interactions, and optimal settings are proposed [2]. The optimal conditions of the process are defined for the general improvement of the surface roughness. Surface roughness is the degree of surface structure. It is quantified because of the perpendicular deviances of the actual surface of this ideal shape. If these anomalies are high, the surface is uneven; when they are slight, the surface is even. Normally, roughness is designating be the quantity of the surface, part of the shortwave component with a higher frequency. An important role has taken the roughness in revealing how a real object acts together with its environment. Uneven surfaces are generally used faster and have used more quickly and the friction factors are higher than with smooth surfaces. Roughness is often an indicator of the effectiveness of a good mechanical component because the surface abnormalities can form vertical layers or corrosion points. While unevenness is generally not desirable, controlling production is difficult and expensive. The reduction of surface roughness will generally increase exponentially for its production. This often results in trade between the cost of manufacturing a component and its action in the application.

## 2 Selective Laser Sintering

This is a three-dimensional printing method where pieces are formed by sintering when the CO<sub>2</sub> laser beam hits a layer of thin and selective material. The procedure starts with the CAD model and then converts it into an STL file where the parts share the data for each layer. The thickness and replacement of each layer depend on the equipment used. The Selective Laser Sintering (SLS) provides fast, flexible, and economical components for 3D CAD data [3]. The first finished layer passes under a layer of the object, the roller circulates the next layer of the powder, and this process continues until the product is finished. The powder does not melt during process or fuse but acts as a built-in support structure. Therefore, the support requirements are not required separately and when the component is complete, the incomplete powder material is completely removed. SLS technology has sufficient strength in the part and no support is required. The drawback is the excessive consumption of energy.

### 3 Experimental Design

The experimental part building material is PA 2200, and the building models tensile test specimens prepared. The STL setup was produced by SOLIDWORKS -17 and uploaded to the 3D system SLS FORMIGA P100 EOS Rapid Prototyping machine. The control factors orientation (0°, 45°, 90°), part bed temperature (167, 170, 173 °C), and refresh rate (percentage of one time used and fresh material by volume) (0, 30, 60%) are presented in Table 1. The sample profile of surface roughness tests of SLS prototype, tests have given below in Figs. 2 and 3. The surface roughness which is treated as quality properties index, the lowest variability and optimal designs are achieved using the S/N ratio. Advantages of the S/N ratio include increasing the influence of weighting factors, reducing interactive performance, at the same time processing the average, variation and enhancing the quality [4].

### 4 Arithmetic Average Height (Ra)

The average arithmetic height ( $R_a$ ), (Eq. 1) also known as centerline average (CLA), is a maximum common standard of a characteristic regulator. It is well-defined as the outright deviance of the irregularity of the centerline shown in Fig. 1, for the specimen interval. This factor is simple to describe, easy to compute and provides a good description of the variation. It is not sensitive to small changes in the profile and it does not furnish information on wavelengths [5]. The numerical accomplishment of the arithmetic parameter and the mathematical description of average height are the following:

$$R_a = \frac{1}{l} \int_0^l |y(x)| dx \tag{1}$$

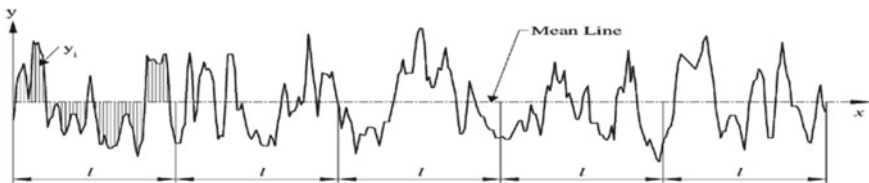


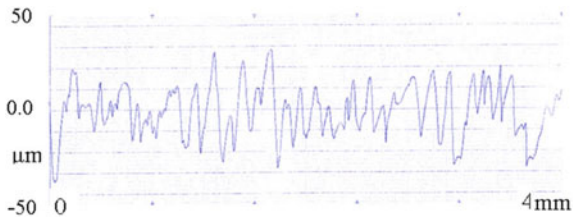
Fig. 1 Arithmetic average height (Ra), description



Fig. 2 Specimen 2, Profile of Mitutoyo SJ-301 roughness Tester



Fig. 3 Roughness profile of specimen 2, built orientation at 0°



## 5 Results and Analysis

### 5.1 Analysis of the Experimental Results

Investigation of experimental facts taken from Taguchi’s experimental L9 (3 × 3) array design runs was carried out on MINITAB R18 software that was used at 95% level of confidence.

### 5.2 Signal to Noise (S/N) Investigation

The response table of surface roughness for the S/N ratio is shown in Table 2 and the plot of S/N ratio for smaller is better given in Fig. 4. The basic method for formatting

**Table 2** L9 (3 × 3) Orthogonal Array, control parameters, and S/N ratio of  $R_a$

Experimental run	Coded values			Actual values			$R_a$ surface roughness Avg $\mu\text{m}$	S/N Ratio for $R_a$ surface roughness	Mean
	A	B	C	A-Orientation degrees	B- Part-Bed temperature °C	C- Refresh rate by % of volume (%)			
T1	1	1	1	0	173	0	9.113	-19.193	9.113
T2	1	2	2	0	170	30	9.563	-19.612	9.563
T3	1	3	3	0	167	60	8.716	-18.807	8.716
T4	2	1	2	45	173	30	10.086	-20.075	10.086
T5	2	2	3	45	170	60	9.633	-19.675	9.633
T6	2	3	1	45	167	0	10.191	-20.163	10.190
T7	3	1	3	90	173	60	9.523	-19.575	9.523
T8	3	2	1	90	170	0	10.88	-20.732	10.880
T9	3	3	2	90	167	30	10.203	-20.174	10.203
Average mean in $\mu\text{m}$							9.7676		

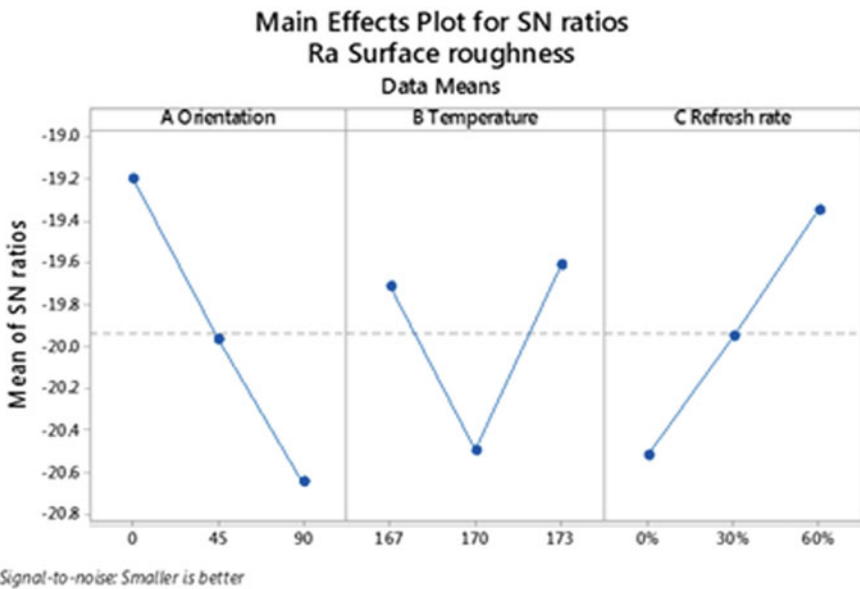


**Fig. 4** Main effect plot for S/N ratios of  $R_a$  surface rough

the Taguchi method converts the objective parameter into an S/N ratio. The stable quality can be attained as the smaller the ratio of S/N is small. As per the response variable, smaller the better is applied for the surface roughness analysis [6, 7]. The quantity of surface roughness is the relative sliding one upon another surface cross-sectional area. The results of an experiment and S/N ratios are provided in Table 2.

**Table 3** Response Table for signal to noise ratios of  $R_a$

Level	A	B	C
1	-19.20	-19.61	-20.03
2	-19.97	-20.01	-19.95
3	-20.16	-19.72	-19.35
Delta	0.96	0.39	0.68
Rank	1	3	2

From this table, the mean S/N was calculated as  $-19.7788$ . The response table for S/N ratios of control factors like part orientation, part bed temperature, and refresh rate were obtained using Taguchi technique given in Table 3. The optimum factors A1, B3, C<sub>3</sub> were has been determined best for the surface roughness from Table 3. Figure 4 plotted the S/N graph to find optimum parameters. According to Fig. 6, for the S/N ratios, the combination of optimal parameters was decided for factor A, level 1 (S/N =  $-19.20$ ), factor B level 3 (S/N =  $-19.72$ ), Factor C level 3 (S/N =  $-19.35$ ). The surface roughness response table for the S/N ratio is shown in Table 4 and the plot of S/N ratio for smaller is better presented in Fig. 4. In this test, the quality function “the smaller, the better” is used. For “smaller the better” quality characteristics S/N (Y) is expressed as in Eq. (3)

$$Y = -10 \log_{10} (\text{MSD}) \tag{2}$$

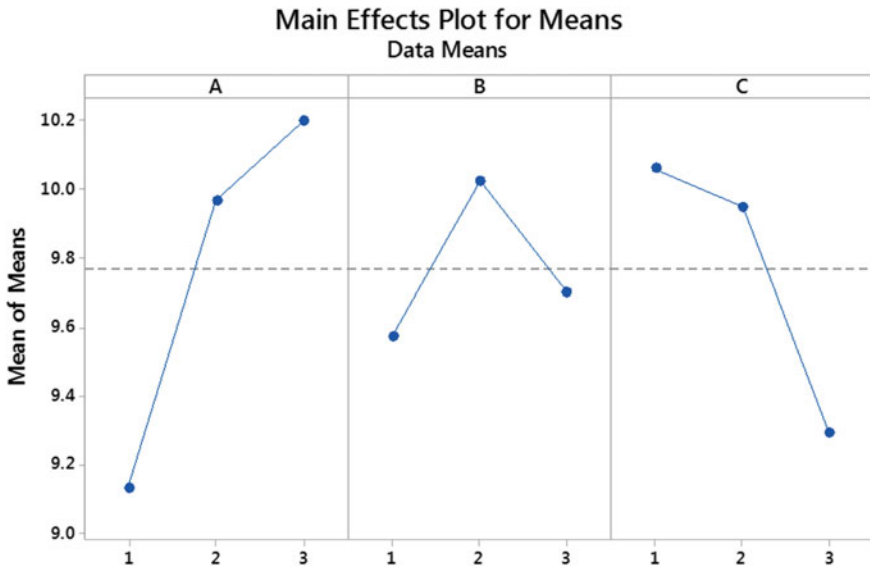


**Fig. 5** Main effect plot of means for ( $R_a$ ) surface roughness

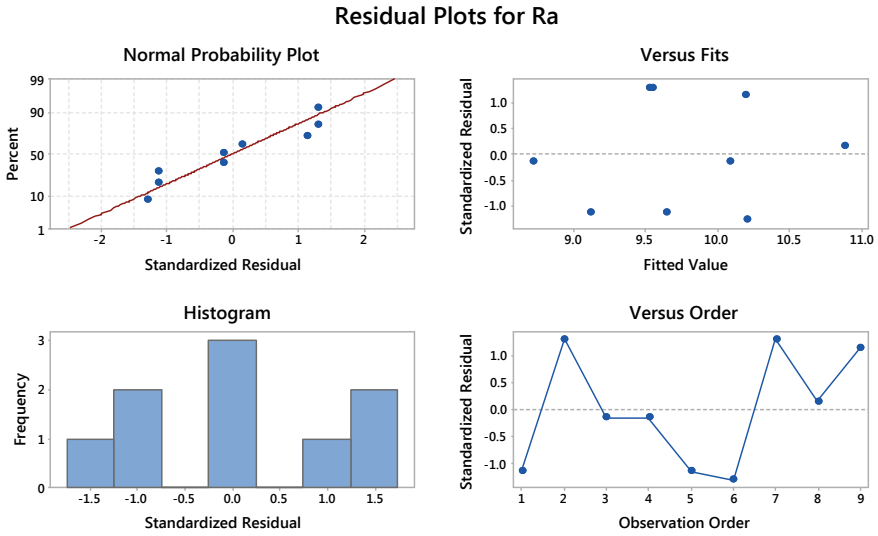


**Fig. 6** Standardized plot for Ra

**Table 4** Response Table for means

Level	A	B	C
1	9.131	9.574	10.061
2	9.970	10.026	9.951
3	10.202	9.703	9.291
Delta	1.071	0.451	0.770
Rank	1	3	2

$$MSD = \alpha^2 + (m_{avg} - m_0) \tag{3}$$

where  $\alpha^2$  is called variance,  $m_{avg}$  is the average of the data, and  $m_0$  is the target value, in this case, it is zero. Experiment analysis carried out using Minitab-R18 software. The main effect plot S/N ratio is used to determine optimum factor level. Respective influence of each factor is estimated ANOVA. Calculations necessary for ANOVA are given in Eq. (4).

$$Ts = \sum_{k=1}^N (Y_k - \bar{Y})^2 \tag{4}$$

where the overall sum of squares is Ts, N is number of observations and  $\bar{Y}$  is the overall mean of S/N Ratio

$$TTj = \sum_{k=i}^j (Y_{ji} - \bar{Y})^2 \tag{5}$$

where the sum of square deviation of *j*th factor is *TTj*, *j*th factor for the *i*th level

$$U_j = \frac{TTj}{f_j} \tag{6}$$

where *U<sub>j</sub>*, *f<sub>j</sub>* are variance and degrees of freedom respectively of *j*th parameter.

$$F_j = \frac{U_j}{U_e} \tag{7}$$

where *F<sub>j</sub>* is F statistics of *j*th factor and the error of variance is *U<sub>e</sub>*.

From Fig. 4, it exhibits that the surface roughness reduces an increase in part orientation from 0° to 90°; the reason is Orientation cause stair-stepping in SLS parts, which leads to the inferior surface finish. As the temperature increases from 167 to 170 °C, reduce the surface roughness and then after increase in temperature to 173 °C the surface roughness increases, the cause is explained as follows as the temperature increases strength and density increases, the powder particles are fused together closely with proper sintering and leads to decreases in surface roughness. Further increase in temperature, decreases the density it heads to increase in surface roughness. Increase in refresh rate (the combination of fresh and single time used material) from 0 percentage, 30 to 60% the surface roughness increases, the reason for this the particles of refresh material fused together closely with suitable sintering it helps to increase in surface roughness. The response Table of means has shown in Table 4 and the plot for means of *R<sub>a</sub>* given in Fig. 5.

If the error rate reaches zero, F and ANOVA cannot be calculated. In these cases, it can predict and control the observed values using a combination of factor levels as in this following Eq. (7):

$$\begin{aligned} Y_{\text{pred}}(\text{O, T, RF}) &= \overline{Y \text{ mean}} + (\overline{A_o} - \overline{Y \text{ mean}}) + (\overline{BT} - \overline{Y \text{ mean}}) + (\overline{CRF} - \overline{Y \text{ mean}}) \\ &= 9.7676 + (9.7676 - 9.7676) + (9.7676 - 9.7676) + (9.7676 - 9.7676) \\ Y_{\text{pred}}(\text{O, T, RF}) &= 9.7676 \mu\text{m} \end{aligned} \tag{7}$$

where *Y<sub>pred</sub>* is predicted S/N ratio of response,  $\bar{Y}$  is the sum of experimental average,  $\overline{A_o}$ ,  $\overline{BT}$ , and  $\overline{CRF}$  are the average response for factors of A, B, and C. The insignificant factors and the interactions were generally omitted from Eq. (7) [8]. It gives the influence of independent variables, as well as the percentage of the contributions of these dependent variables to the response variable. ANOVA analysis was performed in this study at 95% confidence level and 5% significance level. The F values (*F* > *P*) shown the significance of control factors. Table 5, shows the percentage of response factor variables with ANOVA. Therefore, the significance of each parameter is identified from the ANOVA table. Based on the analysis of variance (ANOVA)

**Table 5** Comparison of predicted and experimental value for surface roughness

Parameter optimal setting	Orientation	Temperature	Refresh rate	Experimental value	Predicted value of S/N	Mean value	Regression model value
1	0	173 °C	60%	9.8 μm	9.76 μm	9.76 μm	9.11 μm

**Table 6** Regression analysis:  $R_a$  versus A, B, C

Source	DF	Seq SS	Contribution (%)	Adj SS	Adj MS	F-Value	P-Value
Regression	6	3.358	99.98	3.35888	0.5598	1895.25	0.001
A	1	1.7208	51.22	0.1854	0.1854	627.89	0.002
B	1	0.0249	0.74	0.0052	0.0052	17.65	0.052
C	1	0.8893	26.47	0.5101	0.5101	1727	0.001
A * B	1	0.0024	0.07	0.3265	0.3265	1105.42	0.001
A * C	1	0.2575	7.67	0.6926	0.6926	2344.85	0.000
B * C	1	0.4637	13.80	0.4637	0.4637	1570	0.001
Error	2	0.0005	0.02	0.0005	0.0002		
Total	8	3.3594	100.00				

for surface roughness (Table 6) f-value can be concluded the surface roughness has mainly influenced by the factor A—part orientation [9, 10]. The choice of factors of experimental parameters and their corresponding levels, the analysis of variance (ANOVA) controls the experimental results to decide the effect of each parameter against the objective function [11]. Residual plots for surface roughness is given in Fig. 6.

## 6 Recognition of Significant Parameters

The process parameters (Orientation, Temperature, and Refresh rate) which were influences much on response Variable, has recognized by means of the percentage of influence of each parameter. A-Orientation Parameter through more percentage of influence 51.22% and is followed by factor C-Refresh Rate 26.47% and interaction factor B \* C with 13.80% are a significant parameter for the response variable, the part bed Temperature, the interaction factors A \* B and A \* C are insignificant factors. Analysis of variance for corresponding response variables the percentage of influence of the parameters is shown in Table 5, [11, 12]. Hence, from the ANOVA Table 6, the significance of each parameter is identified; the comparison of predicted and experimental value for surface roughness has given in Table 5.

It shows that  $R^2$  value is 99.98%; this is the confirmation that has a significant impact on the surface roughness. Therefore, the null hypothesis is refused and the

**Table 7** Confirmation test results

Experimental run	Orientation angle	Temperature (°C)	Refresh rate (%)	Surface roughness (μm)
1	0°	173	60	9.83
2	0°	173	60	9.77
3	0°	173	60	10.64

surface roughness values are valid from my experimental results shown in Table 2. The average roughness ( $Ra$ ) value from the regression equation is 11.2 mm [13].

Regression Equation

$$Ra = 6.7219 + 0.7033 A - 0.1179 B + 2.6815 C + 0.5290 A * B - 0.7705 A * C - 0.6305 B * C$$

$$Ra = 9.11 \mu\text{m}$$

## 7 Confirmation Test

The confirmation test has been brought out after recognition of significant factors to verify and found out the most set of optimal level factor combinations. In this present research work, has shown that the significant combination parameters A1, B3, C3. Three tests were conducted with optimal parameters on surface roughness, the results shown in Table 7 [14].

## 8 Conclusions

The analysis of experiments was conducted using the Taguchi method L9 (3 × 3) orthogonal method. The study on the ratio of S/N for surface roughness has taken as “smaller the better”. It is evident that from this analysis, the significant parameters play a crucial role in building a quality prototype. Optimization parameters for surface roughness discussed. The building of a quality prototype by SLS process for various part orientations, part bed temperature, and refresh rate is analyzed. The significant combination parameters A1, B3, and C3 were identified at the level of 95% confidence using ANOVA, and the parameters contribution has carried out as A-orientation influenced 51.22%, followed by parameter C-refresh rate influenced 26.47% and interaction factor B \* C with 13.80% has influenced. The factors B-part bed temperature, and interaction factors A \* B and A \* C were pinpointed as insignificant factors. This empirical technique is applied to other RP processes to

optimize parameters with several materials. The model of this process may be further improved by means of using non-conventional techniques of optimization, for instance, neural networks and genetic algorithms.

## References

1. Guo N, Leu MC (2013) Additive manufacturing: technology, applications and research needs. *Front Mech Eng* 8(3):215–243
2. Park R et al (2014) Establishment of process model for rapid prototyping technique (stereolithography) to enhance the part quality by Taguchi method. *Procedia Eng.* 180(1):1150–1159
3. Guan G et al (2015) Evaluation of selective laser sintering processes by optical coherence tomography. *Mater Des* 88:837–846
4. Schmidt J et al (2015) A novel process chain for the production of spherical sls polymer powders with good flowability. *Procedia Engineering* 102:550–556
5. Soliman HH, Gadelmawla ES, Koura MM, Maksoud TMA, Elewa IM (2002) Roughness parameters. *J Mater Process Technol* 123:pp. 133–145
6. Sood AK, Ohdar RK, Mahapatra SS (2009) Improving dimensional accuracy of fused deposition modelling processed part using grey Taguchi method. *Mater Des* 30(10):4243–4252
7. Sood AK, Ohdar RK, Mahapatra SS (2009) Grey Taguchi method for improving dimensional accuracy of FDM process. *Mater Des* 30(10):4243–4252
8. Raju BS, Sekhar UC, Drakshayani DN (2014) Optimizing multiple quality characteristics of stereolithography process via Taguchi method-based grey analysis for SL5530 epoxy resin material to enhance part quality. *Procedia Mater Sci* 5:2532–2541
9. Maiyar LM, Ramanujam R, Venkatesan K, Jerald J (2013) Optimization of machining parameters for end milling of Inconel 718 super alloy using Taguchi based grey relational analysis. *Procedia Eng* 64(June 2015):1276–1282
10. Rahul SH, Balasubramanian K, Venkatesh S (2017) Optimizing inkjet printing process to fabricate thick ceramic coatings. *Ceram Int* 43(5):4513–4519
11. Raju BS, Shekar UC, Venkateswarlu K, Drakashayani DN (2014) Establishment of process model for rapid prototyping Technique (stereolithography) to enhance the part quality by Taguchi method. *Procedia Technol* 14:380–389
12. Guo J, Bai J, Liu K, Wei J (2018) Surface quality improvement of selective laser sintered polyamide 12 by precision grinding and magnetic field-assisted finishing. *Mater Des* 138(October 2017):39–45
13. Ferraz EG, Andrade LCS, Dos Santos AR, Torregrossa VR, Freire MDRS, Sarmento VA (2011) Effect of different surface processing protocols in three-dimensional images for rapid prototyping. *Adv Eng Softw* 42(6):332–335
14. Hong M-H, Min B, Kwon T-Y (2016) The influence of process parameters on the surface roughness of a 3D-printed Co–Cr dental alloy produced via selective laser melting. *Appl Sci* 6(12):401



# Scheduling of Flexible Manufacturing System by Hybridizing Petri Net with Improved Scatter Search Algorithm



T. R. Chinnusamy, Prabhakar Kammar, Fathima Praveen, T. Karthikeyan, M. Krishnan, N. Varshitha and Ashika Ananda Shetty

**Abstract** The Flexible Manufacturing Systems (FMSs) are highly advanced and integrated with manufacturing systems to produce products. It consists of two or more robots with machining cells and automated guided vehicles (AGVs) that will function under computer control. This paper highlights the importance of using loop layout and planning in FMS by decreasing the backtracking distance and distance traveled by Automated Guided Vehicle (AGV). A hybrid metaheuristic algorithm is used in this paper and it is called as Improved Scatter Search Algorithm (ISSA). The FMS Scheduling is a complex phenomenon due to the huge variability in the working parameters. Problems related to scheduling for general cases are characterized as NP-hard. From the given size of the problem, the computation time required to obtain the optimal schedule mostly will produce exponential results. In this research paper, the dispatching rules are merged with PNs and also PNs with hybrid Improved

---

T. R. Chinnusamy (✉) · P. Kammar · F. Praveen  
Department of Mechanical Engineering, Gopalan College of Engineering and Management,  
Bangalore, India  
e-mail: [chinnu\\_samy80@yahoo.co.in](mailto:chinnu_samy80@yahoo.co.in)

P. Kammar  
e-mail: [dr.prabhakarkammar@gmail.com](mailto:dr.prabhakarkammar@gmail.com)

F. Praveen  
e-mail: [fathima.kareem@gmail.com](mailto:fathima.kareem@gmail.com)

T. Karthikeyan  
MIET, Tirchy, India  
e-mail: [drtkarthikeyan@gmail.com](mailto:drtkarthikeyan@gmail.com)

M. Krishnan  
Tamil Nadu Water Supply Drainage Board, Maintenance Sub Division-1, Namakkal, India  
e-mail: [mkrishnanksrct@gmail.com](mailto:mkrishnanksrct@gmail.com)

N. Varshitha · A. A. Shetty  
Department of Electronics and Communication Engineering, Gopalan College of Engineering and  
Management, Bangalore, India  
e-mail: [nvarshitha099@gmail.com](mailto:nvarshitha099@gmail.com)

A. A. Shetty  
e-mail: [ashikashetty2017@gmail.com](mailto:ashikashetty2017@gmail.com)

Scatter Search algorithm for FMSs performance measure. These traditional hybrid techniques were used for comparing and verifying simulation results. Finally, the test problems were chosen from the review paper for better comparison and PN hybrids with Improved Scatter Search algorithm provide better result in terms of machine utilization, AGV idle time and makespan considering with and without breakdown condition when it is compared with dispatching rules and Petri net with dispatching rule techniques.

**Keywords** Flexible manufacturing system · Scatter search · Improved scatter search · Scheduling · Petri net · Dispatching rules

## 1 Introduction

Customer demand and requirements of any product changes are very rapid in the present market scenario. The manufacturing system is to accommodate the above changes as quickly as possible to compete in the global market. The above advancement will induce conflict in the manufacturing system as the variety of parts increases then there will be productivity decreases. The FMS was a better combination of medium variety of parts with medium production rate. The scheduling problems were solved to determine sequencing of operation considering every job in the process so that, the makespan of each job in the process is minimized or in other words the machines utilization will be maximized. The FMS is a fully automatic manufacturing system and may be used in several parallel production environments for better production rate. The layout of FMS has an impact on production time and efficiency of the system. The physical layout of designing the FMS is an important issue in utilization of machines and material handling systems in the industrial field. In late 1970s, scheduling of FMSs has been published and many researchers are undergone in this popular topic. In FMS, it usually consists of several numerically controlled manufacturing machines and automated material handling systems that transport materials from machines to tool systems and vice versa. Routing flexibility in facility layout where each product can be manufactured via any one of several available routes. Some criteria will optimize with the use of high-level control system and used to decide that which resources are assigned to which product at specific time duration. The system process planning or process scheduling is to determine the allocation of parts to machines considering the sequence of operations to be done. Finally, the constraints of the system are met and performance criteria are optimized. The scheduling process in manufacturing system is a typical optimization problem for which it decides the time of start of the process and allocations of jobs to be processed in the system.

## 2 Literature Survey

A proposed problem of multiterminal Net Assignments by Scatter Search in FPGA-based logic emulation was used. A new mathematical model for the above problem and a powerful heuristic approach also called scatter search algorithm, is adopted. Heuristics techniques are effectively incorporated in many processes for accelerating the optimization search. The experimental results always demonstrate that the promising performance of techniques used [1]. A hybrid scatter search technique or electromagnetism metaheuristic algorithm is used for project scheduling. In the last few years, there are several effective algorithms had been used for solving the problem, which is related to resource-constrained project scheduling. However, the challenging natures of the above problem having relatively small instances that summarize the strongly hard status which restricts the effectiveness of exact optimization. The authors used a new metaheuristic technique for the above-said problem, in which it is able to provide near-optimal heuristic solutions for relatively large instances too if right technique is used for the exact problem [2]. A scatter search technique for the optimum disassembly sequence problem was discussed. Few difficult problems faced by researchers in determining an efficient sequence of disassembly for a product and its end of the product. In this research work, a scatter search (SS) technique is presented which aim to deal with optimum sequence problem for disassembly. The SS algorithm was tested with few case studies of 48 products which consisting of 25, 50, 75, and 100 components of right-angled parallelepiped that is connected by different joints type [3]. The Scatter Search technique for the periodic capacitated arc routing problem is used. Its objective is to assign a set of service days to each edge in a given network. Heuristic techniques were developed by the author and he evaluated on PCARP instances, which are derived from classical CARP studies [4]. To solve the clustering problem, the author proposed a scatter search technique with a given set of customers. The ultimate objective of the paper is to minimize the summation of distances from every cluster centers to all other clients in their cluster. The final computational results on a set of instances show that the heuristic is the best heuristics developed for the above one. [5].

The process scheduling shows that it is an alternative plan to share resources and it will assign resources to the selected activities, which are already planned [6]. In any manufacturing system, the resources will represent as machines, operators, robots, etc... and activities represent the processing of products on the machines or it may be the transport of products between each machines. In FMSs, the complexity is more to calculate the performance measures accurate. The author extensively used computer simulation to get the optimum result of extremely intricate flexible manufacturing systems [7–9]. PNs are mathematical modeling and graphical tool, which is applicable to frequent systems. The most important advantages of using PNs technique in the manufacturing system scheduling over other tools is its ability to represent lots of states in a concise mode, model deadlock situation, conflicts in the system, multi-resource constraints, etc... [10]. In manufacturing system, the total production cost incurred because of the material handling cost. The author

Eynan and Rosenblatt [11] specified that the material handling cost is about 30% of the cost of total production. Hence in FMSs automated material handling system plays an important role. The stochastic colored PNs (SCPNs) model results to be live and bounded. The liveness and boundness can be analyzed using simulation or reachability analysis. The better result will depend on the size of the model, but it cannot perform quantitative analysis [12]. To perform the scheduling in cell-level, the heuristic dispatching rules are integrated with colored timed Petri net simulation [13]. The dispatching rules algorithm which is integrated with hybrid search algorithm provided by the PN simulation to analyse the system [14]. The author used modeling and scheduling techniques using PNs and AI for analyzing FMSs. Here, two-hybrid search algorithms are proposed to decrease the difficulty of large systems [15].

### 3 Methodology

In FMS loop layout, one of the objectives is to reduce the distance traveled and backtracking distance of material handling system (Automated Guided Vehicle). This paper proposes hybridizing PNs with dispatching rules and PNs with Improved Scatter Search techniques for measuring the FMSs performance.

#### 3.1 *Improved Scatter Search (ISS)*

Scatter Search (SS) is a metaheuristic technique and a population-based approach was recently proposed in 1992 by Marco Dorigo et al. to solve several discrete optimization problems. The Improved Scatter Search (ISS) imitate like real ants and find the shortest route between a food source and their nest. Each ant communicates with another ant by pheromone deposit and the optimum path is selected by exchanging their information. More number of ants will traces on a path, so that the pheromone deposit of each ant will increase the deposition which attractive the other ants to follow the path. This type of ants characteristic is adapted on Improved Scatter Search optimization technique to solve real problems.

##### **Algorithm of Improved Scatter Search**

Step 1: Generate the initial sequence and find the objective function value from the initial sequence.

Step 2: Using diversification method to obtain the new set of sequences.

Step 3: Using improvement method from diversification method to get new sequence.

Step 4: Objective function is calculated for all the sequences and arranges them all in ascending order.

Step 5: The crossover and mutation operation is to be done for the inferior sequence. For each newly generated sequence the objective function value.

Step 6: The best or worst solution in the iterations are updated.

Step 7: If Best solution is updated, the process continues from step 2 and it is repeated.

Step 8: If worst solution is updated the process continues with step 5.

Step 9: The process is stopped if the Z value remains the same for n number of iterations.

### ***3.2 Petri Net Dispatching Rules***

The solution methodology is based on dispatching rules that are extensively used to search for a solution given search space. In general, there are two methods used to overcome the complication in the computation. First, a better heuristics function can be employed and the second one is to implement hybrid heuristics search techniques. The target state is selected depends on the minimization of makespan using dispatching rules. Finally, the rule and the optimum path were selected.

#### **Algorithm of Petrinet with Dispatching Rule**

Step 1: Initialize the machine sequence on open.

Step 2: Initialize the operation time matrix array (machine processing times for the jobs).

Step 3: If open is empty, leave the program.

Step 4: Obtain the list of possible states using the dispatching rules on open.

Step 5: Remove the identical markings from the list.

Step 6: Firing the target states, which have the highest priority (minimum makespan) in the table.

Step 7: If marking m is a final marking, exit successfully with the solution.

Step 8: Else go to Step 3.

Step 9: Find the optimal path from the priority table.

Step 10: For every markings  $m'$  to m, the makespan is calculated and optimum path was selected.

Step 11: Display/print the results.

### ***3.3 Dispatching Rules***

This paper discusses hybridizing PNs with dispatching rules for measuring the performance of FMSs. Dispatching rules play a vital in scheduling FMS. A variety of simple and complicated dispatching rules was proposed and many investigations were carried out toward a combination of dispatching rules in-order to obtain a feasible rule which performs better when compared to others. To evaluate the performance of variety of dispatching rules under different conditions of the system, simulation

**Table 1** Dispatching rules and their descriptions

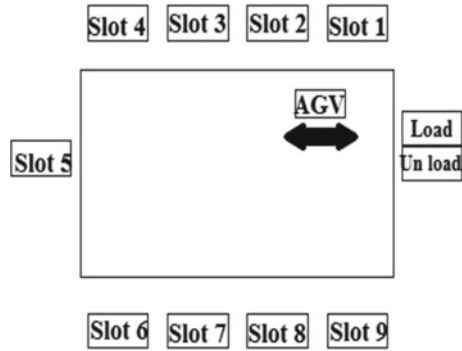
S. No.	Dispatching rules	Description
1.	Shortest Processing Time (SPT)	Select a job having minimum processing
2.	Longest Processing Time (LPT)	Select a job having maximum processing
3.	Least Operations Remaining (LOR)	Select a job with the least operations total processing time for unfinished operations
4.	Most Operations Remaining (MOR)	Select a job with the most operations remaining in the processing sequence
5.	Least Work Remaining (LWR)	Select a job with the least total processing time
6.	Most Work Remaining (MWR)	Select a job with the most total processing time remaining

techniques were used. Simulation techniques exhibit the execution of various dispatching rules and finally the rule which performs the best is selected. The following are the dispatching rules were used to study the performance of FMS: Shortest Processing Time (SPT), Longest Processing Time (LPT), Least Operations Remaining (LOR), Most Operations Remaining (MOR), Least Work Remaining (LWR), and Most Work Remaining (MWR) (Table 1).

## 4 Problem Description

A set of machines and set of jobs or products are taken for the sequential operations. For each product say  $P_i$  is processed by machine  $M_i$  for representing machines and jobs in a layout. The processing requirements are scheduled as per the operations/jobs matrix for “P” products on “M” machines. Thus, the optimum routing of the parts is determined by applying the heuristic or metaheuristic techniques. Normally, dispatching rules are most frequently applied heuristic techniques in production scheduling due to their ease of implementation of process and low time complexity. During the process, a rule inspects the waiting jobs and selects the job with the priority to be processed. The FMS loop layout has high flexibility and low initial costs in handling the material and it is considered for performance measures. Figure 1 shows the sample FMS loop layout problem, which shows the load/unload stations and there is the single AGV which is bidirectional and the machines are arranged (in slots) in the closed-loop layout.

**Fig. 1** Sample FMS loop layout



### 4.1 Input Data for Test Problems

The simulation test problems were taken from Rizvan [16] to illustrate the effectiveness of the proposed hybrid algorithm. The performance of the ISS Algorithm is compared with dispatching techniques. Table 2 shows the distance matrix between the machine slots for the test problems. Table 3 shows the part machine incidence matrix, ie., the job sets used in the test problems.

**Table 2** Distance matrix between the machine slots

Layout	Slots	S1	S2	S3	S4
Loop layout (LL)	L/UL	2	4	10	12
	S1	0	2	8	10
	S2	12	0	6	8
	S3	6	8	0	2
	S4	4	6	12	0

**Table 3** Part machine incidence matrix

Job set 1	Jobs	Machine sequence (operation time)	Job set 2	Jobs	Machine sequence (operation time)
	J1	1(8) 2(16) 4(12)		J1	1(6) 2(12) 4(9)
J2	1(20) 3(10) 2(18)	J2	1(18) 3(6) 2(15)		
J3	3(12) 4(8) 1(15)	J3	3(9) 4(3) 1(12)		
J4	4(14) 2(18)	J4	4(6) 2(15)		
J5	3(10) 1(15)	J5	3(3) 1(9)		

## 5 Results and Discussion

The simulation time of 400 min is used to study the performance of the layout. For every 60 min, a breakdown of 5 min is given to study the breakdown analysis.

### 5.1 Dispatching Rules

Table 4 shows the results of dispatching rules for the test problem (LL  $\times$  JS1). The AGV idle time, Makespan, and average % of machine utilization are calculated using the dispatching rules technique for the test problem (LL  $\times$  JS1). Figure 2 shows the % machine utilization of dispatching rules for the test problem (LL  $\times$  JS1) considering without breakdown. Individual dispatching rules and combined dispatching rules are used to find the AGV idle time, makespan and average % of machine utilization for the test problem (LL  $\times$  JS1). From the result, the average % of machine utilization of MOR dispatching rule performs better (26.25 average % of machine utilization) when compared to other dispatching rules under without breakdown condition. Figure 3 shows the % machine utilization of dispatching rules for the test problem (LL  $\times$  JS1) considering with breakdown. From the result, the average % of machine utilization of L(IT/TPT) and MOR dispatching rules performs better (26.38 and 26.06 average % of machine utilization) when compared to other dispatching rules under with breakdown condition.

Figure 4 shows the makespan of dispatching rules for the test problem (LL  $\times$  JS1). While considering the makespan, the LOR dispatching rule performs better (205) when compared to other dispatching rules under without breakdown condition. While considering the makespan, the LOR dispatching rule performs better (205) when compared to other dispatching rules under with breakdown condition. Figure 5 shows the AGV Idle Time of Dispatching Rules for the test problem (LL  $\times$  JS1). By considering the idle time of material handling system (Automated Guided Vehicle) for with and without breakdown condition, the single dispatching rule performs better for most of the run when compared to combined dispatching rules.

Table 5 shows the results of dispatching rules for the test problems (LL  $\times$  JS2). The AGV idle time, makespan and average % of machine utilization is calculated using the dispatching rules based on the parts sequence and the layout of FMS for the test problem (LL  $\times$  JS2). Figure 6 shows the % machine utilization of dispatching rules for the test problem (LL  $\times$  JS2) considering without breakdown. Individual dispatching rules and combined dispatching rules are used to find the AGV idle time, makespan and average % of machine utilization for the test problem (LL  $\times$  JS2). From the result, the average % of machine utilization of MOR dispatching rule performs better (19.75 average % of machine utilization) when compared to other dispatching rules under without breakdown condition. Figure 7 shows the % machine utilization of dispatching rules for the test problem (LL  $\times$  JS2) considering with breakdown. From the result, the average % of machine utilization of MOR



**Table 4** Results of various dispatching rules for the test problem (LL × JS<sub>1</sub>)

Dispatching rules	Condition	No. of parts completed					AGV idle time (units)	Makespan	% of machine utilization			
		P1	P2	P3	P4	P5			M1	M2	M3	M4
SPT + FIFO	WOB	2	1	2	2	2	33	225	35.50	24.00	23.25	20.00
	WB	2	1	2	2	2	38	225	33.00	24.00	20.00	24.00
L(IT/TPT)	WOB	2	2	2	2	2	22	208	35.50	29.00	19.00	20.00
	WB	2	2	2	2	2	24	208	33.50	29.00	19.00	24.00
L(IT + TPT)	WOB	1	1	2	2	2	24	250	33.00	24.00	22.00	24.00
	WB	1	1	2	2	2	33	250	33.00	24.00	22.00	24.00
L(IP/T/TPT)	WOB	1	1	2	2	2	24	256	33.00	24.00	22.00	24.00
	WB	1	1	2	2	2	28	256	33.00	24.00	22.50	22.00
S(IP/T/TPT)	WOB	2	2	1	2	1	24	209	28.75	29.00	19.00	24.00
	WB	1	2	1	2	1	44	209	28.75	29.00	19.00	20.50
LOR	WOB	2	2	2	2	2	30	205	31.75	29.00	19.00	20.00
	WB	2	2	2	2	2	30	205	32.25	29.00	19.00	20.00
MOR	WOB	2	2	2	2	2	24	218	35.50	29.00	20.50	20.00
	WB	2	1	2	2	2	31	219	33.75	24.00	22.50	24.00
LOR + SPT	WOB	2	1	2	2	2	33	225	35.50	24.00	23.25	20.00
	WB	2	1	2	2	2	38	225	33.00	24.00	20.00	24.00
MOR + LPT	WOB	2	1	2	2	2	33	225	35.50	24.00	23.25	20.00
	WB	2	1	2	2	2	38	225	33.00	24.00	20.00	24.00
LWR	WOB	1	1	2	2	2	24	256	33.00	24.00	22.00	24.00
	WB	1	1	2	2	2	28	256	33.00	24.00	22.50	22.00

(continued)

**Table 4** (continued)

Dispatching rules	Condition	No. of parts completed					AGV idle time (units)	Makespan	% of machine utilization				
		P1	P2	P3	P4	P5			M1	M2	M3	M4	
MWR	WOB	1	1	2	2	2	24	256	33.00	24.00	22.00	22.00	24.00
	WB	1	1	2	2	2	28	256	33.00	24.00	22.50	22.50	22.00
Due date	WOB	2	2	2	2	2	22	218	33.00	29.00	22.50	22.50	20.00
	WB	2	2	2	1	1	38	218	29.25	27.50	19.00	19.00	20.00

WOB—Without Breakdown; WB—With Breakdown

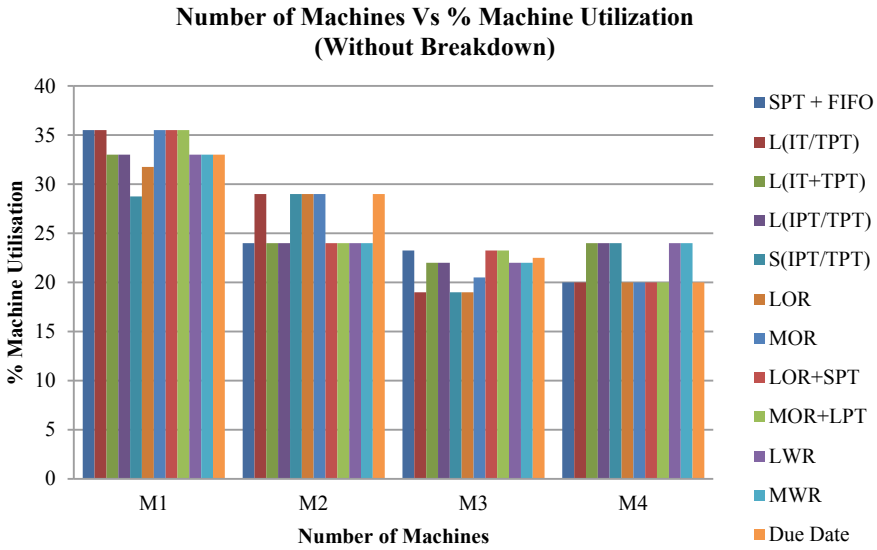


**Fig. 2** % machine utilization of dispatching rules for the test problem ( $LL \times JS_1$ ) (Without breakdown)

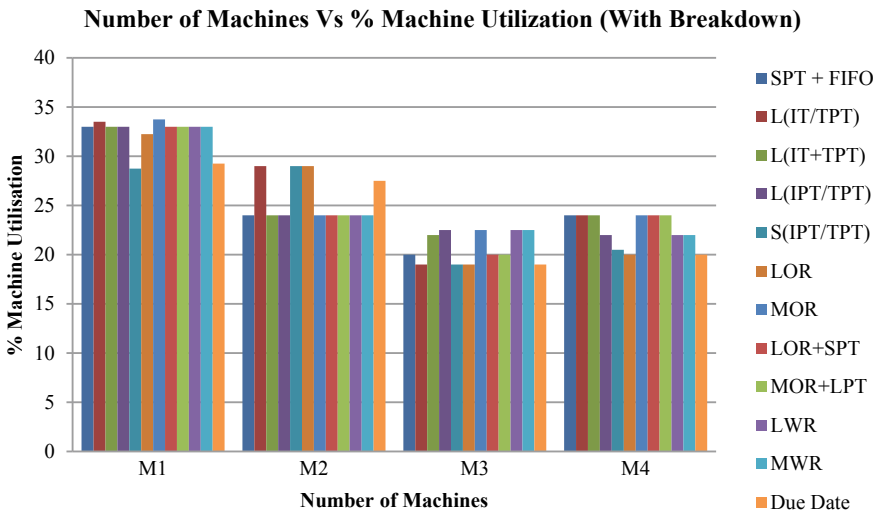


**Fig. 3** % machine utilization of dispatching rules for the test problem ( $LL \times JS_1$ ) (With breakdown)

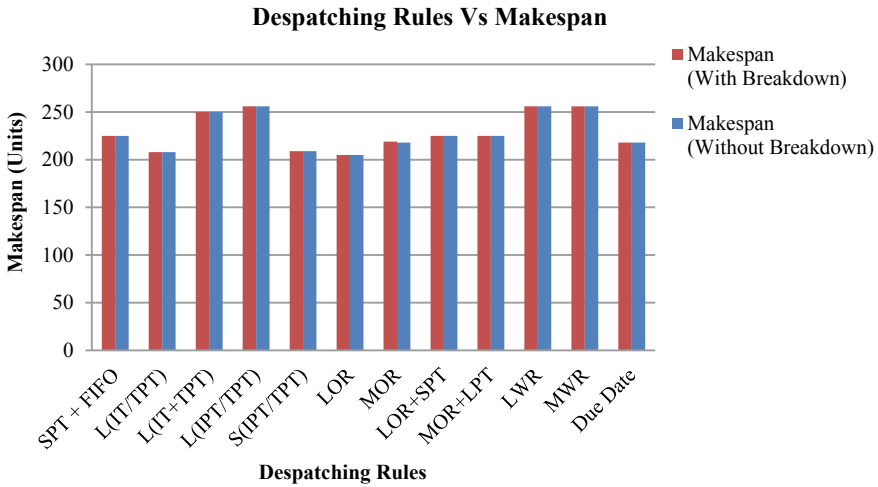


Fig. 4 Makespan of dispatching rules for the test problem (LL × JS<sub>1</sub>)

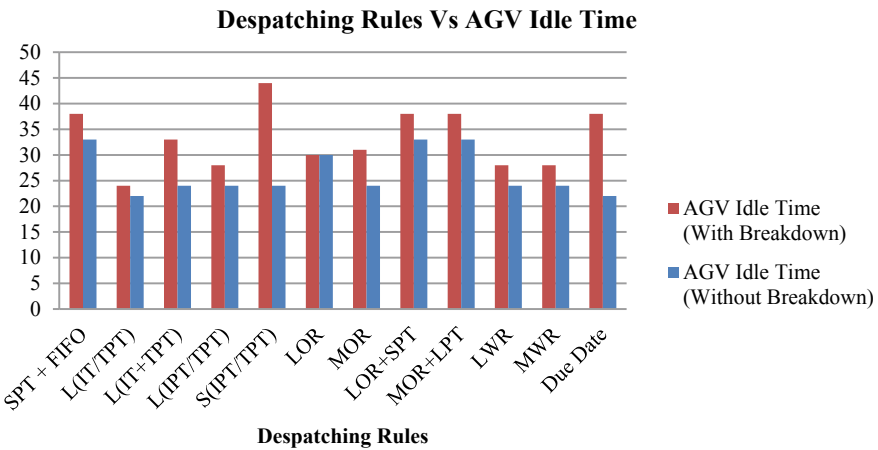


Fig. 5 AGV idle time of dispatching rules for the test problem (LL × JS<sub>1</sub>)

dispatching rule performs better (19.69 average % of machine utilization) when compared to other dispatching rules under with breakdown condition. Figure 8 shows the makespan of dispatching rules for the test problem (LL × JS<sub>2</sub>). While considering the makespan, the L(IT/TPT) dispatching rule performs better (193) when compared to other dispatching rules under without breakdown condition. While considering the makespan, the L(IT/TPT) dispatching rule performs better (193) when compared to other dispatching rules under with breakdown condition. Figure 9 shows the AGV Idle Time of Dispatching Rules for the Test Problem (LL × JS<sub>2</sub>). By considering the idle time of material handling system (Automated Guided Vehicle) for with and

**Table 5** Results of various dispatching rules for the test problem (LL × JS<sub>2</sub>)

Dispatching rules	Condition	No. of parts completed					AGV idle time (units)	Makespan	% of machine utilization			
		P1	P2	P3	P4	P5			M1	M2	M3	M4
SPT + FIFO	WOB	2	2	2	1	2	25	230	28.50	22.00	13.25	12.00
	WB	2	2	2	2	2	25	230	28.50	24.00	13.25	12.00
L(IT/TPT)	WOB	2	2	2	2	2	22	193	29.00	24.00	12.00	12.00
	WB	2	2	2	2	2	22	193	26.50	24.00	12.50	12.00
L(IT + TPT)	WOB	2	1	2	2	3	22	233	29.25	19.75	13.25	12.00
	WB	2	1	2	2	2	24	233	26.50	19.75	11.75	14.00
L(IPT/TPT)	WOB	2	1	2	2	2	22	269	28.50	19.75	13.25	12.00
	WB	1	1	2	2	2	24	269	26.50	19.75	12.25	14.00
S(IPT/TPT)	WOB	2	2	2	1	2	22	199	30.50	19.75	12.00	12.00
	WB	2	2	2	1	2	37	199	26.50	21.00	12.00	12.00
LOR	WOB	2	2	2	2	2	22	200	26.50	24.00	12.00	14.00
	WB	2	2	2	2	2	22	200	26.50	24.00	12.00	14.00
MOR	WOB	2	1	3	2	2	24	215	30.00	19.75	16.00	13.25
	WB	2	1	2	2	2	26	215	26.50	23.75	13.25	15.25
LOR + SPT	WOB	2	2	2	1	2	25	230	28.50	22.00	13.25	12.00
	WB	2	2	2	2	2	25	230	28.50	24.00	13.25	12.00
MOR + LPT	WOB	2	2	2	1	2	25	230	28.50	22.00	13.25	12.00
	WB	2	2	2	2	2	25	230	28.50	24.00	13.25	12.00
LWR	WOB	1	1	2	2	2	26	269	26.50	19.75	14.00	11.25
	WB	1	1	2	2	2	26	269	26.50	19.75	14.00	11.25

(continued)

**Table 5** (continued)

Dispatching rules	Condition	No. of parts completed					AGV idle time (units)	Makespan	% of machine utilization			
		P1	P2	P3	P4	P5			M1	M2	M3	M4
MWR	WOB	1	1	2	2	2	26	269	26.50	19.75	14.00	11.25
	WB	1	1	2	2	2	26	269	26.50	19.75	14.00	11.25
Due date	WOB	2	2	2	1	2	22	211	28.00	22.75	12.00	12.00
	WB	2	2	2	1	2	22	211	28.00	22.75	12.00	12.00

WOB—Without Breakdown; WB—With Breakdown

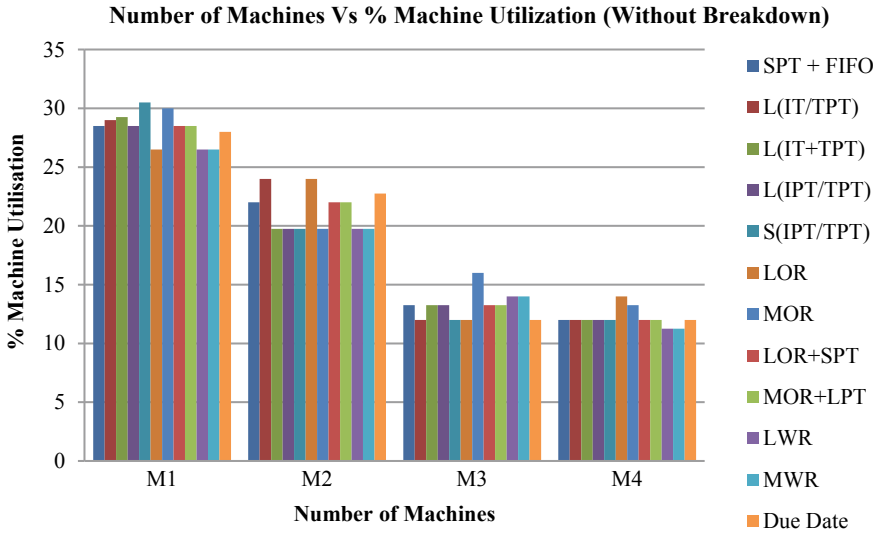


**Fig. 6** % machine utilization of dispatching rules for the test problem ( $LL \times JS_2$ ) (Without breakdown)

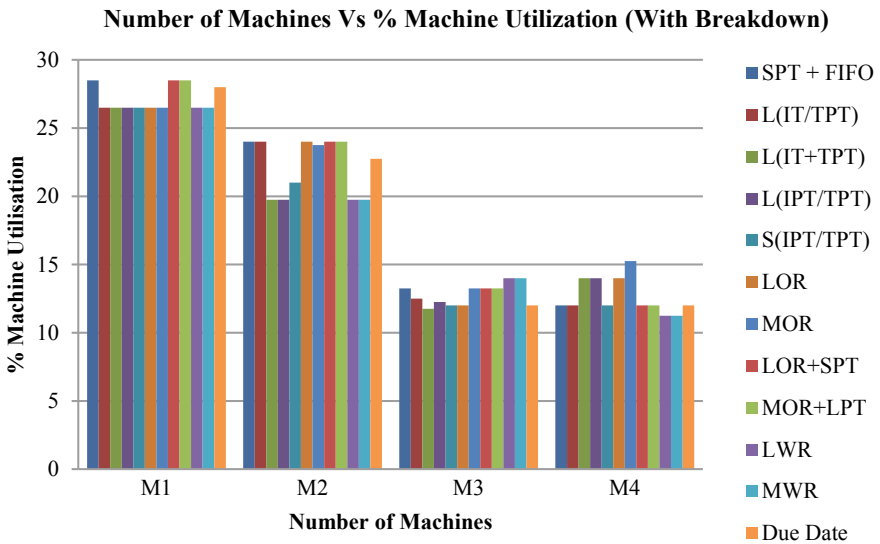


**Fig. 7** % machine utilization of dispatching rules for the test problem ( $LL \times JS_2$ ) (With breakdown)

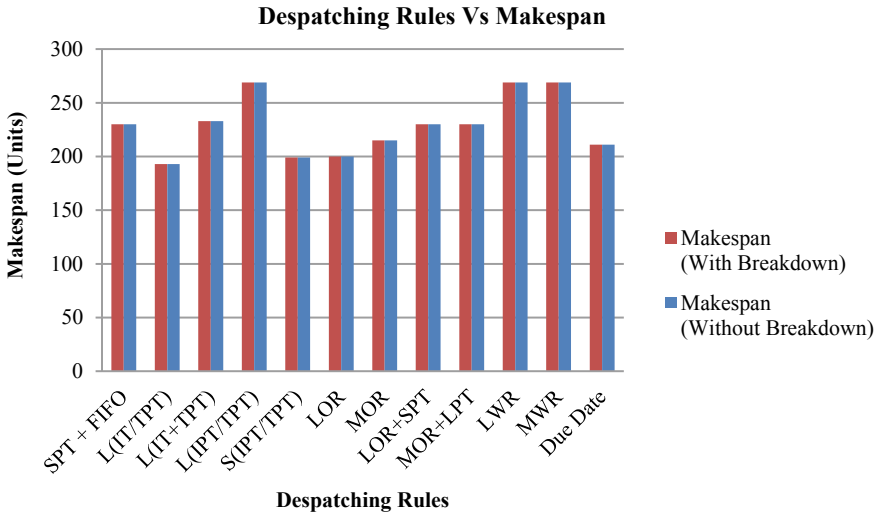


Fig. 8 Makespan of dispatching rules for the test problem (LL × JS<sub>2</sub>)

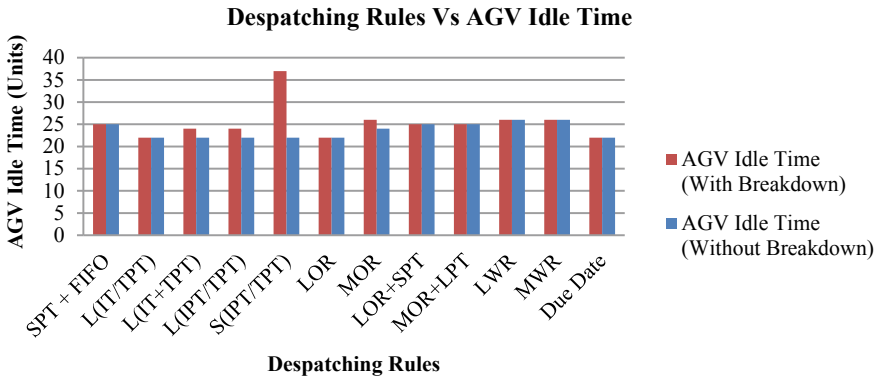


Fig. 9 AGV idle time of dispatching rules for the test problem (LL × JS<sub>2</sub>)

without breakdown condition, the L(IT/TPT) and Due Date dispatching rules perform better (22 and 22) when compared to other dispatching rules.

### 5.2 Hybrid Petrinet with Dispatching Rules

The results of hybrid PETRI NETs with dispatching rules for the test problems (LL × JS<sub>1</sub>) by considering with breakdown and without breakdown is shown in Table 6. Individual dispatching rules and combined dispatching rules with PN are used to



**Table 6** Results of hybrid Petrinet with dispatching rules for the test problem (LL × JS<sub>1</sub>)

PNDR	WB/WOB	No. of parts completed					AGV idle time (units)	Makespan	% of machine utilization			
		P1	P2	P3	P4	P5			M1	M2	M3	M4
SPT + FIFO	WB	4	3	4	4	4	40	94	65.75	53	35	40
	WOB	4	4	5	4	4	48	94	72.75	58	44.5	46.5
L(IT/TPT)	WB	3	3	3	3	3	34	116	56.25	43.5	28.5	30
	WOB	3	3	3	4	4	40	116	61.75	53	38	36.5
L(IT + TPT)	WB	3	3	3	3	4	38	97	56.25	48	35	34
	WOB	4	3	4	4	4	40	97	66	57	38	40
L(IP/TPT)	WB	4	4	5	5	5	48	86	76	63	44.5	46.5
	WOB	5	4	5	5	5	50	86	82.5	71.25	47.5	50
S(IP/TPT)	WB	4	4	4	3	3	38	102	61.75	58	35	40
	WOB	4	5	4	4	4	44	102	74	67.5	41	40.5
LOR	WB	3	3	3	3	3	34	124	57.5	43.5	28.5	30
	WOB	4	3	3	4	4	40	124	61.75	53	38	40
MOR	WB	4	4	4	4	4	42	96	68.5	58.25	38	40
	WOB	5	5	5	4	4	48	96	78.25	69	44.5	50
LOR + SPT	WB	4	3	4	4	4	40	94	65.75	53	35	40
	WOB	4	4	5	4	4	48	94	72.75	58	44.5	46.5
MOR + LPT	WB	4	3	4	4	4	40	94	65.75	53	35	40
	WOB	4	4	5	4	4	48	94	72.72	58	44.5	46.5
LWR	WB	4	4	5	5	5	48	86	76	63	44.5	46.5
	WOB	5	4	5	5	5	50	86	82.5	71.25	47.5	50

(continued)

**Table 6** (continued)

PNDR	WB/WOB	No. of parts completed					AGV idle time (units)	Makespan	% of machine utilization			
		P1	P2	P3	P4	P5			M1	M2	M3	M4
MWR	WB	4	4	5	5	5	48	86	76	63	44.5	46.5
	WOB	5	4	5	5	5	50	86	82.5	71.25	47.5	50
Due date	WB	4	4	4	4	4	42	96	68.5	58.25	38	40
	WOB	5	5	5	4	4	48	96	78.25	69	44.5	50

find the AGV idle time, makespan and average % of machine utilization for the test problem (LL × JS1). From the result, the average % of machine utilization of L(IPT/TPT), LWR and MWR dispatching rules performs better (62.81 average % of machine utilization) when compared to other dispatching rules under without breakdown condition. From the result, the average % of machine utilization of L(IPT/TPT), LWR and MWR dispatching rules performs better (57.50 average % of machine utilization) when compared to other dispatching rules under with breakdown condition. While considering the makespan, the L(IT/TPT), LWR and MWR dispatching rules perform better (86) when compared to other dispatching rules under without breakdown condition. While considering the makespan, the L(IT/TPT), LWR and MWR dispatching rule perform better (86) when compared to other dispatching rules under with breakdown condition. By considering the idle time of material handling system (Automated Guided Vehicle) for with and without breakdown condition, the L(IT/TPT), LWR and MWR dispatching rules relatively having more idle time because of its more machine utilization time when compared to other dispatching rules.

The results of hybrid PetriNets with dispatching rules for the test problems (LL × JS2) by considering with breakdown and without breakdown is shown in Table 7. Individual dispatching rules and combined dispatching rules with PN are used to find the AGV idle time, makespan and average % of machine utilization for the test problem (LL × JS2). From the result, the average % of machine utilization of L(IPT/TPT), LWR and MWR dispatching rules performs better (57.75 average % of machine utilization) when compared to other dispatching rules under without breakdown condition. From the result, the average % of machine utilization of L(IPT/TPT), LWR and MWR dispatching rules performs better (46 average % of machine utilization) when compared to other dispatching rules under with breakdown condition.

While considering the makespan, the L(IT/TPT), LWR, and MWR dispatching rules perform better (69) when compared to other dispatching rules under without breakdown condition. While considering the makespan, the L(IT/TPT), LWR and MWR dispatching rule perform better (69) when compared to other dispatching rules under with breakdown condition. By considering the idle time of material handling system (Automated Guided Vehicle) for with and without breakdown condition, the L(IT/TPT), LWR, and MWR dispatching rules relatively having more idle time because of its more machine utilization time when compared to other dispatching rules.

### ***5.3 Result of Hybrid Petrinet with ISS Algorithm***

The simulation results of hybrid PN with ISS for the test problem (LL × JS1) by considering with breakdown and without breakdown is shown in Table 8. Individual dispatching rules and combined dispatching rules are used to find the AGV idle time, makespan and average % of machine utilization for the test problem (LL × JS1).

**Table 7** Results of hybrid Petrinet with dispatching rules for the test problem (LL × JS<sub>2</sub>)

PNDR	WB/WOB	No. of parts completed					AGV idle time (units)	Makespan	% of machine utilization			
		P1	P2	P3	P4	P5			M1	M2	M3	M4
SPT + FIFO	WB	3	3	3	3	4	38	126	44.5	39.5	22	24
	WOB	4	3	4	4	4	40	126	53	44.75	24	24
L(IT/TPT)	WB	3	3	3	4	4	40	106	52.5	43.75	24	21.25
	WOB	4	4	4	4	4	44	106	55.5	48	24	24
L(IT + TPT)	WB	4	3	4	4	4	40	130	53	46.75	24	24
	WOB	4	4	4	4	5	48	130	57.75	50.25	28	26
L(IPT/TPT)	WB	5	4	5	5	5	50	69	66.25	57.75	30	30
	WOB	6	6	6	6	7	64	69	82.25	73.5	37.25	38
S(IPT/TPT)	WB	4	5	4	4	4	44	76	60	55	26	24
	WOB	5	6	5	5	5	54	76	73.25	67.75	32	30
LOR	WB	4	3	3	4	4	40	107	49.5	43.75	24	24
	WOB	4	4	4	4	4	44	107	57.5	48	24	24
MOR	WB	5	5	5	5	5	52	82	66.25	60	30	30
	WOB	6	6	6	5	5	58	82	76.75	48	24	24
LOR + SPT	WB	3	3	3	3	4	38	126	44.5	39.5	22	24
	WOB	4	3	4	4	4	40	126	53	44.75	24	24
MOR + LPT	WB	3	3	3	3	4	38	126	44.5	39.5	22	24
	WOB	4	3	4	4	4	40	126	53	44.75	24	24
LWR	WB	5	4	5	5	5	50	69	66.25	57.75	30	30
	WOB	6	6	6	6	7	64	69	82.25	73.5	37.25	38

(continued)

**Table 7** (continued)

PNDR	WB/WOB	No. of parts completed					AGV idle time (units)	Makespan	% of machine utilization			
		P1	P2	P3	P4	P5			M1	M2	M3	M4
MWR	WB	5	4	5	5	5	50	69	66.25	57.75	30	30
	WOB	6	6	6	6	7	64	69	82.25	73.5	37.25	38
Due date	WB	5	5	5	5	5	52	82	66.25	60	30	30
	WOB	6	6	6	5	5	58	82	76.75	71.75	34.75	36

**Table 8** Results of hybrid PNISS for the test problem (LL × JS<sub>1</sub>)

WB/WOB	Part sequence	No. of parts completed					AGV idle time (units)	Makespan	% of machine utilization			
		P1	P2	P3	P4	P5			M1	M2	M3	M4
WB	3-1-2-4-5	4	4	5	4	4	44	98	72.75	62.5	41.5	42.75
WOB	3-4-5-1-2	5	5	6	6	5	56	86	91	77.5	54	56.5

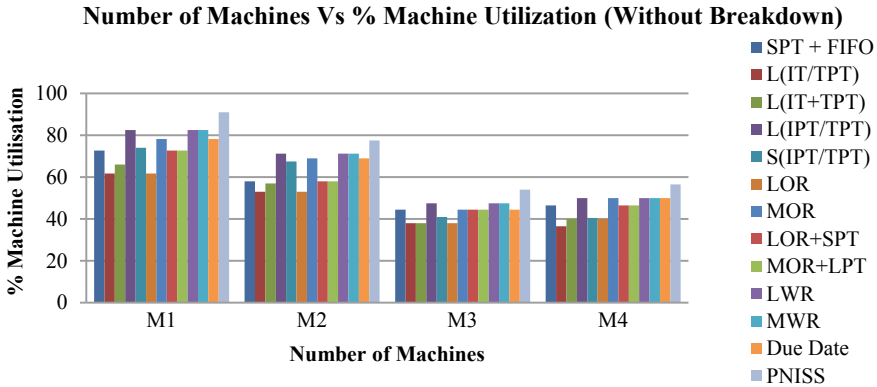


**Fig. 10** % machine utilization for the test problem ( $LL \times JS_1$ ) without breakdown

Figure 10 shows the average % of machine utilization of PNISS performs better (69.75 average % of machine utilization) when compared to other dispatching rules and PNDR under without breakdown condition. Figure 11 shows the average % of machine utilization of L(IPT/TPT), LWR and MWR dispatching rules perform better (57.50 average % of machine utilization) when compared to PNISS (54.88 average % of machine utilization) under with breakdown condition.

Figure 12 shows the makespan for the test problem ( $LL \times JS_1$ ), the PNISS (86) performs the same as L(IPT/TPT), LWR and MWR perform (86) under without breakdown condition. While considering the makespan under with breakdown condition, the L(IT/TPT), LWR and MWR dispatching rule perform better (86) when compared to PNISS (98). Figure 13 shows the idle time of material handling system (Automated Guided Vehicle) for with and without breakdown condition, the L(IT/TPT), LWR and MWR dispatching rules perform better when compared to PNISS. PNISS

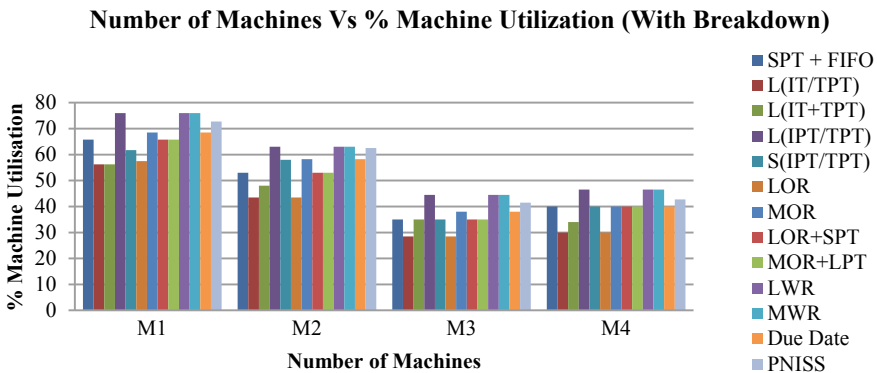


**Fig. 11** % machine utilization for the test problem ( $LL \times JS_1$ ) with breakdown

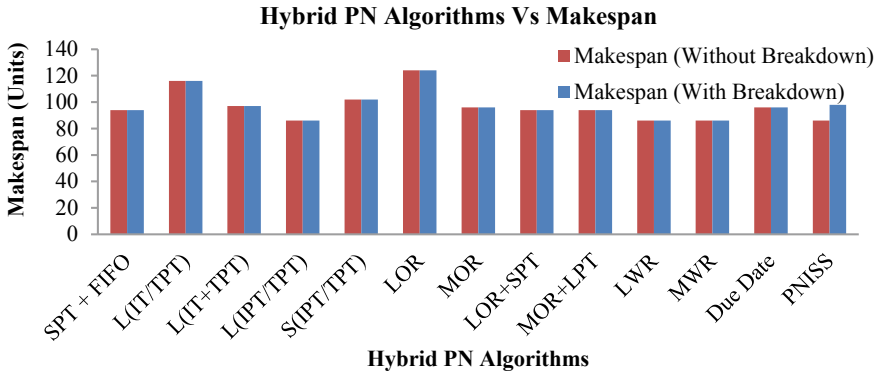


Fig. 12 Makespan for the test problem (LL × JS<sub>1</sub>)

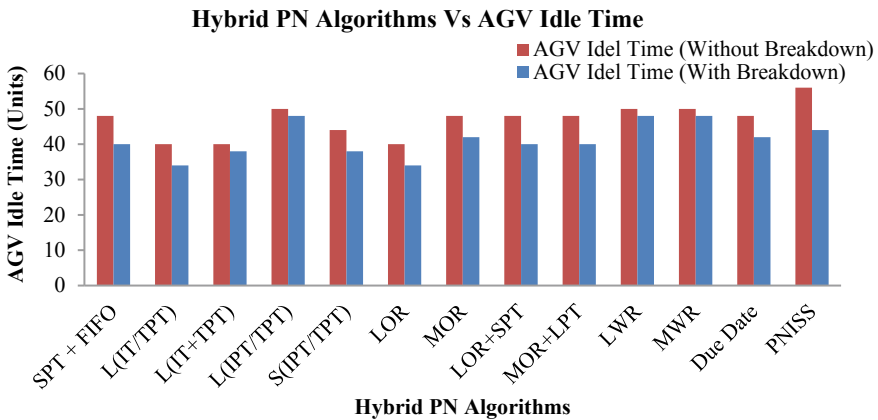


Fig. 13 AGV idle time for the test problem (LL × JS<sub>1</sub>)

relatively having more idle time because of its more machine utilization time when compared to other dispatching rules and PNDR.

The simulation results of hybrid PN with ISS for the test problem (LL × JS<sub>2</sub>) by considering with breakdown and without breakdown is shown in Table 9. Individual dispatching rules and combined dispatching rules are used to find the AGV idle time, makespan and average % of machine utilization for the test problem (LL × JS<sub>2</sub>).

Figure 14 shows the average % of machine utilization of PNIS performs better (66.88 average % of machine utilization) when compared to other dispatching rules and PNDR (57.75 average % of machine utilization) under without breakdown condition. Figure 15 shows the average % of machine utilization of PNIS performs better (50.69 average % of machine utilization) when compared to L(IPT/TPT), LWR and MWR dispatching rules (46 average % of machine utilization) under with breakdown condition. Figure 16 shows the makespan of the test problem (LL × JS<sub>2</sub>),



**Table 9** Results of hybrid PNISS for the test problem (LL × JS<sub>2</sub>)

WB/WOB	Part sequence	No. of parts completed					AGV idle time (units)	Makespan	% of machine utilization			
		P1	P2	P3	P4	P5			M1	M2	M3	M4
WB	2-1-4-3-5	5	6	5	5	5	54	76	73.25	67.5	32	30
WOB	2-3-4-1-5	7	7	7	7	7	72	76	97.75	84	43.75	42

**Number of Machines Vs % Machine Utilization (Without Breakdown)**

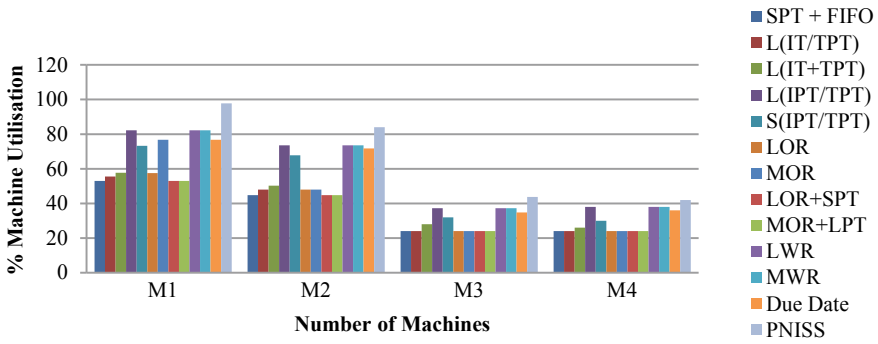


**Fig. 14** % machine utilization for the test problem (LL × JS<sub>2</sub>) without breakdown

**Number of Machines Vs % Machine Utilization (Without Breakdown)**

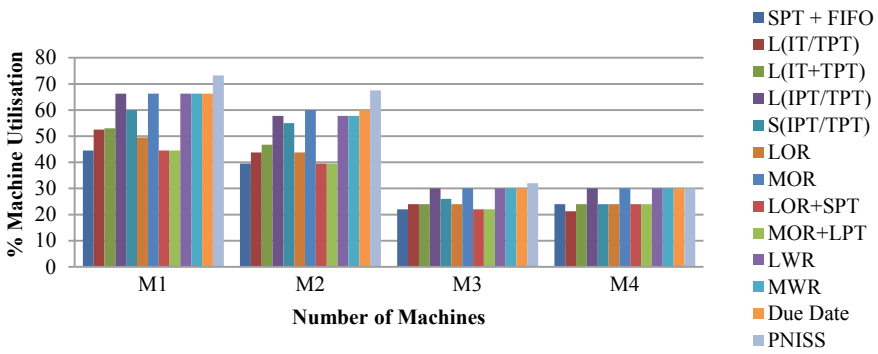


**Fig. 15** % machine utilization for the test problem (LL × JS<sub>2</sub>) with breakdown

**Hybrid PN Algorithms Vs Makespan**

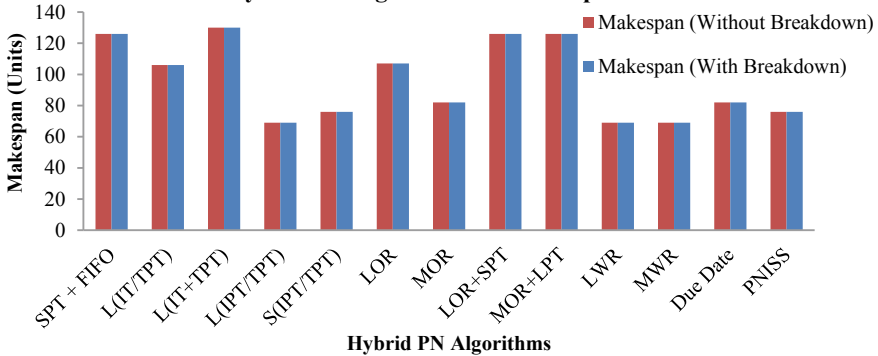


**Fig. 16** Makespan for the test problem (LL × JS<sub>2</sub>)

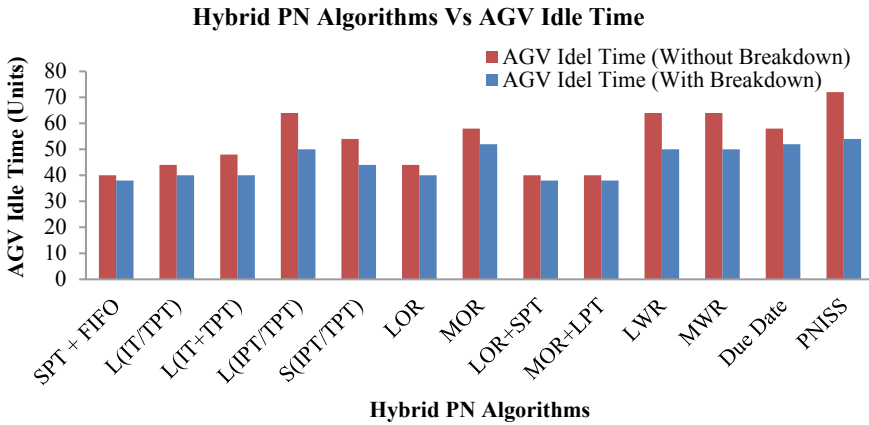


Fig. 17 AGV idle time for the test problem (LL × JS<sub>2</sub>)

L(IPT/TPT), LWR and MWR performs better (69) when compared to PNISS (76) under with and without breakdown condition.

Figure 17 shows the idle time of material handling system (Automated Guided Vehicle) for with and without breakdown condition, the L(IT/TPT), LWR and MWR dispatching rules perform better when compared to PNISS. PNISS relatively having more idle time because of its more machine utilization time when compared to other dispatching rules and PNDR.

The utilization results of PN with ISS show the optimum when compared to dispatching rules. Similarly, from Figs. 10, 11, 12, 13, 14, 15, 16, and 17 the results of the test problems (LL × JS<sub>1</sub>) and (LL × JS<sub>2</sub>) shows that the PNISS performs better when compared to PNDR.

## 6 Conclusion

An arrangement of layout in flexible manufacturing system is extremely important to achieve high productivity. The various algorithms have been developed to solve the layout problem and scheduling in FMS environment. A variety of modifications have been carried out by the researchers to improve its performance. Many attempts have been made to apply algorithms individually to solve these problems. A system that is based on PNs integrated with rule based has been highly used to find optimal decisions for scheduling analysis. In the present research work, hybridizing the existing algorithms with new algorithms (FMS scheduling with hybrid PNDR and PNISS) and were validated against the benchmark problems.

Benchmark problems from the previous literature were carried out for parts requiring different operations and operation sequences. The proposed methodology PNISS performs better for the objective function and yield better solution for both the test

problems. From the test problems, the results were comprehensible and promising in terms of optimality, also the superiority of the proposed hybrid method (PNISS) when compared to other dispatching rules and PNDR techniques considering with and without breakdown.

## References

1. Blum C (2005) Ant colony optimization: introduction and recent trends. *Physics of Life Reviews* 2:353–373
2. Thiruvadyet D, Singh G, Ernst AT, Meyer B (2013) Constraint based SS for a shared resource-constrained scheduling problem. *Prod Econ* 141:230–242
3. Chan Felix TS, Swarnkar Rahul (2006) Ant colony optimization approach to a fuzzy goal programming model for a machine tool selection and operation allocation problem in an FMS. *Robot Comput-Integr Manuf* 22:353–362
4. Bell JE, McMullen PR (2004) Ant colony optimization techniques for the vehicle routing problem. *Adv Eng Inform* 18:41–48
5. Kumar R, Tiwari MK, Shankar R (2003) Scheduling of flexible manufacturing systems: an ant colony optimization approach. *Dep Manuf Technol* 26:1443
6. Desrochers AA, Jaar RY (1995) Applications of Petri nets in manufacturing systems. Institute of Electrical and Electronics Engineers Press, New York, NY
7. Eynan A, Rosenblatt MJ (1993) An interleaving policy in automated storage/retrieval systems. *Int J Prod Res* 31(1):1–18
8. Moore Kendra E, Gupta Surendra M (1995) Stochastic colored Petri net models of flexible manufacturing systems: material handling systems and machining. *Comput Ind Eng* 29(1–4):333–337
9. Lin James T, Lee Chia-Chu (1997) A Petri netbased integrated control and scheduling scheme for flexible manufacturing cells. *Comput Integr Manuf Syst* 10(2):109–122
10. Yu H, Reyes A, Cang S, Lloyd S (2003) Combined Petri net modeling and AI based heuristic hybrid search for flexible manufacturing systems—Part 1. Petri net modeling and heuristic search. *Comput Ind Eng* 44:527–543
11. Yu H, Reyes A, Cang S, Lloyd S (2003) Combined Petri nets modelling and AI-based heuristic hybrid search for flexible manufacturing systems part II. Heuristic hybrid search. *Comput Ind Eng* 44(4):545–566
12. Zhou MC, Jeng MD (1998) Modeling, analysis, simulation, scheduling, and control of semiconductor manufacturing systems: a Petri net approach. *IEEE Trans Semicond Manuf* 11(3):333–357
13. Ahmad F, Huang H, Wang X (2011) Analysis of the Petri net model of parallel manufacturing processes with shared resources. *Inf Sci* 181:5249–5266
14. Murata T (1989) Petri nets: properties, analysis and applications. *Proc IEEE* 77(4):541–580
15. The MathWorks Inc. (2000) Building GUIs with MATLAB, Natick, MA
16. Rizvan E (2012) A multi-agent based approach to dynamic scheduling of machines and automated guided vehicles in manufacturing systems. *Appl Soft Comput* 12(6):1720–1732

# An Image Processing Approach for Detecting Solidification Crack in Pipeline Girth Welds



Nirmala Madian, Somasundaram Devaraj, Santhi Krishnamoorthi and Rajagopal Dhanasekaran

**Abstract** Welding is the most significant component in day-to-day life. Without welding, nothing is possible which relates aircraft to skyrocket, the pipeline to high-ways, cars to workplace constructions. The major problem related to welding is the occurrence of crack at high temperatures during solidification. Sulphide stress corrosion cracking is a major problem to be analysed during pipeline girth welds. The crack occurs when the test stress level approaches 100%. The crack analysis is an important indicator that reflects the safety status in weld quality. It is also important to understand the severity of the crack formed which will help in improving the safety measures better. This will help in selecting the required materials and the proportion ratio which can handle more stress during testing. The paper is about introducing image processing techniques to analyse the crack region and perform segmentation of crack region.

**Keywords** Pipeline girth welds · Solidification · Sulphide stress corrosion · Crack detection · Image processing

---

N. Madian (✉)

Sri Shakthi Institute of Engineering & Technology, Coimbatore, TN, India  
e-mail: [nirmalaooty@gmail.com](mailto:nirmalaooty@gmail.com)

S. Devaraj

Dr N G P Institute of Technology, Coimbatore, TN, India  
e-mail: [somgce@gmail.com](mailto:somgce@gmail.com)

S. Krishnamoorthi

ECE, Guru Nanak Institutions Technical Campus, Hyderabad, Telangana, India  
e-mail: [drsanthignitc@gmail.com](mailto:drsanthignitc@gmail.com)

R. Dhanasekaran

Mechanical, Guru Nanak Institute of Technology, Hyderabad, Telangana, India  
e-mail: [dhanagnit@gmail.com](mailto:dhanagnit@gmail.com)

© Springer Nature Singapore Pte Ltd. 2020

G. S. V. L. Narasimham et al. (eds.), *Recent Trends in Mechanical Engineering*,  
Lecture Notes in Mechanical Engineering,  
[https://doi.org/10.1007/978-981-15-1124-0\\_28](https://doi.org/10.1007/978-981-15-1124-0_28)

## 1 Introduction

Solidification crack [1] is formed in weld metal when the solidification process is performed. The reason is that the hot metal loses its ductility, which results in cracking. The cracking involves (i) hot cracking, (ii) crater cracking, and (iii) centreline cracking. Weld metal is subjected to cracking during the conditions like (i) sensitive chemical composition of parent metal, (ii) irregular shape and size of weld, and (iii) unfavourable stress level. The work is about analysing the behaviour of the crack due to sulphide stress corrosion (SSC) [2] from pipe girth weld, which is strained due to pipe reeling and layout process and is analysed through image processing.

SSC test helps in analysing the sulphide stress cracking in pipe welds done using NACE-TM 0177-90 method-A. Metallographic assessment needs to be carried out to know the influence of heat input and steel chemistries for the SSC resistance on heat-affected regions. The geometry of the SSC samples is investigated. There is always threshold stress for any application. This threshold is affected due to the geometry and the concentration of hydrogen in steel. So care should be taken to reduce the hydrogen concentration to improve the SSC resistance in heat-affected regions. Various methods [3–6] are reported for the SSC testing for detecting crack and the solution to reduce the crack in heat-affected area during the solidification process.

Four unstrained samples are considered where the testing is performed with weld root [2]. The test is performed through dead weight loading considering the surface tension in the inner pipe. The stress test level is set to 100% at various levels compared to parent metal stress. The duration of the test is 30 days. The samples are examined through a microscope to detect the crack and the photomicrographs are recorded to find the feature of interest in analysing the crack.

There are two types of strain cycles for characterising the metal which are (i) Tensile–Compression–Tensile–Compression (T-C-T-C) and (ii) Compression–Tensile–Compression–Tensile (C-T-C-T). The sample tested at 100% shows the formation of a crack within the test period. The obtained crack is associated with SSC. The photomicrograph images are considered as input for the work. Any image can be analysed using the histogram. The histogram is a bar chart representation of the intensity level. When the contrast of an image is low it can be improved using histogram equalization techniques [7, 8]. The image binarization helps in detecting the region of interest along with contour analysis that is used to detect cracks [9].

The paper proposes a methodology for analysing the photomicrographs of the images recorded through the microscope. Image processing algorithms are used for analysing the photomicrographs to detect the location and segment the crack in the weld metal.

## 2 Methodology

The image processing algorithms can be applied to analyse the crack in weld metal due to SSC testing. The methodology involves image preprocessing, region of interest identification through which the crack region is segmented as shown in Fig. 1.

The input image considered is the photomicrographs of solidification crack formed during SSC testing at high temperatures. The images are initially analysed for quality. The quality analysis is based on taking a histogram of the image. The histogram is nothing but the intense study of an image. The histogram is represented as

$$N = \sum_{i=1}^m h_i \tag{1}$$

Where  $N$  is the total observations,  $m$  is the total bin count. The number of bin count is calculated based on bin width  $w$  given as

$$m = \lceil \text{max} - \text{min} / w \rceil \tag{2}$$

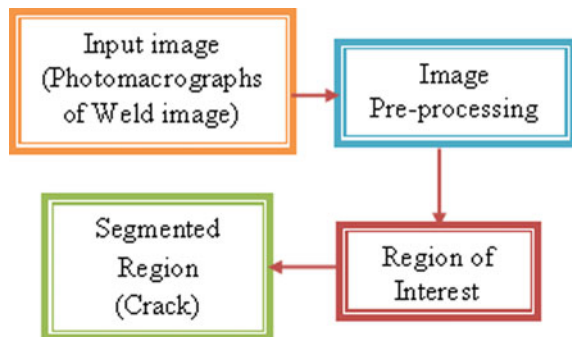
Based on the histogram the image contrast is analysed. If the contrast is low then equalization techniques should be employed to enhance the image quality. The improved quality helps to detect the crack region. Histogram based equalization is performed to enhance the quality of an image which is represented as

$$h_{eq}(i) = \text{round} \left( \frac{cdf(i) - cdf_{\min}}{(M \times N) - cdf_{\min}} \times (L - 1) \right) \tag{3}$$

Where  $cdf$  is the cumulative distribution function,  $M \times N$  matrix size of image,  $L$  number of grey levels.

After enhancement, image binarization is done. The binarization converts the image into two dark bands and bright bands. The bright bands are the region of

Fig. 1 Methodology



interest. The image binarization is represented as where  $(x, y)$  is a coordinate point.

$$b(x, y) = \begin{cases} 1 & \text{foreground} \\ 0 & \text{background} \end{cases} \quad (4)$$

The binarization helps in separating the crack region from the other region including the background. The projection of the image is performed on the binarized image. The projection gives us information about the region where the crack is formed. The projection can be performed along all rows or columns of an image. The projection gives the 1D view of a 2D image. The image is then subjected to segment the crack region. Now the region of interest is analysed for segmenting the crack region. The binary mask of the region of interest is formed. The features from the binary mask are calculated which helps to classify the images with a larger database.

### 3 Results and Discussion

The input considered for the work is photomicrographs of the strained specimen after SCC testing. The test stress till 70% under T-C-T-C and C-T-C-T strain has no crack formation as shown in Fig. 2. The strained specimen at 100% shows crack under T-C-T-C and C-T-C-T strain as shown in Fig. 3a, b. The quality of the image is analysed based on histogram of the image. The histogram of the image is shown in Fig. 4a, b. As the intensity is spread throughout the entire duration from 0-255 the image does not need enhancement.

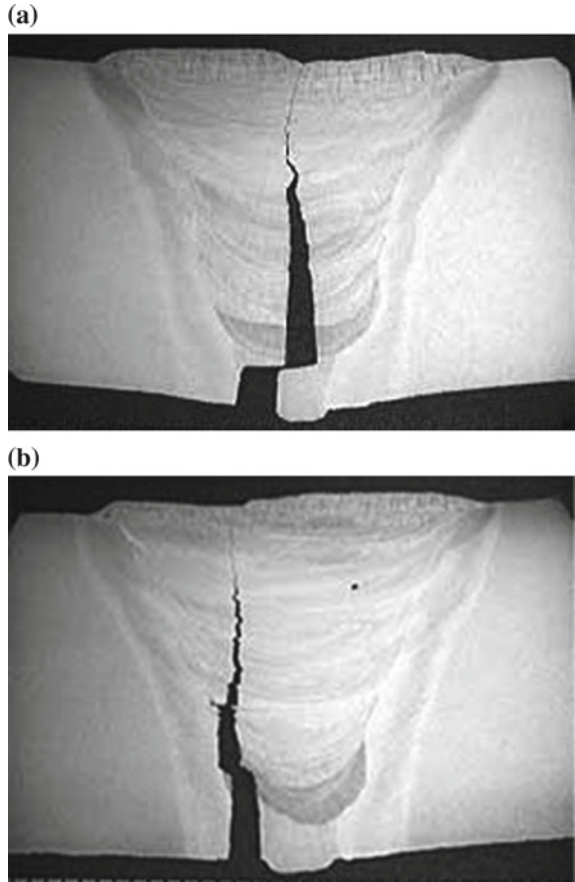
The image then has to be binarised for further analysis. The binary image is shown in Fig. 5a, b. The binary image obtained shows two-band regions (dark and Bright bands). Figure 5a (i) gives us the information of crack region as dark bands and other weld regions as a bright band. But it is noted that the background is also similar to

**Fig. 2** Photomicrographs after SCC testing at 70%, root in tension





**Fig. 3** Photomacrographs after SCC testing at 70%, root in tension under **a** C-T-C-T. **b** T-C-T-C



the crack region. This should be solved and only the region of interest (crack region) should be segmented.

The procedure for the above problem is detecting the binary mask, which helps in separating the crack region irrespective of other regions. One important procedure to detect the crack region is through projections. The crack regions have a low intensity as they look similar to the background. The crack results in gap formation which means a space between two regions and will not have any intensity so the pixel value is zero.

The projection of the normal images as shown in Fig. 6a and there is no dip in intensity which shows no crack in the image. Considering Fig. 6b, c there is a dip region which reflected there is a crack region or a discontinuity in the image region. This is studied through the projection graph. The crack and disjoint region are mentioned in the graph plotted.

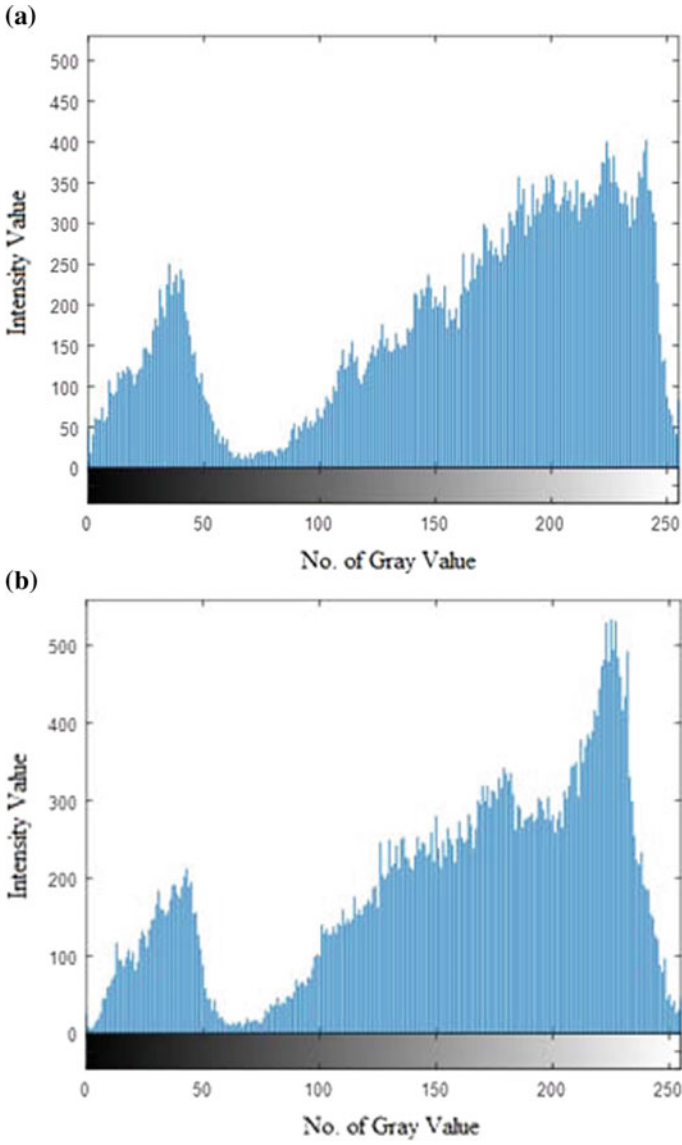
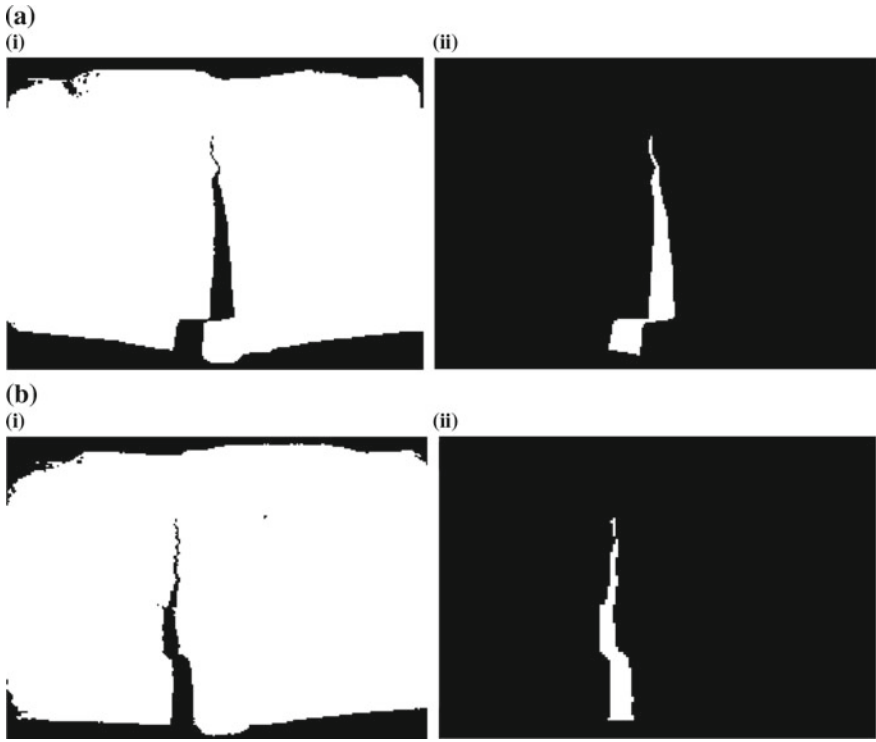


Fig. 4 a Histogram of Fig. 3a. b Histogram of Fig. 3b



**Fig. 5** a (i) Binary Image of Fig. 3a (ii) Segmented binary crack region. b (i) Binary Image of Fig. 3b (ii) Segmented binary crack region

After confirming the presence of crack the binary mask is obtained. The segmentation is performed based on boundary tracking on the mask region to segment the crack region as in Fig. 7a, b.

The feature extracted from the segmented images is given in Table 1.

The features are obtained for crack region obtained for the stress level at 100%. The future scope is to analyse various crack regions at 100% stress level and evaluate the features. From the feature analysis, a conclusion can be obtained on the severity of the stress and have a proper understanding to reduce the causing factor of crack.

## 4 Conclusion

The paper is about detecting the crack formed during the solidification procedure. Welding plays a vital role in all applications. So it is important to have a proper procedure to perform welding. One main drawback is crack formation during the welding process. Here an image processing approach is presented to detect the crack region

**Fig. 6** **a** Projection graph of Fig. 2. **b** Projection graph of Fig. 3a. **c** Projection graph of Fig. 3b

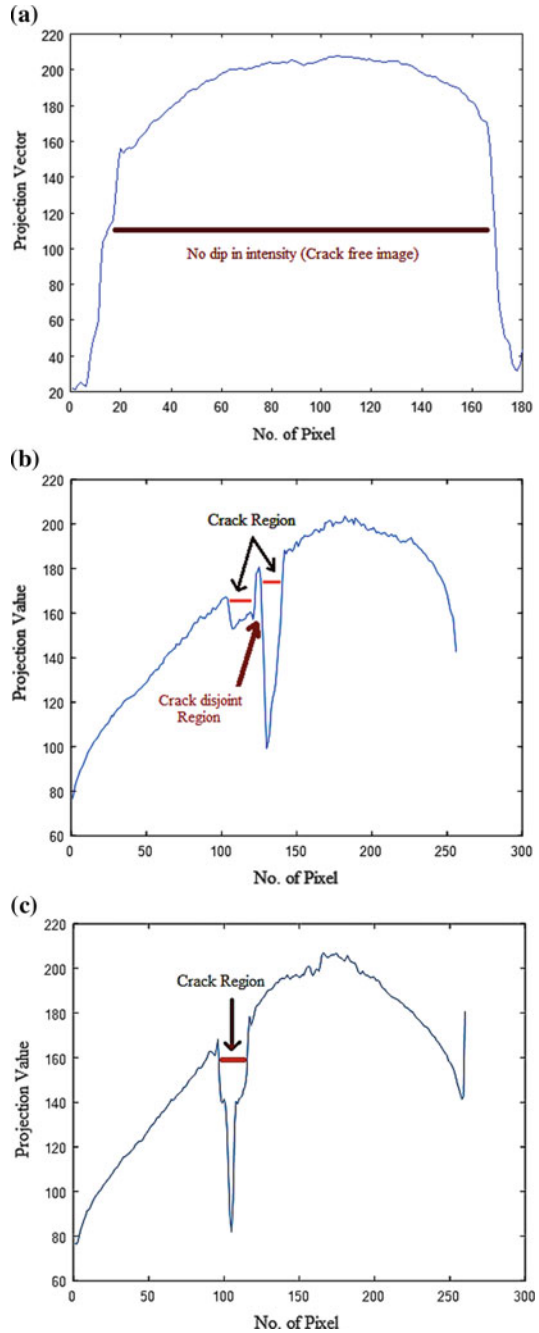


**Fig. 7** Crack segmented image **a** Fig. 3a. **b** Fig. 3b

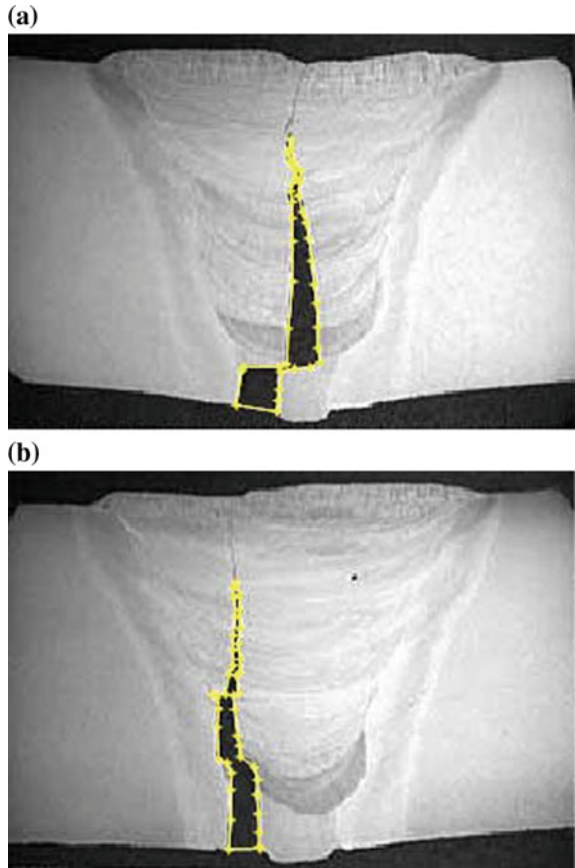


**Table 1** Features of crack region

Image	Area	Perimeter	Axis length	
			Major	Minor
Figure 5a (ii)	949	267.60	116.18	16.24
Figure 5b (ii)	<b>1210</b>	<b>299.01</b>	<b>121.58</b>	<b>31.30</b>

at 100% stress level. Various features are calculated which can help in analysing the severity of the crack region.

## References

1. Agarwal G, Gao H, Amirthalingam M, Hermans M (2018) Study of solidification cracking susceptibility during laser welding in an advanced high strength automotive steel. *Metals* 8(9):673
2. Shenton PA (2005) The effect of strain on the susceptibility of the pipeline girth welds of sulphide stress cracking. In: *Proceedings of NACE 2005, Texas*
3. Zhang W, Zhang Z, Qi D, Liu Y (2014) Automatic crack detection and classification method for subway tunnel safety monitoring. *Sensors* 14(10):19307–19328
4. Tsay LW, Chen YC, Chan SLI (2016) Sulfide stress corrosion cracking and fatigue crack growth of welded TMCP API 5L X65 pipe-line steel. *Int J Fatigue* 23(2):103–113
5. Woollin P (2001) Sulphide stress cracking of welded joints in weldable martensitic stainless steels. TWI Group
6. Endo S, Nagae M, Kobayashi Y, Ume K (1994) Sulfide stress corrosion cracking in welded joints of welded linepipes. *ISIJ Int* 34(2):217–223
7. Mustafa WA, Mydin M, Kader A (2018) A review of histogram equalization techniques in image enhancement application. *J Phys Conf Ser* 37:74–84
8. Santhi K, Wahida Banu RSD, Dhanasekaran R (2014) Contrast enhanced for microstructure of steel materials and engine components. *Adv Mater Res* 984–985:1375–1379
9. Mohan A, Poobal Sumathi (2018) Crack detection using image processing: a critical review and analysis. *Alexandria Eng J* 57(2):787–798

# Experimental Investigation to Optimize Process Parameters in Drilling Operation for Composite Materials



K. Amarnath, P. Surendernath and V. Kumar

**Abstract** This paper optimizes the influence of process parameters in drilling and improves the surface finish quality of GFRP (glass fiber reinforced polymer) composites workpiece by using different drill bits such as 8 mm, 10 mm and 12 mm diameter HSS (M2) drill. A series of experiments will be done by varying the different drilling parameters and different spindle speeds, feed rate, and point angle are varied. The impact of parameters and setup correlation of parameters with respect to the Taguchi approach is explained. Validations of the drilling operation for GFRP will be carried out at CITD and its experimental records will be maintained.

**Keywords** Composite materials · Process parameters · GFRP

## 1 Introduction

Drills are classified by fabric, duration, form, wide variety, and sort of helix or flute, shank, factor characteristics, and length series. Drills are produced from excessive-velocity metal (HSS), strong carbide, or with carbide brazed inserts. Most drills are made for proper-hand rotation. Right-hand drills, as regarded from their point, with the shank going through far away from our view, are turned around in a counterclockwise course on the way to reduce. Left-hand drills cut when turned around clockwise in a comparable way [1–3].

Because of the super pressure carried out with the aid of the device in drilling, it is important to ensure the tension of each reducing tool and workpiece. In drilling operations, the quality of the hole is an important requirement for many applications. Optimized cutting parameters are essential for controlling the required quality [4, 5].

---

K. Amarnath (✉) · P. Surendernath · V. Kumar  
Kamala Institute of Technology and Science, Huzarabad, Karimnagar (Dist), Telangana (State),  
India  
e-mail: [amarnath.kandagatla@gmail.com](mailto:amarnath.kandagatla@gmail.com); [amar428@yahoo.co.in](mailto:amar428@yahoo.co.in)

P. Surendernath  
e-mail: [yadavk026@gmail.com](mailto:yadavk026@gmail.com)

© Springer Nature Singapore Pte Ltd. 2020  
G. S. V. L. Narasimham et al. (eds.), *Recent Trends in Mechanical Engineering*,  
Lecture Notes in Mechanical Engineering,  
[https://doi.org/10.1007/978-981-15-1124-0\\_29](https://doi.org/10.1007/978-981-15-1124-0_29)

## 2 Experimental Investigation

The experiments are done on the drilling machine with the following parameters:

**WORKPIECE MATERIAL**—GFRP (glass fiber reinforced polymer)

**DRILL BIT DIA**—8 mm, 10 mm, 12 mm

**CUTTING SPEED**—1500 rpm, 2000 rpm, 2500 rpm

**POINT ANGLE**—116°, 118°, 120°.

**EXPERIMENTAL PHOTOS** (Figs. 1, 2, Tables 1, 2)

### Taguchi Approach to DOE

- Traditional Design of Experiments (DOE) focused on how different design factors affect the *average* result level.
- From every trial series, we can obtain an average result level and a measure of the variation,  $s_i, i = 1, 2, \dots, 9$  can then be used as levels that provide the most robust design [6].

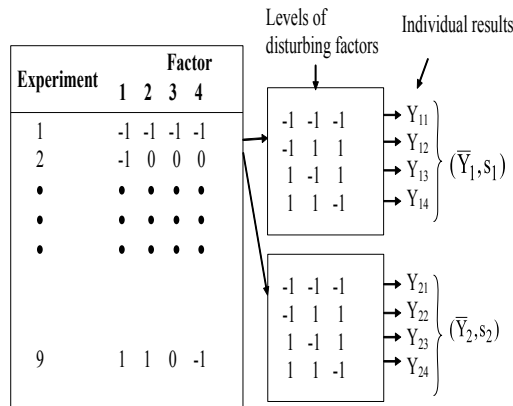
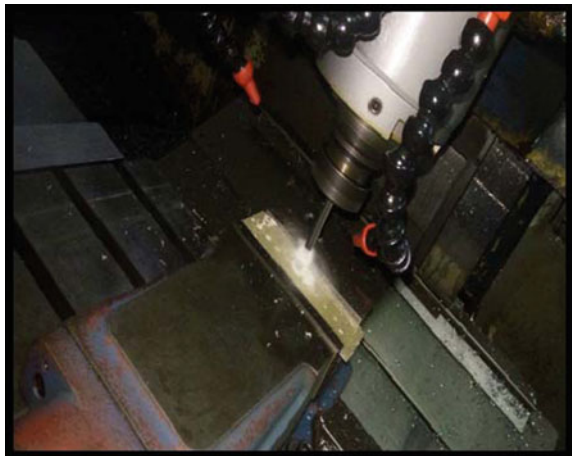


Fig. 1 Drilling process





**Fig. 2** Final component



**Table 1** Input parameters

Process parameters	Level 1	Level 2	Level 3
Speed (rpm)	1500	2000	2500
Drill bit dia (mm)	8	10	12
Point angle	116°	118°	120°

**Table 2** Surface finish values

Job no.	Speed (rpm)	Drill bit dia (mm)	Point angle (°)	Surface finish (R <sub>a</sub> )
1	800	8	116	0.565
2	800	10	118	0.727
3	800	12	120	0.912
4	1000	8	116	1.05
5	1000	10	118	1.21
6	1000	12	120	1.64
7	1200	8	116	2.145
8	1200	10	118	2.521
9	1200	12	120	2.742

### 2.1 Taguchi Parameter for Drilling Process

In order to identify the process parameters affecting machine quality characteristics of milling, preliminary experiments are conducted [7].

**Orthogonal Array Process:**

From the table, to study the two-factor effects of process all the 3 parameters interaction on the selected characteristics are studied while milling.

**Results:**

Using randomization technique, experimental data for the cutting forces have been formulated and S/N ratio is given below:

$$S/N \text{ ratio} = -10 \log \left[ \frac{1}{n} (y_1^2 + y_2^2 + \dots + y_n^2) \right] \tag{1}$$

Where  $y_1, y_2, \dots, y_n$  are machining characteristics for each parameter (Tables 3, 4).

**Table 3** Taguchi orthogonal array

Job no.	Speed (rpm)	Drill bit dia (mm)	Point angle (°)
1	800	8	116
2	800	10	118
3	800	12	120
4	1000	8	116
5	1000	10	118
6	1000	12	120
7	1200	8	116
8	1200	10	118
9	1200	12	120

**Table 4** Surface finish

Surface finish ( $R_a$ ) $\mu\text{m}$
0.565
0.727
0.912
1.05
1.21
1.64
2.145
2.521
2.742

### 3 Observation

The following are the observations made by running the experiments. The cutting forces are measured using a dynamometer.

### 4 Optimization by Minitab Software

To calculate the S/N ratio, means array is designed in Minitab17:

**Type of Design:**

Figures 3 and 4.

**Fig. 3** Selection of Taguchi design

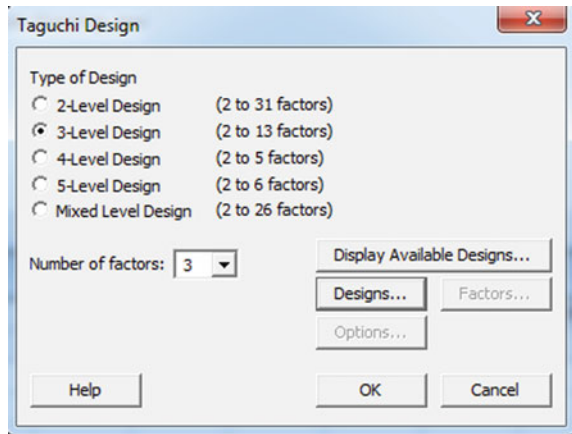
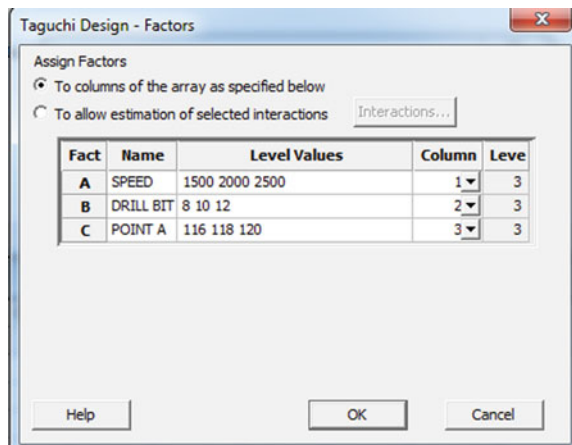


**Fig. 4** Assigning factors



↓	C1	C2	C3
	SPEED	DRILL BIT DIA	POINT ANGLE
1	1500	8	116
2	1500	10	118
3	1500	12	120
4	2000	8	118
5	2000	10	120
6	2000	12	116
7	2500	8	120
8	2500	10	116
9	2500	12	118

Fig. 5 Parameters

↓	C1	C2	C3	C4	C5
	SPEED	DRILL BIT DIA	POINT ANGLE	SURFACE FINISH	SURFACE FINISH 1
1	1500	8	116	0.565	0.610
2	1500	10	118	0.727	0.717
3	1500	12	120	0.912	0.941
4	2000	8	118	1.050	1.040
5	2000	10	120	1.210	1.209
6	2000	12	116	1.640	1.562
7	2500	8	120	2.145	2.146
8	2500	10	116	2.521	2.491
9	2500	12	118	2.742	2.781

Fig. 6 Parameters

### 4.1 Optimization of Parameters

Figures 5 and 6.

Analyze Taguchi Design—Select Responses (Figs. 7, 8, 9, 10, 11).

## 5 Results and Discussion

Taguchi method stresses the importance of studying the response variation using the signal-to-noise (S/N) ratio plays a major role in the Taguchi method.

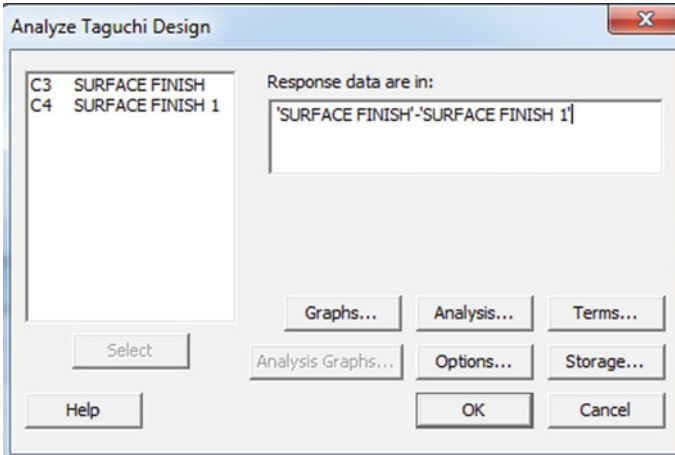
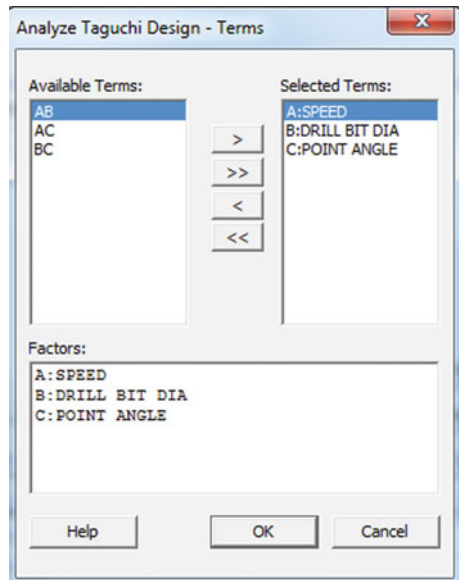


Fig. 7 Design analysis

Fig. 8 Terms\_analyze



$$S/N = -10 * \log\left(\sum (Y^2)/n\right)$$

$n = 1$  (number of measurements in a trial/row)

Performance characteristics, a greater  $S/N$  value corresponds to better performance and it is noted with optimum spindle speed is 2500 rpm (Fig. 12).

	C1	C2	C3	C4	C5	C6	C7
	SPEED	DRILL BIT DIA	POINT ANGLE	SURFACE FINISH	SURFACE FINISH 1	SNRA1	MEAN1
1	1500	8	116	0.565	0.610	-4.63896	0.5875
2	1500	10	118	0.727	0.717	-2.82988	0.7220
3	1500	12	120	0.912	0.941	-0.66628	0.9265
4	2000	8	118	1.050	1.040	0.38203	1.0450
5	2000	10	120	1.210	1.209	1.65212	1.2095
6	2000	12	116	1.640	1.562	4.08009	1.6010
7	2500	8	120	2.145	2.146	6.63057	2.1455
8	2500	10	116	2.521	2.491	7.97915	2.5060
9	2500	12	118	2.742	2.781	8.82225	2.7615

Fig. 9 Work sheet

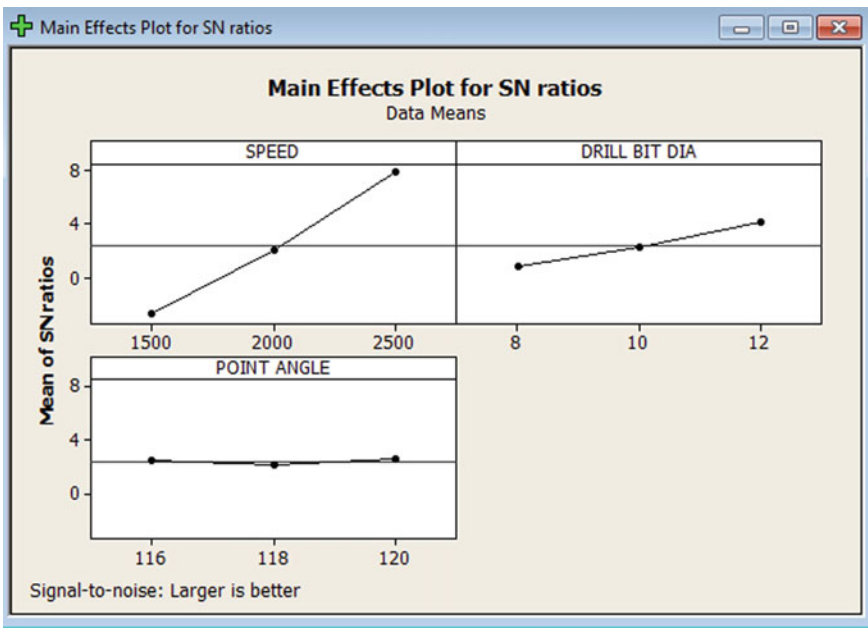


Fig. 10 S/N ratio plot

## 6 Conclusion

In this paper an attempt to make use of the Taguchi optimization technique to optimize drilling parameters during workpiece material fiber.

In this work, the optimal parameters of cutting speed are 1500, 2000, and 2500 rpm, drill bit diameters are 8, 10, and 12 mm and point angles 116°, 118°, and 120°. Experimental work to validate with different parameters and results are

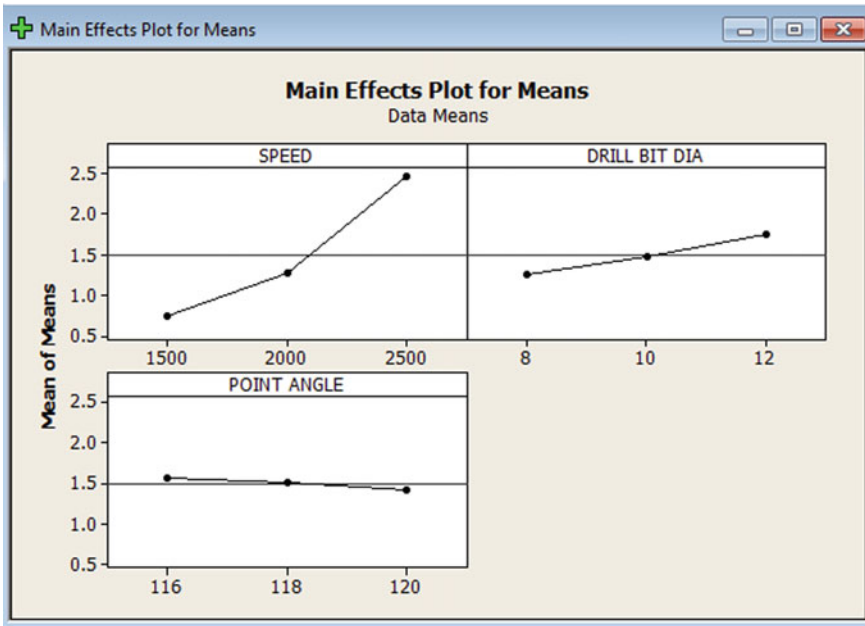


Fig. 11 Means plot

↓	C1	C2	C3	C4	C5	C6	C7
	SPEED	DRILL BIT DIA	POINT ANGLE	SURFACE FINISH	SURFACE FINISH 1	SNRA1	MEAN1
1	1500	8	116	0.565	0.610	-4.63896	0.5875
2	1500	10	118	0.727	0.717	-2.82988	0.7220
3	1500	12	120	0.912	0.941	-0.66628	0.9265
4	2000	8	118	1.050	1.040	0.38203	1.0450
5	2000	10	120	1.210	1.209	1.65212	1.2095
6	2000	12	116	1.640	1.562	4.08009	1.6010
7	2500	8	120	2.145	2.146	6.63057	2.1455
8	2500	10	116	2.521	2.491	7.97915	2.5060
9	2500	12	118	2.742	2.781	8.82225	2.7615

Fig. 12 Final worksheet results. Test report from CITD

validated experimentally the results based on the Taguchi method for which optimal valves obtained are—1200 rpm, drill bit diameter—12 mm and point angle—118°.

## References

1. Davim JP, Reis P (2003) Study of delamination in drilling carbon fiber reinforced plastics (CFRP) using design experiments. *Compos Struct* 59:481–487
2. Krishnaraj V, Prabukarthi A, Ramanathan A, Elanghovan N, Senthil Kumar M (2010) Optimization of machining parameters at high speed drilling of carbon fiber reinforced plastic (CFRP) laminates. *Compos B* 43:1791–1799
3. Krishnamurthy A, Rajendra Boopathy S, Palanikumar K, Paulo Davim J (2010) Application of grey fuzzy logic for the optimization of drilling parameters for CFRP composites with multiple performance characteristics. *Measurement* 45:1286–1296
4. Karnik SR, Gaitonde VN, Campos Rubio J, Esteves Correia A, Abrao AM, Paulo Davim J (2006) Delamination analysis in high speed drilling of carbon fiber reinforced plastics (CFRP) using artificial neural network model. *Mater Des* 29:1766–1776
5. Shyha I, Soo SL, Aspinwalla D, Bradley S (2010) Effect of laminate configuration and feed rate on cutting performance when drilling holes in carbon fibre reinforced plastic composites. *J Mater Process Technol* 210:1023–1034
6. Madhavan S, Prabhu SB (2010) Experimental investigation and analysis of thrust force in drilling of carbon fibre reinforced plastic composites using response surface methodology. *Int J Mod Eng Res (IJMER)* 2(4):2719–2723
7. Enemuoh EU, El-Gizawy AS, Okafor AC (2001) An approach for development of damage-free drilling of carbon fiber reinforced thermosets. *Int J Mach Tools Manuf* 41:1795–1814



# Hardness Characteristics of Grinding Wheel Using Al<sub>2</sub>O<sub>3</sub> with Boron Nitride



Shivashankara, Rudra Naik and Mahadev Gouda Patil

**Abstract** Different techniques used to measure the hardness of the grinding wheel based on the grinding wheel surface of various grain sizes and the bond contents present in the wheel structure. Two different techniques are identified to accept entirely their capacity to differentiate the wheels of various commercial hardness. In production industries, hardness of the grinding wheels is one of the key parameters which shows its strength of the grinding wheel. During the operating condition (dynamic), is the first method to easily relate in the workshop, quite more complex to analyze. One more technique in research studies of grinding wheel hardness obtained through statistical analysis result. This research highlights the further improvement of hardness of grinding wheel by combining two different abrasive materials (Al<sub>2</sub>O<sub>3</sub> with Boron nitride). By mixing these two abrasive materials with vitrified bonding system involves the adjustments in order to maintain grinding performance, mainly the wheel hardness, grain holding capability, cutting strength, and wheel safety during the machining. It is a major outcome on mixing proportion, mixing quality, stability, and skill to manage the wheel in its green state during the heat treatment, while the proper composition of the bonding material tends to influence the strength and hardness of the grinding wheel. The present work reports the influence of the hardness of the wheel in terms of improving the wear rate and durability and power consumed during the grinding operation which highly affects the grinding business. The final parts of this article give the improved hardness of the grinding wheel and combined grain topography, wheel morphology would represent a clear step development of grinding wheel technology and that each of value in its own sphere of application in grinding.

**Keywords** Grinding wheel · Hardness · Bonding material and wheel morphology · Topography

---

Shivashankara (✉)

Department of Mechanical Engineering, Gopalan College of Engineering and Management, Bangalore, India

e-mail: [shivmtech@gmail.com](mailto:shivmtech@gmail.com)

R. Naik · M. G. Patil

Department of Mechanical Engineering, BMS College of Engineering, Bangalore, India

© Springer Nature Singapore Pte Ltd. 2020

G. S. V. L. Narasimham et al. (eds.), *Recent Trends in Mechanical Engineering*,

Lecture Notes in Mechanical Engineering,

[https://doi.org/10.1007/978-981-15-1124-0\\_30](https://doi.org/10.1007/978-981-15-1124-0_30)

## 1 Introduction

Grinding operation is the process of obtaining the required surface roughness on the work where it is required to machine precision components in an aerospace application. Here the tool is called abrasive wheel which acts like a cutting edge rubs against the work material and it removes the very thin layer of material in the form of dust and produces a smooth surface. In production industry the cost per product is subsequently higher because of complex geometry of parts to be finished and grinding wheel manufacturing cost. These two major issues are not much affected in large scale production industries, because the super abrasive wheels (CBN and Diamond) have shown their potential applications with higher production rates. In other production companies (small and medium scale) are shows minimum production rate, customer satisfaction compared to large scale companies, because of using the conventional abrasives  $\text{Al}_2\text{O}_3$  and SiC abrasive wheels for machining the parts. These abrasives do not have enough mechanical properties like cutting ability, strength, hardness, and toughness compared to super abrasives wheels. In order to satisfy the customer satisfaction in terms of cost reduction, quality of products, grinding wheel manufacturer come forward to increase the mechanical properties like hardness, strength, machineability, and re-sharpening of the grain during the operation. Wheel hardness is one of the grinding parameters which plays an important role during grinding operation. In addition to the hardness present in the conventional abrasive wheel, it is required to increase little more hardness to the existing grinding wheel ( $\text{Al}_2\text{O}_3$ ) with small weight percent of (HBN) hexagonal boron nitride. The blend proportions of these two abrasives with proper binding materials can changes in grain characterization using Scanning Electron Microscope (SEM). The improvement of hardness properties has a major outcome on mixing proportion, mixing quality, stability, and skill to manage the wheel in its green state during the heat treatment, while the proper composition of the bonding material tends to influence the strength and hardness of the grinding wheel. The present work reports the influence of the hardness of the conventional wheel in terms of improving the wear rate and durability and power consumed during the finishing operation which highly affects the grinding business. The final parts of this paper present the increase in the hardness properties by combining the basic abrasive materials ( $\text{Al}_2\text{O}_3$ ) with HBN and the wheel morphology and grain topography to improve the performance of the grinding wheel.

## 2 Literature Review

The present issues on the hardness strength of the grinding wheel which is not enough to make the product into finished parts as per the customer satisfaction. Hardness is the properties of the abrasive material which helps to remove the small number of materials and produce the smooth surface on the workpiece [1]. Hussein Talab and Marwa Marza [2] have presented the paper an experimental studying for

manufacturing grinding wheel using various abrasive particles alumina and SiC and the bonding agent use was vitrified. This study produces to assess on the mechanical and physical properties for manufacturing grinding wheel, with the percentage of vitrified bond in the laboratory. The physical (porosity and density) and mechanical properties like hardness, compressive strength, and wear rate were evaluated for the samples. The final results showed that the hardness, density increase, and compressive strength increased by reducing the porosity with increasing bond percentage.

Umashankar and Ramesh Babu [3] have studied about the grinding wheels life. During the grinding operation, the wheel is continuously in contact with the work part in order to obtain the required surface finish, sometimes it undergoes the fracture of bond, grain, and grain pullout finally it leads to wheel degradation because of less hardness of the wheel. When compared to conventional abrasive wheels, super abrasives wheels expect the more Babu, N.R. et al. [4] hardness during dressing with particular dressing capability which reduced by greater depth rate due to the high contact angle between the work and abrasive wheel surface causing more grain fracture. According to Daire et al. [5] formulate the high abrasive hardness and the wear rate was achieved by fusing alumina in the existence of a carbonaceous substance based on the alumina and alumina carbides. For preparations of this product and its usefulness in all the machining operation including material removal from the parts. For machining of 304 stainless steel and carbon steel part, the material removal rate was high using a combination of sintered alumina gel type abrasive with cofused alumina–zirconia, but less effective was identified Narayanan et al. [6] as compared to fused alumina. Vipin Gopana and Leo Dev Wins [7] have presented the quantitative analysis of grinding wheel loading that can give the facts about the machining conditions of the grinding wheel. With the improvement in the area of machine vision and image processing from his study which concentrates on succeeding a system for the quantitative evaluation of wheel loading using image capturing and image processing.

Suya Prem Anand et al. [8] have worked on the grindability of the pre-sintered zirconia that was examined using a vitreous bonded silicon carbide grinding wheel with the various grinding parameters such as speed of the wheel, depth of cut, and feed rate which are varied to investigate its grindability in terms of surface finish, G-ratio, force ratio, and ground surface under both wet and MQL cooling condition. From there study, by using various types of grinding wheel, such as diamond, CBN, and SiC wheels. Out of these wheels, the results obtained are specific energy, grinding force, and surface finish using SiC wheel and were found to be effective towards ground zirconia. Annamalai et al. [9] silicon carbide wheel of grit 220 with low porosity vitreous bonds is used to machine the zirconia and also less cost for SiC wheel is cheaper than using the diamond grinding wheel.

Odiro et al. [10] have discussed the characteristics of the grinding wheel as well as theoretical consideration of the operations of wheel materials. These characteristics of grinding wheel include the wheel material, grain size and its spacing, grade of the wheel, and bond type. The grain size determines the physical appearance of the wheel and grade determines how the bonding material tightly holds the grain on the wheel and the grain affects almost all consideration of the grinding operation. According

to their study the relationship among the different grinding parameters such as radial force  $f$ , the force acting on the single grit  $og$  the wheel  $F$ , grinding wheel velocity  $gV$ , workpiece velocity  $wV$ , wheel diameter, and diameter of the workpiece were established for the required grinding operation.

Pulmer et al. [11] studied the impact on the topography of the abrasive wheel exhibiting that the increase and decrease of wheel roughness and wheel density as increasing the more dressing effect. According to Klocke and Linke et al. [12] designate that the weakens of bonded wheel model using FEA, leads to larger gain breakout and more wear rate with the less hardness on wheel surface. Effort from Palmer et al. [13] indicated that the response of the dressing over the surface of the wheel in terms of two in deep feed rate and speed ratio which evaluated the impact of dressing on grit fracturing based on the developed grinding wheel surface morphology that was identified by using a spam of surface roughness parameter. From his viewpoint important changes in dressing between conventional and engineered grit morphology were also observed.

Breidenstein et al. [14] presented the fact that was focusing on the procedure for the verification of the grinding wheel topography, these topographies enable the product manufacturing to forecast and thus identify the surface of the machined parts. During the machining process influences the quality of machined parts which as the last step of most production chains, the innovation method is more assuring. Due to wear characteristics of the grinding grains, the topography of the grinding tool changes as more as the obtained surface does. Fritz Klocke et al. [15] discussed about the kinematic energy that gets converted into heat during grinding process which is outstandingly influenced by the wheel morphology. Accordingly the grain arrangement and the shape of the cutting edge have to be considered in order to introduce an advance towards the characterization of the cutting edges of a wheel topography while taking the material behavior of the work material into account. This paper highlights the kinematic geometric arrangement model which easily evaluates the geometrical shape of the cutting edge of the measured topography.

### 3 Methodology of Research

A literature study is like a birds eye view for collecting the lack of information on previous research work done by the different investigators. According to the previous research information on the grinding application, many advanced technologies have been adopted for improving the standard quality of abrasive tools. The research information involves the grinding wheel parameters based on the wheel hardness, surface roughness, and wheel morphology and grain topography which plays central role in grinding application. The surface hardness of the conventional abrasive ( $Al_2O_3$ ) wheel is not enough to improve the wheel life and quality of machined surface as per the customer requirement. To achieve the grinding wheel hardness like super abrasive

wheel standard, it is required to increase the grinding wheel hardness characteristic by conducting the hardness test on the sample which is made up of aluminum oxide grinding wheel with the boron nitride. The evaluation of the grinding wheel is on the basis of wheel surface hardness which shows the optimum results on the test sample.

## 4 Experimental Test Procedure

### 4.1 Grinding Wheel Hardness Test

The experiment designated were based on two types of grinding wheel made of vitrified bonded abrasive wheel samples. The first wheel is made of aluminum oxide abrasive particle used as a basic wheel and another wheel is made of combination of two different abrasive particles (Al<sub>2</sub>O<sub>3</sub> and HBN) with composition of Al<sub>2</sub>O<sub>3</sub> plus 10% of boron nitride. This composite wheel dimensions of 25 mm × 25 mm × 6 mm (External diameter × width × internal diameter) was employed. The prepared grinding wheel sample was placed on the anvil of high precision Micro Hardness Testing machine with full automation as shown in Fig. 1, which is specially used for research purposes in Central Manufacturing Technology Institute, Bangalore. The hardness tests were conducted, with the test method and force application variant is Q10-30-60A/A + using ½ inch carbide ball indenter with the basic load of 58 kg was applied for few seconds to know the actual hardness value of the wheel surface.



**Fig. 1** Micro hardness tester with a fully automatic loading system

**Table 1** Hardness values of the wheels

Sl. no.	Sample identification	Hardness measure in HR 15Y			Avg. values
		1st value	2nd value	3rd value	
1	Al <sub>2</sub> O <sub>3</sub> with 10% HBN	87.2	91.2	95.5	91.3
2	Al <sub>2</sub> O <sub>3</sub> basic wheel	90.9	92.3	89.5	90.9

Three hardness values were taken in three different places on the wheel surface by adjusting the wheel position and results were tabulated for both the types of grinding wheel. The average hardness result is shown in Table 1.


## 4.2 Measurement of Grinding Wheel Morphology

Grinding wheel morphology and grain topography were carried out with the Field Emission Scanning Electron Microscope (FEGSEM), SE2 (EhThomly detector)—for wheel Topography and the optical resolution: Up to 0.8 nm with magnification factor range from 12 to 100,000X (SE); 100–100,000X (BSE). The measuring range of a single scan limited around 15 cm × 15 cm the measuring of larger surface area was obtained by merging multiple scans. Measuring range of the investigated grinding wheel topographies was selected so that the grain distribution characteristics reached a quasi-state. There are six scanned images that were taken from each grinding wheel samples. From these samples wheel morphologies and grain topography were selected with magnification factors 200X, 500X, 1000X and WD and height was 9.8, 2.00. So that the distribution of basic wheel grain shape characteristics and the boron nitride wheel were analyzed. From the SEM analysis, it was observed that the basic wheel morphology shows the more porous, not uniform mixture of grain with bond and absence of cutting edges when compared to boron nitride wheel. This SEM analysis was carried out in Central Manufacturing Technology Institute, Bangalore (Fig. 2).

## 5 Results and Discussion

### 5.1 Grinding Wheel Hardness

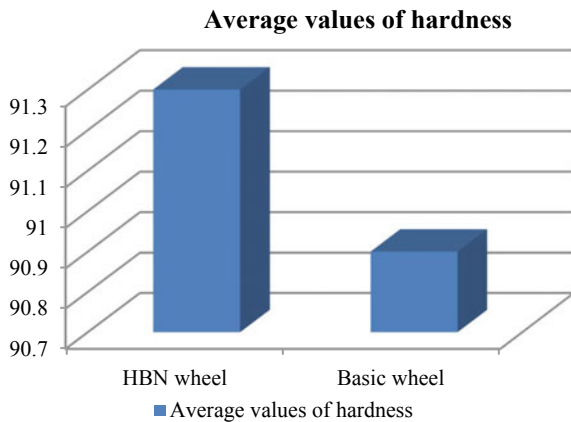
The results in Table 1 show the grinding wheel hardness using the two different types of grinding wheels samples. The type-1 wheel used Al<sub>2</sub>O<sub>3</sub> as a Basic wheel and Type-2 Wheel used an Al<sub>2</sub>O<sub>3</sub> with boron as nitride particles.

<b>Model</b> : Ultra Plus Field emission Scanning Electron Microscope (FEGSEM) <b>Manufacturer</b> : Carl Zeiss <b>Supplier</b> : Carl Zeiss Group	
 <p style="text-align: center;"><b>SCANING ELECTRON MICROSCOPE (SEM)</b></p>	<b>SPECIFICATIONS</b>
	In lens detector- for surface structure
	SE2 (EhThomly detector)- for Topography
	EsB detector- for Pure material contrast
	AsB detector- for Channeling contrast (crystal orientation)
	CL detector- for Luminescent materials
	STEM- Scanning Tunneling Electron Microscope Resolution: Upto 0.8nm
	Magnification: 12- 100,000X (SE); 100-100,000X (BSE)

**Fig. 2** Ultra plus field emission scanning electron microscope (FEGSEM)

As per the result obtained from the tabulated values, it is clearly shown that the differences in wheel hardness from two types of grinding wheel, in that the type-2 wheel (Al<sub>2</sub>O<sub>3</sub> with boron nitride) shows the more hardness than the Basic wheel. Figure 3 shows the increased hardness value compared with basic wheel hardness.

**Fig. 3** Average hardness values of the grinding wheel



## 5.2 Grinding Wheel Morphology and Grain Topography

The result in Figs. 7 and 8, show the homogeneous mixture of grain topography that is generated for improving the hardness of the grinding wheel. From the SEM image, the uniform grain distribution was observed by grain topographies, and wheel hardness characteristics which appeared in wheel morphology by the combination of aluminum oxide with the boron nitride grinding wheel. This has shown to be more effective than either the aluminum abrasive alone.

## 6 Characterization of Aluminum Oxide with Boron Nitride Particles

The Fig. 4 shows there is a chance of grain pullout to be very fast during grinding because of improper holding of grain with the bond in Fig. 5a than Fig. 5b.

Figure 5 indicates clearly, the topography of the wheel which is having more cutting edges projection with the boron nitride abrasive material when compared to basic wheel topography.

Figure 6 illustrates the grain topography analysis of two different types of grinding wheel investigation and the smaller grain size led to a more number of cutting edges with the small greater chip thickness. The sizes of the grain had no significant recommendation on the grain distribution of size and shape of the grain character.

Figure 7 Due to the combining of  $\text{Al}_2\text{O}_3$  with Boron nitride grinding wheel insist the results clearly confirm, that the grain morphology with minimize porous and the above two grinding wheel types were the same and the grain sizes were separately distributed.

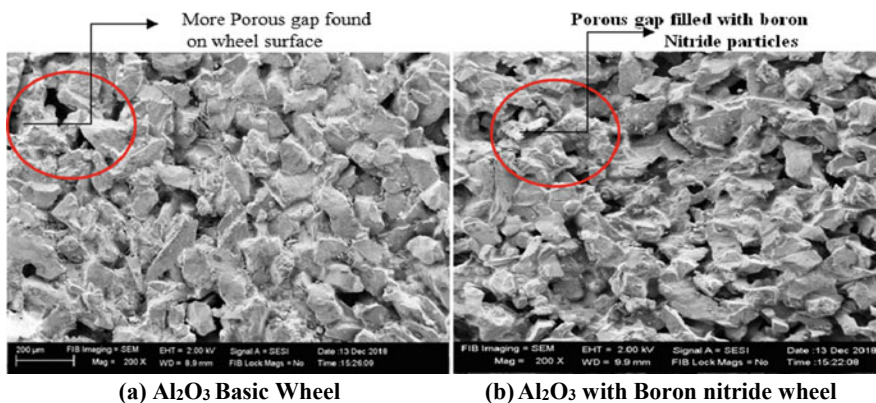


Fig. 4 Topography of different crystalline forms of  $\text{Al}_2\text{O}_3$  with boron nitride grinding wheel



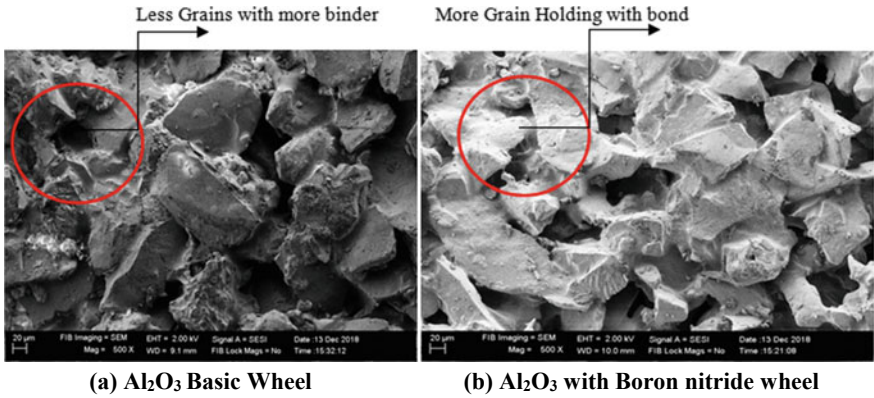


Fig. 5 Grain topography of a crystalline form of Al<sub>2</sub>O<sub>3</sub> with boron nitride

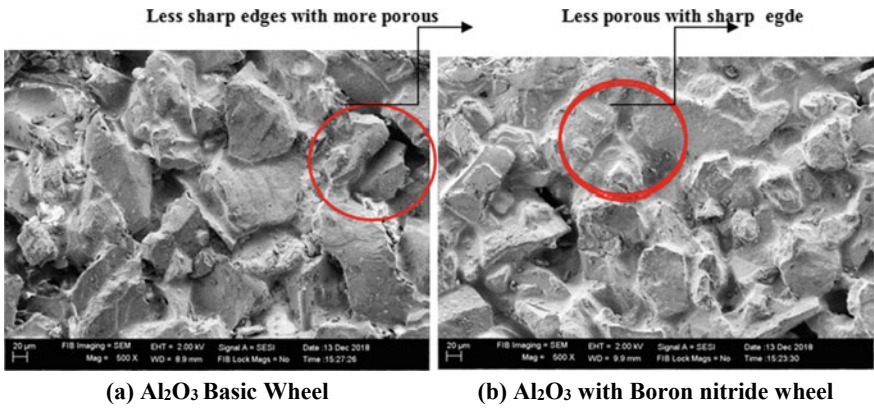


Fig. 6 Grain topography of crystalline form of Al<sub>2</sub>O<sub>3</sub> with boron nitride grinding wheel

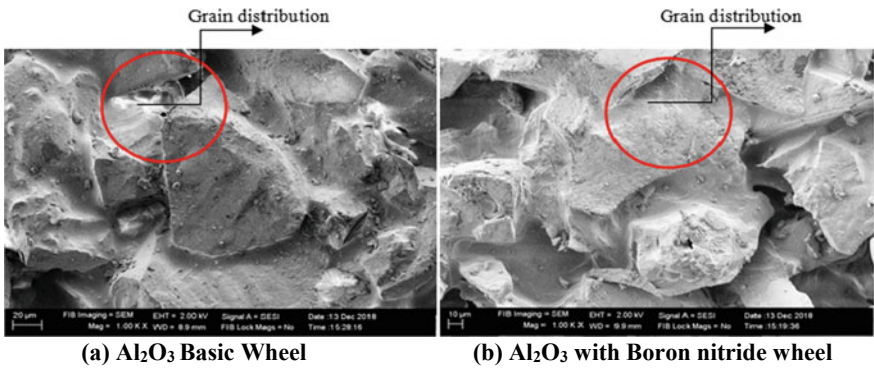
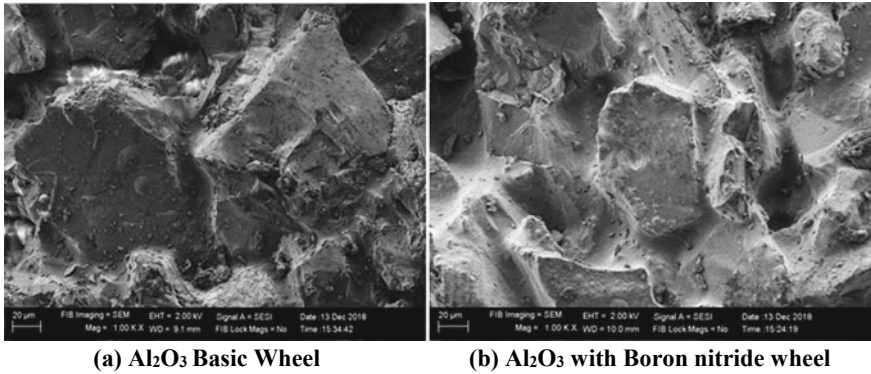


Fig. 7 Topography of crystalline form of Al<sub>2</sub>O<sub>3</sub> with boron nitride grinding wheel



**Fig. 8** Topography of crystalline form of Al<sub>2</sub>O<sub>3</sub> with boron nitride grinding wheel

Figure 8 show the topography of crystalline form of boron nitride wheel surface, it clearly shows that the homogeneous mixture of the abrasive particles with porous free surface of the wheel. A combination of the aluminum oxide with the boron nitride grinding wheels with different topography is shown to be more effective than the either the aluminum oxide abrasive alone.

## 7 Conclusion

1. Strongly identified the increased hardness value on the manufactured composite grinding wheel using aluminum oxide with boron nitride.
2. Hardness result of the manufactured grinding wheel from the aluminum oxide and boron nitride increases with increasing the percentage of vitrified bond, and the hardness value of manufactured abrasive wheels from boron nitride (HBN) was higher than that of manufactured grinding wheels from aluminum oxide (Al<sub>2</sub>O<sub>3</sub>).
3. The porosity of the manufactured wheel from aluminum oxide and boron nitride decreases with increasing the bonding percentage, and the manufactured abrasive wheel from aluminum oxide with boron nitride improves the uniform grain distribution.
4. The density of the manufactured grinding wheel using aluminum oxide and boron nitride increases with an increase in the bonding percentage.
5. The strength of the manufactured abrasive wheels from aluminum oxide with boron nitride increases with increasing the hardness value, and the strength of the grinding wheels using aluminum oxide (Al<sub>2</sub>O<sub>3</sub>) with boron nitride is higher than that of the wheel manufacture using aluminum oxide (Al<sub>2</sub>O<sub>3</sub>).

6. The hardness of the manufactured abrasive wheel using aluminum oxide with boron nitride increases the workpiece, then the increased hardness characteristic is good for wheel life.
7. SEM analysis of the manufactured abrasive wheel highlights the grain topography that showed the uniform grain distribution on the wheels and the wheel morphology showing the homogeneous mixture of aluminum oxide with boron nitride grain and vitrified bond.

## References

1. Odior AO, Oyawale FA (2010) Manufacture of abrasive grains from locally sourced raw materials in Nigeria. *J Emerg Trends Eng Appl Sci* 1(1): 40–47
2. Talab H, Marza M (2017) Study Some properties for manufactured grinding wheels by use different abrasive materials. *Aust J Basic Appl Sci* 11(2):50–58
3. Shankar U, Ramesh Babu N (2018) A model for predicting the geometry of crater on grinding wheel surface ablated with a single pulsed laser. *Procedia Manuf* 26:509–520
4. Babu NR, Radhakrishnan V, Murti YV (1989) Investigations on laser dressing of grinding wheels part I: preliminary study. *J Eng Ind* 111(3):244–252
5. Daire et al. High-hardness abrasive product based on alumina and aluminum oxycarbides and process for preparing same United State Patents [11], [19], [45]4,341,533 45 July 27, 1982
6. Narayanan KS, et al. (1988) Grinding wheel with combination of fused and sintered abrasive grits 18,11, Patent Number: 4,741,743 (45) Date of Patent: May 3, 1988
7. Vipin Gopana, Leo Dev Wins K (2016) Quantitative analysis of grinding wheel loading using image processing. *Procedia Technol* 25:885–891
8. Suya Prem Anand P, et al. (2017) Investigation on grindability of medical implant material using a silicon carbide wheel with different cooling conditions. *Procedia Manuf* 10:417–428
9. Annamalai VE, et al. (1993). Efficient grinding of Ce-TZP with SiC wheels. *J Eur Ceram Soc* 11:463–469
10. Odior O et al (2013) Theoretical considerations of machining with grinding wheels. *Int J Eng Technol* 2(2):126–133
11. Palmer J, Ghadbeigi H, Novovic D, Curtis D (2018) An experimental study of the effects of dressing parameters on the topography of grinding wheels during roller dressing. *J Manuf Process* 31:348–355
12. Klocke F, Linke B (2008) Mechanisms in the generation of grinding wheel topography by dressing. *Prod Eng* 2(2):157–163
13. Pulmer J, et al. (2018) The Influence of Abrasive Grit Morphology on Wheel Topography and Grinding Performance. In: 8th CIRP Conference on High Performance Cutting (HPC 2018), *Procedia CIRP*, vol 77, pp 239–242
14. Breidenstein B, Denkena B, Mörke T, Hockauf R (2016) Markierungsfreie Bauteilidentifikation, Submitted to *wt-Werkstattstechnik online*, vol. 6
15. Klocke F et al (2016) Approach of characterization of the grinding wheel topography as a contribution to the energy modelling of grinding processes. *Procedia CIRP* 46:631–635

# Optimization of Process Parameters on EDM for Inconel 718



Ch. Shekar, U. Ashok Kumar, K. Kishore and P. Laxminarayana

**Abstract** Inconel 718 super alloy are highly used in gas turbine, space vehicles, aircraft, nuclear reactors, submarine, petrochemical equipments and other high temperature applications. Due to the excellent mechanical properties, high strength at elevated temperature, it's hard to machine in traditional machining process. EDM is one of the most suitable techniques to shape this alloy into desire shape. The present study is to investigate the machining characteristics of Inconel 718 material on CNC—EDM using copper and graphite electrodes. Taguchi L9 orthogonal array had been used for design of experiment, where the input parameters are current, Pulse-ON, Pulse-OFF and the experimental outcomes are material removal (MRR). Analysis of variance (ANOVA) is employed to indicate the level of significance of machining parameters.

**Keywords** Inconel 718 · Design of experiments—Taguchi L9 OA · Material removal rate · S/N ratio-larger the better · Anova-significant factor

## 1 Introduction

Electrical discharge machining (EDM) has been used in the machining of tough and complex materials used in the industries [1, 2]. In the EDM process, material removal is by the action of spark discharges between the electrode tool and the workpiece. The spark discharges produces per second take place in a tiny crater by melting and vaporization, thus reproducing the shape of the tool into the work piece. A dielectric

---

Ch. Shekar (✉) · U. A. Kumar · P. Laxminarayana  
Department of Mechanical Engineering, College of Engineering, Osmania University, Hyderabad, India  
e-mail: [shekar\\_cipet@yahoo.co.in](mailto:shekar_cipet@yahoo.co.in)

U. A. Kumar  
e-mail: [uak.oumech@gmail.com](mailto:uak.oumech@gmail.com)

K. Kishore  
Department of Mechanical Engineering, Vasavi College of Engineering, Hyderabad, India

© Springer Nature Singapore Pte Ltd. 2020  
G. S. V. L. Narasimham et al. (eds.), *Recent Trends in Mechanical Engineering*,  
Lecture Notes in Mechanical Engineering,  
[https://doi.org/10.1007/978-981-15-1124-0\\_31](https://doi.org/10.1007/978-981-15-1124-0_31)

fluid flushes out the “chips” that are the products of the discharge. Many complex shapes can be reproduced in the workpiece [3, 4].

Inconel materials are used in many industries like aerospace, medical instruments, and nuclear plants because of good mechanical properties [5]. Electrical discharge machining (EDM) is an alternative method for machining Inconel alloys in required shapes w.r.t to the tool design. Therefore, EDM is capable of efficiently machining various parts with hardness properties. Experiments have been carried out to see the effects of input parameters such as current, time-on, and time-off and tool electrode on the performance of material removal rate. Taguchi’s method has been used as a design of experiments technique for experimental investigation. Experiments have been designed as per Taguchi’s L 9 Orthogonal array. Analysis of variance (ANOVA) is done to indicate the significance of machining parameters [6–9].

## 2 Experimental Details

### 2.1 Work Piece Material

Samples are of square segment of Inconel 718 steel having size of 80 mm × 80 mm × 10 mm thick and the properties with Composition in percentage by weight are given in Table 1 with the copper electrode and graphite electrode of 10 mm diameter for machining.

Design of Experiments was based on the factors and levels using Taguchi L9 Orthogonal array with input parameters and their levels shown in Table 2. Table 3 shows the experiments were carried out according to the Taguchi L9 Orthogonal array.

**Table 1** Composition of Inconel 718

Elements	N	Ti	Al	Cr	Mo	N	Ferrous
Composition	50–55	17–21	0.2–0.8	17–21	2.8–3.3	4.75–5.5	Balance

**Table 2** Selected process parameters for machining conditions of Inconel 718

Parameters	Level 1	Level 2	Level 3
Current	4	6	8
Pulse-On	5	7	9
Pulse-Off	2	3	5

**Table 3** Shows the L9 Orthogonal array experimental for EDM of Inconel 718 by using copper and graphite electrode

Expt. No	Current	Pulse-On	Pulse-Off
1	4	5	2
2	4	7	3
3	4	9	5
4	6	5	3
5	6	7	5
6	6	9	2
7	8	5	5
8	8	7	2
9	8	9	3

### 3 Results and Discussions

Higher Material Removal Rate (MRR) is calculated by dividing the difference between the weight of workpiece before (wb) and after (wa) machining, against the machining time (tn). With copper and graphite electrodes on machining of Inconel 718 as shown in Table 4.

$$MRR = \frac{\text{Before and after machining weight of work piece}}{\text{Machining Time}}$$

**Table 4** Experimental results of Inconel 718 by EDM with copper and graphite electrode

Expt. No	Current	Pulse-On	Pulse-Off	MRR with copper electrode (mm/min)	MRR with graphite electrode (mm/min)
1	4	5	2	0.066	0.085
2	4	7	3	0.069	0.074
3	4	9	5	0.125	0.092
4	6	5	3	0.128	0.098
5	6	7	5	0.169	0.132
6	6	9	2	0.173	0.138
7	8	5	5	0.300	0.183
8	8	7	2	0.386	0.198
9	8	9	3	0.467	0.293

### 3.1 Signal to Noise Ratio of MRR with Copper Electrode on Inconel 718

From Table 5 shows the S/N Ratios of MRR with copper electrode machining on Inconel 718 w.r.t input parameters of Current, Pulse-ON, and Pulse-OFF and the optimum combination is A3B3C2 from Fig. 1 for Material removal rate for which higher the better is considered.

**Table 5** Response table for S/N Ratios of MRR with copper electrode on Inconel 718

Level	Current	Pulse-On	Pulse-Off
1	-17.66	-15.96	-15.61
2	-15.51	-15.59	<b>-15.36</b>
3	<b>-13.38</b>	<b>-15.00</b>	-15.58
Delta	4.28	0.96	0.25
Rank	1	2	3

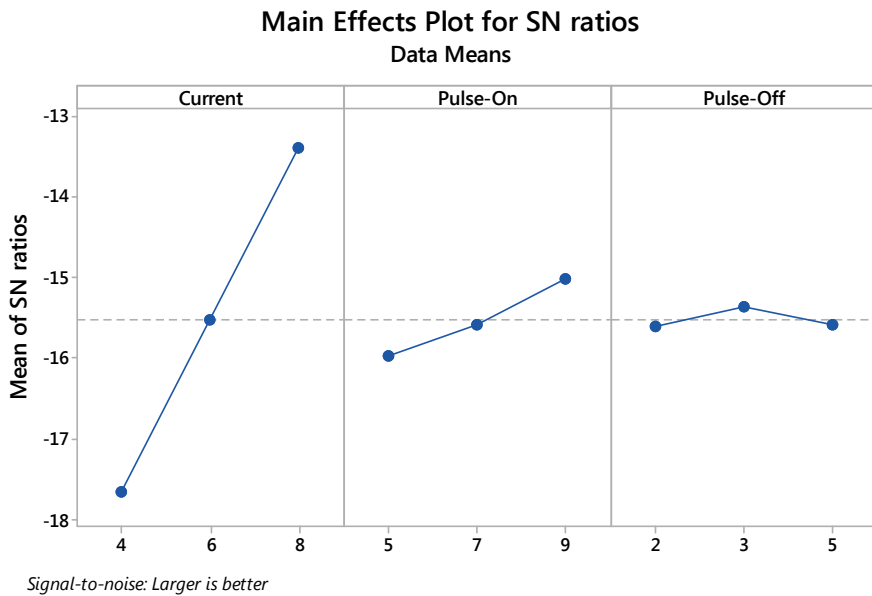


**Fig. 1** Graph S/N Ratios of MRR with copper electrode machining on Inconel 718

**Table 6** ANOVA of MRR with copper electrode

Source	DF	Adj SS	Adj MS	F-value	P-value	% Contribution
Current	2	0.01064	0.00532	61.79	0.016	92.11
Pulse-On	2	0.00064	0.00032	3.69	0.213	5.51
Pulse-Off	2	0.00010	0.00005	0.61	0.623	0.90
Error	2	0.00017	0.00009			1.49
Total	8	0.01155				100

### 3.2 ANOVA for of MRR with Copper Electrode by EDM on Inconel 718

From Table 6 Shows the ANOVA for MRR with copper electrode by EDM on Inconel 718 in which the most contribution percentage factor is current 92.11%, which shows the highest value in machining process followed by less pulse-on 5.51% and pulse-off 0.90%, and error contribution 1.49%.

### 3.3 Signal to Noise Ratio of MRR with Graphite Electrode on Inconel 718

From Table 7 shows the S/N Ratios of MRR with graphite electrode machining on Inconel 718 w.r.t input parameters of Current, Pulse-ON, and Pulse-OFF and the optimum combination is A3B3C2 from the graph of Fig. 2 for Material removal rate for which higher the better is considered.

**Table 7** S/N Ratios of MRR with graphite electrode on Inconel 718

Level	Current	Pulse-On	Pulse-Off
1	-21.02	-16.28	-15.81
2	-14.55	-15.87	<b>-15.47</b>
3	<b>-11.73</b>	<b>-15.15</b>	-16.02
Delta	9.29	1.13	0.54
Rank	1	2	3



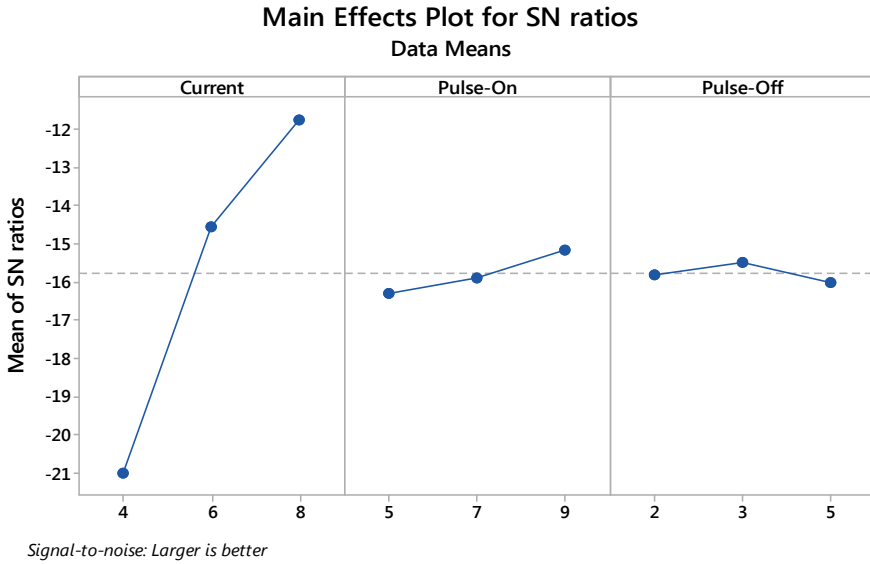


**Fig. 2** Graph S/N Ratios of MRR with graphite electrode machining on Inconel 718

### 3.4 ANOVA for of MRR with Graphite Electrode by EDM on Inconel 718

From Table 8 the ANOVA for of MRR with Graphite electrode by EDM on Inconel 718 in which the most contribution percentage factor is current 95.76%, which shows the highest value in the machining process followed by less pulse-on 2.54% and pulse-off 1.05%., and error contribution 0.64%.

**Table 8** ANOVA of MRR with graphite electrode

Source	DF	Adj SS	Adj MS	F-value	P-value	% Contribution
Current	2	0.04435	0.02218	149.06	0.007	95.76
Pulse-On	2	0.00118	0.00059	3.96	0.202	2.54
Pulse-Off	2	0.00049	0.00024	1.63	0.38	1.05
Error	2	0.00030	0.00015			0.64
Total	8	0.04632				100.00

## 4 Conclusions

In this study, material removal rate is the most important performance measure using Taguchi L9 design of experiments. In order to improve productivity in EDM machining of Inconel 718, the optimum level of copper and graphite are calculated as follows:

- The material removal rate of Inconel 718 with copper and graphite electrode shows the maximum removal rate. The optimum combination is A3B3C2, i.e., Current 8Amps, Pulse-On 9  $\mu$ s, Pulse-Off 3  $\mu$ s is 0.467 and 0.293 mm/min which is matching within the Taguchi L9 Orthogonal Array of Design of Experiment
- From the ANOVA it was found that the current is the most significant factor which is contributing to MRR w.r.t electrodes of copper 92.11% and graphite 95.76% and error estimation is 0.64% for graphite and 1.49% for copper electrode.

## References

1. Ezugwu E (2005) Key improvements in the machining of difficult-to-cut aerospace superalloys. *Int J Mach Tools Manuf* 45:1353–1367
2. Rajesha S, Sharma A, Kumar P (2011) On electro discharge machining of Inconel 718 with hollow tool. *J Mater Eng Perform* 21(6):1–10
3. Tzeng Y (2008) Development of a flexible high-speed EDM technology with geometrical transform optimization. *J Mater Process Technol* 203(1–3):355–364
4. Bharti PS, Maheshwari S, Sharma C (2010) Experimental investigation of Inconel 718 during die-sinking electric discharge machining. *Int J Eng Sci Technol* 2(11):6464–6473
5. Kuppan P, Rajadurai A, Narayanan S (2008) Influence of EDM process parameters in deep hole drilling of Inconel 718 international. *J Adv Manuf Technol* 38:74–84
6. Ashok Kumar U, Laxminarayana P (2017) Study of tool wear optimization in micro holes machining of SS316 by die sinker electrical discharge machining. *Int J Sci Res Multidiscip Stud* 3(7):1–4
7. Ashok Kumar U, Laxminarayana P (2017) Optimization of process parameters of material removal rate in micro hole machining by die sinker EDM. *IOSR J Eng (IOSRJEN)* 7(7):61–65 ||V||
8. Ashok Kumar U, Laxminarayana P (2018) Optimization of electrode tool wear in micro holes machining by die sinker EDM using Taguchi approach. *Mater Today Proc* 5(1):824–1831. <https://doi.org/10.1016/j.matpr.2017.11.281> (Elsevier)
9. Ashok Kumar U, Laxminarayana P (2018) Experimental optimisation of process parameters on micro hole machining by die sinker EDM. *Int J Adv Mater Manuf Charact (IJAMMC)* 8(2). <http://dx.doi.org/10.11127/ijammc2018.09.06>

# Profile Optimization in Tooltip for FSW Process—A Numerical Investigation



R. Saravanan, M. S. Sreenivasa Rao, T. Malyadri  
and Nagasrisaihari Sunkara

**Abstract** Friction Stir Welding (FSW) is employed for welding the metal surfaces without changing their phase. The major process variables of FSW are the profile of tooltip including plain or grooved surfaces, rotary speed of the tooltip, the angle of the tool fixed, and the vertical force on the tooltip. This investigation focuses the tooltip geometry with plain surface in FSW of AA6061. Initially conventional cylindrical profile is considered with a predefined tool spinning speed of the tool and compressive force which applied over it axially, for a specific welding application. The factors varied four levels. The stability related, thermal, and transient investigations were performed. The observations were compared with different geometries including two different truncated cone profiles and a hexagonal prismatic profile. The best profile suggested based on the investigation results.

**Keywords** FSW · Tooltip geometry · Numerical investigation · Transient analysis · Thermal analysis · Stability investigations

## 1 Introduction

Friction Stir Welding (FSW) attracts the researcher due to its significant performance. Pavan Kumar et al. [1] investigated the material flow pattern responses in FSW of AA 6061 with respect to various tooltip geometries like Knurling, plain cylindrical

---

R. Saravanan (✉)

Mechanical Engineering, Ellenki College of Engineering and Technology, Hyderabad, TS, India  
e-mail: [dr.sarravanan@gmail.com](mailto:dr.sarravanan@gmail.com)

M. S. S. Rao · T. Malyadri · N. Sunkara

Mechanical Engineering, VNR Vignana Jyothi Institute of Engineering and Technology,  
Hyderabad, TS, India

e-mail: [subbusoft2004@gmail.com](mailto:subbusoft2004@gmail.com)

T. Malyadri

e-mail: [malyadri.vnr@gmail.com](mailto:malyadri.vnr@gmail.com)

N. Sunkara

e-mail: [snsaihari@gmail.com](mailto:snsaihari@gmail.com)

© Springer Nature Singapore Pte Ltd. 2020

G. S. V. L. Narasimham et al. (eds.), *Recent Trends in Mechanical Engineering*,

Lecture Notes in Mechanical Engineering,

[https://doi.org/10.1007/978-981-15-1124-0\\_32](https://doi.org/10.1007/978-981-15-1124-0_32)

surface, threaded cylindrical surface, conical, and grooving. The welding joints like butt and lap were considered. But the influence of the tool direction in rotation plays a vital role in material flow patterns than tooltip geometry. Bilici [2] studied the influence of the tool geometry like cylindrical, tapered, threaded cylindrical, and square in the friction stir spot welding of polypropylene sheets. The author reported that the threaded taper tooltip outperformed and the tooltip dimensions were standardized. Indira Rani and Marpu [3] experiment with FSW of AA6061 and AA6351 suggested that the square profile for axial force 6000 N, speed of the weld 60 mm/min at 1000 rpm of tool rotation for AA6061. Meilinger and Török [4] also recommended truncated taper pin for FSW of aluminum alloys. Kadian et al. [5] conducted the experimentation at three levels of tool traverse speed like 1.8, 2, and 2.2 mm/s and varied rotational speeds at three levels as 1000, 1200, and 1400 rpm for welding AA6061. The authors reported that the truncated cone type tooltip reduced the maximum weld temperature and also causes the less quantity of material mixing. The investigation of [6] was Aluminum Alloy (AA-7075) with various spindle speeds, feed, and the tool's depth on work piece. The setting of 1750 rpm of spindle speed at 20 mm weld width, plunge depth 0.16 mm, and feed of 50 mm/min yielded high toughness. Abedini et al. [7] recommended triangular tooltip profile which yielded high weld strength than the tapered tooltip for spot welding of DP780 at 30 kN axial load, 1000 rpm tool rotation and feed is 20 mm/min. The study of [8] was on AA2016-T6 with tool rotation 900 rpm, feed 40 mm/min, axial force 5 kN. The weld by use of taper tooltip yielded Excess of 10% Ultimate tensile strength, 9% of yield strength, and 30% of percent of elongation at 20 centigrade weld temperature. Casalino et al. [9] experimented in butt welding of AA 5754H11 and reported that tapered tooltip produced a regular joint. The smooth surface finish ensured with a little flash. Raguraman et al. [10] investigated numerically about the tooltip geometry influence on FSW of AA 6061 and AZ6 and recommended concave-shaped fluted tooltip geometry than tapered fluted tooltip with highlighting the reason of the required lesser value of heat flux to weld the materials. Rathinasamy and Raju with Smolin [11, 12] recommends simulation can be a tool for analyzing the cases effectively and economically. Smolin [12] depicted the mechanism of FSW by using computer simulation. Investigation of [13] was on AA6061 FSW and focused on thermal effects by tooltip geometries. This study focused on the influence of load applied to the tool axially, rotational speed, and feed. Except the feed, factors like force on tool and rotational speed were directly proportional and linear response to welding temperature. Daneji et al. [14] experimented in FSW of AA6061 (6061-O temper) alloy with cylindrical too profile at 1750 rpm. The variants were welding speeds, thread pitches, and pin lengths. The findings were: the welding speed plays a key role in FSW due to insufficient tooltip length, the pinhole, and insufficient penetration defects occurred. The shoulder and tip diameter are unswervingly relative to the flow velocity of material and the material inside the weld melt, respectively [15]. The influence of shape and size of tooltip geometries in thermo-mechanical

environment, flow of plasticized material, heat generation rate, torque, and traverse force which act on the tool [16]. This numerical investigation entirely different by considering cone angles of truncated profiles, hexagonal shape which circumscribed circle is equivalent diameter of conventional circular tooltip profile. The surface of the tooltip is not grooved. Sufficient numerical investigation techniques like stability analysis, thermal investigation, and transient analysis were carried out to optimize tooltip profiles.

## 2 Materials and Methods

In this study, four different tooltip geometries were considered, viz., cylindrical, hexagonal prismatic, truncated cone with cone angle  $20^\circ$ , and truncated cone with cone angle  $10^\circ$ . Each plate to be welded is of  $50 \times 200$  mm size. Hence final dimension will be  $100 \times 200$  mm. The tooltip is 5.7 mm long. The shoulder has 20 mm diameter. The CAD (CREO) pro-esoftware tool is employed in the design of tools and plates. The Designed tooltips such as cylindrical (Tool-I), hexagonal prismatic (Tool-II), truncated cone with cone angle  $20^\circ$  (Tool-III), and truncated cone with cone angle  $10^\circ$  (Tool-IV) are shown in Fig. 1 and their working philosophy is illustrated in Fig. 2.

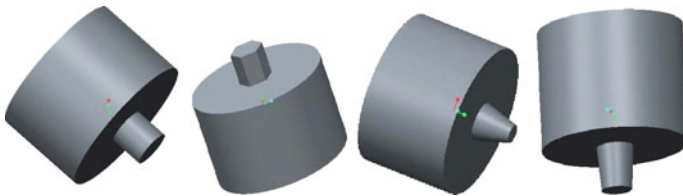


**Fig. 1** Geometry of Tool-I to IV, respectively from left to right

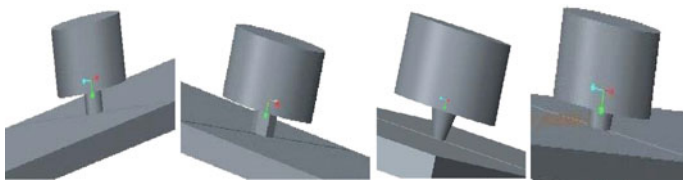


**Fig. 2** Working philosophy of Tool-I to IV, respectively from left to right

### 2.1 Stability Investigation

The CAE tool (ANSYS) is employed for the static analysis. The material properties were defined and meshed for analysis. The tooltip is steel ( $G = 2 \times 10^{11}$  Pa, Poisson's ratio 0.3; Density  $7850 \text{ kg/m}^3$ , and Yield strength 350 Mpa) and the plate to be-welded is aluminum Al-6061 ( $G = 68.9 \times 10^9$  Pa, Poisson's ratio 0.33; Density  $2700 \text{ kg/m}^3$ , and Yield strength 276 Mpa). The gripping load and compression load on the tool were defined such a way that the corners of the plate, as well as the sides, are with fixed support. The tool is subjected to an inertial load of 3 kN with rotation speed of 1000 rpm. Then the stability related analyses were conducted for the four different tooltip geometries. The deformation in mm, strain and stress in MPa, and shear stress in MPa are measures of performances. The results and findings are discussed in the results and discussion section. Figures 3, 4, 5, and 6 illustrates the stability investigations of tool-I to Tool-IV, respectively (Table 1).

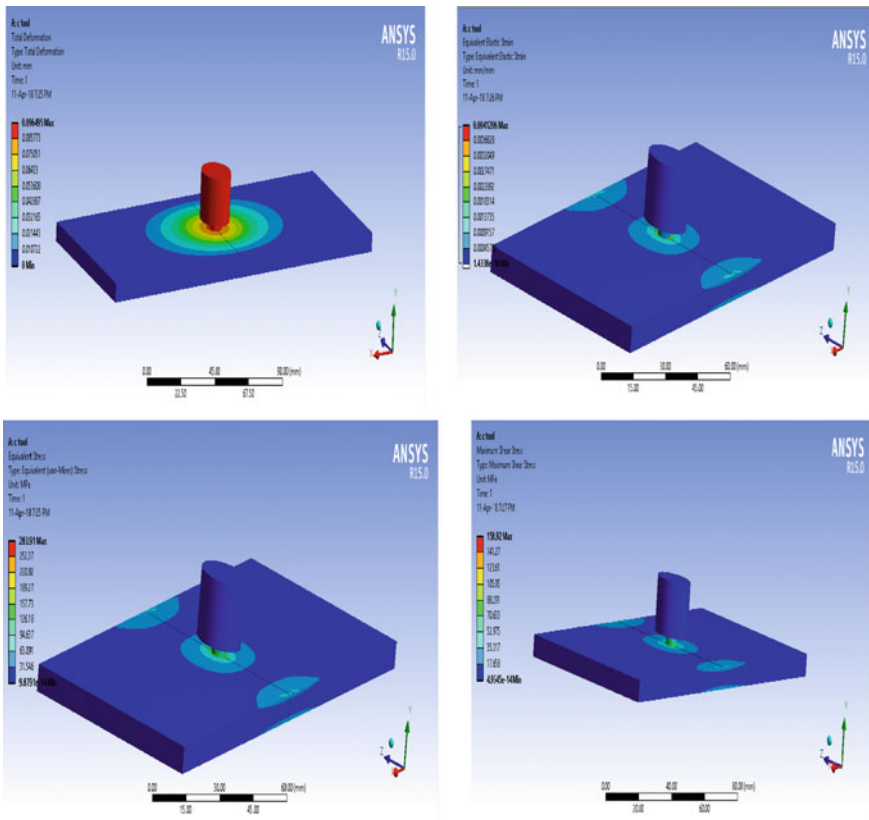


Fig. 3 FSW—stability investigation with Tool-I

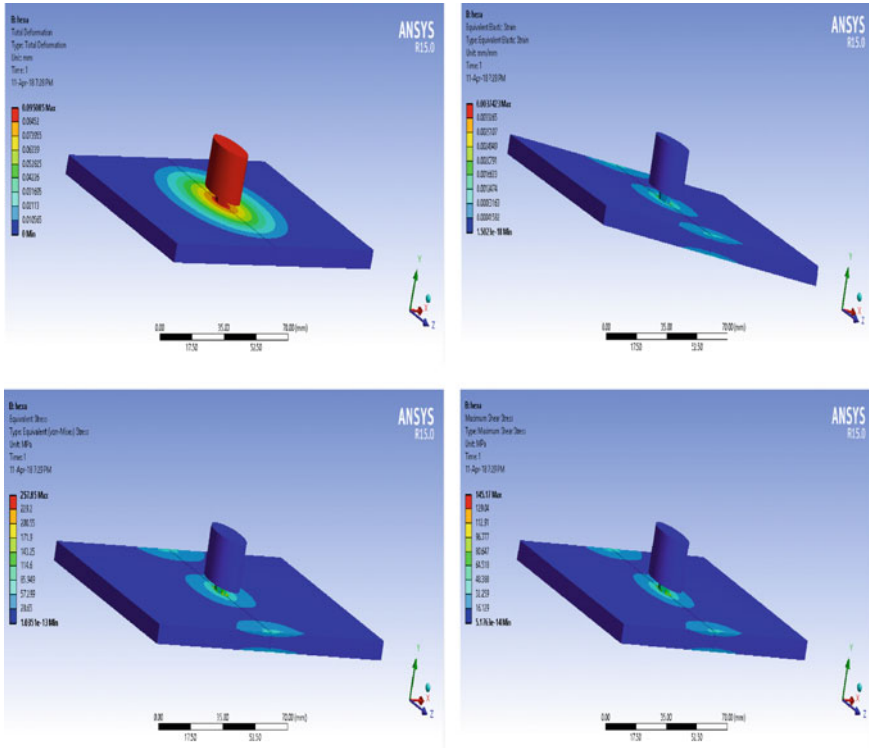


Fig. 4 FSW—stability investigation with Tool-II

### 2.2 Thermal Investigation

The length of the tooltip in FSW is slightly less than the depth of welding. The tooltip penetrates the surface completely to make the butt joint. Then the tool starts to travel along the mid-gap between the plates after a small space. The travel speed can be preset and known as welding speed. The heat generated based on the wear resistance. The material defined steel for tool and Al6061 for the workpiece. The thermal boundary conditions like initial plate temperature equal to ambient temperature as 22 °C, the film coefficient as  $3e-4\text{w/mm}^2$ , the temperature of tooltip is 590 °C, the bottom and top surface temperatures of plates, were 25 °C and 250 °C, respectively. The heat flux and temperature distributions were investigated. The results and findings were discussed in the Result and Discussions section (Figs. 7, 8 and Table 2).

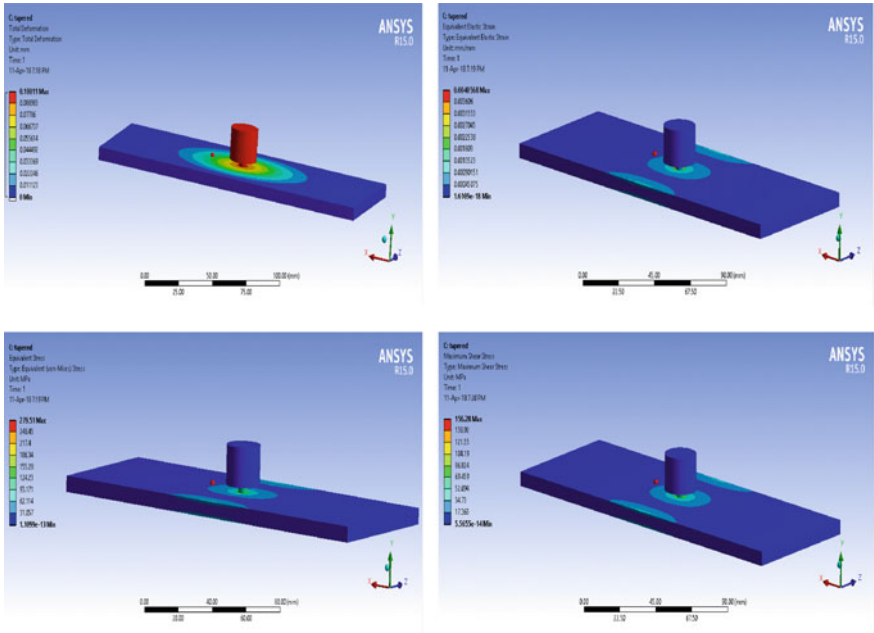


Fig. 5 FSW—stability investigation with Tool-III

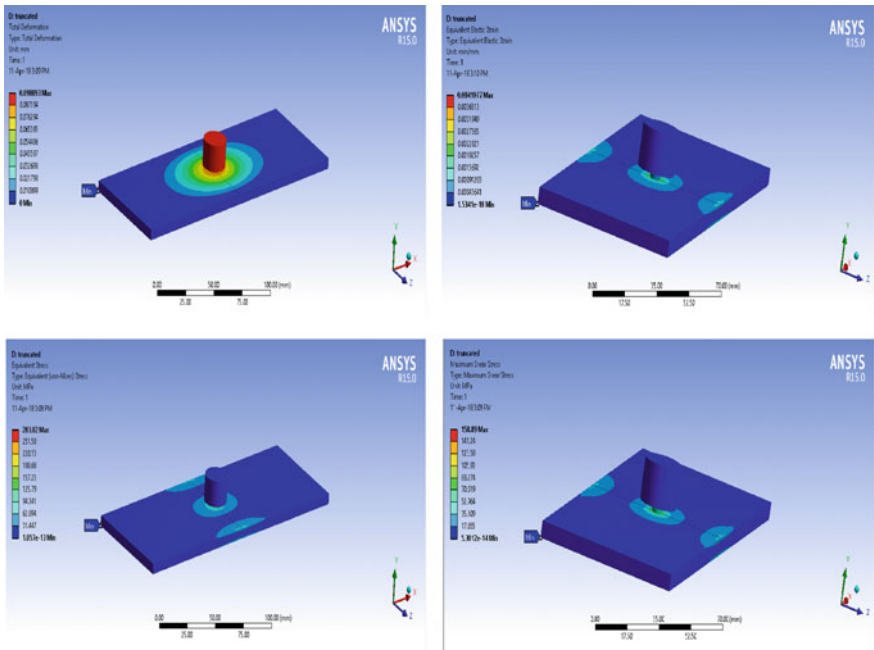
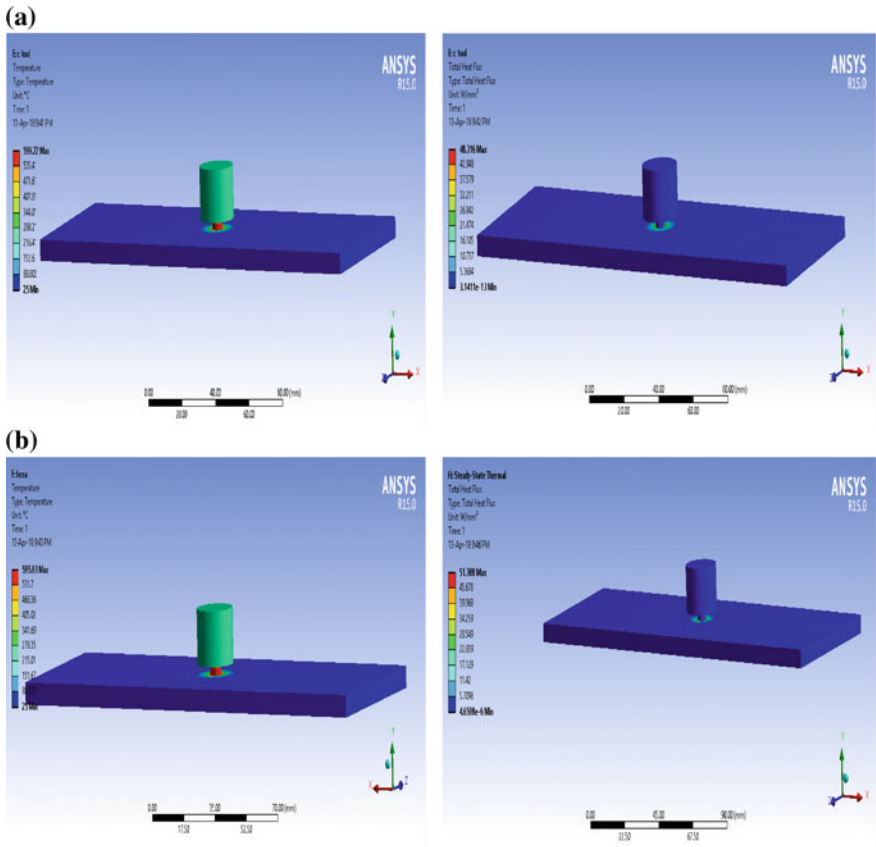


Fig. 6 FSW—stability investigation with Tool-IV



**Table 1** Results of stability investigations

	Range	Deformation	Strain	Stress	Shear stress
Tool-I	Min	0	1.4338E-18	0.9879E-13	4.9545E-14
	Max	0.096495	0.0041206	283.91	158.92
Tool-II	Min	0	1.5023E-18	1.0351E-13	5.1763E-14
	Max	0.095085	0.0037423	257.85	145.17
Tool-III	Min	0	1.6109E-18	1.1099E-13	5.5655E-14
	Max	0.100110	0.0040568	279.51	156.28
Tool-IV	Min	0	1.5341E-18	1.0573E-13	5.3012E-14
	Max	0.098093	0.0041077	283.02	158.89



**Fig. 7** Temperature (left) and Heat flux (right) distribution: Tool-I (a) Tool-II (b)

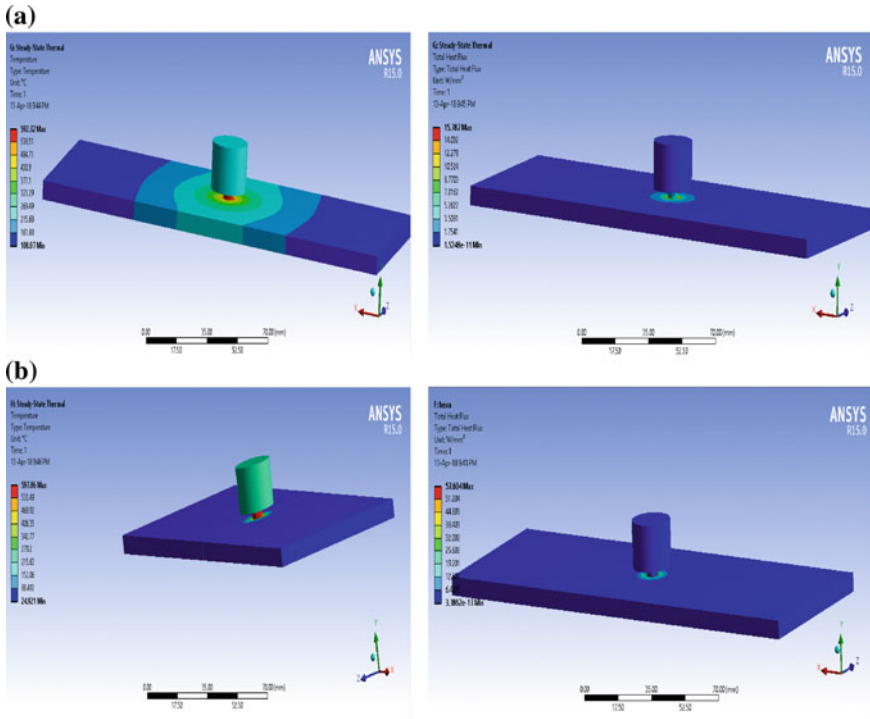


**Fig. 8** Temperature (left) and Heat flux (right) distribution: Tool-III (a) Tool-IV (b)

**Table 2** Results of Thermal Analysis

	Tool-I		Tool-II		Min	Tool-III	Tool-IV	
	Min	Max	Min	Max		Max	Min	Max
Temp.	25	599.22	25	595.03	108.07	592.32	24.921	597.06
Heat flux	3.14e-13	48.316	3.39e-13	51.388	1.53e-11	15.787	4.64e-6	57.604

### 2.3 Transient Investigation

It is the extension of stability and thermal analysis. From the results, it is noted that the high stresses produced by cylindrical tooltip (Type-I) and truncated cone with cone angle 10° (Tool-IV) than other tooltip geometry. Hence, in the Transient investigation the above two profiles of the tooltip were considered. The velocity of the tool varied at four levels such as 0.025, 0.027, 0.028, and 0.030 mm/s. The other conditions remain the same. The sample of model for transient investigation is shown in Figs. 9, 10, 11, and 12 (Right). The deformation, stress, shear stress, and

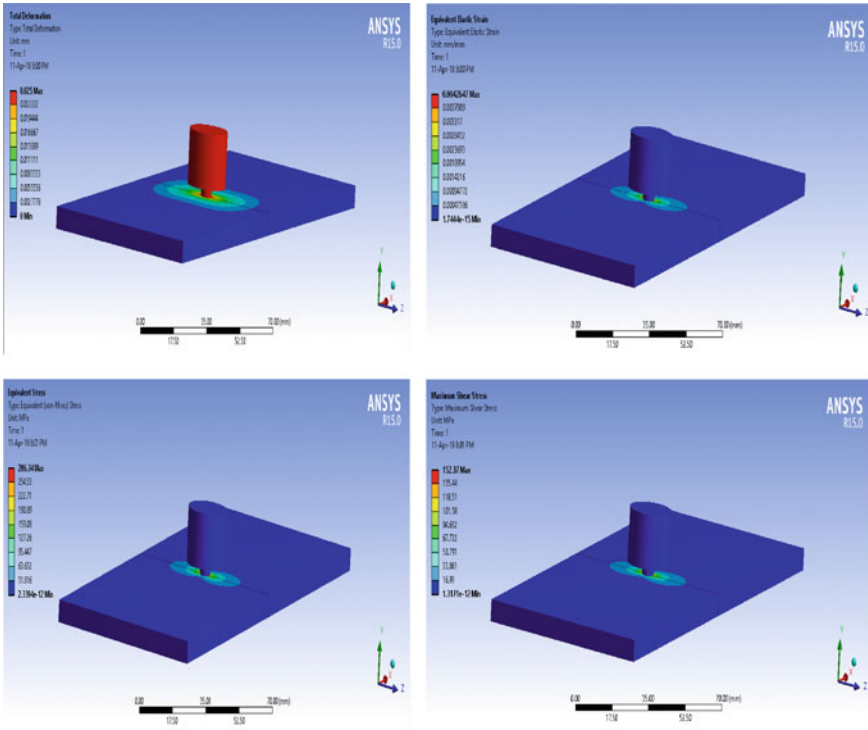


Fig. 9 Transient investigation results for Tool-IV at 0.025 mm/s

strain were observed. The precise results were discussed to suggest the best geometry (Table 3).

### 3 Results and Discussions

The steel tooltip geometry like cylindrical (Tool-I), hexagonal prismatic (Tool-II), truncated cone with cone angle 20° (Tool-III), and truncated cone with cone angle 10° (Tool-IV) were used to stir weld the Al6061 Plates. The tooltip geometry performance was evaluated based on deformation, strain, stress, and shear stress. The deformation, strain, stresses, and shear stress performance of Tool-I, Tool-II, Tool-III, and Tool-IV depicted in Figs. 3, 4, 5, and 6, respectively. Each Figure from the left to right illustrates deformation Performance, strain performance, stress performance, and the shear stress performance, respectively. The lower (min) and higher (max) values appear in blue and red colors, respectively. The numerical investigation results were consolidated in Table 1. From the results it was ensured that all the tooltips were well stabled. The thermal investigations were illustrated tool wise in Fig. 7 for Tool-I and

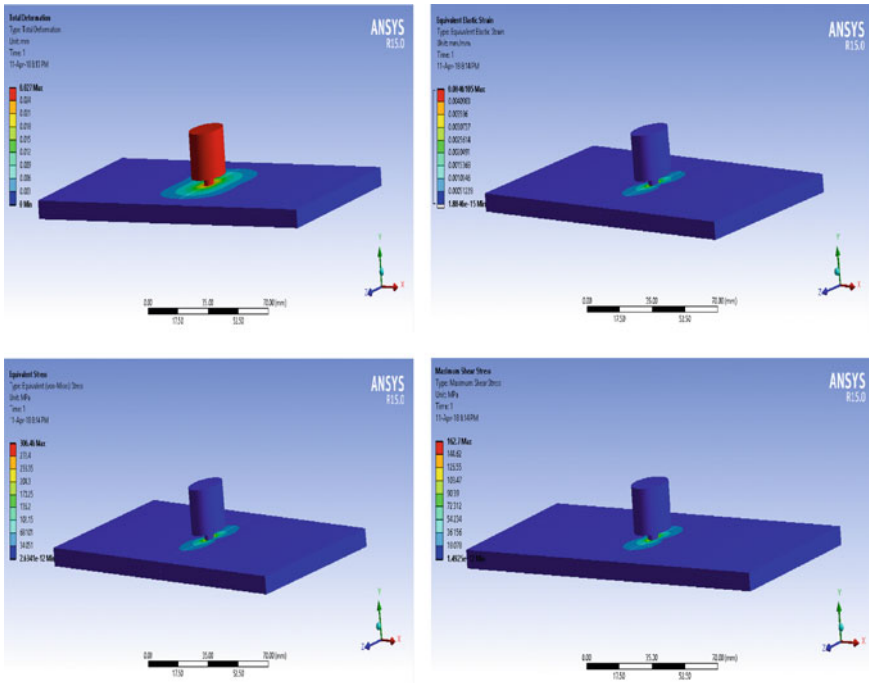


Fig. 10 Transient investigation results for Tool-IV at 0.027 mm/s

Tool-II and in Fig. 8 for Tool-III and Tool-IV, respectively. It was identified that the truncated cone profile with cone angles  $10^\circ$  give high temperature and heat flux. In the transient analysis also, the same tool performed well.

### 4 Conclusion

One of the major factors which influenced the FSW process is the tooltip profile. This paper focused and optimized the tooltip profile for FSW of AA6061 plates. In addition, conventional cylindrical type, hexagonal prismatic, truncated conical with cone angles  $20^\circ$ , and  $10^\circ$  were considered for analysis. All the four profiles were included in the stability analysis and the safe limit of plastic deformation and stress formation were ensured in the stability investigation. In thermal analysis, it was found that the truncated cone profile with cone angles  $10^\circ$  give high temperature and heat flux compared to hexagonal prismatic and truncated cone profile with cone angles  $10^\circ$  (Tool-III). It is noticed that the Tool-III gives a very low heat flux than other profiles including the cylindrical profile. Many investigations recommended the truncated cone profile for their specific cases of FSW, but not stated the importance of cone

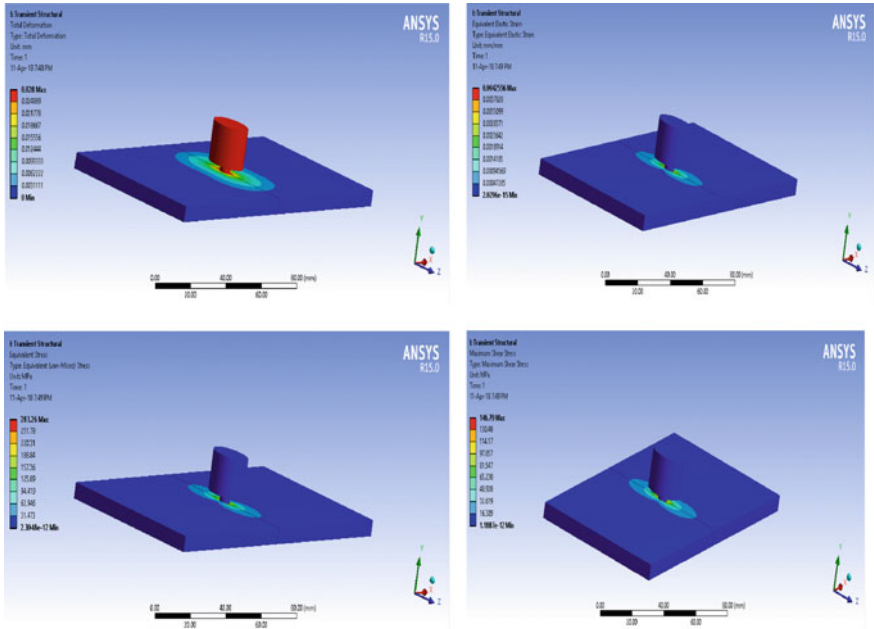


Fig. 11 Transient investigation results for Tool-I at 0.028 mm/s

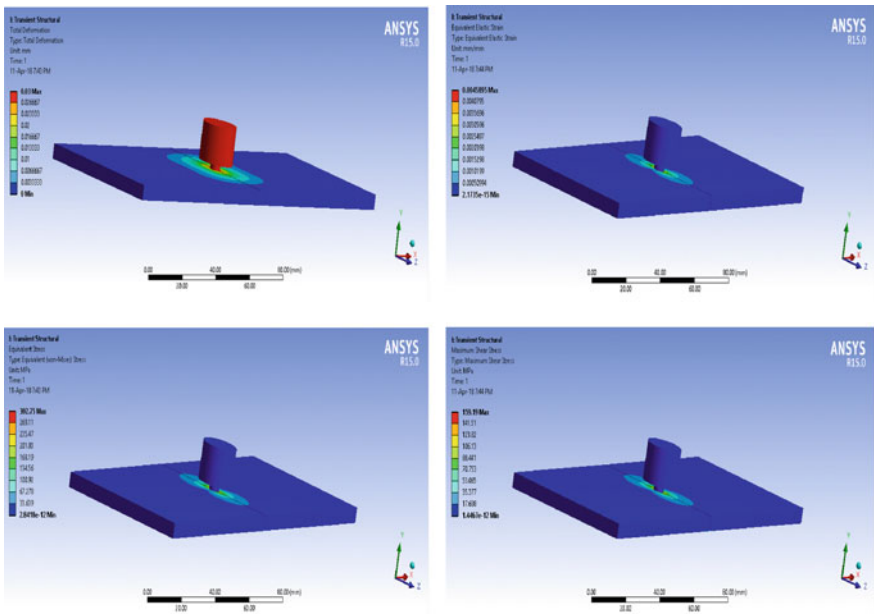


Fig. 12 Transient investigation results for Tool-I at 0.030 mm/s

**Table 3** Results of Transient Analysis

Tool profile	Tool-I		Tool-IV	
Tool velocity	0.030	0.028	0.025	0.027
Deformation	0.03	0.028	0.025	0.027
Stress	302.75	283.26	286.34	306.46
Shear stress	159.19	146.79	152.37	162.7
Strain	0.0046	0.0043	0.0043	0.0046

angle. The investigation extended further with transient analysis. The investigation considered four different tool velocity for selected tooltip profiles and found that at the Tool-IV dissipated more heat than Tool-I. Hence the Tool-IV will consume less power.

## References

1. Pavan Kumar T, Venkata T, Vishnu A, Rakshit S (2014) Influence of tool geometry in friction stir welding on material flow pattern. *Int J Curr Eng Technol* 2:230–235
2. Bilici MK (2012) Effect of tool geometry on friction stir spot welding of polypropylene sheets. *Express Polym Lett* 6(10):805–813
3. Indira Rani M, Marpu RN (2012) The effect of variation of tool geometry on friction stir welded aluminum alloys—an experimental investigation. *Int J Mech Eng Robot Res* 1(1):91–98
4. Meilinger Á, Török I (2013) The importance of friction stir welding tool. *Prod Process Syst* 6(1):25–34
5. Kadian AK, Puri G, Das S, Biswas P (2014) Effect of tool geometry and process parameters on the material flow of friction stir welding. In: 5th International and 26th All India Manufacturing Technology, Design and Research Conference (AIMTDR 2014), December 12–14, IIT Guwahati, Assam, India, pp 28–1
6. Shahabuddin, Dwivedi VK (2018) Effect of tool geometry of friction stir welding on mechanical properties of AA-7075 aluminum alloy. *Int J Mech Eng Technol* 9(6):625–633
7. Abedini O, Ranjbarnezhad E, Marashi P (2017) Effect of tool geometry and welding parameters on the microstructure and static strength of the friction-stir spot-welded DP780 dual-phase steel sheets. *Mater Technol* 51(4):687–694
8. Ugendfer S, Kumar A, Somi Reddy A (2014) Fundamental investigation of tool geometry on mechanical properties of friction stir welding of AA2014 aluminum alloy. *Procedia Mater Sci* 5:824–831
9. Casalino G, Campanelli S, Mortello M (2014) Influence of shoulder geometry and coating of the tool on the friction stir welding of aluminum alloy plates. *Procedia Eng* 69:1541–1548
10. Raguraman D, Muruganandam D, Kumaraswamidhas LA (2014) Study of tool geometry on friction stir welding of AA 6061 and AZ61. In: Proceedings of National Conference on Contemporary Approaches in Mechanical, Automobile and Building sciences-2014. *IOSR J Mech Civ Eng*, pp 63–69
11. Rathinasamy S, Raju R (2010) Sequencing and scheduling of non-uniform flow pattern in parallel hybrid flow shop. *Int J Adv Manuf Technol* 49(1–4):213–225
12. Smolin AY (2018) Understanding the mechanisms of friction stir welding based on computer simulation using particles. *Defense Technology*. <https://doi.org/10.1016/j.dt.2018.09.003>

13. Elangovan K, Balasubramanian V, Valliappan M (2008) Effect of tool pin profile and tool rotational speed on mechanical properties of friction stir welded AA6061 aluminium alloy. *Mater Manuf Process* 23(8):251–260
14. Daneji A, Ali M, Pervaiz S (2017) Influence of tool geometry and processing parameters on welding defects and mechanical properties for friction stir welding of 6061 aluminum alloy. *IOP Conf Ser Mater Sci Eng* 346:1–9
15. Jil S, Jin Y, Yue Y, Zhang L, Lv Z (2013) The effect of tool geometry on material flow behavior of friction stir welding of titanium alloy. *Eng Rev* 33(2):107–113
16. Rai R, De A, Bhadeshia HKDH, DebRoy T (2011) Review: friction stir welding tools. *Sci Technol Weld Joining* 16(4):325–342

# Effect of Composition and Process Parameter on Mechanical Properties of Composite Coating by Laser Cladding: An Overview



Ranit Karmakar and Subrata Kumar Ghosh

**Abstract** Laser cladding is one of the finest surface modification techniques, to incorporate greater hardness, less wear and corrosion, resistance to oxidation at elevated temperature as well as very low coefficient of friction. Coating with different characteristics can be synthesized by control of the matrix and reinforcement composition of the coating, substrate material, and process parameters of laser beam precisely. Before starting any investigation or research, an investigator have to gather a thorough idea about previous studies in the relevant field. Hence, this article depicts the effect of input parameter on quality of laser cladded coating. In addition, effect on performances and different mechanical properties like microhardness, wear resistance, corrosion resistance, and adhesion strength are also overviewed. Finally, the trends of future development are forecasted which will help a new research scholar to find interest in the field of laser cladded coating and its quality.

**Keywords** Laser cladding · Coating · Microhardness · Wear resistance · Corrosion resistance

## 1 Introduction

Engineering components must have quality, reliability, and long service life which fully depend upon the bulk properties such as toughness, strength, machinability, and formability as well as surface dependent properties like microhardness, wear, corrosion, oxidation, and fatigue resistance. Both can hardly be achieved simultaneously with reasonable cost. So, surface engineering comes into the field which is very efficient to reduce the losses by wear, tear, corrosion, and oxidation in addition to keeping constant bulk properties of materials. A coating on substrate to protect the materials is an efficient technique of surface modification. Almost any type of substrate can be protected by a wide-ranging coating material through various techniques for the application in Aerospace, and Power generation to microelectronics

---

R. Karmakar (✉) · S. K. Ghosh  
Department of Mechanical Engineering, NIT Agartala, Agartala 799046, India  
e-mail: [ranit.karmakar15@gmail.com](mailto:ranit.karmakar15@gmail.com)

© Springer Nature Singapore Pte Ltd. 2020  
G. S. V. L. Narasimham et al. (eds.), *Recent Trends in Mechanical Engineering*,  
Lecture Notes in Mechanical Engineering,  
[https://doi.org/10.1007/978-981-15-1124-0\\_33](https://doi.org/10.1007/978-981-15-1124-0_33)



[1]. Thin, thick, and hardfacing coatings are produced by various processes like physical vapor deposition (PVD), chemical vapor deposition (CVD), thermal spraying, electrodeposition, plasma spraying, laser cladding, electroplating, etc. But most of the coatings are susceptible to delamination at intense mechanical interaction. In this scenario, the Laser Cladding uses a beam of high power laser source to melt the coating material as well as a very thin interface layer of substrate material to generate a crackless and poreless coating and having tremendous bonding with substrate too. As a rapid solidification takes place fine microstructure is obtained leading to high hardness and better mechanical properties of the coating. There are many advantages [2] of laser cladding technique, such as

- I. Greater metallurgical bonding strength between coating and substrate materials;
- II. The process is comparatively fast and related to rapid cooling;
- III. The coating is free from crack and pore applying appropriate process parameter;
- IV. The coating can be generated locally and can cover larger surfaces by overlapping of adjacent tracks of laser scanning path;
- V. The process is employed in an ambient atmosphere with a local laser beam and coaxial shielding by inert gas.

This article is focused on the type of laser used, types of laser cladding process, and process parameters of cladding. In addition to that the coating constituents and various substrate materials which are already done by many researchers are discussed throughout. Finally, the effect of all this input parameter on mechanical properties like wear resistance, hardness, corrosion resistance, and the phase constituents are overviewed thoroughly to help researcher to their recent work and as well as for future study.

## 2 Types of Laser and Cladding Processes

Santo [3] described the different processes involved in laser cladding in his review. The alloying or coating materials can be incorporated in the molten pool either in a form of pre-placed layers or by feeding directly by means of co-depositing instrument and materials in the powder, sheet or wire form. Pre-deposited method is the simplest way of laser cladding where the full area is surrounded by inert gas. Co-depositing technique consists of wire feeding, lateral, and coaxial power feeding or injection. When laser beam scans the surface, the powder is blown under laser by a carrier gas stream. Overlapping of scanning tracks is required to cover a larger surface area. Normally, Argon gas is used as shielding and carrier medium. The pre-deposited power system consumes more time and wire feeding system can be hardly controlled precisely. But the powder injection process is the most efficient and attractive application in complex geometry also. The thickness of clad from 50  $\mu\text{m}$  to 2 mm can be achieved by one step. For thicker clad layer, the process is applied again and again. The average power densities in laser cladding are 102–104  $\text{W}/\text{cm}^2$  and average interaction time is  $10^{-3}$  to 0.5 s.

Types of laser which have enough power for laser cladding are CO<sub>2</sub> lasers, Nd:YAG lasers, Fiber lasers, and High Power Diode Lasers (HPDLs). Nd:YAG and CO<sub>2</sub> lasers are rigorously used in repairing and cladding purposes in automotive industry. Fiber and HPDL lasers are going to be used in new establishment of research.

### 3 Process Parameter of Laser Cladding

Quality of cladding is fully depended on input process parameter of cladding process which has to be studied thoroughly [4]. The cause-effect diagram is shown in Fig. 1 indicates the various process parameters and the output quality of cladding layer in detail.

The effect of some important process parameter is discussed as follows:

#### 3.1 Scanning Speed

Scanning speed is one of the important parameters for controlling the quality of clad layer which includes proper height, width, and thickness of cladding as well as free from pores and cracks and good bonding with base metal. Zhang [5] have showed that with the increase of scan speed from 100 to 300 mm/min, the average microhardness

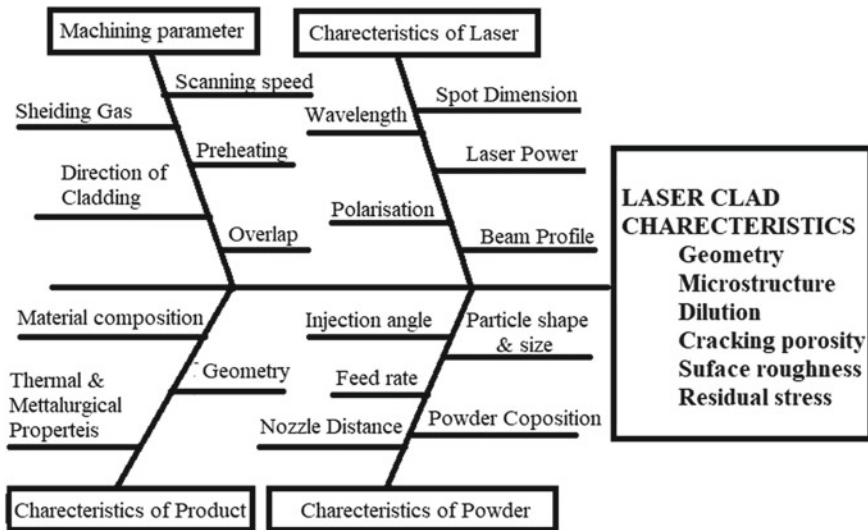


Fig. 1 Cause-effect diagram for the process of laser cladding [4]

of cladding also increases from 388 to 580 HV<sub>0.2</sub>. In addition to that, from 100 to 300 mm/min scan speed, the microstructure is changed from cellular dendritic and fish-bone like interdendritic carbide to the primary cementite and also Martensite at a speed of 500 mm/min. With the increasing speed from 25 to 65 cm/min in iron base cladding, [6] the height and width of track in drastically decreased but depth remained almost same throughout. The dilution rate is almost constant about 64.23% with a variation of scanning speed from 5 to 15 mm/s and decreased (37.06%) at 20 mm/s scan speed [7].

### **3.2 Laser Power**

The power of laser is an essential parameter to determine hardness and other qualities. If the power is less, the microcracks will be formed due to poor melting of powder, whereas at high power dilution rate is good. Bykovskiy et al. [6] have studied in a graphical form that with the increasing laser power from 300 to 600 W the geometry (height, width, depth) was enlarged in all respect. In coating of TiN/Al on Ti6Al4V, the cladding layers had no cracks and pores when the laser power is between 1.8 and 3.0 kW, but above it some microcracks and pores were seen [8]. Farayibi et al. [9] studied the effect of laser power on the cladding of Ti-6Al-4V (in wire and powder form) on steel substrate. They concluded that height and width of clad are inversely and directly proportional to the laser power (1400, 1600, 1800 W).

### **3.3 Powder Feed Rate**

Powder feed rate plays a very crucial role to determine the thickness of clad layer. Generally, the thickness of coating is directly proportional to the powder feed rate [4]. The clad or coating height and width are directly and inversely proportional to powder feed rate when it was varied from 10 to 30 g/min while cladding of Ti-6Al-4V (in wire as well as powder form) was done on steel substrate [9]. Decreasing the mass or powder flow rate, a higher clad depth and wider tracks can be obtained. But for the increment of clad height the feed rate must be increased [10].

### **3.4 Overlapping Factor and Pulse Duration**

Farina et al. [11] have discussed the effect of overlapping factor and pulse duration of Stellite 6 cladding on Carbon steel by pulsed Nd:YAG laser. At high value of overlapping factor, the total clad area on volume is increased, whereas for low value the clad length is decreased. At high pulse duration, the melting ratio increases due to increased interaction time. But for low pulse duration the effect of decreased energy

density is dominated. A cross-sectional analysis of iron base cladding [6] shows more even melt through the substrate material at an overlapping rate of 2/3 of single-layer coating when compared with rate of 1/3 and 1/2.

### 3.5 *Composition of Cladded Coating*

Composition of cladding consists of reinforcement material as well as matrix. The reinforcement material can be introduced in two ways. The ceramic powder can be introduced in the matrix directly, called “Ex situ”, whereas if the ceramic material is dispersed in the matrix indirectly by the chemical reaction, called “In situ” coating. By varying the composition, researchers can precisely tailor their desired properties in the coating. Yan et al. [12] have done Ni-based Nano h-BN MMC coating on medium carbon steel using Nd:YAG laser. They observed that friction coefficient of coating is dramatically decreased (to 0.35) in addition to Nano h-BN which is a high self-lubricant material. The high harness value from 590 to 690 HV<sub>0.3</sub> was obtained in the cladding of WC powder—Inconel 625—on AISI-304 Stainless steel owing to the presence of hard phase like W<sub>2</sub>C and Fe<sub>3</sub>W<sub>3</sub>C [13]. In addition to that low dissolution of WC particle was observed at high scanning speed. Chien et al. [14] conducted an experiment in laser cladding of TiO<sub>2</sub> on Ti-6Al-4V. As the melting point of TiO<sub>2</sub> is very high, upon increasing the percentage of it, the penetration depth decreases owing to supercoiling effect.

## 4 **Effect on Performances**

### 4.1 *Microhardness*

Microhardness profile indicated a novel change with depth of the laser cladding of Ni-base TiC on Ti-6Al-4V [15]. Figure 2a shows that highest microhardness at surface was 681.3 HV, at the base it reached up to 839.9 HV and then it is dramatically decreased. Halder et al. [16] found microhardness up to 2200 HV<sub>0.05</sub> in the tailored surface of multicomponent metal matrix composite coating (MMC) on Ti-6Al-4V. This high hardness is due to different hard reinforcement particles (TiO<sub>2</sub>, TiB<sub>2</sub>, TiN, V<sub>2</sub>O<sub>3</sub>, VN, C, etc.) formed by in situ reaction with B<sub>4</sub>C, Ti, and hBN. The microhardness of the cladding of WC reinforced NiCrBSi MMC can be achieved from 350 to 900 HV if the concentration of WC particle is varied from 5 to 45%. But too much concentration is avoided due to loss of binder effect at higher concentration as concluded by Varela et al. [17]. Sahu et al. [18] have done an in situ composite coating (TiB<sub>2</sub>–TiC–Al<sub>2</sub>O<sub>3</sub>) on Al alloy. On average 1000–1950 HV<sub>0.05</sub> was found depending upon powder composition and process parameter combination as a result

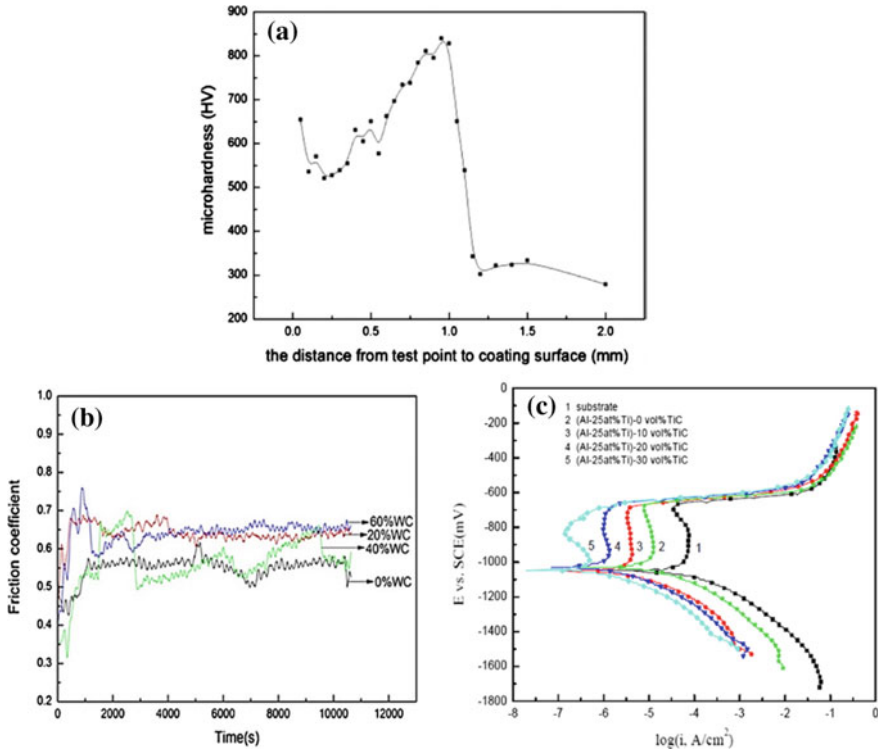


**Fig. 2** Effect on different properties: **a** Microhardness profile with depth [14], **b** Variation of friction coefficients at 700 °C [19], **c** Potentiodynamic anodic polarization curves of Al/TiC composite cladding [23]

of very hard ceramic particle present in the matrix formed during in situ reaction and rapid cooling.

## 4.2 Wear Resistance and Friction Coefficient

Mass losses in wear testing at room temperature are 28.5 and 6.3 mg for Ni45-5 wt% BN and Ni60-10 wt% BN, respectively, which clearly showed the increment of wear resistance by the addition of Nano h-BN [11]. Weng et al. [19] conducted an experiment to determine the wear resistance and friction coefficient of Ni/WC laser cladded coating at low-to high-temperature range. They concluded that wear resistance is consistently increasing at the room temperature and 600 °C with increasing WC content. Figure 2b shows the variation of friction coefficient with sliding time at 700 °C and indicates reduced friction and wear at 40–60% WC contentment due to greater formation of oxide film at this high temperature.

The durability of cladding of a component is examined by the overall wear of component with and without cladding. Bartkowski et al. [20] showed beneficial effect of Stellite-6/60% WC cladding on durability in the service life of an agricultural tool. The mass loss at wear testing in this tool without coating is about 1100 g whereas with coating is around 800 g. The in situ Ni/WC coating has lower resistance to wear at 100 N and 200 N and higher under 300 N than the ex situ coating. In addition to that the average friction coefficient of the cladding by in situ is the lowest and steadier than that of the ex situ one [21]. Wang et al. [22] compared the wear resistance of Ni60 cladding without rare-earth oxide (REO) and cladding with REO ( $\text{La}_2\text{O}_3$ ,  $\text{Y}_2\text{O}_3$ ,  $\text{CeO}_2$ ). The loss in without REO cladding was  $0.0974 \text{ mm}^3$  whereas the cladding with  $\text{La}_2\text{O}_3$ ,  $\text{Y}_2\text{O}_3$ , and  $\text{CeO}_2$  were 0.0018, 0.0159, and  $0.0031 \text{ mm}^3$ , respectively. It indicates the cladding with  $\text{La}_2\text{O}_3$  and  $\text{CeO}_2$  have sufficient effect in wear resistance of Ni60 cladding layer.

### 4.3 Corrosion Resistance

Generally, the component subjected to marine as well as salty environment must have high corrosion resistance. The corrosion resistance is measured by potentiodynamic polarization technique and indicated by current densities. Corrosion can be reduced by increasing the amount of TiC on AA6063 cladding [23]. Here, it was shown that if the TiC content is varied from 0 to 30%, the current density was drastically reduced from  $199.46$  to  $1.15 \mu\text{A cm}^{-2}$  (as shown in Fig. 2c) which indicated a sharp increase in corrosion resistance. Lei et al. [24] have shown that the corrosion current density of Ni/Carbon fibers (CFs) coating was only 7% of those in Ni-base coating. And what was more corrosion resistance of Ni/CFs coating is also increased with laser scanning speed. A study on AISI420/VC MMC coating proved the negative effect of Vanadium Carbide particle on the properties of corrosion resistance of the cladding [25]. Even no significant improvement in erosion resistance of 420 steel can be observed when the wt% of VC was increased.

### 4.4 Adhesive Strength

This may be in between metallic materials, ceramic materials or the combination of both. Adhesive strength depends upon oxide present as well as mutual affinity of the component of composite coating. Adhesion test is done as per ASTM D4541 standard [26]. Paul et al. [27] found an adhesion strength of 60 MPa at the interface of WC-12 wt% Co cladding on low carbon steel. But few researchers have done this test so far in case of composite coating by laser cladding.

## 5 Inference and Scope of Future Research

1. Laser cladding is the most efficient surface modification method. Most of the surface coatings are prone to failure easily by delamination. But coating by laser cladding is only the exception because it has greater adhesion to substrate due to better dilution of coating layer into substrate materials. So the rate of dilution is a measure of performance of cladding layer. Laser scanning speed, powder feed rate, and laser power, overlapping factor are the most important laser cladding parameters on which hardness, surface roughness, etc. are dependent. But the effect of parameters like spot size, nozzle distance, focusing of laser, and profile of the beam are hardly considered in the published article still now. In addition to changing the shielding gas and cladding direction can be the considerable parameter, which should be considered by modern researchers. Hardness, wear resistance, and corrosion resistance are measured for checking the quality of the coating.
2. The recent scientist can look into the measurement of residual stress induced in cladding layer and adhesion strength of coating with various combinations of laser parameters and composition MMC coating too. These two cases are also overlooked by the researcher so far.
3. Most of the published work is concentrated on the effect of weight or volume percentage of ceramic particle in MMC coating on the quality of coating mentioned earlier. Generally, on increasing this amount these aforementioned parameters are increased to a certain limit. But it has been seen that VC has an adverse effect on stainless steel. So researcher can try with two or more combinations of reinforcement particle in future and observed the positive effect on performances and negative as well. It will be very helpful for repair technology by laser cladding in aerospace, power generation, and automotive industry.
4. There is also a scope to do research in the field of hybrid cladding techniques.

## References

1. Vilar R (1999) Laser cladding. *J Laser Appl* 11:64–79
2. Ocelk V, Heeswijk VV, Hosson JTMD, Csach K (2004) Foam coating on aluminum alloy with laser cladding. *J Laser Appl* 16:79
3. Santo L (2008) Laser cladding of metals: a review. *Int J Surf Sci Eng* 2:327–336
4. More SR, Bhatt DV, Menghani JV (2017) Resent research status on laser cladding as erosion resistance technique—an overview. *Mater Today Proc* 4:9902–9908
5. Zhang W (2013) Influence of scanning speed on microstructure and hardness during laser cladding high-Cr cast iron. *Appl Mech Mater* 395–396:1127–1131
6. Bykovskiy DP, Petrovskiy VN, Murzakov MA, Mironov VD, Dzhujaev PS, Polski VI (2015) Formation of multilayer claddings using high-power fiber laser radiation. In: 18th conference on plasma-surface interactions, pp 227–231. *Physics Procedia*, Moscow
7. Chen JL, Li J, Song R, Bai LL, Shao JZ, Qu CC (2015) Effect of the scanning speed on microstructural evolution and wear behaviors of laser cladding NiCrBSi composite coatings. *Opt Laser Technol* 72:86–99

8. Yao F, Zhang XC, Sui JF, Tu ST, Xuan FZ, Wang ZD (2015) Microstructure and wear resistance of one-step in-situ synthesized TiN/Al composite coatings on Ti6Al4V alloy by a laser nitriding process. *Opt Laser Technol* 76:78–85
9. Farayibi PK, Murray JW, Huang L, Boud F, Kinnell PK, Clare AT (2014) Erosion resistance of laser clad Ti-6Al-4 V/WC composite for waterjet tooling. *J Mater Process Technol* 214:710–721
10. Riveiro A, Mejías A, Lusquiños F, Val JD, Comesaña R, Pardo J, Pou J (2014) Laser cladding of aluminium on AISI 304 stainless steel with high-power diode lasers. *Surf Coat Technol* 253:214–220
11. Farnia A, Ghaini FM, Sabbaghzadeh J (2013) Effects of pulse duration and overlapping factor on melting ratio in preplaced pulsed Nd:YAG laser cladding. *Opt Lasers Eng* 51:69–76
12. Yan H, Wang AH, Zhang XL, Huang ZW, Wang WY, Xie JP (2010) Nd:YAG laser cladding Ni base alloy/nano-h-BN self-lubricating composite coatings. *Mater Sci Technol* 26:461–468
13. Abioye TE, Folkes J, Clare AT, McCartney DG (2013) Concurrent Inconel 625 wire and WC powder laser cladding: process stability and microstructural characterisation. *Surf Eng* 29:647–653
14. Liu YH, Li J, Xuan FZ (2012) Fabrication of TiC reinforced Ni based coating by laser cladding. *Surf Eng* 28(8):560–563
15. Liu YH, Li J, Xuan FZ (2012) Fabrication of TiC reinforced Ni based coating by laser cladding. *Surf Eng* 28:560–563
16. Haldar B, Karmakar S, Saha P, Chattopadhyay AB (2014) In situ multicomponent MMC coating developed on Ti-6Al-4V substrate. *Surf Eng* 30:256–262
17. Varela JA, Amado JM, Tobar MJ, Mateo MP, Yañez A, Nicolas G (2015) Characterization of hard coatings produced by laser cladding using laser-induced breakdown spectroscopy technique. *Appl Surf Sci* 336:396–400
18. Sahu JK, Sahoo CK, Masanta M (2015) In-situ TiB<sub>2</sub>-TiC-Al<sub>2</sub>O<sub>3</sub> composite coating on aluminum by laser surface modification. *Mater Manuf Process* 30:736–742
19. Weng Z, Wang A, Wu X, Wang Y, Yang Z (2016) Wear resistance of diode laser-clad Ni/WC composite coatings at different temperatures. *Surf Coat Technol* 304:283–292
20. Bartkowski D, Bartkowska A (2017) Wear resistance in the soil of Stellite-6/WC coatings produced using laser cladding method. *Int J Refract Met Hard Mater* 64:20–26
21. Shu D, Li Z, Yao C, Li D, Dai Z (2017) In situ synthesised WC reinforced nickel coating by laser cladding. *Surf Eng* 34:276–282
22. Wang C, Gao Y, Zeng Z, Fu Y (2017) Effect of rare-earth on friction and wear properties of laser cladding Ni-based coatings on 6063Al. *J Alloys Compd* 727:278–285
23. He H, Fu YC, Guo WH, Xiao M, Pang XZ, Shen XM, Zeng JM (2013) Microstructure and corrosion behavior of laser cladding Al<sub>3</sub>Ti-based composite coatings on AA6063 aluminum alloy. *Adv Mater Res* 634–638:2973–2978
24. Lei J, Shi C, Zhou S, Gu S, Zhang LC (2018) Enhanced corrosion and wear resistance properties of carbon fiber reinforced Ni-based composite coating by laser cladding. *Surf Coat Technol* 334:274–285
25. Zhang Z, Yu T, Kovacevic R (2017) Erosion and corrosion resistance of laser clad AISI 420 stainless steel reinforced with VC. *Appl Surf Sci* 410:225–240
26. Brito VRSS, Bastos IN, Costa HRM (2012) Corrosion resistance and characterization of metallic coatings deposited by thermal spray on carbon steel. *Mater Des* 41:282–288
27. Paul CP, Alemohammad H, Toyserkani E, Khajepour A, Corbin S (2007) Cladding of WC-12 Co on low carbon steel using a pulsed Nd:YAG laser. *Mater Sci Eng A* 464:170–176



# Influence of ZrB<sub>2</sub> Particles on Dry Sliding Wear Behaviour of AA7075/ZrB<sub>2</sub> In-Situ Composites



M. Nallusamy, S. Sundaram and K. Kalaiselvan

**Abstract** AA7075/ZrB<sub>2</sub> Aluminium Matrix Composites (AMCs) were successfully fabricated using the in-situ fabrication method. The inorganic salts (K<sub>2</sub>ZrF<sub>6</sub> and KBF<sub>4</sub>) reacted with molten aluminium at 900 °C and formed ZrB<sub>2</sub> inside the melt itself. AMC castings were obtained in different volume fractions (0, 3, 6 and 9%) of ZrB<sub>2</sub>. The dry sliding wear behaviour of AA7075/ZrB<sub>2</sub> in-situ AMCs was evaluated using pin-on-disc wear apparatus. The wear experiments were executed as per Design of Experiments (DoE). The effect of wear parameters such as sliding velocity, sliding distance, content of ZrB<sub>2</sub> and normal load on wear rate was analyzed. It was evident that ZrB<sub>2</sub> particles influenced the wear resistance of fabricated AMCs. The worn surfaces revealed an increase in number of cracks when sliding velocity, sliding distance and normal load increased. The worn surface of AA7075/ZrB<sub>2</sub> AMCs was observed using Field Emission Scanning Electron Microscopy (FESEM). The wear rate was decreased and the corresponding wear resistance was increased when the volume fraction of ZrB<sub>2</sub> particles increased in the fabricated AMCs.

**Keywords** AMCs · DoE · Wear rate

---

M. Nallusamy (✉) · K. Kalaiselvan  
Department of Mechanical Engineering, Dr. N.G.P. Institute of Technology, Coimbatore 641048,  
Tamil Nadu, India  
e-mail: [nallusamy1979@gmail.com](mailto:nallusamy1979@gmail.com)

K. Kalaiselvan  
e-mail: [kalaiselvanmohit@gmail.com](mailto:kalaiselvanmohit@gmail.com)

S. Sundaram  
Muthayammal Engineering College (Autonomous), Rasipuram 637408, Tamil Nadu, India  
e-mail: [sundaram1160@gmail.com](mailto:sundaram1160@gmail.com)

© Springer Nature Singapore Pte Ltd. 2020  
G. S. V. L. Narasimham et al. (eds.), *Recent Trends in Mechanical Engineering*,  
Lecture Notes in Mechanical Engineering,  
[https://doi.org/10.1007/978-981-15-1124-0\\_34](https://doi.org/10.1007/978-981-15-1124-0_34)

## 1 Introduction

In recent years, many engineering applications require the materials which are having the significant properties like high strength, lightweight, high thermal, wear and corrosion resistance, etc. AMCs have been offering such customized property combinations of materials for the applications in aerospace, automotive, automobile, defence, marine, sports and recreation industries [1, 2]. Basically, aluminium alloys have inferior mechanical and tribological properties. AMCs improve the superior properties by enhancing the material's mechanical behaviour [3, 4].

The properties of AMCs depend upon the shape, size and distribution volume of reinforcement materials in aluminium matrix [5]. The bonding and nature of the interface between aluminium matrix and ceramic particles will also help to enhance the properties [4]. Nowadays, AMCs are generally fabricated by several conventional methods include powder metallurgy, plasma spraying, spray atomization and co-deposition, squeeze casting and stir casting [5]. The cost of AMCs fabrication method is also very important for increasing its applications [6]. All the processing methods are classified into two basic categories such as solid state processing and liquid state processing. The researcher has adopted one of the liquid state technique called in-situ fabrication technique to form the required wt% of AMCs. This technique is primarily adopted for low processing cost and to produce AMCs with high interfacial bonding strength, uniform dispersion of particles with fine size and its thermodynamic stability [7].

Several studies on in-situ fabricated MMCs with various reinforcements were reported in the literature. Michael Rajan et al. prepared AA7075/TiB<sub>2</sub> AMCs by in-situ reaction of salts K<sub>2</sub>TiF<sub>6</sub> and KBF<sub>4</sub> with aluminium melt and found the uniform dispersion of cubical, spherical and hexagonal shapes particles with clear interface and fine bonding with aluminium matrix [8]. Dinaharan et al. fabricated AA6061/ZrB<sub>2</sub> in-situ composites and observed the enhancement of ultimate tensile strength, wear resistance and hardness of AA6061 with increase in content of ZrB<sub>2</sub> [9]. Naveen Kumar et al. prepared AA6351-ZrB<sub>2</sub> in-situ composites and indicated that the wear rate was decreased and wear resistance was increased with increase in the content of ZrB<sub>2</sub> particles [10]. Kumar et al. produced Al-4Cu/TiB<sub>2</sub> composites and demonstrated that the wear resistance was considerably improved with increase in TiB<sub>2</sub> particles [11]. Song-Li Zhang et al. manufactured AMCs reinforced by Al<sub>3</sub>Zr and ZrB<sub>2</sub> particulates from Al-K<sub>2</sub>ZrF<sub>6</sub>-KBF<sub>4</sub> and showed that weight loss due to wear of the composites decreases with an increase in Al<sub>3</sub>Zr and ZrB<sub>2</sub> particulates [12].

In the present investigation, wear experiments were executed as per DoE using pin-on-disc wear apparatus to evaluate dry sliding wear behaviour of AA7075/ZrB<sub>2</sub> in-situ AMCs. The wear rate ( $W$ ) of AA7075/ZrB<sub>2</sub> in-situ AMCs were analyzed. The influence of sliding velocity ( $v$ ), sliding distance ( $D$ ), normal load ( $P$ ) and content of (wt%) of ZrB<sub>2</sub> particles ( $c$ ) on fabricated AMCs were reported.

## 2 Experimental Procedures

AA7075/ZrB<sub>2</sub> AMCs were fabricated by the addition of inorganic salts K<sub>2</sub>ZrF<sub>6</sub> and KBF<sub>4</sub> with aluminium melt. The melt was upheld at 900 °C and it was stirred periodically for 60 min. The required amount of ZrB<sub>2</sub> particles were produced due to the chemical reaction between the weighed amounts of inorganic salts with aluminium melt. After the slag removal, the melt was decanted with preheated die. The castings with different volume fractions (0, 3, 6, and 9%) of ZrB<sub>2</sub> were obtained and presented in Fig. 1. The specimens were made with the dimensions of 25 mm × 25 mm × 6 mm and polished as per the metallographic standard for characterization. The polished samples were etched with a colour etchant and observed microstructure using optical microscope (OM).

The wear specimens were machined for required dimensions (8 mm × 8 mm × 30 mm) as shown in Fig. 2 and the wear test was carried out by a pin-on-disc wear testing machine under dry lubricating conditions in accordance with ASTM G99-05

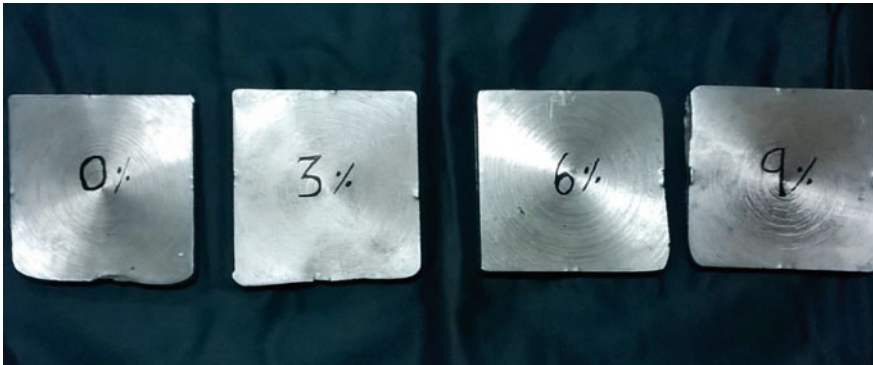
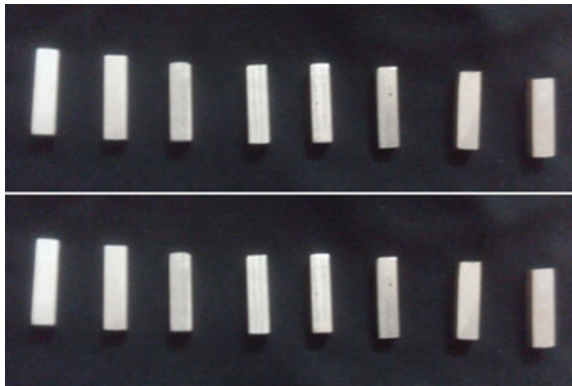


Fig. 1 AA7075/ZrB<sub>2</sub> in-situ AMCs with (0, 3, 6 and 9%) of ZrB<sub>2</sub>

Fig. 2 Specimens before wear test



**Fig. 3** Specimens after wear test



**Table 1** Dry sliding wear parameters and their levels

Parameter	Notation	Unit	Level			
			1	2	3	4
Sliding velocity	$V$	m/s	0.4	0.8	1.2	1.6
Sliding distance	$D$	M	250	500	750	1000
Normal load	$P$	N	5	10	15	20
ZrB <sub>2</sub> content	$C$	wt%	0	3	6	9

standards. Before testing, the specimen surface was polished by using grit paper. A polished surface of the pin was loaded on hardened chromium steel rotating disc. The height loss of the pin was monitored by a computer interfaced data acquisition system. The wear test was carried out at room temperature. The wear surface of selected specimens is presented in Fig. 3.

The principal parameters which influence the wear rate of AA7075/ZrB<sub>2</sub> in-situ AMCs are sliding velocity, sliding distance, content of ZrB<sub>2</sub> and normal load [13]. The selected parameters range and levels are given in Table 1.

The volumetric loss of pin was calculated as the cross section of the test pin multiplied by its loss of height [14]. The experiments were executed in accordance with DoE at random and the wear rate of each specimen was recorded and presented in Table 2. The wear surface of selected specimens was observed using FESEM.

### 3 Results and Discussion

The influence of selected parameters such as sliding velocity, sliding distance, content of ZrB<sub>2</sub> and normal load on the wear rate of AA7075/ZrB<sub>2</sub> in-situ composites were

**Table 2** DoE matrix and experiment results

Experiment no.	Sliding wear parameters				Wear rate (10 <sup>-5</sup> mm <sup>3</sup> /m)
	<i>v</i>	<i>D</i>	<i>P</i>	<i>C</i>	
1	1	2	2	3	135
2	1	4	4	1	180
3	2	2	2	3	143
4	1	3	3	2	155
5	1	1	1	4	130
6	2	1	1	4	102
7	3	4	4	1	158
8	3	1	1	4	135
9	2	3	3	2	157
10	3	2	2	3	147.5
11	2	4	4	1	186
12	4	3	3	2	153
13	3	3	3	2	149
14	4	4	4	1	165
15	4	2	2	3	152
16	4	1	1	4	120

obtained and represented in graphical form. The feasible effects of the parameters on wear rate are detailed as follows.

### 3.1 Sliding Velocity

The influence of sliding velocity on the wear rate of AA7075/ZrB<sub>2</sub> in-situ composite is shown in Figs. 4a–c. It is very clear that the wear rate significantly increases with the increase of sliding velocity. Hence, it is confirmed that the frictional heat is created between the counter surfaces influenced by the sliding velocity [15]. The softness of the pin surface is directly proportional to the frictional heat. The pin surface is softened when the frictional heat increases. The degree of frictional heat depends on the degree of sliding velocity.

When sliding velocity significantly increases, the pin surface is proportionately softened due to more frictional heat and hence the counter surface penetrates more into the pin surface. As the counter surface penetration is more, the wear rate becomes high. The thermal disparity between the aluminium matrix alloy and ZrB<sub>2</sub> reinforcement particles is also playing a crucial function in sliding wear [12]. When two surfaces are sliding each other, the interface stress is created due to the thermal disparity. Hence, The ZrB<sub>2</sub> particles are dislocated from the matrix and formed as

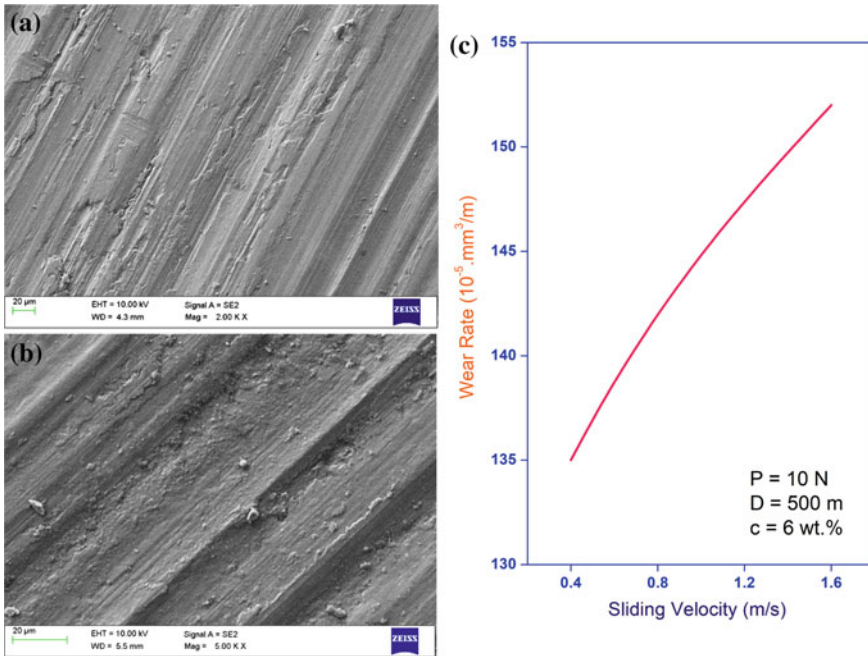


**Fig. 4** FESEM micrographs of wear surfaces on AA7075/ZrB<sub>2</sub> in-situ composites at sliding velocity of **a** 0.4 m/s, **b** 1.6 m/s and **c** effect of sliding velocity on the wear rate

wear debris while the interface stress is increased. It effects to cause of cracks and scratches on the surfaces. When the sliding velocity considerably increases, the more reinforcement particles are dislocated from the matrix causing more wear rate.

The FESEM micrographs of wear surfaces of fabricated AA7075/ZrB<sub>2</sub> in-situ composites at sliding velocities of 0.4 m/s and 1.6 m/s are presented in Fig. 4a, b, respectively. Figure 4a depicts the patches and grooves on the worn surface owing to misplacement of ZrB<sub>2</sub> particles at sliding velocity of 0.4 m/s. Figure 4b shows the deepest grooves, abrasions and severely damaged surface at sliding velocity of 1.6 m/s. It is clear from Fig. 4c that the wear rate of AA7075/ZrB<sub>2</sub> in-situ composites increases with increase of sliding velocity.

### 3.2 Sliding Distance

Figure 5a–b depict the FESEM micrographs of wear surfaces on sliding distance of AA7075/ZrB<sub>2</sub> in-situ composites. It is proved from Fig. 5c that the wear rate is linearly increased with the increase of the sliding distance at constant sliding velocity of 0.8 m/s. Figure 5a depicts the division of asperities and wear debris of fabricated AMCs at the sliding distance of 250 m. The deep grooves and fewer cracks are seen

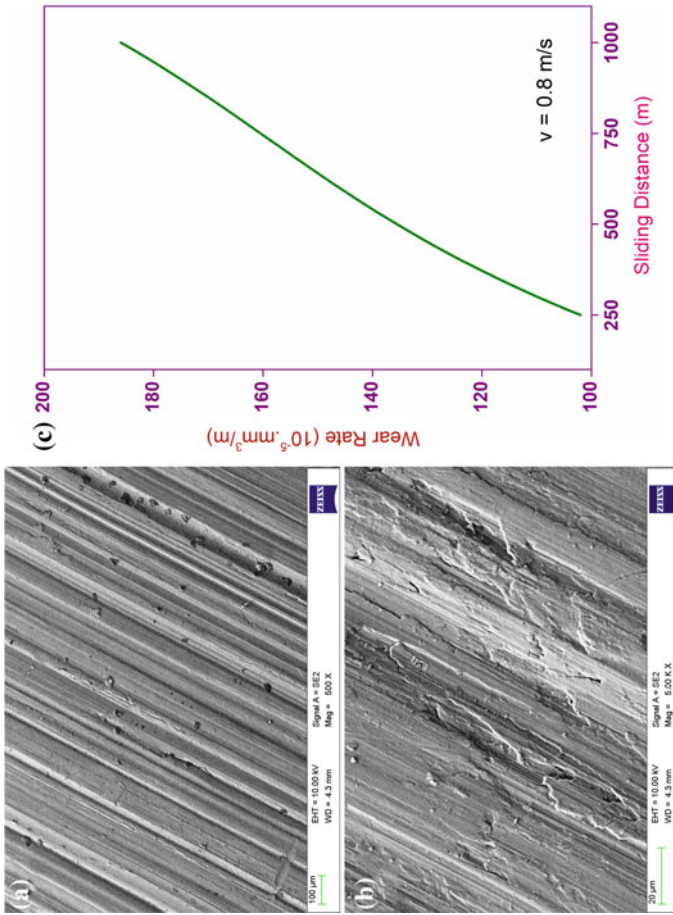


**Fig. 5** FESEM micrographs of wear surfaces on AA7075/ZrB<sub>2</sub> in-situ composites at sliding distance of **a** 250 m, **b** 1000 m and **c** effect of sliding distance on the wear rate



in Fig. 5b and it is obvious that the size and propagation of cracks are more at the sliding distance of 1000 m. The wear surface indicates that it is subjected to more frictional heat and thus, the wear rate of the AMCs increases with increase of sliding distance.

### 3.3 Normal Load

Figures 6a–b depict the FESEM micrographs of wear surfaces on the normal load applied on AA7075/ZrB<sub>2</sub> in-situ composites. It is proved from Fig. 6c that the wear rate is significantly increased with increase of the applied load at constant sliding velocity of 1.2 m/s. The counter surfaces will involve in relative motion under normal load during sliding. The penetration of the pin increases when increase of the normal load. A higher amount of material transfer between the counter surfaces takes place. It is clear from Figs. 6a–b that the formation of cracks and fragmentation of asperities are more at normal load of 20 N when compared on the wear surface at normal load of 5 N.

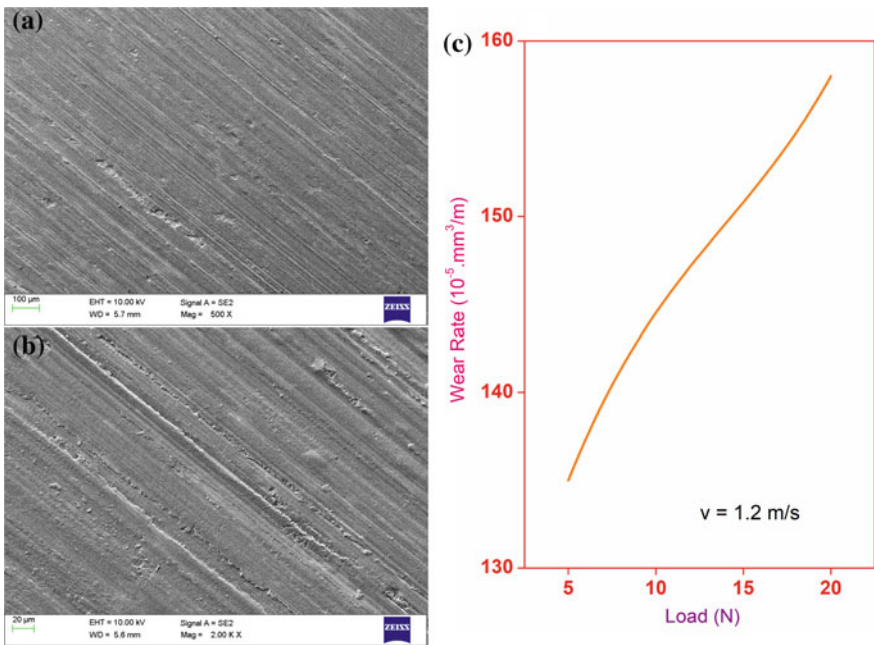


**Fig. 6** FESEM micrographs of wear surfaces on AA7075/ZrB<sub>2</sub> in-situ composites at a normal load of **a** 5 N, **b** 20 N and **c** effect of normal load on the wear rate



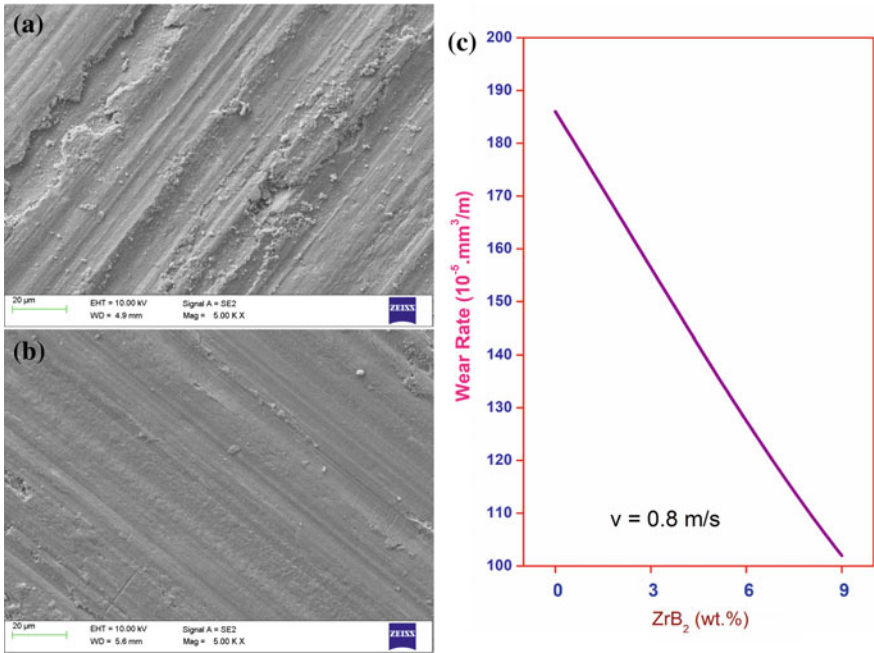


**Fig. 7** FESEM micrographs of wear surfaces on AA7075/ZrB<sub>2</sub> in-situ composites at ZrB<sub>2</sub> content of **a** 0%, **b** 9% and **c** effect of ZrB<sub>2</sub> content on the wear rate

### 3.4 Content of ZrB<sub>2</sub>

Figure 7a–b depict the FESEM micrographs of wear surfaces on 0 wt% and 9 wt% of ZrB<sub>2</sub> content on AA7075/ZrB<sub>2</sub> in-situ composites. It is proved from Fig. 7c that the wear rate is significantly increased with the increase of ZrB<sub>2</sub> content. The thermal expansion coefficients of AA7075 and ZrB<sub>2</sub> particles are about  $23.1 \times 10^{-6} \text{ K}^{-1}$  and  $6.5 \times 10^{-6} \text{ K}^{-1}$ , respectively. The thermal expansion coefficients disparity between the matrix material and reinforcement material leads larger amount of density dislocation and load-carrying capacity resulting to enhance the wear resistance of composites. It is obvious from Fig. 7a that the formation of wear debris, pits and grooves in higher amount at 0 wt% of ZrB<sub>2</sub> content. Figure 7b shows the lesser formation of wear debris and pits at 9 wt% of ZrB<sub>2</sub> content. It is clear from Fig. 7c that the wear resistance increases when increasing the content of ZrB<sub>2</sub> in AMCs.

## 4 Conclusions

- AA7075 alloy reinforced with ZrB<sub>2</sub> AMCs were successfully fabricated by in-situ reaction of the inorganic salts K<sub>2</sub>ZrF<sub>6</sub> and KBF<sub>4</sub> with aluminium melt.
- The dry sliding wear behaviour of AA7075/ZrB<sub>2</sub> AMCs was evaluated using a Pin-on-disc apparatus. The in-situ formed ZrB<sub>2</sub> particles increased the wear resistance of the composites. The wear parameters like sliding velocity, sliding distance and normal load were proportional to the wear rate. FESEM photomicrographs clearly revealed the higher degree of cracks, pits and grooves when sliding velocity, sliding distance and normal load were increased. It was also confirmed that the wear rate was significantly reduced with an increase in the content of ZrB<sub>2</sub> particles in the fabricated AMCs.

## References

1. Miller WS, Zhuang L, Bottema J, Wittebrood AJ, Smet PD, Haszler A, Vieregge A (2000) Recent development in aluminium alloys for the automotive industry. *Mater Sci Eng, A* 280:37–49
2. Heinz A, Haszler A, Keidel C, Moldenhauer S, Benedictus R, Miller WS (2000) Recent development in aluminium alloys for aerospace applications. *Mater Sci Eng, A* 280:102–107
3. Miracle DB (2005) Metal matrix composites—from science to technological significance. *Compos Sci Technol* 65:2526–2540
4. Dinaharan I, Murugan N (2012) Dry sliding wear behavior of AA6061/ZrB<sub>2</sub> in-situ composite. *Trans Nonferrous Met Soc China* 22:810–818
5. Bayraktar E, Masounave J, Caplain R, Bathias C (2008) Manufacturing and damage mechanisms in metal matrix composites. *J Achiev Mater Manuf Eng* 31(2):294–300
6. Kala H, Mer KKS, Kumar S (2014) A review on mechanical and tribological behaviors of stir cast aluminum matrix composites. *Procedia Mater Sci* 6:1951–1960
7. Michael Rajan HB, Ramabalan S, Dinaharan I, Vijay SJ (2013) Synthesis and characterization of in situ formed titanium diboride particulate reinforced AA7075 aluminum alloy cast composites. *Mater Des* 44:438–445
8. Wang H, Li G, Zhao Y, Chen G (2010) In situ fabrication and microstructure of Al<sub>2</sub>O<sub>3</sub> 410 particles reinforced aluminum matrix composites. *Mater Sci Eng, A* 411(527):2881–2885
9. Dinaharan I, Murugan N, Parameswaran S (2011) Influence of in situ formed ZrB<sub>2</sub> particles on microstructure and mechanical properties of AA6061 metal matrix composites. *Mater Sci Eng A* 528:5733–5740
10. Naveen Kumar G, Narayanasamy R, Natarajan S, Kumaresh Babu SP, Sivaprasad K, Sivasankaran S (2010) Dry sliding wear behaviour of AA 6351-ZrB<sub>2</sub> in situ composite at room temperature. *Mater Des* 31:1526–1532
11. Kumar S, Subramanya Sarma V, Murty BS (2007) Influence of in situ formed TiB<sub>2</sub> particles on the abrasive wear behaviour of Al–4Cu alloy. *Mater Sci Eng A* 465:160–164
12. Zhang S-L, Zhao Y-T, Chen G, Cheng X-N, Huo X-Y (2008) Fabrication and dry sliding wear behavior of in situ Al–K<sub>2</sub>ZrF<sub>6</sub>–KBF<sub>4</sub> composites reinforced by Al<sub>3</sub>Zr and ZrB<sub>2</sub> particles. *J Alloy Compd* 450:185–192

13. Sannino AP, Rack HJ (1995) Dry sliding wear of discontinuously reinforced aluminum composites: review and discussion. *Wear* 189:1–19
14. Mandal A, Chakraborty M, Murty BS (2007) Effect of TiB<sub>2</sub> particles on sliding wear behaviour of Al–4Cu alloy. *Wear* 262:160–166
15. Rao RN, Das S (2011) Effect of SiC content and sliding speed on the wear behaviour of aluminium matrix composites. *Mater Des* 32:1066–1071

# Fibre Reinforced Polymer (FRP) Nanocomposites for Radar Absorption Application in the X-Band



Puppala Siva Nagasree, Koonam Ramji, Killi Krushna Murthy,  
Mantri Kannam Naidu and Tammareddy Haritha

**Abstract** Microwave radar absorbing properties are effectively achieved due to the unique structure and electrical properties of nanostructured materials. The main objective of the present work is to show that by utilizing lower weight fractions of MWCNTs an efficient and thin microwave absorber with load bearing capacity can be developed. Fibre reinforced polymer (FRP) nanocomposites for radar absorbing applications in the X-band (8.2–12.4 GHz) were prepared using MWCNTs as dielectric lossy material. The complex permittivity values obtained from Vector Network Analyzer were used to evaluate the reflection loss of double-layered structures using transmission line theory. A reflection loss of less than  $-10$  dB for entire band was obtained for RAS 8 with a total thickness of 3 mm. At central frequencies of 10.6 GHz and 11.0 GHz RAS 6, RAS 3 shown  $-32$  dB and  $-35$  dB, respectively, corresponding to 99% absorption of incident electromagnetic radiation. The proposed double-layered RAS are lightweight promising structures for radar absorption application.

**Keywords** Fibre reinforced polymer · Radar absorbing structure · MWCNTs · Dielectric material · Input impedance · Vector network analyzer

---

P. S. Nagasree (✉)

Department of Mechanical Engineering, D.M.S.S.V.H. College of Engg, Machilipatnam, India  
e-mail: [psnagasree@gmail.com](mailto:psnagasree@gmail.com)

K. Ramji

Dr.B.R.Ambedkar University, Srikakulam, India  
e-mail: [ramjidme@gmail.com](mailto:ramjidme@gmail.com)

K. K. Murthy

Department of Chemistry, Indian Institute of Technology, Hyderabad, India  
e-mail: [krushna@iith.ac.in](mailto:krushna@iith.ac.in)

M. Kannam Naidu

Department of Mechanical Engineering, M.V.G.R. College of Engg, Vizianagaram, India  
e-mail: [mknaidu09@gmail.com](mailto:mknaidu09@gmail.com)

T. Haritha

Department of Mechanical Engineering, N.R.I. Institute of Technology, Pothavarappadu, India  
e-mail: [haritha\\_gorijala@yahoo.com](mailto:haritha_gorijala@yahoo.com)

© Springer Nature Singapore Pte Ltd. 2020

G. S. V. L. Narasimham et al. (eds.), *Recent Trends in Mechanical Engineering*,  
Lecture Notes in Mechanical Engineering,  
[https://doi.org/10.1007/978-981-15-1124-0\\_35](https://doi.org/10.1007/978-981-15-1124-0_35)

## 1 Introduction

Composite structures to increase the operational capability and durability have been the needs for high-performance weapon systems in the stealth technology [1, 2]. For commercial and military purposes interference shielding and microwave absorption are the main issues in the X-band (8.2–12.4 GHz). Microwave radar absorbing properties are effectively achieved by nanostructured materials due to their unique structure and electrical properties. The most attractive polymer because of its commercial availability, relative ease in processing, corrosion resistance is Epoxy resin.

By blending lower filler content Fibre reinforced polymer composites (FRP) are the most feasible materials for Radar Absorbing Structures as they possess both load carrying potentiality and absorbing capability [3]. As the Electromagnetic (EM) wave consists of both electric and magnetic energy, the lossy materials are classified as dielectric and magnetic absorbers which absorb the corresponding energy component [4]. Due to high values of specific gravity of the magnetic absorber materials [5] there prevails a need for lightweight, corrosion-resistant, structurally sound, efficient microwave absorber. Therefore, Microwave absorbers consist of dielectric materials like CNTs, Carbon nanofibres, carbon black, graphene are the most suitable as found in literature [6–15]. By blending carbon black with epoxy gives 2.4 GHz bandwidth for less than  $-10$  dB with a thickness of 2.55 mm [6]. The combination of carbon fibres with carbon black resulted in a reflection loss of  $-31.8$  dB and a bandwidth of 2.4 GHz less than  $-10$  dB [10]. Graphite, SWCNTs, MWCNTs, CNFs and Fullerenes absorbing properties were evaluated at microwave frequencies to reveal the configuration of nano inclusions particularly alter the EM performance [14]. According to Electromagnetic percolation theory to form a conductive matrix and to reach threshold percolation the necessary conditions are high conductivity and high aspect ratio of the filler material in the polymer matrix. MWCNTs satisfies these conditions.

In this research E-glass epoxy nanocomposites with different weight proportions of MWCNTs were fabricated by the in situ polymerization process. The electromagnetic characteristics were evaluated by estimating the complex permittivity and permeability. The radar absorbing properties of double-layered RAS were obtained by Numerical simulation.

## 2 Experimental Work

### 2.1 Materials and Characterization

E-glass fabric of plain weave type having 12000 strands per tow was procured from High Chem Laboratories India with an aerial weight of  $387 \text{ gm/m}^2$ . The filler material for the Radar absorbing structures was MWCNTs (Intelligent Materials Pvt Ltd) having a purity of 99% with O.D of 10–20 nm and a length of 3–8  $\mu\text{m}$ . Epoxy

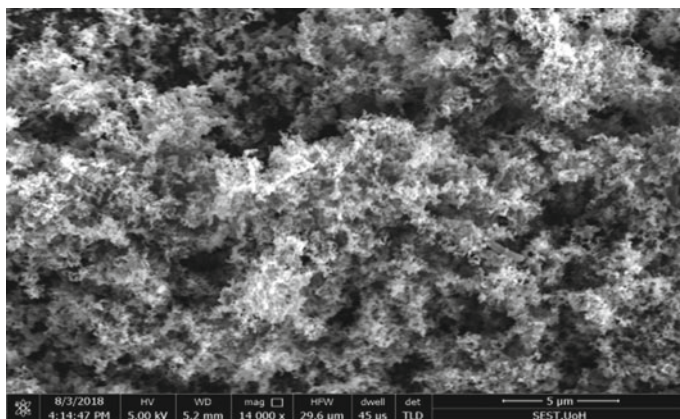
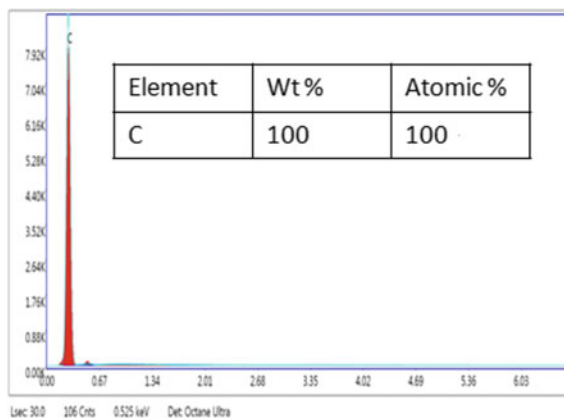


**Fig. 1** FESEM image of MWCNTs

**Fig. 2** EDX of MWCNTs



(Epofine) a thermoset resin was the matrix with DETDA (Di Ethyl Tetra Di Amine) as hardener having a density of  $1.2 \text{ g/cm}^3$ . The FESEM and EDX spectra of MWCNTs were shown in Figs. 1 and 2. MWCNTs were more tend to agglomerate because of Van der Waals forces and high purity was confirmed by EDX.

## 2.2 Fabrication of Samples

The measured amounts of Epoxy resin and MWCNTs were mixed with acetone for better blending [16]. After the complete evaporation of acetone the solution was ball milled (In smart systems) for 1 h at 500 rpm and with a ratio of 100:24 hardener was added. Bath type sonication (Trans-O-Sonic, M/S Shanti Industrial Estate) at

80 kHz frequency for 30 min was utilized to get homogeneous mixture. By heating the solution to 90°C the viscosity reduced to facilitate the uniform impregnation on E-glass fabric using hand layup method. The hot air oven as shown in Fig. 3. at different temperatures was employed to cure the samples for 6 h. The obtained specimens with a thickness of 1.5 mm were machined to a size of 22.9 mm × 10.2 mm to fit into X-band waveguide sample holder. The five samples of varying MWCNT weight percentages from 0.4% to 2% were fabricated (Fig 4).



**Fig. 3** Curing of Samples in hot air oven

**Fig. 4** Vector network analyzer



### 2.3 Measurement of Complex Permittivity

Measuring S-parameters by Vector Network Analyzer (Rhodes and Schwarz model ZVB 20), the complex permittivity values were given by material measurement software inbuilt with VNA. TRL method was used for calibration purposes. The reflection loss of multilayered samples was obtained from MATLAB code developed based on transmission line theory.

## 3 Results and Discussions

### 3.1 Complex Permittivity

The performance of the composites for absorption was given by their permittivity values. The relative complex permittivity of the material was given by  $\epsilon_r = \epsilon'_r + j^* \epsilon''_r$ . In a lossy dielectric material, the electromagnetic field propagation induces two categories of electrical currents: displacement current and current due to conduction. Interaction of bound charges, i.e. displacement current causing the polarization effect describes the complex permittivity real part also known as storage capacity of lossy material. The imaginary part indicates the capacity of dissipation due to free electrons increase (conduction current) [17]. Figure 5 shows the dielectric permittivity real part of epoxy—MWCNT composites as a frequency function for different weight percentages of MWCNT. It is observed that variation in dielectric constant with respect to change in frequency is negligible and also increase in loading of MWCNT increases the real part of permittivity as found in previous literature with other carbon materials also [5, 14]. The value of real part for lowest weight percentage is 3.4 and for the highest loading of MWCNT 2% gives rise to 5.84. The variation in imaginary

**Fig. 5** Real values of complex permittivity of the samples

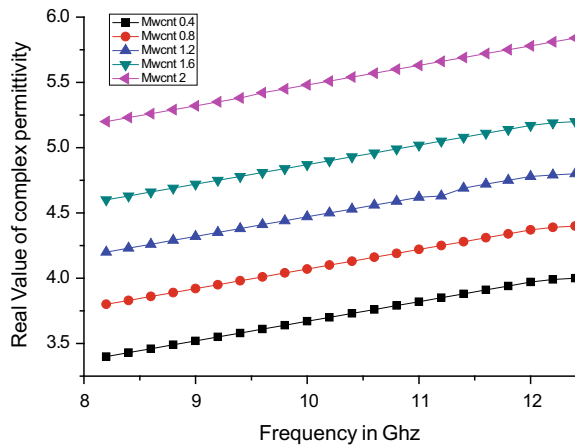
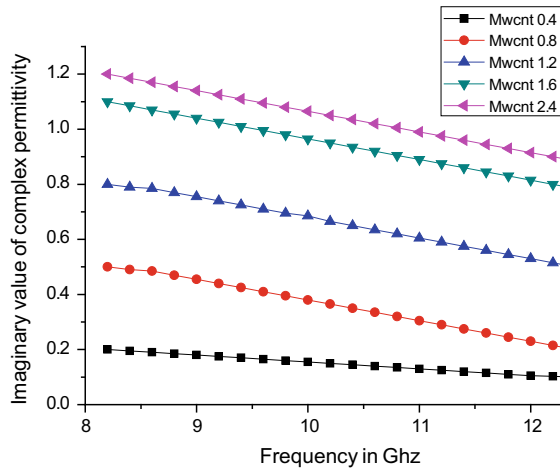




**Fig. 6** Imaginary values of complex permittivity of the samples

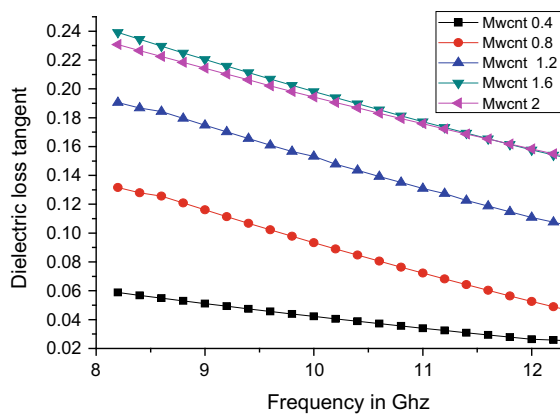


part of the complex permittivity is shown in Fig. 6. Here the variation with respect to frequency is significant and also the values increases for higher loadings and it attains a maximum value of 1.2 at the frequency of 8.2 GHz. An increase in MWCNT content favours the development of conductive network, porosities formation which leads to the increase in permittivity values. Due to increase of viscosity with increase in MWCNT weight percentage in the epoxy matrix higher loadings than 2% were not preferred.

### 3.2 Dielectric Loss Tangent

Figure 7 shows the average values of the dielectric loss tangent of the prepared samples. Loss tangent is the factor of attenuation to convert the stored energy to the

**Fig. 7** Dielectric loss tangent values



heat dissipation [18]. The absorption improves with the raise in loss tangent. The values of dielectric loss tangent of MWCNT-epoxy composites increased from 0.06 to 0.23.

### 3.3 Reflection Loss and Simulation

The Radar absorbing properties of the structures were determined by the following Eqs. (1 and 2) [14, 15]

$$z_{in} = \sqrt{\frac{\mu_r}{\epsilon_r}} * \tan h \left\{ \frac{j2\pi}{c} * \sqrt{\mu_r * \epsilon_r} * f * d \right\} \tag{1}$$

$$R.L = 20 \log[(Z_{in} - 1)/(Z_{in} + 1)] \tag{2}$$

where  $Z_{in}$  is the normalized input impedance,  $\mu_r, \epsilon_r$  are the complex permittivity and permeability of the lossy material, and  $d, f, c$  are the thickness, frequency, velocity of light, respectively. Double-layered structures for radar absorption were designed based on impedance matching condition where the first layer was anticipated to offer the best impedance match with free space whereas the absorbing layer has to deplete the microwave energy utmost and the last layer predicted to be reflective to simulate actual operating conditions, i.e. it must be Perfect Electric Conductor (PEC). By using a MATLAB programme developed for multilayer structures based on transmission line theory the reflection losses of double-layered structures were found for different weight percentages of MWCNTs. The details of double-layered RAS with a thickness of 1 mm for the first layer and 2 mm for the second layer were considered for numerical simulation as shown in Table 1 (Fig. 8).

**Table 1** Various double-layered radar absorbing structures

Sample	First layer	Second layer	Third layer
RAS 1	MWCNT 0.4	MWCNT 0.8	PEC
RAS 2	MWCNT 0.4	MWCNT 1.2	PEC
RAS 3	MWCNT 0.4	MWCNT 1.6	PEC
RAS 4	MWCNT 0.4	MWCNT 2	PEC
RAS 5	MWCNT 0.8	MWCNT 1.2	PEC
RAS 6	MWCNT 0.8	MWCNT 1.6	PEC
RAS 7	MWCNT 0.8	MWCNT 2	PEC
RAS 8	MWCNT 1.2	MWCNT 1.6	PEC
RAS 9	MWCNT 1.2	MWCNT 2	PEC
RAS 10	MWCNT 1.6	MWCNT 2	PEC

**Fig. 8** Schematic representation of double-layered RAS

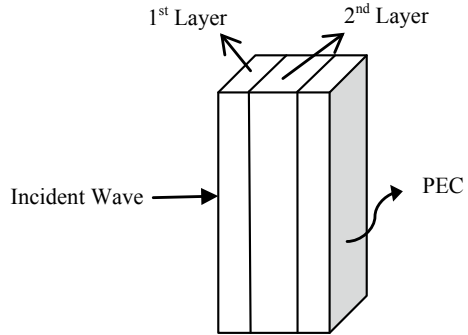
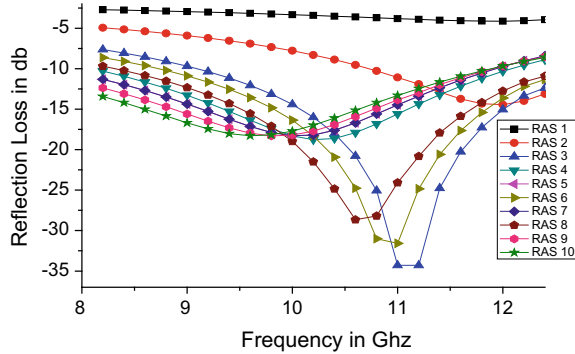


**Fig. 9** Reflection loss values



The reflection loss values of the proposed radar absorbing structures with a thickness of 3 mm in the X-band were shown in Fig. 9. The three structures RAS 10, RAS 9, and RAS 5 have exhibited a bandwidth of 3.8 GHz with a reflection loss of less than  $-10$  dB, i.e. from 8.2 GHz to 12.0 GHz corresponding to 90% absorption and at central frequency of 9.8 GHz shown less than  $-18$  dB. Out of all structures RAS 8 maintained less than  $-10$  dB in the entire frequency range of the X-band. RAS 6 and RAS 3 has reflection loss less than  $-10$  dB for bandwidth of 3.4 GHz and at central frequencies of 10.6 GHz and 11.0 GHz exhibited reflection loss of  $-32$  and  $-35$  dB, respectively, corresponding to 99% absorption of incident electromagnetic radiation. All the structures except RAS 1 displayed a reflection loss of less than  $-5$  dB. Evaluation of Mechanical properties of the designed RAS and verification of simulated results by experimentation is the future scope.

## 4 Conclusions

In this work, we fabricated the E-glass/epoxy-MWCNT radar absorbing structures with different loadings of MWCNTs. The complex permittivity values were measured. Numerical simulations were performed to obtain the absorption performance of double-layered radar absorbing structures. The better reflection loss was obtained for RAS10 with less than  $-15$  dB for a bandwidth of 2 GHz corresponding to 95% absorption. The designed RAS with a thickness of 3 mm was a promising lightweight structure for Radar absorption application.

## References

1. Park K-Y, Lee S-E, Kim C-G, Han J-H (2006) Fabrication and electromagnetic characteristics of electromagnetic wave absorbing sandwich structures. *Compos Sci Technol* 66:576–584
2. Fan Z, Luo G, Zhang Z, Zhou L, Wei F (2006) Electromagnetic and microwave absorbing properties of multi-walled carbon nanotubes/polymer composites. *Mater Sci Eng B* 132:85–89
3. Kim J-B, Lee S-K, Kim C-G (2008) Comparison study on the effect of carbon nano materials for single-layer microwave absorbers in X-band. *Compos Sci Technol* 68:2909–2916
4. Chin WS, Lee DG (2007) Development of the composite RAS (radar absorbing structure) for the X-band frequency range. *Compos Struct* 77:457–465
5. Teber A, Cil K, Yilmaz T, Eraslan B, Uysal D, Surucu G (2017) Manganese and zinc spinel ferrites blended with multi-walled carbon nanotubes as microwave absorbing materials. *Aerospace* 4(2):4010002
6. Oh J-H, Oh K-S, Kim C-S, Hong C-H (2004) Design of radar absorbing structures using glass/epoxy composite containing carbon black in X-band frequency ranges. *Compos B* 35:49–56
7. Micheli D, Marchetti M (2012) Mitigation of human exposure to electromagnetic fields using carbon foam and carbon nanotubes. *Engineering* 4:928–943
8. Micheli D, Pastore R, Apollo C, Marchetti M, Gradoni G (2012) Optimization of multilayer shields made of composite nanostructured materials. *IEEE Trans Electromagn Compat* 54(1)
9. Lee S-E, Kang J-H, Kim C-G (2006) Fabrication and design of multi-layered radar absorbing structures of MWNT-filled glass/epoxy plain-weave composites. *Compos Struct* 76:397–405
10. Lv X, Yang S, Jin J, Zhang L, Li G, Jiang J (2009) Microwave absorbing characteristics of epoxy composites containing carbon black and carbon fibers. *Polym (Korea)* 33(5):420–428
11. Choi I, Kim JG, Seo GS, Lee DG (2012) Radar absorbing sandwich construction composed of CNT, PMI foam and carbon/epoxy composite. *Compos Struct* 94:3002–3008
12. Kim PC, Lee DG (2009) Composite sandwich constructions for absorbing the electromagnetic waves. *Compos Struct* 87:161–167
13. Folgueras LC, Alves MA, Rezende MC (2010) Dielectric properties of microwave absorbing sheets produced with silicone and polyaniline. *Mater Res* 13(2):197–201
14. Micheli D, Apollo C, Pastore R, Marchetti M (2010) X-band microwave characterization of carbon-based nanocomposite material, absorption capability comparison and RAS design simulation. *Compos Sci Technol* 70:400–409
15. Micheli D, Pastore R, Apollo C, Marchetti M, Gradoni G (2011) Broadband electromagnetic absorbers using carbon nanostructure-based composites. *IEEE Trans Microw Theory Tech* 59(10)
16. Jin-Bong Kim (2012) Broadband radar absorbing structures of carbon nanocomposites. *Adv Compos Mater* 21(4):333–344

17. Giorcelli M, Savi P, Miscuglio M, Yahya MH, Tagliaferro A (2014) Analysis of MWCNT/epoxy composites at microwave frequency: reproducibility investigation. *Nanoscale Res Lett* 9:168
18. Nwigboji IH, Ejembi JI, Wang Z, Bagayoko D, Zhao G-L (2015) Microwave absorption properties of multi-walled carbon nanotube (outer diameter 20–30 nm)—epoxy composites from 1 to 26.5 GHz. *Diam Relat Mater* 52:66–71

# Synthesis and Microwave Absorption Properties of MnZn Ferrite Nanocomposite



Tammareddy Haritha, Koonam Ramji, Killi Krushna Murthy,  
Puppala Siva Nagasree and Dukkipati Bala Nagesh

**Abstract** Manganese zinc ferrite nanopowder was prepared by sol–gel auto combustion method. XRD analysis was carried to estimate the crystal structure and average diameter. Hysteresis behavior of the synthesized nanoparticles was studied with VSM. Composite laminates were prepared to study the microwave absorption properties like permittivity, permeability, and reflection loss in X-band frequency. The laminates were fabricated with epoxy as the matrix containing MnZn ferrite as magnetic fillers in different weight percentages using the hand layup method. Complex permittivities and complex permeabilities were measured using a vector network analyzer in the X-band frequency. Reflection loss of multilayered composite structures was estimated using a MATLAB code developed based on transmission line theory. A maximum reflection loss of  $-25$  dB is obtained for a four-layered structure at 10.2 GHz.

**Keywords** Permittivity · Permeability · Radar absorbing structure · Reflection loss

---

T. Haritha (✉)

Department of Mechanical Engineering, NRIIT, Pothavarappadu, Vijayawada, India  
e-mail: [haritha\\_gorijala@yahoo.com](mailto:haritha_gorijala@yahoo.com)

K. Ramji

Dr. B.R. Ambedkar University, Srikakulam, India  
e-mail: [ramjidme@gmail.com](mailto:ramjidme@gmail.com)

K. K. Murthy

Department of Chemistry, IIT, Hyderabad, India  
e-mail: [krushna@iith.ac.in](mailto:krushna@iith.ac.in)

P. S. Nagasree

Department of Mechanical Engineering, D.M.S.S.V.H. College of Engineering, Machilipatnam, India  
e-mail: [psnagasree@gmail.com](mailto:psnagasree@gmail.com)

D. B. Nagesh

Department of Mechanical Engineering, DIET, Vijayawada, India  
e-mail: [dukkipati.balanagesh@gmail.com](mailto:dukkipati.balanagesh@gmail.com)

© Springer Nature Singapore Pte Ltd. 2020

G. S. V. L. Narasimham et al. (eds.), *Recent Trends in Mechanical Engineering*,  
Lecture Notes in Mechanical Engineering,  
[https://doi.org/10.1007/978-981-15-1124-0\\_36](https://doi.org/10.1007/978-981-15-1124-0_36)

## 1 Introduction

Microwave absorbers can eliminate electromagnetic waves and make target visualization difficult to the RADAR. This ability depends on the materials used as microwave absorbers. Composite materials with dielectric, magnetic, and dielectric/magnetic fillers are developed to achieve microwave absorption. Some of the dielectric fillers are carbon black (CB), carbon nanofibers (CNF), carbon nanotubes (CNT), etc.; magnetic fillers include ferrites of NiZn, CoZn, NiFe, MnZn, Ba, and Cu. Composite materials find a wide range of applications because of their lightness, strength, resistance to corrosion, design flexibility, and improved microwave absorption properties.

## 2 Literature Review

A lot of research has been carried out to examine the effects of magnetic materials such as Fe–rubber, Ni–Zn, Ni–Ti, Fe–Ni, Fe–Ni–Co alloy nanoparticles, Fe<sub>3</sub>O<sub>4</sub>, NiFe<sub>2</sub>O<sub>4</sub>, and Zr–Mn [1–16] on the microwave absorption behavior in resin/paraffin matrix in the microwave frequency range. The reflection loss measured in Fe–rubber composite is below –10 dB [1] in between 8 and 10.64 GHz –13 dB [2] in between 8 and 12 GHz for Fe–NiTi composite and –20 dB at 1.59 GHz for Ni–Zn ferrite nanocomposite [8]. In addition, the matching frequency and thickness were precisely predicted in X-band for the ferrite–rubber composite materials using a numerically derived solution and were observed to be consistent with the experiment results. From the results of Ni–Zn ferrite composites, it is observed that the process of combining surface modification with cross-linking has improved microwave absorption properties with RL less than –20 dB with a smaller matching thickness than conventional microwave absorber using a spinel-type ferrite. Fe–Ni alloy nanoparticles [3, 6, 7 and 10] were dispersed into a paraffin wax/resin matrix to investigate complex permittivity, permeability, and reflection loss in the frequency range 2–18 GHz using the transmission line theory. The calculated RL is observed to be less than –20 dB [3] and –10 dB [6, 7, 10] in composites consisting of Fe–Ni alloy nanoparticles which are prepared by arc discharge method, facile hydrogen-thermal reduction method, surface modified planar anisotropy, and sol–gel method, respectively. The wt% of alloying elements, range of frequency for the abovementioned RL, and thickness of these composites are 49 wt% of Ni, 15 and 50 vol. % of Fe–Ni and Fe<sub>0.64</sub>Ni<sub>0.36</sub>, 7.6–16 GHz, 11–15 GHz, 0.8–1.8 GHz, and 3.1–15.1 GHz, 1.02–1.70 mm, 1.9–2.5 mm, 2.5–1.2 mm, and 1–4 mm, respectively. The effective absorption bandwidth for 15 vol. % of Fe–Ni alloy particles exceeds 4 GHz and the maximum RL of –14 dB is witnessed at 13 GHz with thickness of 2.1 mm and a reflection loss of –40 dB is attained

at 1.1 GHz for a layer of thickness 2.3 mm for 50 vol.% of Fe<sub>50</sub>Ni<sub>50</sub> particle–resin composites. Synthesized ferrite polymer nanocomposite (CoMn-Fe<sub>2</sub>O<sub>4</sub>/epoxy) [11] with a thickness of 2 mm exhibited RL of –59.60 dB at 12 GHz. The nanocomposites displayed higher electromagnetic absorption frequency and broad absorption bandwidth with RL less than –20 dB because of larger magnetic anisotropy of Co and ferrite nanoparticles. Furthermore, nanocrystalline Zr–Mn substituted Co ferrite composites [12] demonstrating enhanced reflection loss by 50% at specific frequency with addition of Zr–Mn to Co nanoferrites. A maximum reflection loss of 27 dB is observed at matching frequency of 2.45 GHz. The electromagnetic parameters of Fe–Ni–N nanocomposite [13, 14] revealed that they possessed multi-resonance peaks in the high frequencies. The magnetic and microwave absorbing properties investigated in Fe–Ni–N/paraffin matrix with different elemental compositions [14] have revealed the best microwave absorbing properties with optimum reflection loss of –17.5 dB at 12.0 for a thickness of 2 mm.

Various studies have been conducted to investigate the microwave absorption properties. Investigations were mostly carried out on Radar absorbing materials (RAM). In this work, Mn<sub>0.5</sub>Zn<sub>0.5</sub> ferrite powder has been synthesized by sol–gel auto combustion method. Composite laminates containing epoxy and ferrite nanopowder coated on e-glass were fabricated. These composite laminate structures were tested in X-band frequency for estimating complex permittivity and complex permeability. Numerical simulation is used for estimating microwave absorption of the multilayered structure.

### 3 Experimentation

#### 3.1 *Synthesis of Manganese Zinc Ferrite Nanoparticles*

Manganese zinc ferrite nanoparticles were synthesized by sol–gel auto combustion method. In this method, MnZn ferrite was prepared by dissolving equimolar mixture of iron nitrate, urea, zinc nitrate, and manganese nitrate in distilled water. This solution was evaporated using a magnetic stirrer at 200 rpm at a temperature of 60 °C until the concentration becomes thick. Then the concentrated mixture was placed in a furnace at a temperature of 400 °C for about 60 min. The obtained ferrite was collected in a crucible and calcinated for 120 min at a temperature of 600 °C in a furnace and allowed to cool in the furnace to room temperature. The ferrite was collected from the furnace and the ball was milled for 120 min to obtain uniform size as shown in Fig. 1.



**Fig. 1** Ferrite nanopowder

### ***3.2 Sample Preparation***

Epoxy resin (Epofine LY 556), e-glass fiber (10,000 strands per Tow), and high-temperature hardener Di Ethyl Tetra Di Amine (DETDA) used in the preparation of composite were purchased from High Chem. Laboratories, India. The composite samples have been prepared by the hand layup method.

Nanocomposite samples were prepared in the desired concentration following the below procedure:

1. MnZn ferrite nanopowder and epoxy were weighed using the digital balance in the desired weight percentage.
2. Magnetic fillers have been preliminarily dispersed in acetone and the mixture is dispersed in epoxy, then to get a well-dispersed solution, the mixture is ball milled in a conventional ball milling apparatus (in Smart Systems Pvt. Ltd., Hyderabad, India) at 800 rpm for about 2 h. The first 1 h in clockwise and the next 1 h in anticlockwise direction.
3. It is followed by sonication at 18 MHz frequency with a bath type sonicator (Trans-O-Sonic; M/s Shanti Industrial Estate, Mumbai, India) for 60 min
4. The sonicated mixture was further sonicated for 30 min after adding curing agent (100:24 epoxy: hardener) to nanopowder–epoxy mixture.
5. E-glass fabric has been cut into required dimensions and impregnated with the MnZn-dispersed resin hardener mixture.
6. Impregnated fabric layers were stacked and compressed to attain the desired thickness.

7. The prepared composite was cured in the oven at 80 °C for 60 min, then at 110 °C for the next 60 min, at 150 °C for the next 120 min and at 180 °C for the next 120 min.
8. The same procedure was repeated for all weight percentages (10, 20, and 30%) of MnZn alloy nanopowders.

## 4 Experimental Results

### 4.1 XRD, VSM, SEM, and EDAX Analysis

Figure 2 shows the XRD pattern of manganese zinc ferrite powder. The pattern shows good agreement with the JCPDS file for Mn<sub>0.5</sub>Zn<sub>0.5</sub> ferrite. The magnetic hysteresis loop at room temperature is shown in Fig. 3. The hysteresis loop was used to determine saturation magnetization and coercivity values for the synthesized nanoferrite particles. The coercivity is found to be 104.97G, magnetization 7.9269e-3, and retentivity 971.77e-6 emu. Figure 4 shows the SEM image of the ferrite with various particles in the range of 30 nm–40 nm size and spheroidal particle shape and Fig. 5 gives the elemental analysis. The EDAX analysis confirms the presence of Mn, Zn, Fe, and O in the synthesized powder.

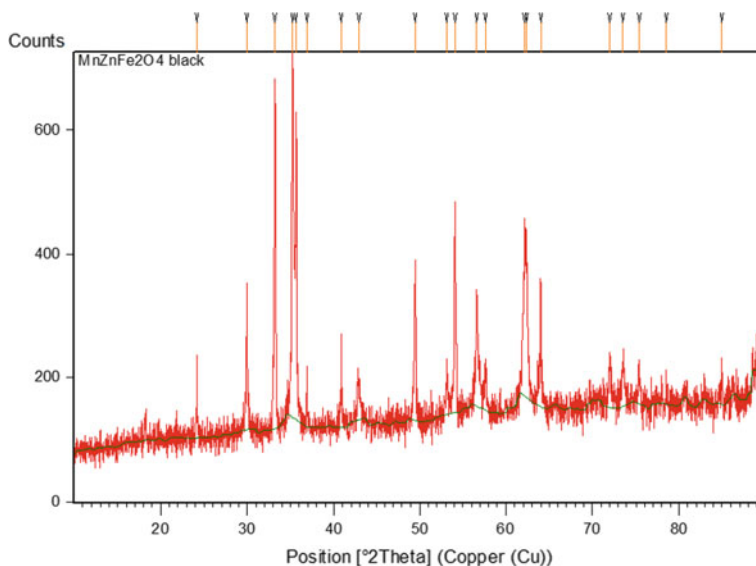


Fig. 2 XRD pattern of MnZn ferrite powder

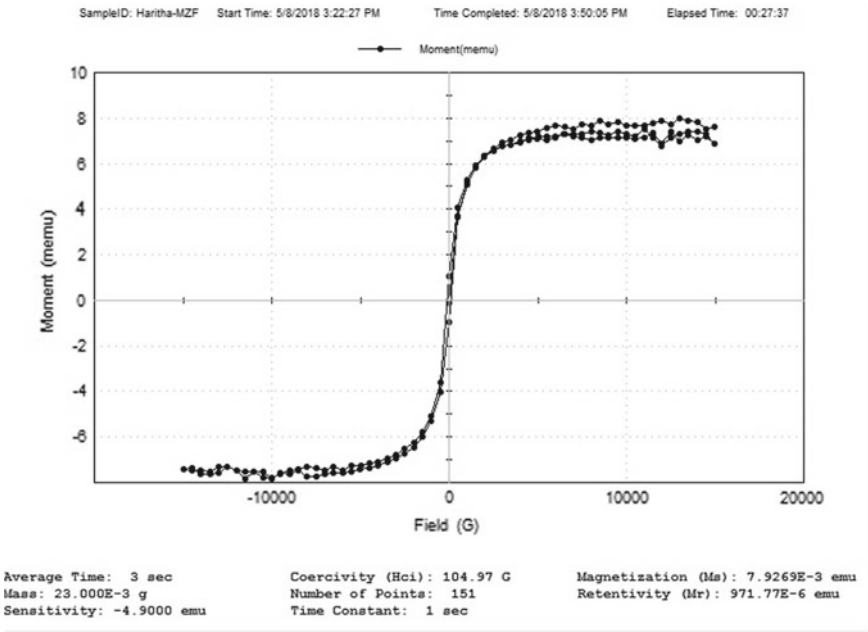


Fig. 3 VSM graph for MnZn ferrite

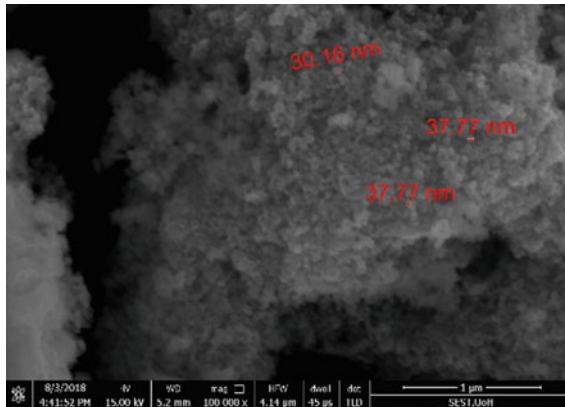
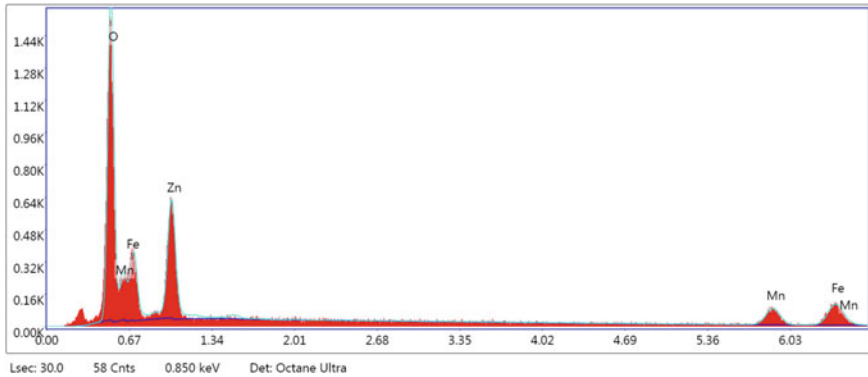


Fig. 4 SEM image of MnZn ferrite

### 4.2 Permittivity and Permeability Studies

Microwave absorption properties depend on the values of permittivity and permeability. The values of complex permittivity and complex permeability of the samples



**Fig. 5** EDAX analysis of MnZn ferrite

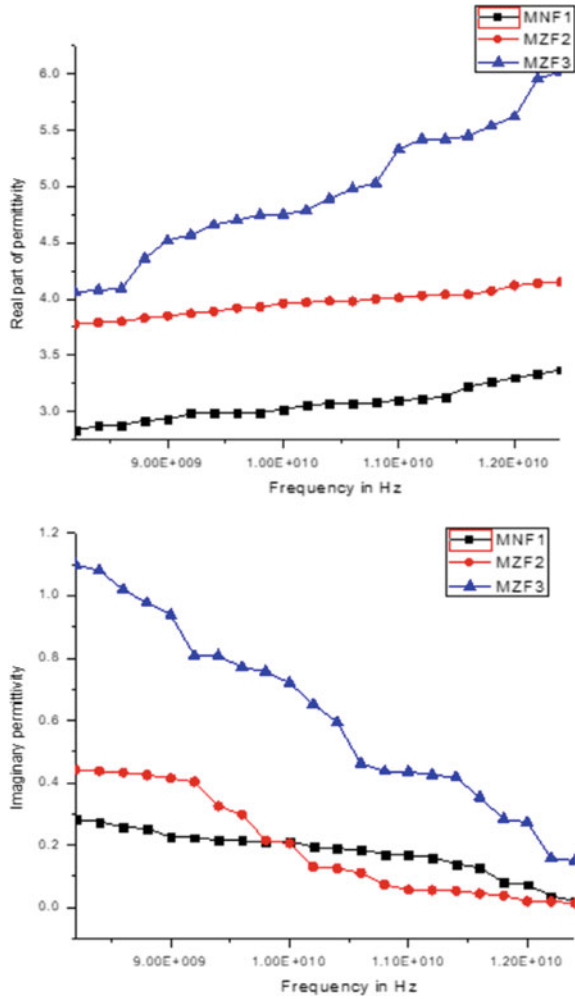
fabricated are as shown in Figs. 6 and 7. From the results, it was noticed that the higher the filler concentration, the greater are the permittivity and permeability. This is because of the conductive behavior of the filler material.

### 4.3 Reflection Loss

With the complex permittivity and complex permeability data, reflection loss of the multilayered structures for various thickness of the samples was estimated. Simulation of the multilayered RAS is carried out by using electromagnetic wave theory to measure absorption in terms of RL of the structure. RL of the multilayered RAS depends on the electromagnetic properties such as complex permittivity and permeability, and thickness and frequency. A MATLAB code was developed based on the fundamentals of the EMW theory using impedance matching conditions and transmission line theory to measure microwave absorption.

Simulation studies were carried out for radar absorbing structures (RAS) by considering epoxy as the first layer. Different combinations of single-layered, double-layered, three-layered, and four-layered structures were analyzed. Out of the various combinations, a four-layered structure has a reflection loss of  $-7$  dB in the frequency range of 8.2 GHz–11.0 GHz and the central frequency is found to be  $-25$  dB at 10.2 GHz. The reflection loss of a four-layered pure ferrite sample is shown in Fig. 8.

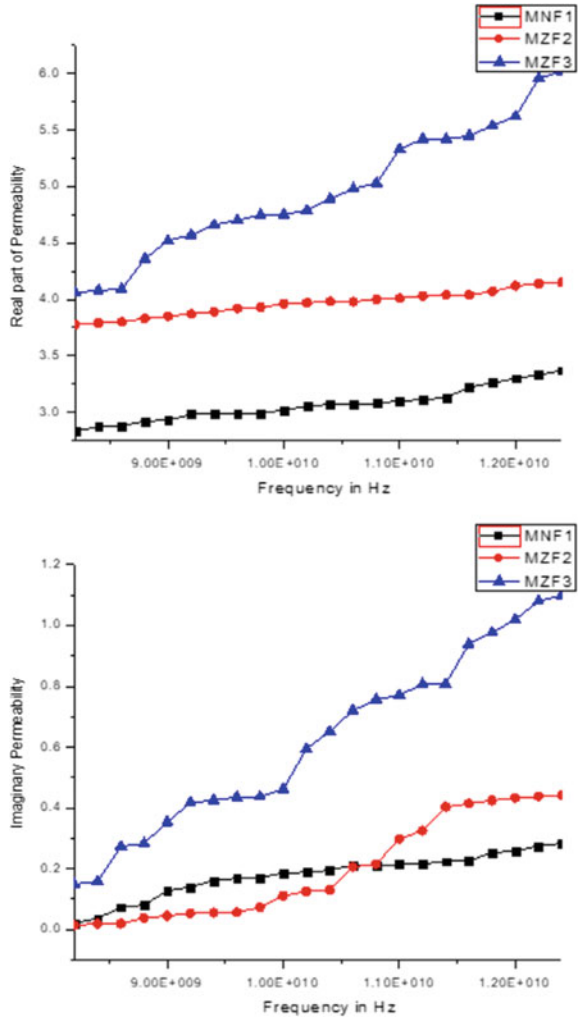
**Fig. 6** Real and imaginary parts of permittivity of ferrite powder



### 5 Conclusions

In the present work, ferrite nanopowder of MnZn was synthesized. Multilayered radar absorbing structures were simulated and the reflection loss is measured in the X-band frequency range based on the permittivity and permeability data of single-layered samples. The results obtained prove that composite material containing pure magnetic material like MnZn ferrite has the potential for radar absorption.

**Fig. 7** Real and imaginary parts of permeability of ferrite powder



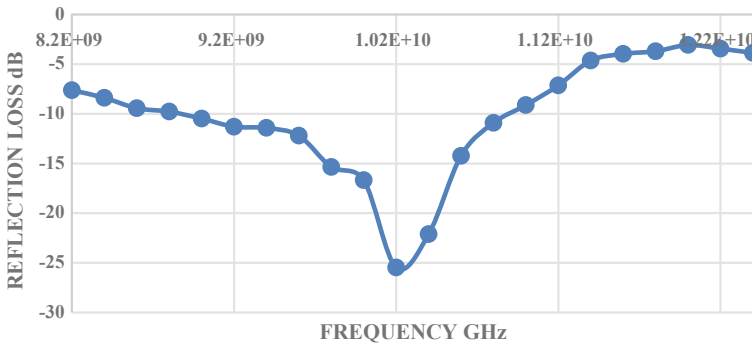


**Fig. 8** Reflection loss of pure ferrite sample

## References

1. Kim SS, Jo SB, Gueon KI, Choi KK, Kim JM, Chum KS (1991) Complex permeability and permittivity and microwave absorption of ferrite-rubber composite in x-band frequencies. *IEEE Trans Magn* 27(6):5462–5464
2. Singh P, Babbar VK, Razdan A, Srivastava SL, Goelastava TC, Goel TC (2000) Microwave absorption studies of Ca–NiTi hexaferrite composites in X-band. *Mater Sci Eng* 78:70–74
3. Lu B, Huang H, Dong XL, Zhang XF, Lei JP, Sun JP, Dong C (2008) Influence of alloy components on electromagnetic characteristics of core/shell-type Fe–Ni nanoparticles. *J Appl Phys* 104:114313
4. Yang C, Jingjie D, Peng Q, Qiao R, Chen W, Chuanlai X, Shuai Z, Gao M (2009) Polyani-line/Fe<sub>3</sub>O<sub>4</sub> nano particle composite: synthesis and reaction mechanism. *J Phys Chem B* 113(15):5052–5058
5. Deng LJ, Zhou PH, Xie JL, Zhang L (2007) Characterization and microwave resonance in nanocrystalline FeCoNi flake composite. *J Appl Phys* 101:103916
6. Zhen L, Gong YX, Jiang JT, Shao WZ (2008) Electromagnetic properties of FeNi alloy nanoparticles prepared by hydrogen-thermal reduction method. *J Appl Phys* 104:034312
7. Wei J, Zhang Z, Wang B, Wang T, Li F (2010) Microwave reflection characteristics of surface-modified Fe 50 Ni 50 fine particle composites. *J Appl Phys* 108:123908
8. Shimba K, Furuta K, Morimoto N, Tezuka N, Sugimoto S (2011) Microwave absorption properties of polymer modified ni-zn ferrite nanoparticles. The Japan Institute of Metals. *Mater Trans* 52(4):740–745
9. Yan SJ, Zhen L, Xu CY, Jiang JT, Shao WZ, Lu L, Tang J (2011) The influence of Fe content on the magnetic and electromagnetic characteristics for Fe x (CoNi)<sub>1-x</sub> ternary alloy nanoparticles. *J Appl Phys* 109:07A320
10. Yan X, Xue D (2012) Fabrication and microwave absorption properties of Fe<sub>0.64</sub>Ni<sub>0.36</sub>-NiFe<sub>2</sub>O<sub>4</sub> nanocomposite. *Nano Micro Lett* 4(3):176–179
11. Bayrakdar H (2012) Electromagnetic propagation and absorbing property of ferrite-polymer nanocomposite structure. *Progress Electromagn Res M* 25:269–281
12. Khan K, Rehman S (2014) Microwave absorbance properties of zirconium–manganese substituted cobalt nanoferrite as electromagnetic (EM) wave absorbers. *Mater Res Bull* 50:454–461
13. Pan H, Cheng X, Zhang C, Gong C, Yu L et al (2013) Preparation of Fe<sub>2</sub>Ni<sub>2</sub>N/SiO<sub>2</sub> nanocomposite via a two-step route and investigation of its electromagnetic properties. *Appl Phys Lett* 102:012410

14. Pan H, Cheng X, Gong C, Yu L, Zhang J, Zhang Z (2013) Preparation of  $(\text{Fe}_x\text{Ni}_{1-x})_4\text{N}$  ( $0.5 < x < 0.8$ ) compounds and evaluation of their magnetic and microwave absorbing properties. *J Appl Phys* 113:113906
15. Li G, Wang L, Li W, Ding R, Yao X (2014) CoFe<sub>2</sub>O<sub>4</sub> and/or Co<sub>3</sub>Fe<sub>7</sub> loaded porous activated carbon balls as a lightweight microwave absorbent. *Royal Society of Chemistry. Phys Chem Chem Phys* 16:12385–12392
16. Feng HT, Zhuo RF, Chen JT, Yan D, Feng JJ, Li HJ, Cheng S, Wu ZG, Wang J, Yan PX (2009) Synthesis, characterization and microwave absorption property of the SnO<sub>2</sub> nanowire/paraffin composites. *Nanoscale Res Lett* 4:1452–1457



# An Experimental Investigation of New Hybrid Composite Material Using Ramie-Flax and Its Mechanical Properties Through Finite Element Method



**Dara Ashok, Sukumar Puhan, Raghuram Pradhan, P. Kiran Babu and Y. Srinivasa Reddy**

**Abstract** This article describes the occurrence of the recent natural fiber hybrid composite mistreatment as strengthening with the hybrid materials using fiber and polyester matrix and polyester resins. The sheets of the composites were made from Ramie fiber with the matrix of Flax fiber and polyester. The resin used was polyester resin. The composite weight division was maintained at 20% fiber and 80% resin. To verify the mechanical characteristics of the natural hybrid composite fiber, the cutting of the specimen is finished within the required shape after the hybrid composites have been made. Thus, fashioned material permitted tensile, flexural, effect and compression tests at entirely in distinct orientations. In order to match experimental outcomes, the finite element inquiry is administered. The conclusions were taken as to the differentiation of the effects of these hybrid composites on the various characteristics of materials.

**Keywords** Hybrid composite · Ramie fibers · Flax · Modulus of elasticity · Finite element method

---

D. Ashok (✉) · S. Puhan · R. Pradhan · P. Kiran Babu · Y. Srinivasa Reddy  
Department of Mechanical Engineering, Pace Institute of Science and Technology, Ongole, India  
e-mail: [ashok.dara1@gmail.com](mailto:ashok.dara1@gmail.com)

S. Puhan  
e-mail: [sukumar\\_p@pace.ac.in](mailto:sukumar_p@pace.ac.in)

R. Pradhan  
e-mail: [raghuram\\_p@pace.ac.in](mailto:raghuram_p@pace.ac.in)

P. Kiran Babu  
e-mail: [kiran\\_p@pace.ac.in](mailto:kiran_p@pace.ac.in)

Y. Srinivasa Reddy  
e-mail: [srinivasareddy\\_y@pace.ac.in](mailto:srinivasareddy_y@pace.ac.in)

## 1 Introduction

Hybrid composites [1–4] add more than two components together to create a novel material with greater features than the first components. The material comprises a woven ply reinforcing fiber and a matrix material that binds the plies along and provides rigidity that forms the fibers into structures. These unique characteristics disagree with those of golden alloys as each of the composite materials still retains its initial chemical, physical, and mechanical characteristics. Composites are widely used in regional trade as a latest trend. In the region sector, there are basically two types of fiber composites that are used, carbon/epoxy and glass/phenolic. Carbon/epoxy is usually implemented on major supporting structures, while glass/phenolic supports cabin furniture.

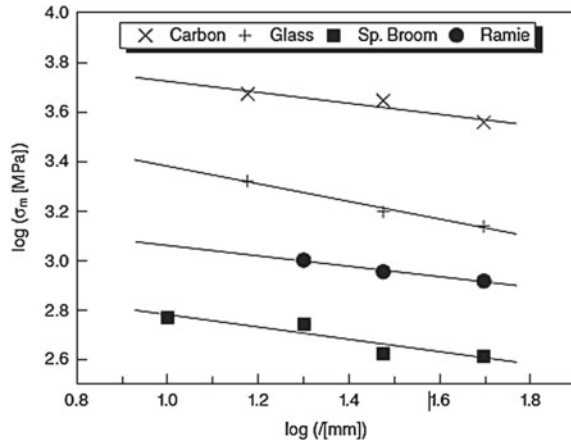
Polymeric materials reinforced with artificial fibers such as glass, coal, and aramid provide the advantages of greater rigidity and strength to weight the quantitative relationship as compared to custom building materials such as timber, concrete, and steel. Mechanical characteristics of fiber-reinforced composites rely on a number of variables including mechanical characteristics of fiber and polymer, adhesion of fiber/matrix, fiber geometry and orientation, and fraction of fiber quantity. The impacts of interfacial bonding of fiber and/or polymer, polymer type, and fiber matrix [5].

Despite these advantages, the epidemic use of man-made fiber-reinforced chemical compound composites involves a tendency to say no, due to tethering elevated original rates and conflicting environmental influence. With the structural materials, the natural fiber composites have drawn considerable standing in latest years. In the composites, there has been a rapidly increasing interest in the unfairness of the natural fibers as an underpinning. Natural fibers enticing alternatives (such as bamboo, banana, sisal, jute, coir, etc.) are low prices, lightweight, high particular modules, renewability, and biodegradability [6].

There are significant requirements that are eco-friendly for low-cost materials with excellent mechanical characteristics. Glass fiber has long been used, but there is now a demand for material that has the same or better characteristics to substitute it. The world currently trying to substitute products that are not recyclable [1]. We look at natural fibers that can exhibit good mechanical properties for material to avoid the disadvantage. Ramie is the strongest of the natural fibers. When wet [7], it shows superior strength.

Especially for its ability to carry shape, cut back wrinkling, and smooth luster to the material look, Ramie fiber is good. It is not as robust as other fibers and is usually used as a mixture with other fibers such as cotton or wool. In permeability, density, and microscopic look, it is a kind of like flax. Due to its elevated molecular crystallinity, Ramie is inflexible, fragile, low resilience and elasticity. Ramie Fibers' advantages are merging with other fibers. It resists microorganism attack, mildew attack, and various insects. Its ability to absorb is exceptionally high [8].

**Fig. 1** Impact of gauge length on strength of Spanish broom, ramie, carbon and glass fibers (reprinted from Elsevier © 2015)



## 2 Literature Survey

Weibull [9] developed an applied mathematics approach for material strength that assumes a distribution of weak spots (for example cracks or dislocations) that result in material failure. In line with this approach, a quantifiable matter is just as strong because the volume component containing the weakest defect and larger volumes of matter a lot of possible to own a lot of defects, therefore the strength of a Weibull material is powerfully keen about its volume.

Bevitori et al. [10] and Monteiro et al. [11] described that tensile strengths of bog hemp fibers exhibited a hyperbolic kind of contrary association with the fiber diameter. Angelini et al. initiate that strengths of bog hemp and three different forms of fibers exaggerated with a decrease within the gauge length (Fig. 1) [12]. So in natural fibers the exceptional strength of ramie fibers behavior leads us to take for the hybrid composites with flax.

Table 1 Recapitulates the data for tensile strength, Young’s modulus, elongation, and corresponding fiber diameter of ramie fibers reported in the literature. The mechanical properties of ramie fibers variances could be due to fiber production methods, fiber diameters, and/or differences in testing methods [13–24].

## 3 Materials and Methods

This section contains the main points regarding materials and also the procedure that was thought about for the production of composite and also the check procedure followed for testing the characterization of composites, severally. The raw materials used for fabrication are

**Table 1** Mechanical properties of ramie fibers

Tensile strength (MPa)	Young's modulus (GPa)	Elongation (%)	Diameter ( $\mu\text{m}$ )	References
800–1000	65	1.7–2.3	40–60	[13]
621	47.5	1.9	48.5	[10]
402	30–40	–	36	[15]
730	42	–	30	[16]
526	15.5	3.5	120	[17]
560	–	2.5	34	[18]
–	48.6	2.4		
627	31.8	2.7	120	[19]
1250	36.0	3.8	20.3	[20]
768	42	2.6	–	[21]
494	24	2.57	33.6	[22]
333	24.7	1.63	25–30	[23]
936	25	–	15–40	[24]

- (a) Ramie fiber
- (b) Flax fiber
- (c) Hardener
- (d) Epoxy Resin

(a) **Ramie Fiber**

Ramie goes to the *Boehmeria* genus, unremarkably referred to as white ramie, China grass, inexperienced China grass, and rhea. It is persistent plant, mowed six times in a year from family order Urticaceae or nettle. It is one of the oldest vegetable fibers and has been used for millenniums. It produces an outsized range of branchless stems from underground rhizomes and incorporates a crop life from six to twenty years. Remedial treatment needed to removal of gums and pectins inside the bark.

Ramie in China is typically harvested by hand because the canes mature. Uneven strands of Chinese silk plant makes gathering a tough task. Drubbing and scratching are necessary processes to discrete the fibers. After separation of fibers from woody matter and soft tissues, fibers stay in ribbon-like strips as they are controlled along by gums and cellulose. Machines are not nevertheless capable of playacting all the essential stages that are why Chinese silk plant is not wide used.

Forming plain-woven and knit products is generally mixed with cotton. It is used in clothing items, tablecloths, serviettes, and handkerchiefs. Chinese silk plant is used in nets, canvas, fabric products, straw hats, and heart hoses apart from textile trade. Ramie has higher tensile strength, eight cotton times, and seven silk times. Ramie fiber, first grade in reverence for strength and durability among all herbal fibers. When subjected to weather circumstances or immersed in water, it has an exclusive representative of repelling rot (Figs. 2, 3, Table 2).



**Fig. 2** a Initial ramie fiber b Final ramie fiber

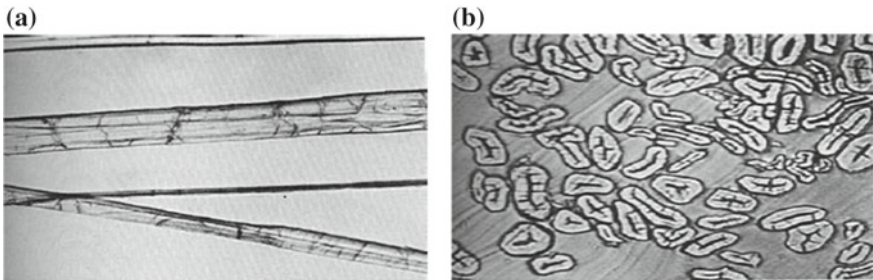


**Fig. 3** a Longitudinal view b Ramie fibers cross section

**Table 2** Physical and chemical characteristics of ramie and other cellulosic fibers

Characteristics	Ramie	Flax	Hemp	Cotton
Ultimate fiber length (mm)	5	1	5	9
Minimum	120–150	13–14	15–25	20–30
Average	620	130	55	63
Maximum				
Ultimate fiber diameter (microns)	13	5	10	12
Minimum	40–60	17–20	15–30	14–16
Average	126	40	50	20
Maximum				
Tensile strength (kg/mm <sup>2</sup> )	95	78	83	45
Moisture regain in %	12	12	12	8
Chemical composition (%)	72–97	64–86	67–78	88–96
Cellulose	1–0	5–1	6–4	0
Lignin	27–3	31–14	27–18	12–4
Hemicelluloses, pectin, and others				

Ramie fibers display the improved mechanical properties when mixed with bast fibers (45–88 cN/tex). The fiber dimensions range 120–150 mm in length and 40–60 μm in diameter. The major problem with ramie is its low elasticity of 3–7% which means it is stiff and brittle.

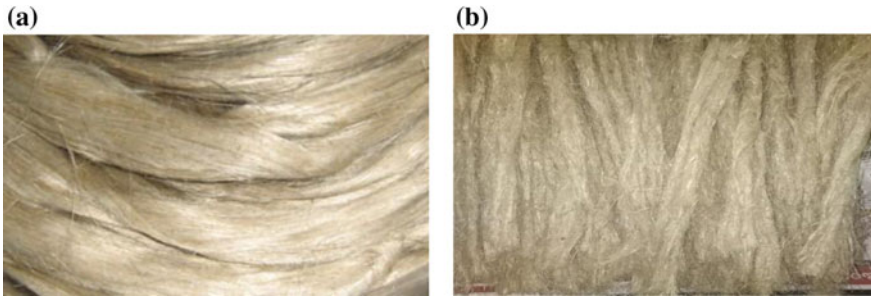


**Fig. 4** a Initial flax fiber b Final flax fiber

### (b) Flax Fiber

Flax is 2–3 times tougher than cotton fiber, thus it is a lot of proof against wear and abrasion. It absorbs wetness well and could be a terribly breathable fiber. As flax fibers do not have abundant physical property, materials created with flax do not tend to lose their form simply. It is additionally hypoallergenic so a superb selection of fiber for those with allergies. Flax could be a member of *Linum* within the family *Linaceae*. The scientific name of the plant is *Ustatissimum*. Flax is cultivated in cooler places of the globe. The gather of flax needs special talent, operations, and specific machines (Figure 4).

### (c) Hardner(HY 951) [25]

Hardeners square measure always needed to produce synthetic resin of associated degree useful for its alleged purpose. Epoxies do not succeed anywhere near the dramatic mechanical and chemical properties they might have with the hardener without a hardener. To ensure that the epoxy combination can fulfill the appliance's requirements, the right type of hardener should be chosen. Research should be done on each of the resins, so the hardener can perform satisfactorily to create some of the ultimate epoxy mixtures. Common samples of a square-based epoxy hardeners measure hydride, amine-based, polyamide, open chain, and cycloaliphatic.

### (d) Epoxy Resin(LY 556) [26]

The term 'resin' encompasses a good many artificial substances of comparable mechanical properties (Dense liquids that stabilize into clear solids). The term 'resin' has been applied within the nowadays to just about any element of a liquid that forms a tough lacquer or enamel-like end. An example is enamel, a contemporary product that contains resins that area unit organic compounds, but not traditional plant resins.

The amount of resin between layers must be controlled as follows: surface of mat 90%; chopped strand mat 70%; plaid 50%. Two layers of glue can be used according to the following equation:

$$w_{total} = w_{laver} + w_{roller} + w_{other}^{[1]}$$

$w_{total}$  = the volume of the total plastic layer;  
 $w_{layer}$  = the actual volume of resin in the layer;

$$W_{layer} = W_r w_g / (1 - w_r);$$

$w_r$  = the amount of resin with standard requirements;  
 $w_g$  = the total weight of enhanced material;  
 $w_{roller}$  = the volume of resin on the roller;  
 $w_{other}$  = the amount of resin lost for other reasons.

## 4 Composite Fabrication

Fabrication of composite is completed by standard methodology known as hand lay-up methodology. A mold of dimension  $300 \times 300 \times 6 \text{ mm}^3$  is used. Polyester resin with its conforming hardener in a ratio of 10:1 is methodically mixed. Mold liberating silicon spray is applied to mold releasing sheet and then the sliced fiber, assorted with the resin is mildly poured on the sheet, which is located inside the mold. The persistence of emotional agent is to simplify simple subtraction of the composite from the mold once natural process. The mixture is enabling to line within the mold for an amount of 24 time unit below forged pressure of 20 kg. Then the specimen is dividing into appropriate dimension for mechanical and physical tests. In this fabrication procedure, three categories of composites are prepared with different compositions. Ramie and Flax fiber are added in a weight percentage of 80% and 20% for improving the mechanical properties of composites.

### 4.1 Hand Lay-Up Technique

The described process procedures used for manufacture ramie fiber-reinforced thermoset polymer composites were all established methods are compression molding [27–30], hot pressing [31], filament winding, prepreg plus hot pressing or molding, and resin transfer molding. For the economical to reveal better mechanical properties, we are choosing hand lay-up Technique.

The fibers were balanced and accordingly the resin and hardeners were assessed. Epoxy and hardener were mixed properly with absence of bubbles to avoid premature failure of material. The consequent fabrication process consisted of first setting a film on the mold surface and polymer coating was applied on the sheets for rolling. Again resin applied to next fiber ply of another kind was placed and rolled. Cylindrical mild steel rod used as Roller for rolling. This process was repeated until eight alternating fibers layers have been laid. On the highest of the last ply a compound coating is completed, that serves to make sure a good surface finish. Finally, 20 kgf weight was

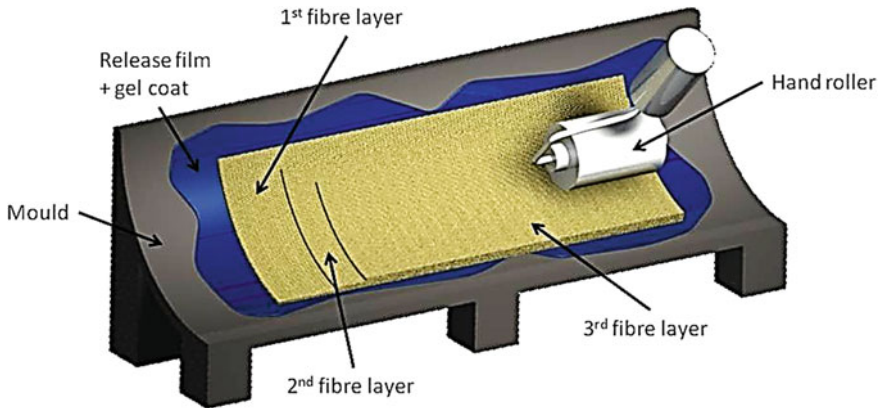


**Fig. 5** Process of hand lay-up technique

applied on the composite over 72 h to badge contented time for solidification and subsequent hardening (Fig. 5).

## 4.2 Hybrid Composite Preparation

Pre-early the mold for the composite is ready. We have to prepare mold of size  $300 \times 300 \times 3$  mm for the provision of required composite. A clean smoothened surfaced wood board is taken and splashed completely. We give a cover to the wooden board with a nonreactive thin plastic sheet called OCB (Odet-Cascadec-Bollore) Sheet. Then the Ramie and Flax are taken of equal size that of the mold.

Raw Ramie and Flax are washed and dried with water. After that, for right weight, it is measured and unbroken. The measurement of the samples should be right to create good composite and therefore the blend should be extremely uniform. We bring the right amount of compound we calculated previously and 100% of its hardener. Then this blend is fully stirred until it turns into a touch heat. Hardener should take very minute because by forming the tiny lathers, little extra hardener can ruin the composite. The experiments have been researched and discussed to evaluate the strengths of flexural, impact strength, tensile, and compression.

## 5 Experimental Procedure

The tensile tests of the composites were accomplished as per the ASTM D3039 standards. The tests were ended by using a universal testing machine (Tinius Olsen H10KS). The specimen of the required dimension  $120 \times 20 \times 3$  mm<sup>3</sup> aspect was



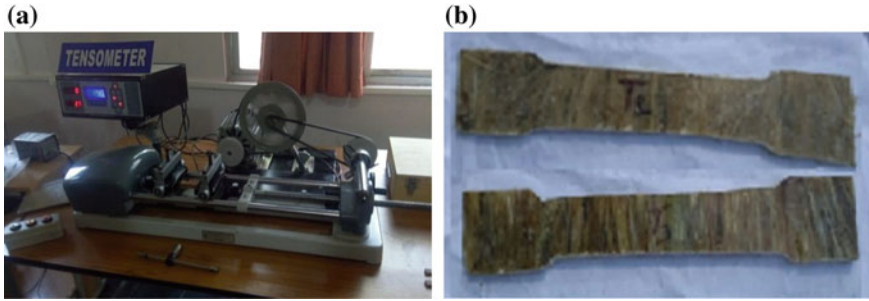


**Fig. 6** a Tensile test b Tensile test specimen

chopped from the composite cast. The check was accompanied at a continuing strain rate of 2 mm/min. The tensile test prearrangement is shown in the figure. Tensile strength ( $\sigma$ ) was calculated by

$$\sigma = \frac{F}{A}$$

where

$F$  = the maximum load (in newtons);

$A$  = the area of the specimen.

The maximum bending stress of a composite is the flexural strength that it can withstand during bending before reaching the breaking point (Fig. 6). As per ASTM D790-03 test standards, The flexural tests of the composites were performed. The flexural strength ( $\sigma_b$ ) was calculated by

$$\sigma_b = \frac{3FL}{2bt^2}$$

where

$F$  = the maximum load (newtons);

$L$  = the distance between the supports (millimeters);

$b$  = the breadth of the specimen (millimeters) and

$t$  = the thickness (millimeter) (Fig. 7).

In Charpy impact test, specimens were subjected to a huge quantity of force for a very short interval of time. The higher amount of impact strength indicates that it can absorb a large amount of energy before failure and its plasticity will be also large. The size of the specimen for the impact test was  $50 \times 15 \times 3 \text{ mm}^3$  and has a 2 mm deep notch on one face. The three tested results from three specimens at any one temperature (in J) are averaged (Fig. 8).

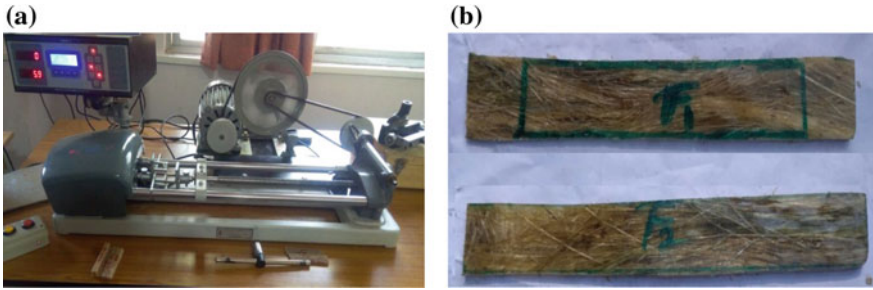


**Fig. 7** a Flexural testing specimens b Flexural testing specimen

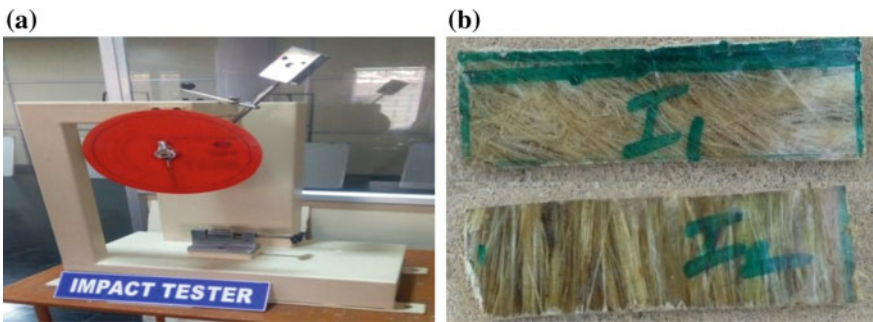


**Fig. 8** a Impact tester b Charpy testing specimens

The size of the specimen for the impact test was  $10 \times 10 \times 3 \text{ mm}^3$ . The resulting stress-strain diagram delivers information on proportional limit, elastic limit, yield strength, and compressive strength (Fig. 9).

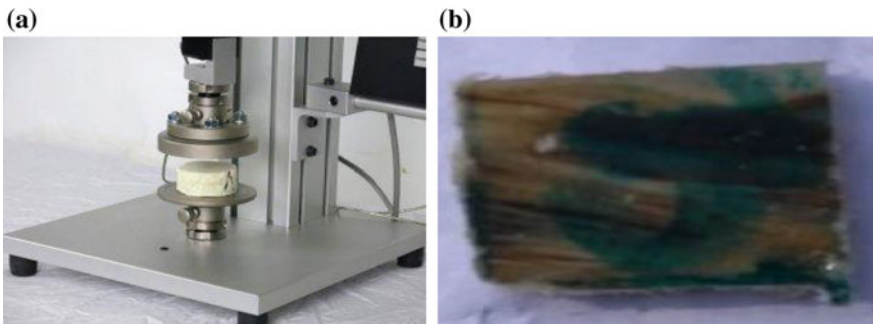


**Fig. 9** a Compression testing machine b Compression testing specimen

## 6 Finite Element Analysis

A hybrid composite is made up of using more than two or more types of materials, either it is created from fibers-matrix or not. In this paper, one type of hybrid composite with composition of natural fiber and flax with resin is modeled in ANSYS Workbench 16.0. The structural experiments are tested in ANSYS Composite Prep-Post (ACP) Workbench. In this paper, composites are made by changing their orders and orientations as like the Experimental specimen but keeping all the same conditions and loads, which are directly applied to the composites. From these results a mark ready result came out, which is able to be useful to form associate composite of high strength with victimization same fibers of several properties. This sort of study is extremely useful to see the manner of creating a composite by selecting a correct lay-up to style the fabric.

## 7 Results and Discussion

The results which comprise assessment of tensile strength, flexural strength, impact strength, and Compression strength have been studied and discussed. The understanding of the results and the evaluation among various composite samples are also presented. The consequence of fiber content on tensile properties of the composite is shown in table (Figs. 10, 11, Table 3).

The significant variation of tensile strength for different systems specifies fiber content is not only a major factor which affects the mechanical performance, interfacial adhesion and the fibers influences polyester matrix properties also have a significant effect. Generally, in the case of little strains while not interface fracture reflects the modulus performance of each fiber and matrix interface transfer the elastic

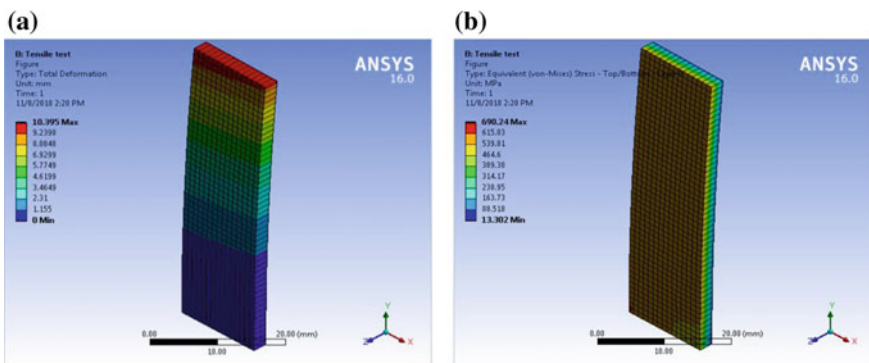
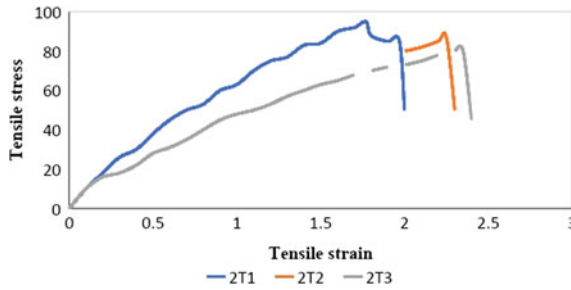


Fig. 10 FEA results for tensile test a Total displacement b Tensile stress



**Fig. 11** Results comparison between three test specimens

**Table 3** Results assessment between experimental results and FEA for tensile test

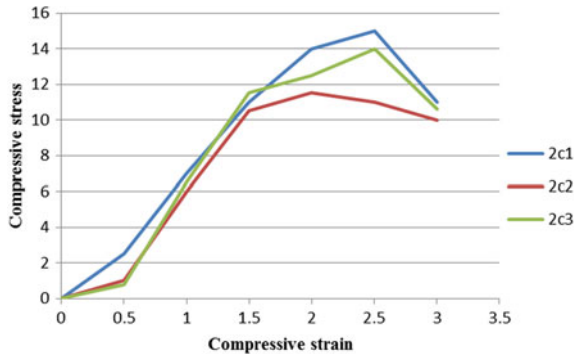
S. no	Specimen label	Experiment results			FEA results		
		Maximum load (N)	Displacement (mm)	Tensile stress at maximum load (Mpa)	Mean load (N)	Displacement(mm)	Tensile stress at maximum load (Mpa)
1	2t1	2802.84	13.15	697.9	2790.5	10.395	690.24
2	2t2	2787.83	12.34	680.2			
3	2t3	2780.39	12.92	691.3			

deformation. The tensile strength is rise due to the cross-linking network construction among the fibers and the resin materials in polymer matrix. The variations of the compressive load and compressive stress of Ramie and Flax fiber content shown in following figure. It is found that the compressive load and compressive stress of fiber composites linearly increased as the content of the natural fiber is increased. This is due to excellent scattering of fiber and active stress transmission between the fiber and the matrix (Table 4).

The variation of the Flexural strain and flexural stress of Ramie and Flax fiber content shows in the following table. It is found that the flexural load and flexural stress of fiber composites linearly increased as the content of the natural fiber is increased. This is due to excellent dispersion of fiber and actual stress transmission between the fiber and the matrix (Graph. 1, Fig. 12, Table 5).

**Table 4** Results experimental results compression test

S. no	Specimen label	Maximum load (N)	Compressive stress (Mpa)	Bulk modulus (Mpa)
1	2c1	1888	14.86	912.16336
2	2c2	1470	11.65	949.66788
3	2c3	1528	12.58	935.19525



Graph 1 Compressive test graph details

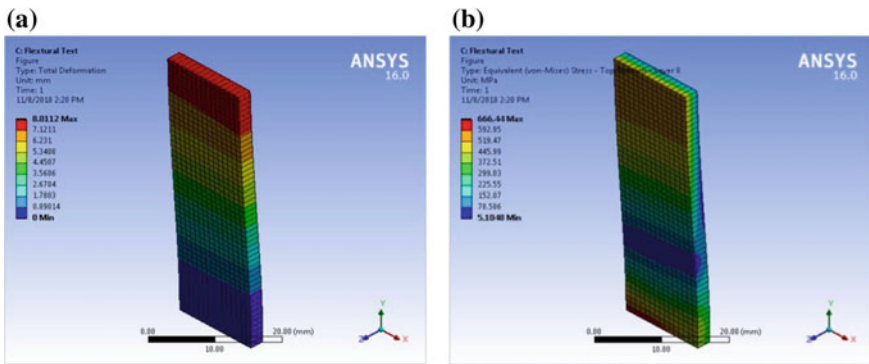


Fig. 12 FEA results for flextural test. a Total displacement. b Flextural stress

Table 5 Results assessment between experimental results and FEA for tensile test

S. no.	Specimen label	Experimental results			FEA		
		Maximum load (N)	Displacement (mm)	Maximum stress (Mpa)	Mean load(N)	Displacement (mm)	Maximum stress (Mpa)
1	2f1	1680	7.9	641.72	1692.6	8.0112	666.44
2	2f2	1701	8.1	637.23			
3	2f3	1697	8.0	643.23			

In Charpy test, when the striker impacts the specimen, endures to absorb energy till failure against plastic deformation. Table 6 shows the variation of energy absorbed by the Ramie and Flax fiber content. It is originated that there is no considerable change in the impact test by changing the fiber orientation. (Fig. 13).

**Table 6** Results comparison between experimental results and FEA for tensile test

S. no.	Specimen	Experimental results		FEA	
		Stress (MPa)	Energy absorbed (KJ) (Charpy test)	Stress (MPa)	Energy absorbed (KJ)
1	I <sub>1</sub>	270.015	40 kJ	271.9	45.6 kJ
2	I <sub>2</sub>	277.19	42 kJ		
3	I <sub>3</sub>	273.21	40 kJ		

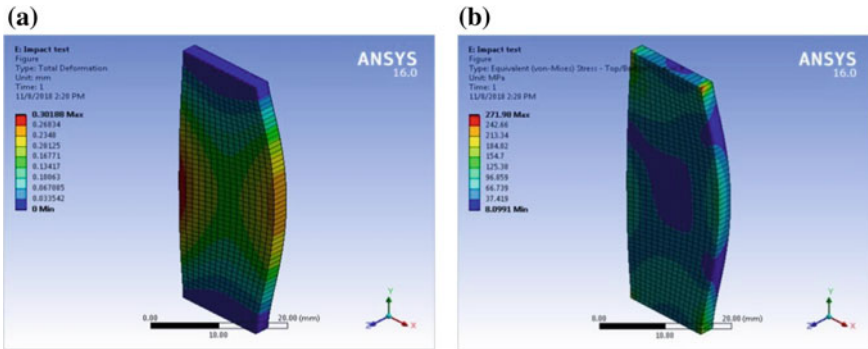


**Fig. 13** FEA results for flextural test **a** Total displacement. **b** Flaxtural stress

## 8 Conclusion

Hybrid Ramie and Flax fiber-reinforced polyester composite, has fabricated by simple hand lay-up technique. Based on the Experimental and Finite element Analysis (FEA) through ANSYS, It has been perceived that the Mechanical properties of the composites are greatly influenced by the fiber loading and fiber length. The micro hardness value rises with raise in fiber length. As far as the effect of ramie fiber loading is exercised on composites with 5 wt% fiber loading displays improved hardness value as compared to 10 wt% irrespective of fiber length except for 30 mm length. A progressively increase 15% in tensile and flexural strength is observed. However, there is a reduction in the strength properties with 8%. It can be experiential that the tensile modulus increases irrespective of fiber loading but increase in fiber length.

On the whole, it is concluded that ramie-flax Hybrid composites can exhibit good mechanical properties for the green engineering application where the recycling is needed.

## 9 Scope for Future Work

There is a very wide scope for future scholars to explore this area of research. This work can be promoted to study added features of such composites with other prospective fillers and alignment of layers/fibers for augmentation of hybrid composites and their mechanical and physical behavior.

## References

1. Wang R-M, Zheng S-R, Zheng Y-P (2011) Introduction to polymer matrix composites. In: *Polymer Matrix Composites & Technology*. Woodhead Publishing Series in Composites Science and Engineering, pp 1–25
2. Fiorea V, Calabrese L, Scalicia T, Bruzzaniti P Valenza A (2018) Experimental design of the bearing performances of flax fiber reinforced epoxy composites by a failure map. *Compos B Eng* 148: 40–48
3. Fragassa C, Pavlovic A, Santulli C (2017) Mechanical and impact characterisation of flax and basalt fibre vinylester composites and their hybrids. *Compos B Eng* S1359–8368(17):30048-3
4. Hamidon MH, Sultan MTH, Ariffin AH (2019) Investigation of mechanical testing on hybrid composite materials. *Fail Anal Bio-compos Fibre-Reinf Compos Hybrid Compos*:133–156
5. Yan Y (2016) Developments in fibers for technical non wovens. *Adv in Techn Nonwovens*
6. Hamdan A, Mustapha F, Ahmad KA, Mohd Rafie AS, Ishak MR, Ismail AE (2016) The bonded macro fiber composite (MFC) and woven kenaf effect analyses on the micro energy harvester performance of kenaf plate using modal testing and Taguchi method. *J Vibroeng*:18
7. Hendra (2017) A study on cotton-ramie fabric reinforced composites. *Int J Mater Sci* 12(1):117–125, ISSN 0973–4589
8. Müssig J (2008) Cotton fibre-reinforced thermosets versus ramie composites: a comparative study using petrochemical- and agro-based resins. *J Polym Environ* 16(2):94–102
9. Elmahdy, EE (2015) A new approach for Weibull modeling for reliability life data analysis. *Appl Math Comput* 250:708–720
10. Bevitori AB, Silva ILAD, Carreiro RS, Margem FM, Monteiro SN (2012) Elastic modulus variation with diameter for ramie fiber. Paper presented at the Characterization of Minerals, Metals, and Materials—TMS 2012 Annual Meeting and Exhibition, Orlando, FL
11. Monteiro SN, Satyanarayana KG, Ferreira AS, Nascimento DCO, Lopes FPD, Silva ILA, Bevitori AB, Inácio WP, Bravo Neto J, Portela TG (2010) Selection of high strength natural fiber. *RevistaMateria* 15(4):488–505
12. Du Y, Yan N, Kortschot M (2015) The use of ramie fiber as reinforcements in composites. University of Toronto, Canada, *Biofiber Reinforcements in Composite Materials*. Book edited by Omar Faruk, MohiniSain, pp 104–136
13. Weibull W (1939) A statistical theory of the strength of materials, vol 151. *IngeniörsvetenskapsakademiensHandlingar*, Stockholm
14. Nam S, Netravali AN (2006) Green composites. Physical properties of ramie fibers for environment-friendly green composites. *Fibers and Polym* 7(4):372–379
15. Suizu N, Uno T, Goda K, Ohgi J (2009) Tensile and impact properties of fully green composites reinforced with mercerized ramie fibers. *J Mater Sci* 44(10):2477–2482
16. Goffin AL, Raquez JM, Duquesne E, Siqueira G, Habibi Y, Dufresne A, Dubois P (2011) From interfacial ring-opening polymerization to melt processing of cellulose nanowhiskered poly(lactide)-based nano composites. *Biomacromolecules* 12(7):2456–2465
17. Junior de Menezes A, Siqueira G, Curvelo AAS, Dufresne A (2009) Extrusion and characterization of functionalized cellulose whiskers reinforced polyethylene nanocomposites. *Polymer* 50(19):4552–4563

18. Marsyahyo E, Soekrisno, Rochardjo HSB, Jamasri (2008) Identification of ramie single fiber surface topography influenced by solvent-based treatment. *J Ind Text* 38(2):127–137
19. Munawar SS, Umemura K, Kawai S (2008) Manufacture of oriented board using mild steam treatment of plant fiber bundles. *J Wood Sci* 54(5):369–376
20. Lee TS, Choi HY, Choi HN, Lee KY, Kim SH, Lee SG, Yong DK (2013) Effect of surface treatment of ramie fiber on the interfacial adhesion of ramie/acetylated epoxidized soybean oil (AESO) green composite. *J Adhes Sci Technol* 27(12):1335–1347
21. Pal SK, Mukhopadhyay D, Sanyal SK, Mukherjee RN (1988) Studies on process variables for natural fiber composites—effect of polyesteramide polyol as interfacial agent. *J Appl Polym Sci* 35(4):973–985
22. Lu Y, Weng L, Cao X (2006) Morphological, thermal and mechanical properties of ramie crystallites—reinforced plasticized starch biocomposites. *Carbohydr Polym* 63(2):198–204
23. Alloin F, D'Aprè A, Kissi NE, Dufresne A, Bossard F (2010) Nano composite polymer electrolyte based on whisker or microfibrils polyoxyethylene nano composites. *Electrochimica Acta* 55(18):5186–5194
24. Kumar N, Siddesh Chincholia, Hegde PR, Shivagiria SY, Revanasiddappa M (2018) Synthesis and characterization of fly ash/wooden fiber reinforced epoxy resin polymer composite. *Mater Today: Proc* 5(1), Part 1:501–507
25. Pothnis JR, Ravikumar G, Joshi M, Akella K, Kumar S, Naik High NK (15 March 2012) Strain rate compressive behavior of epoxy LY 556: radial constraint effect. *Mater Sci Eng A* 538:210–218
26. Goda K, Asai T, Yamane T (2003) Development of ramie fiber reinforced biodegradable resin matrix composites by press forming and effect of chemical treatments. *Zairyo/J Soc Mater Sci Jpn* 52(10):1245–1252
27. Kimura T, Kurata M, Matsuo T, Matsubara H, Sakobe T (2004) Compression molding and mechanical properties of green-composite based on ramie/PLA non-twisted commingled yarn. *Zairyo/J Soc Mater Sci Jpn* 53(7):776–781
28. Alsina OLS, De Carvalho LH, Ramos Filho FG, D'Almeida JRM (2005) Thermal properties of hybrid lignocellulosic fabric-reinforced polyester matrix composites. *Polym Test* 24(1):81–85
29. Müssig J (2008) Cotton fibre-reinforced thermosets versus ramie composites: a comparative study using petrochemical- and agro-based resins. *J Polym Environ* 16(2):94–102
30. Lodha P, Netravali AN (2005) Characterization of stearic acid modified soy protein isolate resin and ramie fiber reinforced 'green' composites. *Compos Sci Technol* 65(78):1211–1225



# Effect of MgO Particulates on Dry Sliding Wear of Al LM13 Metal Matrix Composite



C. S. Ravindra Sagar, T. K. Chandrashekar and Batluri Tilak Chandra

**Abstract** Al LM13 alloy reinforced with MgO particulates of 0–10wt% in terms of 2wt% were developed by the stir casting technique and the prepared samples were characterized on the basis of microstructure, Brinell hardness, XRD, and SEM. The hardness test indicated increased hardness of the MMC as the MgO particulate percentage increased. Optical microscope studies indicate the MgO particulate distributed randomly in the Al LM13 matrix. The presence of MgO was also identified in XRD. The wear performance of Al-LM13/MgO composite was examined on pin-on-disk equipment. The experimental studies on the MgO particulate increased the wear rate and decreased proportionately indicating the active role of the MgO particulate in reducing the wear. SEM suggests the presence of adhesive and abrasive wear mechanism with evidence of transfer films. The development in the wear resistance is due to the presence of MgO particulates in the Al LM13 matrix alloy.

**Keywords** MgO particulate · Al-LM13 · Dry sliding wear

## 1 Introduction

MMCs are capable of attaining wear and mechanical properties owing to the existence of reinforcement. Aluminum which is less in weight, in various applications [1]. Wear decreases the effectiveness by collective material loss, utilization of fuel, and replacement of component; due to this, the wear behavior of MMCs is assigned and it is essential [2]. To study the behavior of wear of aluminum–silicon carbide, MMCs show the increasing wt% of SiC which decreases the weight of aluminum

---

C. S. R. Sagar (✉) · B. T. Chandra  
Department of Mechanical Engineering, Sri Siddhartha Institute of Technology, Tumkur 572105,  
Karnataka, India  
e-mail: [csravindrasagar19@gmail.com](mailto:csravindrasagar19@gmail.com)

T. K. Chandrashekar  
Department of Mechanical Engineering, Mangalore Institute of Technology, Moodabidre,  
Mangalore 574225, Karnataka, India

© Springer Nature Singapore Pte Ltd. 2020  
G. S. V. L. Narasimham et al. (eds.), *Recent Trends in Mechanical Engineering*,  
Lecture Notes in Mechanical Engineering,  
[https://doi.org/10.1007/978-981-15-1124-0\\_38](https://doi.org/10.1007/978-981-15-1124-0_38)

**Table 1** Al LM13 alloy chemical composition

Elements	Cu	Mg	Si	Fe	Mn	Ni	Zn	P	Sn	Ti	Al
wt%	0.83	1.2	12	1	0.5	1.5	0.5	0.1	0.1	0.2	Balanced

**Table 2** MgO particulate chemical composition

Appearance	White powder
Particulate size	5–8 $\mu\text{m}$
Solubility	Partly soluble in water
Molecular formula	MgO
Molecular weight	40.30
Density	3.70 g/cc
Melting point	2300 °C

[3]. Al7075/SiC developed by metallurgical technique its wear resistance improved [4]. The wear rate of MMC decreased with an increased wt% of SiC particulates [5].

From the above literature survey, the Al-LM13/MgO particulate composite is not explored extensively. Thus the present work focused on wear behavior of Al-LM13/MgO particulate composite produced through the stir casting technique.

## 2 Development of the Metal Matrix Composite

LM13 and MgO particulate chemical composition is as shown in Tables 1 and 2.

In the stir casting technique, the LM13 alloy is heated to a temperature of 750 °C in a crucible, then the particulate is at 400 °C; it is preheated and agitated at the rapidity of 545 rpm for a period of 15 min and the MMC is discharged to die.

## 3 Results and Discussion

### 3.1 Optical Microstructure Studies

Microstructural studies show that the conformation of porosity is negligible in both the LM13 and composite shows the even scattering of MgO in MMC (Figs. 1 and 2)

**Fig. 1** Al LM13 (as-cast) alloy

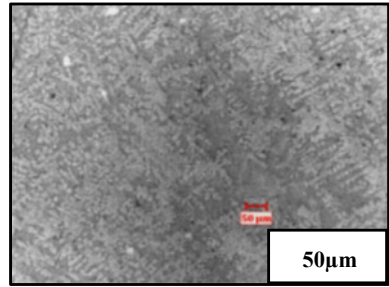
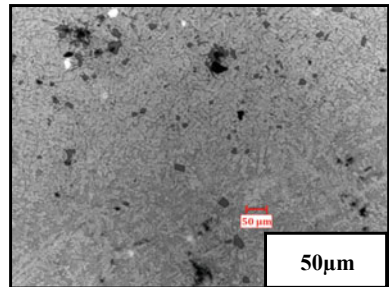


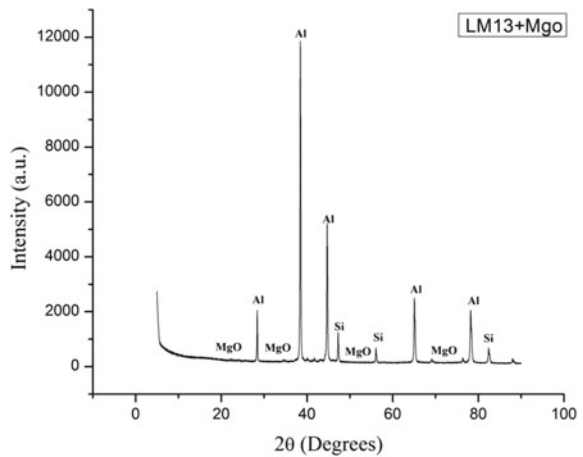
**Fig. 2** Al-LM13/MgO composite



### 3.2 XRD Studies

Figure 3 shows the XRD pattern of Al-LM13/MgO composite, the graph shows the diffraction pattern belonging to Al LM13 matrix and MgO particulate. The XRD analysis shows the presence of aluminum, silicon, and magnesium oxide. There is no presence of any intermediate phase in the analysis of the composite.

**Fig. 3** XRD Al-LM13/MgO composite



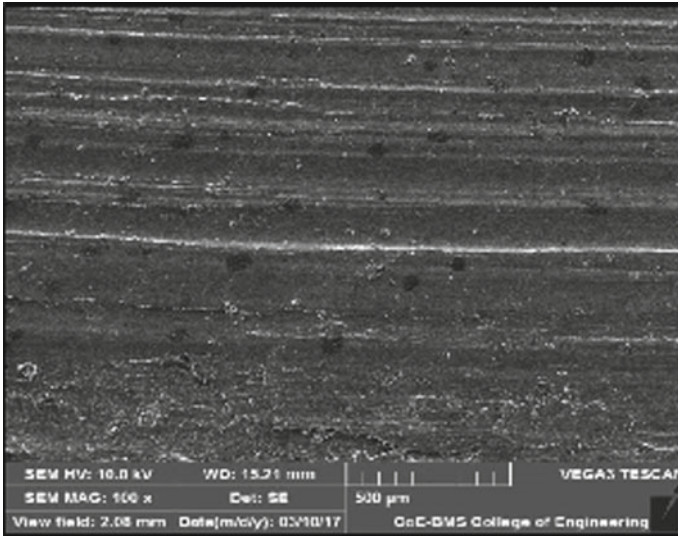


**Fig. 4** SEM of Al LM13 (as-cast) alloy

### ***3.3 Scanning Electron Microscope Studies***

The wear of Al-LM13/MgO was enhanced due to the existence of MgO particulate in Al LM13 matrix alloy; the wear that occurs in the MMC is owed to plastic deformation; hard MgO particulates and gouging will crush the minute hard particulates and forms a tiny sub-external layer designated as MML which safeguard the alloy [6] (Figs. 4 and 5).

### ***3.4 Brinell Hardness and Wear Behavior***

Figure 6 shows that as the wt% of the MgO particulate reinforcement increases, the hardness of the composite improves significantly owing to the existence of hard reinforcement [7].

Figures 7, 8, and 9 show that Al LM13 suffers from the highest wear rate as compared to other reinforced composites; it can be referred that the wear rate decrease more or less linearly as the percentage of the MgO particulate is increased in the Al LM13 matrix. This result is in agreement with the experimental data by Tang et al. [8]; further, the addition of the particulate increases the wear conflict of alloy decreases in wear rate suggests a strong bond strength in between Al LM13 matrix and MgO particulates. MgO particulates are embedded in the Al LM13 matrix and have a relatively higher hardness as compared to the matrix alloy; consequently, most of the load applied on the MMC is sustained by the hard MgO particulates leading to

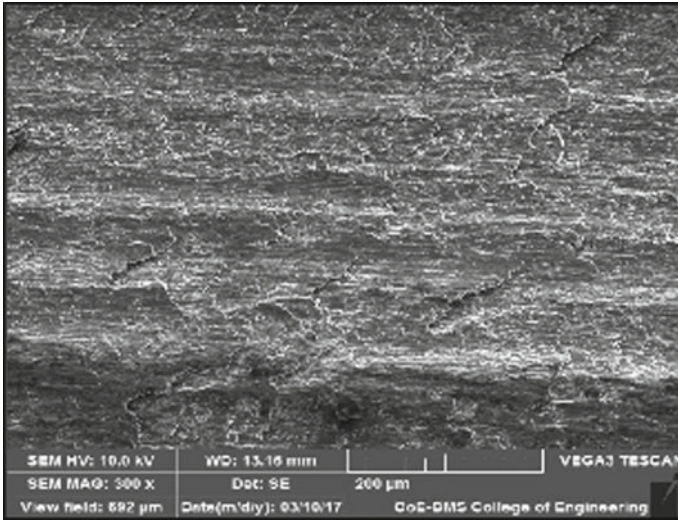


Fig. 5 SEM of Al-LM13/MgO composite

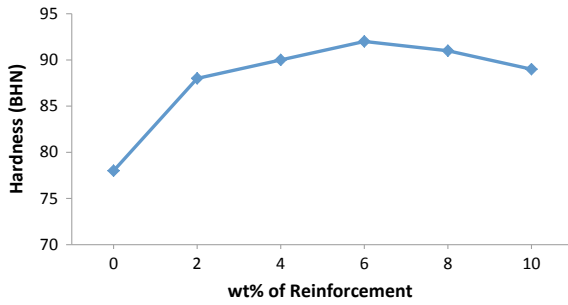


Fig. 6 Brinell hardness at different wt% of reinforcement for Al LM13 and its composite

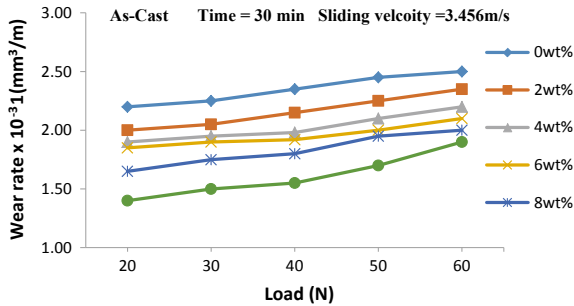
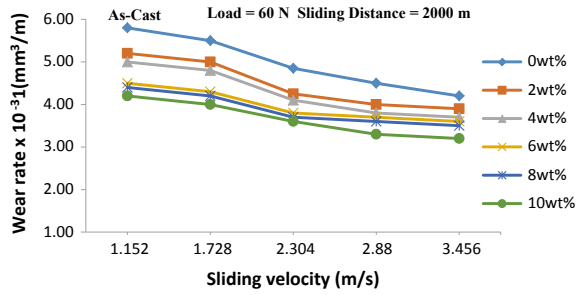
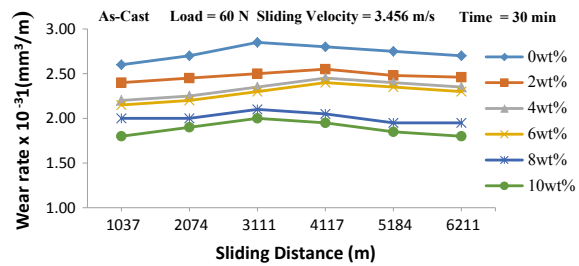


Fig. 7 Wear rate of Al LM13 and its composite for various applied load in the as-cast condition

**Fig. 8** Wear rate of Al LM13 and its composite for various sliding velocity in as-cast condition



**Fig. 9** Wear rate of Al LM13 and its composite for various sliding distance in as-cast condition



reducing the wear percentage in the matrix. Thus, more stress is developed by MgO particulates during dry sliding wear resulting in a decrease in the wear rate of the Al LM13 matrix.

### 4 Conclusion

1. Al LM13 alloy and its MMC have been successfully developed with uniformly dispersed MgO particulate using the stir casting technique.
2. Microstructure clearly exposes the even scattering of the MgO particulate in the Al LM13 matrix alloy.
3. The hardness of MMCs increases significantly with increase in the MgO particulate reinforcement.
4. Wear rate of Al LM13 and its composite declines with increase in the reinforcement wt% and also by increasing the applied load the composite wear rate increases, by varying with sliding velocity the wear percentage of the composite declines when sliding distance is constant and percentage of grooving in worn-out layer of MMC is reduced when the reinforcement wt% increases indicating lesser removal of the material.

## References

1. Altunpak Y, Akbulut H (2009) Effects of aging heat treatment on machinability of alumina short fiber reinforced LM 13 aluminum alloy. *Int J Adv Manuf Technol* 43(5):449–454
2. Hayajneh MT, Hassan AM, Al-Omari MA (2001) The effect of graphite particles addition on the surface finish of machined Al-4 wt% Mg alloys. *J Mater Eng Perform* 10(5):521–525
3. Sathyabalan P, Selladurai V, Sakthivel P (2001) ANN based prediction of effect of reinforcements on abrasive wear loss and hardness in a hybrid MMC. *Am J Eng Appl Sci* 2(1):50–53
4. Venkataraman B, Sundararajan G (2000) Correlation between the characteristics of the mechanically mixed layer and wear behaviour of aluminium, Al-7075 alloy and Al-MMCs. *Wear* 245(1–2):22–38
5. Das S (2004) Development of aluminium alloy composites for engineering applications. *Trans Indian Inst Met* 57:325–334
6. Savaskan T, Bican O, Alemdag Y (2009) Developing aluminium-zinc based a new alloy for tribological applications. *J Mater Sci* 44:1969–1976
7. Pai BC, Ray S, Prabhakar KV, Rohatgi PK (1976) Fabrication of aluminium alumina (magnesia) particulate composites in foundries using magnesium additions to the melts. *Mater Sci Eng* 24:31
8. Tang F, Wu X, Ge S, Ye J, Zhu H, Hagiwara M, Schoenung JM (2008) Dry sliding friction and wear properties of B4C particulate-reinforced Al-5083 matrix composites. *Wear* 264:555–561. <https://doi.org/10.1016/j.wear.2007.04.006>

# Flexural Fracture Analysis on 2D and 3D Weaved Carbon–Silicon Carbide Composites



S. Sapthagiri and S. Nagakalyan

**Abstract** Propelled materials, for example, constant fiber-fortified artistic grid composites offer huge improvements in an assortment of properties when contrasted with their mass, solid partners, etc. These properties incorporate essentially the ductile pressure, flexural stress, and crack parameters. Anyway to date, there are not really any logical examinations that gave an account of carbon fiber based propelled earthenware composites where SiC is utilized as the lattice. The present work is an endeavor to draw out the flexural fractural quality properties alongside a nitty-gritty examination of the crack conduct of 2D and 3D woven carbon ceaseless fiber strengthened (silicon carbide) ceramic–matrix composite (CFCC) materials. The crack propagation conduct has been dissected in two symmetrical indents and the introduction and its esteem are available in this paper.

**Keywords** Ceramic–matrix composite · Flexural strength · Fracture behavior · Three-point bend test

## 1 Introduction

Normally, earthenware frameworks are the conspicuous decision for high-temperature applications. High modulus of flexibility and low pliable strain, which most earthenware production have, that have joined to make the disappointment of endeavors add fortifications to acquire quality enhancement. The utilization of support with high modulus of versatility may deal with the issue to some degree and present pre-worrying of the fiber in the earthenware grid is as a rule progressively turned to as an alternative. At the point when earthenware production has a higher

---

S. Sapthagiri

Department of Mechanical Engineering, Geetanjali College of Engineering and Technology, Hyderabad, India

S. Nagakalyan (✉)

Department of Mechanical Engineering, Guru Nanak Institutions Technical Campus, Hyderabad, India

e-mail: [kalyan502@gmail.com](mailto:kalyan502@gmail.com)

© Springer Nature Singapore Pte Ltd. 2020

G. S. V. L. Narasimham et al. (eds.), *Recent Trends in Mechanical Engineering*,

Lecture Notes in Mechanical Engineering,

[https://doi.org/10.1007/978-981-15-1124-0\\_39](https://doi.org/10.1007/978-981-15-1124-0_39)



warm extension coefficient than fortification materials, the resultant composite is probably not going to have a prevalent dimension of solidarity. All things considered, the composite will create quality inside earthenware at the season of cooling bringing about miniaturized scale breaks reaching out from fiber to fiber inside the framework. Small scale breaking can result in a composite with rigidity lower than that of the framework.

The flexural quality speaks to the most elevated pressure experienced inside the material at its snapshot of the crack. Flexural Testing is commonly done in a three-point and four-point stacking frameworks. In three-point stacking, at the purpose of stacking, the best surface of the example is put in a condition of pressure while the base surface is in strain. Since the rigid qualities of earthenware production are around one-tenth of their compressive qualities and since break happens on the elastic example confront, the flexure test is a sensible substitute for the malleable test for pottery. Stress is processed from the example thickness, the bowing minute, and the snapshot of idleness of the cross section.

## 2 Fabrication of C–SiC Composite

The C–SiC composite was made by the liquid silicon invasion (LSI) process. This procedure comprises three organizes as shown. Starting with a Carbon Fiber Reinforced Clay (CFRC) made of a coal tar pitch with high carbon content, a green-body preform is made. This preform is then pyrolyzed under the latent climate at temperatures more prominently 900 °C, changing over the CFRC into a higher permeable carbon–carbon (C–C) composite. In the last advance, the permeable material is penetrated with fluid silicon under vacuum to produce the last C–SiC clay. The liquid silicon invasion (LSI) process offers numerous potential focal points, for example, a single-step process, low handling temperature, and close net-shape preparing. Be that as it may, the procedure has a few constraints as the span of the examples are restricted to basic shapes, and the examples must be hot-squeezed at high temperatures, close to 1900 °C, which causes debasement of fortifications.

### 2.1 Specimen Preparation

The indents with various square root radii were presented by methods for ISO-met low-speed cutting saw and Electric Discharge Machine (EDM).

The ISO-met low-speed cutting saw is an exactness separating saw intended for cutting different sorts of materials with negligible distortion. The ISO-Met low speed saw was utilized for removing indents with lower root radii utilizing 0.15 mm and 0.3 mm thick jewel wafer edges.

The Electric Release Machine has a metallic wire as a cutting device. A start is produced between the cutting device and the example which dissolves the ideal

bit of the example and evacuates it. The slicing device was customized to move in characterized ways for evacuating the material. The EDM was utilized for removing indents with bigger root radii of 1 mm and 3 mm.

Delta TM 35  $x - y$  profile projector was utilized for estimating the components of the score. The examples were set on the phase of the projector which at that point anticipated a picture of the example on a bigger screen. The split length and score root span were estimated from the screen. Utilizing fitting amplification, the genuine split length and root sweep were determined.

### 2.2 Specimen Configuration

The example arrangement was allowed by the E 399: the Single-Edge Notched Beam (SENB) example as shown in Fig. 1. The crack strength assessment is done for the most part using the Single-Edge Notched Beam (SENB) example. They are for the most part weakness pre-broken with the goal that the split length/width proportion lies somewhere in the range of 0.45–0.55. This guarantees that the key measurements ( $a$ ,  $B$ , and  $W - a$ ) are commonly roughly equivalent. In any case, for pottery and their composites, the exhaustion pre-splitting is not important.

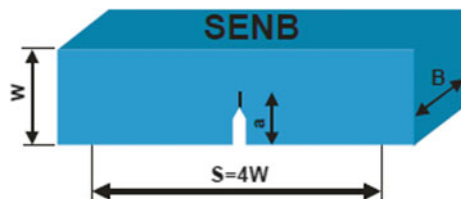
To ensure that the specimen fractures under nominally elastic conditions, i.e., the plastic zone must be small compared to the specimen cross section: ASTM recommends the following limitations on the specimen dimensions

$$B, a, (W - a) \geq 2.5 (K_{IC}/\sigma_y)^2; \quad 0.45 \leq (a/W) \leq 0.55, \text{ and } (P_{\max}/P_Q) \leq 1.1 \tag{1}$$

where “ $B$ ” is the specimen thickness, “ $a$ ” is the crack length, and “ $W$ ” is the specimen width. If the above conditions are satisfied, then the  $K_{IQ}$  values obtained to give the plane strain fracture toughness  $K_{IC}$  of the material.

The initial selection of specimen dimensions, from which valid  $K_{IC}$  values will be obtained, may be based on an estimated value of  $K_{IC}$ .  $K_{IC}$  can be estimated on the basis of experience with similar materials or by employing various empirical correlations with other types of notch toughness such as  $CVN$  values. Alternatively, the ratio of yield strength to Young’s modulus,  $\sigma_y/E$ , can also be employed.

**Fig. 1** A schematic of Single-Edge Notched Beam specimen with dimensional specifications



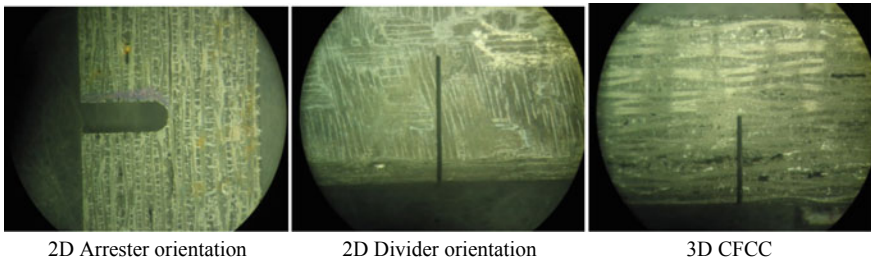


Fig. 2 Notch profile under stereomicroscope

### 3 Experimentation Summary

All the fracture toughness tests were led on a PC controlled, servo water-powered INSTRON 8801 test framework using a self-articulating three-point twist installations of the INSTRON 5500 test framework. The tests were led at encompassing temperature (23 °C) and in research facility air environment. The indented examples were stacked in slope control at a consistent inclined rate of 0.5 mm/min.

The test method includes three-point twist stacking or stick stacking of scored examples. Load versus uprooting information of the material is naturally gotten from the testing machine. Secant lines with inclined at 5% not exactly the flexible areas were gotten on the bends for assurance of  $P_Q$ . Contingent upon the material and the kind of bend obtained, the  $P_Q$  esteem is acquired. The proportion of  $P_{max}/P_Q$  must be guaranteed to be under 1.1. The restrictive esteem  $K_Q$  is then determined from this heap using conditions that have been set up based on flexible pressure examination.  $K_Q$  meets all requirements to be  $K_{IC}$  if previously mentioned conditions are fulfilled. Score Profile under a stereomicroscope of three distinct examples is shown in Fig. 2.

## 4 Result and Discussion

### 4.1 Flexural Strength

Flexural tests in three-point bend loading were led on examples of rectangular cross-sectional territory with a settled range length of 40 mm. For each case (3D, 2D crack arrester, and 2D crack divider), two examples were tried and the information acquired was exposed to the measurable investigation. The heap uprooting information got for flexural quality assessment of 3D, 2D crack arrester, and 2D crack divider introductions have been shown in Figs. 3, 4, and 5 separately and the example subtleties are given in Table 1.

The tensile stress is for the most part in charge of the disappointment of the example and not compression. The diagrams display a progressive increment in the

**Fig. 3** Load versus Displacement, 3D CFCCs

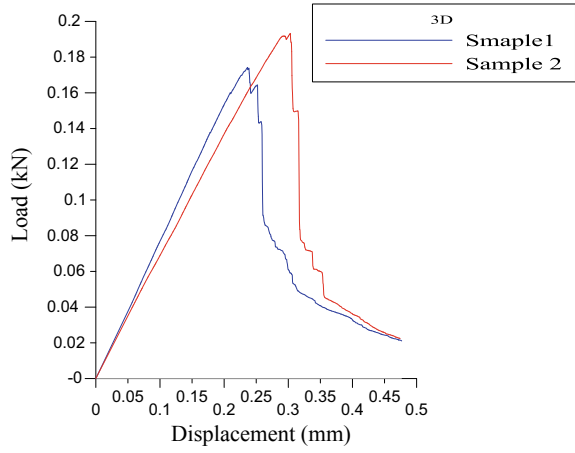


**Fig. 4** Load versus Displacement, 2D CFCCs Crack Arrester Orientation

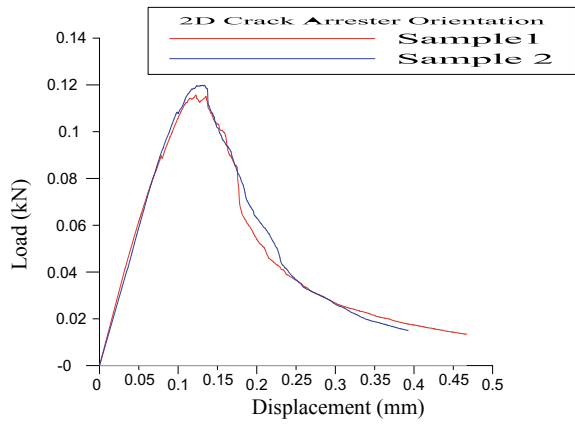


**Fig. 5** Load versus Displacement, 2D CFCCs Crack Divider Orientation

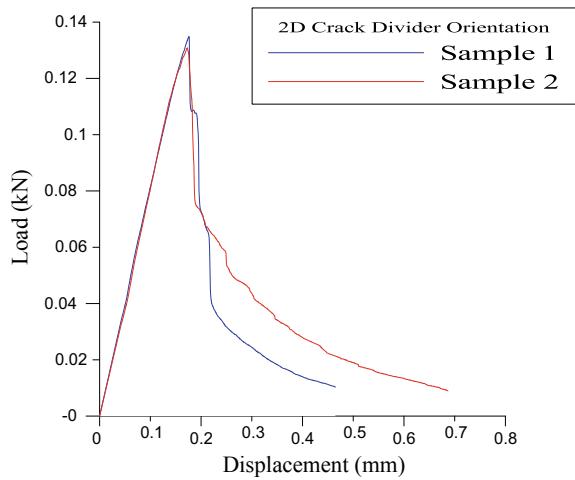


**Table 1** Specimen details

Sample Id	Span length, S (mm)	Width, b (mm)	Thickness, d (mm)
<i>2D Crack Arrester Orientation CFCCs</i>			
1.	40	13.64	4.03
2.	40	13.85	4.15
<i>2D Crack Divider Orientation CFCCs</i>			
1.	40	6.68	5.01
2.	40	6.83	5.01
<i>3D CFCCs</i>			
1.	40	7.85	3.53
2.	40	6.95	3.50

heap alongside an expansion in relocation up to an explicit point and afterward demonstrate a lofty decline with the falling slant. The progressive increment in the flexible zone is because of the nearness of filaments opposite the heading of break engendering. This is trailed by the little degree of quick fall in the worry with a further increment in the relocation. The precarious fall in load is trailed by a steady decline with relocation. This area shows the shear method of disappointment. In this locale, the split spreads through the framework and this prompts the advancement of “T” and “L” breaking. Right off the bat, a gathering of strands at the surface, where the greatest pressure is experienced takes an interest in the heap conveying stage. At the point when the heap starts to expand, a couple of more packages of strands participates and by this stage, the main heap of filaments is totally worried. The sudden fall in load begins when the principal heap of filaments starts to break/come up short and in this way this split proliferation is completed to alternate packs of strands.

## 4.2 Flexural Strength Evaluation

The maximum tensile stress (**Flexural strength**) of the composite material, (parallel to the fibers) on the outermost surface is given by

$$\sigma_f = (3P_{\max}S)/(2bd^2) \quad (2)$$

where “P” is the load applied, “S” is the span length, “b” is the width of the specimen, and “d” is the thickness of the specimen (Table 2).

It was plainly seen from the table that 3D situated CFCCs have **3.96** occasions higher flexural quality when contrasted with the 2D CFCCs (crack arrester introduction) [1]. This is credited to the way that in 3D CFCCs, the carbon strands organize ties the SiC-network all the more widely and successfully contrasted with 2D CFCCs.

**Table 2** Flexural strength measurements

Sample Id	P <sub>max</sub>	L (mm)	B (mm)	D (mm)	Flexural strength (MPa)	Mean flexural strength (MPa)
<i>2D CFCCs Crack Arrester Orientation</i>						
1.	115.5	40	13.64	4.03	31.27355	30.7
2.	119.8	40	13.85	4.15	30.14003	
<i>2D CFCCs Crack Divider Orientation</i>						
1.	134.9	40	6.68	5.01	48.25767	47.0
2.	130.8	40	6.83	5.01	45.77076	
<i>3D CFCCs</i>						
1.	174.2	40	7.85	3.53	106.9	121.5
2.	193.3	40	6.95	3.50	136.2	

This is on the grounds that in 3D CFCCs, the 2D carbon fiber layers are interconnected by sewing them a third way. This outcome is more grounded holding among network and the fortification in 3D CFCCs. It is additionally observed that the flexural quality of the 2D split divider introduction is **1.53** occasions higher than the 2D crack arrester introduction. This is on the grounds that in the divider introduction, the carbon strands are longitudinally situated while in the arrester introduction, the carbon filaments are arranged in transverse way. As the longitudinally arranged strands grant more opposition than the transverse filaments, the flexural quality of 2D crack divider is higher than the 2D split arrester (Fig. 6).

It can be clearly seen that 3D CFCCs exhibit a high flexural strength than 2D CFCCs.

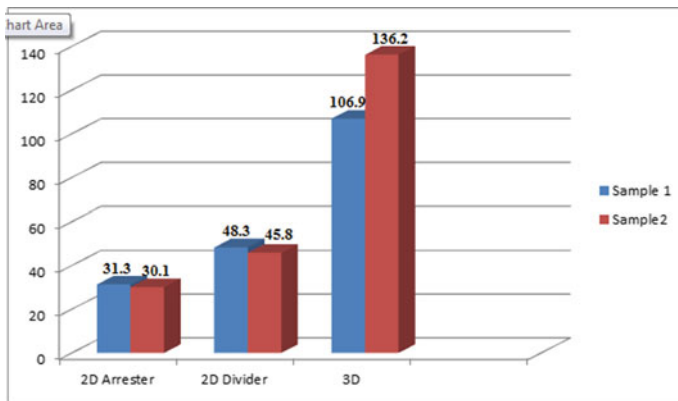


**Fig. 6** Flexural strength of 2D Crack Arrester, 2D Crack Divider, and 3D CFCCs

### 4.3 Fracture Toughness

The load–displacement data obtained for **Fracture Toughness** evaluation of 3D, 2D crack arrester, 2D crack divider orientations are shown in Figs. 3, 4, and 5, respectively. The specimen details of 3D, 2D crack arrester, 2D crack divider orientations are shown in Tables 3, 4, and 5, respectively [2, 3].

It is clearly observed from Fig. 7 that the heap relocation bends for all the 3D CFCCs tests, the heap at first increments directly with removal. This relates to the

**Table 3** Specimen details of 3D CFCCs

Sample Id	W (mm)	B (mm)	a (mm)	$2\rho$ (mm)	a/W
1.	6.12	3.50	2.13	0.16	0.35
2.	6.93	3.53	3.65	0.22	0.53
3.	6.95	3.53	3.71	0.20	0.53
4.	7.30	3.51	4.50	0.21	0.62
5.	6.50	3.54	2.97	0.32	0.46
6.	6.68	3.49	3.61	1.28	0.54
7.	6.51	3.50	3.32	3.65	0.51

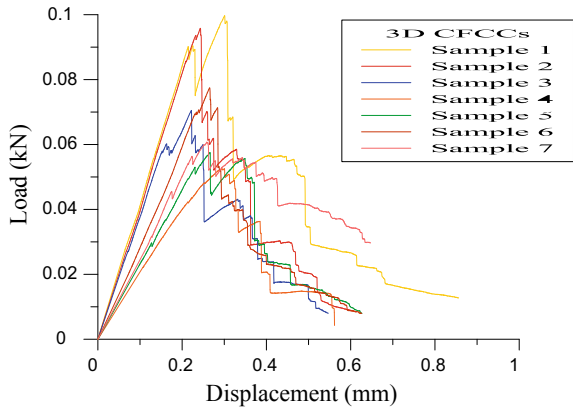
**Table 4** Specimen details of 2D Crack Arrester CFCCs

Sample Id	W (mm)	B (mm)	a (mm)	$2\rho$ (mm)	a/W
1.	13.6	4.07	4.54	0.20	0.33
2.	13.6	4.03	6.33	0.19	0.47
3.	13.6	4.03	6.50	0.22	0.41
4.	13.6	4.02	6.91	0.20	0.51
5.	13.6	4.04	7.33	0.31	0.54
6.	6.25	2.64	3.14	1.21	0.50
7.	7.08	2.64	3.51	1.33	0.50
8.	6.31	2.6	3.02	3.59	0.48
9.	6.88	2.6	3.40	3.70	0.49

**Table 5** Specimen details of 2D Crack Divider CFCCs

Sample Id	W (mm)	B (mm)	a (mm)	$2\rho$ (mm)	a/W
1.	13.89	3.95	4.57	0.16	0.33
2.	13.76	3.97	7.01	0.16	0.509
3.	13.70	4.01	7.83	0.31	0.57
4.	13.88	4.57	7.04	0.21	0.507
5.	13.88	4.67	7.21	0.28	0.52

**Fig. 7** Load versus Displacement, 3D CFCCs



phase in which the example to a great extent encounters elastic stresses. In this area, the material displays the quality of the composite which is ascribed to a great extent because of the nearness of strands and a minor commitment of the matrix. Pursued by this stage, stable split augmentation happens. This is reflected in nonlinear increase in load with displacement. This stage is trailed by an observable soak drop in load with a further increment in uprooting demonstrating mode I disappointment. This is because of the disappointment of fiber packs at the indenting tip. The further increment in load is because of the opposition development in the example in light of the worrying of fresher filaments.

The load-bearing capacity of samples of Figs. 8 and 9 are noticeably different. This is because; the specimen width and thickness of Fig. 9 samples are nearly half of Fig. 8 samples and from Fig. 10, it is evident that the load initially increases linearly with displacement in all the cases. This corresponds to the stage in which the specimen largely experiences elastic stresses. Followed by this stage, crack extension takes place. This is reflected in nonlinear increase in load with displacement followed by

**Fig. 8** Load versus Displacement, 2D CFCCs Crack Arrester Orientation

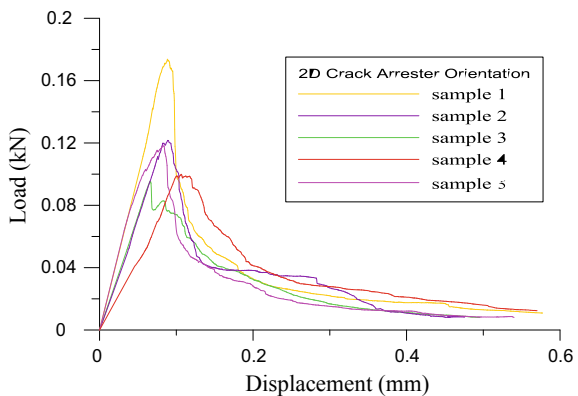




**Fig. 9** Load versus Displacement, 2D CFCCs Crack Arrester Orientation

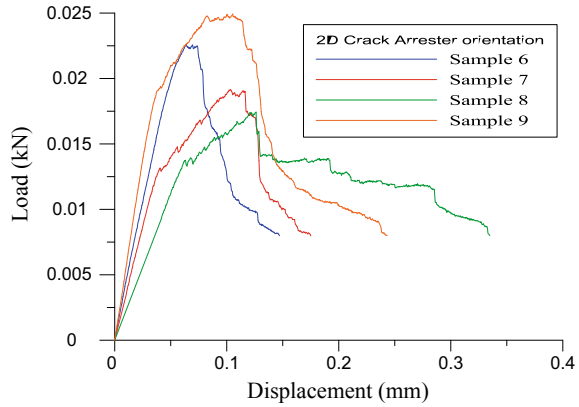
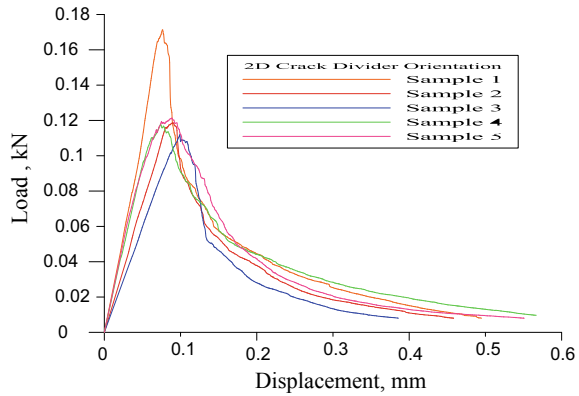


**Fig. 10** Load versus Displacement, 2D CFCCs Crack Divider Orientation



noticeable drop in load with further increase in displacement. The load-displacement curves show distinctly different characteristics at this stage of crack extension in all the orientations.

The contingent fracture toughness ( $K_Q$ ) of 3D and 2D weaved  $C_f$ -SiC CFCC material was assessed in the split arrester and break divider introductions as indicated by the ASTM standard E 399. Figures 7, 8, 9, and 10 demonstrate the essential information of the heap variety with relocation. From the previously addressed literature, it gives the subtleties of the examples and the information got from these fracture toughness tests [4]. The estimations of  $K_{max}$  and  $K_Q$  determined for each test are additionally recorded in these tables. These information demonstrate that the material displays valid  $K_{max}/K_Q$  values ( $<1.1$ ) for a few examples, indicating stable break augmentation. Along these lines, just these qualities are considered to yield legitimate  $K_{IC}$ . Under these conditions, the material displays altogether higher break sturdiness esteem in the crack divider introduction when contrasted with the crack arrester introduction. Under such conditions, the CFCC material shows a fundamentally high crack sturdiness esteem in 3D weaved introduction. A normal estimation

of contingent crack strength ( $K_Q$ ) 3.93 MPa√m is gotten for 3D CFCCs. A normal estimation of restrictive break sturdiness ( $K_Q$ ) for 2D weaved split divider introduction is observed to be 1.82 MPa√m though the contingent break toughness ( $K_Q$ ) of 2D weaved crack arrester introduction is observed to be 1.52 MPa√m. This study reveals that the conditional fracture toughness of 3D CFCCs is 2.58 times of 2D CFCCs crack arrester orientation. This is because of the higher flexural strength of 3D CFCCs. The conditional fracture toughness of 2D CFCCs crack divider orientation is 1.2 times of 2D CFCCs crack arrester orientation. Amid the three-point twist trial of CFCCs, as the heap is connected continuously, a procedure zone frames at the leader of the crack tip. Higher the measure of this procedure zone, higher is the opposition of the material to crack along these lines, and higher is the fracture toughness of the material. The disappointment in crack divider introduction happens basically through the mode I along these lines bringing about the bigger procedure zone. The disappointment in crack arrester introduction happens basically through mode II in this manner bringing about the littler procedure zone. Subsequently, the fracture toughness estimation of split divider introduction is higher than that of the crack arrester introduction.

#### 4.4 $K_{IC}$ Validation

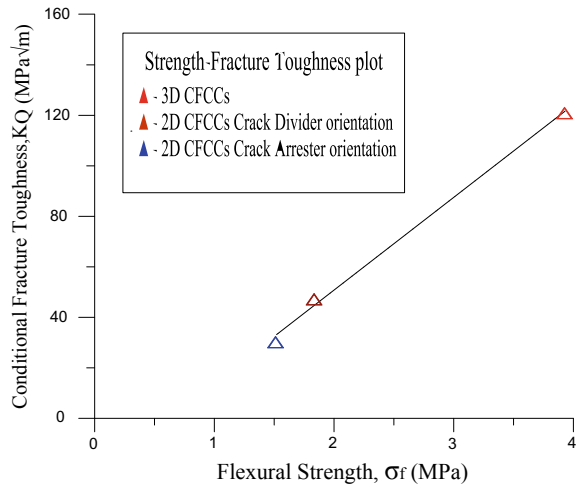
**3D CFCCs:** The CFCCs material exhibits a significantly high fracture toughness value in 3D weaved orientation. It can be seen from Table 2 that the specimen numbers of 5 and 7 are considered for  $K_{IC}$  because they are satisfying the  $K_{IC}$  validation criteria. An average value of  $K_{IC}$  3.36 MPa√m (corresponding to the  $a/W$  ratios of 0.46 and 0.509) is obtained for **3D CFCCs**.

**2D CFCCs:** The  $K_Q$  values derived from specimens 4 and 5, corresponding to  $a/W$  ratios 0.507 and 0.52, in the 2D weaved crack divider orientation are considered to yield valid  $K_{IC}$ . It can be seen from Table 3 that the specimen numbers of 4 and 5 are considered for  $K_{IC}$  because they are satisfying the  $K_{IC}$  validation criteria. An average value of plain strain fracture toughness ( $K_{IC}$ ) for 2D weaved **crack divider** orientation is found to be 1.50 MPa√m. In the 2D weaved crack arrester orientation, no sample satisfied all the conditions mentioned above for a valid  $K_{IC}$  test, so the conditional fracture toughness ( $K_Q$ ) is calculated for these samples.

#### 4.5 Strength–Fracture Toughness Correlation

It is observed from Fig. 11 that fracture toughness increases as the strength of material increases. From this, it is evident that CFCCs follow Linear Elastic Fracture Mechanics (LEFM). The corresponding relation between fracture toughness and strength is given by  $K_I = 36.72 * \sigma_f - 22.64$  [5, 6].

**Fig. 11** Correlation of strength and fracture toughness plot



#### 4.6 Effect of Notch Root Radius ( $\rho$ ) on Fracture Toughness

The apparent fracture toughness ( $K_{IQ}$ ) is a function of the notch root radius. There exist a critical notch root radius ( $\rho$ ) above which  $K_{IQ}$  varies linearly with  $(\rho)^{0.5}$  and below this critical value,  $K_{IQ}$  is independent of  $\rho$  or in other words it is invariant, that is, it is solely a material property. But, in our study, contradictory results are obtained for some samples giving irregular trends. This may be due to the damage occurred to the samples while cutting the notches through EDM wire cut machine. A spark generated between the cutting wire and the specimen causes the melting of sample and due to this, there may be damage to the fiber bundles present at the notch tip resulting in irregular fracture toughness values.

## 5 Conclusions

3D-oriented CFCCs have 3.96 occasions higher flexural quality when contrasted with the 2D CFCCs arrester orientation in view of a progressively broad and viable system of carbon fibers. Flexural quality of 2D crack divider orientation is 1.53 occasions higher than the 2D crack arrester introduction because of longitudinally situated fibers in the crack divider orientation. Flexural quality of the 2D crack arrester introduction is low as a result of transverse situated fibers. The restrictive fracture toughness ( $K_Q$ ) of 3D CFCCs is 2.58 occasions of 2D CFCCs-crack arrester orientation. This is a result of the higher flexural quality granted to 3D CFCCs via carbon fibers. The restrictive fracture toughness ( $K_Q$ ) of 2D CFCCs-crack divider orientation is 1.2 occasions of 2D CFCCs-crack arrester orientation in view of expansive process zone estimate in crack orientation. Plain strain fracture toughness ( $K_{IC}$ ) of 3D CFCCs

and 2D crack divider introduction are  $3.36 \text{ MPa}\sqrt{\text{m}}$  and  $1.50 \text{ MPa}\sqrt{\text{m}}$ . The chart between flexural strength and restrictive fracture toughness is observed to be straight which demonstrates that CFCCs pursue Linear Elastic Fracture Mechanics (LEFM).

It saw from the outcome and discourses that 3D Situated CFCCs has more strength than both the introductions of 2D CFCCs.

**Acknowledgements** We heartily thank the management of Geethanjali College of Engineering and Technology, Hyderabad, for their cooperation and support related to this research work as well as technical staff members who have directly and indirectly extended help to carry out the experimental work.

## References

1. Eswara Prasad N, Kumari S, Kamat SV, Vijaykumar M, Malakondaiah G (2004) Fracture behaviour of 2D-weaved, silica–silica continuous fibre-reinforced, ceramic–matrix composites (CFCCs). *Eng Fract Mech* 71:2589–2605
2. Eswara Prasad N, Dakshinamurthy K, Kamat SV, Vijayakumar M (2005) Flexural behaviour of 2d silica–silica continuous fibre-reinforced, ceramic-matrix composites. *Trans Indian Inst Met* 58:883–895
3. Ramavath P, Mahender V, Hareesh US, Johnson R, Kumari S, Eswara Prasad N (2011) Fracture behaviour of chemical vapour deposited and hot isostatically pressed zinc sulphide ceramics. *Mater Sci Eng A* 528:5030–5035
4. Dutta A, Eswara Prasad N, Deepak, Bhandari B (2012) National Metallurgists' Day—Annual Technical Meet of Indian Institute of Metals. <https://www.researchgate.net/publication/264039464>
5. Anderson TL (2005) *Fracture mechanics*, 3rd edn. Taylor & Francis, Boca Raton
6. Broek D (1986) *Elementary engineering fracture mechanics*, 4th edn. <https://doi.org/10.1007/978-94-009-4333-9>

# Characterization of Aluminium Alloy 6063 Coated Over Mild Steel by Aluminization Process



B. Vijaya Kumar and K. John William

**Abstract** The main objective of present study is to see the feasibility of aluminum alloy deposition over mild steel using aluminization technique to improve the corrosion resistance by developing an economically feasible technique. Aluminum alloy coating has been done by dipping the mild steel in hot liquid metal of aluminum alloy at above 800 °C for various time intervals; hot dipped mild steel rods were allowed to air cool. Coatings were characterized to observe the grains diffusion between coating and base metal, it is found that coating metal is diffused into mild steel surface and formed a corrugated grain profile that is facilitating interlocking between both surfaces and this is desired to improve bond strength. Hardness test and toughness test were conducted to observe the strength of the coating and found that coating strength is improved. This process assures a tight bond between the base metal and coating metal.

**Keywords** Aluminization · AA6063 · Mild steel (IS 2062) · Mechanical properties · Microstructure

## 1 Introduction

Surfacing is playing vital role to improve the corrosion resistance on iron alloys and wear resistance on ferrous and nonferrous alloys. There are many traditional surface coating techniques available [1]; apart from these techniques, aluminization is one of the best methods to deposit Aluminum alloys over Ferrous alloys to improve corrosion resistance. Aluminization is the process, in which Aluminum is melted above 800 °C and at that temperature Ferrous alloys are dipped in metallic liquid bath and kept for some time to diffuse the Aluminum into Iron. The Ferrous alloy is

---

B. V. Kumar (✉)

Department of Mechanical Engineering, Guru Nanak Institute of Technology, Ranga Reddy Dist., Ibrahimpatnam 501506, Telangana, India  
e-mail: [hodme.gnit@gniindia.org](mailto:hodme.gnit@gniindia.org)

K. J. William

TATA Consultancy Service, London, UK

© Springer Nature Singapore Pte Ltd. 2020

G. S. V. L. Narasimham et al. (eds.), *Recent Trends in Mechanical Engineering*,

Lecture Notes in Mechanical Engineering,

[https://doi.org/10.1007/978-981-15-1124-0\\_40](https://doi.org/10.1007/978-981-15-1124-0_40)

reaching to Austenitic Temperature due to which it allows or permits the Aluminum grains into Ferrous alloy grains by adjusting at intermolecular spaces. After few seconds or completion of the dipping time, depending upon the base metal character, it will be taken out from the liquid metal bath and allowed for air cooling, the air cooling starts from the temperature 730 °C to room temperature and the cooling takes place as per heat treatment cycle. In this study, an experiment was conducted using Mild Steel (IS 2062) by surface alloying with aluminum (AA 6063) through diffusion. Aluminum coating provides steel with excellent oxidation and corrosion resistance at elevated temperatures up to 1000 °C, and with reasonable scaling resistance [2].

Hot-dip aluminizing is also a kind of most widely used processes for coating steel with aluminum, to increase corrosion, and oxidation resistance as well as hardness [3]. The current study deals with the influence of process parameters on microstructure and microhardness of aluminized and diffused specimens. In aluminizing, the surface layer is impregnated with aluminum to the specified thickness in the temperature range of 600–1000 °C.

It gives greater wear resistance, hardness, and corrosion resistance. In order to find the suitable coating method for Aluminum alloys on all kinds of surfaces, a comparative study was conducted to conclude the best method. The results of this comparison are shown in Table 1. Based on the comparison, mild steel samples were chosen to dip in aluminum liquid bath [4].

**Table 1** Vickers microhardness values for different temperatures and time (with silica)

Load applied (gms)	Distance between indentation points in (mm)	Vickers microhardness values (Hv) For different temperatures and time		
		700 °C and 3 min	800 °C and 5 min	900 °C and 7 min
50	−0.7	172 Hv	172 Hv	167 Hv
50	−0.6	167 Hv	166 Hv	168 Hv
50	−0.5	170 Hv	175 Hv	175 Hv
50	−0.4	179 Hv	176 Hv	177 Hv
50	−0.3	611 Hv	671 Hv	719 Hv
50	−0.2	626 Hv	683 Hv	727 Hv
50	−0.1	630 Hv	729 Hv	730 Hv
10	0	354 Hv	401 Hv	401 Hv
10	0.1	78 Hv	73 Hv	67 Hv
10	0.2	75 Hv	71 Hv	68 Hv
10	0.3	74 Hv	70 Hv	69 Hv

## 2 Experimentation

Mild steel (IS 2062) was used as the substrate material. The sample of 12 diameter and 120 mm length was used. This was cut from 1 m rod and sent for turning and approximately 1 mm of layer is removed from the mild steel rod, Aluminum blocks. The specimen was thoroughly cleaned before aluminizing. Rinsing was carried out with water followed by acetone solution for 1 min and then dried. Mild steel rod of 12 mm diameter  $\times$  120 mm long specimen was taken. Then, it was sent for turning and approximately 1 mm is removed from 12 diameter rod. After turning process, the specimen rod was found to be 11.85 in diameter and 120 mm in length. Now the rods were rinsed with water followed with acetone solution then and dried. Aluminum blocks were melted in crucible by using furnace. At 660 °C, aluminum was melted and then we added degassing tablet to it, then aluminum got purified; waste gases were sent out and slag was floating up, we removed slag with strainer.

The same experiment was carried out but now in case II we have added silica to molten metal. Mild steel rod of 12 mm diameter  $\times$  120 mm long specimen was taken. Then, it was sent for turning and approximately 1 mm was removed from 12 diameter rod. After turning process, the specimen rod was found to be 11.85 in diameter and 120 mm in length. Now, the rods were rinsed with water followed with acetone solution then and dried. Aluminum blocks were melted in crucible by using furnace. At 660 °C aluminum got melted and then we added degassing tablet to it then aluminum got purified; waste gases were sent out and slag was floating up, we removed slag with strainer. Now, we started increasing the temperature of molten aluminum because as we added silica it will reduce the boiling point of the aluminum.

Then we added 10% of silica to molten aluminum and the temperature of molten aluminum got reduced. Now, the rod was dipped in molten aluminum, this mild steel specimen was then dipped in bath for 3 min at 700 °C and the mild steel specimen was stirred in liquid bath for effective coating over mild steel, after that the specimens were allowed to cool in air.

The same experiment was carried out for two times at different temperatures. Again mild steel specimen was taken and dipped in aluminum bath for time period of 5 min at 800 °C. The mild steel specimen was stirred in liquid bath for effective coating over mild steel, after that the specimen was allowed to cool in air. The same mild steel specimen was dipped in bath for time period of 7 min at 900 °C. The mild steel specimen was stirred in liquid bath for effective coating over mild steel, after that it was allowed to cool in air.


### 3 Characterization of Coating

The coating characterization is as follows; and after coating, the specimen rods were visualized and we got a smooth finish on rods that were at higher temperature and for more dip time. The list of pictures can be seen below. These are the visualized picture of aluminum coated rods without silica (Figs. 1, 2, 3, and 4).

#### Microstructure Test

The microstructural examination is carried out by putting well polished, properly etched, and dried samples on the base of the microscope. An appropriate combination


**Fig. 1** Aluminum coated rods with silica 3 min 700 °C

Dip time & Temperature	Aluminium coated rods without silica
3 min. 700°C	


**Fig. 2** Aluminum coated rods without silica 5 min 800 °C

Dip time & Temperature	Aluminium coated rods without silica
5 min. 800°C	

**Fig. 3** Aluminum coated rods without silica 7 min 900 °C

Dip time & Temperature	Aluminium coated rods without silica
7 min. 900°C	

**Fig. 4** Aluminum coated rods with silica 5 min 800 °C

Dip time & Temperature	Aluminium coated rods with silica
5 min. 800°C	



of objective and eyepiece of known magnification is selected to view the sample. The microscope is illuminated and the image of sample surface is focused [5]. Details of the surface vision are examined by either direct (eye) viewing or by taking a photograph to be analyzed later. The microstructural examination of metals and alloys is generally accomplished for the following purposes.

Observation of grain growth, study of grain boundaries and grain shapes, study of phases present in material, study of crystal irregularities, to reveal microdefects like inclusions, microcracks, etc. determination of compositions and distribution of metals in an alloys, study of the heat treatment, and other process on mechanical properties of metals/alloys [5]. After aluminizing process, the sample was selected and cut to a suitable size of 1 inch with the help of band saw. After this, the samples were mounted by using polymeric material catalyst and resin. The mounting process was completed for an hour by curing process. This mounted sample was polished by using standard metallurgical process [6] (Figs. 5 and 6).

### Micro Hardness Test

Microhardness test was carried out on the Aluminized test samples across the interface using Vicker's microhardness tester. The test was carried out at a load of 500 gms. Samples are prepared as per the standard mounting methods as prepared for microstructural analysis.

**Fig. 5** Mounting samples of aluminum coating rods (with silica)

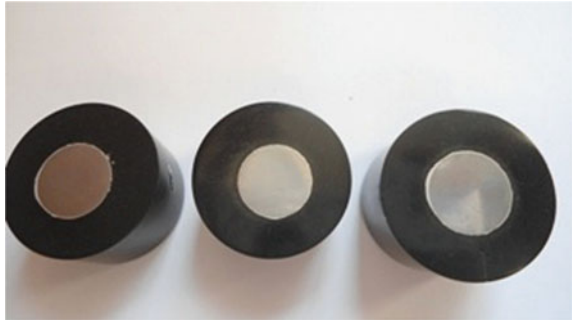


**Fig. 6** Mounting samples of aluminum coating rods (without silica)



## 4 Results and Discussion

### Visualization

The coating was absorbed with smooth surface finish, as the machining is not required for the application of the components. Two different experiments were carried out and mild steel specimen rods were dipped in aluminum alloy with silica and without silica. When compared to first sample, without silica the coating was not so uniform and we did not get shining on rods, but when silica added specimen rods were observed extra shining could be seen on rods with good surface finish.

### Microstructure

The mild steel coated specimen rods were absorbed and the aluminum alloy has got refined grains size with slight corrugated shape on mild steel and it is reported that diffusion has been taken place due to the higher temperature. It is also absorbed that ferrite flakes have been formed on mild steel surface. Six samples were given for testing, in which three specimen rods samples were aluminum coated mild steel rods (with and without adding of silica). Sample 1—Aluminum coated mild steel specimen rods without silica at 700 °C and 3 min dip time, microstructure shows the growth of ferrite at interface is less. Sample 2—Aluminum coated mild steel specimen rods without silica at 800 °C and 5 min dip time, microstructure shows the growth of ferrite at interface is more. Sample 3—Aluminum coated mild steel specimen rods without silica at 900 °C and 7 min dip time, microstructure shows the growth of ferrite at interface is more. Sample 4—Aluminum coated mild steel specimen rods with silica at 700 °C and 3 min dip time, microstructure shows with silica growth of ferrite at interface is less and uniform ferrite and pearlite structure have been formed. Sample 5—Aluminum coated mild steel specimen rods with silica at 800 °C and 5 min dip time, microstructure shows the growth of ferrite at interface is increased progressively larger than the pearlite structure. Sample 6—Aluminum coated mild steel specimen rods with silica at 900 °C and 7 min dip time, microstructure shows the growth of pearlite structure is improved in size as compared to five samples and also ferrite structure is smaller than other five samples (Figs. 7, 8, 9, 10, 11, and 12).

**Fig. 7** Microstructure of aluminized specimens without silica at 700 °C, 3 min



**Fig. 8** Microstructure of aluminized specimens without silica at 800 °C, 5 min



**Fig. 9** Microstructure of aluminized specimens without silica at 900 °C, 7 min



**Fig. 10** Microstructure of aluminized specimens with silica at 700 °C, 3 min



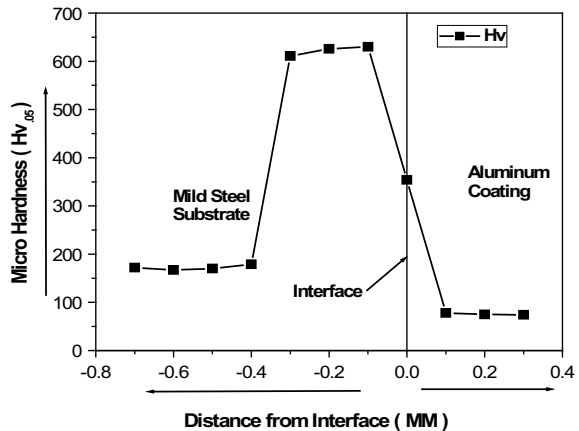
**Fig. 11** Microstructure of aluminized specimens with silica at 900 °C, 7 min dip time



**Fig. 12** Microstructure of aluminized specimens with silica at 800 °C, 5 min



**Fig. 13** Graph for 700 °C, 3 min dipping temperature and time



**Mechanical Properties**

It is observed that the hardness of the coating is increased with increase in dipping temperature and time, whereas the thickness of coating is inversely proportional to the temperature and dip time, that is, when the thickness of coating increases at lower temperature (below 700 °C), while the thickness of coating decreases from 700–900 °C. Hence, the coating hardness is absorbed to be increased with temperature. The hardness of the substrate is increased very near to the interface at the temperature above 700 °C, 800 °C, 900 °C. The reason for increase hardness along interface is due to phase transformation in mild steel. The mild steel surface as we absorbed the ferrite and pearlite structure be grown as it is seen to be formed Martensite structure (Figs. 13, 14, and 15).

**5 Conclusion**

Hence, we conclude that the aluminum alloy can be coated on mild steel and the strength of coating depends on the dipping temperature, if the temperature increases then the also hardness increases. This more hardness may lead to peel of the coating

**Fig. 14** Graph for 800 °C, 5 min dipping temperature and time

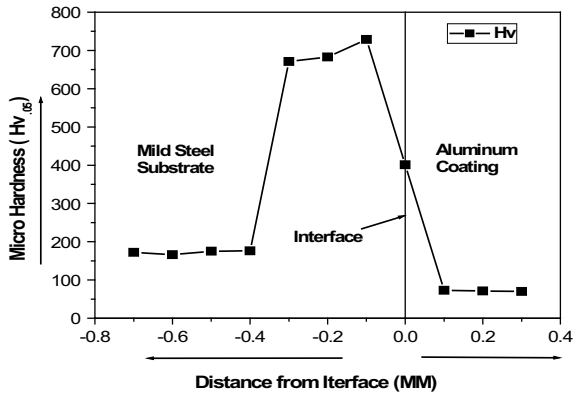
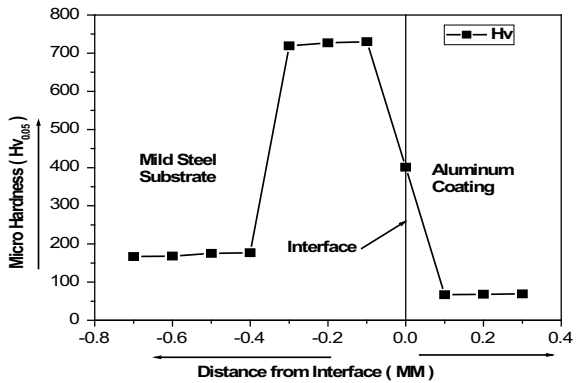


**Fig. 15** Graph for 900 °C, 7 min dipping temperature and time



at lower load; it is concluded that the process should be carried out just above the melting temperature (660–700 °C) and the dip temperature of 3 min. The coating thickness depends on dip time and temperature. At high melting temperature with less dipping time, the coating thickness increases, for high temperature and more dip time, the thickness decreases and metal gets more hard. The reason for low thickness coating over mild steel rod is high fluidity of aluminum alloy at higher temperatures.

Finally, the net conclusion is that the aluminum alloy coating on mild steel specimen rod at the temperature of 700 °C and 3 min dip time gave the best results for the mechanical properties like toughness, hardness, and corrosion resistance.

**Future Scope**

The materials suitable for aluminising include low alloy steels, stainless steels, nickel-base alloy, and nickel-iron alloys, etc. Similar studies can be performed by changing the diffusion temperature and time and it can also be made by changing the quenching time, soaking time, and temperature.

## References

1. Jagielski J et al (2000) Effect of chromium nitride coating on the corrosion and wear resistance of stainless steel. *Appl Surf Sci* 156(1–4):47–64
2. Richards RW et al (1994) Metallurgy of continuous hot dip aluminizing. *Int Mater Rev* 39(5):191–212
3. Ryabov VR (1985) *Aluminizing of Steel*. Oxonian Press, New Delhi, pp 48–51
4. Dovey DM, Waluski A (1963) Continuous dip aluminizing of steel. *Metallurgia* 67:211–217
5. Young WB, McComb JA (1990) New piston ring face coatings using design of experiments. *SAE Trans*, Section 3, Part 2, 99:1228–1235
6. Hunter CE, Gardner TP, Zakrajsek CE (1990) Simultaneous optimisation of diesel engine parameters for low emissions using Taguchi methods. *SAE Trans*, Section 3, Part 2, 99:2068–2078

# Investigation of Mechanical and Wear Characteristics of Aluminum Reinforced with Quartz Composites



T. Thirumalai, A. Harsha Vardhan Reddy, S. Nagakalyan  
and Rajagopal Dhanasekaran

**Abstract** The interest for lightweight, less expense, and prevalent material required the improvement more up to date materials and consequently an exertion has been taken to create aluminum lattice composites by stir casting technique, which is the easiest and affordable path for delivering aluminum matrix composite. The creation of aluminum matrix composite was finished by strengthening with different weight % of quartz. The result demonstrates that increasing of quartz in aluminum composite increased the hardness and rigidity. The wear test uncovered that expansion of quartz diminished the wear loss and expands the wear resistance. The SEM result on microstructure demonstrates the no throwing imperfection and wear resistance of the composites.

**Keywords** AMC · Hardness · Tensile strength · Wear resistance

## 1 Introduction

The interest for lightweight, financial, and great quality materials prompts the advancement of new materials that meet these necessities. One of the recently created materials is aluminum metal-matrix composites (Al-MMCs). These days, there are

---

T. Thirumalai (✉) · A. H. V. Reddy · S. Nagakalyan  
Department of Mechanical Engineering, Guru Nanak Institutions Technical Campus,  
Ibrahimpattanam, Telangana, India  
e-mail: [tmala@rediffmail.com](mailto:tmala@rediffmail.com)

A. H. V. Reddy  
e-mail: [krishharsha225@gmail.com](mailto:krishharsha225@gmail.com)

S. Nagakalyan  
e-mail: [kalyan502@gmail.com](mailto:kalyan502@gmail.com)

R. Dhanasekaran  
Guru Nanak Institute of Technology, Khanapur, Telangana, India  
e-mail: [dhanagni@gmail.com](mailto:dhanagni@gmail.com)

different results of MMCs were utilized particularly for car and designing applications. This is a result of their high quality, high elastic modulus, and low thermal coefficient of thermal extension, lightweight, low thermal shock, great wear resistance, and a lot more focal points.

## 2 Literature Survey

Aluminum-based MMCs make up a category of cutting edge designing materials over regular Al alloys. Improvement of new forming methods and utilization of less cost particulate reinforcing materials, the utilization of these composites is increasing in a wide assortment of businesses. A. Rutecka et al. [1], explore the strain rate, weakness properties, creep resistance, and lifetime of Al/SiC MMC. By including silicon carbide in aluminum, the weakness properties get expanded. The rate of harm parameters increment winds up more prominent for higher substance of the SiC content particles. Greatness of the mean strain is diminished by including silicon carbide.

J. Jebeebmoses et al. [2], examined and depicted the creation of aluminum with support of different measures of silicon carbide. By including silicon carbide particles the hardness and elasticity get expanded. Because of the expansion in support particles the mechanical properties get expanded contrasted with network composite and furthermore it changes the crack mode. R. Dhanasekaran and T.S. Mahesbabu et al. [3, 4], considered and researched the turning task in Al356 aluminum MMC including silicon carbide and boron carbide as fortification. Polycrystalline precious stone is utilized for turning activity. In light of the feed rate, just the surface harshness will get expanded or diminished. In ANOVA when feed rate change to 0.1 mm/rev the surface harshness gets diminished.

C. Dhavamani et al. [5], explore the boring of aluminum silicon carbide. By alluring useful methodology, the limiting surface harshness and amplifying metal expulsion rate are examined. To speak about the connection among info and yield variable, a various relapse model is utilized and hereditary calculation is utilized to upgrade the procedure. In view of speed, feed, and dia of cut completing of penetrating of the composite will be great. David Raja Selvam et al. [6], examined and produced the aluminum matrix composite including fortified as SiC and consistent load of fly fiery remains by mix throwing strategy. By including magnesium the wet capacity of SiC and fly fiery remains gets improved. By including fly fiery debris the disintegration of SiCp was avoided and Al4C3 development was additionally averted. The rigidity of the aluminum network gets expanded by including silicon carbide. C.M. Friend [7], examined Al compounds discovered application in transportation designing because of its better quality than weight proportion. Be that as it may, less wear opposition of Al combinations can be overwhelmed by utilizing Al-based MMCs produced for tribological applications. K. Kalaiselvan [8], considered and created the aluminum composite Al6061 metal grid composite with clay Al2O3 utilizing fluid metallurgy course in mix throwing strategy. The fortifications were



prewarmed before blend in the aluminum combination. Consequently, the present work was taken up to comprehend the adjustment in wear of the quartz fortified aluminum composites. Dhanasekaran and Hamid Reza Ezatpour et al. [9, 10], contemplated and explore the impact of nanoalumina when added to Al606 amalgam and expulsion properties on mechanical and small scale properties improved. In this, the processed nano-Al<sub>2</sub>O<sub>3</sub>/Al composite powder infused into dissolve by argon gas. V. Bharath et al. [11], contemplated test has fine grain smaller scale structure with high porosity utilizing nano Al<sub>2</sub>O<sub>3</sub> which was scattered with low agglomeration, so the quality and flexibility get expanded.

### 3 Material and Method

Quartz is the second most mineral found at Earth's surface and its intriguing properties make it a champion among the most profitable trademark substances. LM9 aluminum gives splendid assurance from utilization under both standard barometrical and marine conditions. LM9 can be anodized by any of the customary methods, the ensuing cautious film reaching out in concealing from diminishing to dull darker, dependent upon the procedure used (Table 1). Stir casting technique has been utilized for assembling irregular molecule strengthened composites. In a stir casting process, the fortifying material stages are spread into liquid network in mechanical mixing, by planning metal lattice composites by the blend throwing technique. In this, various variables are required for significant consideration, including the trouble of accomplishing a uniform circulation of the fortification material, wet ability between the two primary substances, porosity in the cast metal framework composites, and composite responses between the support material and the matrix alloy (Table 2).

**Table 1** Chemical composition of Aluminum LM9

Material	% of Composition
Copper	0.04
Magnesium	0.51
Silicon	11.37
Iron	0.48
Manganese	0.42
Nickel	0.002
Zinc	0.02
Lead	0.009
Tin	0.002
Titanium	0.01
Aluminum	Remaining

**Table 2** Process parameters of stir casting

Parameters	Units	Value
Spindle speed	RPM	400
Stirring time	Min.	5
Temperature of melt	°C	920
Preheated temperature of quartz particles	°C	300
Preheated temperature of mold	°C	250
Power feed rate	g/s	0.8–1.2

## 4 Design of Experiments

Taguchi methods are measurable techniques created by Genichi Taguchi to show signs of improvement nature of produced products, and all the more as of late likewise connected to building. Proficient analysts have respected the objectives and upgrades realized by Taguchi techniques, especially by Taguchi's improvement of structures for considering variety, yet have censured the wastefulness of a portion of Taguchi's recommendations.

The Taguchi method includes decreasing the variety in a procedure through plan of examinations. The rule motivation behind the strategy is to make great items requiring little to no effort to the maker.

## 5 Methodology

A batch of aluminum composite has been softened at 920 °C with a suppress heater. Before stirring the Quartz ought to be prewarmed at a temperature of 300 °C. When the melting temperature achieves the aluminum composited is solved and mixing done by utilizing the mechanical stirrer. The dissolve was irritated with the assistance of a mechanical stirrer to shape a fine vortex. The mixing of preheated SiO<sub>2</sub> particles was included at a steady feed rate into the vortex. The procedure parameters utilized are given in the table. In the wake of mixing the liquid mix, it was filled the preheated lasting mold. The MMCs having different weight percentage rates (8.9 and 13%) of quartz were manufactured by a similar methodology.

## 6 Results and Discussion

Wear mechanism is a hazardous factor and it impacts the administration life Wear is particular as the progressive loss of material from solid because of mechanical activity, i.e., contact or relative movement against a strong or liquid. Propelled designing materials and composites are utilized, where high wear resistance is required.

The abrasive wear resistance of the particle strengthened with metal-matrix composites increments with adds to in the volume division option of particles, under both high and low stress and high wear resistance conditions.

### 6.1 Hardness and Tensile and Wear with Volume Fraction % of Quartz

Because of the support of quartz in aluminum LM9, the hardness of the composite gets increased. During machining the outcome indicates that constant and spasmodic chips are framed at sporadic interim at 8% of volume and discontinuous chip shaped at 13% of volume. It demonstrates an increase in hardness and strength of the composite (Table 3).

Wear of components is a critical factor and it influences the service life span. Wear loss is minimum at 13% composition of quartz and it is compared with 8, 9% of other samples. It is shown in Fig. 1.

**Table 3** Increasing of hardness value

S. NO.	Amount of quartz added in LM9 (%)	Rockwell hardness in MPa	Tensile strength in MPa
1.	0	49.04	178
2.	8	50.33	180
3.	9	55.53	183
4.	13	56.70	175

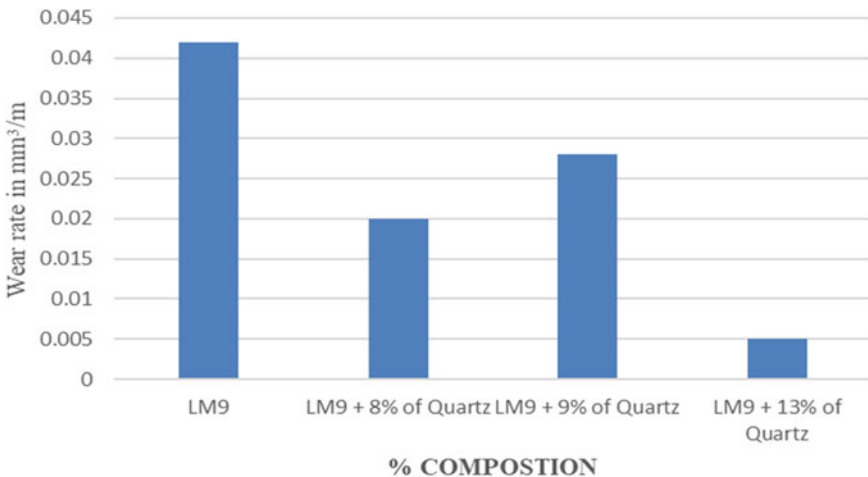


**Fig. 1** Wear loss of AMC

## 6.2 Microstructure and SEM Analysis

The microstructural characterization of aluminum LM9 reinforced with various quartz level was appeared beneath Figs. 2, 3, 4, and 5. Figure 2 demonstrates the impact of normal load on the wear rate. As the typical load increases the coefficient of grating likewise increment which prompts more wear rate. This is most basic wonder in the greater part of the material. Normal load has the most elevated impact on the sliding wear rate.

Figure 3 gives the quantity of scratches on the surfaces which is more. This uncovers the essential wear instrument that is rough wear. The investigation of wear surface of the LM9 and composite of lower magnification reveals distinct patterns of grooves and edges running parallel to each other the sliding way.

In Figs. 4 and 5 there were high scratches on the wear surfaces. This multifaceted that the essential wear instrument is abrasive wear. The aftereffect of wear surface

**Fig. 2** SEM images for mixture 1 (8% quartz reinforcement)



**Fig. 3** SEM image for mixture 2 (9% quartz reinforcement)

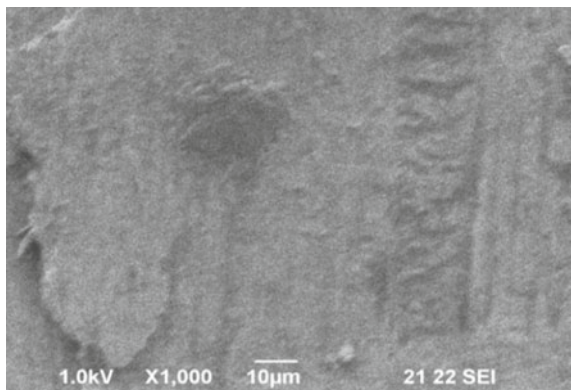


**Fig. 4** SEM images for mixture 3 (quartz 13% reinforcement)

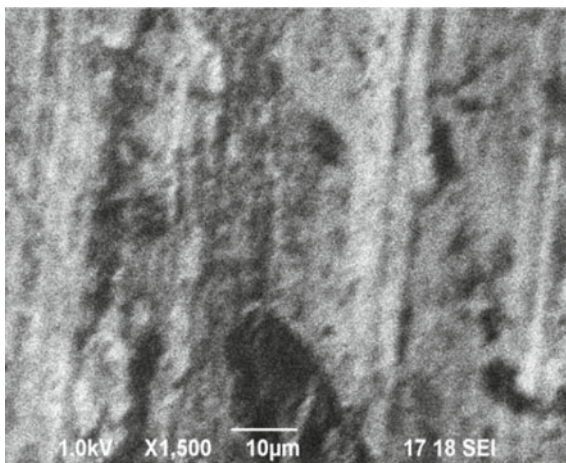
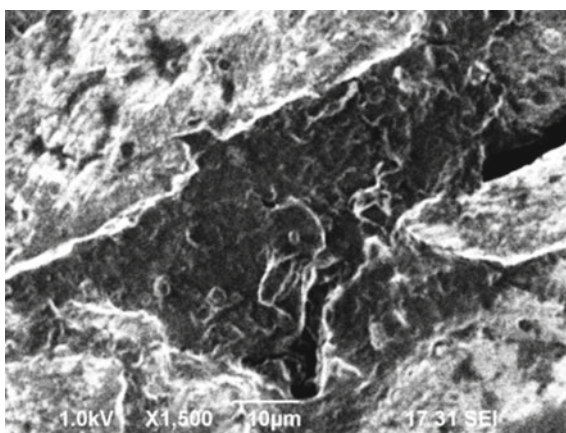


**Fig. 5** SEM images for mixture 3 (quartz 13% reinforcement)



of the combination and composite of lower magnification indicates the grooves and of scores and edges running parallel to each other the sliding way.

The outcome gives the surface that was described by long and continuous grooves which have heavy scores. The nearness of small scale deformity on the sliding surface is another significant marvels watched. The wear surface shows unmistakable parallel sections all through the surface.

## 7 Conclusion

Stir casting method is employed for the manufacture of aluminum matrix composite reinforced with various levels of quartz to get the desired properties.

Reinforcing quartz with aluminum alloy in the respective percentages (8–13%) has shown an appreciable improvement in its mechanical properties and wear resistance.

The hardness and tensile strength were increased with the addition of weight percentage of quartz. The SEM result revealed the distribution of quartz in aluminum matrix as fairly homogeneous.

**Acknowledgements** The authors are grateful and thanks to AICTE-RPS scheme for sanctioning the project fund and also thanks Dr. R. Subramanian, PSG College of Technology, Coimbatore and Dr. B. Ravishankar, NIT, Trichy for their help and constructive suggestions rendered during the study.

## References

1. Ruteckaa A, Kowalewska ZL, Pietrzakb K, Dietricha L, Makowskab K, Woniakc J, Kosteckic M, Bochniakc W, Olszynac A (2011) Damage development of Al/SiC metal matrix composite under fatigue, creep and monotonic loading conditions. *Procedia Eng* 10:1420–1425
2. Jabeenmoses J, Dinaharan I, Josephsekhar S (2014) Characterization of silicon carbide particulate reinforced AA6061 aluminium alloy composites produced via stir casting. *Procedia Mater Sci* 5:106–112
3. Dhanasekaran R, Senthil Kumar P, Santhi K (2012) Microstructure and wear behavior of planetary gear material and metal carbide coating. *Int Rev Mech Eng* 6(6):1321–1325
4. Mahesbabu TS, Aldrin Sugin MS, Muthukrishnan N (2012) Investigation on the characterization of surface quality on machining of hybrid metal matrix composite. *Procedia Eng* 38:2617–2624
5. Dhavamani C, Alwarsamy T (2012) Optimization of machining parameters for aluminium and silicon carbide composite using genetic algorithm. *Procedia Eng* 38:1994–2004
6. David Raja Selvam J, Robinson Smart DS, Dinaharan I (2013) Synthesis and characterization of Al6061-Fly Ashp-SiCp composites by stir casting and compocasting methods. *Energy Procedia* 34:637–646
7. Friend CM (1987) The effect of alumina fiber array on the age hardening characteristics of and Al/Mg/Si alloy. *J Mater Sci* 22:2997–3005
8. Kalaiselvan K, Murugan N, Parameswaran Siva (2011) Production and characterization of AA6061-B4C stir cast composite. *Mater Des* 32:4004–4009
9. Dhanasekaran R, Senthil Kumar P, Baskaran S, Santhi K (2012) Wear behavior of surface treated alloy steel with assorted blends of fine particles by using plasma spray process. *Adv Mater Res* 383–390:893–897
10. Ezatpour HR, Sajjadi SA, Sabzevar MH, Huang Y (2014) Investigation of microstructure and mechanical properties of Al6061-nanocomposite fabricated by stir casting. *Mater Des* 55:921–928
11. Bharath V, Nagara M, Auradi V, Kori SA (2014) Preparation of 6061Al-Al<sub>2</sub>O<sub>3</sub> MMC's by stir casting and evaluation of mechanical and wear properties. *Procedia Mater Sci* 6:1658–1667

# Studies on Application and Mechanism of Self-Healing Polymer and Nanocomposite Materials



S. Sreenatha Reddy, Rajagopal Dhanasekaran, Sujeet Kumar, Shiv Shankar Kanwar, R. Shruthi and T. Navaneetha

**Abstract** From the last few decades, self-healing techniques came into existence which has wide applications in the aerospace, automobile industries, biomedicine, etc. The polymers have the ability to repair the damages caused by various actions of impact, fatigue, and erosion and restore the original characteristics of material. Its lightweight, good processability, chemical stability, low cost, and high strength make it smart material. Self-healing is inspired by biological study. There are three main concepts of self-healing: capsule-based self-healing mechanism, vascular self-healing mechanism, and intrinsic self-healing mechanism. The aim of this article is to give a complete idea about the application and mechanism of self-healing polymers and its nanocomposites. Impact damages, fatigue, puncture, and corrosion are reviewed by this article. Safer, long-lasting, and economical products can be produced using self-healing polymers. Finally, this article wraps up with great scope in research and developments. Sources of information were from scientific articles, patents, and different materials.

**Keywords** Self-healing material · Fatigue · Nanocomposites · Capsule · Vascular mechanism

## 1 Introduction

Polymer is a lightweight, high strength, good processability, chemical stability, and low-cost smart material which has capability to heal the damages caused by various thermal, mechanical, and ballistic actions at nanolevels [1]. Composite materials

---

S. Sreenatha Reddy · R. Dhanasekaran · S. Kumar (✉) · S. S. Kanwar · R. Shruthi · T. Navaneetha  
Department of Mechanical Engineering, Guru Nanak Institute of Technology, Hyderabad,  
Telangana, India

e-mail: [kumarsujeet28782@gmail.com](mailto:kumarsujeet28782@gmail.com)

S. Sreenatha Reddy

e-mail: [principal.gnit@gniindia.org](mailto:principal.gnit@gniindia.org)

R. Dhanasekaran

e-mail: [dhanagnit@gmail.com](mailto:dhanagnit@gmail.com)

© Springer Nature Singapore Pte Ltd. 2020

G. S. V. L. Narasimham et al. (eds.), *Recent Trends in Mechanical Engineering*,

Lecture Notes in Mechanical Engineering,

[https://doi.org/10.1007/978-981-15-1124-0\\_42](https://doi.org/10.1007/978-981-15-1124-0_42)

consists of two different natural materials to get a good characteristics performance. In recent years, it has found its wide scope in aerospace, automobile, etc. Materials go natural consequences by getting degraded, damaged, fiber fracture, delamination, and failures that occur over time. These may affect the material strength, stiffness, conductivity properties, and dimensional stability [2]. The fractures and ruptures are at micro levels which cannot be detected. The cracks further grow due to mechanical stress which lead to failure of component. Engineering researchers only focused on developing new products with high strength and better properties. But due to all the failures of high inspection and improved properties, self-healing comes into picture.

Self-healing technique is based on biological strategy which is the source of inspiration [3]. It was first developed by White et al. The concept of self-healing has been successfully tested to a number of materials that are nanostructured. Self-healing materials have the potential to heal the cracks, fractures, or any damages without any external help. It can heal the fractures caused due to impact, fatigue, erosion, and corrosion. It uses catalyst such as Grubbs and tungsten hexachloride. On the basis of chemistry, self-healing is of two types, namely, autonomous and nonautonomous. In autonomous self-healing, materials do not need any external inducement because the damage itself activates the healing process. On other hand, in nonautonomous, materials require need external agent (heat and light) to activate the healing process. Self-healing is sustainable, safer, and long-lasting. It expands the lifetime and survivability of the product and have higher reliability. It restores the initial characteristic of those materials.

Polymers nanocomposite have superior properties but they face some problems like cavitations. This work gives illustrations on mechanism of recovering the existing properties of materials that undergo damages and focuses on practical applications of artificial self-healing. It restores the material's surface and volume unification by improving the strength, stiffness, and electrical conductivity. The three primary concepts of self-healing are capsule based, vascular, and intrinsic.

## 2 Self-Healing: Concept and Mechanism

Self-healing is the property of material to repair any type of damages automatically without any external help. It was come into attention in 1970s to understand constituent properties of filled elastomers that are used in solid rocket propellants. The concept of self-healing comes from biological concepts and the synthetic version comes to existence. The natural consequences of materials such as damage, degradation, and failures occur over time. Since 2001, a wide range of self-healing material has been developed. The cracks, fractures, or any damages that are caused due to impact, fatigue, erosion, etc. can be healed by self-healing material. When the damages occur, the capsules will break and chemicals will get interacted with the void spaces and that get filled to heal the microscopic level fractures.



Polymers and its composites are the most used materials nowadays and industrial applications. Self-healing materials have the potential of self-repairing of any damages caused due to mechanical, chemical, thermal, and ballistic actions. Traditional materials do not have such properties. Self-healing materials reduce maintenance cost, high strength, better performance ratio, and can heal the imperfections of any size [4]. For all, the self-healing systems rate of healing is equal to rate of damage. So far several researches are going on to focus on the behavior of polymers and its nanocomposite materials as they are widely used. Self-healing material is used to rectify all of the problems and the life of the component will increase as well as survivability. These materials have the ability to block the path of propagation of nanolevel fractures to macroscopic scale. According to congenital approach of self-healing polymers, it works due to synthetic holding in the network itself which has the ability to rearrange accordingly after damage has occurred in the presence of outer inducement [1].

Self-healing materials can be categorized according to general mechanism as Extrinsic and Intrinsic self-healing mechanism [5, 6]. Composite helps in differentiating the above two with respect to damage response and their chemistries.

## ***2.1 Extrinsic Self-Healing Mechanism System***

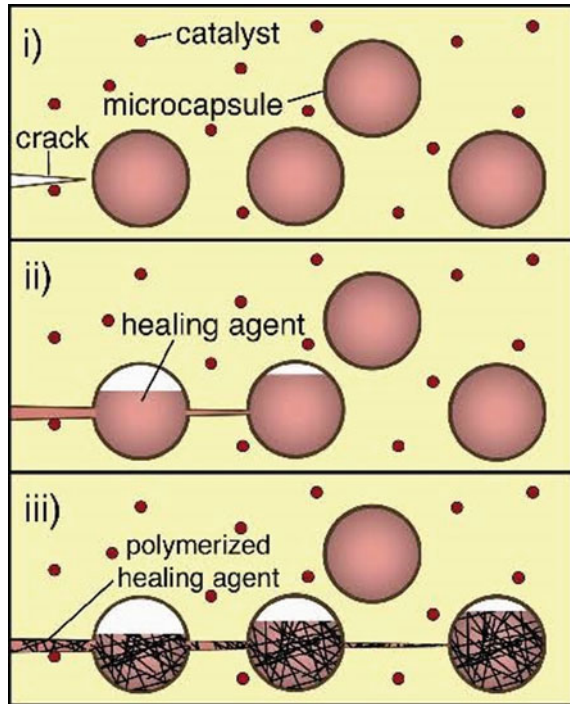
This mechanism deals with the recovery of structural damages using external healing materials in the shape of containers placed in the matrix as capsules or vascular networks [6]. Based on the container, the following are two types.

## ***2.2 Capsules Embedment-Based Self-Healing Mechanism***

In this mechanism, self-healing is started by damages itself. It is also called as microencapsulated self-healing polymer [5–10]. White et al. presented the capsule-based polymer in 2001. Capsules store the healing materials. At the point when ruptures and fractures occur in the component system the capsules get cracked and healing agent will reach the damaged site. The catalyst present helps in the polymerization of healing agent. It also helps in activating most of the healing phenomena and is Grubb's catalyst and tungsten hexachloride.

The selfhealing system works according to the ring-opening metathesis polymerization (ROMP) of dicyclopentadiene (DCPD) using Grubb's catalyst. Polymeric microcapsules are most often prepared by using a miniemulsion polymerisation technique [11]. The procedure includes oil-in-water dispersion mechanism. Poly urea-formaldehyde (PUF), polyurethane, poly melamine-urea-formaldehyde (PMUF), poly melamine-formaldehyde (PMF), and a few are used in making of capsule shells. Effective strength recovery (>90%) can be achieved by increasing the mechanical properties and efficiency of the healing agent material [12].

**Fig. 1** Microencapsulated self-healing mechanism



The two limitations faced by capsule embedment catalyst healing mechanisms are high cost of catalyst (Grubbs) and lack of amount healing agent to heal repeatedly. Figure 1 shows capsule embedment self-healing mechanism.

### 2.3 Vascular Network Self-Healing Mechanism

In this mechanism, the self-healing process is done using the vascular network in the form of capillaries or narrow pipelines into the matrix. The healing materials are organized in 1D, 2D, and 3D matrix. These networks are interconnected until the damages initiated self-healing. These networks contain healing agents into polymer matrix through microchannels. Toohey et al. first gave the idea including the microchannel network which contains dicyclopentadiene (DCPD) in the materials [5]. Grubbs' catalyst with DCPD is delivered to an epoxy surface coating by microchannels. For many years studies were done to use several types of healing and heal the large scale of damages [13–18]. The healing material is released to the damage or crack plane and polymerization occurs. Multiple connection points have increased the reliability as there will be no pipeline blockage and easy accessibility of healing agent in bulk. Hence, 3D connectivity has higher potential to heal damages than 1D [5].

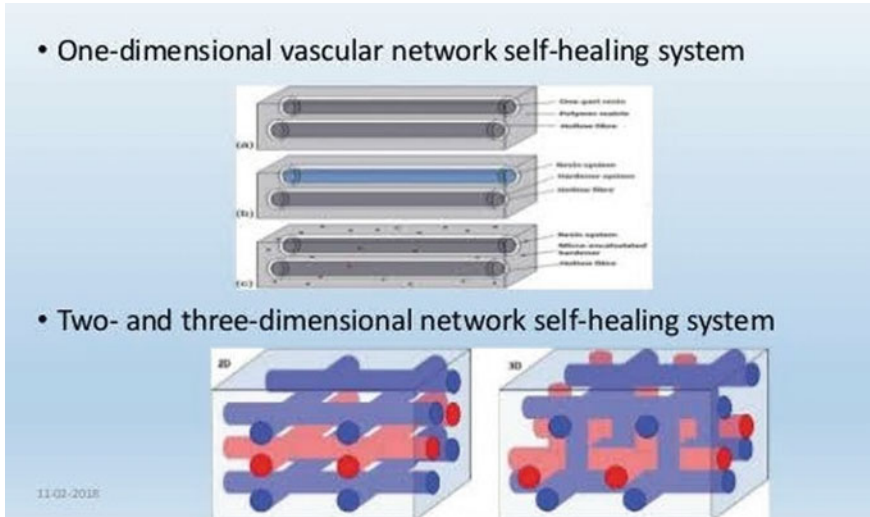


**Fig. 2** Vascular Network self-healing mechanism

The vascular network produced by Koralagundi Matt et al. within conventional glass fiber reinforced polymer matrices composite has self-healing ability which used in composite structure of wind turbine blades [19] (Fig. 2).

### 2.4 *Intrinsic Based Self-Healing Mechanism*

In this type of mechanism, the repair is accomplished by thermally reversible reaction, hydrogen bonding, ionic coupling, or molecular diffusion without any external help such as healing agent and catalyst [20]. Several other reaction mechanisms are used to activate the intrinsic healing in polymers such as irradiation-induced cycloaddition [21], Metathesis reaction [22], photothermal ring-opening reaction [23], photothermal metal-ligand complexation [24], and redox-triggered host-guest complexation and decomplexation reaction [25, 26]. The thermoplastic-based components use this mechanism to heal the damages. This mechanism is less complex than extrinsic self-mechanism (Fig. 3).

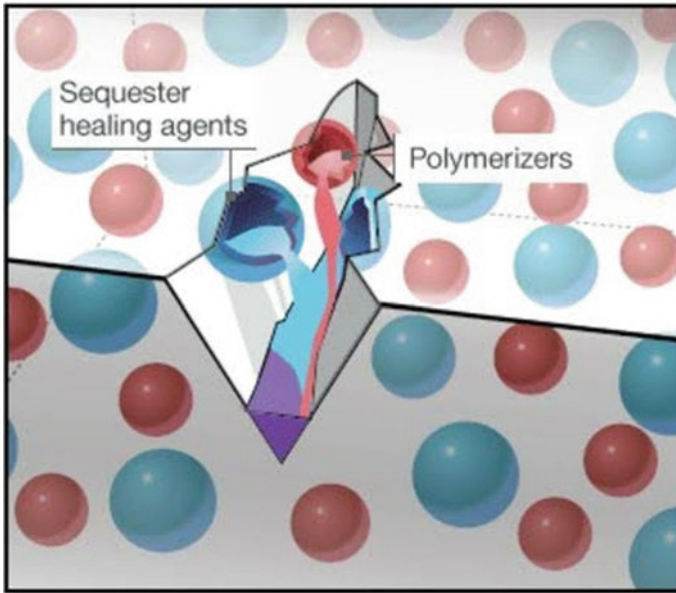


**Fig. 3** Intrinsic Self-Healing mechanism

### **3 Self-Healing Polymer NanoComposites: Applications**

#### ***3.1 Effect of Self-Healing Polymer in Sealing Holes and Size of Bullets***

This technology of self-healing of polymer nanocomposites helps in healing the damages caused by bullets. When bullets are fired on fuel tanks of helicopters, the encapsulating materials heal the holes by sealing it completely without losing any material inside. This technology is mainly used by army helicopter. It can heal full holes immediately.

#### ***3.2 Effect of Self-Healing Polymer on Impact Damage***

Impact is a force caused due to sudden application of load on the component material. The damage caused due to impact loading cannot be traced as it is in microscopic scale. The material receives some impact load and causes punctures, fractures, and mixed-mode cracking which will lead to continuous delamination and damages at nanolevels. It can decrease the efficiency and lifetime of the component. Finally, this microscopic scale damage leads to macroscopic level damage and materials failure will occur. Fiber reinforced composites have low performance due to impact

loading. Using FRC self-healing polymer gained 51% reduction in damage when the materials go under low-velocity impact. By reducing the mechanical properties and increasing healing effect efficiency, there is a possibility of significant recovery of damages (>90%). Williams et al. revealed a result based on true compression after impact (CAI) experiment which tells 95% holding of CAI strength compared to 66% of unrepaired panels [12]. To enable CAI retention, the materials require thermal treatment at 125 °C due to nonautomatically self-healing. Tensile test is designed to specify bulk continuous deformation which leads to failure. Elongation at break, yield point stress [27], and force displacement curve [28] are used to quantify and identify the self-healing performance but the healing is not reflected fully.

To overcome all these hurdles, self-healing nanocomposite materials are used in the polymer matrix when subjected to mechanical loading, the elastomeric network could accept the mechanical energy by opening of nanoclay beams.

### 3.3 Effects of SelfHealing Fatigue Strength

Fatigue is a mechanical property of the material which is responsible for the cyclic load applications. Due to cyclic load on bridge the materials component go deformed and cracks formation occurs. The damage rate depends on the array of the variables such as frequency and amplitude of the stress intensity and mechanical properties. Due to this, the survivability will decrease. These problems occur continuously and finally it leads to failure status. Temperature, mobility, and polymerization rates decide the healing rate. The crack propagation and chemical kinetics decide the fatigue life extension. At 20% DCPD microcapsule, 2.5 wt% catalyst and at low-stress intensity, the fatigue performance was tested and the results came by arresting fatigue crack propagation [29]. According to Brown et al., self-healing under fatigue loading can be measured by using life extension ( $\lambda$ ) and fatigue life ( $N$ ) as given in Eq. (1)

$$\lambda = \frac{N_{healed} - N_{control}}{N_{control}} \quad (1)$$

Stress intensity factor fatigue life extension ( $\lambda$ ). Reduction in stiffness up to 12.5% for 10 min when thermal energy of 120 °C is applied then self-healing fatigue life extension  $\lambda = 2$  for a tensile Mode I [30]. When chemical kinetics are higher than mechanical kinetics then the fatigue crack is completely controlled [31].

Monotonic fracture is less complex than fatigue because it depends on different factors such as applied stress intensity range, the loading frequency, the ratio of applied stress intensity, the healing kinetics, and the rest period employed [32]. Recovery of stiffness is lost due to damage caused by cyclic loading that is considered successful because crack growth rate is reduced due to self-healing.

### 3.4 Effect of Self-Healing on Erosion and Corrosion

Erosion is the process of removing away the materials layer by action of several phenomena such as wind, water, and natural agents. Corrosion is the natural process of gradual destruction of materials by chemical or electrochemical reaction with their environment. To avoid above problems, a layer of coating is coated on the material which is responsible for all the problems that are self-healing in nature, i.e., polymer materials. Xiao fan Luo et al. have made the arrangement and new shape memory which help in self-healing coating. The coatings include isolated morphology with electrospun thermoplastic poly (PCL) stands which pass through shape memory epoxy grid. Through warming mechanical harm of covering can be held which leads to events. First, shape recovery of the matrices to get the split surfaces spatial vicinity and second one to dissolve PCL stands to recover back the break. The harm properties are restored in control recovering test [33]. The coatings have the ability to self-heal. Another test, Aluminum alloys are examined in seawater which is designed to improve the resistance. Aluminum alloy 3003 was applied with 30  $\mu\text{m}$  thick coating. A corrosion test was done in 3% NaCl at 70  $^{\circ}\text{C}$  and pH of 1.5 for 120 h. [34]. The self-healing performance was decided on the basis of corrosion behavior of defect. They show coating damage with no defect or a little damage at the defect.

The erosive behavior cannot be decided by surface roughness [35]. Experimentally, self-healing of erosion damages has not been demonstrated [36] (Fig. 4).

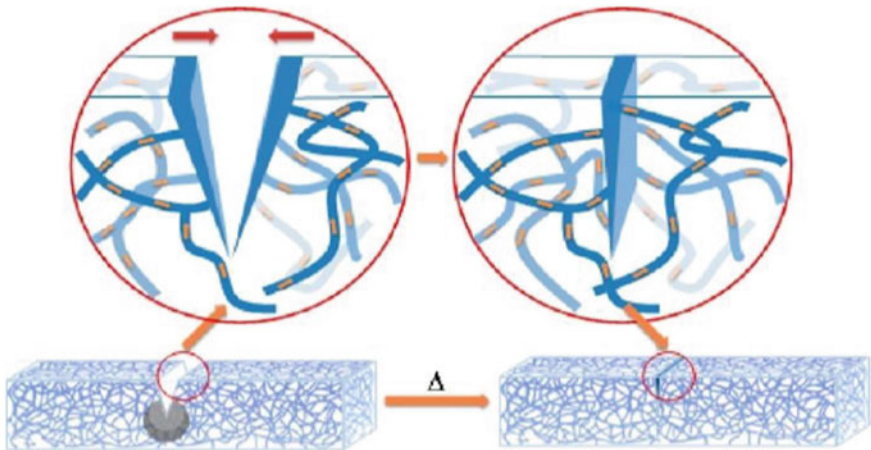


**Fig. 4** Schematic illustration of the coating morphology and the shape memory assisted self-healing (SMASH) concept [33]

### 3.5 Usage of Self-Healing Polymer in Phone Screens and Paints for Cars

When scratch occurs on the phone screens or on the car's body then it can be self-healed. Phone screens contain polymer-based materials that have self-healing property. Hence, lifetime of the phone screens increases. Traditional paints used for painting vehicles do not have such properties of self-healing. Self-healing has applications mainly in automatic, aerospace, and building industries. For example, Nissan Motor Co. Ltd has commercialized world's first self-healing clear coat for car surface. The trade name of this product is "Scratch Guard Coat" [37]. According to the company, scratches on the coated car surface are repaired by hydrophobic paint and it lasts for duration of 3 years. High elastic resins prevent the scratches movement to the inner layer of the painted car surface.

## 4 Conclusion

Recently, several researches and developments occur in the domain of polymer nanocomposites. It is because of lightweight, high strength, and low-cost smart materials. The cracks developed due to various actions are at microscopic scale. The healing of these cracks are not economical and easy. So self-healing is introduced, which is derived from biological concepts. Achievements of self-healing polymers are not satisfactory as fatigue and erosion related problems are not supported. Yet it has several applications in the aeronautical, automobile industries, etc.

Due to self-healing techniques, numerous damages at molecular and structural level defects can be repaired. So mechanical and optical properties can be regained which is favorable path for self-healing research. Transparency can be restored using this technique. From a long-term point of view, intrinsic self-healing would be the reasonable solutions for the molecular design of synthesis polymer.

## References

1. Blaiszik BJ, Kramer SLB, Olugebefola SC, Moore JS, Sottos NR, White SR (2010) Self-healing polymers and composites. *Annu Rev Mater Res* 40:179–211
2. White SR, Sottos NR, Geubelle PH, Moore JS, Kessler MR (2001) Autonomic healing of polymer composites. *Nat Int J Sci* 409:794–797
3. Varghese S, Lele A, Mashelkar R (2006) Metal-ion mediated healing of gels. *J Polym Sci, Part A: Polym Chem* 44(1):666–670
4. van der Zwaag S (2007) An introduction to materials design principles: damages prevention versus damage management. In: *Self healing material*. Springer, AA Dordrecht, The Netherlands, pp 2–9
5. Toohey Kathleen S, Sottos Nancy R, Lewis Jennifer A, Moore Jeffrey S, White Scott R (2007) Self-healing materials with microvascular networks. *Nat Mater* 6(8):581–585

6. Hia IL, Vahedi V, Pasbakhsh P (2016) Self-healing polymer composites: prospects, challenges, and applications. *Polym Rev* 56:225–261
7. Dry C, Sottos NR (1993) Passive smart self-repair in polymer matrix composite materials. In: Proceedings of SPIE: society of photo-optical instrumentation engineers, vol 1916, pp 437–444
8. Aïssa BA, Therriault D, Haddad E, Jamroz W (2012) Self-healing materials systems: overview of major approaches and recent developed technologies. *Adv Mater Sci Eng* 17:854203
9. Brown EN, White SR, Sottos NR (2004) SEM X international national conference
10. Brown EN, White SR, Sottos NR, Mater J (2006) Fatigue crack propagation in microcapsule. *J Mater Sci* 41(19):6266–6273
11. Asua JM (2002) Miniemulsion polymerisation. *Prog Polym Sci* 27:1283–1346
12. Williams GJ, Bond IP, Trask RS (2009) Compression after impact assessment of self-healing CFRP. *Compos Part A—Appl Sci Manuf* 40(9):1399–1406
13. Hamilton AR, Sottos NR, White SR (2010) Self-healing of internal damage in synthetic vascular materials. *Adv Mater* 22(45):5159–5163
14. Norris CJ, Bond IP, Trask RS (2011) Interactions between propagating cracks and bioinspired self-healing vasculature embedded in glass fibre reinforced composites. *Compos Sci Technol* 71(6):847–853
15. Peterson AM, Kotthapalli H, Rahmathullah MAM, Palmese GR (2012) Investigation of interpenetrating polymer networks for self-healing applications. *Compos Sci Technol* 72(2):330–336
16. Grunenfelder LK, Suksangpanya N, Salinas C, Milliron G, Yaraghi N, Herrera S et al (2014) Bio-inspired impact-resistant composites. *Acta Biomaterialia* 10(9):3997–4008
17. Esser-Kahn AP, Thakre PR, Dong H, Patrick JF, Vlasko-Vlasov VK, Sottos NR et al (2011) Three-dimensional microvascular fiber-reinforced composites. *Adv Mater* 23(32):3654–3658
18. Yang T, Wang CH, Zhang J, He S, Mouritz AP (2012) Toughening and self-healing of epoxy matrix laminates using mendable polymer stitching. *Compos Sci Technol* 72(12):1396–1401
19. Korlagundi Matt AK, Strong S, ElGammal T, Amano RS (2015) Development of novel self-healing polymer composites for use in wind turbine blades. *J Energy Resour Technology* 137(5):051202
20. Wang Y, Pham DT, Ji C (2015) Self-healing composites: a review. *Cogent Eng* 2:1075686
21. Chung CM, Roh YS, Cho SY, Kim JG (2004) Crack healing in polymeric materials via photochemical [2+2] cycloaddition. *Chem Mater* 16(21):3982–3984
22. Scott TF, Schneider AD, Cook WD, Bowman CN (2005) Photoinduced plasticity in cross-linked polymers. *Science* 308(5728):1615–1617
23. Ghosh B, Urban MW (2009) Self-repairing oxetane-substituted chitosan polyurethane networks. *Science* 323(5920):1458–1460
24. Burnworth M, Tang I, Kumpfer JR, Duncan AJ, Beyer FL, Fiore GI, Rowan SJ, Weder C (2011) Optically healable supramolecular polymers. *Nature* 472(7343):334–337
25. Vogt AP, Sumerlin BS (2009) Temperature and redox responsive hydrogels from ABA triblock copolymers prepared by RAFT polymerization. *Soft Matter* 5(12):2347–2351
26. Van Der Zwaag S, Grande AM, Post W, Garcia SJ, Bor TC (2014) Review of current strategies to induce self-healing behaviour in fibre reinforced polymer based composites. *Mater Sci Technol* 30(13a):1633–1641
27. Murphy EB (2011) The return of photoelastic stress measurements: utilizing birefringence to monitor damage and repair in healable materials. *J Mater Chem* 21(5):1438–1446
28. Maes F, Montarnal D, Cantournet S, Tournilhac F, Corte L, Leibler L (2012) Activation and deactivation of self-healing in supramolecular rubbers. *Soft Matter* 8(5):1681–1687
29. Brown EN, White SR, Sottos NR (2005) Retardation and repair of fatigue cracks in a microcapsule toughened epoxy composite-Part II: In situ self-healing. *Compos Sci Technol* 65:2474–2480
30. Zako M, Takano N (1999) Intelligent material systems using epoxy particles to repair microcracks and delamination damage in GFRP. *J Intell Mater Syst Struct* 10(10):836–841
31. Brown Eric N, Moore Jeffrey S, White Scott R, Sottos Nancy R (2003) Fracture and fatigue behavior of a self-healing polymer composite. *Mater Res Soc Symp Proc* 735:101–106



32. Brown EN, White SR, Sottos NR (2005) Retardation and repair of fatigue cracks in a microcapsule toughened epoxy composite-part II: in situ self healing. *Compos Sci Technol* 65(15–16):2474–2480
33. Luo X (2013) Shape memory assisted self-healing coating. *ACS Publ* 2(2):152–156
34. Yabuki A (2015) Self-healing coatings for corrosion inhibition of metals. *Mod Appl Sci* 9(7):215
35. Keller MW, Hampton K, McLaury B (2013) Self-healing of erosion damage in a polymer coating. *Wear* 307(1–2):218–225
36. Cho SH, White SR (2009) Braun PV (2009) Self-healing polymer coatings. *Adv Mater* 21:645–649
37. <http://www.nisanglobal.com/en/technology/introduction/details/sgc/index.html> (2008)

# Comparing Fire Penetration Results of Natural Fibre Reinforced Composite Material with Plywood



Rajagopal Dhanasekaran, S. Sreenatha Reddy, Anwar Pasha, Akula Deep Chander, Asar Fayaz Baig and T. Thirumalai

**Abstract** The aim of this experimental study is to determine and compare the fire penetration results of natural fibre reinforced composite material with plywood. Because of their availability, cost, as well as, physical and mechanical properties of natural fibre reinforced composites, they are most widely used in industrial applications like insulating material, building and transportation industries. The application of this composite material needs different properties for different applications, but in case of insulating and building material purposes their thermal properties must be studied, fire penetration rate is one of the important factors in indicating the fire hazard. From this study, it is concluded that fire penetration rate of composite material fabricated by sisal, coconut and palm leaf sheath fibres is less, i.e. 0.206 and time taken for penetration is 87 s that is double the time taken for plywood for penetration.

**Keywords** Natural fibre reinforced composite materials · Fire penetration test · Building and transportation materials · Fire penetration rate

---

R. Dhanasekaran · S. S. Reddy · A. Pasha (✉) · A. D. Chander · A. F. Baig  
Department of Mechanical Engineering, Guru Nanak Institute of Technology, Hyderabad,  
Telangana, India  
e-mail: [amanwar21436@gmail.com](mailto:amanwar21436@gmail.com)

R. Dhanasekaran  
e-mail: [dhanagnit@gmail.com](mailto:dhanagnit@gmail.com)

S. S. Reddy  
e-mail: [principal.gnit@gniindia.org](mailto:principal.gnit@gniindia.org)

T. Thirumalai  
Department of Mechanical Engineering, Guru Nanak Institutions Technical Campus, Hyderabad,  
Telangana, India  
e-mail: [ttmala@rediffmail.com](mailto:ttmala@rediffmail.com)

© Springer Nature Singapore Pte Ltd. 2020  
G. S. V. L. Narasimham et al. (eds.), *Recent Trends in Mechanical Engineering*,  
Lecture Notes in Mechanical Engineering,  
[https://doi.org/10.1007/978-981-15-1124-0\\_43](https://doi.org/10.1007/978-981-15-1124-0_43)

## 1 Introduction

Nowadays composite materials are widely used because of their better properties than conventional materials like metals, glass and wood. Composite is nothing but combination of two or more different materials, this combination leads to greater improvement in the properties of the material. There are two types of composite materials one is synthetic and another one is natural fibre composite material; both are same in case of fabrication but they show different properties during the application of material to the product or any component. Natural fibre reinforced composite material is emerging material in present days because of their physical properties as well as chemical properties, which are better than the artificial or synthetic fibres. These materials are mainly used in building and transportations applications and also used in other different applications, they must exhibit better fire resistance properties in order to use this material.

Fire penetration test is used to determine the penetration resistance of the composite material as well as time taken to burn the composite material, this test can be done by using oxy-acetylene welding machine that produces high intensity and temperature range flame which makes the penetration in the composite material. It was concluded that natural fibre reinforced composite material becomes hard to ignite if fire retardant materials are added during the fabrication process [1]. Flammability as well as machinability properties of sisal fibre reinforced polymer composite material was studied. In present day, composite material is widely used and it is used with the replacement of synthetic fibre composite material; flammability depends on three basic factors they are oxygen supply, ignition source and fuel. Flammability can be controlled by these three factors and reduced by adding fire retardants during the fabrication of natural fibre reinforced composite material. Fire retardants function in the composite material is to delay the fire penetration in the material [2].

In present situation, human is thinking about materials that are energy saving and pollution reducing in nature, these conditions are satisfied by the natural fibre reinforced composite material. These materials are not only energy saving but also improve thermal and mechanical resistance of the building material [3]. Experimental study is conducted on biocomposites that include sisal fibre as a fibre reinforcing material and author discussed about the effect of silicon carbide (SiC) powder in the composite material on the thermal properties, like thermal conductivity, thermal stability and thermal diffusivity, that increases with increase in SiC powder content and specific heat capacity increases up to some limit and decreases [4]. Previously, thermal conductivity behaviour of the bamboo fibre reinforced composite on the basis of varying volume fraction, temperature and fibre angle is mainly focused. Thermal conductivity decreases with volume fraction of fibre and increases with fibre angle variation [5]. Jute fibre composite material gives better thermal behaviour than other composite material, as the amount of filler material increases in the composite it causes the increase of hardness and decrease of its tensile strength. Natural fibres are found to be superior in industrial applications than glass fibres [6].

Thermal properties of natural fibre reinforcement polymer composite materials are studied by considering volume of fibre content in the composite material. As volume of fibre content increases, it increases the insulation characteristics of the material [7]. Investigation on plant stem fibre (*Entada manni*) reveals the thermal degradation and structural characteristics of the fibre. KOH-treated fibres effects on the thermal stability and microstructural behaviour of the fibre [8]. Thermal behaviour of the bamboo fibre composite material is analysed; these fibres have low thermal stability and degradation of material starts from 200 °C [9]. Nanointerstitial material in the natural fibre reinforced polymer improves thermal conductivity of material [10].

Most of the authors discussed the use of fire retardants and filler material in composite material manufacturing and also, they studied the thermal properties of the natural fibre reinforced composite material. This paper deals with the information on the composite material fire penetration resistance result and compared.

## 2 Methodology

Fire penetration test of the natural fibre reinforced composite material includes the different subsections like materials, machines used for testing, fabrication of composite material and fire penetrating testing procedure of the composite material.

### 2.1 Material Used

For fabrication of composite material, different fibres are used like sisal fibre, coir fibre and palm leaf sheath fibre these are the reinforcing materials shown in Figs. 1, 2, and 3, respectively, and resin LY-556 and hardener HY-951 are used as matrix and bonding material in composite material.

### 2.2 Machine Used

Composite materials can be fabricated by different fabrications methods but for this project, composite material is fabricated by hand lay-up method of composite manufacturing.

- Universal Testing Machine (UTM) is used for compression of fibre layers, general use of UTM is to test tensile as well as compression strength of materials. This machine completely works on the hydraulic mechanism, both upper and lower heads of machine moves in column. This movement is used for compression purpose by placing material in between heads with the use of plates as shown in Fig. 4.



**Fig. 1** Sisal fibre laminate

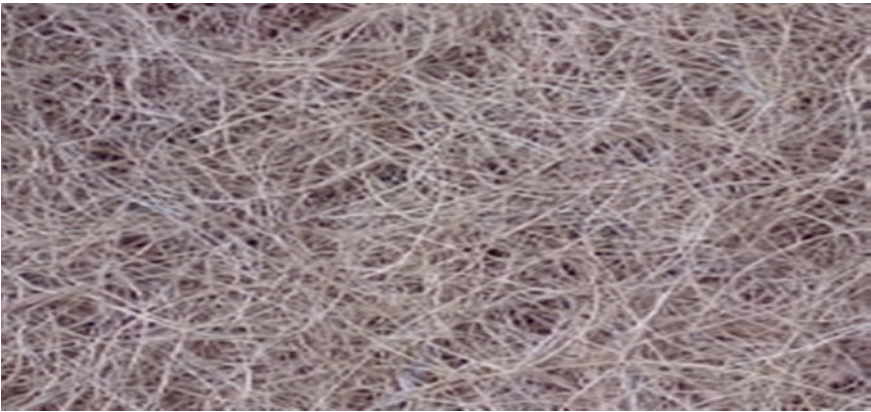


**Fig. 2** Coconut fibre laminate

- Oxy-acetylene welding equipment torch shown in Fig. 5 is used for penetration test; generally, this equipment is used for welding two metals by using high temperature range of heat produced from the equipment. High temperature flame is used for fire penetration test for this study.



**Fig. 3** Palm leaf sheath fibre laminate



**Fig. 4** Universal testing machine

### ***2.3 Fabrication of Composite Material***

Fabrication process of composite material included different stages like fibre selection, fibre preparation, application of resin, compression of layers and curing of material as shown in Fig. 6. Sisal fibre, coconut fibre and palm leaf sheath fibre are used for fabrication of composite material, these fibres are arranged in such a way that they must bind each other and the pattern of this arrangement is sisal–coconut–palm leaf sheath–coconut–sisal as shown in Fig. 7. During fabrication process, laminates of fibres are placed upon other to form complete composite material. By applying resin mixture with the proper proportions in between each and every layer and compress this pattern by using universal testing machine will give natural fibre reinforced composite material.



**Fig. 5** Oxy-acetylene welding torch with flame



**Fig. 6** Fabrication process of composite material

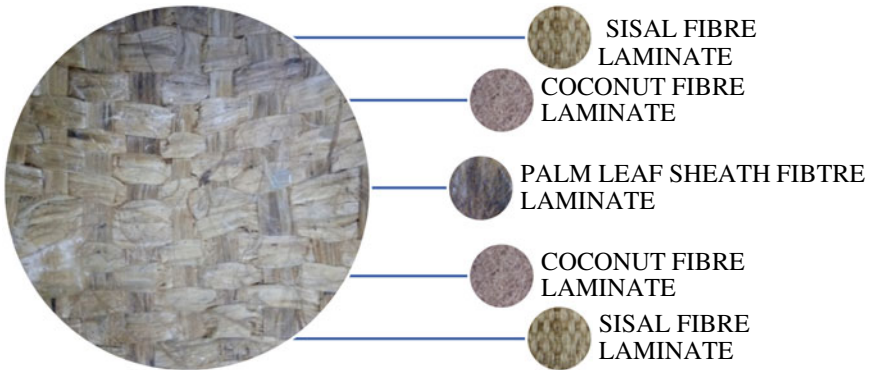


**Fig. 7** Composite material pattern representation



## 2.4 Fire Penetration Testing Procedure

It is necessary to test the natural fibre composite material in order to use in different applications like building and insulating materials, thermal behaviour of the natural fibre composite material must be studied before using it in practical. Fire penetration test is one of the major factors in the thermal behaviour and safety of material using different applications, for this test, flame of the oxy-acetylene welding equipment is used. For comparison of results plywood is tested along with the composite material.

Both the specimens are of  $150 \times 120 \times 18$  mm dimensions as shown in Figs. 8 and 9, these are tested for penetration resistance determination of the composite material

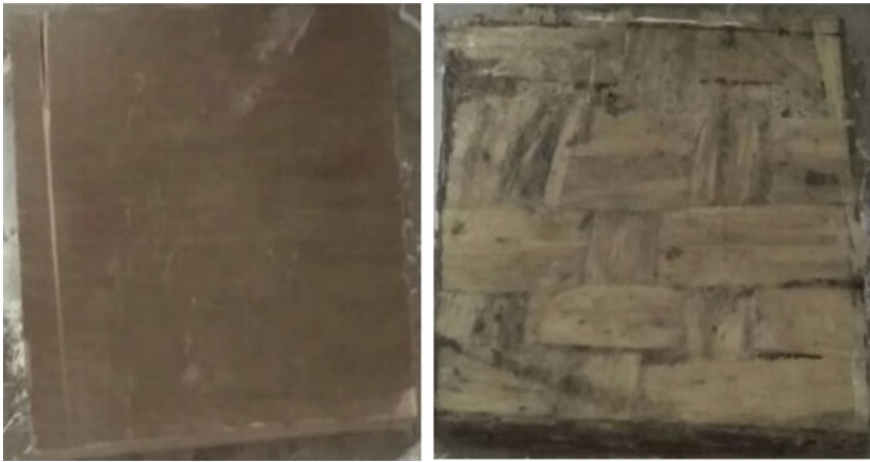


Fig. 8 Plywood and composite material before testing

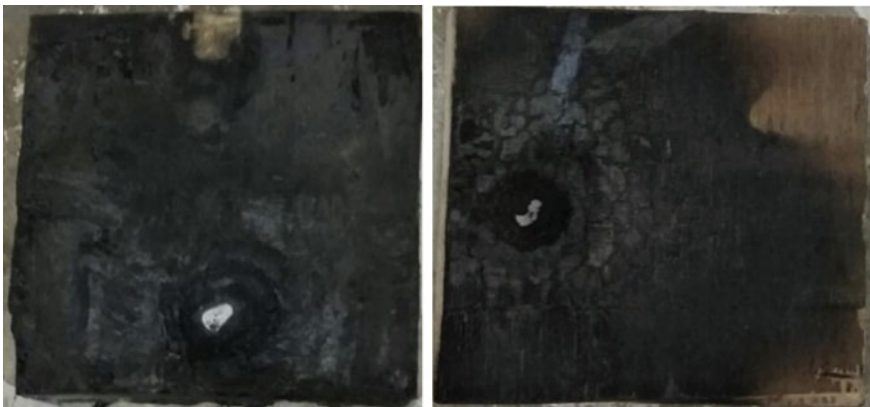


Fig. 9 Plywood and composite material after testing





**Fig. 10** Penetration testing of plywood material



**Fig. 11** Penetration testing of composite material

along with the plywood. These specimens are tested individually to know the time taken to penetrate high intensity of flame in it. During the testing process, nozzle of the oxy-acetylene welding is placed in such a way that flame strikes the front face of the composite material as shown in Figs. 10 and 11, this will continue till the flame is exit from the rear side of the specimens.

### **2.5 Calculations**

Fire penetration test is mainly used to determine the time taken to penetrate the flame in the material and penetration rate of natural fibre reinforced composite material, this includes some theoretical calculations that are as follows:

$$\%P_{comp} = \frac{(P_{ply} - P_{comp})}{P_{ply}} \times 100 \quad (1)$$

$$\%P_{ply} = \frac{(P_{ply} - P_{comp})}{P_{comp}} \times 100 \quad (2)$$

where

$\%P_{comp}$  = Percentage of penetration rate of composite

$\%P_{ply}$  = Percentage of penetration rate of plywood

$$P_{ply} = \text{Penetration rate of ply wood} = \frac{\text{Thickness of plywood}}{\text{Time taken to penetrate}} \quad (3)$$

$$P_{comp} = \text{Penetration rate of composite} = \frac{\text{Thickness of composite}}{\text{Time taken to penetrate}} \quad (4)$$

In order to calculate percentage of penetration rates of composite material and plywood Eqs. 1 and 2 are used, respectively. Percentage rates can be calculated by using individual penetration rates of both materials, penetration rates of materials are calculated by using Eqs. 3 and 4.

### 3 Results and Discussion

Fire penetration experiment of the composite material gives thermal behaviour of the natural fibre reinforced composite material compared to plywood material and this test provides the percentage of penetration rate of composite material and plywood. Fire characteristics of the material depend on composition, fibre content, dimensions of the specimen and intensity of the flame.

Composition of the composite material plays an important role in deciding thermal behaviour of composite material, composition of material includes the number of layers used and type of resins used for fabrication of material. As the number of layers increases penetration decreases. As fibre content increase in composite material it increases the time taken for penetration, when bulk amount of combinational fibres place in front of the flame it is difficult to burn or penetrate in that material. Another reason is that if the fibre content is more it absorbs moisture in large quantities, this absorption restricts some amount of flame.

Dimensions of composite material like thickness, length and width effect on the fire penetrating characteristics of the material. The material which is having large thickness give less penetration rate and time taken for penetration is more, this is because of number of layers that provide restriction from fire increased in the composite material. Oxy-acetylene welding equipment provides high intensity flame this

**Table 1** Final results of fire penetration test

S. no.	Material	Thickness in mm	Time taken in seconds	Penetration rate	Percentage of penetration rate
01	Composite Material	18	87	0.206	48.5
02	Plywood	18	45	0.4	94.17

can affects the penetration rate of composite material. If the intensity of flame is less, rate of penetration is less and penetration time is more, for high intensity flame it is vice versa of low intensity flame.

Compared to plywood material, composite material gives better penetration resistance, because when flame strikes composite material it must burn the first layer of material. Sisal fibre is first layer of this material, it will restrict some amount of fire during the fire penetration test. Composite material does not catch fire at initial stage of testing, penetration is uniform in composite material up to final stage because at initial stage of fire penetration, testing flame of the torch must face thick layer of resin mixture, at that time it is difficult for fire flame to penetrate in composite material.

Percentage of penetration rate of composite material is 48.5%, this means composite material has less penetration rate due to the properties of individual fibres that are used for the composite material fabrication. Rate of penetration depends on the complete physical as well as chemical properties of composite material. Percentage of penetration rate of plywood is 94.7%, this means that plywood does not withstand high temperature flame and it allows the flame easily in it, so penetration rate is more. Plywood does not contain any matter that provides resistance to the composite material; this is the reason that plywood gives fire penetration rate more than composite material.

Time taken for flame to penetrate in the composite material is more, it means composite material restricts the flame to penetrate in it. Time taken for flame to penetrate in the composite material depends upon the arrangement of fibre layers in the composite material fabrication process; this arrangement of the layer will give somewhat restriction of the flame. Time taken for flame to penetrate in the plywood material is less, it means that the material is allowing flame faster than composite material. All the results related to the fire penetration test of composite material and plywood as mentioned in the Table 1.

## 4 Conclusion

Natural Fibre reinforced composite material is having different applications in every field like transportation, building material and industrial applications due to the reason of their easily available nature and also, they are free from environmental pollution.

Natural fibre reinforced composite material can withstand up to high temperature range without catching fire because of the nature of binding material used during the composite material fabrication. It is observed during the penetration process initial and final stages of the flame penetration are constant in the composite material. It depends on thickness of the composite material and fire catching capacity of the individual fibre used in the composite material.

The amount of burning rate of the fibres in the composite material depends on the nature of the resin and resin proportions are used during the fabrication process. If the amount of resin present in the composite material is more then the burning rate of the material is less. If the composite material is fabricated with less amount of resin mixture it will burn as fast as any type of plywood. More time is taken for flame to penetrate the composite material because of only the fibre content and amount of resin present in the composite material. Rate of penetration in composite material less due to its better properties that can be transferred from the resin mixture to the composite material.

## References

1. Kozłowski R, Wadyka Przybylak M (2018) Flammability and fire resistance of composite material reinforced by natural fibres. *J Polym Adv Technol* 19:446–453
2. Vishnu Prabhakar M, Rajashekar T (2018) Machinability and flammability properties of sisal reinforced composite. *IOP Conf. Series: Mater Sci Eng* 402:012035
3. La Gennusa M, Llorach-Massana P, Montero JI, Peña FJ, Rieradevall J, Ferrante P, Scaccianoce G, Sorrentino G (2017) Composite building materials: thermal and mechanical performances of samples realized with hay and natural resins. *Sustainability* 9(3):373
4. Teja MS, Ramana MV, Sriramulu D, Rao CJ (2016) Experimental investigation of mechanical and thermal properties of sisal fibre reinforced composites and effect of SiC filler material. *IOP Conf. Series: Mater Sci Eng* 149:012095
5. Mounika M, Ramaniah K, Ratna Prasad AV (2012) Thermal conductivity characterization of fibre reinforced polymer composite. *J Mater Sci Eng* 3:1107–1116
6. Praveen Kumar K, Manzoor Hussian M, Reddy S (2018) An overview on thermal and mechanical properties of natural fibre reinforced hybrid composites. *Int J Curr Eng Sci Res* 5(1):41–46
7. Mohapatra RC (2018) Experimental study on optimization of thermal properties of natural fibre reinforcement polymer composites. *Libr J* 5:1–14
8. Peter BO, Ajibade OJ, Alaneme KK (2016) Structural characteristics, thermal degradation behavior and tensile properties of hand extracted *Entada manni* fibres. *J Phys Sci* 27(1):89–102
9. Shah AUM, Sultan MTH, Cardona F (2017) Thermal analysis of bamboo fibre and its composites. *BioResources* 12(2):2394–2406
10. Reddy KS, Sreedhar D (2016) Thermal conductivity of natural fibre, glass fibre and CNT's, reinforced epoxy composites. *Int J Curr Eng Technol* 6:1196–1198

# Microstructural Evaluation of Friction Surfaced Aluminium Alloy AA6063 Over Mild Steel



**B. Vijaya Kumar**

**Abstract** AA6063 aluminium alloy coating was deposited over IS2062 mild steel using friction surfacing technique and the microstructural evaluation was studied at various process parametric combinations to obtain relationships between the input parameters and grains interlocking which were observed from microstructural evaluation and with microhardness. The microstructural evaluation of the coating images across the interface using microstructure image analyzer and hardness was also measured across the interface using micro Vickers hardness. Studies revealed that no defect along the interface and very good bond integrity between aluminium alloy and mild steel. Coating exhibited fine grain size microstructure along the interface. It is noticed that aluminium alloy layers are cohesive with mild steel and coating layers dovetailed with base metal which is required for interface strength. Mechtrode rotational speed (N), axial load (F) Table speed ( $V_x$ ) are noteworthy elements and influence the output parameters. Based on the observation of results more metal transfer at the parametric combination of higher axial load and traverse speed with lower rotational speed produced sound coating. Based on various ranges of parameters, combination of strong bond is obtained in a close range of parameters' combination. Coating metal and base metal are incongruous and have propensity to form brittle inter-metallics

**Keywords** Friction surfacing · Mechtrode · Substrate · Microstructure · Sound coating

## 1 Introduction

This is an advanced solid-state welding technique to deposit metallic coatings on dissimilar metals using frictional energy and it is related to friction welding that consists deposition of plasticized metal on flat plate by utilizing the heat developed

---

B. V. Kumar (✉)

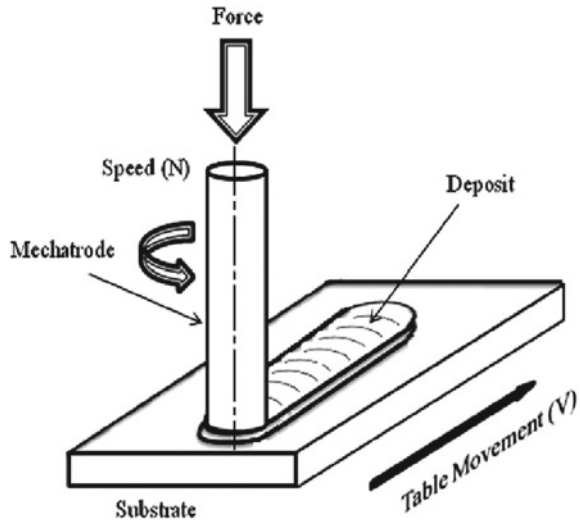
Department of Mechanical Engineering, Guru Nanak Institute of Technology, R.R District, Ibrahimpatnam 501506, Telangana, India  
e-mail: [vkbongarala@gmail.com](mailto:vkbongarala@gmail.com)

© Springer Nature Singapore Pte Ltd. 2020

G. S. V. L. Narasimham et al. (eds.), *Recent Trends in Mechanical Engineering*,  
Lecture Notes in Mechanical Engineering,  
[https://doi.org/10.1007/978-981-15-1124-0\\_44](https://doi.org/10.1007/978-981-15-1124-0_44)

511

**Fig. 1** Schematic of friction surfacing



by radial friction at consumable rod (Mechatrode) and flat plate (Substrate) interface. In this process, a revolving aluminium alloy round rod is forced on a mild steel plate in vertical direction then temperature is developed between the rod end and plate surface due to frictional energy. The rod end starts deforming plastically and increases deformation by heat transfer from the interface. Once the rod stir ends, it deforms completely and lies on the base plate due to shear force offered by the table traverse speed due to relative motion between rod and plate.

Material flow at the area of contact occurs due to combination of mechatrode force, rotation speed and substrate traverse speed. As the substrate moves at a specific rate the plasticized material detaches from the mechatrode and deposits over the substrate. The vertical axial load initiates the plastic deformation in mechatrode that deformed material continuously and metallurgically bonded layers on base metal as shown in the schematic diagram in Fig. 1. Many authors were attempted on friction surfacing technique to deposit with variety of material combinations [1]. They found that ferrous materials, in general, were ready to coat [2] nonferrous materials pose some problems due to their high thermal conductivity and high temperature instability [3]. Among nonferrous materials, Aluminium alloy was found to be more feasible coating material and can be coated at a narrow range of parameter levels owing to that application potential as candidate material for corrosion protection. Traditionally, aluminium coatings were made by cladding and aluminization, to minimize dilution, inter-metallic formation and to retain material chemistry, coatings were done at higher pressure and higher temperature. However, it suffers from problems associated with solidification; in addition, the process is time-consuming and not cost-effective. Therefore a solid-state welding process which do not takes place at melting temperature can report these problems and friction surfacing is the ideal solid-state welding process that can deposit comparatively thick metallic coatings.



**Fig. 2** CNC friction surfacing machine

Friction surfacing of aluminium alloys was reported earlier [3, 4]; however, emphasis was on the feasibility aspects and mechanical properties. Detailed microstructure study of these solid-state deposits of aluminium over mild steel has not been well documented, thus, the present study assumes special significance.

## 2 Experimentation

AA 6063 aluminium alloy rods of 15 mm diameter and 280 mm long with a chemical composition of 0.4Si, 0.35Fe, 0.10Cu, 0.10Mn, 0.65 Mg, 0.10Cr, 0.10Zn, 0.10Ti; balance aluminium (in wt%) as mechatrode (consumable rod) and mild steel (250 mm × 300mm × 10mm) as substrate was used in the present study. Rod ends were faced to ensure flatness and the substrate was milled and surface ground to obtain a flat and even surface free from oxide. Mechatrode and substrate were cleaned with acetone prior to surfacing to minimize contamination [5].

Friction surfacing experiments were carried out on CNC friction surfacing machine having a capacity of 50 kN axial load (F), spindle speed 2400 rpm (N) and table speed of 5000 mm/min (Vx) located at the Defence Metallurgical Research Laboratory, Hyderabad, India. AA6063 aluminium alloy coatings were deposited over a length of 100 mm on mild steel shown in Fig. 3 as per the experimental parameter matrix (Table 1).

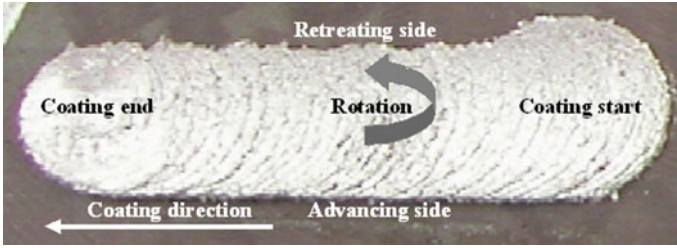


**Fig. 3** Typical friction surfaced layer

**Table 1** Selected parameters and levels

Parameters	Notation	Levels	
		Min. (-)	Max. (+)
Axial force	F (kN)	4	6
Spindle speed	N (rpm)	800	1000
Table speed	Vx (mm/min)	600	800



**Fig. 4** Deposit of aluminium alloy over mild steel by the eight parameter combinations

**2.1 Design of Experiments**

To obtain the optimum parameters, experiments were designed using factorial design for two levels, 3 parameters giving  $2^3 = 8$  parameter combinations as shown in Tables 2 (Fig. 2).



**Table 2** Experimental parametric matrix

Parameter combinations	Parameters		
	F (kN)	N (rpm)	Vx (mm/min)
1	(-) 4	(-) 800	(-) 600
2	(+) 6	(-) 800	(-) 600
3	(-) 4	(+) 1000	(-) 600
4	(+) 6	(+) 1000	(-) 600
5	(-) 4	(-) 800	(+) 800
6	(+) 6	(-) 800	(+) 800
7	(-) 4	(+) 1000	(+) 800
8	(+) 6	(+) 1000	(+) 800

### 3 Characterization of Microstructure

Characterization of microstructure on coated samples was carried out on microstructure image analyzer. Test samples were taken from coated substrate by cutting in cross direction, after that the test pieces were mounted by dry mounting method with Bake-lite powder and polished using the standard metallurgical procedure [6]. Polished samples were etched with two different etchants for revealing the microstructure of mild steel and aluminium, mild steel portion was etched first with Nital solution next aluminium portion was etched with keller’s solution after that the samples were dried and observed their microstructure at 100 × 200 × and 500 × magnification . Microhardness measurements were taken by standard procedure of IS: 1501-2002 using Vickers microhardness tester using 300 gms load [7, 8]. Hardness survey was also conducted across the coating interface using Vickers microhardness. Figure 5(A–H): Microstructure of coating at parametric combinations PC-1to PC-8.

### 4 Results and Discussion

The microstructure of coating material before coating is represented in Fig. 5. A Typical friction surfaced aluminium alloy is shown in Fig. 4. The coating surface obtained as coarser due to formation of ripples; the deposition laid on the substrate as layers one after the other with small upset like onion rings that is inherent characteristics of friction surfacing [9]. The plasticized layer is transferred on to the substrate in linear direction as per the table traverse speed.

From Fig. 5A to Fig. 5H, it is reported that the aluminium coating is cohesive to the base metal and join together with corrugated profile microstructure between coating and substrate which is most inevitable joint [10], and it is evident from the Fig. 5C at parameter combination 3 that is at lower axial force (4KN)) higher rotational speed(100 rpm) and lower table speed (600 mm/min). The grain size of the

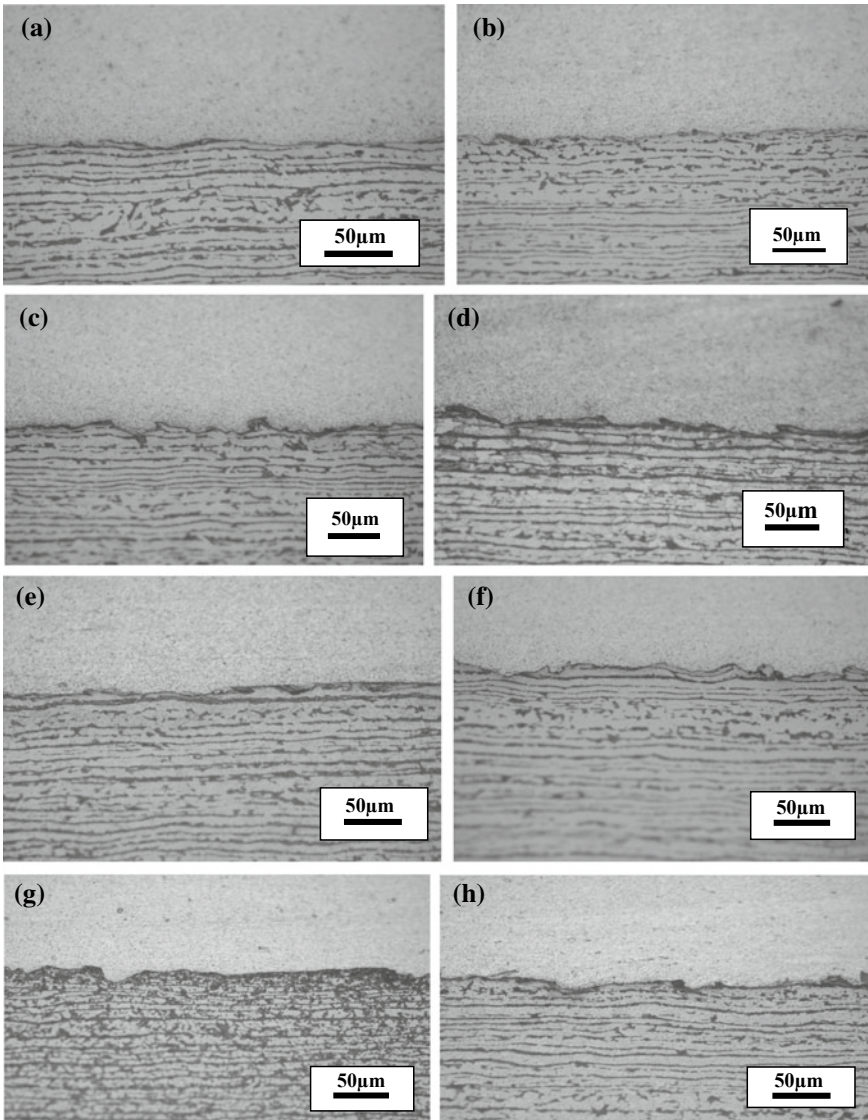


**Fig. 5** **A** Microstructure of coating at parametric combinations PC-1. **B** Microstructure of coating at parametric combinations PC-2. **C** Microstructure of coating at parametric combinations PC-3. **D** Microstructure of coating at parametric combinations PC-4. **E** Microstructure of coating at parametric combinations PC-5. **F** Microstructure of coating at parametric combinations PC-6. **G** Microstructure of coating at parametric combinations PC-7.5. **H** Microstructure of coating at parametric combinations PC-8

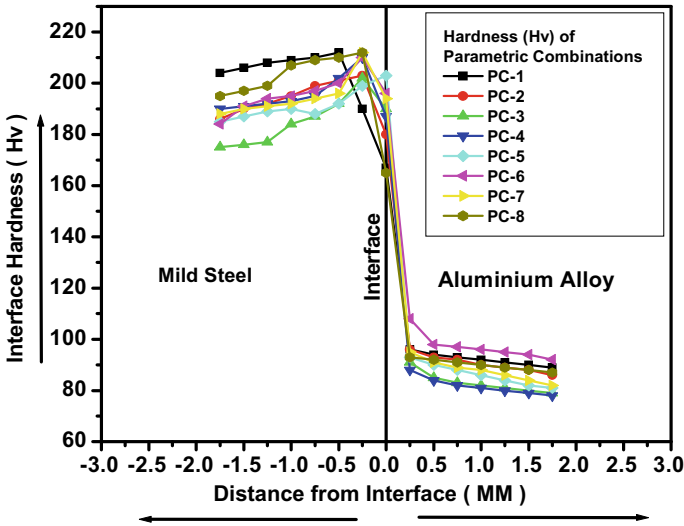


Fig. 6 Hardness distribution around the interface of parameters combination 3

coating is smaller than that in the consumable rod before coating. The fine grain size results that the coating strength is improved. The heat-affected zone is nil because the consumable plasticized layer temperature is lesser than the base metal plastic state temperature [11].

Hence post-weld treatment of coating is not desirable to remove internal stresses like as it is done in conventional welding processes. Hardness gradient across the interface of process parameter is represented in Fig. 6. It is observed that hardness tends to increase as the interface is approached [12]. Maximum hardness is observed in parameter combinations 3 and 7 and least in 6.

## 5 Conclusions

- It is concluded that the aluminium coating is cohesive to the base metal and joined together with corrugated profile microstructure between coating and substrate which is most inevitable joint.
- The grain size of the coating is smaller than that in the consumable rod before coating and improved the coating strength.
- The heat-affected zone is nil because the consumable plasticized layer temperature is lesser than the base metal plastic state temperature.

**Acknowledgements** The authors are thankful to the authorities of Defence Metallurgical Research Laboratory for providing the friction surfacing facilities to carry out the experiments. They would

also like to place on record the support extended by Mr. G. Vijay Kumar for his help in carrying out friction surfacing experiments and Mr. D. S. K. Murali in carrying out the mechanical testing.

## References

1. Tokisue H, Katoh K (2005) Structure and mechanical properties of multilayer friction surfaced aluminium alloys. Report of the Research Institute of Industrial Technology. Nihon University, Number 78
2. Chandrasekaran M, Batchelor AW (1997) Study of the interfacial phenomena during friction surfacing of aluminum with steel. *J Mater Sci* 32:6055–6062
3. Li JQ, Shinoda T (2000) Underwater friction surfacing. *Surf Eng* 16(1):31–35
4. Klopstock H, Neelands AR (1941) An improved method of joining and welding metals. U.K. Patent No. 572, 789, 17 October 1941
5. Sakihama H, Tokisue H (2002) Mechanical properties of friction surfaced 5052 aluminium alloy. *J Jpn Inst Light Metals* 52(8):346–351
6. Shinoda T, Okamoto S (1995) Deposition of hard coating layer by friction surfacing. *J Jpn Weld Soc* 13(3):432–437 (1995-08-05)
7. Madhusudhan Reddy G, Srinivasa Rao K, Mohandas T (2009) Friction surfacing: novel technique for metal matrix composite coating on aluminium-silicon alloy. *Surf Eng* 25(1):25–30
8. Vitanov VI, Voutchkov II (2005) Process parameters selection for friction surfacing applications using intelligent decision support. *J Mater Process Technol* 159:27–32
9. Chandrasekaran M, Batchelor AW (1997) Friction surfacing of metal coatings on steel and aluminium substrate. *J Mater Process Technol* 72:446–452
10. Batchelor AW, Jana S (1996) The effect of metal type and multi layering on friction surfacing. *J Mater Process Technol* 57:172–181
11. Khalid Rafi H, Janaki Ram GD, Phanikumar G, Prasad Rao K (2010) Friction surfacing of Austenitic stainless steel on low carbon steel: studies on the effect of traverse speed. In: Proceedings of the World Congress on Engineering 2010, vol II, WCE, London, 30 June–2 July 2010
12. Liu XM, Zou ZD, Zhang YH, Qu SY, Wang XH (2008) Transferring mechanism of the coating rod in friction surfacing. *Surf Coat Technol* 202(9):1889–1894

# Mechanical Properties of Coconut–Carbon Fiber Reinforced Hybrid Composites



Nampally Yadagiri, B. Naresh, B. Phanindra and P. Varalaxmi

**Abstract** Polymer hybrid composites have superior mechanical composites such that it can be applied for numerous applications. Hybrid polymers composite suggests the design engineer acquires the significant properties in a significant degree by the selection of fibers and matrix. In the present examination, the mechanical properties of coconut fiber and carbon fibers reinforced polyester hybrid composite were investigated. The basic hand lay-up strategy was utilized for the manufacturing of hybrid composites. The mechanical properties, for example, tensile, flexural, and impact strengths of the hybrid composites were assessed according to the ASTM guidelines. Various proportions of the fibers in the composite specimens with random orientation are tested for the mechanical properties. Examination of treated and untreated fibers was additionally considered to know its effect on the mechanical properties. The mechanical properties were enhanced as the carbon fiber content expanded in the composite specimen.

**Keywords** Carbon fiber · Coconut fiber · Polyester

## 1 Introduction

In recent times, fiber reinforced composites are in use for a variety of structures, ranging from aircraft, spacecraft, and buildings and bridges. These broad usages of composites have been facilitated by the introduction of novel materials, development in manufacturing processes and developments of new testing methods as well. Fiber reinforced materials are superior to those of most alloys since it possesses enhanced mechanical properties and its strength-to-weight ratios. Application of composite

---

N. Yadagiri (✉) · B. Naresh · B. Phanindra · P. Varalaxmi  
Department of Mechanical Engineering, Guru Nanak Institute of Technology, Hyderabad 501510, India  
e-mail: [Yadagiri.yantric@gmail.com](mailto:Yadagiri.yantric@gmail.com)

B. Naresh  
e-mail: [naresh.bairagoni08@gmail.com](mailto:naresh.bairagoni08@gmail.com)

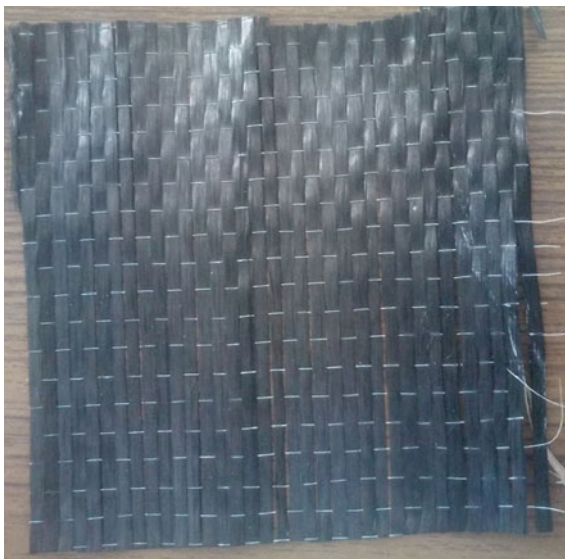
© Springer Nature Singapore Pte Ltd. 2020  
G. S. V. L. Narasimham et al. (eds.), *Recent Trends in Mechanical Engineering*,  
Lecture Notes in Mechanical Engineering,  
[https://doi.org/10.1007/978-981-15-1124-0\\_45](https://doi.org/10.1007/978-981-15-1124-0_45)

materials as structural materials is improving day by day because of these properties, since it makes the designer to design the characteristics of composites is an important advantage [1]. Noorunnisa et al. [2] investigated the mechanical and chemical properties of sisal/carbon hybrid composites and found that the carbon weight % in the hybrid composites enhances the mechanical properties. The treatment of the sisal fibers also improves the mechanical properties. Kiran et al. [3] studied the tensile properties of sisal fiber reinforced polyester composites and found that the fiber weight ratio along with its lengths impacts the tensile strength. Sfiligoj Smole et al. [4] studied the physical properties of grass fibers by considering its impact on treatment with different solutions. Panthapulakkal and Sain [5] investigated on the mechanical and thermal properties of injection-molded short hemp/glass fiber reinforced hybrid composites along with water absorption tests and concluded that the addition of glass fiber content improves the performances properties, thermal properties, and also the water absorption properties of the hemp fiber. Varada Rajulu et al. [6] studied the tensile properties of ridge guard/glass fiber reinforced phenolic composites and reported that the tensile properties are improved with increasing glass fiber content in the hybrid composites. Singha et al. [7] studied the chemical resistance, mechanical, and physical properties of biofiber-based polymer composites. Gangjian et al. [8] investigated on characterization of carbon/wood fiber reinforced hybrid composites by varying polypropylene and carbon percentage. Dobah et al. [9] investigated on tensile and impact properties of a hybrid polyethylene/epoxy combination matrix with carbon fiber fabric. Krishnudu et al. [10, 11] investigated on mechanical properties of natural fiber like coir-luffa cylindrical and prosperous Juliflora hybrid composites by considering the chemical treatments and also the weight proportions in the composite sample. So there is a lot of works carried out by various authors on different fibers but only a few works have been carried out on hybrid composites containing carbon fiber. So, in the present work, investigation is carried out to know the mechanical properties of carbon fiber hybrid composites such as tensile, flexural, and impact strengths. Study on these properties is vital in comparison to physical properties.

## 2 Materials and Methods

### 2.1 Materials

Coconut fibers used in the present study were collected from Nallamalla areas in bark form. Woven cloth carbon fiber was also used in the present study and is shown in Fig. 1. High performance polyester resin and the methyl ethyl ketone peroxide were used as a catalyst and cobalt naphthenate was used as an accelerator. Coconut fibers were extracted from its bark and later it was soaked in 5% NaOH solution for 1 h to remove its greasy and sticky nature and hemicelluloses. Later, it was

**Fig. 1** Carbon fiber

washed thoroughly in distilled water to clean the surfaces and dried for 48 h in room temperature.

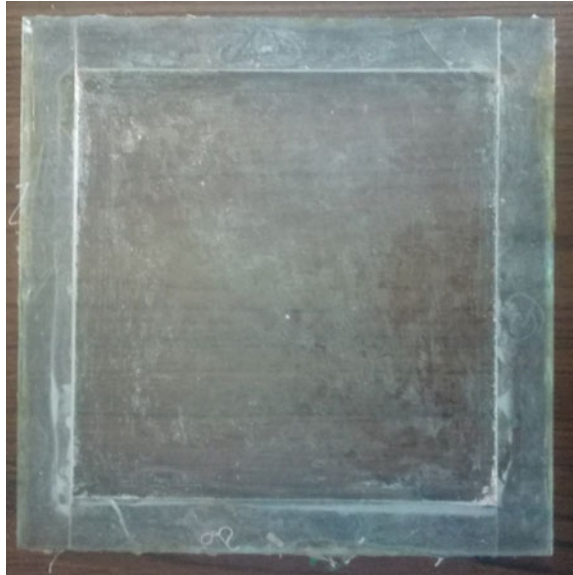
## ***2.2 Preparation of Hybrid Composite***

The different combinations (100/0, 75/25, 50/50, 25/75, 0/100) were selected to make hybrid coconut/carbon/polyester laminates. Hand lay-up technique was used to prepare the composite laminates. Later, the matrix system is poured into a mold made of glass plates with dimensions of 160 mm × 160 mm × 3 mm (Length × Width × Thickness) as shown in Fig. 2. The mold was coated with a thin layer of wax uniformly, which acts as a good releasing agent. Rolling process is used to remove excess resin and air bubbles, and a glass plate was placed on top of it along with weights of about 25 kgs to compress the laminate uniformly and to ooze out the excess matrix. The castings were allowed for 24 h at room temperature and after that, these are heated at 80 °C for 15 min to remove the laminates from the molds easily. With simple tapering method the laminates were removed from the mold.

## ***2.3 Tensile, Flexural and Impact Tests Measurement***

The tensile and flexural strength was determined using INSTRON Universal Testing Machine (UTM). For both the tests the crosshead speed is maintained at 10 mm/min

**Fig. 2** Glass mold used for the fabrication



and 5 mm/min with temperature maintained at 250 °C and relative humidity of 50%. For each test, three samples were prepared as per the ASTM standards. The flexural strength was also determined by using three points bending on the specimens with dimensions 150 mm × 20 mm × 3 mm are cut as per ASTM D 790-07 specifications. The impact strength is determined using IZOD impact tester. The test specimens with dimensions 67.5 mm × 12.7 mm × 3 mm are cut as per ASTM D 256-88 specifications.

### **3 Results and Discussion**

#### **3.1 Tensile Tests**

Tensile strength is one of the most significant and is the most widely specified property. Tensile strength of matrix and coconut/carbon fiber reinforced hybrid composites with both treated and untreated coconut fibers. The composites with different ratios of fiber weight were shown in Table 1. From the table, it was observed that tensile strength increase in carbon fiber content. It was also observed that the treated hybrid composites possess higher strength when compared to untreated hybrid composites, this is due to the removal of hemicellulose and lignin content in the natural fibers (coconut fiber). Moreover, this also increases the interface bonding between



**Table 1** Tensile Strength of hybrid composites for varying proportions of fiber content

S. no.	Fiber ratios	Tensile strength in MPa	
		Untreated	Treated
1	0–100	24	38.14
2	25–75	26	52.64
3	50–50	32	69.81
4	75–25	45	92.49
5	100–0	95.97	96.01

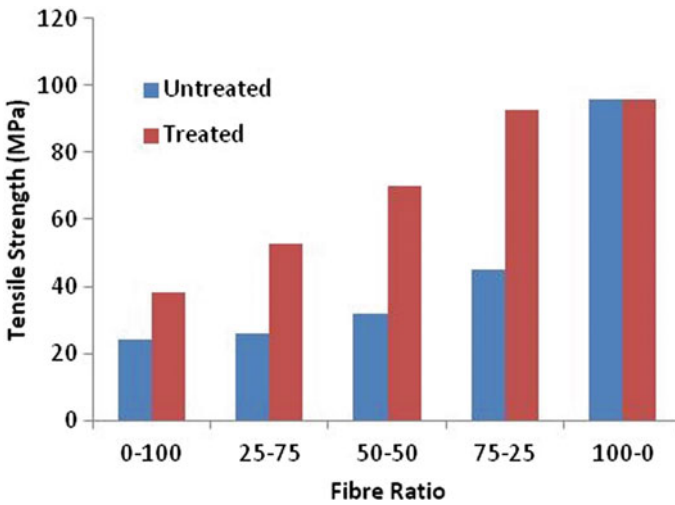


**Fig. 3** Variation of tensile strength with different fiber ratios for treated and untreated fibers

the fiber and the matrix. Figure 3 shows the variation of tensile strength for treated and untreated coconut/carbon fiber reinforced hybrid composites with different fiber weight ratios.

### 3.2 Flexural Tests

Flexural strength of coconut/carbon fiber reinforced hybrid composites with different ratios of fiber weight were shown in Table 2. From the table, it was observed that flexural strength increased with increase in carbon fiber content in the sample. It was also observed that treated posse’s higher strength when compared to untreated hybrid composites due to the removal of hemicellulose and lignin. This also increases the

**Table 2** Flexural strength of coconut/carbon hybrid composites for varying proportions of fibers

S. no.	Fiber ratios	Flexural strength in MPa	
		Untreated	Treated
1	0–100	50.84	68.54
2	25–75	71.19	92.18
3	50–50	102.58	109.49
4	75–25	111.48	119.58
5	100–0	127.01	126.91

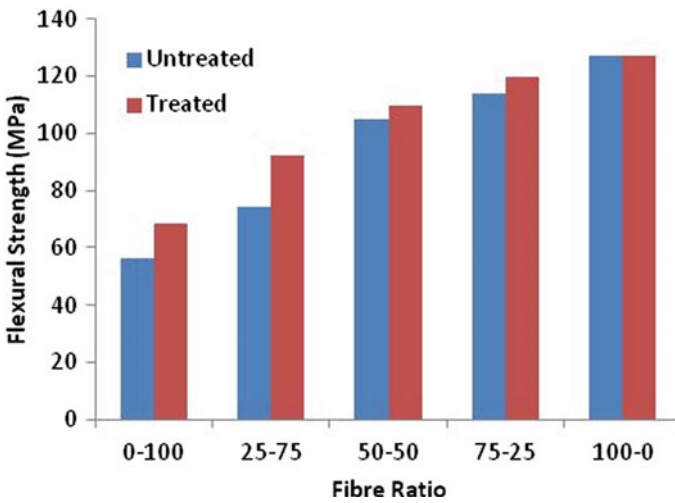


**Fig. 4** Variation of flexural strength with different fiber ratios for treated and untreated fibers composite samples

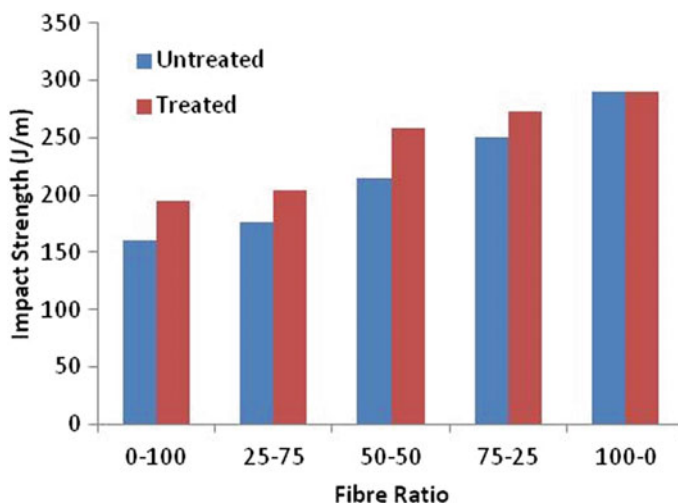
interface bonding between the fiber and the matrix. Figure 4 shows the variation of flexural strength for treated and untreated coconut/carbon fiber reinforced hybrid composites.

### 3.3 Impact Tests

Impact strength results of coconut/carbon fiber reinforced hybrid were shown in Table 3. From the table, it was observed that impact strength also increased with carbon fiber content as the artificial fibers possess higher strength in all the mechanical properties. It was also observed from the table that treated hybrid composites have more impact strength when compared to untreated hybrid composites. Improvement of impact properties for treated composites is due to the removal of hemicellulose

**Table 3** Impact strength of coconut/carbon fiber hybrid composites for different weight ratios

S. no.	Fiber ratios	Impact strength J/m	
		Untreated	Treated
1	0–100	150.11	194.81
2	25–75	171.58	204.54
3	50–50	202.12	258.67
4	75–25	231.45	272.95
5	100–0	289.71	289.79

**Fig. 5** Impact strength for treated and untreated fibers with different fiber ratios in hybrid composites

and lignin. This increases the interface bonding between the fiber and the matrix. Figure 5 shows the variation of impact strength for coconut/carbon fiber reinforced hybrid composites with varying fiber weight content.

## 4 Conclusions

The mechanical properties were tested for the fabricated coconut/carbon hybrid composite samples. Mechanical properties like tensile, flexural, and impact were tested as per the ASTM standards. The fiber treatment with NaOH was also studied in the present work and observed an improvement in all the mechanical properties due to the modification of the surfaces over the natural fibers. Coconut fiber content along

with carbon fiber content varied with proper proportions and its effect was also studied and results revealed that the high carbon fiber content possess high mechanical properties.

## References

1. Ihueze CC, Okafor CE, Okoye CI (2015) Natural fiber composite design and characterization for limit stress prediction in multi-axial stress state. *J King Saud Univ-Eng Sci* 27(2):193–206
2. Noorunnisa Khanam P, Abdul Khalil HPS, Jawaid M, Ramachandra Reddy G, Surya Narayana C, Venkata Naidu S (2010) Sisal/carbon fibre reinforced hybrid composites: tensile, flexural and chemical resistance properties. *J Polym Environ* 18:727–733
3. Udaya Kiran C, Ramachandra Reddy G, Dabade BM, Rajesham S (2007) Tensile properties of sun hemp, banana and sisal fiber reinforced polyester composites. *J Reinf Plast Compos* 26(10):1043–1050
4. Sfiligoj Smole M, Kleinschek KS, Kre T, Strnad S, Mandl M, Wachter B (2004) Physical properties of grass fibres. *Chem Biochem Eng Q* 18(1):47–53
5. Panthapulakkal S, Sain M (2007) Injection-molded short hemp fibre/glass fibre-reinforced polypropylene hybrid composites—mechanical, water absorption and thermal properties. *J Appl Polym Sci* 103:2432–2441
6. Varada Rajulu A, Rama Devi R (2007) Tensile properties of ridge gourd/phenolic composites and glass/ridge gourd/phenolic hybrid composites. *J Reinf Plast Compos* 26:629–638
7. Singha AS, Thakur VK (2009) Chemical resistance, mechanical and physical properties of biofibers-based polymer composites. *Polym Plast Technol Eng* 48:736–744
8. Guo G, Chen JC, Gong G, Lingam MR (2016) Injection molding and mechanical characterization of carbon fiber-woodfiber/polypropylene hybrid composites. *SPE ANTEC Indianapolis* 2016/1106
9. Dobah Y, Ghazzawi Y, Bourchak M (2015, September) Mechanical properties of hybrid carbon fiber reinforced polyethylene and epoxy composites. *ARNP J Eng Appl Sci* 10(16):7053–7057
10. Krishnudu DM, Sreeramulu D, Reddy PV, Rao HR (2018) Effect of alkali treatment on mechanical properties of Prosopis Juliflora hybrid composites. *Int J Appl Eng Res* 13(5):2933–2935
11. Krishnudu DM, Sreeramulu D, Reddy PV (2018, April) Optimization the mechanical properties of coir-luffa cylindrica filled hybrid composites by using Taguchi method. In: AIP conference proceedings, vol 1952, no. 1. AIP Publishing, p 020058

# Frequency Analysis of Aircraft Wing Using FEM



Akhil Basutkar, Kunal Baruah and Shashidhar K. Kudari

**Abstract** Aircraft wings are slender because of their high aspect ratios resulting from large spans and they are susceptible to vibration problems. Hence, in the design of aircraft wings, frequency analysis is a very important input. In this work dynamic behavior of Boeing 747-400 (having aerofoil number BAC 465) aircraft wing is carried out using finite element analysis. A CAD model of the wing is prepared including aerofoil, the engine attached to the wing and the details of the winglet. Detailed frequency analysis in the range 0–300 Hz of the wing with respect to maximum displacement and von Mises stress is conducted. The results obtained are useful inputs for analyzing resonant frequencies and the design of the wing.

**Keywords** Aircraft wing · Vibration · Frequency analysis · FEM

## 1 Introduction

The vibration of a mechanical system is an undesirable issue due to its dangerous failure effects on the system structure. It is important to safe the vibrating structure from failure to prevent disastrous effects, particularly if the structure is in direct contact with humans like aircraft. Among all aircraft parts, dynamic analysis of the wings is important because their performance is critical for the overall aircraft safety. The dynamic stability of the aircraft wings is a major consideration in the design of the aircraft. The major function of an aircraft wing structure is to resist the aerodynamic loads. For this reason, it is stiffened by several frames to enable it to resist loads like bending, compressive and torsion. The wing is subjected to undesired vibration because of the aerodynamic effect, engine attached to it and the vortex caused at the winglet. The important requirement to carry out an aeroelastic and dynamic loads response is the modal analysis of aircraft wings. Several researchers [1–9] have published papers in related areas. Generally, the finite element method (FEM) is widely used to investigate the dynamic behavior of aircraft wings.

---

A. Basutkar · K. Baruah · S. K. Kudari (✉)  
Department of Mechanical Engineering, CVR College of Engineering, Hyderabad, India  
e-mail: [s.kudari@rediffmail.com](mailto:s.kudari@rediffmail.com)

© Springer Nature Singapore Pte Ltd. 2020  
G. S. V. L. Narasimham et al. (eds.), *Recent Trends in Mechanical Engineering*,  
Lecture Notes in Mechanical Engineering,  
[https://doi.org/10.1007/978-981-15-1124-0\\_46](https://doi.org/10.1007/978-981-15-1124-0_46)

Wing resonance is undesirable because it can lead to a dangerous failure of the wing structure. To prevent it, an investigation under what circumstances the resonance occurs is required. Fundamentally frequency analysis of the structure is essential. It is required to explore dependencies between the structure's oscillation frequencies (modal analysis) and its operational conditions (e.g., flight speed, engine rpm or other cyclic loadings, which makes the structure to oscillate). The simplest way to avoid the resonance is avoiding corresponding operational conditions (e.g., certain engine rpm range).

It is observed from the literature that modal analysis of the plane wing is carried out without considering important secondary elements like engine and winglet attached to it. The secondary structures are also of equal importance as the primary structures so that analysts can identify the actual modes of vibration and its effects on the stability of the wing. The engine and the winglet attached to the wing provide different dynamic characteristics of the wing. The main emphasis of this research work is to obtain various modes and to conduct frequency analysis of Boeing 747-400 aircraft wing having important secondary structures like engine and winglet considering the forces generated by the engine and the winglet using FEA.

## 2 CAD Model of the Wing

Wings surface is used to produce lift and ensure flight. Hence, the geometry of the wing determines its aerodynamic quality of a wing, which is expressed as the lift to drag ratio, and can reach high values, up to 60 for some gliders. The swept-wing configuration is the most appropriate wing used for airliners. It needs more forward speed to produce lift than the rectangular wing and produces much less drag which facilitates the aircraft to fly faster. It also works well at the higher altitudes, where most commercial aircraft operate.

A three-dimensional CAD model of the wing of Boeing 747-400 (having aerofoil number BAC 465) including engine and winglet attached to it is carried out using SOLIDWORKS version 24 software. The dimensions of the wing used in this analysis are given in Table 1, the CAD model of the wing constructed is shown in Fig. 1.

It is not possible to obtain the complete information of the aircraft wing from the manufacturing company. All the information and the technical specifications that have been used in this work such as material specification, geometry, dimensions, and loading conditions are taken from relevant books and published work that has dealt with the problem previously.

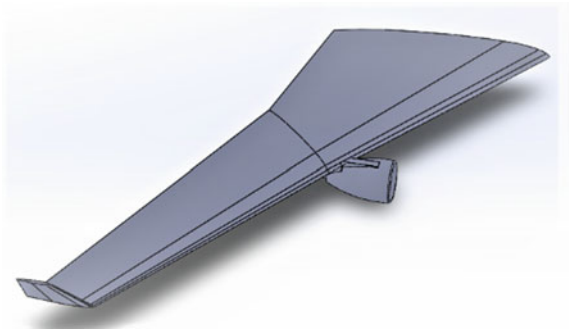
## 3 Finite Element Model of the Wing

The CAD model of the wing including engine and winglet shown in Fig. 1 is imported to ANSYS FEM software. The discretization of the analysis domain of the wing is

**Table 1** Dimensions and material properties of the wing

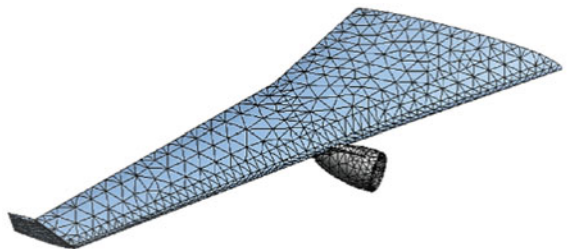
S. no.	Description	Measurement
1	Total length of the wing	24.95 m
2	Root chord length	13.711 m
3	Tip chord length	4.01 m
4	Width at root chord	1.5 m
5	Area of the wing	525 m <sup>2</sup>
6	Taper ratio	0.275
7	Aspect ratio	7.39
8	Material	Aluminum 7076
9	Modulus of elasticity	71.7 GPa
10	Tensile yield stress	503 MPa

**Fig. 1** Wing CAD model



done using SOLID 187, 10 noded tetrahedral solid elements. The number of elements used in the FE analysis is 4407 and the number of nodes is 8823. A 3-dimensional FE mesh of the analysis domain is shown in Fig. 2. The displacement boundary conditions used are all displacements are fixed on the surface of the wing attached to the fuselage of the wing. The material information used in this work is given in Table 1.

**Fig. 2** FE mesh of the wing model used in the analysis



## 4 Finite Element Analysis

### 4.1 Modal Analysis

The first modal analysis (natural frequencies) of the wing including engine and the winglet is carried out using ANSYS version 15. It is decided to obtain the natural frequencies between 0–300 Hz so that it can be simulated with the engine operating frequencies for resonance analysis. We obtained 60 frequencies (modes) in the range 0–300 Hz. Typically, modal analysis of the fifth mode  $f = 13$  Hz is shown in Fig. 3. To indicate all the modal frequencies, a plot of the maximum amplitude versus modal frequencies is shown in Fig. 4.

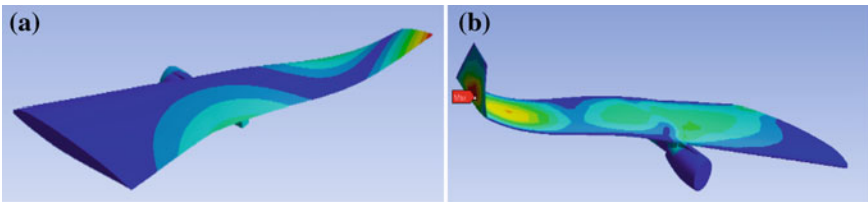


Fig. 3 Typically a modal analysis b von Mises stress distribution of the fifth mode  $f = 13$  Hz

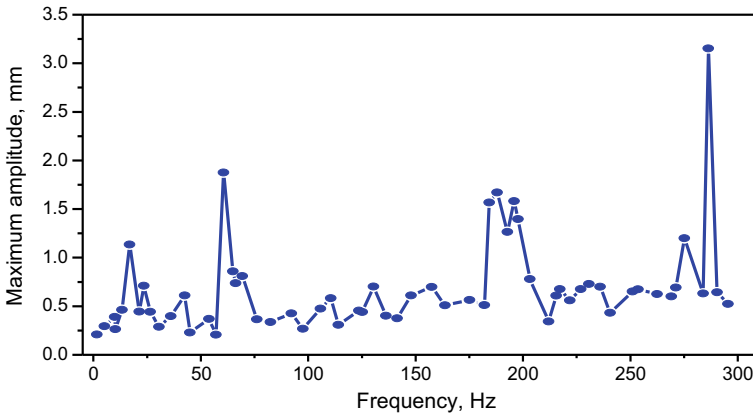


Fig. 4 Maximum amplitude vs. modal frequencies



**Fig. 5** Wing loading considered in the analysis



## 4.2 Frequency Analysis

In this work, a frequency analysis is conducted in the range of 0–300 Hz in steps of 1 Hz to evaluate the dangerous frequencies. The analysis is done to consider dynamic forces generated due to (i) the engine operating speed and (ii) wingtip vortices at winglet. It is known from the literature that the operating speed of the engine of the Boeing aircraft is between 10,000–18,000 rpm, which is 166–300 Hz. As details of the force generated due to the engine is a limitation of this work due to lack of details as said in Sect. 2, we have assumed a typical force of 1 kN acting on the wing at the engine attachment point of the wing as shown in Fig. 5. The load generated due to winglet vortex acting at the winglet is approximated as 0.5 kN for the analysis as shown in Fig. 5. The frequency analysis is carried out for three cases (a) considering engine force of 1kN acting at the engine attached point and (b) vortex force of 0.5 kN generated at winglet and (c) considering both forces.

A typical plot of frequency versus maximum amplitude of vibration of the wing due load case-III is shown in Fig. 6a, b shows the maximum von Mises stress induced in the wing due to various frequencies. It is clear from this figure and results of other cases that more dangerous vibration is expected at frequency 286 Hz, which accounts to be the engine, speed of 17,160 rpm. The results of all three cases for maximum amplitude of vibration and maximum von Mises stress in the wing are shown in Table 2. The results infer that the Boeing engine speeds less than 17,160 rpm are safe for the wing to be stable and to be out of dangerous vibration. It is known that through design, extensive analysis, and certification tests, all configurations of commercial jet airplanes are free from flutter vibration for all design conditions within the aeroelastic stability envelope [10]. Hence, the results obtained in this analysis would be more useful inputs in the safe design of an aircraft wing.

## 5 Conclusions

In this work frequency analysis of Boeing 747-400 aircraft wing is carried out in the range 0–300 Hz. As the details of the loading on the wing are not clearly available, the analysis is carried out using load due to engine and wingtip vortex. The following conclusions are drawn from the present analysis.

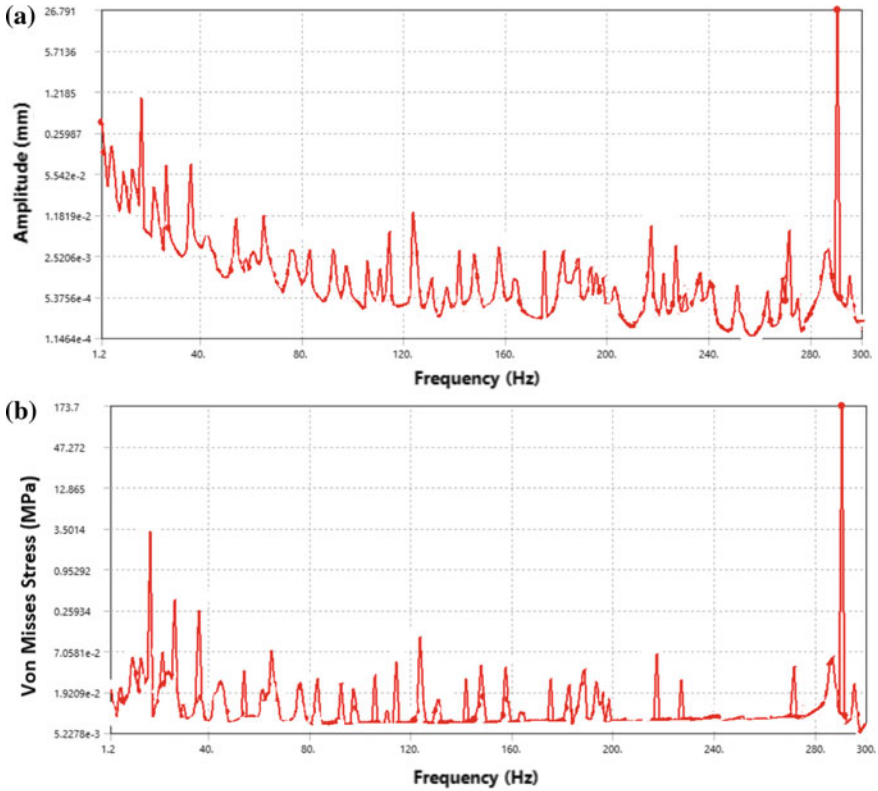


**Fig. 6** The frequency plot generated due to case-III **a** amplitude and **b** von Mises stress

**Table 2** Maximum amplitude of vibration and maximum von Mises stress in the wing

S. no.	Load case	Critical frequency, Hz	Amp, mm	von Mises Stress, MPa
1	Case-1	286	14.8	95.98
2	Case-2	286	11.98	77.78
3	Case-3	286	26.8	173.78

The wings’ dangerous resonant frequency is identified as 286 Hz for the considered conditions of the wing. At the engine operating frequency of 286 Hz wing can have high amplitudes of vibration and generate high stresses in the wing, which can lead to failure of the wing. It is clear from this analysis that the Boeing wing considered in this work is having safe dynamic stability for load frequencies less than 286 Hz. The aircraft engine operating speed less than 286 Hz is safe for the safety of the aircraft.

## References

1. Jia P, Lai SK, Zhang W, Lim CW (2014) Experimental and FEM modal analysis of a deployable-retractable wing. *Mod Mech Eng* 4:183–197
2. El Maani R, Radi B, El Hani A (2017) Vibratory reliability analysis of an aircraft's wing via fluid structure interactions. *Aerospace* 4:40
3. Flore L, Cubillo AA (2015) Dynamic mechanical analysis of an aircraft wing with emphasis on vibration modes change with loading. In: *International conference of scientific paper AFASES*, pp 28–30
4. Santosh KN, Yihun Y, Hamid ML (2015) Finite element analysis and vibration testing of a simple replicate beam-type aircraft wing with and without secondary structure attached. *Int J Aeronaut Sci Aerosp Res* 2(3):27–38
5. Benerjee JR (2016) Modal analysis of sailplane and transport wings using the dynamic stiffness method. *J Phys* 721:1742–6596
6. Krishnamurthy T, Frank, T (2008) Static and dynamic structural response of an aircraft wing with damage using equivalent plate analysis. In: *American institute of aeronautics and astronautics, Schaumburg, IL*
7. Abdulameer HA, Dr. Wasmi HR (2015) Vibration control analysis wing by using smart material. *Innov Syst Des Eng* 6(8):2222–2871
8. Bertrand J, Fellouah H, Alsaif K (2017) Experimental evaluation of the critical flutter speed on wings of different aspect ratio. *J Appl Fluid Mech* 10(6):1509–1514
9. Pavlov B. Determining resonance frequencies of an airplane wing. <http://stc.fs.cvut.cz/history/2009/sbornik/Papers/pdf/PavlovBogdan-340622.pdf>
10. [http://www.boeing.com/commercial/aeromagazine/aero\\_16/vibration\\_story.html](http://www.boeing.com/commercial/aeromagazine/aero_16/vibration_story.html)

# Structural and Vibrational Analysis of Femur Bone Using FEA



Sonu Kumar Kharatmal, Pranav Ravindrannair, Karthik Sridhar, Mir Akber Mohsin Ali and V. Rajashekhar

**Abstract** The femur bone happens to not only be the largest bone in the human body but also one that is most susceptible to fracture. In this paper, a study has been made on the structural and vibrational analysis of the femur bone by making use of a finite element solver (FES) in this case ANSYS. The purpose of the work is to gain an insight into the effective design of bio aided equipment. The femur bone is subjected to (free–free) and (fixed–fixed) boundary conditions were for both the cases natural frequency is in the range of 0–1382.5 Hz and 1254.3–8497.3 Hz. The mode shape and the fracture location can be determined and identified. The results are compared with results available in the literature and it was found to be acceptable with a variation of only 1–2%. It was observed that sudden impact repeated vibrations excitation is a major reason for femur bone failure and the results of this study show that the critical failure occurs at bone shaft (the region between two joints) and neck region.

**Keywords** Femur · Natural frequency · Vibration · Finite element analysis · Biomechanics

## 1 Introduction

Humans are extremely skilled when it comes to everyday movements such as walking, standing, or even climbing stairs. It is such an essential trait that even human babies display skills in such activities by the age of two. However, a lack of physical activity can be a prerequisite for multiple chronic diseases. In the modern world, a plethora of professions such as Physical Educators, Athletic Coaches, Strength and Conditioning Trainers, etc. exist that help an individual attain the required physical workout. These professions rely on training in the fields of Kinesiology and Biomechanics. Kinesiology is the branch of science that studies human movement whereas biomechanics involves the analysis of relevant information that helps understand

---

S. K. Kharatmal · P. Ravindrannair (✉) · K. Sridhar · M. A. M. Ali · V. Rajashekhar  
Aurora's Technological and Research Institute, Hyderabad, India  
e-mail: [Pranavturbokat91@gmail.com](mailto:Pranavturbokat91@gmail.com)

© Springer Nature Singapore Pte Ltd. 2020

G. S. V. L. Narasimham et al. (eds.), *Recent Trends in Mechanical Engineering*,  
Lecture Notes in Mechanical Engineering,  
[https://doi.org/10.1007/978-981-15-1124-0\\_47](https://doi.org/10.1007/978-981-15-1124-0_47)

535

effective and safe movement patterns, equipment, and relevant exercises required to improve movement. The study of these fields is of particular interest and often critical in Sports and it helps prevent injuries or injured athletes. Hence Biomechanics is a powerful ally that provides information on the mechanical properties of tissues, mechanics involved in the movement, not to mention preventive and rehabilitative therapy. Engineers also make use of biomechanics to design specialized equipment to prevent injuries related to overuse.

The Femur bone or thigh bone happens to be the longest and largest bone in the human body. It forms both the hip joint and the knee joint by connecting to the Pelvis and the Tibia respectively. The Femur bone is taken as the topic of study in this paper as the Femur is one of taking a large percentage he commonly fractured bones in a Human body owing to it taking a large percentage of the weight. Hence while designing sports equipment care must be taken to prevent the resonant frequencies from coinciding with excitation frequencies. Finite Element Analysis (FEA) is a method of solving certain problems in Engineering and Science often encountered in engineering. Also, FEA is a cost-effective method to study the effect of vibrations and has been made use of in this paper.

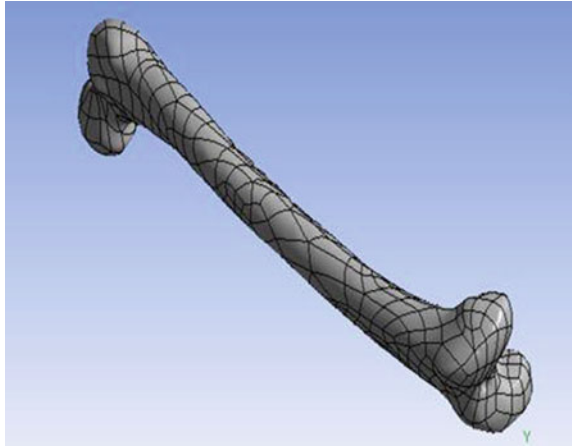
Kumar et al. [1] proposed that the primary objective in the analysis of the Femur bone is to obtain the natural frequencies, natural vibration modes and to identify the probable locations of fracture in the bone through computer simulation formulated by Finite Element Analysis (FEA). Natural frequencies and natural vibration modes are calculated by subjecting the femur bone to both free–free and fixed–fixed boundary conditions.

Khalil et al. [2] made use of experiments and analysis to obtain the natural frequencies of a Femur bone. The experimental and analytical results were obtained by making use of the Fourier analysis and Transfer Matrix method, respectively. However, this study was conducted on a freely vibrating bone.

Shieh et al. [3] conducted a study where finite element analysis was made use of in order to compare stemmed hip joint, resurfacing hip joint, and natural hip joint with respect to both lateral and medial femur stress, and strain distribution on the femur in order to discuss the applicative characteristics of the different surgical procedures of artificial hip joint replacement. The effect of vibrations on the femur bone was studied by Thomas et al. [4] whereas finite element analysis was made use of to predict the fracture in a Femur by Grassi et al. [5], Keyak et al. [6] and Haider et al. [7]. Voo et al. [8] presented a methodology involving the use of computational models and biomechanical stress analysis in a human femur to assess risks.

Hight et al. [9] studied the vibrational analysis on the tibia bone and compared the analytical results with the experimental results. Various other studies were also conducted to measure the effect of impact on bone using FEA [10], Applications of FEA [11–13] and CFD [14, 15] in biomechanics. Vibrational analysis of human brain neck [16], while material properties were determined by making use of modal analysis [17].

**Fig. 1** Meshed model of the femur bone



## 2 Material and Methodology

Based on a volume reconstruction of the coronal computer tomography (CT) images of the left femur bone of a healthy male (37 years of age, weight 65 kg) a 3D finite element model was developed. CT scan properties were set at a resolution and side spacing of 0.5 mm and 0.75 mm, respectively. The material properties considered for the study of the femur bone possess Young's modulus of 7.585 GPa, Poisson ratio of 0.35, and a Bone density of 866 kg/m<sup>3</sup>. The CT dataset was then imported into MIMICS, software used for medical image processing (Materialize, Leuven, Belgium) following which the segmentation of the images was done and the point clouds of femur bone was obtained. The point clouds of the femur bone are converted into surface models using Geomagic Studio software (Fig. 1).

During analysis geometrical model is subjected to two different boundary conditions. For the free–free boundary condition, the lateral condyle, the median condyle, and the femur neck are free whereas in the fixed–fixed boundary condition they are a constraint to move. When the results have been compared with the literature result, it was observed that fixed–fixed boundary condition is more appropriate and describes precise human body behavior. We have taken into account the first 10-order vibration mode shape (Figs. 2, 3, 4).

## 3 Modal Analysis

Modal analysis using FE was performed on ANSYS Workbench 15. The governing dynamic response equation was given by

$$[M]\{x(t)\} + [C]\{x(t)\} + [K]\{x(t)\} = \{F(t)\} \quad (1)$$

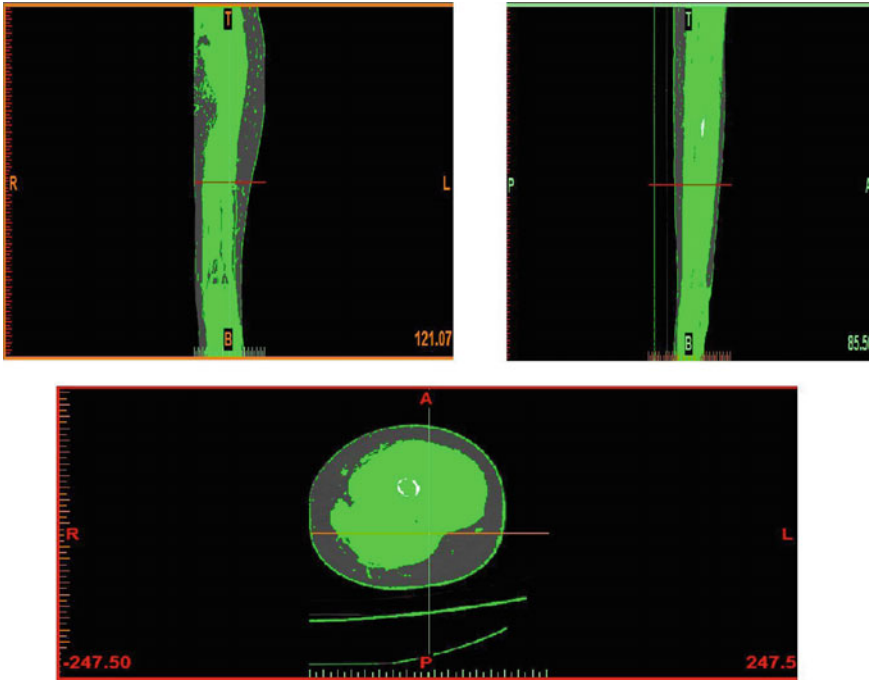


**Fig. 2** Segmentation of bone from soft tissue

Where  $[M]$ ,  $[C]$ ,  $[K]$  are the global mass, Damping and Stiffness Matrix of the model, respectively;  $\{\ddot{x}(t)\}$ –Acceleration Vector,  $\{\dot{x}(t)\}$ –Velocity Vector,  $\{x(t)\}$ –Displacement vector.

For undamped free vibration analysis, both the external excitation force and damping are zero ( $[F] = 0$ ,  $[c] = 0$ ). So the Eq. (2) can be represented as undamped free vibration.

$$[M]\{\ddot{x}(t)\} + [K]\{x(t)\} = 0 \tag{2}$$

The solution for the above equation can be written as:

$$\{x\} = \{X\}e^{i\omega t} \tag{3}$$

where  $\{X\}$  represents the amplitudes of vibration of all the masses (mode shape or eigenvector's),  $\omega$  eigen frequency ( $\text{rads}^{-1}$ ), so the Eq. (2) reduces to:

$$([K] - \omega^2[M])\{X\} = 0 \tag{4}$$

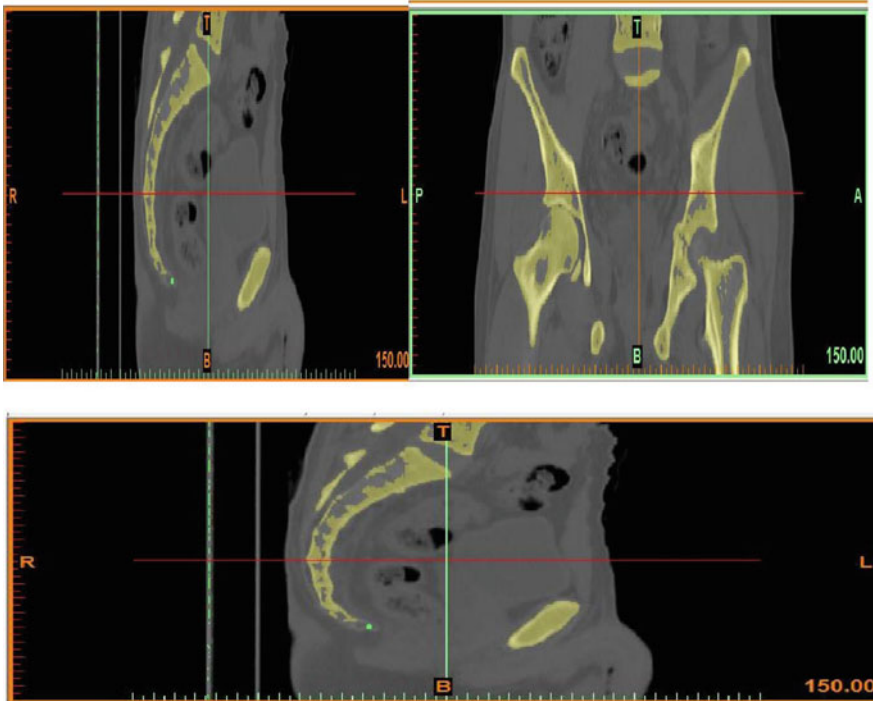


Fig. 3 Region growing of soft bone

If we replace  $\omega^2$  by  $\lambda$ , Eq. (4) becomes a linear problem in matrix algebra.  $\{X^i\}$  has a nonzero solution, then the coefficient matrix must be equal zero. Each eigenvector  $\{X\}$  and corresponding eigenvalues  $\{\omega_i^2\}$  is solved using ANSYS.

## 4 Results

### 4.1 Free-Free Boundary Condition

The result from the modal analysis gives us the following 10 natural frequencies and mode shapes with free-free boundary conditions (Table 1 and Figs. 5, 6, 7, 8, 9, 10, 11, 12, 13, 14).



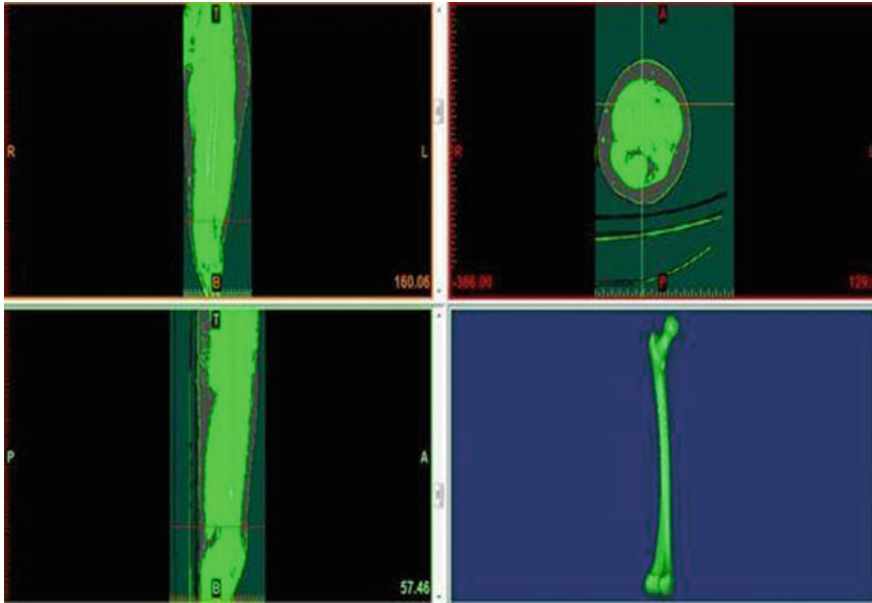


**Fig. 4** Segmented models of CT scan

**Table 1** Mode and natural Frequencies in free–free boundary condition

Mode number	Natural frequency (Hz)
1	0
2	0
3	0
4	4.8134e-004
5	7.4685e-004
6	8.9801e-004
7	449.56
8	523.51
9	1112.80
10	1382.50

**4.2 Fixed–Fixed Boundary Condition**

The result from the modal analysis gives us the following 10 natural frequencies and mode shapes with fixed–fixed boundary condition (Table 2 and Figs. 15, 16, 17, 18, 19, 20, 21, 22, 23, 24).

Fig. 5 Mode Shape 1

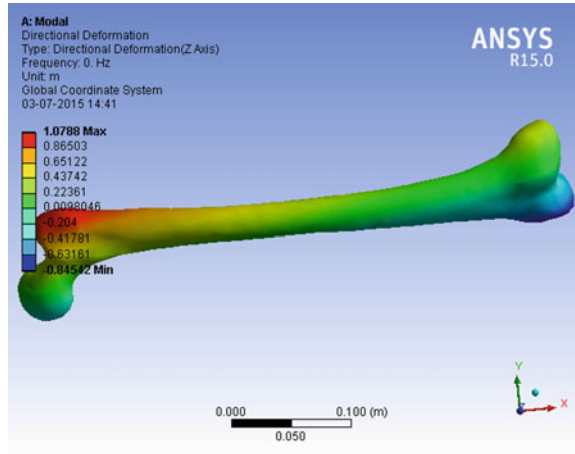
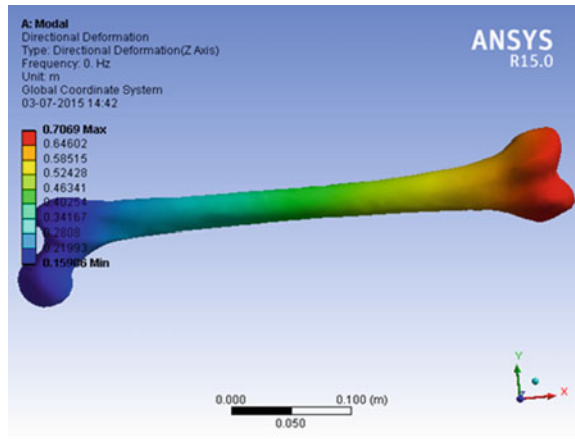


Fig. 6 Mode Shape 2



### 4.3 Results of Structural Analysis

The variations observed in the equivalent stress are shown in the Fig. 25.

The variations in the total deformation of the Femur bone is shown in the Fig. 26.

## 5 Discussions

If the external excitation frequency corresponds with the natural frequency of the bone, then it can lead to the bone being fractured. The analysis performed for the free-free boundary condition gives us a frequency range from 0 Hz to 1382.50 Hz and

Fig. 7 Mode Shape 3

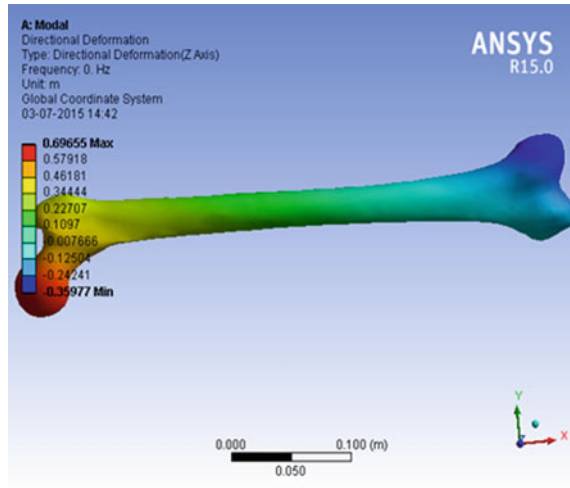
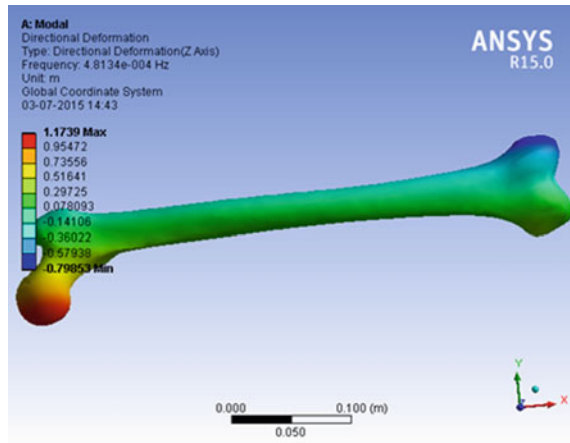


Fig. 8 Mode Shape 4



the analysis performed for the fixed–fixed boundary condition gives us a frequency range of 1254.30 Hz to 8497.31 Hz. The results are in agreement with the literature taken for reference [1, 2]. The variations observed in the free–free boundary condition can be accounted for by the fact that this is not a real case.

Since the fixed–fixed boundary condition gives us an accurate representation of the human body we can discuss the results of the fixed–fixed analysis. The mode shape can also be used to predict the location of the fracture. For example in mode 1 having a natural frequency of 1254.30 Hz, the fracture occurs in the shaft region of the bone whereas, in mode 10, the fracture occurs toward the neck of the bone as

Fig. 9 Mode Shape 5

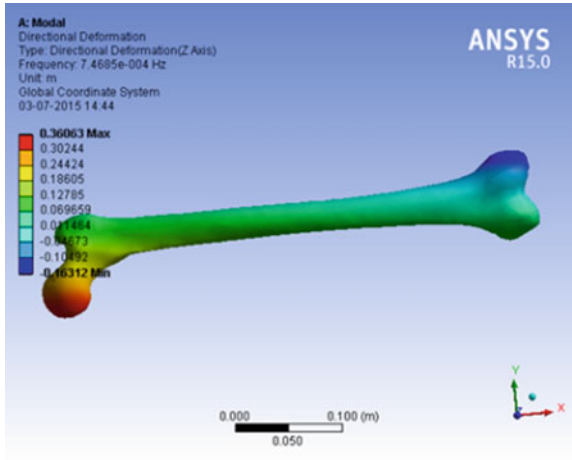


Fig. 10 Mode Shape 6

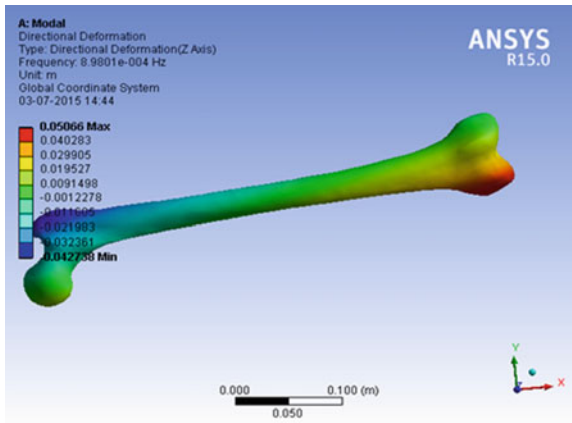


Fig. 11 Mode Shape 7

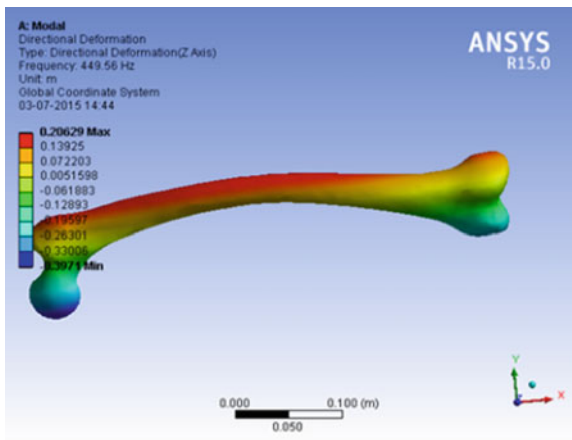


Fig. 12 Mode Shape 8

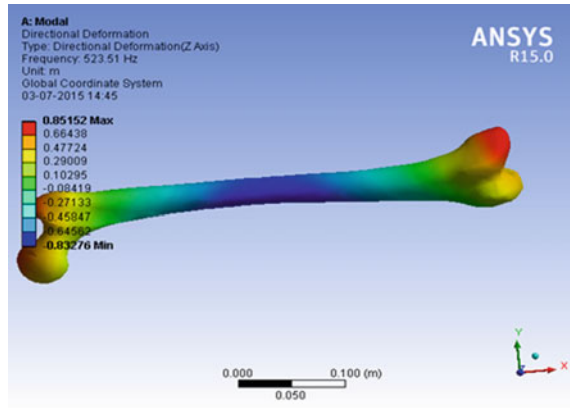


Fig. 13 Mode Shape 9

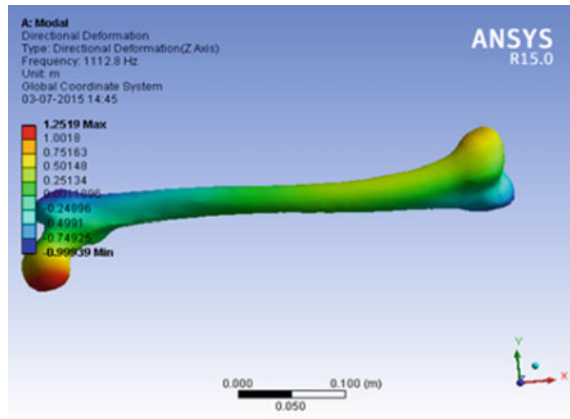
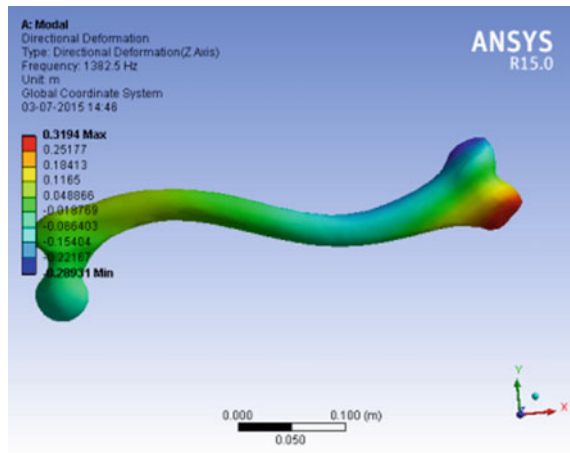


Fig. 14 Mode Shape 10



**Table 2** Mode and Natural Frequencies in fixed–fixed boundary condition

Mode number	Natural frequency (Hz)
1	1254.30
2	1321.11
3	2994
4	3151.52
5	5035.30
6	5362.69
7	5601.10
8	7456.82
9	8244
10	8497.31

**Fig. 15** Mode Shape 1

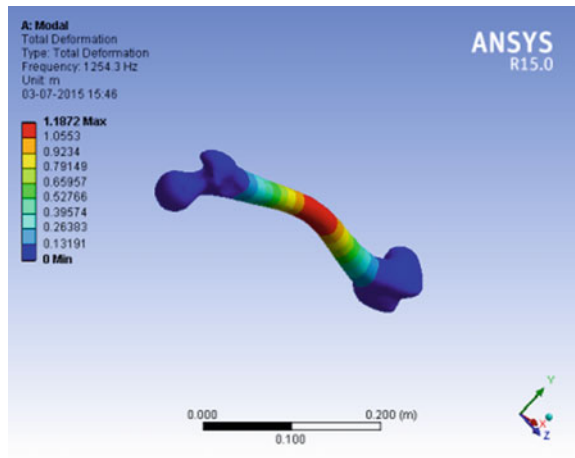


**Fig. 16** Mode Shape 2

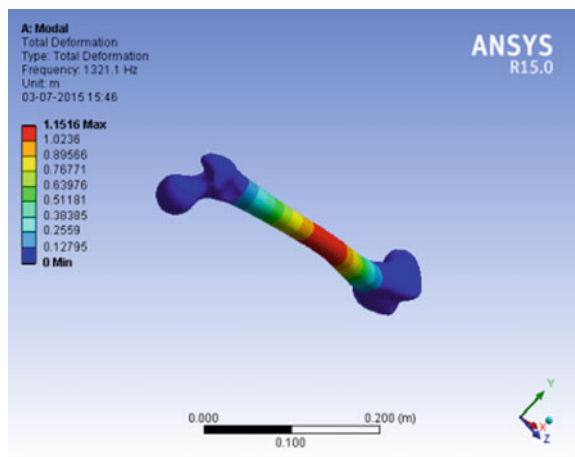


Fig. 17 Mode Shape 3

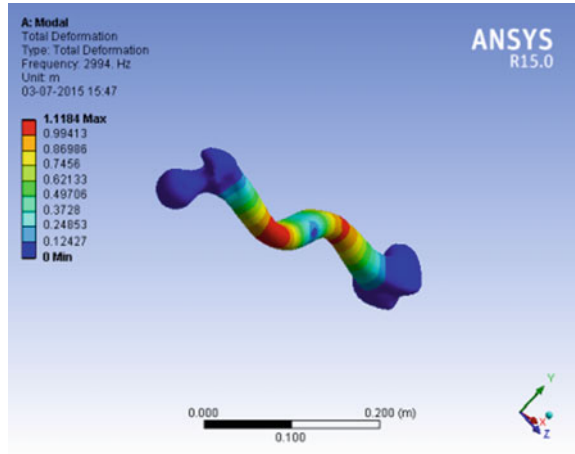
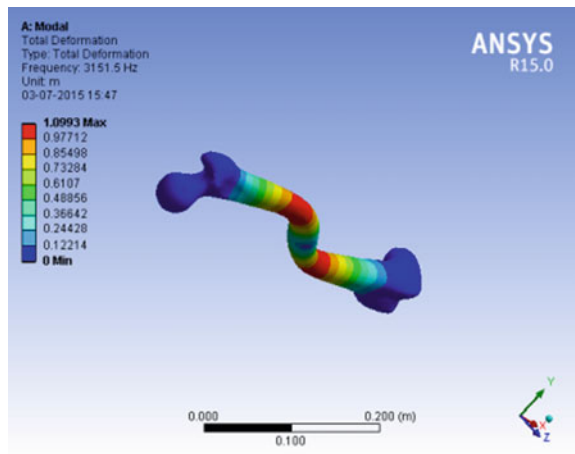


Fig. 18 Mode Shape 4



shown in images Fig. 15 and Fig. 24. We can notice that the fracture of the femur bone seems to occur either at the shaft or the neck region for different frequencies. Although an external load can excite any mode from the first mode to any higher mode, the lower nodes are comparatively easier to excite.

## 6 Conclusions

A sudden and continuous vibration is the primary culprit that causes a failure of the femur bone. If its excitation frequency corresponds to the natural frequency of the bone, then the critical failure of the bone can occur due to resonance. It was observed

Fig. 19 Mode Shape 5

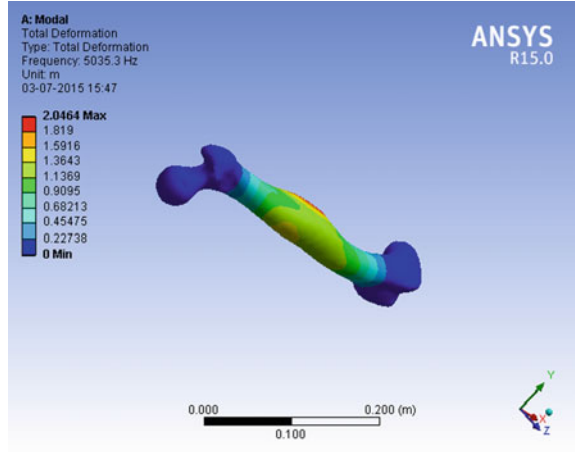
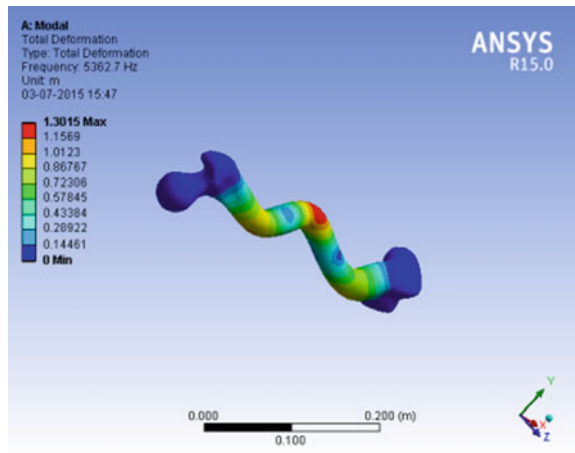


Fig. 20 Mode Shape 6



that the fracture can occur at either the neck region or the bone shaft region of the bone. The natural frequencies for the femur bone were identified and the results were found to be in good agreement with those obtained from the literature.



Fig. 21 Mode Shape 7

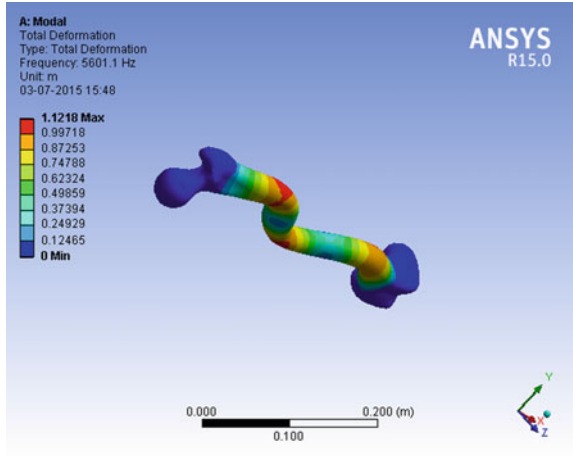


Fig. 22 Mode Shape 8

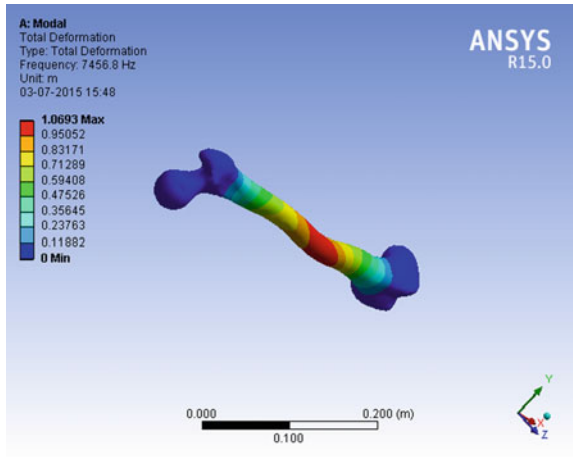


Fig. 23 Mode Shape 9

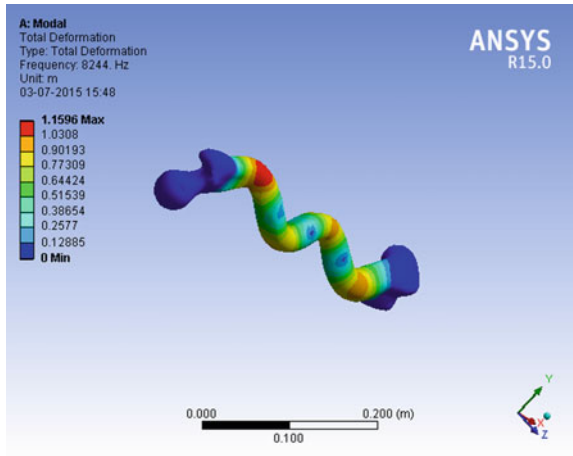
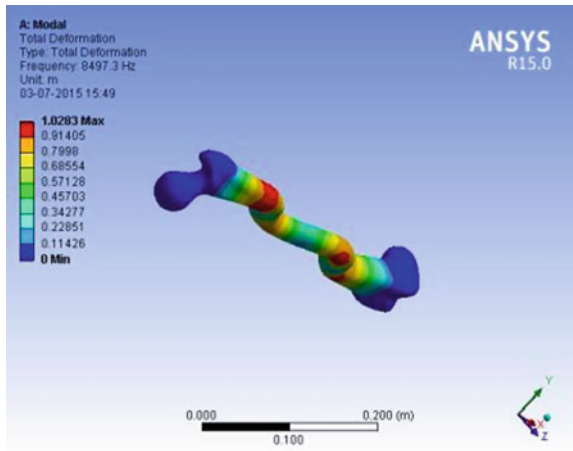
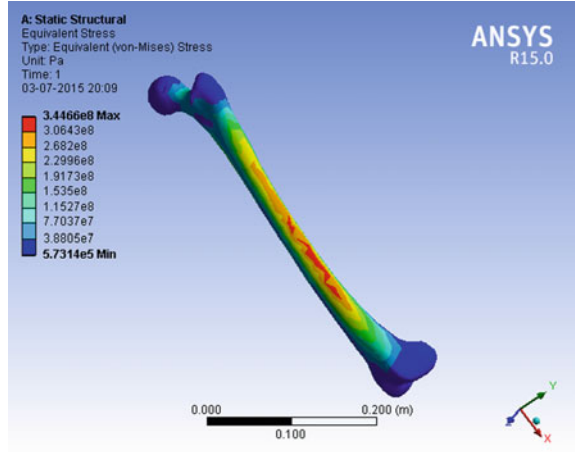


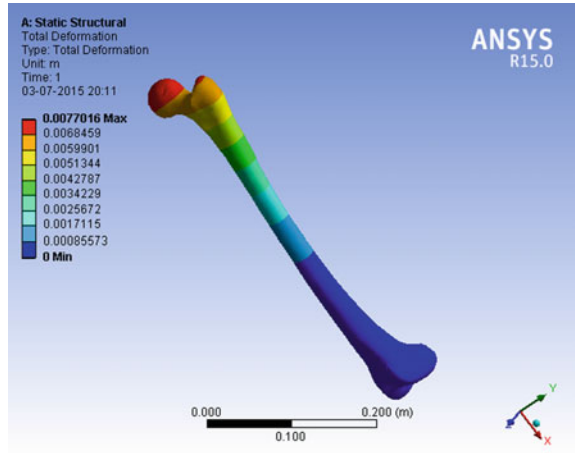
Fig. 24 Mode Shape 10



**Fig. 25** Variation of equivalent stress in a femur bone



**Fig. 26** Variations in total deformation of a femur bone



## References

1. Kumar A, Jaiswal H, Gag T, Patil P (2014) Free vibration modes analysis of femur bone fracture using varying boundary conditions based on FEA. *Procedia Mater Sci* 6:1593–1599
2. Khalil TB, Viano DC, Taber LA (1981) Vibrational characteristics of the embalmed human femur. *J Sound Vib* 75(3):417–436
3. Shieh M-C, Lin AC (2012) CAD-model-based design and stress analysis of resurfacing hip joint prosthesis. *Comput-Aided Des Appl* 9(5):609–619
4. Thomas AM, Luo DZ, Dunn JW (1991) Response of human femur to mechanical vibration. *J Biomed Eng* 13(1):58–60
5. Grassi L, Schileo E, Taddei F, Zani L, Juszczak M, Cristofolini L, Viceconti M (2012) Accuracy of finite element predictions in sideways load configurations for the proximal human femur. *J Biomech* 45(2):394–399

6. Keyak JH, Rossi SA, Jones KA, Les CM, Skinner HB (2001) Prediction of fracture location in the proximal femur using finite element models. *Med Eng Phys* 23(9):657–664
7. Haider IT, Speirs AD, Frei H (2013) Effect of boundary conditions, impact loading and hydraulic stiffening on femoral fracture strength. *J Biomech* 46(13):2115–2121
8. Voo L, Armand M, Kleinberger M (2014) Stress fracture risk analysis of the human femur based on computational biomechanics
9. Hight TK, Piziali RL, Nagel DA (1980) Natural frequency analysis of a human tibia. *J Biomech* 13(2):139–147
10. Pashah S, Massenzio M, Jacquelin E (2008) Prediction of structural response for low velocity impact. *Int J Impact Eng* 35(2):119–132
11. Lee SJ, Liong K, Tse KM, Lee HP (2010) Biomechanics of the deformity of septal L-Struts. *The Laryngoscope* 120(8):1508–1515
12. Bin Tan L, Tse KM, Lee HP, Tan VBC, Lim SP (2012) Performance of an advanced combat helmet with different interior cushioning systems in ballistic impact: experiments and finite element simulations. *Int J Impact Eng* 50:99–112
13. Tse KM, Lee HP, Shabana N, Loon SC, Watson PG, Thean SYLH (2012) Do shapes and dimensions of scleral flap and sclerostomy influence aqueous outflow in trabeculectomy? a finite element simulation approach. *Br J Ophthalmol* 96(3):432–437
14. Tse KM, Chang R, Lee HP, Lim SP, Venkatesh SK, Ho P (2013) A computational fluid dynamics study on geometrical influence of the aorta on haemodynamics. *Eur J Cardiothorac Surg* 43(4):829–838
15. Tse KM, Chiu P, Lee HP, Ho P (2011) Investigation of thermodynamics in the development of dissecting aneurysm within patient specific dissecting aneurysmal aortas using computational fluid dynamics (CFD) simulations. *J Biomech* 44(5):827–836
16. Tse KM, Tan LB, Lim SP, Lee HP (2012) Characterization of human head-brain-neck vibration behavior. In: 4th American Conference on Human Vibration, pp 19–20
17. Taylor WR, Roland E, Ploeg H, Hertig D, Klabunde R, Warner MD, Hobatho MC, Rakotomanana L, Clift SE (2002) Determination of orthotropic bone elastic constants using FEA and modal analysis. *J Biomech* 35(6):767–773

# CFD Analysis, Analytical Solution, and Experimental Verification for Design and Analysis of Air Intake of Formula Student Car



S. Vivek, Rabi Pathak and Rishabh Singh

**Abstract** The main aim of this paper is to Design, Analyze, and Fabricate an air intake for CBR 600rr, which is a 4-cylinder engine that is intended to be used in Formula Student Competition. The mass flow rate to the engine has to be fed by a 20 mm restrictor as per rules portrayed by SAE and Formula Bharat. In order to satisfy the rules, a venturi-type restrictor along with a cylindrical shaped plenum with 4 cylindrical runners is included in the design. The restrictor has a converging and diverging angle of 14 and 6 degree, respectively. The main objective is to achieve appropriate velocity at the outlet for proper mixing of fuel with air and minimum pressure drop across the inlet to the throat. The analytical study has also been properly discussed here to make other researchers and students have a clear understanding of the theoretical study on the air intake. It makes use of the Bernoulli theorem and continuity equation to find pressure difference between downstream flow end pipe narrow sections. The design of air intake is done using Solid Works, ICEM CFD is used to generate the mesh to the model where the hybrid mesh is implemented to this model. ANSYS Fluent is used to run the case and simulate. Further to validate our results experimentally, a mass flow rate sensor and a pressure sensor are included. The air intake is fabricated using aluminum as it has the capability to withstand vibrations from the engine and also the suction pressure of the engine.

**Keywords** CBR 600rr · Formula student · Restrictor · CFD · ICEM

## 1 Introduction

Formula Student competitions are held every year worldwide as well as in India to give students hands-on experience in design, analysis, and manufacturing of formula student cars and its parts. The committees like Formula SAE and Formula Student Germany has imposed a rule of adding a 20 mm restrictor to intake manifold and

---

S. Vivek (✉) · R. Pathak · R. Singh  
Department of Mechanical Engineering, Nitte Meenakshi Institute of Technology, Bangalore  
560064, India  
e-mail: [svivekkumar007@gmail.com](mailto:svivekkumar007@gmail.com)

© Springer Nature Singapore Pte Ltd. 2020  
G. S. V. L. Narasimham et al. (eds.), *Recent Trends in Mechanical Engineering*,  
Lecture Notes in Mechanical Engineering,  
[https://doi.org/10.1007/978-981-15-1124-0\\_48](https://doi.org/10.1007/978-981-15-1124-0_48)

553

states that all air flowing to the engine should pass through this single restrictor bet irrespective of it being a single cylinder or multi-cylinder engine. This is done to limit the maximum power of the engine by reducing the mass flow rate.

The engine used is CBR 600rr having a maximum power of 118 HP 13500 rpm and 599 cc displacement. A venturi-type air restrictor is connected to the plenum. The inlet of it converges till the restrictor and then diverges towards the plenum. The diameter of the part diverging near to the plenum is more than the diameter at the inlet for ensuring better pressure and velocity according to the requirement as per the hit and trail method adopted. A plenum is designed to make sure that all the runners are delivering the equal flow of fluid and damp out pulsation caused by intake stroke of the engine. The right size of a plenum is also very important as the high volume can cause poor throttle response and low volume can cause negative pressure created in the plenum chamber [1].

The theme of all this design is to ensure that there is a minimum pressure drop for maximum mass flow rate. Thus we found this design to achieve a uniform distribution of air across the four intake ports of the engine. In this research, the old designs have been refined and improved to accommodate the most recent developments brought about on the engine.

## 2 Literature Survey

**F.M. White, Fluid Mechanics [2]** provided the conceptual foundation of fluid mechanics. Chapters on ducts, immersed bodies, potential flow, compressible flow, open channels, and turbomachinery show the major applications of the field.

**R. Yerram and N. Prasad in 2006 [3]** states that filter is important as it doesn't allow the dust and dirt to pass through to the engine except pure air required for combustion which keeps the engine healthy and efficient.

**A. Cevizm and M. Akin in 2010 [4]** provided the concept for the proper design of plenum and suggests that volume should be six times the engine cylinder for better flow of air in intake specifically for formula student cars.

**Logan M. Shelagowski and Thomas A. Mahank in 2015 [5]** explain the importance of three main characteristic, i.e., Plenum volume, runner length and runner area for proper breathing of the engine.

**John D. Anderson Jr., Computational Fluid Dynamics in 1995 [6]** presented the application of governing equations like continuity equation, NS equation and Bernoulli equation in physical phenomenons and also shows the importance of grid generation, boundary conditions, and other fluid flow parameters.

### 3 Methodology



### 4 Analytical Study

The analytical study was carried out by using Bernoulli Theorem and continuity equation. The venturimeter formula was studied and carried out to find the pressure and velocity at different cross sections. The suction pressure was also considered during the calculation. All necessary formulae are listed below for understanding (Fig. 1) [7].

**Bore length (B) = 67 mm**

**Stroke (S) = 42.5 mm**

**Length of Rod (L) = 91.8 mm**

**Crank Angle ( $\Theta$ ) = 0.2 rad = 11.5 degree**

**Engine Speed ( $\omega$ ) = 1352 rad/sec**

**Area of Piston ( $A_p$ ) =  $3.525 \times 10^{-3} \text{ m}^2$**

**Velocity ( $V_p$ ) =  $[(S/2)\sin\Theta + \{(S/2)^2\sin\Theta\cos\Theta\}/\{(L^2 - (S/2)^2\sin^2\Theta\}^{1/2}]$**

**$V_p = 7 \text{ m/s}$**

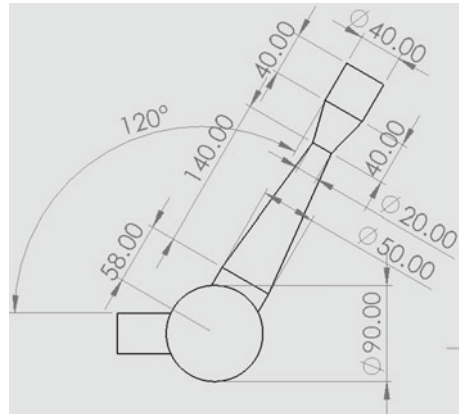
**Area of Inlet Port ( $A_{ip}$ ) =  $1.256 \times 10^{-3} \text{ m}^2$**

**Velocity at Inlet Port ( $V_{ip}$ ) =  $(A_p \cdot V_p) / A_{ip} = 19.64 \text{ m/s}$**

**Pressure at Inlet of Air Intake Manifold = 1 bar**

**Theoretical Discharge at Inlet Port (Q) =  $A_{ip} \cdot V_{ip} = 0.02195 \text{ m}^3/\text{s}$**

**Fig. 1** Air intake with all dimensions in mm



Now to calculate Maximum Discharge as per condition of Choking i.e.  $M = 1$ , we

Require:

Stagnation Temperature ( $T_0$ ) =  $T_{room} + Vp^2/2Cp = 300.19 \text{ k}$

Stagnation Pressure ( $P_0$ ) =  $P_{atm} * (T_0/T_1)^{(k/(k-1))} = 101550.965 \text{ pa}$

$Q_{Choked} = M_{max}/Density = [(A * P_0)^{(k/RT_0)^{1/2} * (2/k + 1)^{(k+1)/(2*(k-1))}] / \rho = 0.0184 \text{ m}^3/\text{s}$

Theoretical Coefficient of Discharge considering losses = maximum discharge during Choking/Theoretical Discharge =  $0.0184/0.02195 = 0.84$

Velocity at Inlet Port = Velocity in Runner due to same Area( $V1$ ) =  $19.64 \text{ m/s}$

Now there will be change in Velocity and Pressure in the Plenum.

Thus, Velocity inside Plenum( $V2$ ) =  $(Vip * Aip) / A_{plenum} = 3.39 \text{ m/s}$

Similarly, Velocity at intersection of Plenum and Venturi

$V3 = 10.99 \text{ m/s}$

Also, Velocity at Restrictor

$V4 = 68.734 \text{ m/s}$

Again, Velocity at end of Venturi(Venturi inlet),

$V5 = 17.18 \text{ m/s}$

For Pressure,

$Q = [Cd * Area * (2 * (P1 - P2) / \rho)^{1/2}] / (1 - B^4)^{(1/2)}$

Where  $P1$  is the preceding pressure

$P2$  is the succeeding pressure

From calculations, we have

Inlet Manifold Pressure =  $101325 \text{ pa} = 1 \text{ bar}$

Pressure at Restrictor =  $95245 \text{ pa} = 0.94 \text{ bar}$

Pressure drop =  $0.06 \text{ bar}$

Pressure in Plenum =  $0.76 \text{ bar}$

Pressure at Inlet Port(outlet) =  $0.43 \text{ bar}$



## 5 CFD Analysis

The CFD analysis consists of steps like designing, modeling, meshing, applying boundary and initial conditions and solving to obtain results in required plots or animations.

### 5.1 Design and Modeling of Air Intake

The design of air intake is done in Solid Works (Fig. 2). A lot of consideration has been taken while designing the air intake. After many attempts and analysis finally, this design was approved for presentation.

The geometry of the intake system has been optimized by adding venturi-type guideway. The outlet has a more expanded area than the inlet of venturi as it has been found experimentally that expanding areas induces low losses near the inlet to the plenum. The converging angle of 14 degrees and the diverging angle of 6 degrees ensured the maximum airflow rate with a very high coefficient of discharge. This design also avoids boundary layer separation. The material used for fabrication of the air intake system was aluminum as it facilitated in better machining and cheaper than other materials as well as in very cheaper. The manufactured restrictor is basically an obstruction venturimeter. The constrictor complies with the rules and induces less pressure drop with very high discharge. The flow efficiency and acoustic performance for this design were very good.

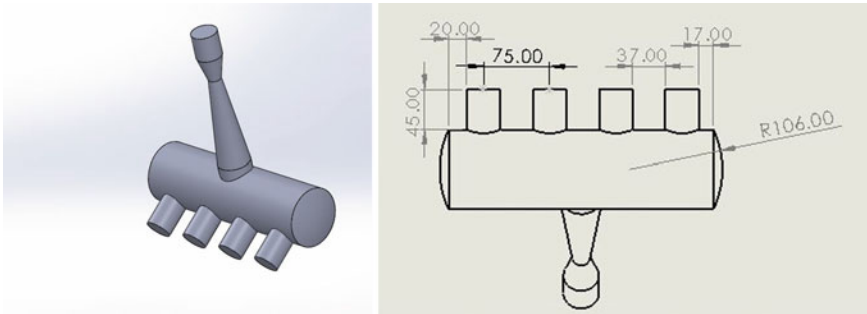


Fig. 2 Solid model in Solid Works

## 5.2 Meshing

It is the process of dividing the entire geometry into a finite number of subdomains which are called cells or elements. The term mesh is also called a grid. The governing equations are then discretized and solved inside these cells or elements individually.

There are 2 main types of mesh.

1. Structured mesh—It generally consists of hexa elements in 3D and quad elements in 2D. In this type of mesh, the coordinate of each node can be given as the input for grid generation. It is not necessary that hexa elements are always structured; we can also have pyramids, triangles in a structured mesh.
2. Unstructured mesh—It consists of tetra elements, however, it can also consist of quad elements. The major difference between structured and unstructured mesh is the way the computer stores the data.

We have different software for mesh generation, but we have used ICEM CFD which is developed by ANSYS. We have selected this software considering its advantage over other available software. In ICEM CFD we can import the geometry from any other commercial designs, in our case we have imported the geometry from Solid Works in step file as it helps to capture the surfaces in a better way [8].

We have implemented hybrid mesh to solve our problem; a hybrid mesh is a combination of tetra mesh and hexa mesh. The geometry was split into 3 different parts namely plenum, restrictor and runner. The plenum is an air storage tank that stores air which will be utilized by the engine for combustion. The plenum was equipped with a tetra mesh by controlling the size of the elements; we had 14–15 lakh elements approximately only in the plenum. The restrictor is a converging–diverging nozzle, which is used to suck the air from the atmosphere and send it to the plenum. The restrictor has been equipped with a body-fitted mesh. Body-fitted mesh technique is used for cylindrical bodies; it captures the entire cylindrical body so that there is negligible skewness error on the walls of the body. The finer mesh is implemented near the walls of the body so that the wall function can be captured. The spacing between the finer elements is set as 0.05 with ratio of 1.2. The runner is the connector between the plenum and engine inlet, the length of the runner influences in acceleration, the optimum length of runner results in better acceleration. The runner is also equipped with body-fitted mesh or O-grid with 0.05 spacing and 1.2 ratios for the finer elements near the wall. The number of elements in the entire geometry came up to 30 lakh which is a decent number for analysis. The quality of the mesh was maintained well above 0.65 (Figs. 3, 4, 5, 6).

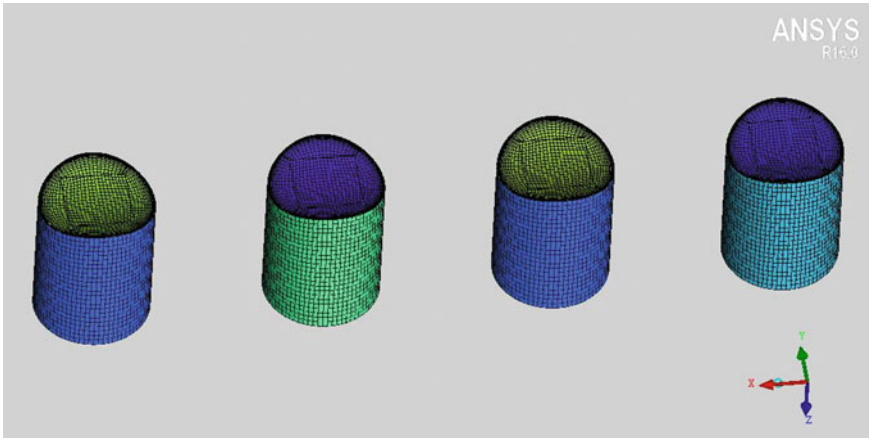


Fig. 3 Runners with O-grid

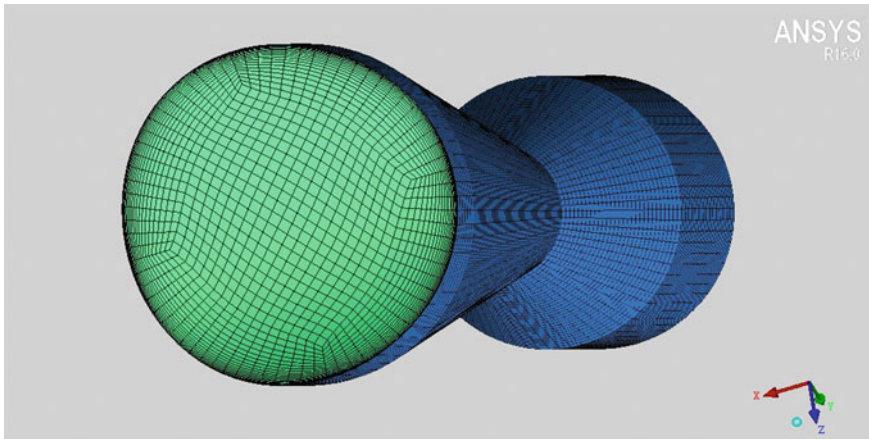


Fig. 4 Restrictor with O-grid

### 5.3 Analysis and Simulation Results

**ANSYS Fluent** was used to analyze and simulate the case, the model was solved on pressure based since it was a subsonic incompressible flow. K-e model was implemented as we had a small body with turbulent flow, and K-e is very good in capturing the near-wall functions due to friction when compared to other models that are available. Inlet velocity and outlet pressures are the boundary conditions mentioned to the solver. The intersections between all the three geometries were defined to the

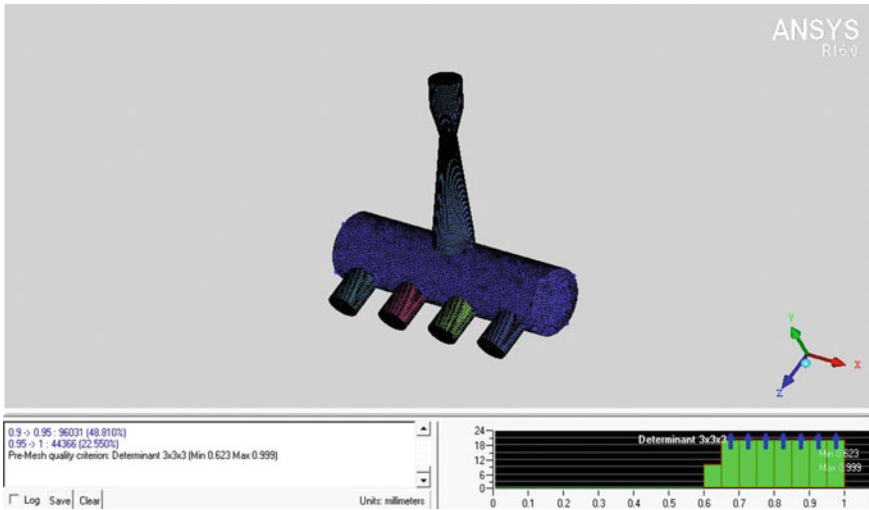


Fig. 5 Mesh of air intake with quality index

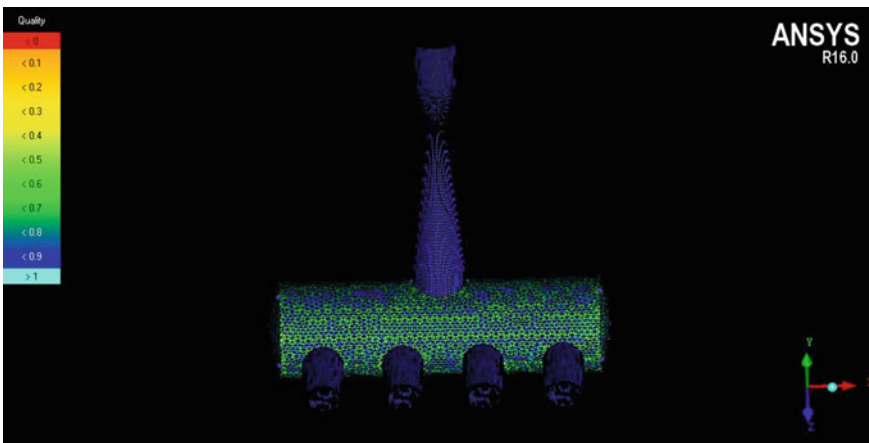


Fig. 6 Overall mesh quality

software. Initially, the solver was set to first-order equations and later after slight convergence, it was changed to second-order equations to obtain more accurate results (Figs. 7, 8, 9, 10, 11).

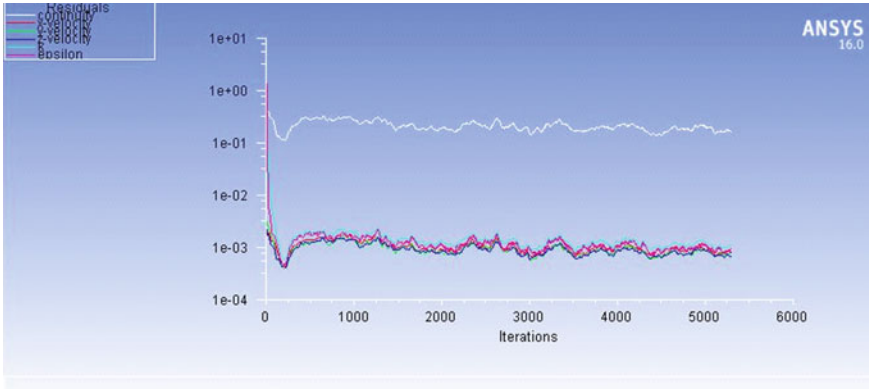


Fig. 7 Convergence graphs

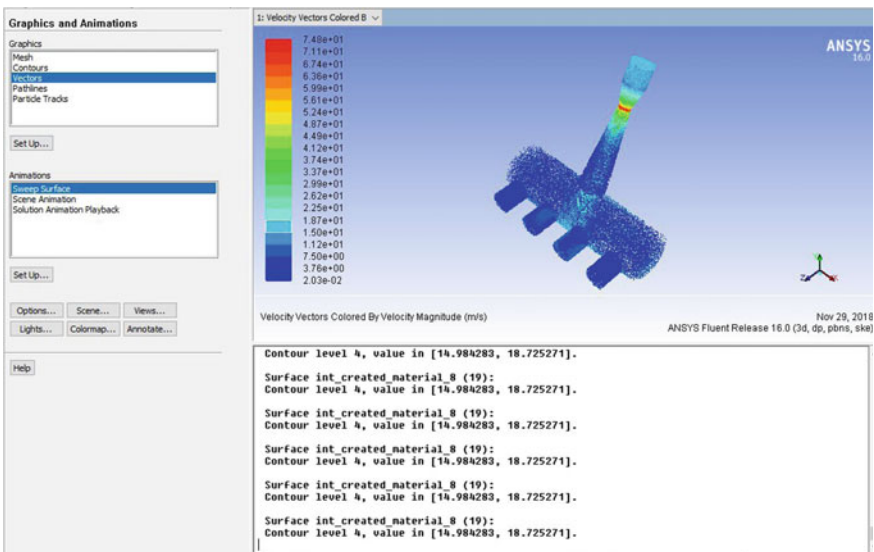


Fig. 8 Velocity at outlet of air intake or Engine inlet port

## 6 Experimental Method

### 6.1 Mass Flow Sensor (MAF)

The mass airflow sensor is used to measure the amount of air an engine takes in for its operation. It measures the volume of air and compensates for its density also. It is installed between the air filter and intake manifold of output (analog) and the other produces a frequency output (digital). Both designs work on the “hot wire”

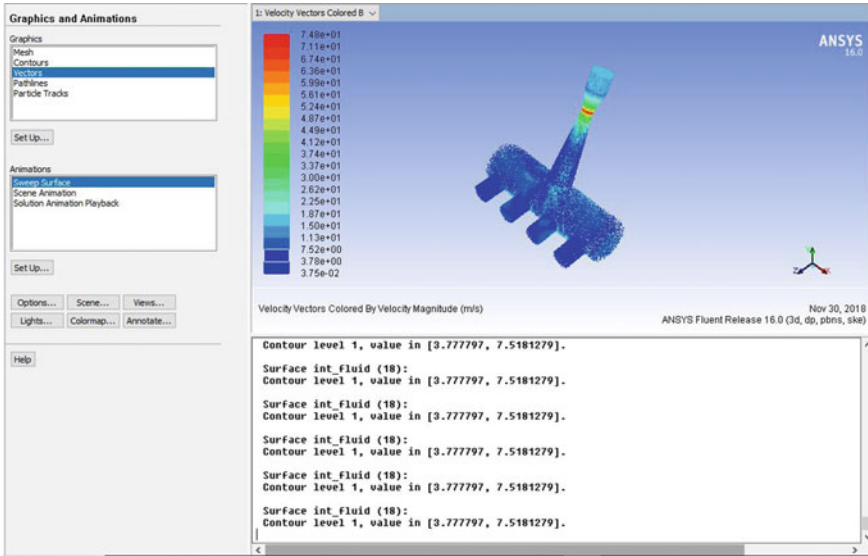


Fig. 9 Inlet velocity of the air intake manifold

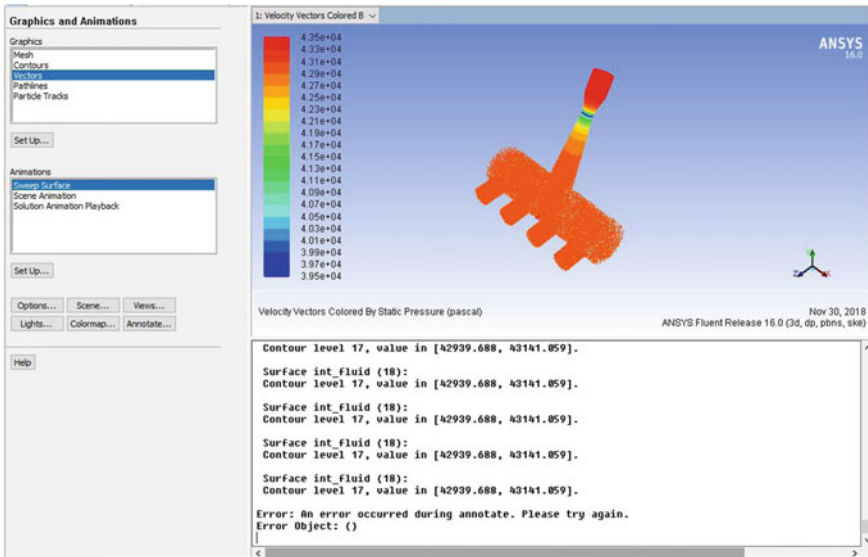
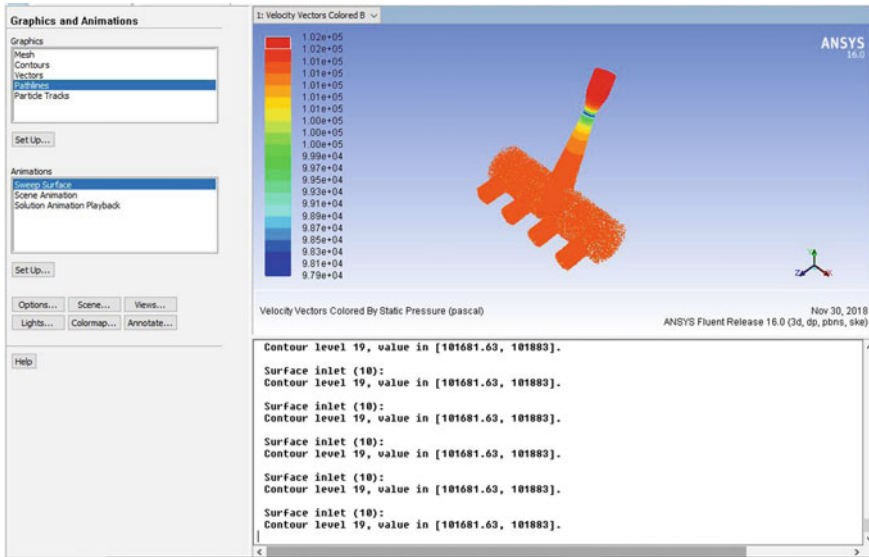


Fig. 10 Inlet pressure for air intake manifold



**Fig. 11** Outlet pressure for air intake manifold

principle. A hot wire MAF sensor has a small electrically heated wire and a small temperature sensor installed close to the hot wire. The temperature sensor measures the temperature of the air near the hot wire. When the engine is idling, a very little air flows pass the hot wire, so it takes very small electrical current to keep the wire hot. When the accelerator is pressed, the throttle opens allowing more air to flow over the hot wire. The passing air cools the hot wire down, more the air flows more will be electrical current is needed to keep it hot. The amount of this electrical current is proportional to the amount of airflow. The engine computer uses airflow signal to calculate the proper amount of fuel injected into the cylinders in order to keep the air/fuel ratio at the optimal level. The value obtained for mass flow at runner was found to be 0.0218 m<sup>3</sup>/s and velocity was 17.36 m/s forthe engine (Fig. 12).

## 6.2 Manifold Absolute Pressure Sensor (MAP)

Manifold absolute pressure (MAP) sensor measures the pressure inside the intake manifold. When the engine is not in running condition then the pressure inside the intake manifold is the same as that of outside pressure but when the engine starts, a vacuum is created inside the manifold by the throttle plates which create pumping action of pistons and the restriction. Intake vacuum drops to almost zero at full

**Fig. 12** MAF sensor

throttle with the engine running and the pressure inside the intake manifold again becomes equal to outside pressure. The vacuum inside an engine's intake manifold, by comparison, can range from zero up to 22 inches Hg or more depending on operating conditions. Vacuum at idle is always high and typically ranges from 16 to 20 inches Hg in most vehicles. The highest level of vacuum occurs when decelerating with the throttle closed. The pistons are trying to suck in air but the closed throttle chokes off the air supply creating a high vacuum inside the intake manifold (typically four to five inches Hg higher than at idle). When the throttle is suddenly opened when accelerating hard, the engine sucks in a big gulp of air and vacuum plummets to zero. Vacuum then slowly climbs back up as the throttle closes. The value obtained was 0.51 bar (Fig. 13).

## 7 Conclusion and Comparison

The design of air intake is very important for the proper and efficient functioning of the engine. The design becomes much more important when there is no use of turbochargers or superchargers and the air intake is totally dependent on the design





**Fig. 13** MAP sensor

and construction of air intake and inlet manifold. The pressure inside the engine is less than that of atmosphere thus the air is driven inside it, but the mass flow rate and velocity of air are dependent on obstruction meter (venturimeter, orifice meter, etc.), air restrictor, plenum, runner, and inlet port. The design presented in this paper ensures maximum flow rate with a very high coefficient of discharge and less losses. This design and manufacturing also have ensured better performance, efficiency, suitable speed of air, appropriate pressure and low-pressure drop with a high mass flow rate.

The design is really beneficial and can be a great choice in formula student competitions as verified with CFD analysis, analytical study, and experimental approach (Table 1).

**Table 1** Comparison of analytical, experimental, and CFD analysis results

S. No	Position	Theoretical Approach		Experimental Approach		CFD Analysis	
		P(bar)	V(m/s)	P(bar)	V(m/s)	P(bar)	V(m/s)
1.	Engine inlet port	0.43	19.64	0.51		0.43141	18.725
2.	Plenum	0.76	3.39			0.89	3.78
3.	Restrictor	0.94	68.73			0.964	71.1
4.	Inlet of the intake manifold	1.015	17.18		17.36	1.01	16.86
5.	Pressure drop	0.06				0.046	

**Acknowledgements** We would like to thank our college NMIT and its project lab, where we performed experimental tests and CFD analysis. We would also like to acknowledge all the people who contributed their time and helped us writing this paper and completing in a timely manner. We also express our gratitude to all the staff members of the Department of Mechanical Engineering and the professors for constant guidance and encouragement.

## References

1. Sullivan DA (1939) Intake manifold. Available [www.google.com/patents/us2160922](http://www.google.com/patents/us2160922)
2. White FM (2003) Fluid mechanics. McGraw-Hill, New York
3. Yerram R, Prasad N (2006) Optimization of intake system and filter of an automobile using CFD analysis. SAE ARAI Paper 2006
4. Cevizm A, Akin M (2010) Design of a new SI engine intake manifold with variable length plenum
5. Logan M, Shelagowski and Thomas A. Mahank (2015) Formula SAE intake restrictor design and performance. Saginaw Valley State University
6. Anderson Jr. JD (1995) Computational fluid dynamics: the basics with applications, 4th edn. McGraw Hill International Editions, New York, pp 4–82
7. Chopade, MR, Valavade AP, Barhatte SH (2012) Performance enhancement of air filter by design optimization. IJAET III(2012). E-ISSN 0976-3945
8. AnsysInc, ANSYS Fluent user manual

# Noncontact Surface Roughness Assessment Using Machine Vision System



Dhiren Patel, Kiran Mysore and Kartikkumar Thakkar

**Abstract** The use of the optical device for the measurement of surface roughness reduces complexity and time for measurement. In the current study, surface roughness parameters were measured after machining on a shaper machine using the machine vision system which was compared with that obtained through the stylus method. Machining operation involves complexity and produces different surface finish with different cutting conditions, therefore in the present study correlation between surface roughness parameters (viz. arithmetic average height ( $R_a$ ); maximum height of peaks ( $R_p$ ); root mean square roughness ( $R_q$ ); maximum height of the profile ( $R_t$ ), and ten-point height ( $R_z$ )) and optical surface finish parameters (i.e., mean, standard deviation, skewness and kurtosis) has been developed for varied values of cutting parameters (i.e., depth of cut and RPM of pulley drive). The linear relation model with optical parameters and surface roughness parameters has been developed. It was observed that all the roughness parameters can be estimated with a fair degree of accuracy ( $R^2 > 0.92$ ) using optical statistical parameter kurtosis, while means, skewness, and standard deviation obtained through the same image processing data fail to estimate roughness parameters.

**Keywords** Machine vision system · Roughness parameters · Surface profilometer · Kurtosis

## 1 Introduction

Super Superior surface finish after any machining operation is an essential parameter that adds quality ingredients in any finished product. Surface roughness inspection is an important activity for the quality control department of many manufacturing industries. Moreover, it is widely accepted that surface finish is an important parameter affecting the useful life of the material, fatigue strength, corrosion resistance, wear resistance and aesthetic appeal of the product [1]. Major involvement of the

---

D. Patel (✉) · K. Mysore · K. Thakkar  
Pandit Deendayal Petroleum University, Gandhinagar 382421, Gujarat, India  
e-mail: [dhirenpatel85@gmail.com](mailto:dhirenpatel85@gmail.com)

© Springer Nature Singapore Pte Ltd. 2020  
G. S. V. L. Narasimham et al. (eds.), *Recent Trends in Mechanical Engineering*,  
Lecture Notes in Mechanical Engineering,  
[https://doi.org/10.1007/978-981-15-1124-0\\_49](https://doi.org/10.1007/978-981-15-1124-0_49)

surface roughness in the modern manufacturing arena leads to the requirement of efficient and accurate surface roughness assessment [2]. Since many years, accurate measurement of the surface roughness has been subject of attention and it is still a challenge due to surface roughness of machined components is a vital property for those who studying tribology, wear, corrosion and even lubrication [3]. Various methods have been proposed for the evaluation of the roughness which covers the qualitative assessments based on visual and hepatic perception, to quantitative instrumental measurement methods [4, 5]. Instrumental methods are divided into two groups: contact methods, including atomic force microscopy, and stylus Profilometry [4], and noncontact methods such as light interferometer [4] and machine vision [5]. Use of stylus contact method to measure vertical displacement is a conventional and widely accepted method for industries around the globe for surface roughness measurement, however, the method is time consuming and lacks in benefit where automation is the prime need for mass production [6]. Moreover, the stylus cannot cover all the valleys on the workpiece and works as a low pass filter [7]. Furthermore, the stylus method is not effective when a higher temperature surface is to be inspected [8]. Surface finish after any machining operation depends mainly upon tool wear, feed rate, depth of cut and cutting speed. For a superior surface finish, all such cutting parameters are needed to be optimized during operation. Simultaneous and fast monitoring of surface roughness parameters during cutting operations can help to optimize cutting parameters for better surface finish. Such a fast and easy measurement of surface roughness parameters can be accomplished by a machine vision system [9]. Hence, noncontact method for inspecting the surface roughness has remained the interest area of the researchers since the last decade [10–13].

There are many methods of noncontact surface roughness measurement using image texture extraction, i.e., laser beam, ultrasound, microscopic and light scattering. Machine vision and light scattering based surface roughness measuring techniques are suitable for different machining operations in mass production [14]. Many researchers have obtained good results of surface roughness measurement using vision-based noncontact measurement technologies which use light source type design, various algorithms for image processing, roughness evaluation and prediction model [15–21]. The same system can be used for different machining operations; however different correlations and regression equations are needed to be calculated for each machining operation. The aim of the present study is to develop a correlation between the image capturing data obtained through the histogram of scattered light and surface roughness parameters which can be useful to calculate different surface roughness parameters with required accuracy during the machining operation.

## 2 Experimental Details

A mild steel specimen with a  $40 \times 40 \times 17$  mm dimension was prepared after machining under a shaper machine with different drive speed and depth of cut. Mild steel used for specimen preparation was used from a single batch and of the same quality. The HSS tool used for each specimen preparation was identical.

A portable surface profilometer (Handysurf E 35A) with a stylus contact method was used for measuring surface roughness parameters (see Fig. 1). Measuring conditions of surface profilometer are given in Table 1. A machine vision system used to extract texture and roughness features is shown in Fig. 2. It was coupled with a Charge Coupled Device (CCD camera) PULNIX.



Fig. 1 Surface profilometer (HANDYSURF-35A)

Table 1 Measuring conditions of profilometer

Sr. No.	Parameters	Value
1	Evaluation length (mm)	8.00
2	Measuring speed (mm/s)	0.6
3	Cutoff value (mm)	0.8
4	Type of filter	Gaussian
5	Measuring range ( $\mu\text{m}$ )	80
6	Form Remove	Straight

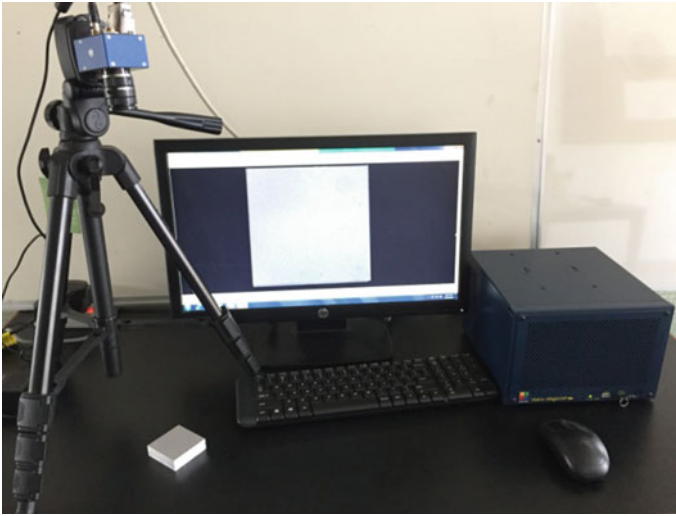


Fig. 2 Setup of machine vision system

### 3 Methodology

Totally 12 mild steel specimens of the same dimensions were prepared using shaping operation with variation in depth of cut and pulley speed to obtain variation in roughness parameters of the specimen. Different roughness parameters, viz., arithmetic average height ( $R_a$ ); maximum height of peaks ( $R_p$ ); root mean square roughness ( $R_q$ ); maximum height of the profile ( $R_t$ ) and ten-point height ( $R_z$ ) were measured using surface profilometer. Different machining conditions used to prepare specimens are shown in Table 2. The experiments have been performed in a randomized order to reduce the effects of uncontrolled error in measurements caused due to environmental and other unknown factors. Moreover, all the roughness parameter measurements were performed in triplicate and the average of the values have been reported.

Machine vision setup shown in Fig. 2 was used to enhance the image captured using CCD and was processed to obtain histogram of the reflected and scattered light. The captured image was enhanced to de-noise and remove other digital asperities which may distort the result. Mean ( $R_m$ ), standard deviation ( $R_{st}$ ), skewness ( $R_{sk}$ ), and kurtosis ( $R_{ku}$ ) have been calculated from the histogram analysis for each specimen. Since it is known that the machine vision technology is a light-sensitive technique, all the experiments were conducted at approximately similar surrounding luminance.

Skewness can be defined as the asymmetry in the peaks or valleys distribution from the normal distribution. Equation (1) shows that skewness is the measure of value up to which a distribution is distorted either left or right. As shown in Eq. (2), Kurtosis is the measurement of the sharpness of the distribution. In the sense of roughness of the surface, these two parameters affect the friction coefficient of the

**Table 2** Cutting conditions of shaper machine

Specimen no.	Pulley speed (RPM)	Depth of cut (mm)
1	125	0.75
2	216	0.5
3	125	1
4	125	0.5
5	350	0.5
6	216	0.75
7	216	1
8	350	0.75
9	350	1
10	583	0.5
11	583	1
12	583	0.75

surface. When the kurtosis is higher and skewness is negative, the friction coefficient tends to be less. It is caused because of small depths of the dimple and wide spacing between dimples. The general formula for skewness and kurtosis is

$$Skewness = \frac{3 \times (\bar{X} - median)}{S} \tag{1}$$

$$kurtosis = \frac{\sum_{i=1}^N \frac{(Xi - \bar{X})}{N}}{S^4} \tag{2}$$

Where  $\bar{X}$  is the mean,  $S$  is the standard deviation, and  $N$  is the sample size.

Correlation coefficients for each roughness parameter with all statistical parameters obtained through image processing are calculated; moreover, regression equations are also obtained to predict all the roughness parameters using the machine vision system.

## 4 Result and Discussion

Roughness parameters ( $R_a, R_z, R_q, R_p, R_t$ ) measured using surface profilometer with varying conditions of machining parameters is given in Table 3. It can be observed from the table that surface roughness is dependent on pulley speed and depth of cut parameters of machining operation. 8-bit grayscale images enhanced using machine vision systems is shown in Fig. 3. Statistical parameters have been calculated from the histogram of grayscale image and are shown in Table 4. The correlation coefficient between surface roughness parameters obtained through profilometer and machine vision system has been calculated (see Table 5). It is clear from Table 5 that kurtosis

**Table 3** Roughness parameters measured using surface profilometer

Specimen no.	Pulley speed (RPM)	Depth of cut (mm)	$R_a$ ( $\mu\text{m}$ )	$R_z$ ( $\mu\text{m}$ )	$R_q$ ( $\mu\text{m}$ )	$R_p$ ( $\mu\text{m}$ )	$R_t$ ( $\mu\text{m}$ )
1	125	0.75	4.230	21.880	5.100	10.390	31.700
2	216	0.5	4.500	22.500	5.400	11.400	28.900
3	125	1	4.700	24.700	5.600	11.600	34.200
4	125	0.5	5.000	24.800	6.100	12.300	32.700
5	350	0.5	5.100	24.900	6.200	13.200	32.500
6	216	0.75	5.500	28.000	6.600	12.600	33.400
7	216	1	5.600	26.900	6.600	13.500	35.400
8	350	0.75	5.680	28.710	6.980	15.000	35.100
9	350	1	5.700	30.000	7.000	15.700	41.800
10	583	0.5	6.600	33.300	8.100	18.000	47.000
11	583	1	7.500	36.500	9.100	19.700	54.900
12	583	0.75	8.200	38.800	9.900	21.700	56.200

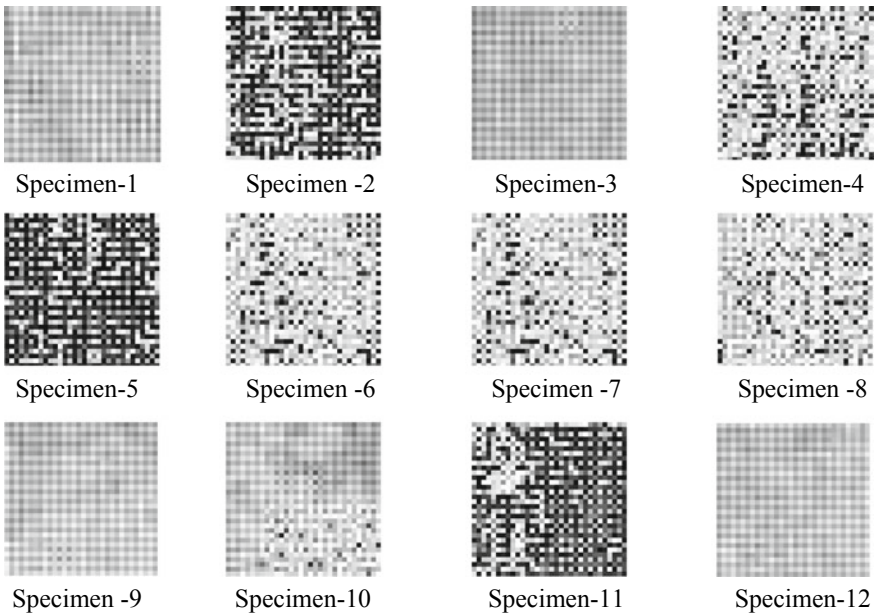


**Fig. 3** Grayscale images of specimen captured by the machine vision system



**Table 4** Statistical parameters measured using a machine vision system

No.	$R_m$	$R_{st}$	$R_{sk}$	$R_{ku}$
1	93.011	27.839	-1.366	-1.612
2	99.495	27.972	-1.272	-1.424
3	107.809	30.164	-0.949	-1.279
4	112.972	30.474	-0.435	-0.804
5	162.863	40.883	-0.072	-0.737
6	169.150	67.688	-0.050	-0.674
7	171.994	71.368	-0.025	-0.656
8	178.121	71.973	0.005	-0.647
9	181.265	82.828	0.209	-0.502
10	181.438	89.177	0.384	0.475
11	181.638	89.230	0.584	0.640
12	187.076	93.847	0.752	1.172

**Table 5** Correlation between roughness parameters and machine vision parameters

Roughness parameters	$R_m$ (%)	$R_{st}$ (%)	$R_{sk}$ (%)	$R_{ku}$ (%)
$R_a$ ( $\mu\text{m}$ )	77	87	89	98
$R_z$ ( $\mu\text{m}$ )	79	91	89	98
$R_q$ ( $\mu\text{m}$ )	78	88	90	99
$R_p$ ( $\mu\text{m}$ )	77	89	88	98
$R_t$ ( $\mu\text{m}$ )	69	83	82	96

has the highest correlation with the surface roughness parameters with a correlation coefficient of 0.98, 0.98, 0.99, 0.98, and 0.96 for  $R_a$ ,  $R_z$ ,  $R_q$ ,  $R_p$ , and  $R_t$  respectively. Thus, it is evident that surface roughness parameters can be predicted from the value of kurtosis with the desired accuracy and is comparable with that of profilometer measurements. However, mean, standard deviation, and skewness has a lower value of correlation coefficient with roughness parameters compared to kurtosis (see Table 5). This is due to the fact that kurtosis is a fourth-order moment and responds to a small deviation in the profile very sensitively, therefore it respond to the smallest irregularity of the surface and predicts nearly the exact value of each roughness parameters [22]. Although, being important statistical measures, the values of mean, standard deviation and skewness do not predict the surface roughness parameters accurately. However, these terms provide important information about the type of irregularities on the surface.

Regression equations are obtained for the prediction of roughness parameters using each of the statistical parameters obtained through the machine vision system (see Table 6). The value of the coefficient of variation  $R^2$  for the regression equation indicates the ability of the equation to explain data variations. All the regression

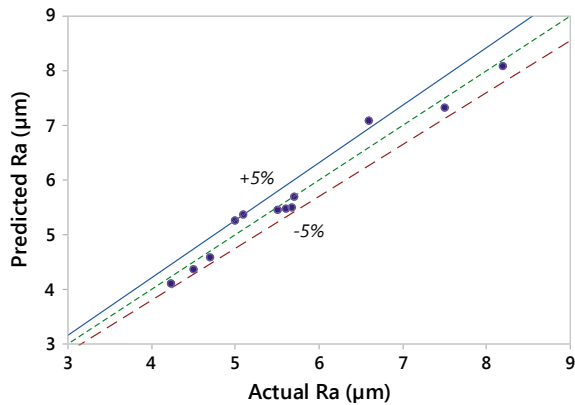
**Table 6** Regression equations for the prediction of roughness parameters as a function of machine vision parameters

Roughness Parameters	Mean		Standard deviation		Skewness		Kurtosis	
	Linear equation	$R^2$ (%)	Linear equation	$R^2$ (%)	Linear equation	$R^2$ (%)	Linear equation	$R^2$ (%)
$R_a$ ( $\mu\text{m}$ )	$X = (Y - 16.6)/23.816$	60	$X = (Y + 50.7)/19.511$	76	$X = (Y + 3.1)/0.5129$	79	$X = (Y + 4.4)/0.6987$	97
$R_z$ ( $\mu\text{m}$ )	$X = (Y + 1.8)/5.4241$	62	$X = (Y + 67.7)/4.5072$	82	$X = (Y + 3.4)/0.1148$	79	$X = (Y + 4.8)/0.1542$	95
$R_q$ ( $\mu\text{m}$ )	$X = (Y - 17.3)/19.578$	61	$X = (Y + 49.8)/15.982$	77	$X = (Y + 3.0)/0.4214$	80	$X = (Y + 4.4)/0.5714$	97
$R_p$ ( $\mu\text{m}$ )	$X = (Y - 35.1)/8.0269$	59	$X = (Y + 37.3)/6.6929$	79	$X = (Y + 2.6)/0.1711$	77	$X = (Y + 3.9)/0.2342$	96
$R_t$ ( $\mu\text{m}$ )	$X = (Y - 45.6)/2.7588$	48	$X = (Y + 33.0)/2.4144$	69	$X = (Y + 2.5)/0.1711$	68	$X = (Y + 3.9)/0.0883$	92

equation for roughness parameter validation has  $R^2$  value of more than 92% which indicates higher predictability of the equation. The fitted equation is a linear equation that indicates kurtosis has a linear relationship with each of the surface roughness parameters.

Moreover, the value of kurtosis and skewness indicates the type of irregularity on the workpiece surface. Negative skewness indicates asymmetry above the mean height of irregularities while positive skewness indicates asymmetry below the mean height. Least skewness (0.005) for specimen 8 which had a speed of 350 rpm with 0.75 mm of the depth of cut indicates the symmetric distribution of the heights above the midplane. The value of kurtosis is less than 4 for the entire specimen who indicates irregularities are in the form of heights above the midplane and there is the absence of any spikes on the specimen surface which is also clear from the gray scale images of the specimen.

**Fig. 4** Prediction of  $R_a$  using machine vision system with the reference to stylus method



It can be observed from Fig. 4 that the use of linear relation with kurtosis can predict the value of  $R_a$  with a higher degree of fitness. The relative error in the measurement with reference to stylus method is observed to be within the permissible limit of  $\pm 5\%$ . All the other roughness parameters could also be predicted using kurtosis with very less error, i.e.,  $R_z (\pm 5\%)$ ,  $R_q (\pm 5\%)$ ,  $R_p (\pm 8\%)$  and  $R_t (\pm 10\%)$  as shown in Figs. 5, 6, 7, 8.

Higher error value in some of the measurements can be due to change in atmospheric conditions like light intensity, diffraction of the light waves, etc. However, the machine vision technology can predict the surface roughness with a fair degree of accuracy as explained and justifies its applicability due to benefits in terms of time, cost, ease and noncontact method with no interference with the workpiece surface.

**Fig. 5** Prediction of  $R_z$  using machine vision system with the reference to stylus method

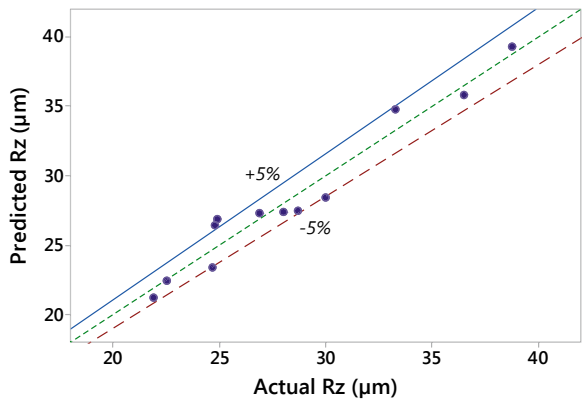


**Fig. 6** Prediction of  $R_q$  using machine vision system with the reference to stylus method

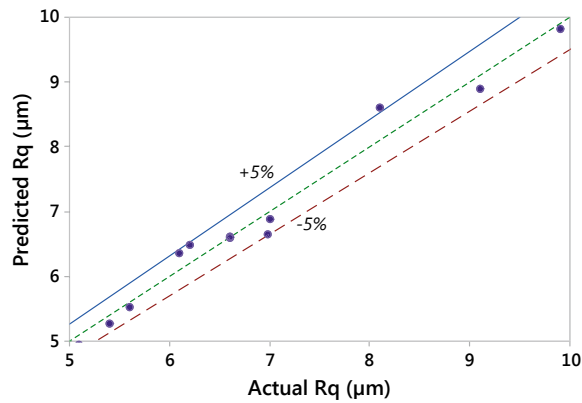


**Fig. 7** Prediction of  $R_p$  using machine vision system with the reference to stylus method

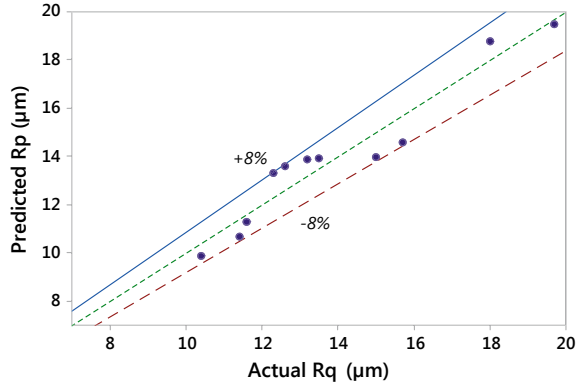
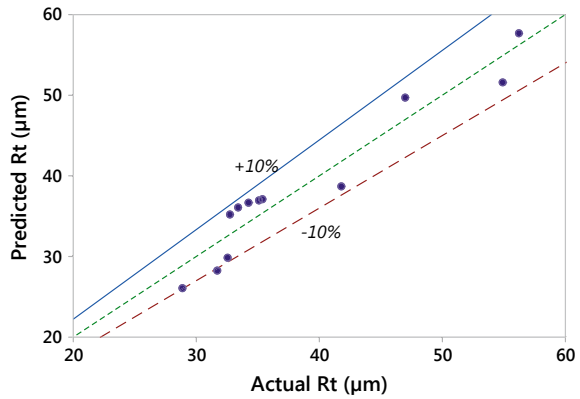


**Fig. 8** Prediction of  $R_t$  using machine vision system with the reference to stylus method



### 5 Conclusions

The present study has been performed to establish a relation between standard surface profilometer method and image processing method, and to compare the results obtained from both the methods on the specimen prepared with shaper under the same cutting parameters. Being a noncontact technique with relatively fast processing speed gives the image processing method an edge over the standard stylus method. Covering all points in the measuring area makes the image processing method a reliable one too. Kurtosis had relatively fewer errors and succeeds to predict all the surface roughness parameters with a fair degree of accuracy.

## References

1. Asiltürk I, Çunkaş M (2011) Modeling and prediction of surface roughness in turning operations using artificial neural network and multiple regression method. *Expert Syst Appl* 38(5):5826–5832
2. Gadelmawla ES, Koura MM, Maksoud TMA, Elewa IM, Soliman HH (2002) Roughness parameters. *J Mater Process Technol* 123(1):133–145
3. Singh SK, Srinivasan K, Chakraborty D (2004) Acoustic characterization and prediction of surface roughness. *J Mater Process Technol* 152(2):127–130
4. Poon CY, Bhushan B (1995) Comparison of surface roughness measurements by stylus profiler, AFM and non-contact optical profiler. *Wear* 190(1):76–88
5. Ghodrati S, Mohseni M, Kandi SG (2015) Dependence of adhesion strength of an acrylic clear coat on fractal dimension of abrasive blasted surfaces using image processing. In: 6th international color and coating congress
6. Radhakrishnan V (1970) Effect of stylus radius on the roughness values measured with tracing stylus instruments. *Wear* 16(5):325–335
7. Sherrington I, Smith EH (1988) Modern measurement techniques in surface metrology: part I; stylus instruments, electron microscopy and non-optical comparators. *Wear* 125(1):271–288
8. Chen S, Feng R, Zhang C, Zhang Y (2018) Surface roughness measurement method based on multi-parameter modeling learning. *Measurement* 129(12):664–676
9. Pfeifer T, Wieggers L (2000) Reliable tool wear monitoring by optimized image and illumination control in machine vision. *Measurement* 28(3):209–218
10. Priya P, Ramamoorthy B (2007) The influence of component inclination on surface finish evaluation using digital image processing. *Int J Mach Tools Manuf* 47(3–4):570–579
11. Al-Kindi GA, Shirinzadeh B (2009) Feasibility assessment of vision-based surface roughness parameters acquisition for different types of machined specimens. *Image Vis Comput* 27(4):444–458
12. Elango V, Karunamoorthy L (2008) Effect of lighting conditions in the study of surface roughness by machine vision—an experimental design approach. *Int J Adv Manuf Technol* 37(1–2):92–103
13. Younis MA (1998) On line surface roughness measurements using image processing towards an adaptive control. *Comput Ind Eng* 35(1–2):49–52
14. Gadelmawla ES (2011) Estimation of surface roughness for turning operations using image texture features. *Proc Inst Mech Eng Part B J Eng Manuf* 225(8):1281–1292
15. Tsai D, Chen J, Chert J (1998) A vision system for surface roughness assessment using neural networks. *Int J Adv Manuf Technol* 14(6):412–422
16. Liu W, Zheng X, Liu S, Jia Z (2012), A roughness measurement method Based on genetic algorithm and neural network for microheterogeneous surface in deep-hole parts. *J Circuits, Syst Comput* 21(1):1–14
17. Lee BY, Tarn YS (2001) Surface roughness inspection by computer vision in turning operations. *Int J Mach Tools Manuf* 41(9):1251–1263
18. Lee BY, Juan H, Yu SF (2002) A study of computer vision for measuring surface roughness in the turning process. *Int J Adv Manuf Technol* 19(4):295–301
19. Kumar R, Kulashakar P, Dhanasekar B, Ramamoorthy B (2005) Application of digital image magnification for surface roughness evaluation using machine vision. *Int J Mach Tools Manuf* 45(2):228–234
20. Demircioglu P, Bogrekcı I, Durakbasa NM (2013) Micro scale surface texture characterization of technical structures by computer vision. *Measurement* 46(6):2022–2028
21. Jeyapoovan T, Murugan M (2013) Surface roughness classification using image processing. *Measurement* 46(7):2065–2072
22. Kostakos J (2013) Relation between surface roughness and adhesion as studied with AFM. Ph.D thesis, University of Twente

# Optimization of Brake Pedal for FSAE Vehicle



Kaustubh Babrekar, Saurabh Bairagi, Jatin Parajiya and Nitin G. Phafat

**Abstract** The brake pedal is used to actuate the brakes of any normal car. It faces a very high load during intensive and repetitive braking. A brake pedal is required to be durable as well as have a low weight. The study is focused toward designing an optimized brake pedal having good durability and a considerable factor of safety along with the lowest weight. First, the brake pedal of Aluminum (7075 T6) is designed using a 3D modeling software (SolidWorks) and then the Finite Element Analysis is carried out to find the stresses induced when a load of 40 kg, i.e., 392 N acts. Once the results are determined for the solid pedal the pedal is then further optimized by removal of material in less stressed zones and analyzed appropriately.

**Keywords** FEA · ANSYS · Brake pedal

## 1 Introduction

Formula SAE India is an engineering design competition, where engineering students from all parts of the country design and fabricate a Formula One prototype. Weight remains a crucial factor in these events as the power increases with a reduction in vehicle weight. Brake is the most crucial part which reduces the speed and brings the vehicle to rest. The design of the brake pedal is made considering the repetitive forces acting on the pedal from the driver's foot during normal as well as hard braking. The

---

K. Babrekar (✉) · S. Bairagi · J. Parajiya · N. G. Phafat  
Department of Mechanical Engineering, MGM Jawaharlal Nehru Engineering College,  
Aurangabad, India  
e-mail: [kaustubh.babrekar@gmail.com](mailto:kaustubh.babrekar@gmail.com)

S. Bairagi  
e-mail: [saurabh.bairagi.434@gmail.com](mailto:saurabh.bairagi.434@gmail.com)

J. Parajiya  
e-mail: [jatinparajiya196@gmail.com](mailto:jatinparajiya196@gmail.com)

N. G. Phafat  
e-mail: [phafatng@gmail.com](mailto:phafatng@gmail.com)

optimized pedal is desired to possess high strength and stiffness along with less weight [1, 2].

### ***1.1 Literature Review***

In the modern-day FSAE car the weight remains the crucial parameter, excess weight of the pedal can be eliminated by proper analysis of the pedal such that it doesn't fail [3]. Weight depends on the material of the pedal and appropriate selection of the material is very important [4]. Machinability and cost of the material is also taken into consideration, optimization of material must not result in failure of the pedal [5]. Conventional pedals need replacement and adequate improvements in every area of the pedal are important [6].

### ***1.2 Methodology***

Firstly, the pedal is studied along with the forces and other design parameters affecting it. This is followed by the selection of proper, lightweight, and rigid Aluminum material. The solid model is designed using SolidWorks and then meshed in ANSYS. Friction between the stud, brackets, and pedal is given and forces are applied on the pedal. Stress Analysis is executed using ANSYS. The parts with little or no deformation are optimized for weight reduction and the results are studied [7].

## **2 Material Selection**

The best material for the manufacturing of brake pedal is Aluminum 7075 T6 due to its high stress-bearing property compared to the other grades, it is comparatively cheap and easily available and has the following properties (Table 1).

## **3 Manufacturing Process**

In the forging process, a metal is given shape after heating it along with constant hammering or putting the heated metal into a die. The formation of the desired shape requires enormous force making the aluminum weak with no benefit. Whereas, in casting the metal in the liquid state is poured into the mold of the product and is then given the desired shape. This is economical in case of mass production, but the cast iron is found to have impurities and hence may become brittle. Machining is done with the help of a VMC, where the unwanted material is removed from a block

**Table 1** Material properties for aluminum 7075 T6

Component	Amount (wt%)
Aluminum (Al)	90%
Magnesium (Mg)	2.5%
Copper (Cu)	1.6%
Zinc (Zn)	5.6%
Chromium (Cr)	0.23%
Density	2.81 g/cc
U. T. S.	572 MPa
Yield Strength	503 MPa
Young's Modulus	71.7 GPa
Machinability	70% (Good)

of metal to obtain a highly finished component that helps in retaining the strength and durability of the metal. For superior finish, rigidity, and strength, machining is preferred [8].

### 4 Stress Analysis

A solid model of Aluminum 7075 was made weighing 117 g (Fig. 1).

Maximum force a driver could apply on the pedal during sudden braking = 40 kg.

Force = Mass \* Acceleration.

40 kg \* 9.81 m/s = 392 N.

Force acting on the pedal was taken to be 392 N and a frictional contact was given between the stud, pedal, and brackets. Rod at the bottom which held the brackets acted as fixed support. Resistance from the master cylinder (oil pressure and spring force) were applied on the pedal's rear side in the opposite direction [9] (Figs. 2, 3, 4, and 5).

**Fig. 1** CAD model of a solid pedal in SolidWorks

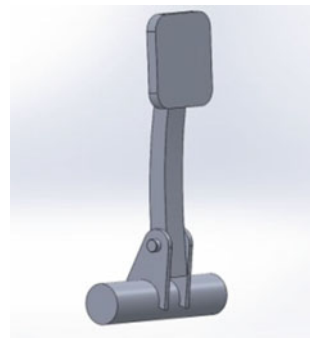




**Fig. 2** Pedal loading  
(applying the forces on solid pedal)

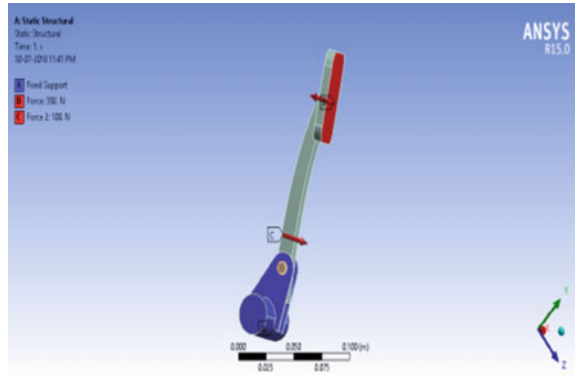


**Fig. 3** Equivalent stress in solid pedal

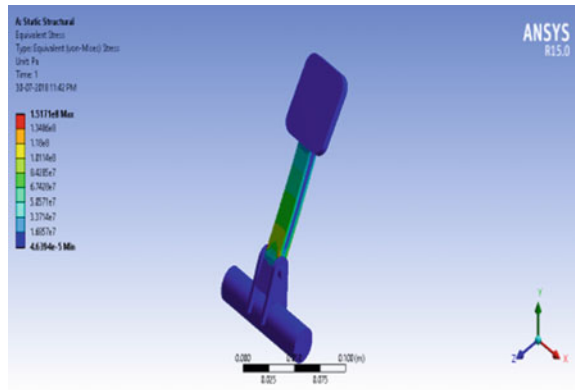
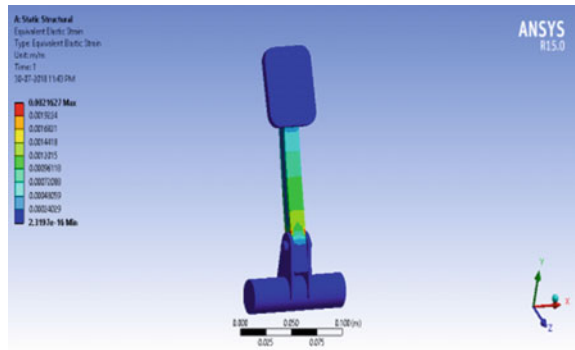
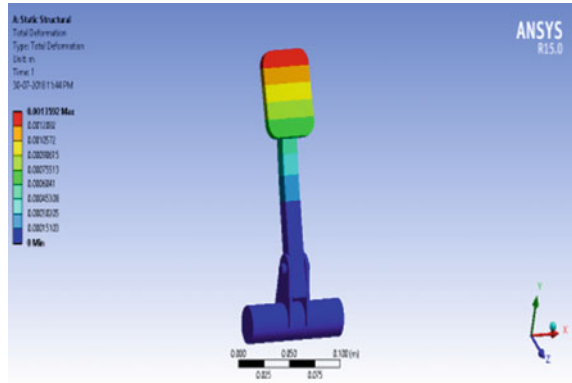


**Fig. 4** Equivalent strain in solid pedal



Equivalent stress (von Mises stress) is considered in design as it allows any arbitrary 3D stress state to be represented as a single positive stress value. Equivalent stress is part of the maximum equivalent stress failure theory used to predict yielding in a ductile material [10].

**Fig. 5** Total deformation in solid model



Equivalent Stress (von Mises) is 151.71 MPa.  
 Total Deformation is 1.3 mm.  
 Factor of Safety is  $503/151.71 = 3.32$ .

It is clear that the component has a very high factor of safety and is oversized. This component is optimized further by removing material from the parts with very little concentration. This method was used to obtain the following geometry. After the stress analysis carried out on the pedal, results were noted [11, 12] (Figs. 6, 7, 8, 9, 10, and 11).

Equivalent Stress (Von Mises) is 378.9 MPa.  
 Total Deformation is 2.3 mm.  
 Factor of Safety is  $503/378.9 = 1.32$ .

Solid pedal weighs 121.92 g while the optimized weighs only 62.52 g. After optimization though the factor of safety has decreased from 3.32 to 1.32 but it is satisfactory until the weight is being lowered down to nearly half (Fig. 12).

**Fig. 6** SolidWorks model of optimized pedal



**Fig. 7** Fine meshing in solid model

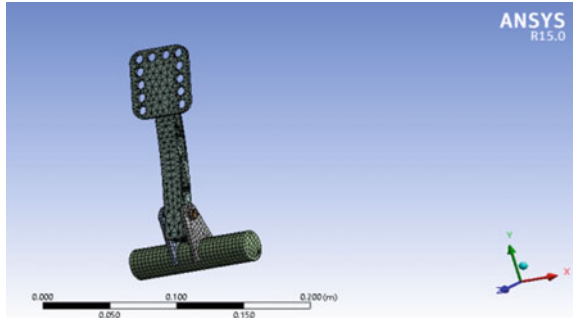


**Fig. 8** Pedal loading (applying the forces on optimized pedal)

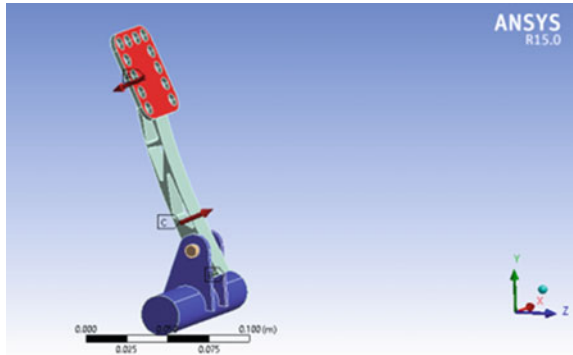


**Fig. 9** Equivalent stress for optimized pedal

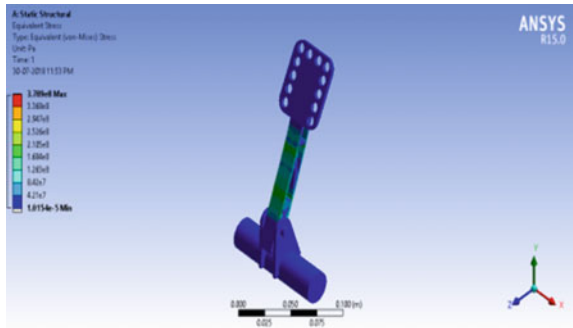


**Fig. 10** Equivalent strain for optimized pedal

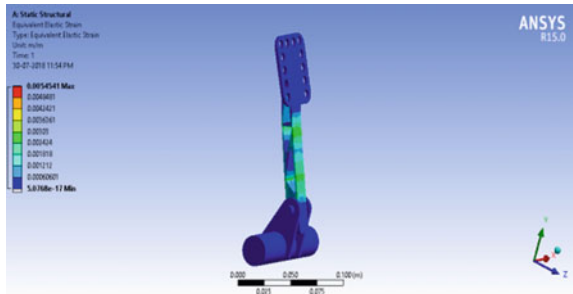


**Fig. 11** Total deformation

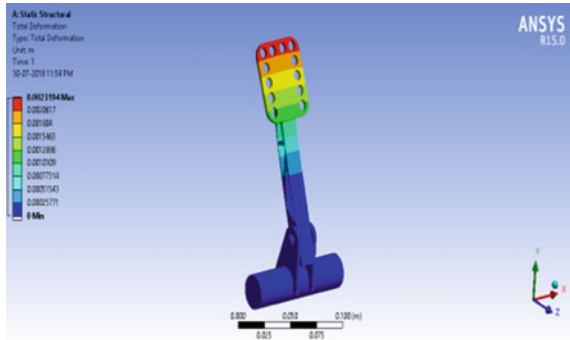


**Fig. 12** Solid pedal versus optimized pedal (modeled in SolidWorks)



## 5 Conclusion

Stress concentration of the optimized model has increased leading to a low factor of safety. The solid pedal was overdesigned to be safe and it unnecessarily increased the vehicle’s weight. Table 2 gives a detailed comparison between the Solid and the Optimized pedal. The volume and the space required by the optimized pedal are less and the weight has reduced by 48.73%. Considering the weight of all the three pedals, i.e., Accelerator, Brake and the Clutch, an overall reduction in weight of about 180 gms is achieved. The equivalent stress in the optimized pedal is 378.9 MPa, giving a factor of safety of 1.32 which is in the very limits. Hence, the design is concluded to be safe.

**Table 2** Solid versus optimized comparison

	Solid	Optimized
Mass	121.92 gms	62.52 gms
Deformation	1.3 mm	2.3 mm
Stress	151.71 MPa	378.9 MPa
F. O. S.	3.32	1.32
Mass	121.92 gms	62.52 gms

## References

1. Kurkure B, Sadaphale DB (2015) Optimization of brake pedal. *Int J Mech Ind Technol* 3(1), 175–183. ISSN 2348-7593 (Online)
2. Chhabra P (2011) Concurrent design and prototyping of composite accelerator pedal. *Int J Adv Technol (IJAT)* 2(4) (October). ISSN 0976-4860
3. Aleksendric D, Cirovic V, Smiljanic D (2015) Brake pedal feel control model. SAE Technical Paper, SAE International, No. 2015-01-2674, September
4. Harzheim L, Graf G (1995) Optimization of engineering components with the SKO method. SAE Technical Paper Series, 951104
5. Dhande KK, Jamadar NI, Ghatge S (2014) Design and analysis of composite brake pedal: an ergonomic approach. *Int J Mech Eng Robot Res* 3(3):474–482
6. Saidpour H (2004) Lightweight high performance materials for car body structure. In: NTI technology conference, CEME, Ford Motor Company, 16 June 2004
7. Jawarikar P, Khan S, Kshirsagar B (2016) Structural optimization, thermal and vibration analysis of two wheeler disc brake rotor. *Int J Innov Res Sci Eng* 2(8):169–186
8. Amandeep AK, Goyal A, Rohilla P (2017) Optimization of brake pedal by finite element simulation. *Int J Mech Solids* 12(1), 27–40. ISSN 0973-1881
9. Dhande K, Jamadar N, Ghatge S (2014) Conceptual design analysis of brake pedal profile. *Int J Innov Res Sci Eng Technol* 3(11):17432–17441 (November)
10. Milliken WF, Milliken DL (1995) Race car vehicle dynamics. SAE International, ISBN I56091-526-9
11. Bhandari VB (2015) Design of machine elements. Tata McGraw Hill, New Delhi
12. Data records, Team VAAYU (2016) FSAE Team MGM's Jawaharlal Nehru Engineering College, Aurangabad

# Design and Analysis of Steering Clevis Joint for Optimization and Steering Stability



Aniket Sawant, Dhananjay Patil, Vedashri Joshi, Amit Trisal and Arvind Chel

**Abstract** The paper describes process of design and analysis for the clevis joint. These are widely used as an extreme to steering rack to drive the power of steering rack to the tie rod of the vehicle. This research aims to design the clevis joint for reducing the weight and increase the steering stability of an all-terrain vehicle (ATV), while considering a satisfaction safety factor for both handling and performance of the vehicle. The first step is modeling the clevis joint as per the operational consideration and the various design constraints. The next stage is stress analysis using finite element software and design adjustments for decreasing weight without conceding the structural strength.

**Keywords** ATV: steering clevis joint · Finite element analysis (FEA) · Weight reduction · Optimization

## 1 Introduction

Weight Reduction is playing a vital role in automobile engineering industry to improve the efficiency and stability. It has been accomplished through advances

---

A. Sawant (✉) · D. Patil · V. Joshi · A. Trisal · A. Chel  
Department of Mechanical Engineering, MGM Jawaharlal Nehru Engineering College,  
Aurangabad, India  
e-mail: [aniketsawant239@gmail.com](mailto:aniketsawant239@gmail.com)

D. Patil  
e-mail: [patiljay014@gmail.com](mailto:patiljay014@gmail.com)

V. Joshi  
e-mail: [vedashrijoshi97@gmail.com](mailto:vedashrijoshi97@gmail.com)

A. Trisal  
e-mail: [amittrisal122@gmail.com](mailto:amittrisal122@gmail.com)

A. Chel  
e-mail: [dr.arvindchel@gmail.com](mailto:dr.arvindchel@gmail.com)

in various fields like method considerations, material selection, design optimization, and fabrication process.

Design optimization must be done to obtain the lowest weight with maximum or greater performance based on elimination of design boundaries and design uncertainties. The clevis on a vehicle is a joint, which is used as an addition to steering rack to drive the power of steering rack to the wheels via tie rods [1].

Clevis joint is connected to tie rod on one end and steering rack on the other end by the thread provided inside the steering rack and the tapping procedure done. The function of a clevis joint is used as an addition to the rack which able to control the position of the tie rod. The tapping procedure is done on clevis joint mating platform with the steering rack.

Structural optimization tool like topology and profile optimization helps to decrease product development time as it gives a mathematical model, which indicates scope for optimization and weight reduction for overdesigned modules [2].

Clevis joint comprises a heim joint and C-shaped cup, which partially houses the heim joint. It connects tie rods with the rack as a bolt passes through the C-shaped structure and the heim joint. The weight reduction of Clevis joint is done such that the strength and life cycle performance of the joint are satisfied.

## 2 Literature Survey

For Design optimization of clevis joint, it is required to study the design aspects and accessible literature so to understand the basic need of the industry for weight reduction and optimization of the components and to establish the increasing role of finite element analysis for the weight reduction and optimization purpose.

Thomas Gillespie in 'Fundamental of Vehicle Dynamics' elaborates that the cornering behavior is a significant performance mode and is associated with the responsiveness of a vehicle to driver input it also describes the front wheel geometry and the forces as well as the torque considered while designing a steering system [2].

A Workshop report published by an agency of the United State government (Feb 2003) focused on the light-weighting of vehicle and the technology gap for light-duty vehicles. It focuses on weight optimization so to develop a light weight vehicle and also had fixed the goal for year 2020–2050 the most light weight vehicle. The target set for weight reduction of UDV Chassis and the suspension system is 25% by the year 2020 [3].

Rajkumar Roy et al. [3] focuses on recent approaches towards the automation of manual optimization processes and its challenges that it presents to the engineering sector. The study describes the scalability as major challenges for design optimization techniques. As now GAs is the most prevalent algorithmic optimization approach. For the large-scale optimization more exploration in topology design, computational power, and effective optimization will be required [3].

Chang and Tang [4] discuss a cohesive design and manufacturing methodology that supports the shape optimization. The main involvement of the work is in the

field of incorporating manufacturing in the design process, where for design the manufacturing cost is considered. The design problematic must be articulated more realistically by integrating the manufacturing cost as both the objective function or constrain function [4].

Rajendran et al. [5] discusses the development of designing an optimized and lightweight knuckle from scratch. Using structure optimization, topology optimization is performed on the design to drive the optimal load required for the load cases. The process of using topology optimization for the load generation and parametric study using shape optimization helps to reduce the design reiteration and intermediate concept models [5].

The disciplines for optimization process are

- (1) Topology optimization—It is a process in which the finest material layout according to the design space and loading case be attained.
- (2) Size optimization—It gives the finest thickness of the object.
- (3) Shape optimization—It gives the optimal filets and the optimum outer dimensions.
- (4) Topology—An progressive form of shape optimization in which a design region is defined and a reinforcement is generated from the shape variable.

### 3 Methodology

A CAD model is designed in three-dimensional interactive application in CATIA V (R28). The model is designed according to its application in the required size and shape.

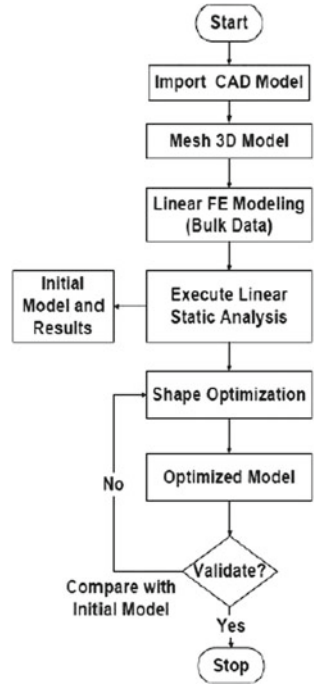
Further finite element analysis is done using FEA simulation software; it helps in validating the CAD model for its durability, strength, and stiffness under certain high loading conditions. The allowable stresses are calculated and compared with the static structural analysis of the designed model. The CAD model is assumed to be sustainable if the allowable stress is less than the static structural analysis (Fig. 1). It is necessary for the long life of the modeled component.

#### 3.1 *Designing a CAD Model*

A CAD model of clevis joint was developed in 3-D modeling software CATIA. It consists of a C-shaped cup, which can be fastened using a bolt to the steering rack. The mating part of the previous design of clevis joint, which is inserted in steering rack was detached and replaced with a simple Allen bolt. It also consists of mounting point for the tie rod. A heim joint can be easily connected to the C shaped structure using a bolt.



**Fig. 1** Methodology [6]



### 3.2 *Material Selection*

In the previous design of clevis joint EN-8 was used as primary material, which has a reasonable tensile strength (Fig. 2).

Optimization was done by changing the design and primary material of clevis joint. Aluminum 7075 T6 was used as a primary material for new clevis joint. Al 7075 T6 is known for its great strength and lightweight quality (Figs. 3 and 4).

### 3.3 *Property Comparison*

The parameters for both materials EN-8 and Al 7075 T6 are given in Tables 1 and 2.

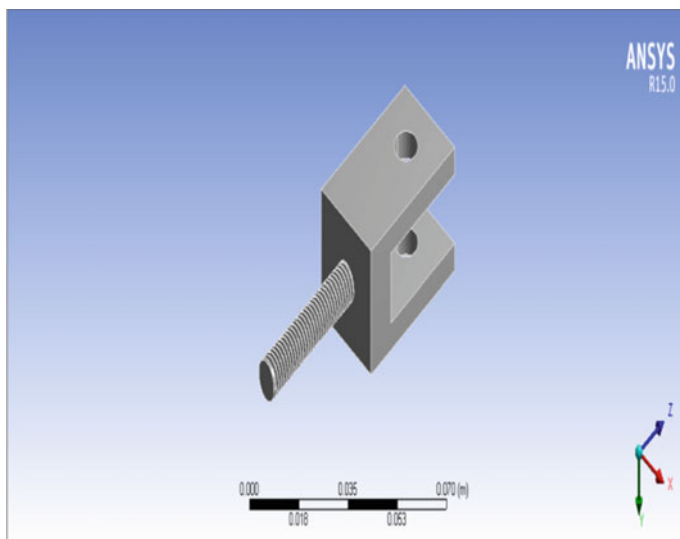


Fig. 2 Old clevis joint design

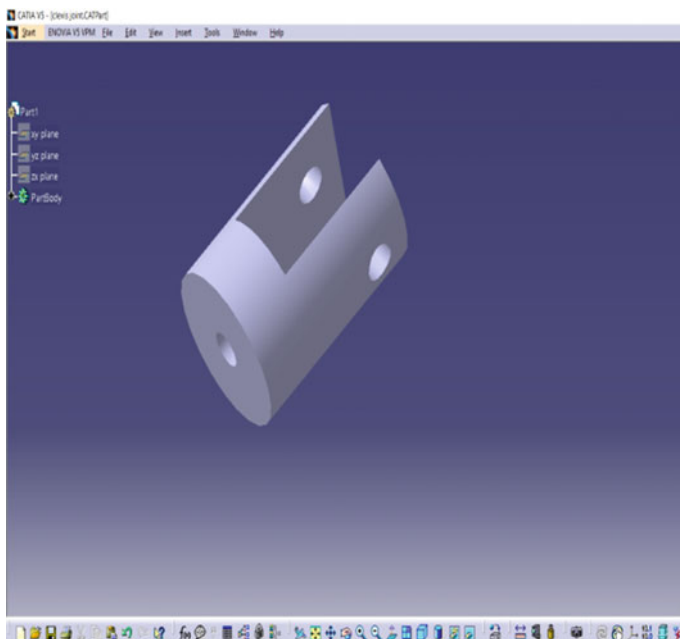
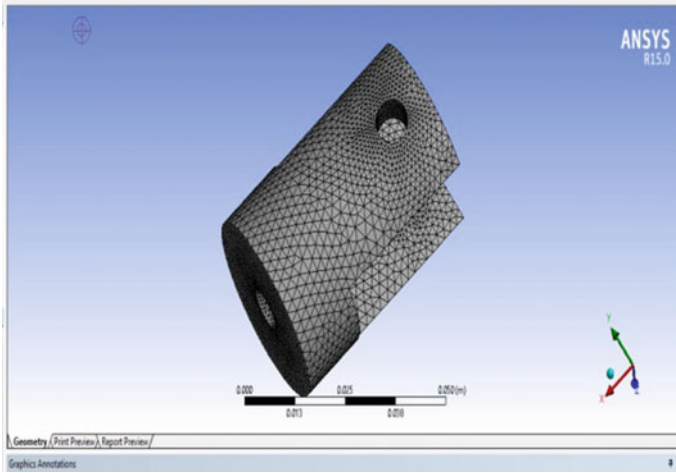


Fig. 3 Optimized new model of clevis joint



**Fig. 4** Meshing in Ansys

**Table 1** Property comparison [2]

Material	EN-8	Al 7075 T6
Density (Kg/m <sup>3</sup> )	7.83	2.77
Young's modulus (GPa)	210	71.7
Yield strength (MPa)	465	503
Ultimate tensile strength (MPa)	700	572
Fatigue strength fracture	0.854	0.87
Allowable strength (MPa)	154.57	82.96
Factor of safety	1.98	1.53

**Table 2** Comparison of old and new design

Parameter	Old design with EN-8 [1]	New design with Al 7075 T6
Mass (g)	125.58	66
Volume (cm <sup>3</sup> )	15997.23	24,250
Surface area (mm <sup>2</sup> )	7673.47	8000

## 4 Calculations

### 4.1 Forces on Clevis Joint from Tie Rod

The forces and torque on the clevis joint can be estimated as follows:

$$\text{Lateral acceleration, } (a) = V^2/R$$

where,  $V$  = Velocity of vehicle (m/s)

$R$  = Turning radius (m)

$$V = 40 \text{ km/hr (11.11 m/s) \& } R = 3.15 \text{ m}$$

$$a = (11.11)^2/3.15 = 39.18 \text{ m/s}^2$$

$$\text{Lateral Force} = \text{wt. of vehicle with driver} \times a$$

$$F = 230 \times 39.18 = 9011.4 \text{ N}$$

$$\text{Wt. distribution ratio} = 60 : 40$$

$$\text{Lateral force on front wheel} = 0.4 \times 9011.4$$

$$= 3604.56 \text{ N}$$

$$\text{Moment on wheel (when stationary)}$$

$$= \text{lateral force} \times \text{mechanical trail}$$

$$= 3604.56 \times 25.5 \times 10^{-3}$$

$$= 91.916 \text{ N-m}$$

$$\text{Moment on wheel (due to traction)}$$

$$= \text{traction force on front wheel} \times \text{scrub}$$

$$= m \times a \times \text{scrub}$$

$$= 230 \times 4 \times 38 \times 10^{-3}$$

$$= 34.96 \text{ N-m}$$

$$\text{Total moment of wheel}$$

$$= 91.916 + 34.96 = 126.876 \text{ N-m}$$

$$\text{Force on tie rod}$$

$$= \text{total moment on wheel/steering arm length}$$

$$= 0.126 / (50 \times 10^{-3})$$

$$= 2.537 \text{ kN}$$

The tie rod is well connected with clevis joint, hence it transmits the force.

$$\text{Force on clevis joint} = 2.537 \text{ kN}$$

$$\text{Stress on clevis joint} = \text{force on clevis joint/area} = 2.537/0.008 = 313.190 \text{ kN/m}^2.$$

The allowable stress for Al 7075 T6 clevis joint is 82960 kN/m<sup>2</sup>, which is 313.190 kN/m<sup>2</sup>. Hence, the clevis joint is safe with Al 7075 T6 material based on the allowable stress (Fig. 5).

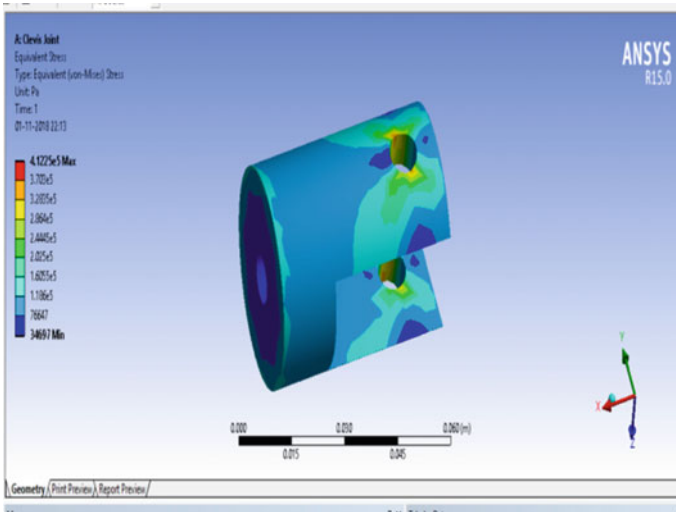


Fig. 5 Analysis for lateral load from tie rod

### 4.2 Forces on Clevis Joint from Steering Rack

Here, the stress exerted by the steering system on the clevis joint is calculated and compared with allowable stress to check the design is safe (Fig. 6).

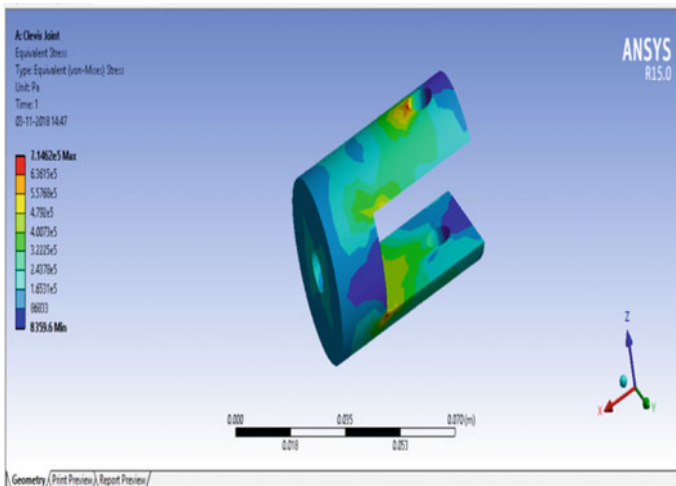


Fig. 6 Analysis for lateral load from steering rack

Let, steering wheel torque = 60 N-m

Steering wheel diameter = 0.3048 m

Force on steering wheel =  $60/0.3048 = 196.504$  N.

**Torque on pinion = torque on steering wheel**

Torque on pinion = 60 N-m

**Force on pinion = torque on pinion/radius of pinion =  $60/36 \times 10^{-3} = 1.666$  kN**

**Force on rack = Force on pinion**

Also, **Force on clevis joint = Force on rack**

Hence Force on clevis joint = 1.66 kN

**Stress = force/area =  $1.666.66/0.008$**

**=  $208.332$  kN/m<sup>2</sup> (allowable stress  $82960$  kN/m<sup>2</sup>)**

### 4.3 Observation

The stress acting on the clevis joint were calculated and compared to the allowable stress. Al 7075 T6 can sustain all the forces as the calculated stress is less than the allowable stress. Using Al 7075 T6 as a primary material in the optimized clevis joint, desired strength and weight reduction in steering system are achieved.

**Weight reduced (For one Clevis Joint)**

**=  $125.58 - 66 = 59.58$  gm.**

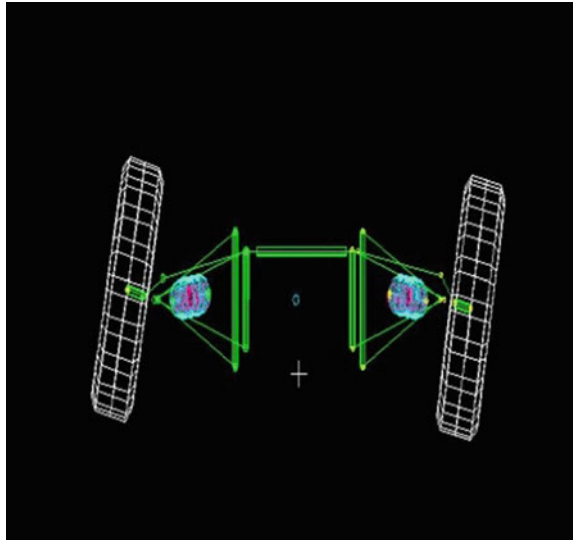
Clevis joint is attached on both extreme ends of steering rack. The total weight reduces by **119.16 gm**.

## 5 Simulation of Steering System

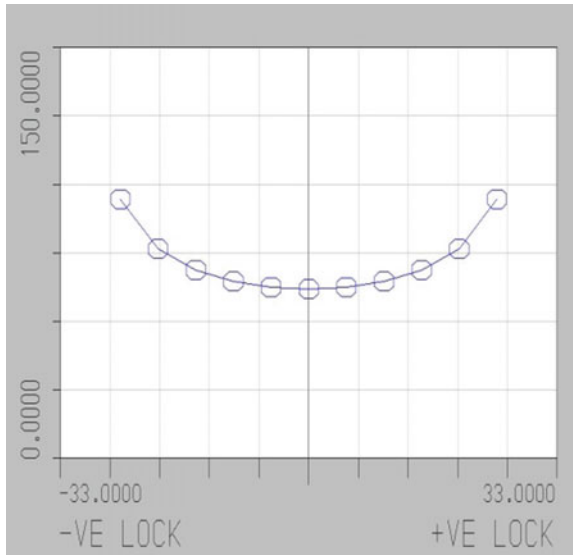
Simulation of steering system is done in LOTUS shark suspension and steering simulator. Dynamic parameters are verified by simulating the geometry. It provides graphs and statistical data of the changes in parameters in dynamic conditions (Fig. 7).

Figure 8 describes the change in Ackermann percentage while cornering from lock to lock on either side. After simulation, statistical data of the parameters is generated. This data is used to validate the design. The simulation shows the effect on parameters in dynamic conditions (Table 3).

**Fig. 7** Steering simulation using LOTUS Shark simulator



**Fig. 8** Ackermann percentage graph



**Table 3** Simulation report (lotus shark simulator)

Lotus suspension analysis v4.03						
*****						
Front suspension-steering travel						
Type 1 double wishbone, damper to lower wishbone						
Incremental geometry values						
Rack travel (Mm)	Toe angle RHS (°)	Toe angle LHS (°)	Camber angle RHS (°)	Camber angle LHS (°)	Ackermann (%)	Turning circle radius (mm)
-45.00	-69.62	49.52	16.71	4.39	51.91	933.47
-40.00	-65.78	43.89	11.92	3.14	66.38	1134.97
-35.00	-61.46	38.40	7.93	2.23	84.00	1375.95
-30.00	-59.27	33.00	6.87	1.55	115.82	1626.29
-25.00	-41.85	27.65	2.72	1.04	94.71	2305.19
-20.00	-29.12	22.31	1.15	0.65	76.43	3225.15
-15.00	-20.25	16.92	0.52	0.36	68.68	4570.39
-10.00	-12.81	11.45	0.20	0.16	64.54	7112.80
-5.00	-6.16	5.84	0.05	0.04	62.42	14516.01
0.00	0.00	0.00	0.00	0.00	61.76	0.00
5.00	5.84	-6.16	0.04	0.05	62.42	14516.01
10.00	11.45	-12.81	0.16	0.20	64.54	7112.80
15.00	16.92	-20.25	0.36	0.52	68.68	4570.39
20.00	22.31	-29.12	0.65	1.15	76.43	3225.15
25.00	27.65	-41.85	1.04	2.72	94.71	2305.19
30.00	33.00	-59.27	1.55	6.87	115.82	1626.29
35.00	38.40	-61.46	2.23	7.93	84.00	1375.95
40.00	43.89	-65.78	3.14	11.92	66.38	1134.97
45.00	49.52	-69.62	4.39	16.71	51.91	933.47

## 6 Conclusion

The new design as well as new material selection has resulted in the desired strength and weight reduction. The following key conclusions can be drawn based on the comparison of the old existing design and newly developed design with new material selection mentioned earlier.



1. As compared to the previous design using EN-8 material the weight of the newly designed clevis joint reduces nearly 48%.
2. In the newly developed clevis joint, the play in transmitting the force has been considerably reduced by 40%. This is because the clevis joint is fixed to the rack using the Allen bolt, which restricts the rotational play.
3. The new design is optimized by removing the mating part, which has been replaced by an Allen bolt with no rotational play.
4. Using the LOTUS suspension software, the Ackermann percentage graph was obtained and shows uniform change from lock to lock on either direction.

## References

1. Kulkarni N, Maid P (2017) Structural design & analysis of steering clevis joint of an ATV for weight reduction and steering stability. *Int J New Technol Res* 3(7):35–37
2. Gillespie T (1992) *Fundamental of vehicle dynamics*. Society of Automobile Engineers, Warrendale, PA
3. Roy R, Hinduja S, Teti R (2008) Recent advances in engineering design optimization. *CIRP Ann Manuf Technol* 57(2):697–715
4. Chang KS, Tang PS (2001) Integration of design and manufacturing of structural shape optimization. *Adv Eng Softw* 32:55–567
5. Rajendran RS, Sudalaimuthu S, Sixth M (2013) Knuckle development process with the help of optimization techniques. In: *Altair technology conference*, India
6. Dumbre P, Mishra AK, Aher VS (2014) Structural analysis of steering knuckle for weight reduction. *Int J Emerg Technol Adv Eng* 4(6):552–557

# Modeling and Structural Analysis of Suspension Rocker for FSAE Vehicle



Saurabh Bairagi, Jatin Parajiya, Kaustubh Babrekar and Nitin G. Phafat

**Abstract** Suspension system plays a vital role in Formula SAE's overall performance as it isolates the vehicle from disturbances and provides a comfortable ride. The motive of this study is concerned with one of the major components of this system; rocker (bellcrank). A solid model of suspension rocker using 3D modeling software Solidworks is prepared and structural analysis is carried out by providing specific boundary conditions. The proposed new optimized model of suspension rocker has less weight and at the same time is competent to perform the function.

**Keywords** Rocker (Bellcrank) · Push rod suspension · FEA

## 1 Introduction

Whenever the vehicle takes a bump or while turning, there is uneven distribution of load which would result in rolling over of the vehicle. Here, the suspension system has its importance as it minimizes the vertical motion along with pitch and roll movements. The suspension system provides a level of comfort and congenial space for driving [1].

FSAE cars mostly used Push-Rod suspension, which consist of double control arm or double wishbone suspension. The reason for using Push-rod suspension is that the push-rods and control arms have airfoil design which allows the air passage smoothly and does not create any sort of turbulent air and provides laminar flow of

---

S. Bairagi (✉) · J. Parajiya · K. Babrekar · N. G. Phafat  
Department of Mechanical Engineering, MGM Jawaharlal Nehru Engineering College,  
Aurangabad, India  
e-mail: [saurabh.bairagi.434@gmail.com](mailto:saurabh.bairagi.434@gmail.com)

J. Parajiya  
e-mail: [jatinparajiya196@gmail.com](mailto:jatinparajiya196@gmail.com)

K. Babrekar  
e-mail: [kaustubh.babrekar@gmail.com](mailto:kaustubh.babrekar@gmail.com)

N. G. Phafat  
e-mail: [phafatng@gmail.com](mailto:phafatng@gmail.com)

© Springer Nature Singapore Pte Ltd. 2020  
G. S. V. L. Narasimham et al. (eds.), *Recent Trends in Mechanical Engineering*,  
Lecture Notes in Mechanical Engineering,  
[https://doi.org/10.1007/978-981-15-1124-0\\_52](https://doi.org/10.1007/978-981-15-1124-0_52)

air. The secondary reason is that it restricts the wheel movement and tends to keep the car at same road level [2].

Further, if one has to provide large room for adjustment Double Wishbone suspension satisfies this need. There are four types of Double wishbone suspension and are mentioned below:

1. Equal length and parallel arms.
2. Equal length and non-parallel arms.
3. Unequal length and parallel arms.
4. Unequal length and nonparallel arms.

Of all the above the fourth type of Double wishbone suspension is widely used [3].

## ***1.1 Literature Review***

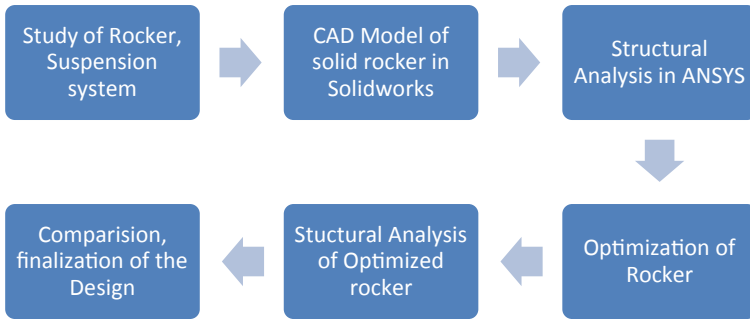
Suspension system is one of the vital elements of a Formula Vehicle; the stability of the car depends irrefutably on it. Improvement in the suspension system from the double wishbone to push rod improves the aerodynamics as well as less in weight [4]. Reduction of weight is majorly possible in the Rocker (BellCrank) [5]. Material selected is Aluminum due to its lightweight and high strength. It has a good response to machinability [6].

## ***1.2 Working Principle***

When the vehicle hits a bump, the force is transmitted from the push-rod to the rocker which results in slight rotational movement of the rocker which turns the torsion bar and the resistant from the bar compresses the damper and further as the heave spring is released it eventually oscillates the damper, which dampens out the force. There are some important parameters, which govern the suspension geometry. They are as follows:

- a. Camber: It is the angle of tire with respect to vertical axis of car and should be negative within the range of  $1^{\circ}$ – $2^{\circ}$ .
- b. Caster: It is the angle of steering axis with respect to the vertical when seen from side view; this angle keeps the tire straight and provides directional stability.
- c. Toe-in: This is the angle when the front portion of tire's are closer than the back portion of the tire and the vice versa is termed as Toe Out [7].

### 1.3 Methodology



### 1.4 Material Selection

We have selected Aluminum 6061 T6 having the following properties: (Table 1).

## 2 Calculations

Dynamic loads should be considered for designing of the suspension system [8, 9] (Tables 2 and 3).

Mass of vehicle without driver = 240 kg

Mass of vehicle with drive,  $M = 310$  kg

**Table 1** Material properties for aluminum 6061 T6

Material	Amount (wt%)
Aluminum (Al)	95.8–98.6%
Magnesium (Mg)	0.8–1.2%
Copper (Cu)	0.15–0.4%
Zinc (Zn)	0.25%
Chromium (Cr)	0.04–0.35%
Density	2.7 g/cc
U. T. S.	310 MPa
Yield Strength	276 MPa
Young’s Modulus	68.9 GPa
Machinability	60% (Good)

**Table 2** Vehicle parameters

Parameters	Front	Rear
Track width	1220.72 mm	1172.61 mm
Camber	-0.734°	0.049°
Roll center height	8.99 mm	30.988 mm
Scrub Radius	33 mm	38 mm
KPI	5°	0°

**Table 3** Suspension details:  
DNM shocks

Suspension properties	Values
Eye to Eye length	190 mm
Stroke	51 mm
Mass	380 gms
Adjustment	4 way external

Mass on front wheels,  $M_F = 108.5$  kg

Mass on rear wheel,  $M_R = 201.5$  kg

Unsprung mass of vehicle,  $M_{us} = 61.233$  kg

Front unsprung mass of the vehicle,  $M_{unF} = 28.779$  kg

Rear unsprung mass of the vehicle,  $M_{unR} = 32.454$  kg

Sprung mass of the vehicle,  $M_s = 310$  kg -  $61.233$  kg =  $248.767$  kg

Front sprung mass of the vehicle,  $M_{sF} = 108.5$  kg -  $28.779$  kg =  $79.721$  kg

Rear sprung mass of the vehicle,  $M_{sR} = 201.5$  kg -  $32.454$  kg =  $169.046$  kg

Natural Frequencies: Front  $N_F = 2.5$  Hz; Rear  $N_R = 2.3$  Hz

Front Motion ratio = 1.428; Rear motion ratio = 1.25

Front track width = 47.468" = 1.2065 m

Rear track width = 46.153" = 1.17228 m

Wheelbase = 64" = 1.6256 m

## 2.1 Spring Rate

### Front Spring Rate

$$K_{sF} = 4\pi^2 \times N_F^2 \times \left( \frac{M_{sF}}{2} \right) \times (\text{Motion Ratio})^2 \tag{1}$$

$$K_{sF} = 4\pi^2 \times (2.5)^2 \times \left( \frac{79.721}{2} \right) \times (1.4285)^2 = 20.055 \text{ N/mm}$$

### Rear Spring Rate

$$K_{sR} = 4\pi^2 \times N_R^2 \times \left(\frac{M_{sR}}{2}\right) \times (\text{Motion Ratio})^2$$

$$K_{sR} = 4\pi^2 \times (2.3)^2 \times \left(\frac{169.046}{2}\right) \times (1.25)^2 = 27.581 \text{ N/mm}$$

### 2.2 Wheel Rate

$$\text{Wheel Rate, } K_w \text{ (N/mm)} = \frac{\text{Spring Rate (N/mm)}}{(\text{Motion Ratio})^2} \tag{2}$$

$$\text{Front Wheel Rate, } K_{wF} = \frac{20.055}{(1.4285)^2} = 9.834 \text{ N/mm}$$

$$\text{Rear Wheel Rate, } K_{wR} = \frac{27.581}{(1.25)^2} = 17.651 \text{ N/mm}$$

### 2.3 Roll Rate

$$\text{Roll Rate } K_{\phi s} = \frac{\pi \times T^2 \times (K_w^2)}{180 \times 2 \times K_w} \tag{3}$$

Front:

$$K_{\phi sF} = \frac{\pi \times (T_F^2) \times (K_{wF}^2)}{180 \times 2 \times K_{wF}}$$

$$K_{\phi sF} = \frac{\pi \times (1.2065)^2 \times (9834.8)^2}{180 \times 2 \times 9834.8} = 124.98 \text{ N} \cdot \frac{\text{m}}{\circ}$$

Rear:

$$K_{\phi sR} = \frac{\pi \times (T_R^2) \times (K_{wR}^2)}{180 \times 2 \times K_{wR}}$$

$$K_{\phi sR} = \frac{\pi \times (1.17)^2 \times (17651.0)^2}{180 \times 2 \times 17651} = 210.85 \text{ N} \cdot \frac{\text{m}}{\circ}$$

## 2.4 Roll Moment at 1G Lateral Acceleration

$$M_{1g} = (h - R_c) \times M_s \times g \quad (4)$$

*Front*

$$M_{1gF} = (h - R_{cF}) \times M_{sF} \times g$$

$$M_{1gF} = (0.2084 - 0.018) \times 79.721 \times 9.81 = 148.904 \text{ Nm}$$

*Rear*

$$M_{1gR} = (h - R_{cR}) \times M_{sR} \times g$$

$$M_{1gR} = (0.208 - 0.037) \times 169.046 \times 9.81 = 283.576 \text{ Nm}$$

## 2.5 Force at Wheel at Ride Height

*Front: Force at each front wheel,*

$$F_{F1} = \left( \frac{M_F}{2} \right) \times g = \left( \frac{108.5}{2} \right) \times 9.81 = 532.1925 \text{ N} \quad (5)$$

*Rear: Force at each rear wheel,*

$$F_{R1} = \left( \frac{M_R}{2} \right) \times g = \left( \frac{201.5}{2} \right) \times 9.81 = 988.3575 \text{ N}$$

## 2.6 Wheel Deflection at Ride Height

*Front: Wheel deflection on each front wheel =*

$$\frac{F_{F1}}{K_{WF}} = \frac{532.1925}{9.8348}$$

$$= 54.1132 \text{ mm} = 2.13'' \quad (6)$$

*Rear: Wheel deflection on each rear wheel =*

$$\frac{F_{R1}}{K_{WR}} = \frac{988.3575}{17.651} = 55.99 \text{ mm} = 2.204''$$

## 2.7 Spring Load

*Front:*

$$\begin{aligned} \text{Spring Load for Front, } F_{SF} &= F_{F1} \times \text{Motion Ratio} = 532.1925 \times 1.428 \\ F_{SF} &= 759.97 \text{ N} \end{aligned}$$

*Rear:*

$$\begin{aligned} \text{Spring Load for Rear, } F_{SR} &= F_{R1} \times \text{Motion Ratio} = 988.3575 \times 1.25 \\ F_{SR} &= 1232.446 \text{ N} \end{aligned}$$

Force on spring is 1232.44 N, for safety let force to be 1500 N. FEA is carried out while applying a maximum force of 3500 N on Rocker arms.

## 2.8 Spring Deflection

*Front:*

$$\begin{aligned} \text{Spring Deflectionon} &= \frac{F_{SF}}{K_{SF}} \\ &= \frac{759.97}{20.055} = 37.89 \text{ mm} \end{aligned}$$

*Rear:*

$$= \frac{1235.446}{27.581} = 44.79 \text{ mm}$$

## 3 Design Procedure and Analysis

Once the material is selected based on the different properties suitable for the rocker to sustain the various forces which are going to act on it and also, after calculating various forces the design procedure starts. The 3D solid model is designed in Solidworks and assembled by providing a bush at one of the hinges.

Further, structural analysis is to be carried out on this model by applying the material ALUMINUM 6061 T6 and providing fine meshing. Manual connections are provided between the hinge and the bush, and the type of contact is selected as frictional contact and a coefficient of friction of 0.1 is applied and appropriate solutions are applied and following results are obtained [10] (Figs. 1, 2, 3, and 4).



**Fig. 1** Solid rocker 3D model

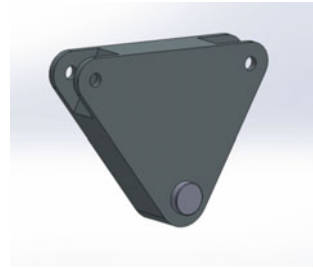


**Fig. 2** Equivalent stress distribution on solid rocker

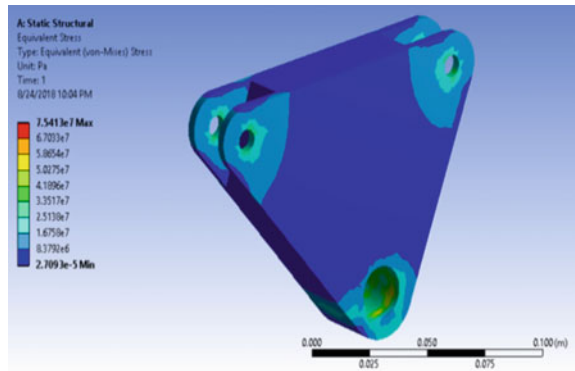
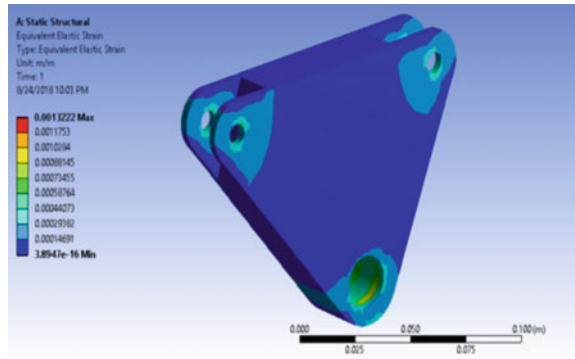


**Fig. 3** Equivalent elastic strain on solid rocker



The same solid model is then heavily optimized by analyzing the above results and FEA is again carried out by applying same material and going through previous procedure. Following are the results of the further optimized rocker: (Figs. 5, 6, 7, 8, 9, and 10).

**Fig. 4** Deformation in solid rocker

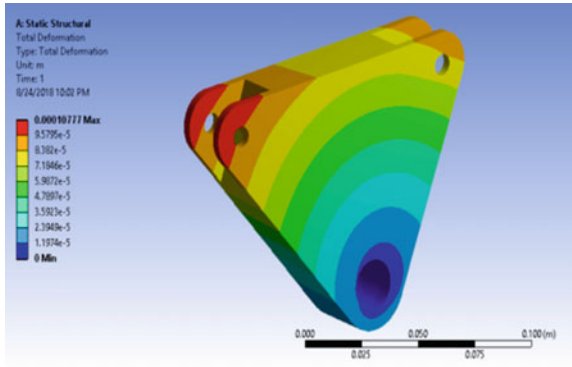


**Fig. 5** Optimized model of rocker



**Fig. 6** Fixed support for bush

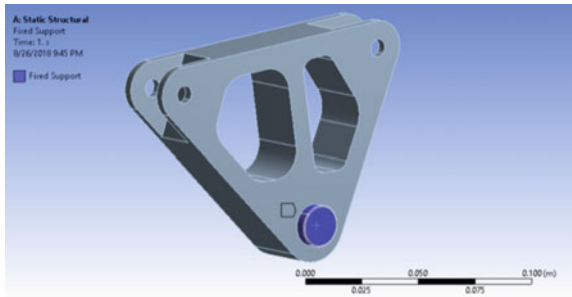


**Fig. 7** Forces & boundary conditions applied

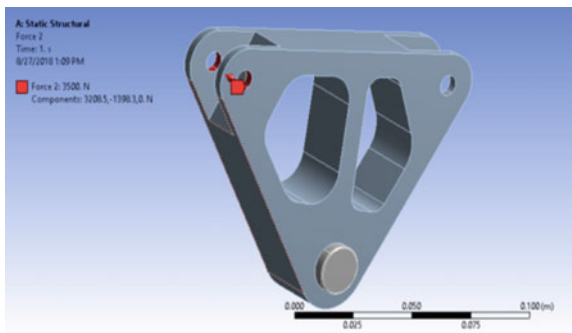


**Fig. 8** Equivalent stress in optimized rocker

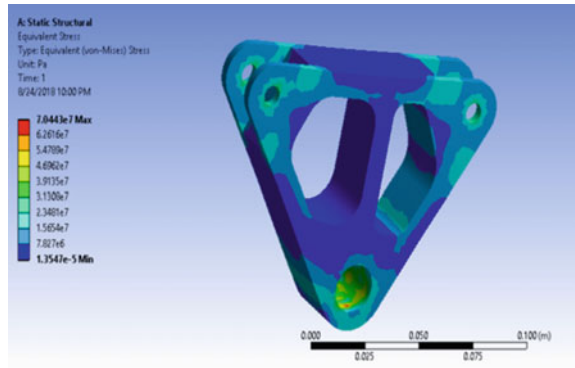


**Fig. 9** Equivalent strain in optimized rocker

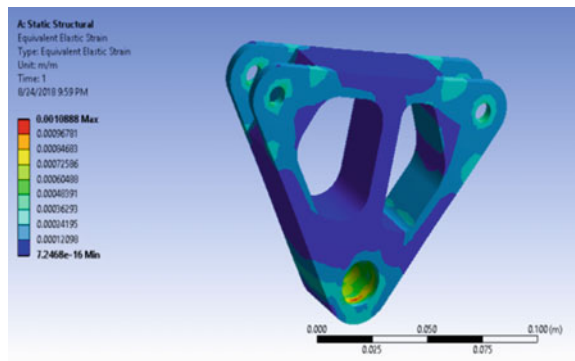
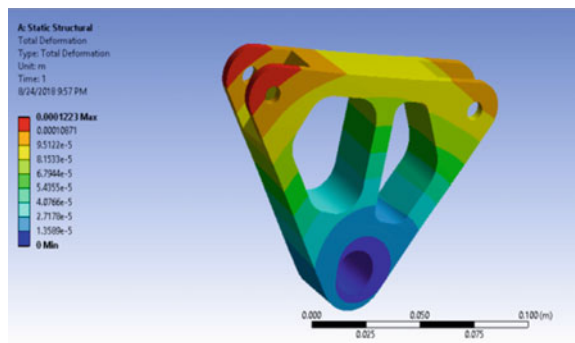


**Fig. 10** Deformation in optimized rocker



## 4 Conclusion

For the rockers, Finite Element Analysis was carried out. The table shows comparison of the results obtained from the FEA on ANSYS software with the required parameters (Table 4).

**Table 4** Solid V/s optimized comparison

	Solid	Optimized
Mass	555.40 gm	344.79 gm
Deformation	0.1077 mm	0.1223 mm
Stress	7.541e7 Pa	7.044e7 Pa
Strain	0.001322	0.001088

From the above data, it was found that the optimized rocker works safely within the specified range of parameters. Range of force rocker can sustain with minimal deformation is up to 4000 N. Weight of the new proposed optimized rocker is reduced by 211 grams for a single rocker, which further results in a total weight saving of 844 grams (4 rockers in FSAE car). Optimization of the rocker has resulted in reduction of C. G. Height, and reduced the rolling effect of the vehicle. The equivalent stress and strain of the optimized rocker are within the confined parameters and hence this design can be concluded structurally safe. The cost of the optimized rocker is also less.

## 5 Appendix

See Table 5.

**Table 5** Appendix

No.	Parameter	Formula	Description
1	Front spring rate	$K_{sF} = 4\pi^2 \times N_F^2 \times \left(\frac{M_{sF}}{2}\right) \times (\text{Motion Ratio})^2$	Amount of weight needed to compress spring by one inch
2	Wheel rate	$K_w = \frac{\text{Spring Rate (N/mm)}}{(\text{Motion Ratio})^2}$	Actual spring rate at tire contact patch
3	Roll rate	$K_{\phi s} = \frac{\pi \times T^2 \times (K_w^2)}{180 \times 2 \times K_w}$	Torque resisting body roll per degree of body roll
4	Roll moment at 1G lateral acceleration	$M_{1g} = (h - R_c) \times M_s \times g$	Moment of inertia of vehicle's sprung mass
5	Force at wheel at Ride height	$F = \left(\frac{M_F}{2}\right) \times g = \left(\frac{108.5}{2}\right) \times 9.81$	Ride height is the clearance between car's base and road which has an Impact on CG.

## References

1. Vadhe A (2018) Design and optimization of FSAE suspension system. *Int J Curr Eng Technol*. E-ISSN 2277-4106, P-ISSN 2347-5161, May
2. Ayman AL (2013) Car suspension control system: basic principles. *Int J Control, Autom Syst* 2(2). ISSN 2165-8277 (Print), July
3. Data Records, Team Vaayu (2016) MGM's J.N.E.C. Aurangabad
4. Vivekanandan N (2014) Design, analysis and simulation of double wishbone suspension system. *Int J Mech Eng* 2(6), 1–7 (June)
5. Das A (2015) Virtual prototype of upright assembly of a race car for SUPRA SAEINDIA competition. *Int J Mech Ind Technol* 2(2). ISSN 2348-7593 (Online)
6. Vishnu CS, Praveen Kumar N, Someshwar Rao K, VVSV Prasad G, Jaswanrh Sai M (2017) Design and analysis of push rod rocker arm suspension using mono spring. *Int J Pure Appl Math* 114(9):465–475
7. Milliken WF, Milliken DL (1995) *Race car vehicle dynamics*. SAE International, Warrendale, PA
8. Davis W (2018) Billy golfer, design and optimization of a formula SAE racecar by Faculty of Worcester polytechnic institute, Project Number: MQP-DCP2012-A11-D12, June
9. Phakatkar HG, Potdar C, Jojode V, Jadhav S (2016) Design of suspension system of formula student car. *Int J Mech Prod Eng* 4(2). ISSN 2320-2092
10. Dixon JC (2009) *Suspension geometry and computation*. Wiley

# Control of End-Effector of a Multi-link Robot with Joint and Link Flexibility



E. Madhusudan Raju, L. Siva Rama Krishna and Mohamed Abbas

**Abstract** Flexibility in manipulators/robots is due to both joint and link flexibility that makes up the system. Flexible robots are preferred over conventional rigid robots in applications like invasive surgeries, space applications, and industries due to their prompt response, low energy requirement, faster operational speeds, and low weight to power ratio. Due to inherent flexibility, accurate positioning of end-effector in required path is difficult. Moreover flexibility of link makes it an infinite degree freedom system and mathematics is very involved. To simplify the problem and get reasonable results, flexible links are modeled based on Euler–Bernoulli beam theory and Assumed mode method is implemented. Joint flexibility is because of small clearances that are inherently present in the joint, because of both manufacturing and assembling constraints, these clearances cause sudden impacts between the joining parts (journal and bearing) resulting in impact force generation as the joints are manipulated. Resulting impact (hertzian contact) forces increase the overall input torque required to manipulate the end-effector according to our wish. This paper's objective is to build a dynamic model of a two-link RR type planar manipulator with link and joint flexibility, and determine the maximum error of tip position between a robot with/without flexibility, as the end effect or travels in required vertical path with payload. Further, apply orthodox control strategies (PD, PI, and PID) to reduce the error. The end-effector carries a payload equals its links mass. Using MSC Adams and MATLAB softwares, a co-simulation approach is developed. Both the controllers (PI, PID) radically reduced error through several iterations, PID control strategy

---

E. Madhusudan Raju (✉) · L. S. R. Krishna  
Department of Mechanical Engineering, University College of Engineering (A), Osmania  
University, Hyderabad, India  
e-mail: [ettaboina@gmail.com](mailto:ettaboina@gmail.com)

L. S. R. Krishna  
e-mail: [lsrkou@gmail.com](mailto:lsrkou@gmail.com)

M. Abbas  
PhD Researcher, Industrial Robotics and Cooperative Robotics, Department of Mechanical  
Engineering, IIT Guwahati, Guwahati, Assam, India  
e-mail: [mohabbas9262@gmail.com](mailto:mohabbas9262@gmail.com)

achieved better results than PI controller and by both approaches, more than 60% of the positional error is reduced.

**Keywords** Link flexibility · Joint clearance · Assumed mode method · Euler–Bernoulli’s beam theory · PI and PID control techniques

## 1 Introduction

Robots/serial manipulators are widely used in repetitive, tiresome and hazardous jobs. These robotic manipulators are designed, built and fabricated with maximum stiffness to limit end-effector vibration for better positional accuracy, resulting in bulky industrial manipulators.

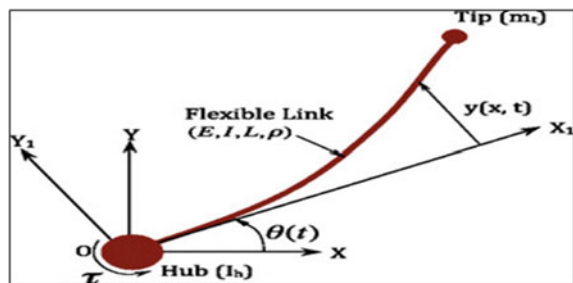
The merits of using a flexible manipulator are high-speed manipulation, low requirement of power and less material for fabrication resulting in a smaller actuator. By reducing manipulator weight, flexibility of the robot increases and the mathematical modeling becomes involved and tedious.

Flexible manipulators, core difficulty is limiting vibrations due to flexibility, it is resolved by including the effects of flexibility and applying various control strategies to accomplish minimum steady-state error and desired transient response. Space research provided the required impetus to study control of flexible manipulators, as they have lightweight reducing the launch cost and responding to issues in weight and space. The joint flexibility results in reduced rigidity of drive, shaft, and gear teeth deformation. Link flexibility results in transverse direction deformation owing to shearing and rotary inertial effects.

A one link flexible robotic system given in Fig. 1 would have rotated by an angle  $\theta(t)$  when actuated, if it was a rigid link robot, but owing to its structural flexibility, it oscillates about a mean position based on the damping of the system, this is seen as a deviation of  $y(x, t)$  from undeformed position from Fig. 1. Therefore,  $y(x, t)$  motion depends on both joint angle  $\theta$  and deformations of the link and joint.

The link flexibility is solved using Assumed mode method. This method is suitable for Euler–Bernoulli links, i.e. (maximum deformation is less than one-tenth of the

**Fig. 1** Flexible beam vibration



link length). Based on this an infinite degree freedom system is reduced to a problem of few prevailing mode shapes solved by Assumed mode method.

The lateral deformation 'y' of the link at a section at a specified time provides the length of position vector. Further, a payload 'MP' at the tip of the link is also attached. The governing equation to represent the vibration of link can be written as given in Eq. (1).

$$EI \frac{\partial^4 y(x, t)}{\partial x^4} + \rho A \frac{\partial^2 y(x, t)}{\partial t^2} = 0 \quad (1)$$

Boundary Conditions: As Eq. 1 involves a second-order derivative in time and a fourth-order derivative in 'x', two initial conditions and four boundary conditions are required for unique solution of  $y(x, t)$  as given by Eqs. 2-7.

$$y(x, t = 0) = y_i \quad (2)$$

$$\frac{\partial y(x, t = 0)}{\partial t} = \frac{\partial y(x, t)}{\partial t} \Big|_{t=0} = y_i' \quad (3)$$

$$y(x, t)|_{x=0} = 0 \quad (4)$$

$$\frac{\partial y(x, t)}{\partial x} \Big|_{x=0} = 0 \quad (5)$$

$$EI \frac{\partial^2 y(x, t)}{\partial x^2} \Big|_{x=L} = -J_L \frac{\partial^2}{\partial t^2} \left( \frac{\partial y(x, t)}{\partial x} \Big|_{x=L} \right) \quad (6)$$

$$EI \frac{\partial^3 y(x, t)}{\partial x^3} \Big|_{x=L} = -M_L \frac{\partial^2}{\partial t^2} (y(x, t)|_{x=L}) \quad (7)$$

The result of Eq. 1 is given as follows:

$$y(x, t) = \sum_{j=1}^n C_{1, j} \sin(\omega_j t) \{ (\cos(\beta_j x) - \cosh(\beta_j x)) - \alpha (\sin(\beta_j x) - \sinh(\beta_j x)) \} \quad (8)$$

where

$$\alpha = \frac{-\beta_j^3 \cos(\beta_j L) - \beta_j^3 \cosh(\beta_j L) + \frac{M_L}{\rho} \beta_j^4 \sin(\beta_j L) - \frac{M_L}{\rho} \beta_j^4 \sinh(\beta_j L)}{-\beta_j^3 \sin(\beta_j L) - \beta_j^3 \sinh(\beta_j L) - \frac{M_L}{\rho} \beta_j^4 \cos(\beta_j L) + \frac{M_L}{\rho} \beta_j^4 \cosh(\beta_j L)} \quad (9)$$

The calculated  $y(x, t)$  is for only single-link and calculations of velocities and accelerations of multi-link manipulators built on Eq. 9 are difficult. Therefore, alternative solutions were investigated and zeroed on MSC Adams software.



## 2 Literature Review

M. Moallem [1] presented a co-simulation method using MscADAMS and MATLAB for solving complex mechanical systems and obtained satisfactory results proving that co-simulation can be used to solve complex dynamic systems. R.M. Mahamood et al. [2] in their work provided a method to solve kinematic and dynamic problems of Stäubli TX40 robot using co-simulation method. D. Zhang and S. Zhou[3] studied Co-simulation using ADAMS and MATLAB for Active Vibration Control of Flexible beam with Piezoelectric Stack Actuator. The virtual prototype of flexible beam with piezoelectric actuator is created in MSC ADAMS. The controller based on FXLMS algorithm is established in MATLAB. A.M. Abdullahi et al. [4] studied the vibration effects on input tracking control of Flexible manipulator using LQR with Non-collocated PID Controller. Jerzy et al. [5] proposed adaptive control method for single-link flexible manipulator.

## 3 Problem Statement

This paper's objectives are to determine the effects of flexibility on tip position variation of a two-link RR type planar robotic arm as the end-effector (tip) is displaced in a specified vertical motion with a specified payload.

Control methods like (PID and PI) were used to minimize the positional error between the Rigid and Flexible-rigid links robots. The key objective is to develop a control strategy so that the ensuing robot system possesses accuracy of a rigid system and swiftness of a flexible system. Depending on the results obtained, a good control strategy will be implemented for future usage. The dimensions and properties reflected in this paper are given in Table 1.

**Table 1** Link parameters

	Length (mm)	Width (mm)	Depth (mm)	Mass (kg)	Density (kg/mm <sup>3</sup> )
Link 1	300	40	20	2	$7.8 \times 10^{-6}$
Link 2	400	40	20	2.6	$7.8 \times 10^{-6}$
End base	80	20	20	0.5	$7.8 \times 10^{-6}$
Gripper 1	50	10	20	0.045	$7.8 \times 10^{-6}$
Gripper 2	50	10	20	0.045	$7.8 \times 10^{-6}$
Payload	–	–	–	5.1	$7.8 \times 10^{-6}$

## 4 Research Methodology

The solution methodology adopted is as follows. The link dimensions were taken to replicate human arm dimensions. Operating MSC Adams software, a Revolute–Revolute-type two-link manipulator made of rigid and flexible (links and joints) are modeled so that end-effector moves in required vertical path with a payload of 5.1 kg (link mass). Torques (input) were applied at the joints (two revolute) triggering the links angular rotation generating end-effector linear motion. The two-link rigid manipulator’s end-effector is forced to move only in identified vertical path as given in Fig. 2. The angular rotations of both links and end-effector motion are the outputs to be monitored. The end-effector moves for 10 s in 2000 steps. The end-effector motion, joint 1 & 2 angular rotations monitored for same 10 s are taken as reference values.

When the rigid links are substituted by flexible links and joints in RR type manipulator and identical input torques are applied at the both the joints. The resulting position of end-effector positions, joints 1 & 2 angular rotations are measured again for same 10 s and in 2000 steps. Figure 3 displays a flexible link built-in MSC Adams. Flexible links are modeled based on Euler–Bernoulli beams, i.e., the maximum deflection should be less than one-tenth of the total length of the beam. MSC Adams solves this problem using Assumed mode method. Positional error is taken as variation between the two (Rigid–Rigid and Flexible link) end-effector tip positions and joint 1 & 2 angular difference for a time of 10 s in 2000 steps. When one link flexible manipulator is made to rotate with various angular speeds the variation between the assumed mode method using MATLAB and Msc Adams was negligibly small. Therefore, Msc Adams software is used for modeling multiple body flexible systems with ease. From the results obtained in Fig. 4 for only link flexibility, one can deduce that as the time and number of steps are increased the positional error



Fig. 2 Model with vertical constraint

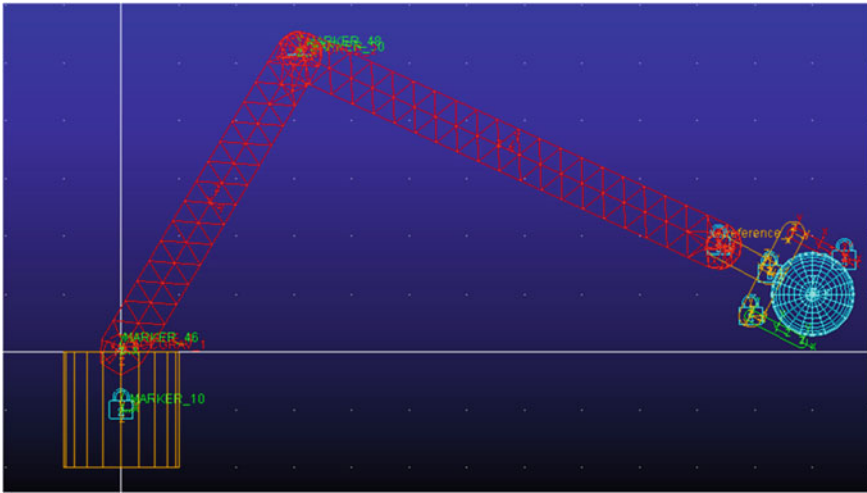


Fig. 3 Building of Flexible model in MSC Adams software

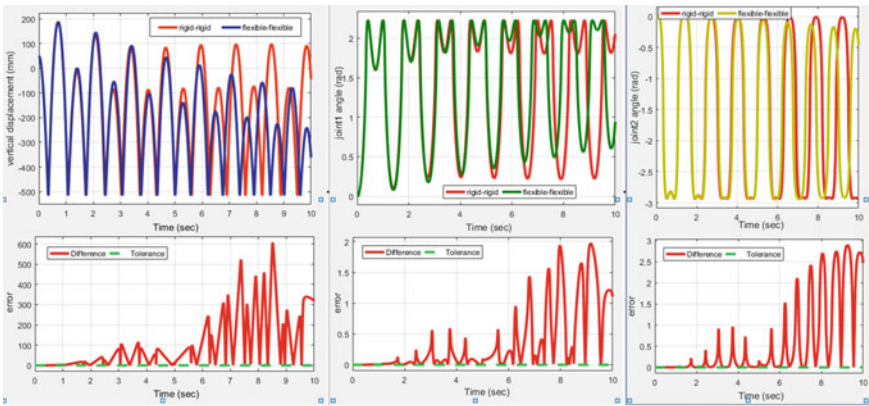


Fig. 4 Errors at end-effector, joint one and two due to link flexibility only

increased. Moreover, the end-effector with a payload of 5.1 kg (mass of two-links) is also affecting the values of positional errors.

When only link flexibility is provided the tip position's maximum error is equal to 561 mm, maximum error at first and second joints is about 1.88 radians and 2.79 radians respectively. The variation of these values with time is provided in Fig. 4.

Figure 5 shows the introduction of clearance of 0.2 mm at the first joint between link one and the base. The joint flexibility because of the clearance gap between the mating parts at the joint (i.e. Journal and the bearing). The clearance at the joints 1 is varied from 0.2 mm to 1 mm in steps of 0.2 mm and 2nd joint is rigid. This variation is shown in Fig. 6. The results show large impact forces are generated at clearance of

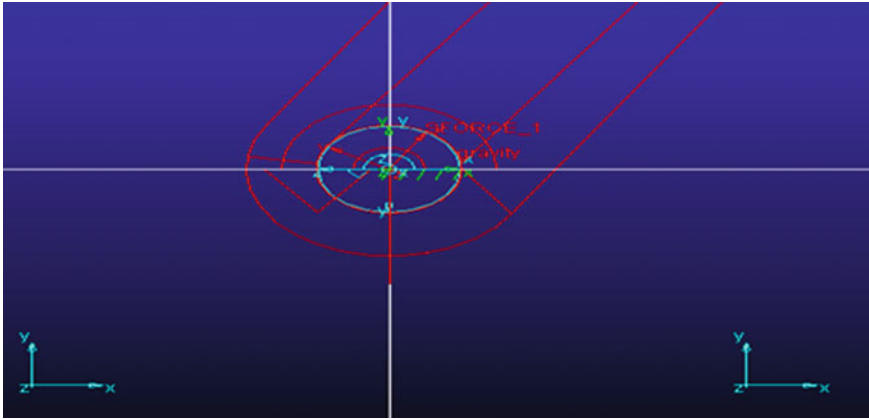


Fig. 5 Creation of clearance of 0.2 mm at joint 1

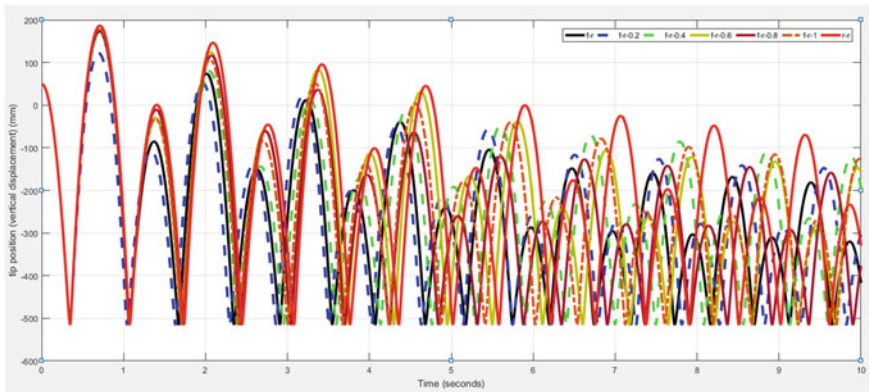


Fig. 6 Variation of end-effector position as clearance is varied from 0.2 mm to 1 mm with flexible links

0.2 mm. If only joint flexibility was present as clearance increased, the impact forces would have increased. However, as the robot system had both link and joint flexibility, and then largest deviation was produced for a clearance of 0.2 mm as shown in Fig. 6. As Hertzian contact forces take into consideration both flexibility and damping of the component into consideration, the results obtained are more realistic compared to other methods. These contacts stresses resulted in higher torques resulting in a bigger and heavier motor/actuator for the same system. Figure 6 shows the results of the variation of three outputs (end-effector motion, angular motions of joint one and two) as the clearance is varied from 0.2 mm to 1 mm. Maximum impact forces were generated for clearance of 0.2 mm. Therefore the same clearance is provided to the flexible link system. Figure 6 shows the error variation for all three outputs.

When both link and joint flexibility are considered, the tip position's maximum error was 574.28 mm; maximum error at first and second joints is about 1.93 radians and 2.82 radians respectively.

To reduce these positional errors for the three outputs (end-effector, joints 1 & 2) to a least value, a control method is required. From the Literature, two conventional controls strategies, i.e., Proportional-Integral Derivate (PID) and Proportional-Integral (PI) control schemes are selected.

### 4.1 Applying Proportional-Integral (PI) Controller at Both Joints

Applying PI and PID control strategies directly in MSC Adams generated problems and getting a solution proved difficult. Therefore, utilizing MSC Adams and MATLAB, a co-simulation method was envisaged. Both flexible and rigid links models were developed in MSC Adams and were imported to MATLAB. Utilizing Simulink, MscAdams model was assimilated in MATLAB environment as displayed in Fig. 7 and as shown in Figs. 6 and 8 block diagrams circuits were generated for both PID & PI control strategies. The tip position's errors the output and the resultant rotations of the joints (angular) are the inputs for the Simulink model. The specific constant values  $K_p$  and  $K_i$  given in Table 2 are chosen such that the magnitudes of all the outputs are minimum resulting in stable behavior. Figure 6 displays the SIMULINK model, so developed in MATLAB. Figure 8 displays the effect of PI controller on the robot system.

When PI control strategy was applied, the tip position's maximum error reduced to 233.84 mm and Average RMS error of 46 mm the at joint 1 & 2 angular position error (maximum) is about 0.98 radians and 1.53 radians, respectively. Figure 7 displays

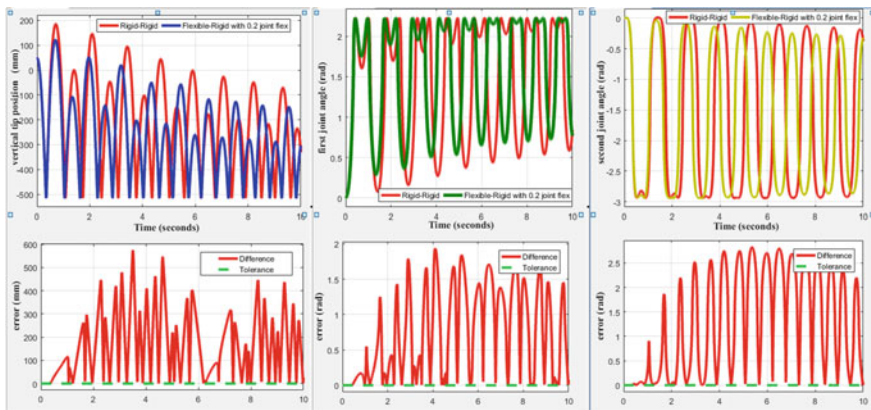


Fig. 7 Errors at end-effector, joint one and two due to both link and joint flexibility

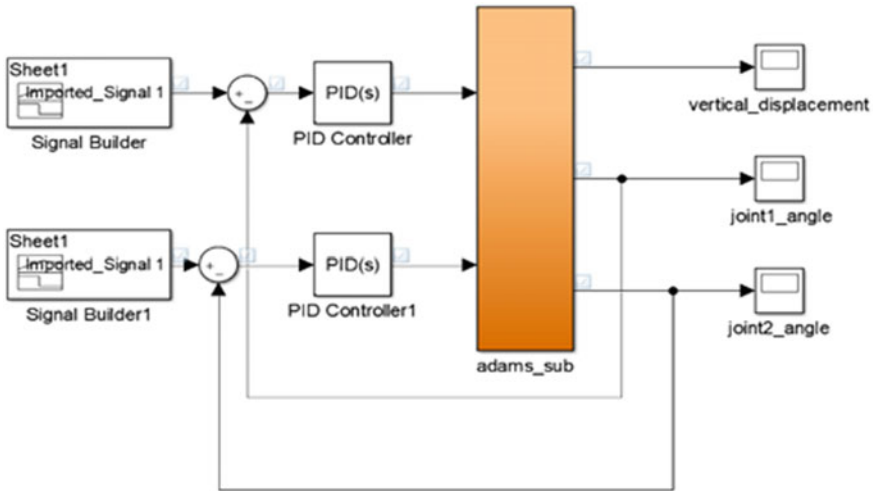


Fig. 8 PID controller Simulink model

Table 2 PI controller constants

	P constant	I constant
Joint 1	2800	2400
Joint 2	200	100

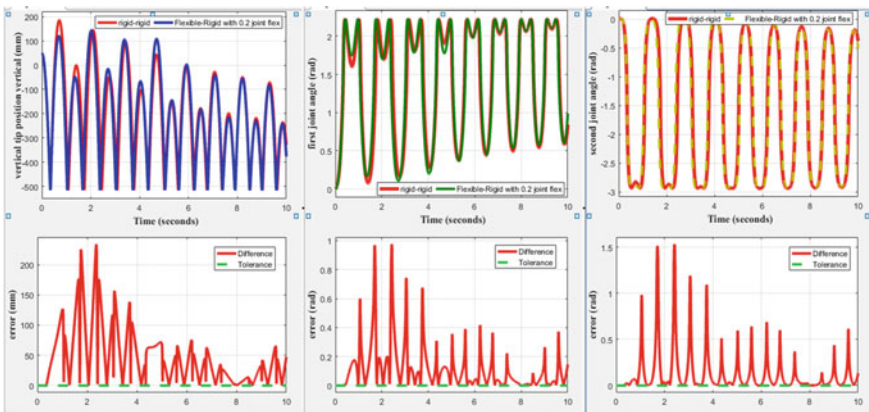


Fig. 9 The errors in tip position, joint 1 & 2 angles with PI controller

these results and one can deduce that these errors are considerably reduced implying that PI control.

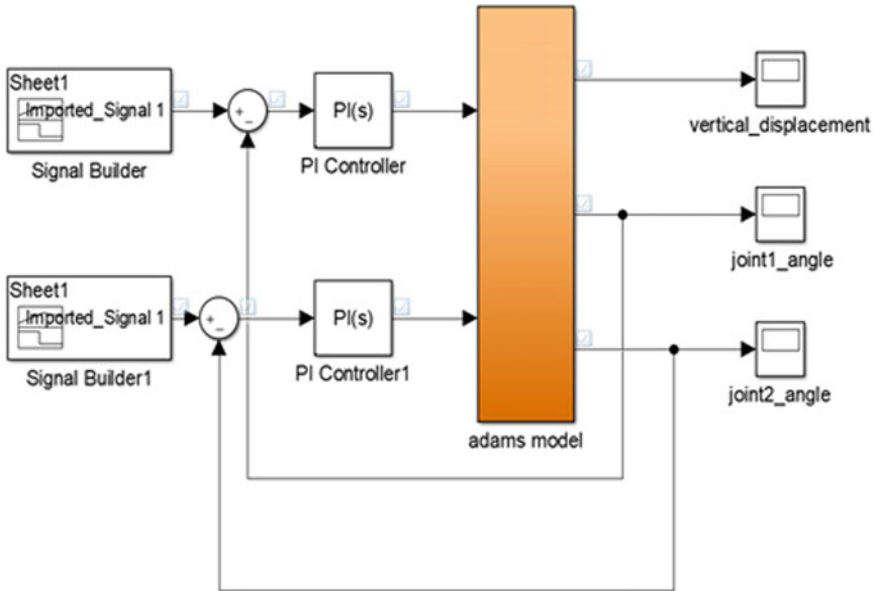


Fig. 10 PID controller Simulink model

### 4.2 Applying Proportional-Integral-Derivative(PID) Controller at the Joints

The constants ( $K_p$ ,  $K_i$ , and  $K_d$ ) in PI and PID controllers are chosen in a trial and error basis (given in Table 3), as the inputs are modified and the outputs are observed as end-effector moves in a vertical path till these error values have become minimum. The tip and joint angles with their corresponding errors in tip position, joint 1 & joint 2 angles with PID controller (Fig. 11).

When PID control strategy was applied, the tip position’s maximum error reduced to 144.53 mm and Average RMS error of 33.2 mm the maximum angular position error at joint 1 & 2 is 0.69 radians and 1.11 radians respectively. Figure 9 shows these results and it can be said that these errors are considerably reduced implying that PID control is satisfactorily countering the effects of flexibility.

Table 3 PID controller constants

	P constant	I constant	D constant	Filter coefficient
Joint 1	2400	1000	1000.2	7.56
Joint 2	200	1000	300	4



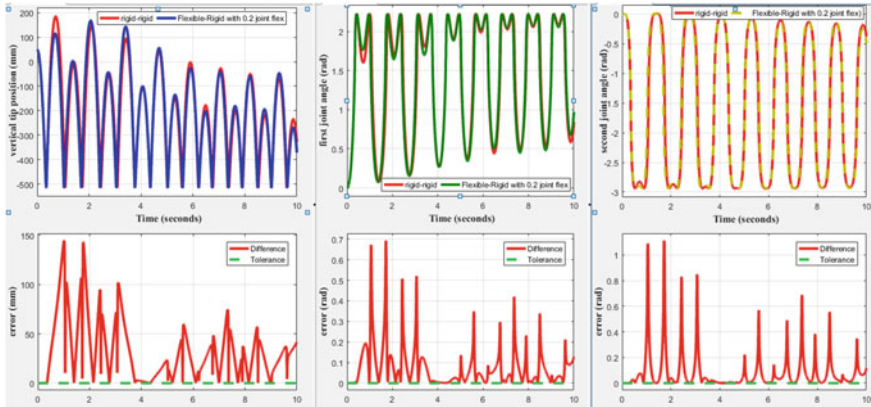


Fig. 11 The error in tip position, joint 1 & joint 2 angles with PID controller

### 4.3 The Effect of the Controllers on the Input and Output Response

Figure 12 provides the effect of PID and PI control strategies to control and reduce the tip position's error and revolute joints 1 & 2 errors no control strategy is adopted. When PI control is adopted the maximum positional error reduced by 59.2 and 74.8% reduction using PID control. The angular error reduced by 49.2% at joint 1 and 45.7% at joint 2 using PI control. When PID control is used, the error at joint 1 reduced by 64.2 and 60.6% at joint 2. It is obvious from Fig. 10 that the PID controller performs

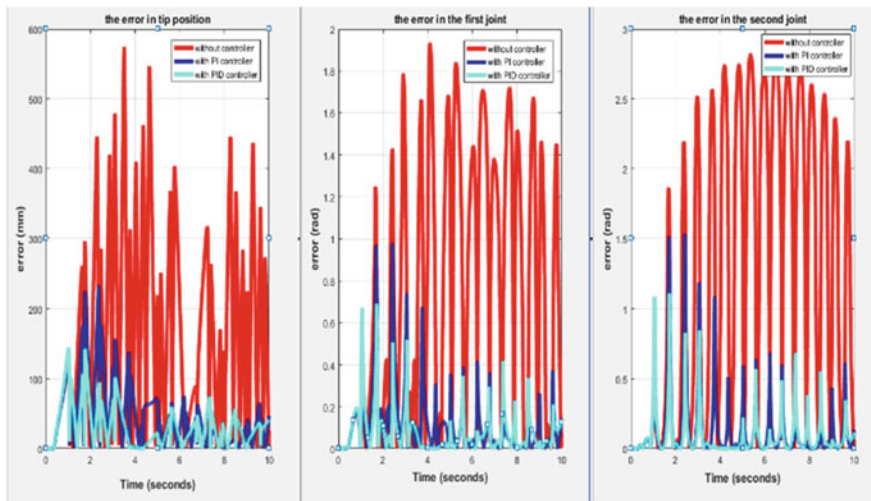


Fig. 12 Effects of PI & PID control strategies



better than PI control for the given conditions and therefore it should be chosen to reduce error and follow the desired path.

## 5 Results and Discussions

When no control strategy was adopted to control link flexibility, the tip position's maximum error was equal to 561 mm and with average RMS error of 158.6 mm. The joints 1 & 2 maximum positional error is 1.88 radians and 2.79 radians respectively. Figure 4 provides these results and it can be deduced that these errors are very large and the flexibility has substantial effect on the tip position's accuracy. By including the joints clearances (0.2 mm clearance at each joint) along with link flexibility we can observe that the tip position's error increased to 574.28 and with average RMS error of 171.2 mm. The angular position error at joint 1 & 2 increased to 1.93 radians and 2.82 radians respectively. Figure 7 provides these results and it can be said, that the joint clearances will affect the tip position increasing the error.

To reduce these errors, two control strategies were used to determine tip position error and see that end-effector follows the specific vertical path.

## 6 Conclusions

A two-link rigid and flexible manipulator has been successfully co-simulated in Adams software and MATLAB. From the model created in ADAMS it is found that link flexibility significantly affects the system behavior. The tip position, first joint angle and second joint angle values are compared by using MATLAB and two types of controllers were (i.e., PID and PI) applied. From the above study, it can be concluded that when joint flexibility (i.e., 0.2 mm clearance) is added to already flexible links the end-effector deflection increased by 2.31%. Whereas when PI control is adopted the maximum positional error reduced by 59 and 74.8% reduction using PID control. The angular error reduced by 49% at joint 1 and 46% at joint 2 using PI control. When PID control is used, the error at joint 1 reduced by 65 and 61% at joint 2. It can be seen from Fig. 12 that PID controller performs better than PI control for the given conditions and therefore it should be chosen to reduce error and follow the desired path.

**Acknowledgements** The authors would like to thank University Grants Commission, South Eastern Region (SERO), Hyderabad for sponsoring this project, as this work is being carried out from UGC Sanctioned Minor Research Project No. F-MRP-6758/16 (SERO/UGC) dated June 30, 2017.

## References

1. Moallem M (1996) Control and design of flexible-link manipulators. Presented in partial fulfillment of the requirements for the degree of doctor of philosophy at Concordia University, Montreal, Quebec, Canada, December
2. Mahamood RM, Aweda JO, Ajao KR, Popoola OT, Odusote JK (2015) PID controller design for two link flexible manipulator. LAUTECH J Eng Technol 9(2):17–22
3. Zhang D, Zhou S (2006) Dynamic analysis of flexible-link and flexible-joint robots. Appl Math Mech 27(5):695–704
4. Ahmad MA, Mohamed Z (2010) Modelling and simulation of vibration and input tracking control of a single-link flexible manipulator. Pertanika J Sci Technol 18(1):61–76
5. Abdullahi AM, Mohamed Z, Muhammad M, Bature AA (2013) Vibration and tip deflection control of a single-link flexible manipulator. Int J Instrum Control Syst (IJICS) 3(4), 17–27 (October)

# Design of Plastic Bottle Shredding Machine and Computational Finite Element Analysis of Shaft in the Shredder



Aluka Dheeraj Reddy, G. V. Niharika and G. Srinivas Sharma

**Abstract** There are many machines available in the market which recycle plastic waste (plastic bottles), but this machine is for small-scale, portable and domestic purpose. The cost of this machine is very low compared to the machines available outside. This machine is designed to cut the large solid material into small pieces. This paper throws light on the mechanism used in the machine and primarily about the analysis (manual and computational) of the shaft, on which the cutting blades are mounted.

**Keywords** Plastic bottle · Shredding · Polyethylene · Shaft · Natural frequency · Finite element analysis

## 1 Introduction

The global problem today is plastic. The pollution caused by plastic effects environment (land, air, water), wildlife, Humans, and a plethora of life cycles on the earth. Plastic cannot be decomposed and the recycled products are much more dangerous to mankind. Plastic is classified mainly into two types, (1) LDPE-Low Density Polyethylene and (2) HDPE-High Density Polyethylene, although there are other forms of plastic such as PET (Polyethylene Terephthalate), PVC (Polyvinyl Chloride), and PP (Poly Propylene).

The plastic bottle is made up of PET. It takes about one-fourth of a bottle of oil that is required to produce a single water bottle, 90% of the bottled water's cost comes from producing the bottle itself. It consumes 17 million barrels of oil to make one year's supply of water bottles, that much oil can be used as fuel for 1.3 million

---

A. D. Reddy · G. V. Niharika · G. S. Sharma (✉)  
Department of Mechanical Engineering, MVSR Engineering College, Hyderabad, India  
e-mail: [sharma.gangaraju@gmail.com](mailto:sharma.gangaraju@gmail.com)

A. D. Reddy  
e-mail: [dheerajreddya@gmail.com](mailto:dheerajreddya@gmail.com)

G. V. Niharika  
e-mail: [gvnih@gmail.com](mailto:gvnih@gmail.com)

© Springer Nature Singapore Pte Ltd. 2020  
G. S. V. L. Narasimham et al. (eds.), *Recent Trends in Mechanical Engineering*,  
Lecture Notes in Mechanical Engineering,  
[https://doi.org/10.1007/978-981-15-1124-0\\_54](https://doi.org/10.1007/978-981-15-1124-0_54)

cars for about one year long or power 1,90,000 houses. With the surge in awareness among people about the recycling of plastics, the demand for shredding machine also rose significantly. There are lots of industrial firms which are dedicated to utilize the recycle management concept. Recycling is more sophisticated than we think. In the whole world, millions of plastic bottles are used every day, but not all are recycled. They are being dumped in the land fields or empty lands, which exacerbate the ground fertility.

This project is about the design of plastic bottle shredding machine and its fabrication. This project helps not only in reducing the collection, packaging, transportation of used plastic but also the labor cost, as this machine itself is portable and can be used anywhere (Domestic purpose). Also, it is very easy to maneuver and does not require any skilled labor for its safe operation.

## ***1.1 Literature Review***

R. Darshan and S. Gururaja [1] have explained in detail the problems involved in the transportation of plastic and importance of its size reduction. They have designed a portable plastic crushing machine for reducing the volume of plastic and further for its recycling. They firmly believe crushing of used water bottles will also ensure that the bottles are no longer used beyond their shelf life and help reduce the space consumed in trucks so that more plastic wastes can be transported without overloading the vehicle, which helps in reducing accidents even.

S. Nithyananth, Libin Samuel, Nithin Mathew, S. Suraj [2] have designed an agricultural waste shredder machine, whose role is to reduce the volume of agro-waste available in the fields and to convert it thereafter to useful fertilizers instead of just decomposing it. They have designed the shredder equipment such that it is attached to a farm tractor, which ploughs the farmlands.

E. Metin, A. Erozturk, C. Neyim [3] have made clear from their detailed survey the problems of plastic recycling in countries like Turkey. They have given a detailed report on solid waste management practices like collection of waste, their restoration and disposal, etc. with their respective costs. They have also included the statistics of the country's household waste generation per capita, population, and municipalities that play a vital role in the survey.

## **2 Methodology**

### ***2.1 Evolution of Shredders***

**First-generation shredders:** Power transmission is through belt drive in order to reduce the noise.

**Table 1** Materials of the components used

Components	Material	Density
Shaft blades washers	AISI 1018 Steel	7870 kg/m <sup>3</sup>
Hopper lid	Aluminum	2700 kg/m <sup>3</sup>

**Table 2** Diameter of the shaft

Formula	$N = 1000$ rpm	$N = 1440$ rpm
$\frac{T_{eq}}{J} = \frac{T_s}{R}$	$d = 29$ mm	$d = 26$ mm
$\frac{M_{eq}}{I} = \frac{\sigma_b}{y}$	$d = 23$ mm	$d = 20.8$ mm
$\frac{T_{eq}}{J} = \frac{G\theta}{l}$	$d = 26$ mm	$d = 23$ mm

**Second-generation shredders:** Gears employed here are made of plastic, which makes the shredding process strenuous for the machine, which results in a very less efficiency.

**Third-generation shredders:** Power transmission here employs a metal sprocket to do the job which has perks like low noise, low power loss and propagates efficient cutting.

**Fourth-generation shredders:** The drive mechanism employs a metal gear in order to increase the efficiency of power transmission; however, the effect of friction and the metal gear sound here is inevitable.

**Fifth-generation shredders:** It employs a completely different method called the Diamond snug movement, which is a fully automatic CNC operation; transmission installation accuracy is very high. (Alloy steel materials are mostly used for the manufacture of machine components here.)

**Sixth-generation shredders (modern):** This latest model grinder has a capacity to even break compact disks and floppies. The embedded buttons panel here ensures the function of forwarding, rewind, and stop, as in the modern world we pay more attention to care for the safety and quality of life.

Our shredder is a sixth-generation model.

## 2.2 Materials

See Table 1.

## 2.3 Machine Components

**Main shaft:** The main shaft has a circular cross section on which it holds the blades and washers without slipping, with the help of a key. It is 30 mm in diameter and is 350 mm long, the effective length is 250 mm, equally distributed on both sides from

the center of the shaft i.e. it is a simply supported type of beam. The diameter of the shaft was calculated considering the twisting, bending and shear forces acting on it.

**Coupling:** There is a Rubber Coupling used here to transmit the power with minimum loss and mainly to absorb the shocks produced during the shredding process.

**Motor:** A Motor of power 1hp (0.746 kW) is likely to be used for satisfying the purpose of the force required for shredding the bottles (Avg. force required for shredding a polyethylene terephthalate-PET bottle is 20 N).

**Gear box:** A Reduction gear box is used here in order to increase the torque (decrease the speed) produced by motor for efficient shredding of plastic bottles, which is placed in between the motor and main shaft in the driveline.

**Cutting blades:** The cutting blades were designed with three sharp corners on each blade to shred the bottles with maximum efficiency and with a thickness of 10 mm to resist the cutting forces acting upon them, and the size of the shredded plastic depends upon the density (number) of the blades mounted on the shaft.

**Washers:** There are washers of same thickness being used, alternate to each blade on the shaft assembly in order to maintain the clearance for the counter shaft-blades, for the smooth running of shredder.

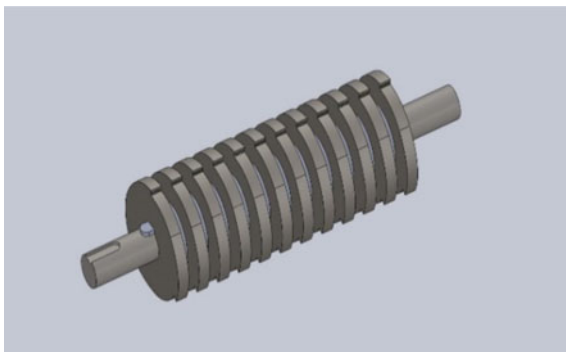
**Hopper:** A hopper is used in the system to easily drop the bottles into the machine; it prevents the bottles from chipping out and guides them directly into the blades. As it is mandatory for any cutting device to operate safely.

**Lid Mechanism:** There is also a Lid mechanism used, in which there is a lid placed on top of the hopper, and the shredder operates only when the lid remains closed. This further increases the safety of the system.

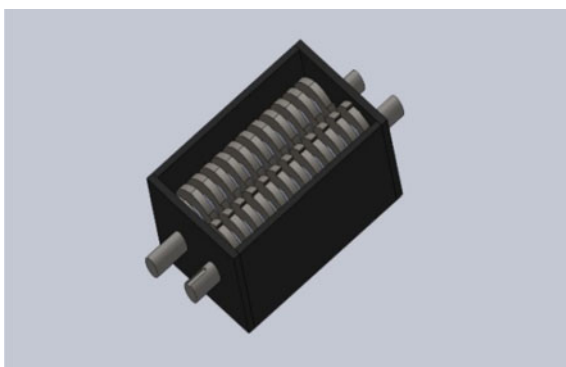
### 3 Working Principle

Our shredder works on the principle of power transmission directly, through a coupling. The machine is powered using a 1HP motor whose speed is reduced from 1440 rpm from 1000 rpm with the aid of a reduction gearbox. The system has two shafts which are mounted at an offset distance. Each shaft has 12 blades and 12 washers mounted alternately. The power is transmitted to one shaft initially, and then to the other shaft with the help of a worm gear arrangement, which makes them rotate in the opposite directions. This shaft assembly (Fig. 1) is enclosed in a cutting chamber (Fig. 2), on top of which a hopper with a lid is attached (Figs. 3 and 4).

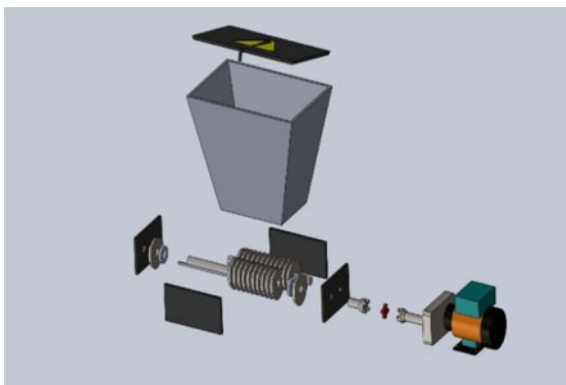
**Fig. 1** Shaft assembly

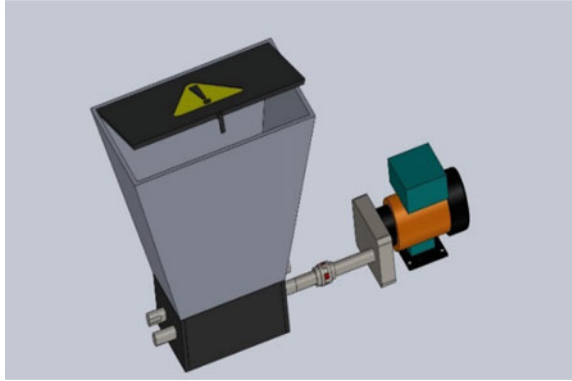


**Fig. 2** Cutting chamber assembly



**Fig. 3** Exploded view of the final assembly



**Fig. 4** Assembled view

## 4 Design Calculations and Construction

### 4.1 Diameter of the Shaft Is Calculated Using

*Twisting Moment:*

$$\frac{T_{eq}}{J} = \frac{T_s}{R}$$

$$I = \frac{\pi}{32}d^4$$

$$J = \frac{\pi}{32}d^4$$

$$T_{eq} = \frac{\pi}{16}d^3T_s$$

$$T_{eq} = \frac{\pi}{16}d^3T_3$$

$$T_{eq} = \sqrt{T^2 + M^2}$$

*Bending Moment:*

$$\frac{M_{eq}}{I} = \frac{\sigma_b}{y}$$

$$M_{eq} = \frac{\pi}{32}d^3\sigma_b$$

$$M_{eq} = \frac{1}{2}\sqrt{T^2 + M^2} + M^2$$



*Shear Force:*

$$\frac{T_{eq}}{J} = \frac{G\theta}{l}$$

$$T_{eq} = \frac{\pi}{32} d^4 \frac{G\theta}{l}$$

Hence as the largest diameter is to be considered, 30 mm is taken as the diameter of the shaft.

## 4.2 Deflection of Beam

(Simply Supported Beam with Uniformly Distributed Load)

$$\delta = 5WL^4/384EI$$

The force required to shred a usual plastic water bottle (100 micron) is about 20 N, but it is taken as 25 N depending upon the safety criterion. The length of the shaft is taken as 35 mm (as it is a small-scale shredding machine), Young's Modulus for the material is 210GPa and the polar moment of inertia is found out from the formula (for a solid circular shaft)

$$I = \pi d^2/64$$

The deflection of the beam is then found to be (1) 5.96E-07 m.

## 4.3 Frequency

**Case 1:** From deflection

$$\omega = (g/\delta)^{1/2} \quad f = \omega/2\pi$$

From here the frequency at the deflection is found to be (2) 645.48 Hz.

**Case 2:** Natural frequency of the shaft (simply supported) is calculated from the formula,

$$f = (k/2\pi) * (EI/\rho AL^4)^{1/2}$$

**Table 3** The natural frequency of shaft for different modes

Modes	<i>K</i> value	Frequency (Hz)
1	9.87	70.5
2	39.5	282.2
3	88.8	6314.4
4	158	1128.8
5	247	1764.68

**Table 4** The harmonic frequency of the shaft under load

Modes	<i>K</i> value	Frequency (Hz)
1	9.87	21.69
2	39.5	86.80
3	88.8	195.17
4	158	347.27
5	247	542.81

The density of the material is 7870 kg/m<sup>3</sup> from Table 1 and the area of the shaft is found to be 0.0344 m<sup>2</sup>. The values of ‘*k*’ for different modes in a simply supported beam is given by,

Mode 1	<i>k</i> = 9.87
Mode 2	<i>k</i> = 39.5
Mode 3	<i>k</i> = 88.8
Mode 4	<i>k</i> = 158
Mode 5	<i>k</i> = 247

See Table 3.

**Case 3:** Frequency of the shaft under UDL (Harmonic frequency) is found using the formula

$$f = (k/2\pi) * (EI/ML^3)^{1/2}$$

where ‘*M*’ being the combined value of the UDL and self-weight of the beam, the frequency of beam under load is and the rest of the values such as Max Stress and Bending Moment are taken from ANSYS as the above results have been validated theoretically.

## 5 Results and Discussions

From the results the maximum diameter arrived for the shaft is 29 mm from Table 2, which is rounded to 30 mm for the safety and availability factors. Given below are the analysis results of the shaft for deflection, stress, bending moment, harmonic and modal analysis.

### 5.1 Deflection of the Shaft

Hence, it is nearly the same value of deflection as calculated theoretically *i.e.*  $5.96E-07$  m (Fig. 5).

### 5.2 Stress in the Shaft

See Fig. 6.

### 5.3 Reactions at Supports

The following *X, Y, Z* solutions are in the Global Coordinate System (Table 5).

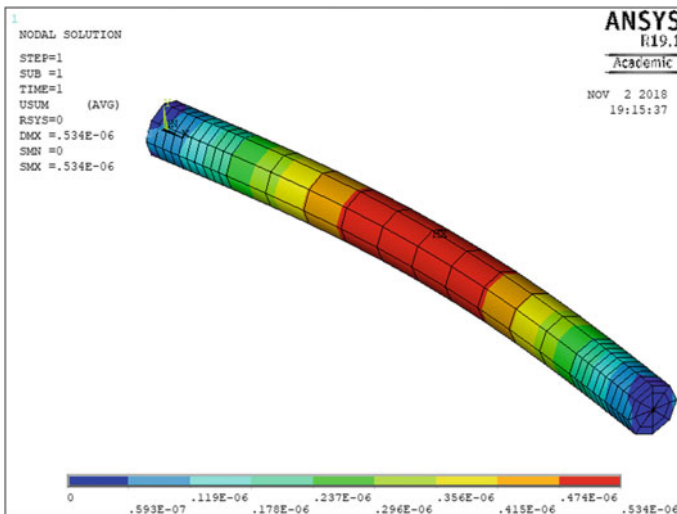
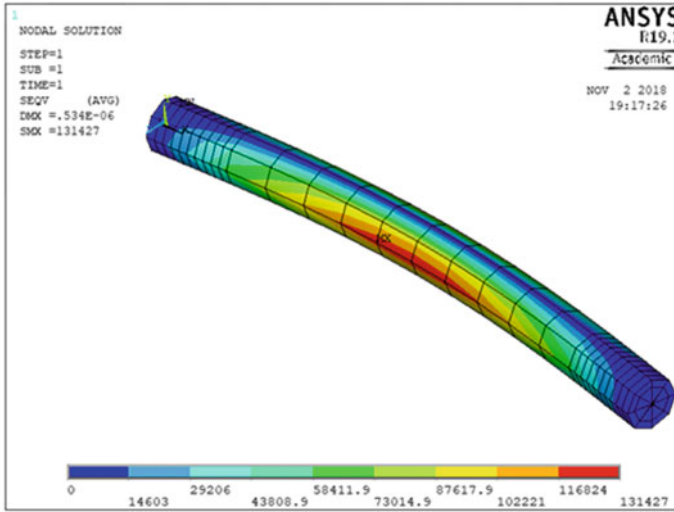


Fig. 5 Deflection =  $5.34E-07$  m



**Fig. 6** Max stress = 131427 N/m<sup>2</sup>

**Table 5** The reactions at joints

Node	FX	FY	FZ	MX	MY	MZ
1	0	0	3.125	-0.227E-017	-	-
22	0	0	3.125	-0.227E-017	-	-
Total values	0	0	6.250	0.455E-017	-	-

### 5.4 Bending Moment Diagram

See Fig. 7.

### 5.5 Maximum Bending Stress

See Fig. 8.

### 5.6 Modal Analysis for the Natural Frequency of the Beam

This is the same frequency as calculated in Case 1 i.e. 645.48 Hz (Figs. 9 and 10).

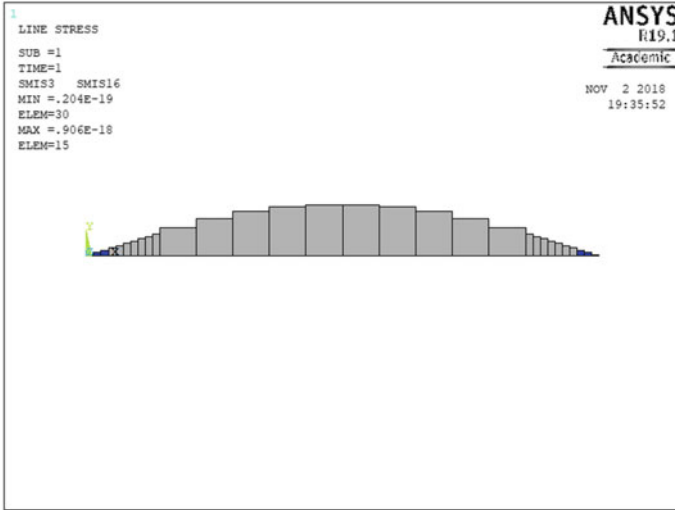


Fig. 7 Max. bending moment =  $0.906E-18$  Nm

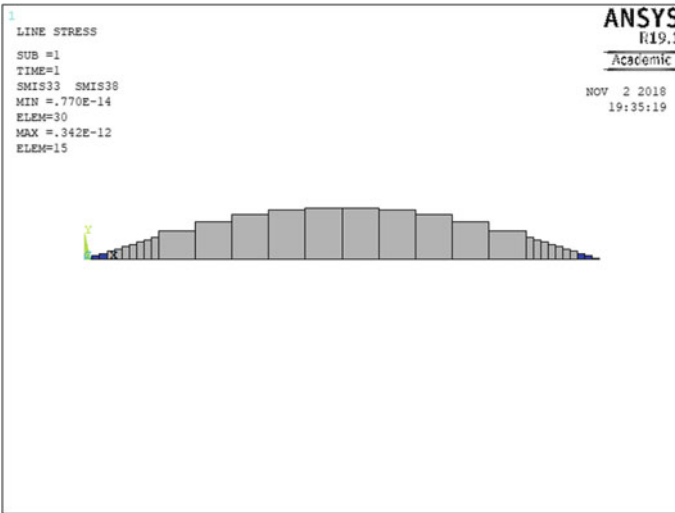


Fig. 8 Max. bending stress =  $0.342E-12$  N/m<sup>2</sup>

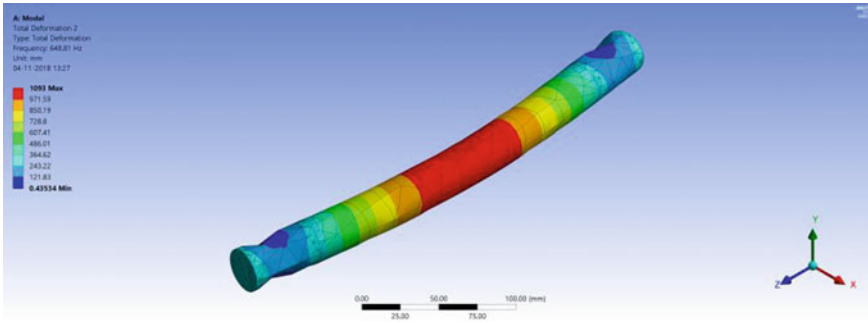


Fig. 9 Mode 1 = 648.81 Hz

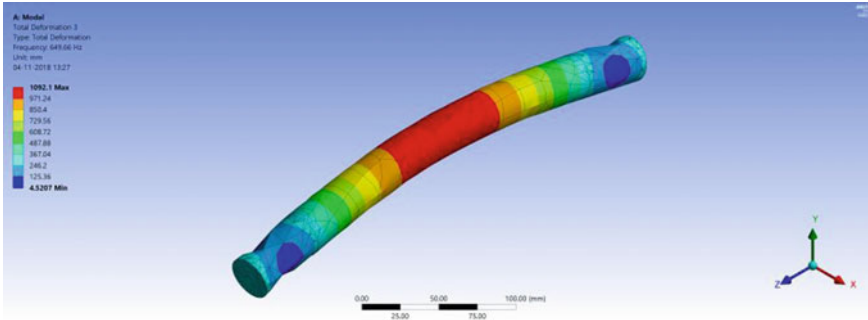


Fig. 10 Mode 2 = 649.66 Hz

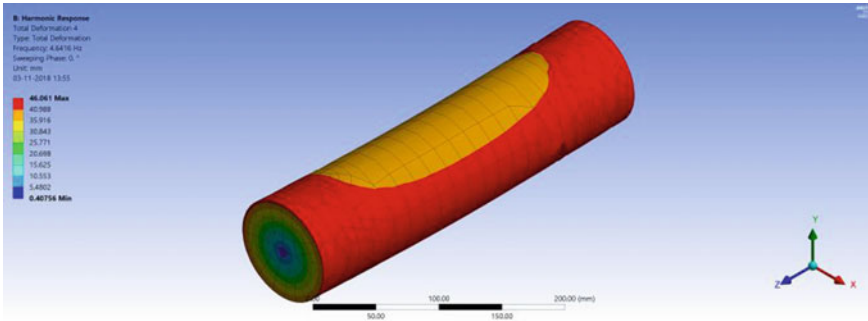


Fig. 11 Mode 1 = 4.641 Hz

### 5.7 Harmonic Analysis for the Frequency of the Shaft with Uniformly Distributed Load

Hence, the Harmonic Frequencies of the shaft for different modes in the range of 1 to 1000 Hz from Fig. 11, 12, 13, 14, 15,16, 17, and 18 are same as the frequencies

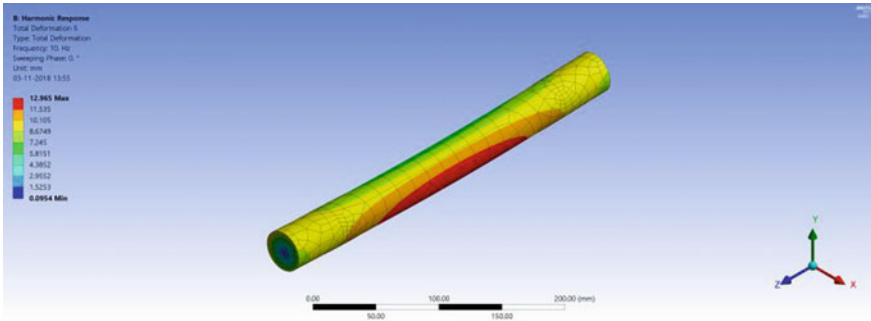


Fig. 12 Mode 2 = 10.0 Hz

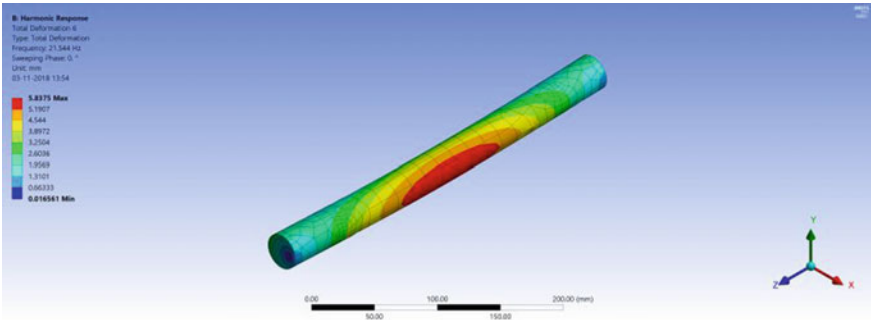


Fig. 13 Mode 3 = 21.544 Hz

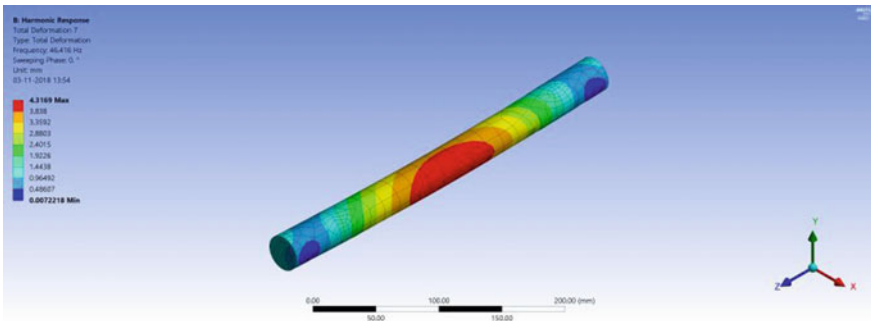


Fig. 14 Mode 4 = 46.416 Hz

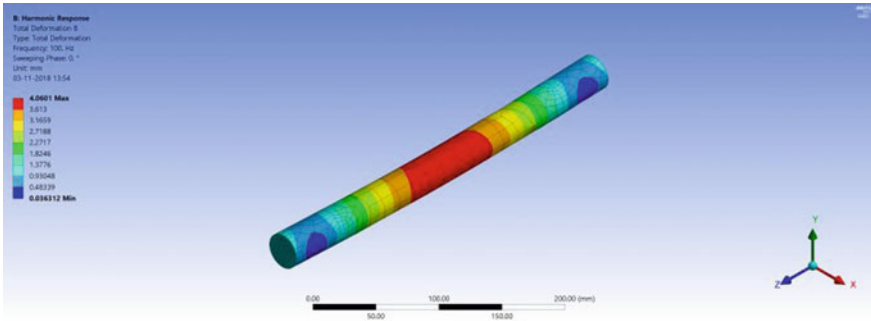


Fig. 15 Mode 5 = 100.0 Hz

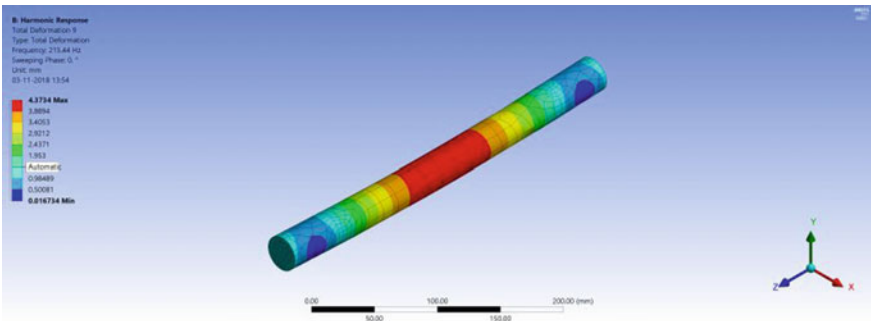


Fig. 16 Mode 6 = 215.44 Hz

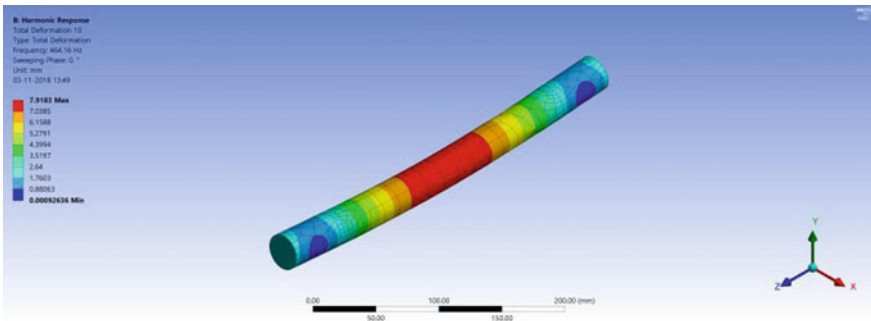


Fig. 17 Mode 7 = 464.16 Hz



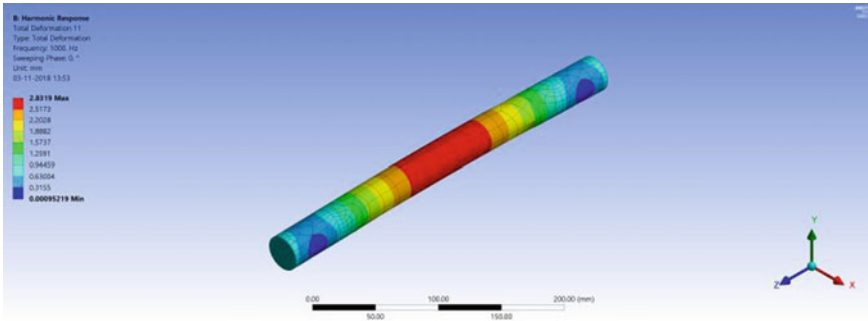


Fig. 18 Mode 8 = 1000 Hz

obtained in Table 4.

## 6 Conclusion

This plastic shredding machine is unique, compact, and portable. The functioning of the machine is simple and easy, to be used by any unskilled personnel. This Low cost and Low maintenance machine are specially designed for plastic recycling. The extension to this is, plastic bottles when shredded to small pieces or powder can be used in making of parking tiles, floating bodies like boats or when mixed with biodegradable powder, it can be decomposed which does not affect the ground fertility. This machine is one best way to recycle and avoid the production of new plastic, to minimize plastic effects on environment.

## References

1. Darshan R, Gururaja S (2017) Design and fabrication of crusher machine for plastic wastes. *Int J Mech Prod Eng* 5(10):55–58
2. Nithyananth S, Samuel L, Mathew N, Suraj S (2014) Design of waste shredder machine. *Int J Eng Res Appl* 4(3):487–491
3. Metin E, Eröztürk A, Neyim C (2003) Solid waste management practices and review of recovery and recycling operations in Turkey. *Waste Manag* 23(5):425–432

# Effect of Temperature on Stress Concentration Factor



Jajula Satish, Shubhashis Sanyal and Shubhankar Bhowmick

**Abstract** In this paper, an isotropic rectangular plate of finite width with a central circular hole has been considered. Plane stress finite element study under uniaxial, uniformly distributed, constant tensile loading, and temperature gradient has been carried out separately and validated. The combined study has been carried out by maintaining the temperature difference between two sides of the plate. By doing so it has been observed that the maximum stress occurring at the discontinuity getting reduced up to some optimum temperature (the temperature at which von Mises stress getting increased) after that it is crossing the maximum value of stress that had occurred in case of structural stress. As a result, the maximum reduction in SCF obtained is 13%. The optimum temperature value is different for different axial loading values.

**Keywords** Plate with hole · Coupled loading · Stress concentration factor · Mitigation · SCF · Temperature

## 1 Introduction

The stress concentration is a major factor when it comes to the case of geometries having discontinuities. There are many research articles available, which discuss the different ways to mitigate the stress at discontinuity and the reduction of stress concentration factor (SCF). P.E. Erikson et al. presented an experimentation results, which shows that the stress concentration factor can be reduced by 13–21% of the initial value as in case of an infinite width plate subjected to axial loading by making auxiliary holes on both the sides of initial hole [1]. T.W. Ulrich et al. also discussed

---

J. Satish · S. Sanyal · S. Bhowmick (✉)  
Department of Mechanical Engineering, NIT Raipur, Raipur, Chhattisgarh, India  
e-mail: [sbhowmick.mech@nitrr.ac.in](mailto:sbhowmick.mech@nitrr.ac.in)

J. Satish  
e-mail: [jajulasatish08@gmail.com](mailto:jajulasatish08@gmail.com)

S. Sanyal  
e-mail: [ssanyal.mech@nitrr.ac.in](mailto:ssanyal.mech@nitrr.ac.in)

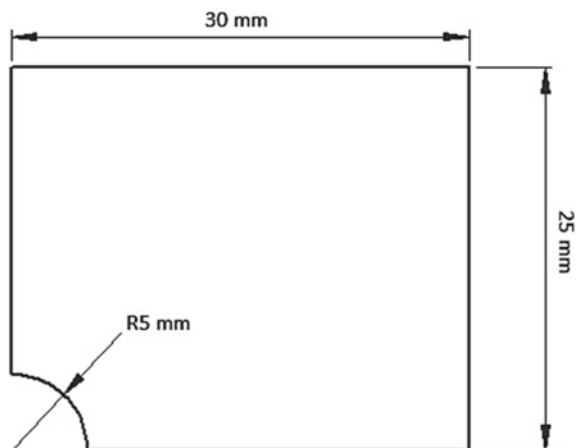
© Springer Nature Singapore Pte Ltd. 2020  
G. S. V. L. Narasimham et al. (eds.), *Recent Trends in Mechanical Engineering*,  
Lecture Notes in Mechanical Engineering,  
[https://doi.org/10.1007/978-981-15-1124-0\\_55](https://doi.org/10.1007/978-981-15-1124-0_55)

the reduction of stress concentration by making auxiliary holes near the initial hole. They had done that analysis by boundary element method in which they divided the boundary of the geometry into finite parts and they converted 2D to 1D [2]. U.C. Jindal stated that by introducing the auxiliary holes of same diameter as the original hole along the axial direction or perpendicular to the axial direction, the maximum SCF reduced by 22% [3]. Like the same way Jain N.K has given a method in which the author made four coaxial holes on either side of the hole so as to achieve the maximum reduction of SCF by 24.4% in an isotropic plate and 31% in orthotropic plate [4]. The isotropic plate has been made as a composite material by G.S. Giare et al. to reduce SCF near the hole. In the original plate made up of Aluminum, the SCF was 2.72. The SCF of new composite material is one (1) [5]. The different attempts to mitigate the SCF near the singularity have been discussed in a review article by S. Nagpal et al. [6]. In all the above-discussed cases, the maximum stress (as well as SCF) has been mitigated by modifying the geometry or changing/improving the properties of the material. But in all the discussed cases, particularly in case of finite width plates it is not an easy task to achieve the required geometrical changes. So as to overcome that difficulties, this paper will be discussing the mitigation of stresses (SCF as well) at the discontinuity/hole/singularity by introducing the thermal field near the hole.

## 2 Methodology

Since the plate is symmetric about both the axes x and y, only a quarter plate was modeled and simulated in ANSYS. The material considered was steel. Because of the symmetric nature of the plate only quarter part was considered. The geometry is shown in Fig. 1.

**Fig. 1** 2D geometry of quarter plate



Initially, axial mechanical loading condition has been considered. A plane eight-noded quadrilateral element (PLANE 183) was considered because it is suitable for both the thermal and mechanical loading conditions. The geometry has been meshed finely (Number of Elements created were 1720) as shown in Fig. 2. The lines on which our concentration lies and where we apply the boundary conditions, those were meshed very finely. Boundary conditions have been assigned such that the quarter plate behaves as a full geometry, i.e., a rectangular plate contained a circular hole at mid-point of its cross section. A constant axial load has been applied on the right side of the geometry as shown in Fig. 3. The force has been uniformly distributed among all the nodes of line. Results were obtained using General Postprocessor.

Separate thermal loading has been applied on the same geometry. The ambient temperature was considered as 30 °C and it is represented with  $T_2$ ; the temperature on the sides which are located adjacent to the hole is given as 35 °C represented as  $T_1$  as shown in Fig. 4. The temperature distribution is observed and the same has

**Fig. 2** Meshing at vicinity of hole

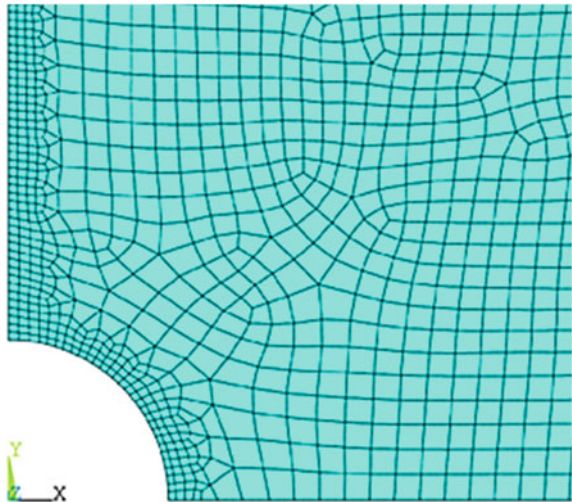


**Fig. 3** Structural loading and boundary conditions

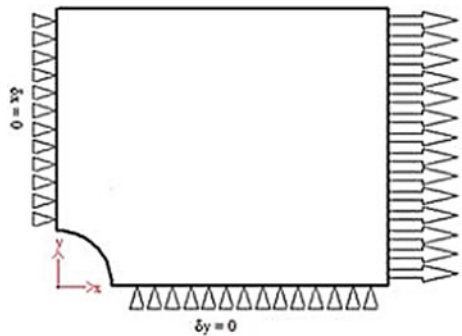
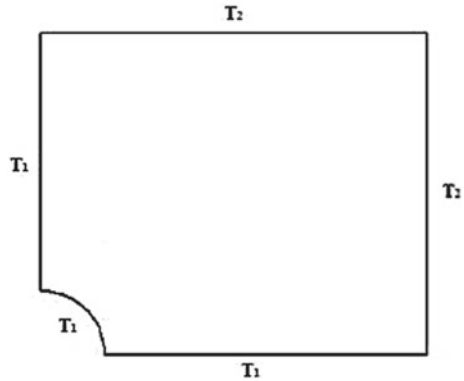


**Fig. 4** Thermal loading



been done for different temperature values of  $T_1$  starting from 35 °C to 80 °C in a 5 °C step. The corresponding temperature distributions were validated [7].

**Coupled Loading.** Initially, the thermal loading has been applied as mentioned above then FE analysis has been done. A file with.rth extension has automatically been created which will be used for structural analysis. Along with the boundary conditions of structural, the rth file has also been imported. The problem has been solved and the results were observed by using ANSYS postprocessor. This process has been repeated by changing the temperature from 35 °C to 80 °C with an interval of 5 °C for the same structural load of 1.95 kN. The results are discussed in the following paragraphs. The same analysis has been done for different axial load values from 1 kN to 2.5 kN at regular intervals of load.

Mathematical equations involved in ANSYS while solving the problem have been mentioned as follows [8]. This involves the conservation of energy.

i.e. Total potential energy ( $P$ ) = Internal Strain Energy ( $U$ )—Potential of an external force ( $E$ )

The effects of initial strain and body forces are neglected, then the strain energy will be

$$U = \int_{vol} \{\varepsilon\}^T [D] \{\varepsilon\} dV \tag{1}$$

$E$  is  $\{f\}^T \{u\}$ ,  $\{f\}$  is an equivalent applied nodal force vector and  $\{u\}$  is nodal displacement vector. In Eq. (1),  $\{\varepsilon\}$  is the strain vector at a point and  $[D]$  is the matrix for constitutive relationships. The strain vector can be defined as

$$\{\varepsilon\} = [B] \{u\} \tag{2}$$

$[B]$  is the matrix of compatibility relations. By substituting Eq. (2) in Eq. (1),

$$U = \{u\}^T \left( \frac{1}{2} \int_{vol} [B]^T [D] [B] dV \right) \{u\} \quad (3)$$

By applying the Minimum Potential Energy Principle,

$$\frac{\partial P}{\partial \{u\}} = 0 \quad (4)$$

By solving the above differential equation using Equations from Eq. (1) to Eq. (3) and substituting in Eq. (4), the following Eq. (5) can be obtained.

$$\left[ \int_{vol} [B]^T [D] [B] dV \right] \{u\} = \{f\} \quad (5)$$

$$\text{Let } [k] = \left[ \int_{vol} [B]^T [D] [B] dV \right]$$

where  $[k]$  is an elemental stiffness matrix in local coordinate system.

For each and every element, ANSYS calculates stiffness matrix and combines all the elemental stiffness matrices according to node numbers to get global stiffness matrix  $[K]$ . For the coupled loading case, the global stiffness matrix for axial loading will be calculated and the same procedure will be followed for thermal loading as well. Both the matrices will be superposed so as to get the final result.

### 3 Results and Discussions

FE Analysis has been done and the results are presented for isotropic finite width plate with central circular hole under in-plane static loading, thermal loading as well as the structural and thermal loading (coupled loading).

**Structural Analysis:** The maximum stress occurred one of the nodes which are located on the circumference of hole and that node is being termed as Node-5 throughout our discussion and our main focus lies on the same node. The stress distribution as in case of axial loading condition is shown in Fig. 5. A detailed view of Node-5 has also been shown in Fig. 5. In case of only mechanical axial loading, the SCF obtained as 2.6 which has been matched with the data given by Bhandari [9, 10].

**Thermal Analysis:** The temperature distribution at all the nodes located on the circumference of the circular hole is validated with the analytical solutions [7].

**Coupled Analysis:** Thermal load has been applied followed by the structural load by choosing suitable elements. As the thermal field has been applied, the maximum stress occurring at Node-5 was decreased and as the temperature is increased at the

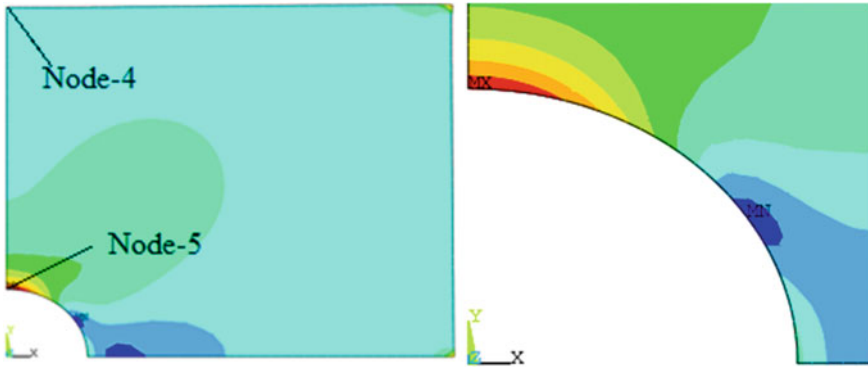


Fig. 5 von Mises stress distribution (Only structural load)

line on which Node-5 is present, the maximum stress was occurring at a different node other than Node-5 (termed as Node-4) as shown in Fig. 6. From the analysis it's also been observed that, as the temperature difference is being increased, the stress at Node-5 is getting decreased and at the same time the maximum stress value is getting decreased up to particular  $\Delta T$  after which it is going beyond the maximum stress of structural case.

The corresponding SCF values at different temperature gradients are mentioned in Table 1. It is been observed that the SCF is decreasing in a linear fashion as  $\Delta T$  is increasing up to critical temperature. After that particular temperature, it is increasing but it is not following a particular pattern. It has also been observed that there would be no difference in the result if the sequence of application of the load is changed

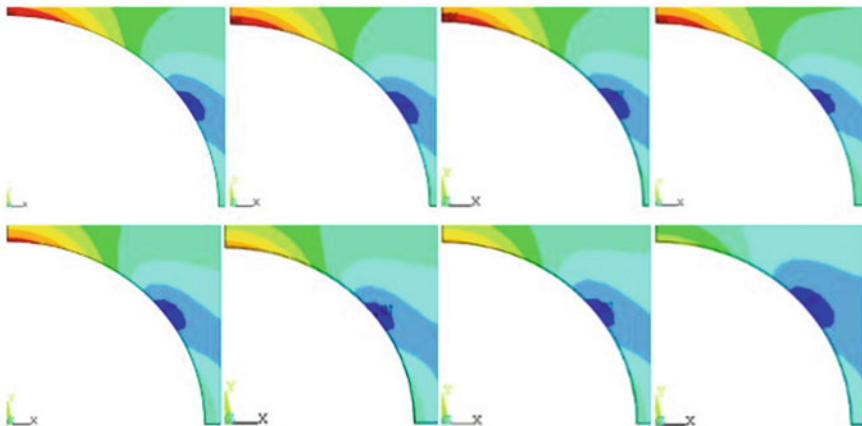


Fig. 6 The stress distribution at Node-5 at different  $\Delta T$  (5, 10, 15, 20, 30, 33, 35, 40 °C, respectively) under axial load of 1.95 kN

**Table 1** SCF values at different temperatures under the axial loading of 1.95 kN

$\Delta T$	SCF @ Node-5	$\Delta T$	SCF @ Node-4
0	2.594	<b>27</b>	<b>2.256</b>
5	2.533	30	2.369
10	2.471	35	2.646
15	2.410	40	3.200
20	2.348	50	3.467
25	2.287		
<b>27</b>	<b>2.256</b>		

(i.e., application of thermal load followed by structural load or vice versa will obtain the same result).

### 4 Conclusion

From the data obtained from combined loading analysis it has been observed that as  $\Delta T$  is being increased, the displacement values are gradually reaching towards the positive values from negative displacement values. It can be better explained as follows. As stated above, the temperature difference is being increased, both the nodes are getting displaced in a positive Y-direction, but they are being displaced in negative Y-direction when only mechanical loading is applied. The final displacement of any of the nodes is being influenced by both the thermal and mechanical loadings. When both the loadings are applied, the resultant displacement at Node-4 is approaching towards the positive displacement value, i.e., at a particular  $\Delta T$  the displacement due to the thermal expansion supersedes the displacement due to axial load. The same behavior can be observed at Node-5 but  $\Delta T$  at which this phenomenon happening is different.

Stress at Node-5 is gradually decreasing as  $\Delta T$  is being increased. It can be justified with the help of following lines. As  $\Delta T$  is increasing, the displacement caused by thermal field superseding the structural displacement. By increasing  $\Delta T$  more, at  $\Delta T$  which is greater than optimum temperature difference ( $\Delta T_{opt}$ ) the magnitude of displacement at Node-4 is greater than that of Node-5. As a result, the strain at Node-4 will be more, so the stress at Node-4 is getting increased and becoming much larger value as  $\Delta T$  is being increased.



## References

1. Erickson PE, Riley WF (1978) Minimizing stress concentrations around circular holes in uniaxially loaded plates. *Exp Mech* 18:97–100. <https://doi.org/10.1007/BF02325003>
2. Ulrich TW, Moslehy FA (1995) A boundary element method for stress reduction by optimal auxiliary holes. *Eng Anal Boundary Elem* 15:219–223. [https://doi.org/10.1016/0955-7997\(95\)00025-J](https://doi.org/10.1016/0955-7997(95)00025-J)
3. Jindal UC (1983) Reduction of stress concentration around a hole in a uniaxially loaded plate. *J Strain Anal Eng Des* 18:135–141. <https://doi.org/10.1243/03093247V182135>
4. Jain NK (2011) The reduction of stress concentration in a uni-axially loaded infinite width rectangular isotropic/orthotropic plate with central circular hole by coaxial auxiliary holes. *IIUM Eng J* 12(6), 141–150 (Special issue in Science and Ethics)
5. Giare GS, Shabahang R (1989) The reduction of stress concentration around the hole in an isotropic plate using composite materials. *Eng Fract Mech* 32:757–766. [https://doi.org/10.1016/0013-7944\(89\)90172-0](https://doi.org/10.1016/0013-7944(89)90172-0)
6. Nagpal S, Jain N, Sanyal S (2012) Stress concentration and its mitigation techniques in flat plate with singularities—a critical review. *Eng J* 16:1–16. <https://doi.org/10.4186/ej.2012.16.1.1>
7. Rao KS, Bapu MN, Ariman T (1971) Thermal stresses in plates with circular holes. *Nucl Eng Des* 15, 97–112 (North-holland publishing company)
8. Kushan DS, Sanyal S, Bhowmick S (2018) Parametric study of interaction effect between closely-spaced nozzles in a thin cylindrical pressure vessel. *Int J Press Vessels Pip* 165:34–42. <https://doi.org/10.1016/j.ijpvp.2018.05.009>
9. Bhandari VB (2008) *Design of machine elements*, 3rd edn. The McGraw-Hill Companies, New Delhi
10. Heywood RB (1952) *Designing by photo elasticity*. Chapman & Hall Ltd, London

# Experimental and Finite Element Analysis of Fracture Parameters of woven Glass/Epoxy Composite



Venkata Sushma Chinta, P. Ravinder Reddy, Koorapati Eshwara Prasad and B. Venkata Sai Kiran

**Abstract** In recent years, Composites are rapidly developing and replacing metals or alloys in numerous Engineering applications as automobiles, Marine Engineering, Aerospace, etc. Due to their properties like resistance to wear, corrosion, high stiffness and strength for reduced weight, superior fatigue characteristics, etc. This study, aimed to analyze the fracture toughness of glass fiber epoxy composite by analyzing the specimen in commercial finite element package in ANSYS environment and there by validating it through experiment. For the experimental process, the glass–epoxy composites plate has been fabricated by hand layup process considering epoxy resin as the matrix and woven roving as the reinforcement. The composite specimens are tested by performing a SENB (single edge notch bend) test to study the fracture toughness and the crack propagation of the glass fiber epoxy composite. The comparison showed good agreement.

**Keywords** Woven roving · Fracture toughness · Epoxy · Three-point bend test

## 1 Introduction

Composites are immensely versatile materials, owing to their ability to inherit the properties of its constituent materials and project a completely new set of properties. Most of the composite materials are made up of two materials; one of them is the matrix or the Binder, surrounds and Binds together the fibers, which are called

---

V. S. Chinta (✉) · P. Ravinder Reddy · B. Venkata Sai Kiran  
Chaitanya Bharathi Institute of Technology (A), Hyderabad, Telangana, India  
e-mail: [venkatasushmachinta@gmail.com](mailto:venkatasushmachinta@gmail.com)

P. Ravinder Reddy  
e-mail: [reddy.prr@gmail.com](mailto:reddy.prr@gmail.com)

B. Venkata Sai Kiran  
e-mail: [b.v.s.k97@gmail.com](mailto:b.v.s.k97@gmail.com)

K. Eshwara Prasad  
Siddhartha Institute of Engineering and Technology, Hyderabad, Telangana, India  
e-mail: [epkoorapati@gmail.com](mailto:epkoorapati@gmail.com)

© Springer Nature Singapore Pte Ltd. 2020  
G. S. V. L. Narasimham et al. (eds.), *Recent Trends in Mechanical Engineering*,  
Lecture Notes in Mechanical Engineering,  
[https://doi.org/10.1007/978-981-15-1124-0\\_56](https://doi.org/10.1007/978-981-15-1124-0_56)

the reinforcement. The drive to improve the properties of composite materials has motivated, material scientists to scrutinize composites with less reinforcement size leading to the development of composites. Composites possess many useful properties such as a specific stiffness, specific strength, dimensional stability, sufficient electrical properties, and appreciable corrosion resistance. The ramifications are easy transportability, reduced stress for rotating parts, high ranges for rockets, which make them alluring for both Civil and defense applications.

## ***1.1 Literature Survey***

Composite materials could easily stand up against the conventional metals or alloys used in engineering areas, yet they pose new problems like interlaminar delamination and fiber cracking, etc. These composite failures can be prevented by improving the fracture toughness of the composite.

In this study test pieces are subjected to flexural loads to evaluate the failure of the specimen in bending conditions, this evaluation helps us in understanding how the composite materials endure bending loads in various applications such as in cooling tower fan blades, and automobile drive shafts. Even though there is much advancement in the field of fracture testing, there are still various problems waiting to be addressed.

Sham Prasad [1] stated that the durability of a composite structure requires a better understanding of the composite's response to the advancement of interlaminar delamination under the three modes and mixed modes of fracture. The study of interlaminar fracture toughness has become popular among researchers, but still a standard test method has not been developed. Tumino [2] after conducting experimental analysis on glass fiber composite and carbon fiber composite through three modes and mixed modes of failure, stated that the dependency between fatigue Paris parameters can be described using a quadratic model, whereas the other monotonic models already existing fail when applied to analyzed materials.

Fiber concentration is the major factor while studying the fracture toughness of a composite laminate. The fracture toughness increases and the crack propagation decreases with the increase in fiber concentration [3, 4]. Ye [5] concluded that the resistance to delamination decreases with the increase of fiber cross-sectional aspect ratio, this can be backed up by the review performed by Nausha [6].

Fiber orientation is the most sought out area of study for researchers. Various authors have analyzed the effect of fiber orientation [7–9], where a majority have agreed that the sequence  $0^\circ/90^\circ/0^\circ/90^\circ$  gives the best results for epoxy–glass fiber composite and also came to a conclusion that the properties such as fracture property and strain energy rate are promising for the above orientation. Adem and Prabhu [10] pointed out that most of the significant mechanical properties show a dependency on strain rate, where the author concluded that the compressive, shear and flexural properties of glass–epoxy composite increase with the increase in strain rate.

Composites tested in labs are done in a controlled and steady environment but in actual applications, these composites are subjected to various adverse environmental factors such as organic oils and acidic waters [12]. In such conditions, predicting the working life of the material is very difficult. For example as the temperature decreases the composites tend to turn brittle [13] and at higher temperatures most of its properties get reduced [14]. Moreover, in practical situations materials seldom experience steady loads; they are mostly subjected to cyclic loads [15] and impact loads [16] where the determination of crack initiation can help in estimating the life of the composites. Venkata Sushma Chinta [17] has found the fracture toughness of jute fiber reinforced epoxy composite and found that fracture toughness of jute epoxy composite is near to that of ceramics like aluminum oxide, silicon carbide, and better than those of polymers and few multi-fiber composites.

## 2 Experimentation

### 2.1 Materials

Woven Roving glass fiber as the reinforcement and epoxy resin (EP-306 grade epoxy resin and EH-758 grade hardener) as a matrix have been selected, Bidirectional Glass fibers of 0.3mm thickness were chosen in this study. Epoxy resins are more expensive than polyester but have superior mechanical properties, higher dynamic strength, and fatigue resistance, which were used to improve the interfacial adhesion and impart strength to the composite. Mechanical characteristics of glass fiber and epoxy resin are shown in Table 1 (Figs. 1, 2).

### 2.2 Preparation of Standard Test Specimens

In this study, the SENB standard specimens are prepared using hand layup method, which are further used to study the fracture mechanics of the glass fiber/epoxy composite.

Initially, the epoxy resin is prepared to be used as the matrix. This matrix is a mixture of epoxy and substance called hardener, mixed in 10:1 ratio. The hardener

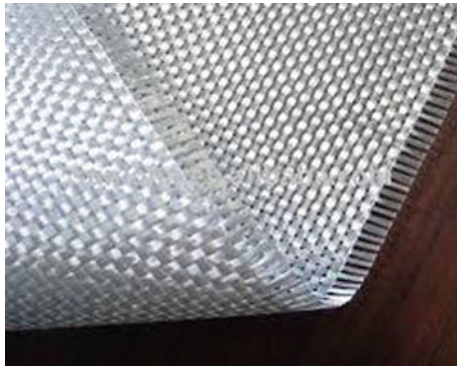
**Table 1** Mechanical properties of glass fiber and epoxy

Properties	Glass fiber	Epoxy resin
Young’s modulus (GPa)	72.4	3.45
Density (gm/cc)	2.6	1.14
Rigidity modulus (GPa)	29.67	1.277
Poisson’s ratio	0.22	0.35

**Fig. 1** Epoxy resin and hardener



**Fig. 2** Woven Roving glass fiber



is highly viscous liquid material, mixed with resin in a suitable proportion, which helps in the solidification of the wet, smooth composite.

Firstly, during the hand layup process, a heavy metallic mold used to prepare the laminate. The surfaces of the mold are cleaned and then a release wax is applied on the surface thoroughly to avoid sticking of epoxy and glass fiber to the surface. The reinforcement i.e, the woven roving glass fiber sheets are cut as per the required dimensions. The woven roving fiber sheet is placed on the surface and the epoxy resin is applied with the help of a brush. To avoid any air bubbles or gaps between the layers, a roller is moved on the surface with mild pressure after each layer till all the layers are stacked up as the requirement. The mold is secured tightly together with the help of bolts and clamps. The laminate is left at room temperature for curing for about 24 h. The laminate is removed from the mold and left at room temperature for further curing.

**Table 2** Glass–epoxy specimen dimension

Specimen	Length (mm)	Width (mm)	Thickness (mm)	Crack length
GF <sub>1</sub>	108	20.1	10.26	9.9
GF <sub>2</sub>	108.04	20.13	10.5	10.4
GF <sub>3</sub>	108.02	20.1	10.3	10.2
GF <sub>4</sub>	108.04	20.1	10.25	10.2
GF <sub>5</sub>	108	20.16	10.2	10.5
GF <sub>6</sub>	108	20.09	10.17	10.2

The specimens are cut from the laminate plate as per the standards to use it in three-point bend test. In total six specimens are fabricated provided with a notch as shown in the below figure and the specimen dimensions are shown in Table 2 (Figs. 3, 4).

**Fig. 3** Test specimens**Fig. 4** Glass–epoxy specimen Gf<sub>1</sub>

### 2.3 Single Edge Notch Bending Test (SENB)

Three-point bending test was performed to calculate the mode I fracture toughness [11]. This test method is used to define the fracture toughness of specimens in terms of critical stress intensity factor. The test method involves loading a specimen in which a crack is initiated by creating a notch. In the SENB test, load is given to the specimen for propagating the already created crack. The test was performed according to test standard ASTM D-5045, using NANO UTM at our institution. Special three-point bending test fixtures are used to fix the specimen. The machine can be used for the maximum load of 25 KN and can bear the maximum weight of 160 kg. Load is applied and feed rate is set as 10 mm/min.

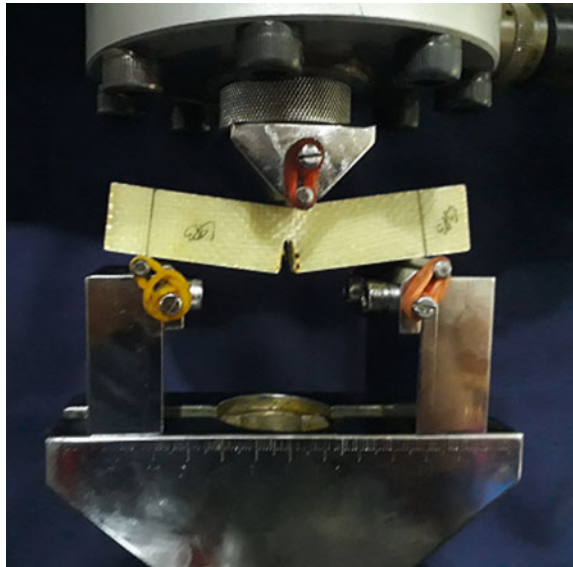
The load at which the crack propagates is noted from the computer attached to the UTM. Later the data excel sheet obtained from the computer is used to plot the LOAD versus Displacement graph (Fig. 5).

**Measurement of compliance of specimen and estimation of load p:** The following Conditions should be satisfied by the specimen as per the standards of ASTM D-5045 to conduct test. For  $Gf_1$  specimen the thickness of the specimen is 10.26 mm. Single edge notch bend is suggested with small thickness to achieve plane strain. An optical microscope is used to measure the notch dimension.

- For straight through notch  $1 \leq \frac{W}{B} \leq 4$  (1)

for  $Gf_1$  specimen  $\frac{W}{B} = \frac{20.1}{10.26} = 1.95$  is satisfied

**Fig. 5** Specimen under test



- The notch width  $N < \frac{W}{10}$  (2)

for  $Gf_1$  specimen  $1.6 < 2.01$  is satisfied

To determine the initial compliance  $C$ , a straight line (AB) is drawn. The reciprocal of the slope of line (AB), is denoted as  $C$ . Draw a second line (AB') with compliance 5% greater than that of line (AB). If the maximum load that the specimen was able to withstand,  $P_{max}$ , falls within lines (AB) and (AB'), use  $P_{max}$  to calculate  $K1$ . If  $P_{max}$  falls outside line (AB) and line (AB'), then use the intersection of line (AB') and the load curve as  $P_Q$ . Furthermore, if  $P_{max}/P_Q < 1.1$ , use  $P_Q$  in the calculation of  $K1$ . However, if  $P_{max}/P_Q > 1.1$ , the test is invalid.

Figure 6 is load versus displacement curve obtained for bending test for  $Gf_1$  specimen. Figure 6 shows value of  $P_Q$  for specimen  $Gf_1$  is 2.135 kN. The maximum load sustained by the specimen,  $P_{max}$  is 2.265 kN.  $P_{max}/P_Q$  for specimen  $Gf_1$  is 1.06, which is less than 1.1. So the test was found to be valid. Stress intensity factor can be considered as an estimate of fracture toughness. The critical stress intensity factor is given by Eq. (3).

$$K_Q = (P_Q/BW^{1/2})f(x) \tag{3}$$

- $P_Q$  Load at which crack propagates in N
- $B$  Thickness of the specimen in mm
- $W$  Specimen width in mm
- $A$  Length of crack in mm



Fig. 6 Estimation of  $P_Q$  for specimen  $Gf_1$



$$x = a/W \quad (4)$$

$$G_Q = (1 - \nu^2)K_{IC}^2/E \quad (5)$$

By using Eq. (3), the stress intensity factor for specimen Gf<sub>1</sub> is determined at the maximum load 2265 N and is found to be 517.35 Mpa.mm<sup>1/2</sup>.  $G_Q$  the strain energy release rate is determined as 9.59 kJ/m<sup>2</sup>.

### 3 Finite Element Analysis

Finite element analysis was performed using analysis software ANSYS 18. A three-dimensional finite element model was created using ANSYS, Mechanical APDL. The element type used was SHELL 8 NODE 281 and a model of required dimension was created. Six such models were created as per the specimens that were put into three-point bending test. The thickness of the created geometry in ANSYS was divided into equal number of glass–epoxy layers in similar stacking sequence as that followed in fabricating the SENB compact test specimen.

During analysis, each layer (lamina) was given its orthotropic mechanical properties shown in Table 3 that were obtained from calculations. The element plot of SENB specimen and element plot in the vicinity of the crack are shown in Figs. (7, 8).

**Table 3** Properties of woven roving glass/epoxy lamina

Properties	Values
E <sub>1</sub>	26536.3 MPa
E <sub>2</sub>	26536.3 MPa
E <sub>3</sub>	11002.6 MPa
ν <sub>12</sub>	0.112
ν <sub>23</sub>	0.348
ν <sub>13</sub>	0.348
G <sub>12</sub>	3878.53
G <sub>23</sub>	3845.67
G <sub>13</sub>	3845.67

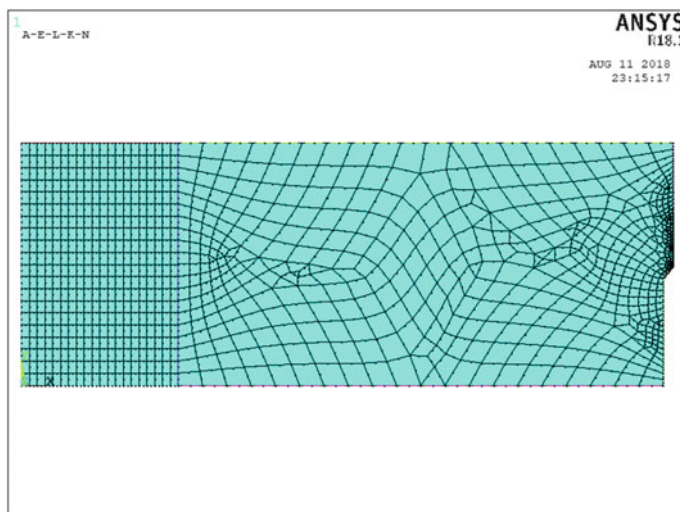


Fig. 7 Element plot for SENB specimen Gf<sub>1</sub>

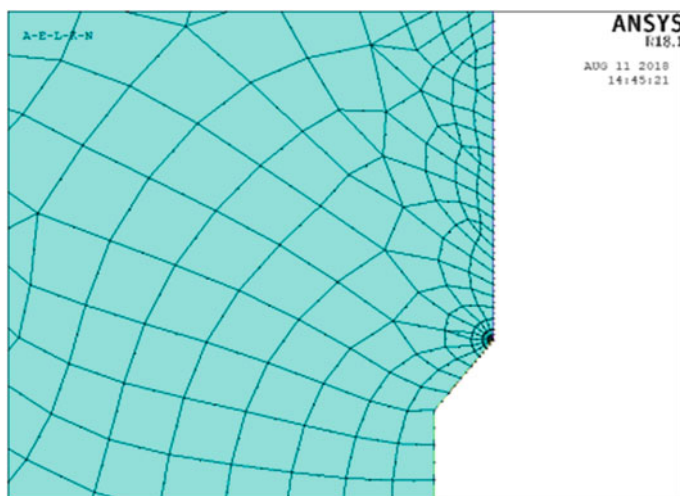
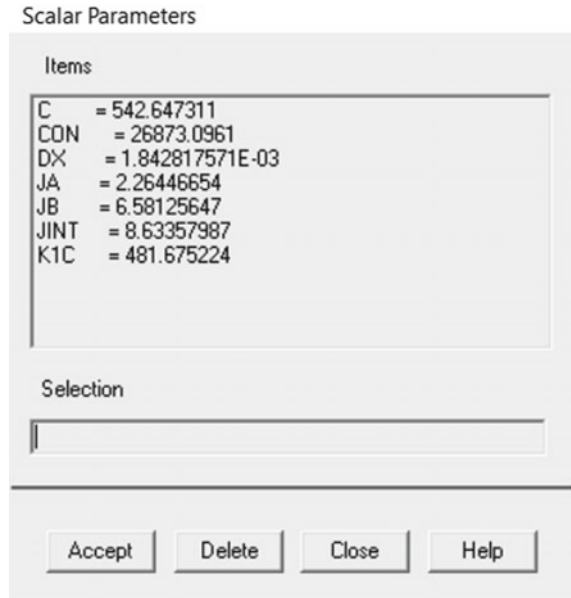


Fig. 8 Element plot in the vicinity of the crack

From Fig. 9 we can observe that  $K_{1C}$  from ANSYS for Gf<sub>1</sub> specimen is 481.67 MPa mm<sup>1/2</sup>.

**Fig. 9** Critical stress intensity factor for  $Gf_1$



### 4 Results and Discussions

In Table 4, the strain energy rate evaluated from experiment and ANSYS are listed. The maximum value of strain energy rate from experiment is 10.30 kJ/m<sup>2</sup> at a load of 2295 N. Stress intensity factor evaluated from experiment and ANSYS are listed in Table 5. The maximum value of stress intensity factor from experiment is 536.54 MPa mm<sup>1/2</sup> at a load of 2303 N. Deviation is observed in estimation of strain energy release rate because a more generalized approach mentioned in ASTM D-5045 has been adopted while conducting the experimental analysis.

**Table 4** Comparison of strain energy released rate between experimental and numerical analysis

Specimen designation	Load $P_{max}$ (N)	Strain energy release rate $G_{Ic}$ (kJ/m <sup>2</sup> )		
		Experiment	Ansyes	% of deviation
$Gf_1$	2265	9.59	8.63	10.01
$Gf_2$	2278	9.51	8.77	8.09
$Gf_3$	2283	9.82	8.91	9.26
$Gf_4$	2297	10.23	9.12	10.85
$Gf_5$	2295	10.30	8.98	12.81
$Gf_6$	2303	10.28	9.11	11.38

**Table 5** Comparison of stress intensity factor between experimental and numerical analysis

Specimen designation	Load $P_{max}$ (N)	Stress intensity factor( $k_{Ic}$ ) Mpa mm <sup>1/2</sup>		
		Experiment	Ansys	% of deviation
Gf <sub>1</sub>	2265	517.35	481.67	6.89
Gf <sub>2</sub>	2278	514.98	486.72	5.4
Gf <sub>3</sub>	2283	523.52	488.12	6.76
Gf <sub>4</sub>	2297	534.15	494.91	7.34
Gf <sub>5</sub>	2295	535.19	491.56	8.32
Gf <sub>6</sub>	2303	536.54	493.32	7.88

## 5 Conclusions

All specimens showed expected behavior during the process of fracture as mentioned in the ASTM D-5045. Results of finite element analysis are found to be reliable with the results obtained experimentally.

In conclusion, the test followed showed a promising insight on fracture toughness of glass–epoxy composite, which is the most common and widely used material. The fracture toughness of glass/epoxy composite determined is on par with materials such as Magnesium alloys and lead alloys. Hence, glass/epoxy composite can serve as an effective substitute for these metals and also further, hybrid composites may be developed and studied, which may be used for space applications, eliminating the use of heavy metals.

## References

1. Sham Prasad MS, Venkatesha CS, Jayaraju T (2011) Experimental methods of determining fracture toughness of fiber reinforced polymer composites under various loading conditions. *JMMCE* 10(13):1263–1275
2. Tumino D, Zuccarellob B (2011) Fatigue delamination experiments on GFRP and CFRP specimens under single and mixed fracture mods. *ELSEVIER Procedia Eng* 1791–1796
3. SrikanthRao D, Ravinder Reddy P, Venkatesh S Determination of mode-i fracture toughness of epoxy-glass fiber composite laminate. *IJMET* 8(11)
4. Mathapati SS, Mathapati SS (2015) Testing and analysis of mechanical properties of E-glass fiber reinforced epoxy polymer composites. *IJRIST* 2(1)
5. Ye L, Deng S Influence of fiber cross-sectional aspect ratio on mechanical properties of glass fiber/epoxy composites. *Compos Sci Technol*
6. Nasuha N A review on mode-I interlaminar fracture toughness of fiber reinforced composites. *J Phys Conf ser.* 908012024
7. FatihDaricik Z (2017) Characterization of delamination crack in multidirectional e-glass/epoxy composite under mode I loading. *Eur Mech Sci* 1(4):117–128
8. Adekomaya O, Adama K (2017) Glass-fiber reinforced composites: the effect of fiber loading and orientation on tensile and impact strength. *NIJOTECH* 36(3):782–787
9. Prabeena T, SrikanthRao D, Gopikrishna N (2017) Evaluation of mode-I fracture toughness of epoxy-glass fiber composite laminate. *IJRSET* 6(1)

10. Adem E, Prabhu P (2015) Tribological behavior of E-glass/epoxy & E-glass/polyester composites for automotive body application. *AJER* 4(10):08–17
11. Sahoo SR, Mishra A (2012) Fracture characterization of plain woven fabric glass-epoxy composites. *Int J Aerosp Mech Eng* 6(7)
12. Masud AKM, Zaman AKB, Al-Khaled A (2007) Effects of environment on fracture toughness of glass fiber/polyester composite. *J Mech Eng* ME38
13. Torabizadeh MA (2013) Tensile, compressive and shear properties of unidirectional glass/epoxy composites subjected to mechanical loading and low temperature services. *IJEMS* 20:299–309
14. Aktas M, Karakuzu R (2009) Determination of mechanical properties of glass-epoxy composites in high temperatures. *Polym Compos* 30(10)
15. Mohamed Ansar A, Singh D, Balaji D (2013) Fatigue analysis of glass fiber reinforced composites. *IJERA* 3(3):588–591
16. Rajesh Mathivanan N, Jerald J (2010) Experimental investigation of woven E-glass epoxy composite laminates subjected to low-velocity impact at different energy levels. *JMMCE* 9(7):643–652
17. Venkata Sushma Chinta, Ravinder Reddy P, Koorapati EP, Sathola Anand (2018) Investigation of fracture toughness of bidirectional jute/epoxy composite and analysis by using FEA. *IJMPERD* 8(6):227–238

# Automatic Gate System with Autofocus Camera Using Node-RED



Basavaraj Talikoti, Ruchira Patole, Amit Pradhan, Allen Thomas, Evin Poullose and Shubham Mane

**Abstract** Automatic gate system makes a property more secure and exclusive. In today's era of automation, it is not just an advanced electronic feature to have an automatic gate but more often a need to provide high-end security. In this paper, an automatic gate system is designed which uses an autofocus camera to automatically recognize the license plate of a vehicle along with the vehicle type and model. The system uses Raspberry Pi 3B + and other sensors along with Node-RED for connecting the processor and different devices to form an Internet of Things (IoT) network. The use of autofocus infrared camera enables accurate recognition of vehicle license plates even with broken or distorted license plates. It also helps in detecting fake license plates with proper programming. Node-RED connects all the devices together by facilitating the flow of data from different sensors to the Raspberry Pi processor and also the uploading of data to an online database. This automatic gate system is easy to set up and has extremely useful features with robust body for unpredictable weather conditions. With the use of Raspberry Pi 3B + the processing is fast and execution is quicker with on-chip Wi-Fi module.

**Keywords** Automatic gate system · IoT · Motor · Autofocus camera

## 1 Introduction

Any kind of property, be it an industrial or a residential property, can be benefitted by the use of automated gate for security. This kind of system along with automatic gate opener and closer also provides security from burglars and stray animals from entering the property [1–4]. It also adds value to the property. The Raspberry Pi 3B + processor acquires data from infrared camera, seven ultrasonic sensors, four infrared sensors, and three motion sensors. Continuous motion-sensing results in good quality surveillance because every time a motion is sensed near the vicinity of

---

B. Talikoti (✉) · R. Patole · A. Pradhan · A. Thomas · E. Poullose · S. Mane  
Pillai College of Engineering, Affiliated to University of Mumbai, New Panvel 410206,  
Maharashtra, India  
e-mail: [btalikoti21@gmail.com](mailto:btalikoti21@gmail.com)

© Springer Nature Singapore Pte Ltd. 2020  
G. S. V. L. Narasimham et al. (eds.), *Recent Trends in Mechanical Engineering*,  
Lecture Notes in Mechanical Engineering,  
[https://doi.org/10.1007/978-981-15-1124-0\\_57](https://doi.org/10.1007/978-981-15-1124-0_57)

the gate, the object is detected and recognized. The infrared camera used enables the detection and recognition of objects at night. Node-RED is used for programming the entire system, which enables the communication between different components of the system; it also enables the accessing of data from the Internet and uploading the required data [5–7].

## 2 Methodology

The methodology of the system as shown in Fig. 1. The data is acquired from the infrared camera, ultrasonic, IR, and motion sensors by the Raspberry Pi 3B + processor. The programming for the system is done in Node-RED programming platform. The detection of object is programmed using different nodes in Node-RED. The code for every node is written in python.

If a license plate is detected, the Automatic License Plate Recognition is done using OpenALPR a cloud-based API used to detect the number of license plate as well as the vehicle model. It is done with the help of Tesseract using Optical Character Recognition (OCR) an online database of OpenALPR. After a recognition, the processor drives the motor using the motor driver circuit.

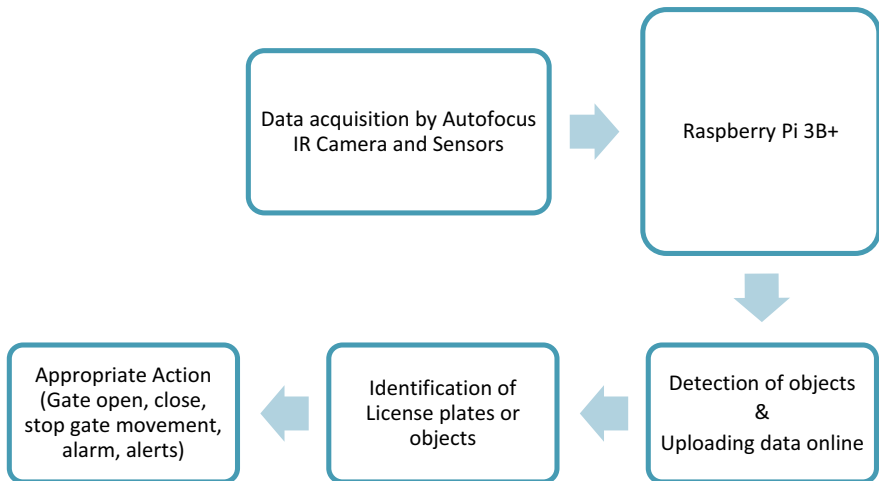


Fig. 1 Methodology

### 3 Automatic Gate System

The brain of the system is the Raspberry Pi 3B + processor, which acquires the input from the camera and auto-focuses the camera according to the requirements. The processor is also connected to ultrasonic sensors and infrared sensors for obstacle detection and object detection. The processor with the help of motor driver circuit controls the motor, which is responsible for the movement (opening or closing) of the gate. Four ultrasonic sensors and four infrared sensors together are responsible for the auto-focusing of the camera with the help of miniature motors to move the camera focal lens. Three 360° Wi-Fi motion sensors are used for motion of the camera. Three ultrasonic sensors are used to stop the gate while closing, if an obstacle is detected to avoid any harm to humans or pets coming in the way of the moving gate. If an unrecognized object is detected in the way of the gate at any stage of execution, immediately an alarm will be set off and alert will be sent to the authorized personnel.

A 220 V 500 W motor has been used with a pinion and chain. The parameters considered for choosing the motor for the gate are the length, height, width, material, and weight of the gate. The other parameters considered for automation are the torque, speed, safety factor. Calculations incorporating the formulae for torque, weight and motor speed relations have been used and the specifications of the motor have been finalized.

Figure 2 and 3 show the programming in Node-RED. It is seen that 28 nodes for various modules have been connected together. The nodes are programmed with

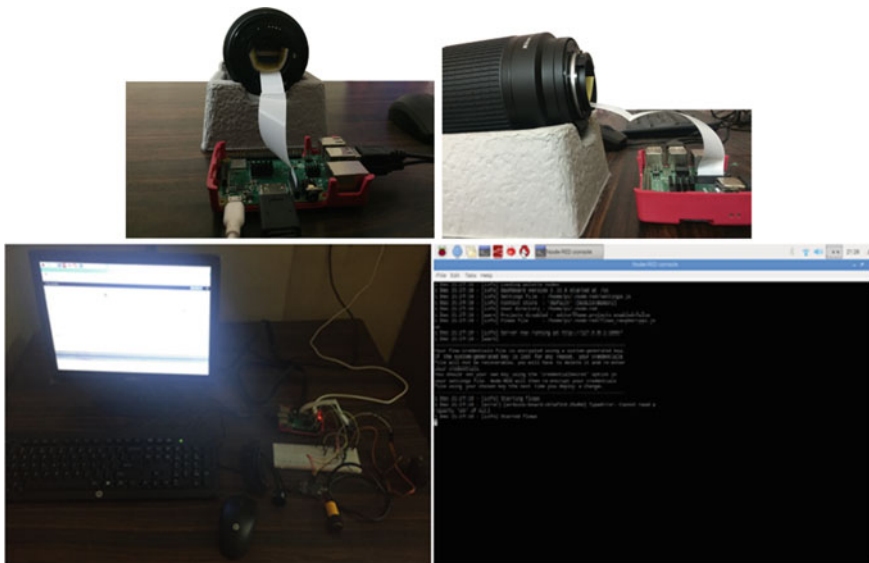


Fig. 2 Hardware and Node-RED console







**Fig. 5** Level-1 autofocus of capture1

**Fig. 6** Level-2 autofocus of capture1



Figure 7 shows the back license plate captured by the camera module. Figures 8 and 9 show the level-1 and level-2 autofocus of the number plate.

Following is the result obtained after debugging. The results clearly indicate the identified number plate.

msg.payload : Object



**Fig. 7** Capture2 number plate



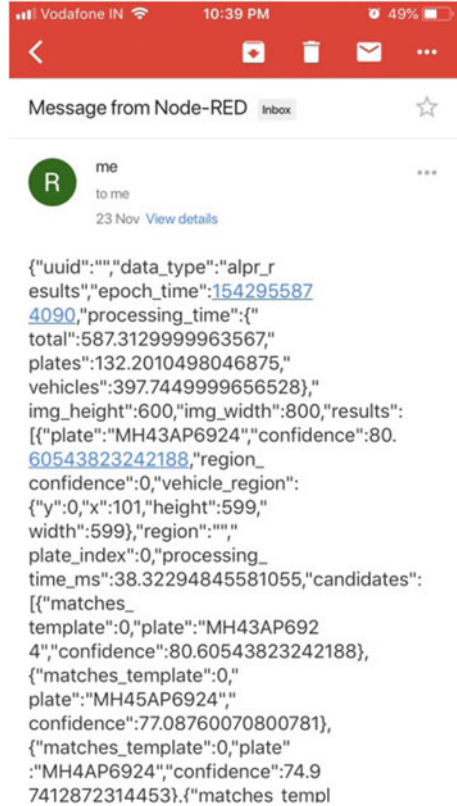
**Fig. 8** Level-1 autofocus of capture2

**Fig. 9** Level-2 autofocus of capture2



```
object
uuid: ""
data_type: "alpr_results"
epoch_time: 1543681938182
processing_time: object
total: 614.6480000024894
plates: 130.6639862060547
vehicles: 434.4749999945634
img_height: 600
img_width: 800
results: array[1]
0: object
plate: "MH43AP6924"
confidence: 92.20283508300781
region_confidence: 0
vehicle_region: object
y: 0
x: 101
height: 599
width: 599
region: ""
plate_index: 0
processing_time_ms: 38.12080764770508
candidates: array[10]
coordinates: array[4]
vehicle: object
matches_template: 0
requested_topn: 10
credits_monthly_used: 2
```

**Fig. 10** Alert received from Node-RED after the recognition of the vehicle



```

version: 2
credits_monthly_total: 2000
error: false
regions_of_interest: array[1]
0: object
credit_cost: 2

```

Figure 10 shows the screenshot of the alert received from Node-RED after the recognition of the vehicle.

## 5 Conclusion

The automatic gate system described in this paper provides high security with automation. The system developed is less expensive and easily installable. The use of an autofocus camera makes it a highly accurate identification system. The amount of focus and zoom is decided by the system after a quick attempt to acquire

a clear image to identify the number. The alert sent to the concerned authorities is quick which enables the user to take appropriate actions in a very short duration of time. The hardware of the system is compact and reprogrammable, it can be easily updated. The system is completely standalone and unmanned; thus, reducing human intervention to a great extent.

## References

1. Davix XA, Christopher CS, Christine SS (2017) License plate detection using channel scale space and color based detection method. In: 2017 IEEE international conference on circuits and systems (ICCS), pp 82–86
2. Tang Y, Zhang C, Gu R, Li P, Yang B (2017) Vehicle detection and recognition for intelligent traffic surveillance system. *Multimed Tools Appl* 76:5817–5832
3. Rodriguez FM, Saburido MG, Castro JLA (2002) New methods for automatic reading of V.L.P.s (Vehicle License Plates), SPPRA 2002 (Signal processing pattern recognition and applications)
4. Anagnostopoulos C, Alexandropoulos T, Loumos V, Kayafas E (2006) Intelligent traffic management through MPEG-7 vehicle flow surveillance. In: Proceedings of IEEE international symposium on modern computing, pp 202–207
5. Shidore MM, Narote SP (2011) Number plate recognition for indian vehicles. *Int J Comput Sci Netw Secur* 11(2):143–146
6. Hidayatullah P, Syakrani N, Suhartini I, Muhlis W (2012) Optical character recognition improvement for license plate recognition in indonesia. In: 2012 Sixth UKSim/AMSS European symposium on computer modeling and simulation, pp 249–254
7. Zhang W, Li X, Ma X (2008) Perspective correction method for chinese document images. In: International symposium on intelligent information technology application workshops, 2008. IITAW '08, pp 467–470

# CFD Analysis of Hydro-Dynamic Lubrication Journal Bearing Using Castor Oil



N. Udgire Manojkumar, H. Jagadish and B. Kirankumar

**Abstract** The overall objectives of the investigation are to decide the journal bearing lubrication features, for example, pressure distribution and oil film thickness. These trademarks can be uncovered by settling the condition that administers the fluid–structure connection happening amongst journal bearing. The pressure distribution of the greasing up oil is controlled by unravelling Navier–Stokes condition; the energy condition gives speed plots, which one used to get the pressure distribution plots by illuminating pressure Poissons condition. The pressure distribution got from Navier–Stokes is utilised to discover the power and removal by settling the anxieties and relations. The weight profile of greasing up oil is fixed consider CASTOR oil as lubricating oil for different length–diameter ratios of the journal bearing by keeping the constant eccentricity value. The overall objectives of the investigation are to decide the journal bearing grease qualities, for example, weight conveyance and oil film thickness. These attributes can be discovered by settling the condition that oversees the fluid–structure cooperation happening between journal bearings. The analysis is also carried out for material like bronze for different length–diameter ratios and constant eccentricity value to find the displacement, stress and pressure profile distribution in the bearing structure by using the boundary condition. For analysis, it is accepted that the flow is laminar and steady and the fluid used for analysis in CFD is CASTOR oil and the boundary condition used is speed 3000 rpm. From this, the result will be the pressure profile for journal bearing. The pressure profile for the CASTOR oil after analysis is found to be as 58092.15, 58212.35, 59162.68 and 59592.64 N/m<sup>2</sup>.

---

N. Udgire Manojkumar (✉) · H. Jagadish · B. Kirankumar  
Department of Mechanical, Hyderabad Institute of Technology and Management, Hyderabad,  
Telangana, India  
e-mail: [udgiremanojkumar@gmail.com](mailto:udgiremanojkumar@gmail.com)

H. Jagadish  
e-mail: [jagadish.jmh@gmail.com](mailto:jagadish.jmh@gmail.com)

B. Kirankumar  
e-mail: [bkiran1426@gmail.com](mailto:bkiran1426@gmail.com)

© Springer Nature Singapore Pte Ltd. 2020  
G. S. V. L. Narasimham et al. (eds.), *Recent Trends in Mechanical Engineering*,  
Lecture Notes in Mechanical Engineering,  
[https://doi.org/10.1007/978-981-15-1124-0\\_58](https://doi.org/10.1007/978-981-15-1124-0_58)

**Keywords** Journal bearing · CFD · CSD · ANSYS · Castor oil · Bronze · L/D ratio and eccentricity

## 1 Introduction

The bearing is a mechanical component that grants relative movement between two sections, for example, the pole and the lodging, with a base rubbing. The capacity of the bearing is as per the following: The bearing backings the pole or the hub and holds it in the correct position. The bearing backings the pole or the pivot and keeps it in the right place. The bearing takes up the power that fallow up on the axis and transmit them to outline or the establishment the bearing guarantees the free turn of the pole or the hub with least contact.

### 1.1 *Classification of Bearing*

Bearings are well-ordered in various ways. Contingent on the course of powers that follows up on them, bearing is grouped into two classes: (1) Radial bearing backings the heap, which is opposite to the hub of the pole. (2) Thrust bearing backings the load, which acts along the centre of the pole. Contingent on the sort of erosion, bearing are ordered into two major gatherings: (1) Sliding contact bearing. (2) Rolling contact bearing. Sliding contact bearing is additionally called plain contact bearing, diary bearing or sleeve heading. For this situation, the surface of the pole glides over the surface of shrub bringing about grating and wear. To decline the grating, these two surfaces are out of the way by a film greasing up oil. The bearing is made of superior bearing material like white metal or bronze. Moving contact bearing is additionally called antifriction bearing or essentially metal roller. Moving components, for example, balls or rollers, are presented between the surfaces that are in relative movement.

### 1.2 *Lubrication and Journal Bearing*

Lubrication is nothing but reducing friction by means of an apt substance called lubricant. The rubbing surfaces of bodies have the relative motion between them. The suitable features of the oil are as follows: (1) To reduce friction. (2) To diminish or avoid wear. (3) To expel out heat generated due to friction. (4) To shield the journal bearing from corrosion. Hydrodynamic lubrication is the elastic distortion of the surfaces engaged as well as the rise in viscosity of the lubricant due to high pressure. The small flexible, flattering parts together with an increase in thickness provides a film, even though very thin, that is much denser than would overcome



**Table 1** Details of circular journal bearing

Journal radius	5 cm
Radial clearance	0.005 cm
Bearing pad thickness	0.5 cm
L/D ratio	2.0, 2.1, 2.2, 2.3, 2.4
Eccentricity ratio	0.8

with completely rigid portions. Or the film that occurs when a lubricant is introduced between the surface that is in rolling contacts, such as mating gears or rolling bearing, decreases friction.

**Governing Equations in CFD:**

(i) *Continuity equation:*

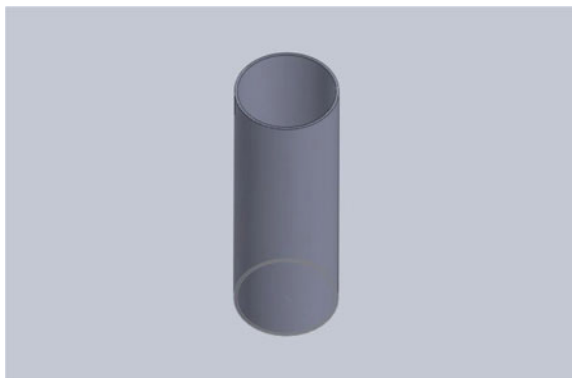
$$\partial u/\partial p + \partial v/\partial q + \partial w/\partial r = 0 \tag{1}$$

In the elasto hydrodynamic lubrication bearing, oil pressure is premeditated by solving the Navier–Stokes equation conforming to fluid flow section subjected to boundary conditions. To get the numerical resolution, journal bearings are modelled using elasto hydrodynamic model, and the solution is attained by using the finite volume method. For this, the commercially available fluid flow solver, ANSYS FLUENT is used. The geometrical model is designed using PRO/E CAD software and is then imported to fluent software. FLUENT solver gives numerical solution for given bearing loading subjected to boundary conditions.

Journal bearings are designed and modelled in PRO/E software using geometrical information shown in underneath the table (Table 1).

*The geometrical models of EHL journal bearings are shown in following figures (Figs. 1, 2, 3, 4, 5).*

**Fig. 1** L/D = 2 and ε = 0.8



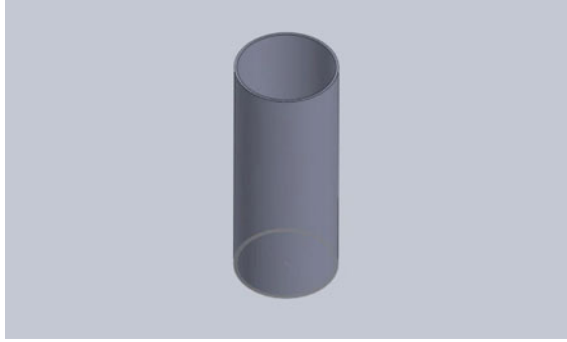


**Fig. 2**  $L/D = 2.1$  and  $\epsilon = 0.8$

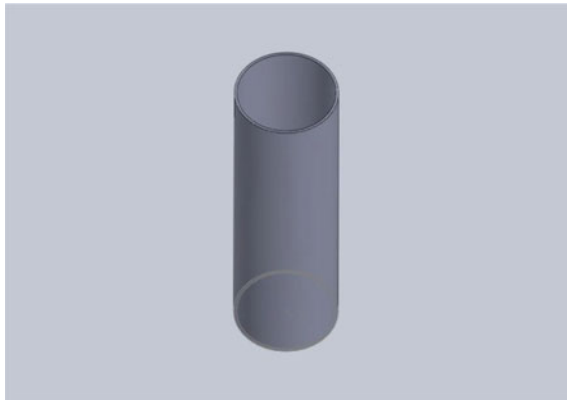


**Fig. 3**  $L/D = 2.2$  and  $\epsilon = 0.8$

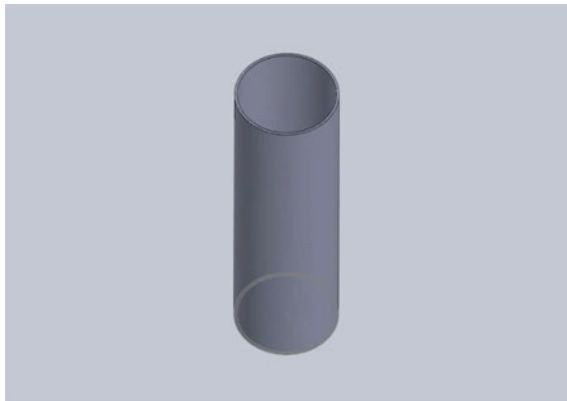


**Fig. 4**  $L/D = 2.3$  and  $\epsilon = 0.8$

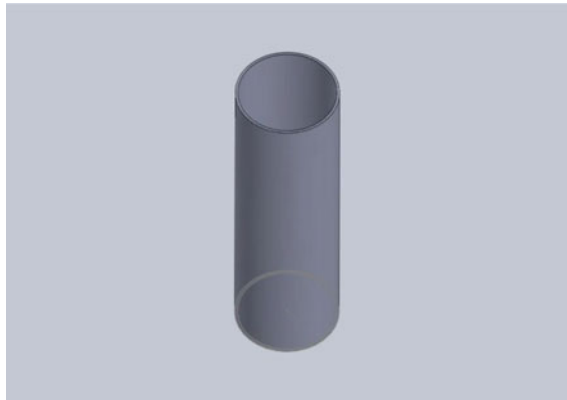


**Fig. 5**  $L/D = 2.4$  and  $\epsilon = 0.8$

## 2 Lubricating Oils

**The required properties of lubricating oil are as follows:**

- It ought to be accessible in a broad scope of viscosities.
- There ought to be little change in consistency of the oil with a change in temperature.
- The oil ought to be artificially steady with the bearing material and air at all temperatures experienced in the application.
- The oil ought to have adequate explicit warmth to divert frictional warmth, without anomalous ascent in temperature.
- It ought to be economically accessible at a sensible expense (Table 2).

*The result for the given fluid flow problem using ANSYS workbench is attained by the below mentioned three critical steps.*

1. Preprocessor.
2. Set-up and solution.
3. Post-processing.

*Imported model (Fig. 6).*

*Meshed mode (Fig. 7).*

*Structural pressure (Fig. 8).*

**Table 2** Castor oil properties

$\rho$	961 kg/m <sup>3</sup>
$C_P$	1800 j/kg k
$k$	0.18 w/m k
$\nu$	0.2844 n-s/m <sup>2</sup>

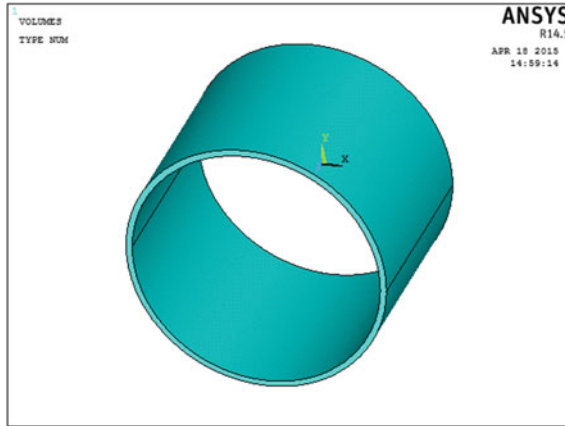


Fig. 6 Imported model in ansys software

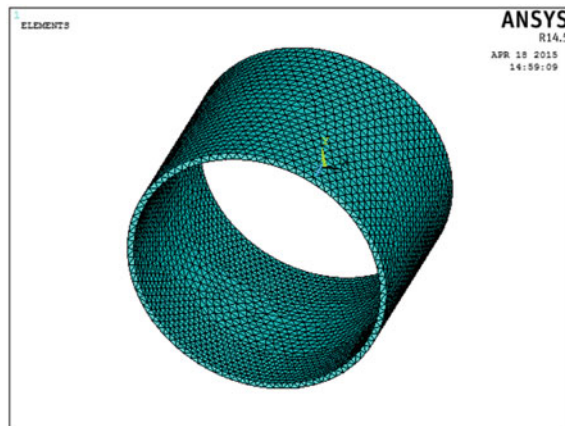
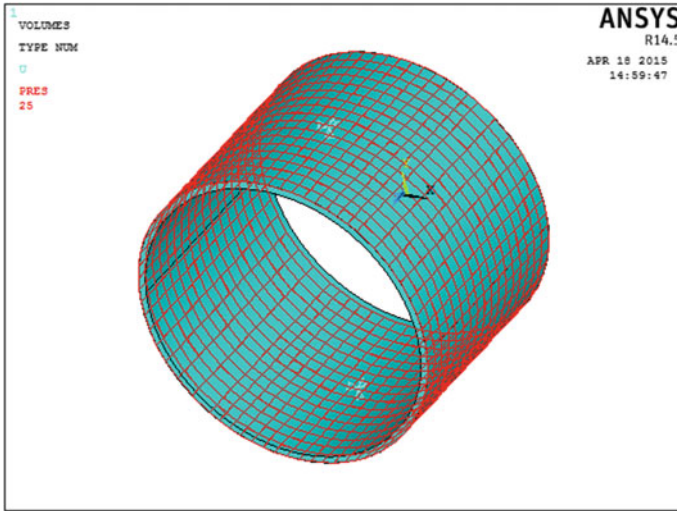


Fig. 7 Meshed model

### 2.1 Structural Analysis of Journal Bearing

The pressure field obtained from fluid subtleties is used in the mechanical analysis to determine the displacement and stresses taking place in mating surfaces. Laminar study floe measured in liquid dynamics and bronze material is used in structural analysis. Commercially available ANSYS software, based on FEM, is used for structural investigation. ANSYS is unanimously useful software to solve the problems numerically of mechanical/civil engineering involving static/changing, auxiliary research (both straight and nonlinear), warmth exchange, and liquid issues and additionally acoustic and electromagnetic problems (Table 3).



**Fig. 8** Applying pressures to model

**Table 3** Bronze material properties

Young’s modulus	75000 MPa
Poisson’s ratio	0.29
Density	0.0000064 kg/mm <sup>3</sup>

### 3 Results and Discussion

The examination of the diary bearing is done by using the FLUENT® programming, and laminar stream condition is employed for this model. Whats more, to which a standard k-ε show is applied for a laminar stream. The significant circumstances that are assessed for the liquid streams are the laminar demonstrating and force condition. The arrangement of Navier-feeds condition gives the speed vectors and weight in the liquid stream locale. FLUENT® can explain the Navier-feeds condition with the standard k-ε laminar model.

In the current research work, journal bearing is analysed using elastic hydrodynamic model to treasure the pressure field, and deformation of bearing coupling surfaces studies fluid dynamics and fluid–structure interface methods. The commercially available ANSYS fluent software is used to envisage oil film pressure deformation and stresses occurring in mating surfaces using CASTOR oil (Figs. 9, 10, 11, 12, 13).

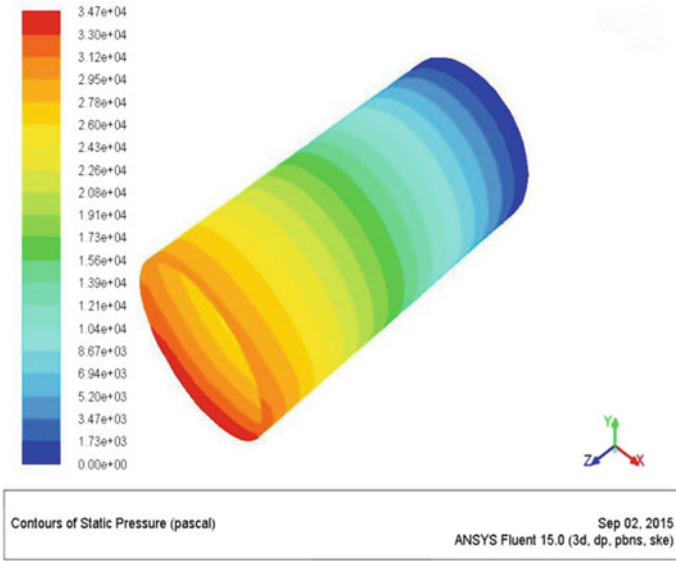


Fig. 9  $L/D = 2.2$  and  $\epsilon = 0.8$

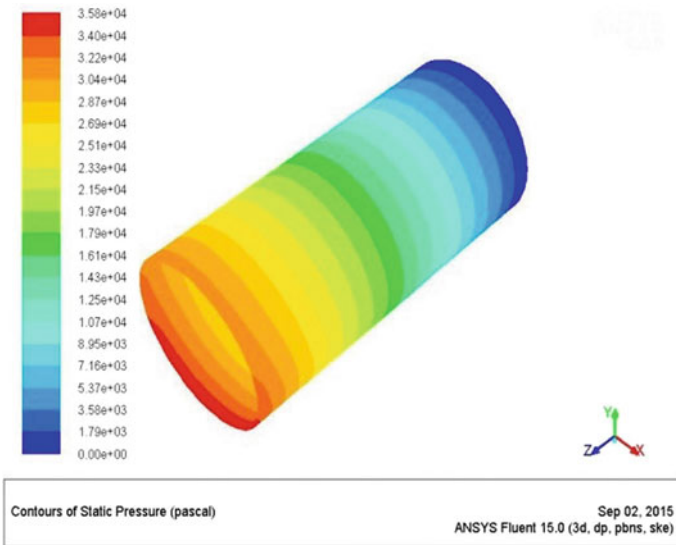


Fig. 10  $L/D = 2.3$  and  $\epsilon = 0.8$

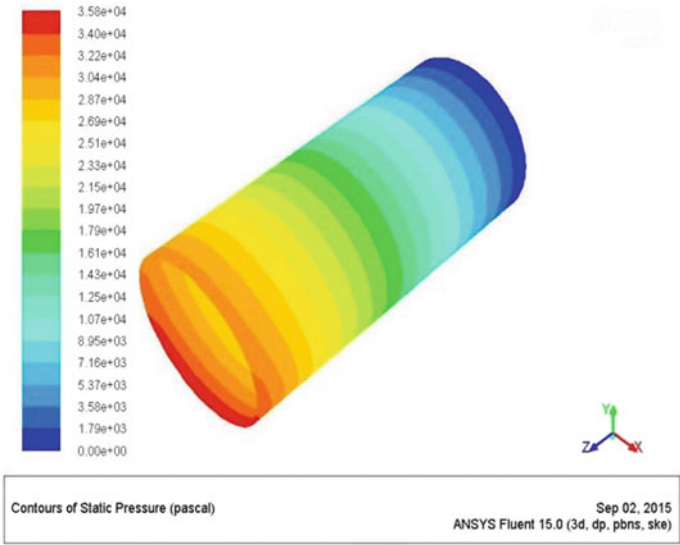


Fig. 11  $L/D = 2.4$  and  $\epsilon = 0.8$

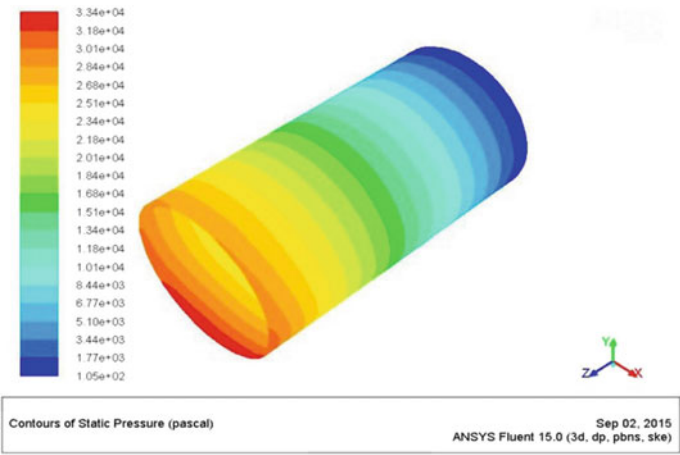
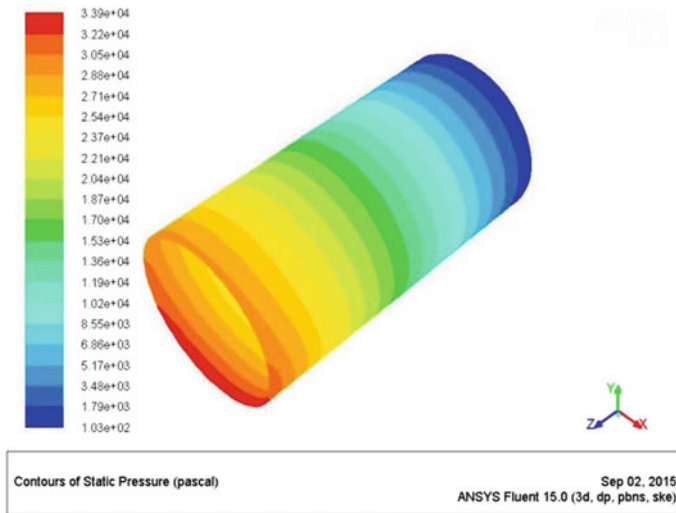


Fig. 12  $L/D = 2.0$  and  $\epsilon = 0.8$



**Fig. 13**  $L/D = 2.1$  and  $\varepsilon = 0.8$

## 4 FSI Results

The outcomes attained from fluid flow analysis are given as input to the structural analysis problem to solve fluid–structure interaction problems. The pressure values obtained from FLUENT is used in the coupled field analysis and is offered in data to structural analysis that has been carried out using ANSYS to get displacement and stress values in journal bearings. The material properties considering structural analysis are listed below. The displacement and stresses are shown for BRONZE material.

$L/D = 2.0$  and  $\varepsilon = 0.8$  (Figs. 14, 15).

$L/D = 2.4$  and  $\varepsilon = 0.8$  (Figs. 16, 17, Graph 1).

## 5 Conclusion

The CFD and structural analysis are done on different models using ANSYS to assess the fluid pressures, Stress distribution and displacement in journal bearing. Different models of journal bearing are designed by varying  $L/D$  ratios 2.0, 2.1, 2.2, 2.3 and 2.4 and eccentricity ratios 0.8. 3D modelling is completed in Pro/Engineer. CFD and structural analysis are completed in ANSYS. By watching the CFD and auxiliary investigation results, the weight is expanding by expanding the  $L/D$  proportions and



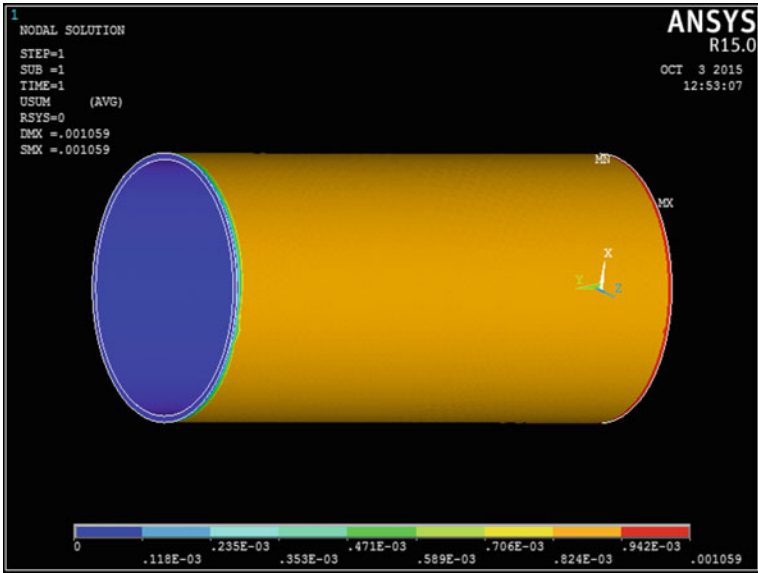


Fig. 14 Displacement

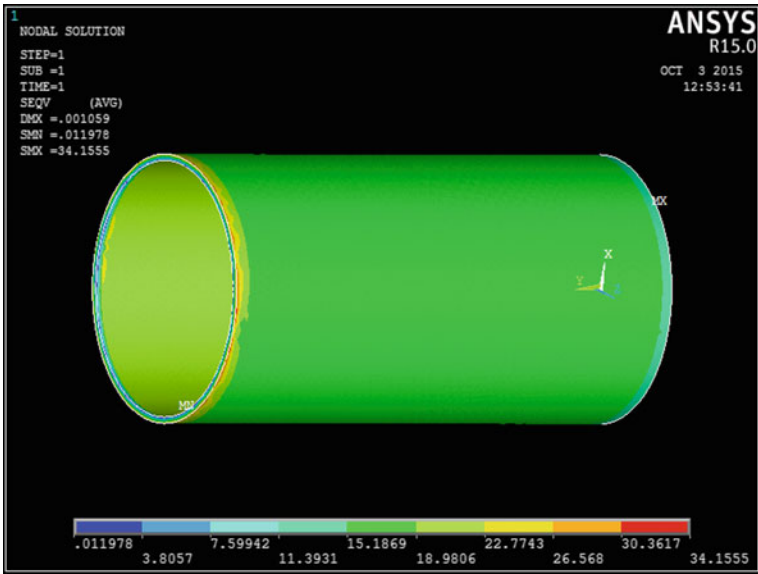


Fig. 15 Stress

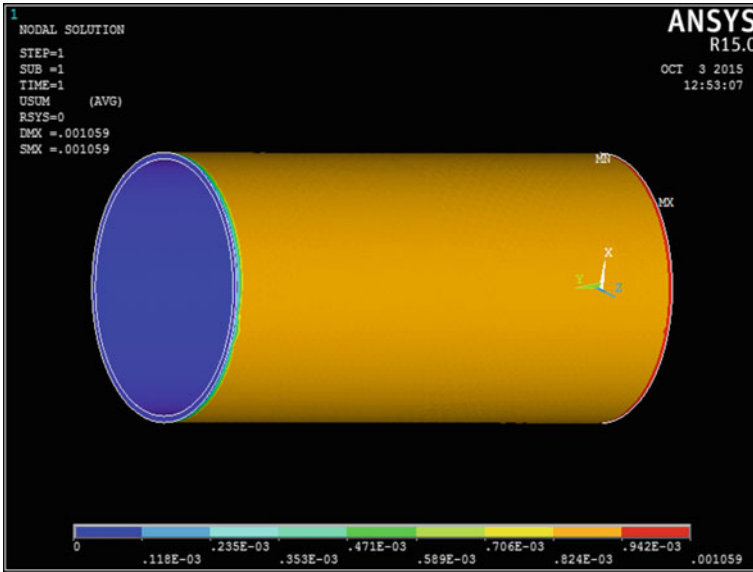


Fig. 16 Displacement

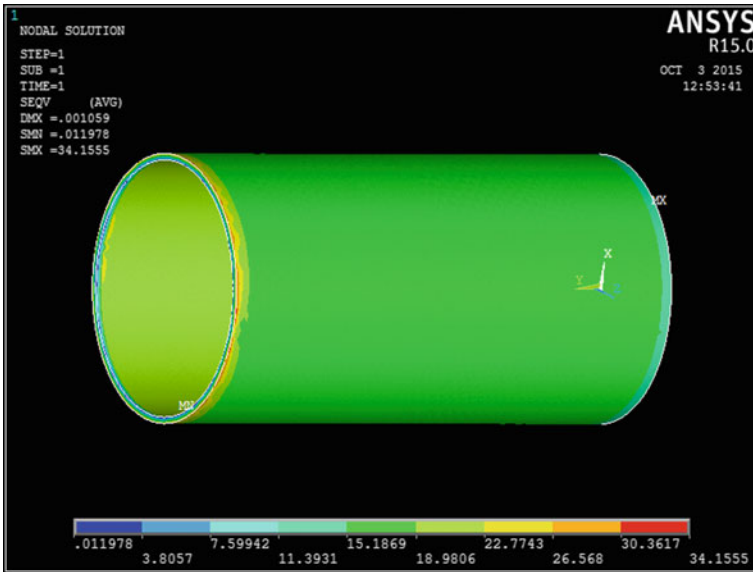
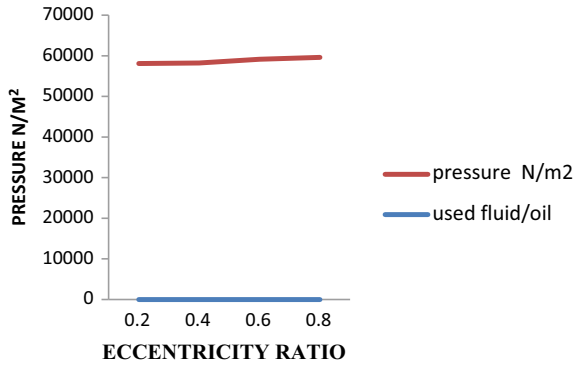


Fig. 17 Stress

**Graph. 1** Castor oil for different L/D ratios



displacement value surges for bronze material for different L/D ratios from 2.0, 2.1, 2.2, 2.3 and 2.4 and same oddness values of 0.8, the displacement are to be 0.0098, 0.01, 0.01, 0.01 and 0.014 m and stresses are to be 29.24, 29.68, 30.36, 35.72 and 36.65 N/m<sup>2</sup>, respectively.

# To Evaluate Chassis Frequency Harmonics of Vehicles by Modal Analysis and Measurement



Nilesh Ahirrao and Santosh Bhosle

**Abstract** Dealing with increased levels of vibrations and annoying noise is a major task in front of today's automotive industry. Uncontrolled vibrations lead to the damage of the vehicle systems. The impact due to large force transmissions introduces large values of unbalanced forces and eventually large stress values. Computational tools are indeed beneficial in resolving the issues through modeling and simulation. Advanced design techniques uses different software and programming methods to evaluate the problems at design stages itself. Harmonic analysis is very critical in the design stages as well as in the operative stages. The unevenness on roads, like speed breakers cause excessive vibrations and uncontrolled dynamics in a vehicle. This paper illustrates the harmonic determination for a vehicle through modal analysis. Modal analysis enhances the capability in determining the modes of vibrations along with frequencies at which these modes occur. The results from modal analysis are compared with the measured values from FFT analyzer. Results from these efforts are discussed, which shows the effectiveness of modal analysis and vibration measurement. Significant reduction in failures of vehicles on roads due to excessive deflections at high vibrating frequencies is a major task. This paper contributes in addressing the issues related to analyzing the vibration levels of vehicle chassis on road surface conditions.

**Keywords** Harmonics · Frequency · Modal · Vibrations · Vehicles

## 1 Introduction

To reduce the unwanted failures and distractive sound levels in vehicles is a major issue related to driving quality and comforts for human beings. It is important to identify the significant cause for such unwanted vibrations and discomforts. To calculate

---

N. Ahirrao (✉) · S. Bhosle

Department of Mechanical Engineering, Maharashtra Institute of Technology, Aurangabad, India  
e-mail: [nileshahirrao15@gmail.com](mailto:nileshahirrao15@gmail.com)

S. Bhosle

e-mail: [spbhosle2001@gmail.com](mailto:spbhosle2001@gmail.com)

© Springer Nature Singapore Pte Ltd. 2020

G. S. V. L. Narasimham et al. (eds.), *Recent Trends in Mechanical Engineering*,

Lecture Notes in Mechanical Engineering,

[https://doi.org/10.1007/978-981-15-1124-0\\_59](https://doi.org/10.1007/978-981-15-1124-0_59)

the unbalanced component of forces in driving conditions is always a tedious task for designers. For Vehicle models, the instability of parameters is always a major concern. On board vibration measurement techniques are very critical in vehicle design and maintenance. For vibration analysis, it is very convenient to indulge in frequency domain. On the contrary it is not so recommended to get involve with time domain. Very high level of confusing signal is available with time domain spectrums. In frequency analysis the amplitude against the time signals is converted to one of amplitude against frequency. This is possible for all types of measured signals in vehicles in majority of chassis point locations [1, 2]. The vibration amplitudes may be displacements, velocities and accelerations. Torsional Vibrations are also very important in measurement and analysis of vibrations in many structures. Modal frequency calibration is very effective in chassis vibration calculations and diagnosis. The very significant role of frequency analysis is to provide high quality information and data about a vehicle from its vibration signals. Vehicles travelling on irregularities produce bouncing and pitching effects. When one wheel is lifted or drops, jumping action occurs. The vehicle lifts to one side which is highly uncomfortable to driver and other passengers. It also reduces the wheel-road adhesion. In addition to these, wheel wobble occurs which is highly dangerous [3–5].

Vibrating panels in a vehicle causes noise levels in a vehicle. We are in the era of modernization of vehicles. A significant fact about all modern cars and other vehicles is that these vehicles are designed in such a fashion that their rigidity mainly comes from platform chassis. Inertial effects like longitudinal speed and rolling plays vital role in stability of a vehicle, provided by chassis. Rigidity does not rely on upper framework of window and door pillars, quarter panels, and windscreen rails. These upper body components are becoming more and more slender. The vehicle main body and frame are mounted on front and rear axles, through springs and shock absorbers. This arrangement is very important for damping purpose. It is expected that suspension system allows minimum amount of shocks getting transmitted to the chassis by the wheels when they roll over on uneven road surfaces. Modeling of such rolling action is very critical to see the amplitude of vibrations against frequency. FFT analyzer along with accelerometer can be effectively used for vibration measurement of a model [6–9]. When shocks are transmitted to the chassis, it creates discomfort to the passengers and driver. Natural frequencies for the inertial structural elements results in many problems. So it is very important to identify these frequencies. Modeling and simulation of a vehicle model along with specific experimental parameters are important for optimized output results. The parameters like mass and structural uncertainties along with and nonlinear parameters plays significant role in evaluating the natural frequencies and modes of vibrations [10–12]. Uneven road conditions are responsible for jerks to passengers. Modeling of vibrating elements is very important in reducing vibration and noise levels. In the conditions of cornering and pitching, the front wheels are lifted or dropped with respect to rear wheels. Pitching also occurs when the vehicle is accelerating or braking. These conditions give very uncomfortable ride to the passengers, as well as high stresses in the vehicle chassis. Vertical movement causes change in moment of inertia for a vehicle. Effective isolating systems are needed to make these vibrations to nullify [13–15].

Random unevenness in road profile and vehicle performance on such surface needs to be evaluated. Resonance is a drastic condition for high level of amplitudes of vibration. In this high amplitude of vibration, stresses may exceed the permissible limits. Rigidity of chassis system is vital in this situation. So, it is very important to predict the resonant conditions for a vehicle chassis. Finite element method identifies the local defects in chassis frame and modal analysis is useful for detecting the frequency ranges of vibrating chassis along with deformations and amplitude of vibrations [16–19].

## 2 Modal Analysis

We consider movement of a vehicle on uneven road surface like speed breakers, which results in pitching and cornering of a chassis. In such a dynamic situation, the system becomes time-dependent. Modal analysis is a way by which we can calculate the natural frequencies of the vibrating chassis. Modal analysis tells us the resonance frequencies of vehicle depending upon geometry of a vehicle.

### 2.1 Hypothesis in Modal Analysis

- We will start with the least value of frequency. The next step is to select the last frequency we want to stop searching.
- It is important to find the resonance frequencies which are in a certain range of operations. A mode superposition method is primarily used for harmonic analysis, which will give the results faster.

### 2.2 Procedure for Modal Analysis in ANSYS and Test-Model Specifications

Foremost step is to attach geometry, then assigning the material properties. Second step is to define the contact regions. Third step is to define mesh controls which is optional. Fourth step is to include the supports. Fifth step is to request for harmonic analysis. Sixth step is to set harmonic analysis options. Final stage is to solve and to review the results.

### 2.3 Test-Model Specifications for Chassis Structure

The major properties and dimensions of a chassis model are shown in Table 1.

**Table 1** Chassis model specifications

Material properties	Values for structural steel
Young's modulus	2e+005 N/mm <sup>2</sup>
Yield stress	250 N/mm <sup>2</sup>
Ultimate stress	460 N/mm <sup>2</sup>
Model dimensions	X:807 mm; Y:500 mm; Z:233.2 mm
Model volume	4.374e+006 mm <sup>3</sup>

### 3 Results—Modal Analysis

The frequencies and deformation values for six modes of vibrations are evaluated in modal analysis. Table 2 shows the frequency values and deformation for all six modes of vibration.

#### 3.1 Deformation for First Mode at 94.663 Hz—Maximum 14.349 mm

See Fig. 1. The highest value of deformation at 94.663 Hz frequency is 14.349 mm in first mode of chassis vibration. This is vertical displacement for first mode. Figure 1 illustrates this deformation in first mode of chassis vibration.

#### 3.2 Deformation for Second Mode at 126.45 Hz—Maximum 15.317 mm

See Fig. 2. The highest value of deformation at 126.45 Hz frequency is 15.317 mm, which is the second mode of chassis vibration. This is also the vertical movement for second mode. Figure 2 illustrates this deformation of chassis model in second mode of vibration.

**Table 2** Frequency and maximum deformation values for different modes

Sr. No	Modes of vibrations	Frequencies (Hz)	Deformations (mm)
1	First mode	94.663	14.349
2	Second mode	126.45	15.317
3	Third mode	126.48	18.696
4	Fourth mode	130.37	16.444
5	Fifth mode	137.61	12.315
6	Sixth mode	150.5	19.075

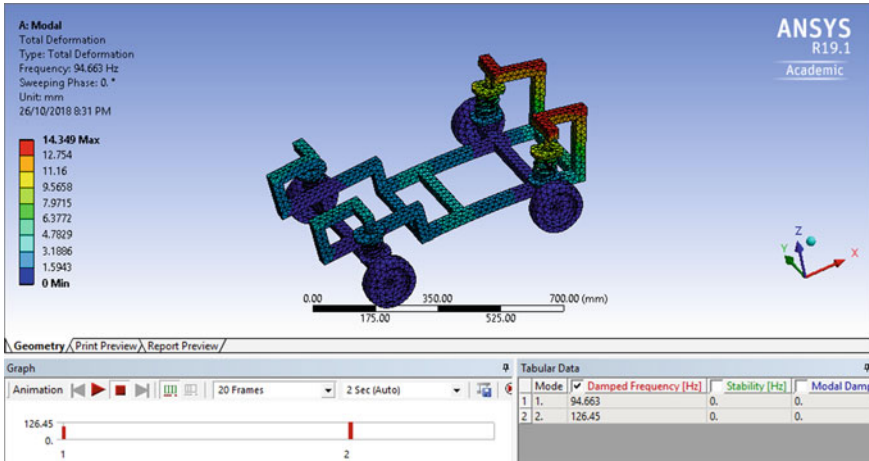


Fig. 1 First mode shape for chassis model vibrations

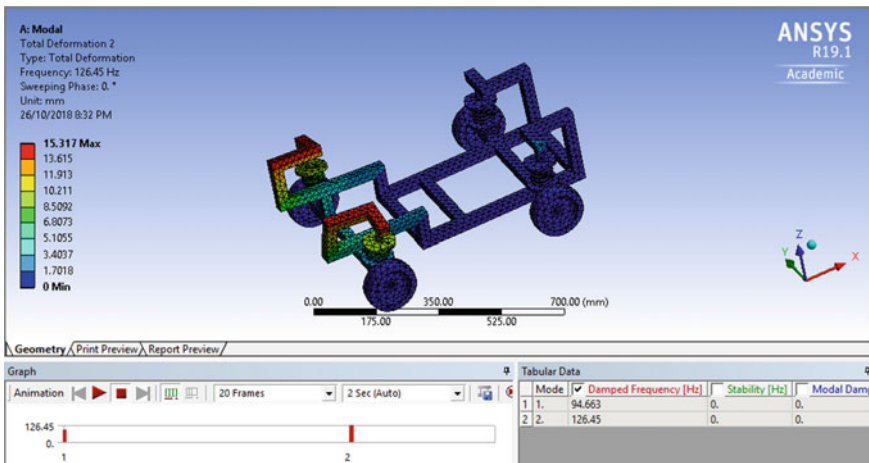


Fig. 2 Second mode shape for chassis model vibrations

### 3.3 Harmonic Analysis of Chassis Model for a Frequency Range 0–100 Hz

See Fig. 3. The harmonic analysis for the narrow range of frequencies 0–100 Hz is done and the results are shown in Fig. 3.



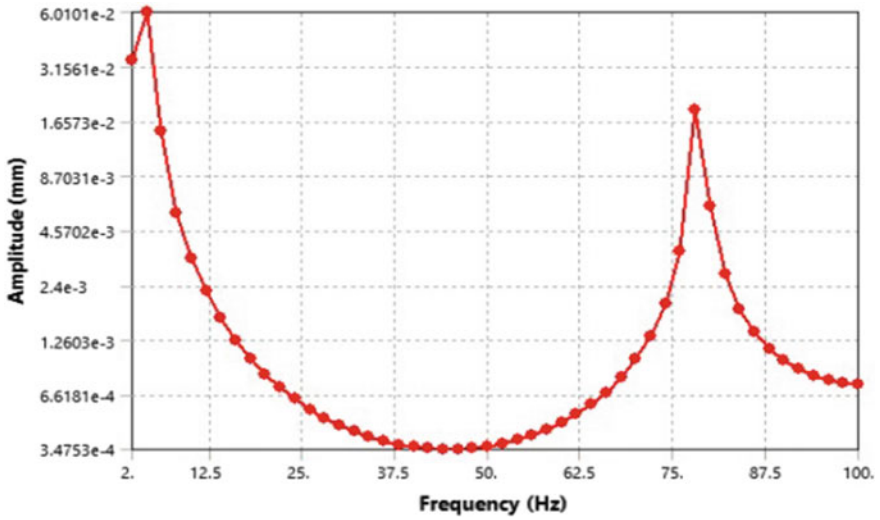


Fig. 3 Harmonic response for 0–100 Hz

### 3.4 Harmonic Analysis of Chassis Model for a Frequency Range 0–200 Hz

See Fig. 4. A frequency range of 0–200 Hz is selected for harmonic analysis and the results are shown in Fig. 4. Major modes of vibrations are covered in this range of frequencies.

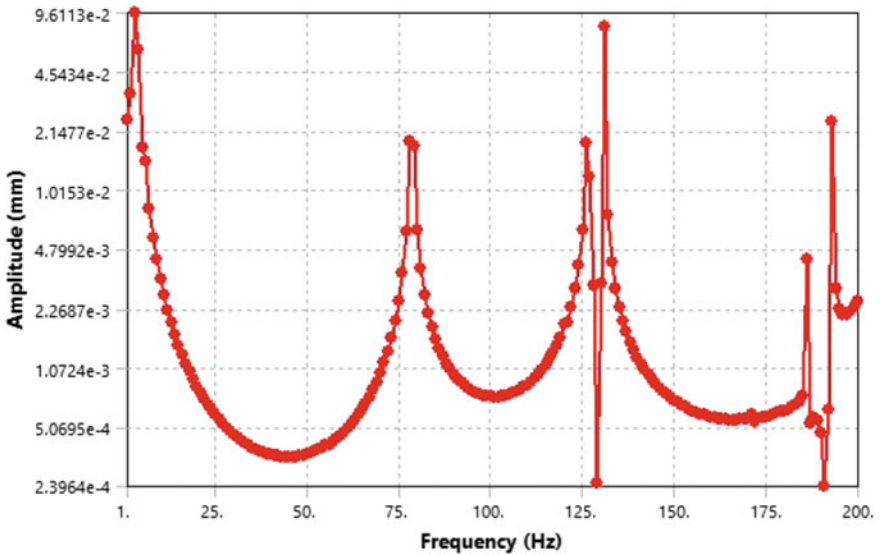


Fig. 4 Harmonic response for 0–200 Hz

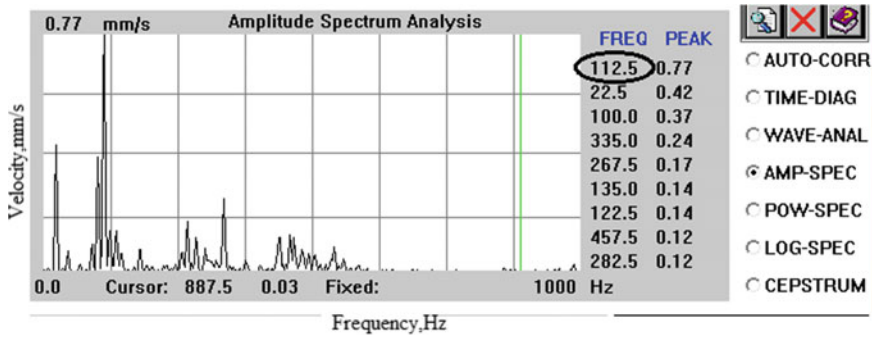


Fig. 5 Frequency value by FFT analyzer

### 4 Experimental Results—Vibration Measurement

A chassis model is built with steel material with the same specifications as given in Table 1. This chassis model is run on a track having some irregularities like speed breakers. FFT Analyzer with accelerometer is used to measure the vibration levels on the chassis frame. The results are shown in Fig. 5. The first two peaks are significant and the value for maximum vibration level is 0.77 mm/s, which is for a frequency of 112.5 Hz.

### 5 Discussion

Table 2 provides the values of frequencies and deformation for all six modes of vibration through modal analysis for a chassis model. The first two mode shapes are obtained at 94.663 Hz and at 126.45 Hz. Figures 1 and 2 represents the two mode shapes along with deformation values. In modal analysis, we have to fix the frequency range of operation. Figure 3 represents harmonic analysis for a frequency range of 0–100 Hz. In this range only first mode of 94.663 Hz is accompanied. We did not achieve the second and consecutive modes in this range. Figure 4 represents harmonic analysis for a frequency range of 0–200 Hz. In this range second mode of 126.45 Hz is also accompanied along with other consecutive frequency values. Figure 5 shows the measured vibration value for chassis model, which is maximum for a frequency of 112.5 Hz. This value is falling beyond the first frequency range of 0–100 Hz. Therefore it indicates that the proper frequency range for modal analysis in this case of a chassis model should be 0–200 Hz.

## 6 Conclusion

This paper describes a method for harmonic modal analysis in case of chassis model which are built with known geometric and material specifications. In this paper, we used structural steel as a material for chassis model. The primary purpose of modal analysis is to find the modes of vibrations and the frequencies at which these occur. As important always, the initial frequency is very critical for observations. We will start with the least value of frequency and the next step is to select the last frequency value, to get a range of frequencies for analysis. It is always important in relation to time saving, and effectiveness, we should not search the full frequency spectrum. But it is important to find the resonance frequencies which are in a certain range of operations. Through vibration measurement on test model we can exactly predict the maximum range of frequency value. It will save the crucial time of calculations and also increases accuracies for further design calculations. We also conclude that minimum two modes of vibrations are important in modal analysis for chassis models. This procedure helps in evaluating proper harmonic frequencies at the design stage itself, which is very important to fix the mass and stiffness properties. Eventually the material selection procedure also gets benefitted with modal analysis. This paper thus describes the significance of modal analysis and vibration measurement for evaluating chassis harmonics.

**Acknowledgements** We are thankful to all the authors of paper we cited in our work. We are also thankful to ANSYS software solution co. for evaluation version.

## References

1. Mannering F (2018) Temporal instability and the analysis of highway accident data. *Anal Methods Accid Res* 17:1–13
2. Cha PD, Buyco K (2015) An efficient method for tuning oscillator parameters in order to impose nodes on a linear structure excited by multiple harmonics. *J Vib Acoust* 137/031018-1
3. Binglin LV, Ouyang H, Li W, Shuai Z, Wang G (2016) An indirect torsional vibration receptance measurement method for shaft structures. *J Sound Vib* 372:11–30 (2016)
4. Wang L, Zhang N, Haiping D (2015) Real time identification of vehicle motion-modes using neural networks. *Mech Syst Signal Process* 50–51:632–645
5. Wedig WV (2016) New resonances & velocity jumps in nonlinear road-vehicle dynamics. In: *Procedia IUTAM symposium analytical method in nonlinear dynamics*, vol 19. Elsevier, pp 209–218
6. Yuksel E, Kamci G, Basdogan I (2012) Vibro-acoustic design optimization study to improve the sound pressure level inside the passenger cabin. *J Vib Acoust* 134/061017:1–9
7. Jihan R, Christian Gerdes J (2004) Integrating inertial sensors with global positioning system (GPS) for vehicle dynamics control. *J Dyn Syst Meas Control* 126:243–254
8. Lin CW, Yang YB (2005) Use of a passing vehicle to scan the fundamental bridge frequencies: an experimental verification. *Eng Struct* 27:1865–1878
9. De Moerloozee K, Al-Bender F, Van Brussel H (2011) Modeling of the dynamic behaviour of system with rolling elements. *Int J Non-Linear Mech* 46:222–233

10. Borboni A, Lancini M (2015) Commanded motion optimization to reduce residual vibration. *J Vib Acoust* 137/031016:1–8
11. Butz T, Simeon B, Stadler M (2010) Optimal design of experiments for estimating parameters of a vehicle dynamics simulation model. *J Comput Nonlinear Dyn* 5/031011:1–7 (2010)
12. Karpel M, Moulin B, Feldgun V (2007) Component mode synthesis of a vehicle system model using the fictitious mass method. *J Vib Acoust* 129:73–83
13. Nishimura K, Terumichi Y, Morimura T, Sogabe K (2009) Development of vehicle dynamics simulation for safety analyses of rail vehicles on excited tracks. *J Comput Nonlinear Dyn* 4/011001:1–9
14. Benaziz M, Nacivet S, Thouverez F (2015) A shock absorber model for structure-borne noise analyses. *J Sound Vib* 349:177–194
15. Tongyi X, Liang M, Li C, Yang S (2015) Design and analysis of a shock absorber with variable moment of inertia for passive vehicle suspensions. *J Sound Vib* 355:66–85
16. Schiehlen W, Iroz I (2015) Uncertainties in road vehicle suspensions. In: IUTAM symposium on dynamics analysis of multibody systems with design uncertainties, *procedia IUTAM* vol 13, pp 151–159 (2015)
17. Heydinger GJ, Salaani MK, Garrott WR, Grygier PA (2002) Vehicle dynamics modeling for the national advanced driving simulator. *Proc Inst Mech Eng Part D J Automob Eng, Spec Issue Pepper* 216:307–317
18. O'Hara PJ, Hollkamp JJ (2014) Modeling vibratory damage with reduced- order models and the generalized finite element method. *J Sound Vib* 333:6637–6650
19. Galluzzi R, Tonoli A, Amati N (2015) Modeling, control and validation of electro hydrostatic shock absorbers. *J Vib Acoust* 137/011012-1

# Analysis of Internal Damping in Rotating Shaft



K. Raju, M. Ravindra Gandhi, Rajasekhar Vangala and N. Suresh

**Abstract** In most of the applications of vibration compared to the elastic and inertia forces, the magnitude of damping forces is small. Under certain circumstances, these small forces may, however, create great influence. Damping is one of the important parameters in the study of dynamic systems. It is generally measured under conditions of cyclic motion and is defined as the energy dissipation in a mechanical system whose free oscillations decrease with time, resulting in a decrease in its amplitude of vibration. From a theoretical point of view, there are two different methods to measure damping, i.e., time response methods and frequency response methods. In rotating machinery, the measurement of damping by applying time response methods and frequency response methods is very difficult. Due to that reason, there is a lack of experiments to measure damping in rotating machinery. This paper discussed Kelvin–Voigt approach for measuring damping in mechanical systems. The mechanical system analyzed in this thesis is a rotating shaft. In general, damping can be explicit through different parameters as damping ratio ( $\zeta$ ) or loss factor ( $\eta$ ). Therefore, the objective about this paper is to determine one of these parameters by means of measuring simple variables such as forces or displacements.

**Keywords** Kelvin–Voigt model · Viscoelastic material · Internal damping

---

K. Raju (✉) · M. R. Gandhi · R. Vangala · N. Suresh  
Department of Mechanical Engineering, Geethanjali College of Engineering & Technology,  
Hyderabad 501301, Telangana, India  
e-mail: [kunchala324@gmail.com](mailto:kunchala324@gmail.com)

M. R. Gandhi  
e-mail: [mails4gandhi@gmail.com](mailto:mails4gandhi@gmail.com)

R. Vangala  
e-mail: [rajasekhar4v@gmail.com](mailto:rajasekhar4v@gmail.com)

N. Suresh  
e-mail: [351Suresh@gmail.com](mailto:351Suresh@gmail.com)

# 1 Methodology

The concept about this project is to determine the damping factor (loss factor ( $\eta$ )) by using simple variables such as force (or) moment. For that, a new methodology is developed and this can be splitted in three steps which are stated as below:

- Step 1:** Relating moments (or) forces with viscosity.
- Step 2:** Relating viscosity with loss factor.
- Step 3:** Relating moments (or) forces with loss factor.

## 1.1 Methodology Implementation

For implementing the above methodology, consider a rotating shaft of simply supported which is subjected to constant central load (see Fig. 1). Assume the shaft is made up of viscoelastic material.

Viscoelastic materials show simultaneously a viscous and an elastic behavior. Different models can represent viscoelastic materials; however, in this project, the Kelvin–Voigt model will only be considered. This model represents the behavior of viscoelastic material by means of a dashpot and a spring as shown in Fig. 2.

In order to have the same deformation, the dashpot constrains the spring. The Kelvin–Voigt model is expressed mathematically by the following expression:

$$\sigma = E\varepsilon + \gamma \frac{d\varepsilon}{dt} \tag{1}$$

where

- $\sigma$  = Stress,
- $E$  = Young’s modulus,
- $\varepsilon$  = Stress, and
- $\gamma$  = Viscosity

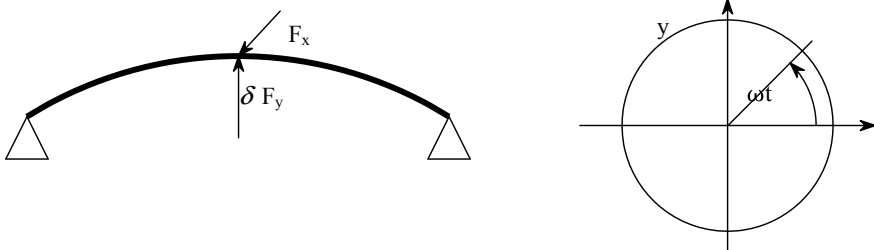
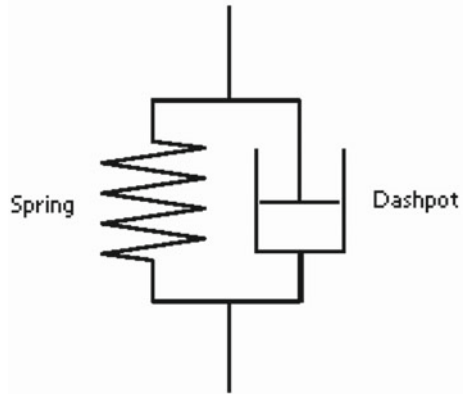


**Fig. 1** Moments and forces

**Fig. 2** Dashpot and a spring



**Step 1: Relating Moments (or) Forces with Viscosity.**

In this analysis, the shaft must be kept in a constant deformed position ( $\delta$ ) as shown in Fig. 1, and is rotating with the angular velocity. The strain at any point will change by the following expression:

$$\varepsilon(r, t) = \frac{\varepsilon_{\max}}{R} \cdot r \cdot \sin(\omega t) \tag{2}$$

where

$R$  = Shaft radius

$r$  = Distance between the point and its center of section

$t$  = Time

$\omega$  = Rotating frequency

$\varepsilon_{\max}$  = Maximum strain

On deriving Eq. (2), the strain rate is obtained, which induces a stationary stress state similar to the bending stress state but is rotated 90°. Equation (3) explicits the strain rate:

$$\frac{d}{dt} \varepsilon(r, t) = \frac{\varepsilon_{\max}}{R} \cdot r \cdot \omega \cdot \cos(\omega t) \tag{3}$$

On the other side, from the following expression, the bending moment about  $x$  can be calculated:

$$M_x = \int_{-R}^R \int_{-\sqrt{R^2-x^2}}^{\sqrt{R^2-x^2}} \frac{\sigma_{\text{Max}} \cdot y}{R} \cdot y \cdot dy \cdot dx \tag{4}$$

The result of the integration is

$$M_x = \frac{\sigma_{Max} \cdot R^3 \cdot \pi}{4} \tag{5}$$

$M_x$  can also be expressed through the following equation:

$$M_x = \frac{\sigma_{y.Max} \cdot R^3 \cdot \pi}{4} \tag{6}$$

Assuming that

$$\sigma = \sigma_x + \sigma_y \tag{7}$$

Then, it would be concluded that  $M_x$  is found as follows:

$$M_x = \frac{E \cdot \epsilon_{Max} \cdot R^3 \cdot \pi}{4} \tag{7a}$$

In the similar way than with  $M_x$ , it is possible to obtain  $M_y$ :

$$M_y = \int_{-R}^R \int_{-\sqrt{R^2-y^2}}^{\sqrt{R^2-y^2}} \frac{\sigma_{Max} \cdot x}{R} \cdot x \cdot dy \cdot dx \tag{8}$$

The result of the integration is

$$M_y = \frac{\sigma_{Max} \cdot R^3 \cdot \pi}{4} \tag{9}$$

Equation (9) can be expressed just as Eq. (10) which is shown below:

$$M_y = \frac{\sigma_{Xmax} \cdot R^3 \cdot \pi}{4} \tag{10}$$

On substituting Kelvin–Voigt model Eq. (1) in the place of  $\sigma_{Xmax}$  of above equation, we get

$$M_y = \frac{\gamma \cdot R^3 \cdot \pi}{4} \frac{d}{dt}(\epsilon_{max}) \tag{11}$$

At this point, the above expression relates a moment with the viscosity which has been obtained.



**Step 2: Relating Viscosity with Loss Factor ( $\eta$ ).**

It will be used by the complex modulus to relate both parameters. As it has been mentioned above, viscoelastic materials show simultaneously a viscous and an elastic behavior. It means that must be represented their modulus by a complex quantity, which possesses components both dissipative and stored energy. This can be expressed about complex modulus in different ways depending on the model used to depict the system. On one hand, the hysteretic model defines through the following expression about the complex modulus:

$$E^* = E(1 + i\eta) = E + i \cdot \eta \cdot E \tag{12}$$

On the other hand, the hysteretic model can also be applied when a material is subjected to cyclic loading. In this case, it is required to assume that both the time histories of the stress cycles and the history of the deformation are harmonic. Moreover, the strain will be delayed in time by a phase angle  $\phi$ , which is considered independent from the frequency. Under these conditions, the strain and strain rate, and time histories of stress can be expressed as follows:

$$\varepsilon = \varepsilon_o \cdot \cos(\omega t - \phi) = \varepsilon_o \cdot e^{-i\phi} \cdot e^{i\omega t} \tag{13}$$

$$\sigma = \sigma_o \cdot \cos(\omega t) = \sigma_o \cdot e^{i\omega t} \tag{14}$$

$$\frac{d}{dt}(\varepsilon) = \varepsilon_o \cdot e^{-i\phi} \cdot e^{i\omega t} \cdot i \cdot \omega \tag{15}$$

where

$\omega$  = Cyclic loading frequency

$t$  = Time

$\phi$  = Phase angle

$\sigma_o$  = Maximum stress

$\varepsilon_o$  = Maximum strain

The complex modulus relates stress and strain according to the following expression:

$$E^* = \frac{\sigma}{\varepsilon} \tag{16}$$

By introducing Eqs. (13) and (14) into Eq. (16), the following expression is obtained for the complex modulus:

$$E^* = \frac{\sigma}{\varepsilon_o \cdot e^{-i\phi}} \tag{17}$$

Now, it is required to relate  $\sigma_o$  with  $\varepsilon_o$ , and by introducing Eqs. (14) and (15) into Eq. (2), the following equation is obtained:

$$\sigma = E(\varepsilon_o \cdot e^{-i\phi} \cdot e^{i\omega t}) + \gamma \cdot e^{-i\phi} \cdot e^{i\omega t} \cdot i \cdot \omega \quad (18)$$

As Eqs. (13) and (18) define the same parameter—stress—it is possible to state that

$$E(\varepsilon_o \cdot e^{-i\phi} \cdot e^{i\omega t}) + \gamma \cdot e^{-i\phi} \cdot e^{i\omega t} \cdot i \cdot \omega = \sigma_o \cdot e^{i\omega t} \quad (19)$$

Consequently,  $\sigma_o$  can be expressed through the following expression:

$$\sigma_o = \varepsilon_o \cdot e^{-i\phi} \cdot (E + i\omega\gamma) \quad (20)$$

If Eq. (20) is introduced into Eq. (17), an equation is obtained, which gives the complex modulus:

$$E^* = E + i \cdot \gamma \cdot \omega \quad (21)$$

If Eqs. (12) and (21) are compared, it is possible to assert that:

$$\gamma \cdot \omega = E \cdot \eta \quad (22)$$

Therefore, viscosity can be expressed in the following equation:

$$\gamma = \frac{E \cdot \eta}{\omega} \quad (23)$$

The equation is interesting because it shows that viscosity depends on the frequency. It also relates viscosity with loss factor.

### **Step 3: Relating Moments (or) Forces with Loss Factor.**

After relating the viscosity with the loss factor ( $\eta$ ), the last step would be to relate the loss factor ( $\eta$ ) with a force instead of a moment because measuring moments can be more complicated than measuring forces.

At this point, it would be possible to express  $M_y$  as function of the loss factor ( $\eta$ ) by introducing Eq. (23) into Eq. (11).

$$M_y = \frac{E \cdot \eta}{4 \cdot \omega} \cdot \frac{d}{dt}(\varepsilon_{\max}) \cdot R^3 \cdot \pi \quad (24)$$

Applying the solid mechanics theory to the shaft shown in Fig. 1, it is required to state that

$$F_x = \frac{4 \cdot M_y}{L} \quad (25)$$

$$F_y = \frac{4.M_x}{L} \quad (26)$$

where  $L$  is the length of the shaft.

One of the parameters of Eq. (24),  $\varepsilon_{\max}$  is unknown; hence, it is necessary to determine it. It is workable to express  $\varepsilon_{\max}$  as function of  $F_y$ .

The value of  $F_y$  is known because it is the force that is introduced to keep about the shaft in a constant.

Deformed position ( $\delta$ ). Introducing Eq. (7a) into Eq. (26), the next expression can be obtained as follows:

$$\frac{1}{4}E.\varepsilon_{\max}.R^3.\pi = \frac{L}{4}.F_y \quad (27)$$

By working out the value of  $\varepsilon_{\max}$  from Eq. (27), the following equation is obtained:

$$\varepsilon_{\max} = \frac{L.F_y}{E.R^3.\pi} \quad (28)$$

Now, relate the loss factor ( $\eta$ ) with the parameters that are known or that can be easily measured. By introducing Eq. (24) into Eq. (25), the following equation is obtained:

$$F_x = \frac{4.E.\eta}{L.4.\omega} \frac{d}{dt}(\varepsilon_{\max}).R^3.\pi \quad (29)$$

If Eq. (28) is introduced into Eq. (3),  $\frac{d}{dt}(\varepsilon_{\max})$  is expressed through the following:

$$\frac{d}{dt}(\varepsilon_{\max}) = \frac{L.F_y}{E.R^3.\pi.R} .r.\omega. \cos(\omega t) \quad (30)$$

Thus,  $F_x$  can be expressed through the following equation:

$$F_x = \frac{4.E.\eta}{L.4.\omega} \frac{L.F_y}{E.R^4.\pi} r.\omega. \cos(\omega t).R^3.\pi \quad (31)$$

By simplifying Eq. (31), the following equation is obtained:

$$F_x = \frac{r}{R} F_y.\eta. \cos(\omega t) \quad (32)$$

As  $F_x$  and  $F_y$  will be measured in the shaft outer part, it is required to state that

$$F_x = F_y.\eta. \cos(\omega t) \quad (33)$$

As the value of  $F_x$  is fluctuating in time, it is possible to assert that the maximum value of  $F_x$  is given by the following equation:

$$F_x = F_y \cdot \eta \quad (34)$$

As a result, the loss factor ( $\eta$ ) may be calculated as function of  $F_y$  and the  $F_x$  maximum value:

$$\eta = \frac{F_x}{F_y} \quad (35)$$

On substituting  $F_x$  value and  $F_y$  value in the equation, we get

$$\eta = \frac{\gamma r \omega \cos(\omega t)}{R E}$$

## 2 Results and Discussions

In this chapter, it may be concluded that the expression which is derived is performed by using MATLAB code. The graphs were drawn between loss factor and parameters ( $R, \omega, r, t$ ) in the derived expression. When the shaft was rotating and constant center loads are acting at the shaft middle portion, the vibrations are obtained in the shaft, and to reduce the amplitude of vibrations some amount of energy is liberated from the shaft t. The energy loss is represented in the analytical form. By varying any one of the parameters ( $R, \omega, r, t$ ) in the derived expression and keeping remaining parameters constant. The input parameters were shown in Table 1.

### 2.1 Loss Factor Versus Radius of the Shaft

Figure 1 shows the variation of loss factor with radius of the shaft. From the figure, it is observed that if the radius of the shaft is increasing, loss factor (energy dissipation) decreases. Because if the radius of the shaft is increased, self-weight of the shaft is

**Table 1** Input data

Young's modulus ( $E$ ) of steel	$2.1 \times 10^5$ N/mm <sup>2</sup>
Viscosity of steel	49 N s/mm
Radius ( $R$ ) of the shaft (mm)	12, 15, 18, 21
Speed of the shaft ( $N$ ) (rpm)	480, 520, 630, 720
Frequency of the shaft (Hz)	31.49, 40.84, 43.98, 54.45
Distance of the point to the center of section ( $r$ ) (mm)	3, 4, 5
Time ( $t$ ) (s)	60, 120, 180, 220

**Table 2** Representation of shaft radius and loss factor

Shaft radius (mm)	Loss factor ( $\eta$ )
12	$2.128 \times 10^{-4}$
15	$1.702 \times 10^{-4}$
18	$1.418 \times 10^{-4}$
21	$1.216 \times 10^{-4}$

**Table 3** Representation of shaft frequency and loss factor

Frequency	Loss factor ( $\eta$ )
31.41	0.0002
40.84	0.0011
43.98	0.0025
54.45	0.0038

also increased, and due to this the vibrations obtained were low initially and to avoid these vibrations, the energy liberated is also low. From Table 2, it is observed that is the loss factor values are obtained less than one, it results in underdamping and due to underdamping the amplitude of vibration is reduced gradually. If loss factor values are equal to one or greater than one, the vibrations are produced continuously in the system and cannot be controlled due to this system failure which has occurred.

### 2.2 Loss Factor Versus Frequency of the Shaft

Figure 4 shows variation of loss factor with frequency of the shaft, and from the figure it is observed that if the frequency of the shaft increases, loss factor also increases because when the speed of the shaft increases, vibrations produced in the shaft also increases, and to reduce these vibrations the energy liberated from the shaft also increases. From Table 3, it is observed that by changing the frequency of the shaft, the loss factor values which are obtained are less than one. The damping which has occurred is underdamped.

### 2.3 Loss Factor Versus Distance of the Point from the Center of Section

Figure 5 shows the loss factor with distance of the point from the center of the section. From the figure, it is observed that if the distance of the point from the center of the section increases, loss factor also increases because the summation of all the energy from all the points liberated from the shaft can reduce the vibration of the shaft. From Table 4, it is observed that all the loss factor values which are obtained are less than

**Table 4** Representation of loss factor and distance of the point from the center of section

Distance of the point from the center of section ( $r$ ) (mm)	Loss factor ( $\eta$ )
3	$1.172 \times 10^{-4}$
4	$2.296 \times 10^{-4}$
5	$2.871 \times 10^{-4}$

**Table 5** Representation loss factor and time

Time ( $t$ )	Loss factor ( $\eta$ )
60	$2.213 \times 10^{-4}$
120	$5.321 \times 10^{-4}$
180	$8.315 \times 10^{-4}$
240	$11.214 \times 10^{-4}$

one, and it represents under damping, and due to this the amplitude of vibration is reduced gradually. If the loss factor values are equal to one or greater than one, the vibrations were produced in the system continuously and cannot be controlled, and due to this, system failure can occur.

## 2.4 Loss Factor Versus Time

Figure 6 shows variation of loss factor with time, and from the graph, it is observed that with the change in the time, the value of loss factor (energy dissipation) also changes. Vibrations obtained in the shaft increase with time. The energy dissipation also increases with time to reduce the vibration of the shaft.

From Table 5, it is observed that all the loss factor values which are obtained are less than one, and it shows underdamping, and due to this the amplitude of vibration is reduced gradually. If the loss factor values are equal to one or greater than one, the vibrations were produced in the shaft continuously and cannot be controlled and due to this system failure occur.

## 3 Conclusion

The thesis of the objective is to determine the loss factor ( $\eta$ ) by using simple variables such as forces (or) moment and for that a new theoretical methodology has been developed. This can be performed in three steps which are relating moments (or) forces with viscosity, relating viscosity with loss factor, and relating moments (or) forces with loss factor.

A rotating shaft of simply supported beam with constant central load is considered for implementing the methodology. Assumption for this case as shaft is made up of viscoelastic material. There are different models to represent the behavior of viscoelastic material. In this project, Kelvin–Voigt model is considered.

Kelvin–Voigt model is expressed mathematically by the following expression:

$$\sigma = E\varepsilon + \gamma \frac{d\varepsilon}{dt}$$

where

- $\sigma$  = Stress,
- $E$  = Young’s modulus,
- $\varepsilon$  = Stress, and
- $\gamma$  = Viscosity.

The theoretical analysis indicates that it is required to measure damping according to the proposed methodology. The expression which is obtained can be accomplished using MATLAB code.

From Figs. 3, 4, 5, and 6, it is observed that the loss factor values are obtained less than one which is underdamped. From the figures, it can be identified that the amplitude of vibration was reduced gradually. Hence, the proposed methodology which is obtained is suitable for measuring damping.

To conclude the thesis from the results, it is observed that the methodology which is proposed can be used for measuring loss factor. The given methodology which is proposed depends on system of single degree of freedom. Using a multi-degree of freedom system, the results should give better and realistic results.

**Fig. 3** Loss factor versus radius of shaft

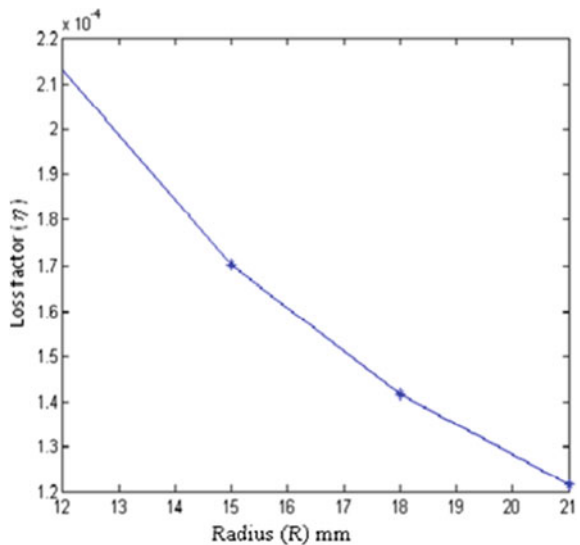


**Fig. 4** Loss factor versus shaft frequency

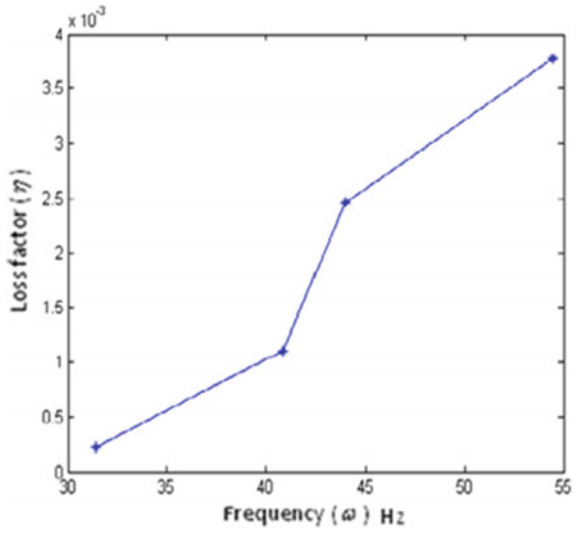


**Fig. 5** Loss factor versus distance of point of the center of section

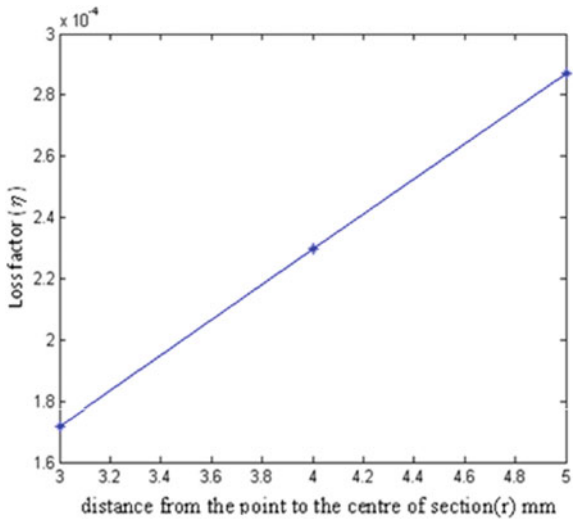
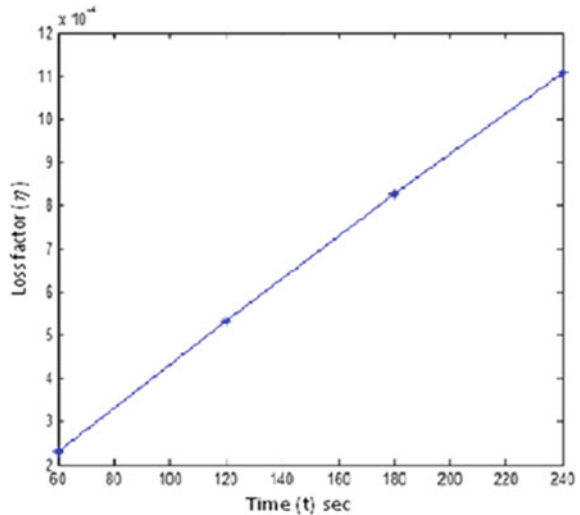




**Fig. 6** Loss factor versus time



## References

1. de Silva CW (2000) *Vibration: fundamentals and practice*. CRC Press, Boca Raton
2. Adhikari S (1998) *Energy dissipation in vibrating structures*. First Year Report, Cambridge University Engineering Department, Cambridge, UK
3. Inman DJ (2001) *Engineering vibration*. Prentice Hall, Upper Saddle River, New Jersey
4. Genta Giancarlo (1993) *Vibration of structures and machines*. Maple-Vail Book Manufacturing Group, York, PA
5. Bert CW (1973) Material damping: an introductory review of mathematical measures and experimental techniques. *J Sound Vib* 29(2):129–153
6. Chopra Anil K (1995) *Dynamics of structures*. Prentice Hall, New Jersey
7. Dukkupati RV. *Mechanical vibrations*. Alpha Science International Ltd.
8. Grover GK. *Mechanical vibrations*. Nemchand and Sons
9. Rao SS, Gupta K. *Theory and practice of mechanical vibrations*. Wiley Eastern Ltd.
10. [http://www.roushind.com/news\\_downloads/white\\_papers/Insight.pdf](http://www.roushind.com/news_downloads/white_papers/Insight.pdf) [online]
11. <http://www.mfg.mtu.edu/cyberman/machtool/machtool/vibration/damping.html> [online]

# An Overview of Harmony Search Algorithm Applied in Identical Parallel Machine Scheduling



P. Sreenivas, Shaik Khaja Peer Saheb and M. Yohan

**Abstract** Harmony Search Algorithms (HSA) is one of new meta-heuristic technique use in optimizing the parallel machine scheduling. HSA has gained much popularity in solving identical parallel machine scheduling problems such as minimizing the maximum makespan time. In HSA, a permutation-based improvisation process implemented in solving different optimization issues in the identical parallel machine scheduling. The HSA has proposed due to various characteristic advantages such as it is efficient, simple, easy and accurate. In this paper has been discussed various researcher's HSA application in identical parallel machine scheduling and summarized their conclusions.

**Keywords** Harmony search algorithm · Identical parallel machine · Meta-heuristic · Optimization

## 1 Introduction

### 1.1 Identical Parallel Machine Scheduling

This paper gives an insight of the identical parallel machine scheduling issue to minimize maximum makespan and minimizing the total tardiness. This situation arises where the completion of job or process is more and more important. This paper deals with Harmony Search algorithm (HSA) one of the popular optimization technique

---

P. Sreenivas (✉) · M. Yohan  
Department of Mechanical Engineering, JNTUA College of Engineering,  
Anantapur 515002, India  
e-mail: [sreenivas.p1616@gmail.com](mailto:sreenivas.p1616@gmail.com)

M. Yohan  
e-mail: [yohan.jntua.me@gmail.com](mailto:yohan.jntua.me@gmail.com)

S. K. P. Saheb  
KLM College of Engineering for Women's, Kadapa 516003, India  
e-mail: [skp.klmcew@gmail.com](mailto:skp.klmcew@gmail.com)

© Springer Nature Singapore Pte Ltd. 2020  
G. S. V. L. Narasimham et al. (eds.), *Recent Trends in Mechanical Engineering*,  
Lecture Notes in Mechanical Engineering,  
[https://doi.org/10.1007/978-981-15-1124-0\\_61](https://doi.org/10.1007/978-981-15-1124-0_61)

which is used in identical parallel machine scheduling. Machine scheduling plays a key role in allocating of different jobs to perform different operations for generating desired shape, form and size on variety of machines in a way which involves in minimization of tardiness, flow time, earliness and make span [1]. Graham et al. [2] made extensive study on identical parallel machine (IPM) scheduling, the IPM scheduling problem is denoted in the mathematical form as  $P||C_{\max}$  where  $P$  is identified as number of identical parallel machines and  $C_{\max}$  is denoted as maximum makespan time. The basis of the harmony search algorithm is the natural phenomena. Most of the metaheuristic techniques are motivated by the nature arrangement. For instance, the popular genetic algorithm technique introduced by the biological process, simulated annealing is based on physical annealing phenomena, ant colony optimization and tabu search algorithms are based on animal's behavior [3]. Gara-Ali et al. [4, 5] have studied and defined the order of the job processing on identical parallel machine to get optimized solution like minimum makespan and they found that this approach simple and easy to implement on identical parallel machine scheduling. Hasani et al. [6] have developed improved harmony search algorithm for scheduling identical machines their objective was to minimize the sum of the completion times. The performance of the proposed algorithm is implements to optimize parallel machine scheduling up to 250 jobs. Chen et al. [7–9] have developed a dynamic harmony search algorithm for solving identical parallel machines scheduling problems to optimize the minimize and maximum makespan. Wang et al. [10, 11] have proposed a hybrid modified global best harmony search algorithm for solving flow shop scheduling problems with objective of minimization of makespan criterion. Parioozfard et al. [12] have developed bio-geography based optimization approach for minimizing the makespan in the job shop scheduling problems. The rest of the article will give an overview of the problem description of the identical parallel machines scheduling and harmony search algorithm in the following sections. The harmony search algorithm applied in different field of engineering applications [13–15].

## 1.2 Problem Description

The identical parallel machine scheduling problem can be described as follows.

Assume that there are set of  $n$  number of jobs  $J = \{J_1, J_2, \dots, J_n\}$  and set of  $m$  identical parallel machines  $M = \{M_1, M_2, \dots, M_m\}$ . At the start time each job  $J$  becomes available for processing, and in which the machine takes up only one operation at a time on one of the  $m$  machines without any tardiness. The processing time of job  $J_i$  is represented as  $p_i$ . Each machine can process only one job at a time and there is no priority and no precedence between the jobs. The objective is to find the optimal scheduling time that i.e. minimization of makespan. Let  $S = \{S_1, S_2, \dots, S_m\}$  represents the identical parallel machine schedule, where  $S_j$  denotes the subset of jobs assigned to machines  $M_j$  with makespan time  $C_j = \sum_{i \in S_j} P_i$ . The mathematical formulation the identical parallel machine problem is given in the following Eqs. (1) to (4).

$$C_{\max} = \min \left( \max_{1 \leq j \leq m} C_j \right) = \min \left( \max_{1 \leq j \leq m} \sum_{i \in S_j} P_i \right) \tag{1}$$

Subject to

$$C_{\max} = \sum_{i=1}^n P_i \cdot x_{ij} \geq 0 \quad j = 1, 2, \dots, m \tag{2}$$

$$\sum_{j=1}^m x_{ij} = 1 \quad i = 1, 2, \dots, n \tag{3}$$

$$x_{ij} = \begin{cases} 1 & \text{if job } J_i \text{ is assigned to machine } M_j \\ 0 & \text{otherwise} \end{cases} \tag{4}$$

As Gragam et al. [2] notified in the scheduling field, the identical parallel machined scheduling problem is represented as  $P \parallel C_{\max}$ , where P is identified as number of identical parallel machines and  $C_{\max}$  is denoted as maximum makespan time and the  $C_{\max}$  is restricted value in the problem definition.

## 2 Harmony Search Algorithm (HSA)

Geem et al. [14] has proposed Harmony Search Algorithm it is a meta-heuristic algorithm and it is based on search space in musical process as jazz improvisation for better state of harmony. Harmony search algorithm has been used in various engineering application for optimizing engineering problems because of its unique advantages. One of the best qualities of Harmony search algorithm is identifying the better search space with in no time that to with high performance and accurate. However, there are few draw backs also in the Harmony search algorithm unlike in all other optimization techniques among them one common drawback is that it fails in its best while searching in numerical applications. Hence, to overcome this problem, some more research is required to utilize at its fullest extent. Mahdavi et al. [15] have studied on this issue and they have proposed new and improved search algorithm which has finer tuning characteristic of numerical technique for outperformance of search algorithm. The common input parameters in harmony search algorithm for finding the solution vector in the search space are pitch adjustment rate (PAR) and harmony memory considering rate (HMCR). The defined set optimization steps of Harmony Search Algorithm are given in Table 1.

### Step1: Initialization of Harmony Memory (HM)

Harmony Memory (HM) is represented in the two-dimensional matrix form which is initialized by setting a initial solutions of Harmony memory size is generated. In Harmony memory matrix the rows are represented as a set of solutions ( $x_i$ ) which

**Table 1** Optimization steps of harmony search algorithm

Step 1	Initialization of harmony memory (HM)
Step 2	Improvisation of a new harmony memory (HM)
Step 3	Updation of the harmony memory (HM)
Step 4	Checking for stopping criteria
Step 5	Otherwise repeat steps 2 and step 3

is termed as population size and the columns are represented as variable of each solution which is termed as jobs. The population size is considered as a dimensional array, the size of this dimensional array depends on the maximum number of jobs exists in any set of problem. Equation (1) show the Harmony Memory representation.

$$HM = \begin{bmatrix} x_1^1 & x_2^1 & \dots & x_{K-1}^1 & x_K^1 \\ x_1^2 & x_2^2 & \dots & x_{K-1}^2 & x_K^2 \\ \vdots & \vdots & \vdots & \vdots & \vdots \\ x_1^{HMS-1} & x_2^{HMS-1} & \dots & x_{K-1}^{HMS-1} & x_K^{HMS-1} \\ x_1^{HMS} & x_2^{HMS} & \dots & x_{K-1}^{HMS} & x_K^{HMS} \end{bmatrix} \tag{5}$$

**Step 2: Improvisation of new Harmony Memory**

In Harmony Search Algorithm, during this step the divergence and convergence have been maintained. Pitch adjusting rate (PAR) and Harmony Memory considering rate (HMCR) are the parameters which are the main input parameters for convergence and divergence search space [5]. The selected parameters are used to construct the solution and this is constructed stochastically based on three operations which are shown in Table 2.

The random consideration variable vales ( $x'_2, x'_3, \dots, x'_K$ ) have also taken in same manner.

$$x'_i \leftarrow \begin{cases} x'_i \in \{x_i^1, z_i^2, \dots, x_i^{HMS}\} & \text{with probability HMCR} \\ x'_i \in X'_i & \text{with probability}(1 - HMCR) \end{cases} \tag{6}$$

**Table 2** Operation parameters

S. No.	Operator	Operator value
01	Memory consideration (based on HMCR)	$x'_1$ this is the first decision variable has been taken from any of the values as specified in HM range ( $x'_1 - x_1^{HMS}$ )
02	Random consideration (based on 1-HMCR)	Refer Eq. (2)
03	Pitch adjustment (based on PAR)	Refer Eq. (3)

In the generated matrix each and every element component obtained by the individual memory consideration is analyzed to determine and confirm whether the pitch should be adjusted or not. The pitch adjustment decision is given in the following Eq. (7). Pitch adjusting decision for  $x'_i$

$$x'_i \leftarrow \begin{cases} \text{Yes with probability} & \text{PAR} \\ \text{No with probability} & (1 - \text{PAR}) \end{cases} \quad (7)$$

If the pitch adjustment decision for  $x'_i$  is Yes, then  $x'_i$  is replaces as shown in the following Eq. (8):

$$x'_i \leftarrow x'_i \pm \text{rand}() * bw \quad (8)$$

where  $bw$  = an arbitrary distance band width  
 $\text{rand}()$  = random number between 0 and 1.

Harmony memory operator value and pitch adjustment operator values has been used to each variable of the new Harmony Memory vector. These steps are followed as same as followed in the Genetic Algorithm optimization technique. In Genetic Algorithm crossover and mutation are the operators unlike in PAR and HMCR in case of Harmony Search Algorithm. The advantage of Harmony Search algorithm is that the HMCR is fully utilized in the optimization analysis, where as in Genetic Algorithm the new chromosomes are generated by crossover of mutation or crossover of two parent. In Genetic Algorithm optimal solution completely depends on the design consideration.

**Step 3: Updation of Harmony Memory**

In this step, the worst harmony is removed from the Harmony memory when the new harmony vector  $x' = (x'_1, x'_2, \dots, x'_K)$  is better than the worst in the generated Harmony memory.

**Step 4: Stopping Criterion**

In the Harmony search algorithm, the stopping criterion is depending on the improvisation satisfaction. It means that if the number of or maximum number of improvisations are deciding the stopping criterion, then the computation of the algorithm terminated. If the maximum number of improvisations are not satisfied then the step 2 and step 3 will be repeated.

### 3 Summary

In this paper, discussed an overview of an effective meta-heuristic technique Harmony Search Algorithm for solving the identical parallel machine scheduling problems. In the IPMS problems there are various characteristics based on realistic rules. Harmony search algorithm is found from the literature one of the popular optimization technique, researchers are focusing on the improvement of the developed algorithms such as discrete harmony search algorithm, hybrid harmony search algorithm, hybrid dynamic harmony search algorithms. Future work could be focused on implementing this meta-heuristic Harmony Search Algorithms to get net solutions in the identical parallel machine scheduling effectively and also in various engineering applications.

### References

1. Lee YH, Pinedo M (1997) Scheduling jobs on parallel machines with sequence-dependent setup times. *Eur J Oper Res* 100(3):464–474
2. Graham RL, Lawler EL, Lenstra JK, Rinnooy Kan AHG (1979) Optimization and approximation in deterministic sequencing and scheduling: a survey. *Ann Discrete Math* 5:287–326
3. Holland JH (1975) *Adaptation in natural and artificial systems*. University of Michigan Press, Ann Arbor, MI 5:1975
4. Gara-Ali A, Finke G, Espinouse M-L (2016) Parallel-machine scheduling with maintenance: praising the assignment problem. *Eur J Oper Res* 252(1):90–97
5. Mahdavi M, Fesanghary M, Damangir E (2007) An improved harmony search algorithm for solving optimization problems. *Appl Math Comput* 188(2):1567–1579
6. Hasani K, Kravchenko S, Werner F (2014) A hybridization of harmony search and simulated annealing to minimize mean flow time for the two-machine scheduling problem with a single server. *Int J Oper Res* 3:9–26
7. Chen J, Pan Q-K, Wang L, Li J (2011) A hybrid dynamic harmony search algorithm for identical parallel machines scheduling. *Eng Optim* 44(1–16)
8. Chen J, Pan Q, Li H (2010) Harmony search algorithm with dynamic subpopulations for scheduling identical parallel machines. In: 2010 sixth international conference on natural computation
9. Chen J, Liu G, Lu R (2011) Discrete harmony search algorithm for identical parallel machine scheduling problem. In: *Proceedings of the 30th Chinese control conference*
10. Wang L, Pan Q-K, Tasgetiren MF (2011) A hybrid harmony search algorithm for the blocking permutation flow shop scheduling problem. *Comput Ind Eng* 61(1):76–83
11. Yuan Y, Xu H, Yang J (2011) A hybrid harmony search algorithm for the flexible job shop scheduling problem. *Appl Soft Comput* 13(7):3259–3272
12. Piroozfard H, Wong KY, Asl AD (2017) An improved biogeography-based optimization for achieving optimal job shop scheduling solutions. *Procedia Comput Sci* 115:30–38
13. Geem ZW, Lee KS, Park YJ (2005) Application of harmony search to vehicle routing. *Am J Appl Sci* 2:1552–1557
14. Geem ZW, Kim JH, Loganathan GV (2002) Harmony search optimization application in pipe network design. *Int J Model Simul* 22(2):125–133
15. Fesanghary M, Mahdavi M, Minary-Jolandan M, Alizadeh Y (2008) Hybridizing harmony search algorithm with sequential quadratic programming for engineering optimization problems. *Comput Methods Appl Mech Eng* 197:3080–3091

# Computational Investigation of Stagnation-Region Gas Injection for Protection of a Locally Heated Skin



Tulasi Tirupati and B. S. Subhash Chandran

**Abstract** Type III and IV shock interactions on the scramjet cowl principal edge produces localized heating of surfaces and leads to thermo-structural failure. One of the methods to protect these surfaces is by blowing shock away with supersonic injection of coolant into stagnation region. The displacement of shock depends on the mass flux ratio of supersonic jet and free stream of projected area. The strength and type of shock interference depends on the location of shock generator. Computational analysis carried out to evaluate the effectiveness of this method with the above parameters. The contours of flow field presented. Shock standoff distance and effective heat flux reduction computed. Geometry and structured grid generated using ICEM CFD. The simulations carried with ANSYS CFX. It found that the minimum shock standoff distance to protect the structure is with mass flow ratio of 0.34. Computed shock standoff distances for the mass flux ratios of zero, 0.17, 0.34, and 0.51 are 4, 8, 12, and 19 mm respectively. The standoff distances are successive integer multiples of zero mass flux standoff distance.

**Keywords** Heat transfer · Shock interaction · CFD · Stagnation region · Gas injection

## 1 Introduction

### 1.1 A Subsection Sample

Intercontinental travelling time possibly will be reducing by the development of hypersonic air breathing vehicles [1]. Hypersonic flow regime is pointed as “the realm of speed where in the physics of flow is dominated by aerodynamic heating”

---

T. Tirupati (✉)

CMR Technical Campus, Kandlakoya (v), Medchal Road, Hyderabad 500010, TS, India  
e-mail: [tirupatitulasi@yahoo.co.in](mailto:tirupatitulasi@yahoo.co.in)

B. S. S. Chandran  
DRDO, Hyderabad, Telangana, India

© Springer Nature Singapore Pte Ltd. 2020  
G. S. V. L. Narasimham et al. (eds.), *Recent Trends in Mechanical Engineering*,  
Lecture Notes in Mechanical Engineering,  
[https://doi.org/10.1007/978-981-15-1124-0\\_62](https://doi.org/10.1007/978-981-15-1124-0_62)



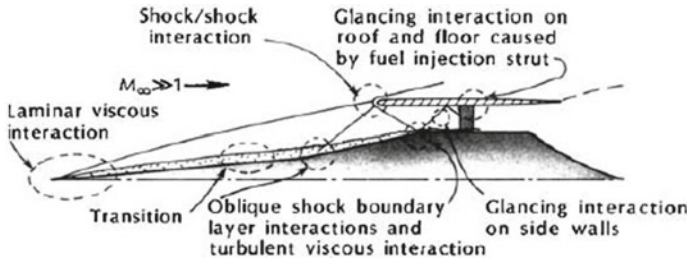


**Fig. 1** Schematic drawing of aerothermal heating factors in hypersonic flow

[2]. Intense technical key factor in the growth of these vehicles is to make them to withstand drastic aero thermal load [3]. Shocks generation and interaction at the leading edges and viscous heat dissipation in the boundary limit are the sources of aero thermal load [4]. Shock–shock interactions at the cowl tip at combustion chamber are necessary to increase flow rate and pressure [5]. Out of the possible interactions, type III and IV results in intense aerothermal load. The schematic sketch represented in Fig. 1 and reproduced from Stollery [6].

One of the methods is to weaken the effect of shock–shock interactions occurring in the stagnation region by modifying type of interaction, i.e., blowing away the shock from the stagnation point and thereby the heat flux generated. To achieve this, gas supersonically injected into the region. The potency of this method is dependent on ratio of mass flux of jet and free stream equivalent to projected area of front leading edge surface.

Love [7] carried the experiments related to gas injection from the nose of an elliptical body of revolution. The objective is to determine drag, pressure distribution and heat flux. Experiments are carried in the supersonic flow field at the Mach number 1.6 He concluded that jet effects are predominant at higher Reynolds number.

Nowak [8] carried out experimental investigation of effect of nitrogen gas ejection from tangential slot located on conical surface at the Mach number 6.7 on the aerothermal environment. The objective of this experiment is to reduce heat flux on surface. He concluded that high mass flux ratios are required to reduce the heat flux generated on the surface due to shock–shock interaction.

Nowak [9] conducted experiments to investigate the effect of transpiration cooling to reduce the heat flux on the cowl leading edge. In his experimental study, helium gas injected with transpiration mass flux of 31%. He recommended that local injection of gas in stagnation region of leading edge.

Holden et al. [10], carried experimental research to study the effect of transpiration cooling over hemispherical nose shapes on the pressure and heat flux distribution. Their study reveals that shock structures of type IV and III can be modified to reduce the heat flux generated in the vicinity of shock–shock interface.

Albertson et al. [11], employed this method in their experimental investigation. Present research presents the CFD simulations of this method and it is the part of doctoral thesis work carried by author.

## 2 Problem Statement and Computational Methodology

Type of shock interference depends on the wedge location from the leading tip of cowl and strength of shock, in turn dependent on the free stream flow conditions. Mass flux ratio,  $m_j/m_\infty$ , jet to free stream influences the shock displacement. Computed  $m'_\infty$  based on  $m'_\infty = \rho_\infty V_\infty A_{le}$ , where  $A_{le}$  is projected area of leading surface.

Albertson et al. [11] carried experimentation on cowl leading edge (radius 2.54 mm) surface similar to NASP scramjet. They injected the gas from four rows of rectangular nozzles, of these two are above and two are below the central part. They generated oblique shock with a wedge of turning angle  $6^\circ$ . The surface modified to house the total 35 rectangular cross section nozzles of 0.035 and 0.005 mm per row. Full nozzles are not included in geometry. Rectangular surfaces created on the leading edge and nozzle outlet conditions employed on this boundary. Geometry modeling and mesh generation is done with ICEM CFD, advanced meshing software. Unstructured hexa mesh created around the geometry with high mesh density in shock regions. Figure 2 represents the schematic of the physical model and computational domain.

3D CFD simulations at the zero angle of attack carried employing the ANSYS CFX, finite volume based software. Shear Stress Turbulence model employed in the analysis. Drag force not considered in the analysis. Investigated parameters are shock generator position and mass flux ratio. Three different ratios investigated in the analysis: 0.17, 0.34 and 0.5. Tables 1 and 2 is the representations of free stream flow properties, nozzle's exit jet conditions and position of wedge.

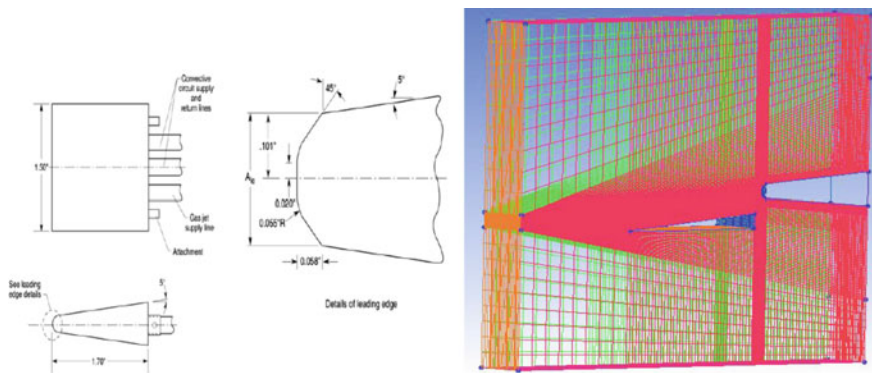


Fig. 2 Schematic of cowl leading edge model and computational mesh for simulations

**Table 1** Free stream conditions for shock interaction control

Run	$M_\infty$	$T_0$ (K)	$T_\infty$ (K)	$p_0$ (bar)	$\rho_\infty$ (kg/m <sup>3</sup> )	$V_\infty$ (m/s)	$Re_\infty$ (1/m)
1	6.0	516.67	62.78	16.62	0.0586	952.942	1.332E+7
2	6.0	502.78	61.11	16.89	0.0610	940.182	1.414E+7
3	6.0	498.89	60.55	16.75	0.0612	935.865	1.423E+7
4	6.0	516.67	62.78	16.48	0.0578	952.942	1.312E+7

**Table 2** Shock generator’s position and jet conditions

Run	$X$ (mm)	$Y$ (mm)	$M_j$	$T_{0j}$ (K)	$p_{0j}$ (bar)	$m_j$ (kg/s)	$m_j/m_\infty$
1	2.54	13.51	2.60	304.44	19.99	0.0055	0.51
2	2.54	11.99	2.60	304.44	19.99	0.0055	0.51
3	2.54	11.99	2.60	305.00	13.37	0.0037	0.34
4	2.54	12.75	2.60	302.78	6.62	0.0016	0.17

### 3 Results and Discussion

#### 3.1 Shock Interference Structure Without Gas Injection

Type III shock interference obtained for the wedge location indicated in run 1 CFD simulations. This shock interference structure is resulted from interaction of weak shock from wedge with bow shock from leading edge. Figure 3 represents the density gradient and Mach number contour of type III interaction. Strong variation in flow observed just below the down portion of the edge in attached mode indicated by yellow and red color region from the density gradient contour. Shock represents the jump condition of the flow properties and shown by spontaneous change of Mach number in the Mach contour.

Type IV shock interference occurs when a weak shock from wedge interact with normal portion of bow shock. The simulations carried with a wedge location of point (-2.54, -13.36) from the center (0, 0) on cowl tip. Figure 4 indicates the contours of density gradient and Mach number for shock interference structure of type IV.

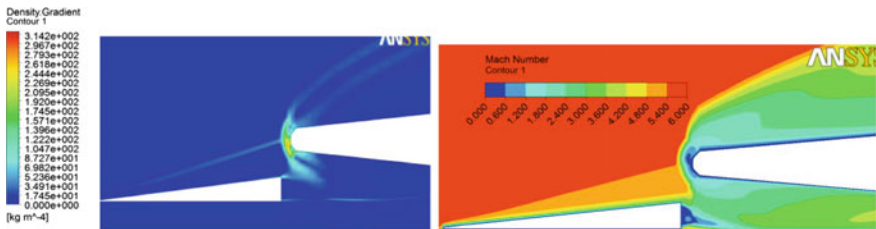


**Fig. 3** Density gradient and Mach number contour for type III shock interaction

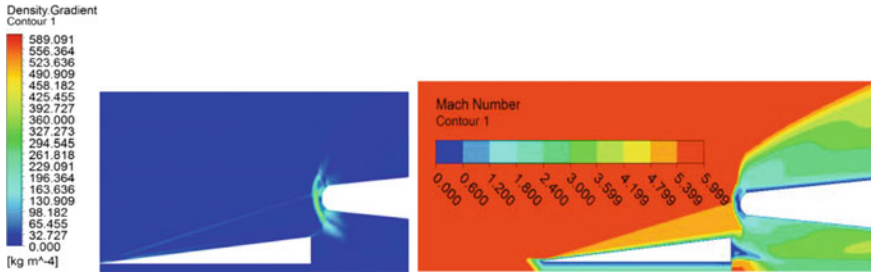


Fig. 4 Density gradient and Mach number contour for type IV shock interference

Interaction of wedge produced shock in the upper section of cowl tip observed from the density gradient contour.

### 3.2 Shock Wave Interference Structure with Gas Injection

Simulations carried for the mass flow ratio of 0.51 for flow conditions indicated in run 1. Bow shock pushed to 19 mm away from the cowl-leading tip, without injection it is at a 4 mm distance. Shock standoff distance is almost five times (an integral multiple) to without injection. Density gradient and Mach number contours presented in Fig. 5. Red color region indicates the supersonic jets from individual nozzles and collapses into single jet. This jet changes its direction in upward direction as observed from the contours.

Figure 6 presents the density gradient and Mach number variation in form of contour for mass flow ratio of 0.34. Bow shock located at a distance of 12 mm approximately, which is lower in comparison to mass flux ratio of 0.51. This mass flux ratio is enough to avoid severe localized heating. Flow field pattern is similar to the mass flux ratio of 0.51.

Density gradient and Mach contour is shown in Fig. 7 for the mass flux ratio of 0.17. Bow shock displaced to 8 mm away from the leading edge from 4 mm distance.

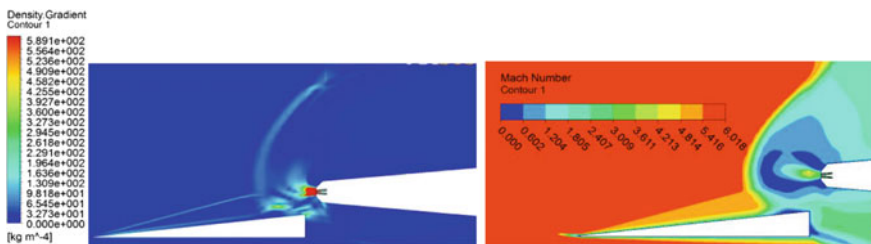


Fig. 5 Density gradient and Mach number contour for mass flux ratio of 0.51 for type III shock structure at the shock generator location of  $y = -13.51$  mm

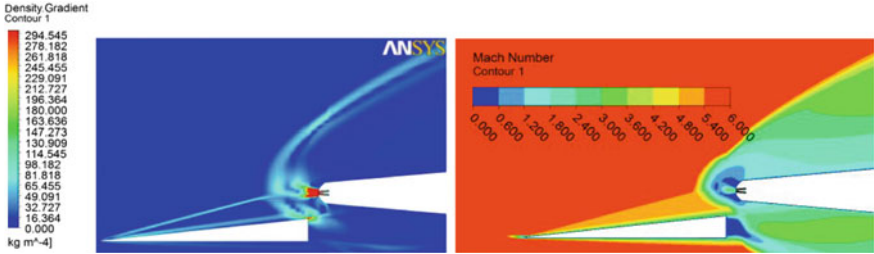


Fig. 6 Density gradient and Mach number contour for mass flux ratio of 0.34

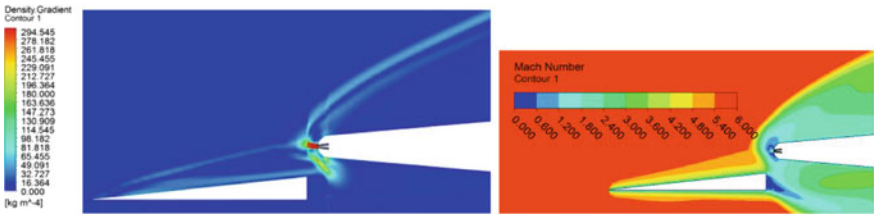


Fig. 7 Density gradient and Mach number contour for mass flux ratio of 0.17

Bow shock standoff distance decrease further in comparison to higher mass flow ratios. Weak shock from generator strikes normally the surface indicating that this ratio is not ample to safeguard the surface from concentrated heat flux.

### 4 Conclusions

Supersonic injection of inert gas through nozzles that are facing free stream is able to modify the shock interference structure and can minimize the heat flux by placing the shock away from stagnation region. It observed that this could be achieved for mass flux ratio of 0.34 and above. Shock standoff distances computed are 4, 8, 12, and 19 mm for mass flux ratios of 0, 0.17, 0.34, and 0.51 respectively. The standoff distances are successive integer multiples of zero mass flux standoff distance.

### References

1. Axdahl EL (2013) A study of premixed shock-induced combustion with application to hypervelocity flight. School of Aerospace Engineering, Georgia Institute of Technology, Atlanta, US, pp 1–7
2. Anderson JD (1992) Aerothermodynamics: a tutorial discussion in thermal structures and materials for high-speed flight. In: Thornton EA (ed) Proceedings of the first thermal structures

- conference, American Institute of Aeronautics and Astronautics
3. Heppenheimer TA (2009) Facing the heat barrier: a history of hypersonics. NASA History Series, Government Printing Office, USA
  4. Thomas JL, Dwoyer DL, Kumar A (1991) Computational fluid dynamics for hypersonic air-breathing aircraft. In: Desideri JA, Glowinski R, Periaux J (eds) Hypersonic flows for reentry problems, vol I. Springer, Berlin (1991)
  5. Gaitonde D, Shang JS (1990) A numerical study of shock-on shock viscous hypersonic flow past blunt bodies. AIAA Paper 90-1491
  6. Stollery JL (1987) Some aspects of shock-wave boundary-layer interactions relevant to intake flows. In: Aerodynamics of hypersonic lifting vehicles, AGARD CP-428
  7. Love ES (1952) The effects of a small jet of air exhausting from the nose of a body of revolution in a supersonic flow. NACA RM L52I19a
  8. Nowak RJ (1988) Gas-jet and tangent-slot film cooling tests of a 12.5 degree cone at Mach number 6.7. NASA TP 2786
  9. Nowak RJ, Holden MS, Wieting AR (1990) Shock/shock interference on a transpiration cooled hemispherical model. AIAA Paper 90-1643
  10. Holden MS, Rodriguez KM (1992) Studies of shock/shock interaction on smooth and transpiration-cooled hemispherical nosetips in hypersonic flows. Technical Report 7931, NASA CR-189585
  11. Albertson CW, Venkat VS (2006) Shock interaction control for scramjet cowl leading edges. AIAA

# Techno-Economic Assessment of Wind/Photovoltaic and Conventional Generator Hybrid Off-Grid Power Systems for Rural Community in Meta Robi District



Kante Mallikarjuna Rao, Robera Daba Bededa, B. Somanath, L. Ranganath and Basam Koteswararao

**Abstract** The intention of this research is to obtain an ideal suited arrangement of hybrid electricity generation system using various renewable energy sources to meet the village load prerequisite reliably, economically, endlessly, and sustainably. Hybrid system consists of sun energy, wind power, and conventional electric generator. The analysis is done in the year 2017–2018 at Deleta Village in Meta Robi District, Oromia region, Ethiopia for hybrid electrification. The required solar potential values and wind speed statistics were taken from NASA. The data shows that the study site has an average wind speed of 2.9 m/s at 10 m anemometer and solar radiation of 5.81 kWh/m<sup>2</sup>/day. The cost of associated hybrid components is collected from various springs and the electric load data was estimated for community and public service's needs. HOMER software was used to perform techno-economic assessment to meet the load requirement using renewable hybrid off-grid configuration. Based on the resources, load, hybrid system, and the component cost input data were considered. The simulation in HOMER gives optimization, sensitivity, and grid comparison results. The optimization result of the simulation demonstrates that the hybrid configuration achieves total NPC of \$1,506,689 and COE of 0.360 \$/kWh at a renewable fraction of 0.6 as the best optimal hybrid configuration considering

---

K. M. Rao · R. D. Bededa · B. Somanath · B. Koteswararao

Civil Engineering, Sri Satya Sai University of Technology & Medical Sciences, Sehare, MP, India  
e-mail: [kmkrao04@gmail.com](mailto:kmkrao04@gmail.com)

K. M. Rao · R. D. Bededa · B. Somanath

Lecturer, Department of Mechanical Engineering, Maddawalabu University, Bale Robe, Ethiopia  
e-mail: [roberadaba@gmail.com](mailto:roberadaba@gmail.com)

B. Somanath

e-mail: [somanathbilihal.g@gmail.com](mailto:somanathbilihal.g@gmail.com)

B. Somanath · L. Ranganath · B. Koteswararao (✉)

Department of Mechanical Engineering, Koneru Lakshmaiah Education Foundation (KLEF),  
Guntur 522502, India  
e-mail: [basam.koteswararao@gmail.com](mailto:basam.koteswararao@gmail.com)

L. Ranganath

e-mail: [lollaranganath@kluniversity.in](mailto:lollaranganath@kluniversity.in)

© Springer Nature Singapore Pte Ltd. 2020

G. S. V. L. Narasimham et al. (eds.), *Recent Trends in Mechanical Engineering*,  
Lecture Notes in Mechanical Engineering,  
[https://doi.org/10.1007/978-981-15-1124-0\\_63](https://doi.org/10.1007/978-981-15-1124-0_63)

economic and environmental point of view. From environmental standpoint of view, the system is characterized with a minimum percentage of carbon dioxide and other GHG emissions of about 195,974 kg/year.

**Keywords** Hybrid system · Electric load · HOMER · Techno-economic · Renewable energy

## 1 Introduction

Ethiopia is a large, landlocked, and diverse country located in the eastern part of Africa between 3° to 15° North and 33° to 48° East. It is the subsequent most populated country in the region (estimated 110.8 million in 2018), out of which 82.5% are rural dwellers. In terms of GDP per capita income of 80.56 USD Billion in 2017, Ethiopia ranks 173 out of 187 according to the HDI 2018 report.

Despite the fact 82.5% of the population of Ethiopia live in countryside areas, power supply from the grid is virtually entirely focused on urban areas. Among other things, dispersed and very low ingesting level of electricity among rural consumers limited grid power penetration to rural dweller which is less than 3% [1]. Based on the hitherto electricity expansion practices, access to electricity does not seem to be the reality of the near future for the greater percentage of the rural communities. However, the current government's approach under UEAP ambitiously increases access to electricity by connecting 5168 new towns and villages to the grid and the country managed to electrify 1700 rural towns and villages per annum. The UEAP aims to increase access level of national per capita consumption of electricity from 28 kWh in 2010 to 137 kWh by the year 2016 [2].

Ethiopia, under UEAP, follows two basic strategies to electrify rural area. These are

- Grid-based large and medium-scale power generation and
- Small-scale renewable energy stand-alone/mini-grid technology options.

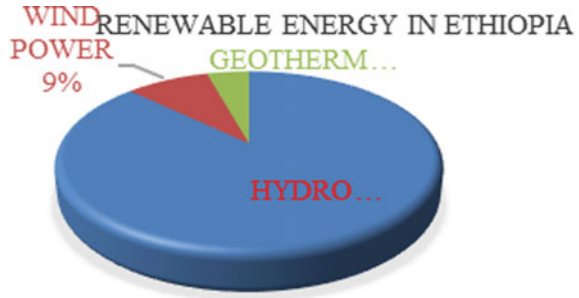
In countryside areas of Ethiopia, 70% of energy demand for food preparation and lighting is from fuelwood. Hence, to access a reliable, affordable, clean, and sustainable energy service, the GoE sets a plan to set an energy mix power generation system (Fig. 1).

## 2 Literature Review

Electrical generation systems containing two or more energy [3, 4] sources such as solar [5, 6] and wind or the combination of these with other unconventional sources such as hydro, geothermal, biomass [3], or with a conventional diesel generator is called hybrid systems. Hybrid systems also contain loading strategies such as batteries or fuel cells. While hybrid energy systems are usually implemented to



**Fig. 1** Ethiopia power generation plan from unconventional energy [2]



electrify the community of rural areas those who detached or far away from national grid, and they can also generate power by the hybrid power generation system.

A research done by A.N. Rahmat et al. [7] in Indonesia results in reduced global warming gases and also it is an off-grid hybrid system, which fulfills the local home needs in the remote areas.

A detailed report given by Gabour et al. [8] in Algeria gives detailed conclusion about renewable, nonrenewable, and hybrid power system. The hybrid system fulfills all requirements with low emissions and power demand.

Ibrahim et al. [9] said that the hybrid renewable system is the best choice for power generation in remote areas when compared to conventional fossil fuel burning. There are researches saying that hybrid renewable power generation system is the best opportunity to generate power in rural areas where there is no grid connection.

### 3 Research Methodology

The overall research methodology is Site Identification. The specific study area is Deleta Village in Meta Robi District (Fig. 2 and 3) The subsequent optimization stage simulates individual of the possible system configurations and displays their list sorted by NPC and cost of electricity (LCOE) to compare and evaluate the most cost-effective option considering factors such as resource availability, load size, fuel price, carbon emissions, and renewable fraction. The final sensitivity analysis helps to reveal how sensitive the outputs are to change for sensitivity input variables such as wind speed, solar radiation, and fuel prices. Sensitivity analysis results are important in answering the generation questions about technology options to inform planning and policy decisions.

**Fig. 2** Map of the study area (Source Google earth)

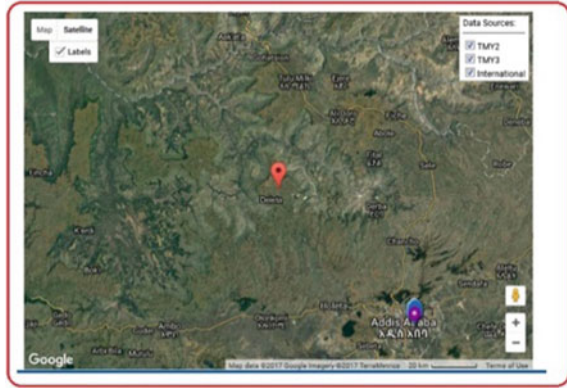
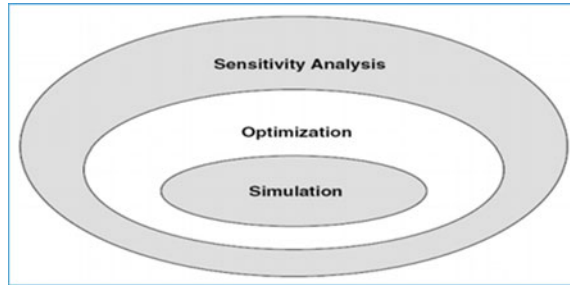


**Fig. 3** The three consecutive steps of HOMER software [10]

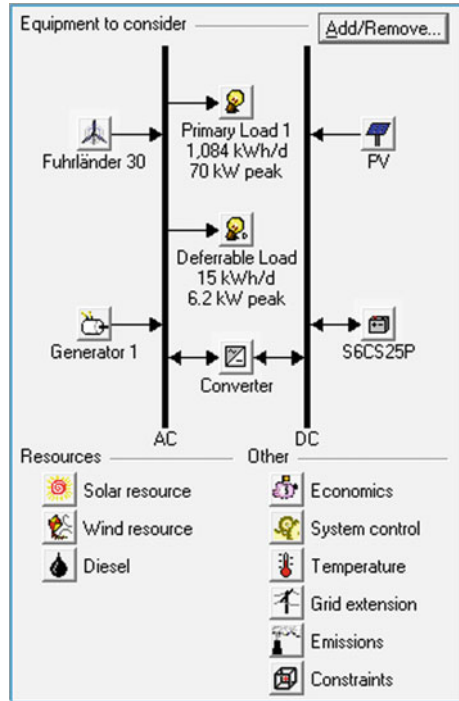


## 4 Hybrid System Components Modeling

HOMER hybrid model requires several inputs which basically describe the technology option, component costs, component specification, and resource availability. Renewable resources available at a location can differ considerably from site to site and it is a vital aspect in developing the hybrid system. Hybrid power generation system modeled in HOMER by using load, resources, component size, cost, and technical parameter is shown in Fig. 4. The wind turbine and diesel generator are connected to AC bus while PV and battery need DC bus and a converter.

The double-headed arrow indicated in the batteries and converters has the following meanings. The converter changes the excessive available power from AC to DC load to charge the batteries after fully meeting the load demand of the system. When the output of the hybrid system is not enough to meet the load, the battery discharges the DC load to the system via the converter to AC power loads.

**Fig. 4** HOMER schematic of hybrid power system modeling



### 4.1 Comparison of Hybrid Off-Grid Systems with Grid Extension

In this study, grid comparison was done to compare the cost of grid extension with the cost of stand-alone system configuration. Homer analyzes the breakeven grid leeway distance by using Eq. 1 [11].

$$D_{grid} = \frac{C_{NPC} \cdot CRF(i, R_{proj}) - C_{power} \cdot L_{tot}}{C_{cap} CRF(i, R_{proj}) + C_{OM}} \tag{1}$$

where  $C_{NPC}$  = total net present cost of stand-alone (\$),  $CRF$  = capital recovery factor,  $i$  = interest rate (%),  $R_{proj}$  = project lifetime (yrs.),  $L_{tot}$  = total primary and deferrable load (kWh/yr),  $C_{power}$  = cost of power from the grid (\$/kWh),  $C_{cap}$  = capital cost of grid extension (\$), and  $C_{OM}$  = operation and maintenance cost of grid extension (\$/kW/yr).

According to the report [11], the average cost of grid extension in remote rural areas varies from \$8,000 to \$10,000 for every kilometer and rapidly increases up to \$22,000/km for extremely difficult terrains. Rural electrification is almost seven to ten times more expensive than that in urban areas. In this work, a \$12,500 for every kilometer or 337,500 birr and the operation and maintenance cost of the system

**Table 1** Grid extension cost

Study area	Grid voltage level	Distance from national grid (km)	Unit capital cost (\$/km)	O&M cost (\$/km/yr)	Total capital cost of grid extension (\$/km)	Grid power price (\$/kwh)
Deleta Village	33 kV	27	12,500	6,750	337,500	0.044

considered was 2% of the capital cost which is \$250 or 6750 birr, whereas the grid power price \$/kWh in 2017 is 0.044 or 1.19 birr/kWh (EEPCo). The grid extension capital cost for the study site is presented in Table 1.

## 4.2 Economic Feasibility Analysis

The concept of LCC is used for cost analysis of the proposed hybrid configuration. The life cycle cost of a component consists of procurement cost, and operation and maintenance cost. Some costs involved in the procurement and operation of a component are incurred at the time of an acquisition (includes costs of purchasing equipment and their installation) and other costs are incurred at later times (includes costs of fuel if exists, operation, and maintenance). LCC accounts for all costs associated with a system over its lifetime, considering the time value of money. Two phenomena disturb the value of money over time [12].

The principal HOMER's economic output indicators are the operating cost, total net present cost (NPC), the levelized cost of energy (LCOE), and the initial capital cost. NPC analysis is an appropriate gauge or scale for the purpose of economic comparison of different energy system classifications and configurations since NPC balances widely divergent cost characteristics of renewable and nonrenewable sources as well it also explores and summarizes [13].

The annualized principal cost of each module is given as follows [14]:

$$C_{acap} = C_{cap} * CRF \quad (2)$$

where CRF is the capital recovery factor [15].

$$CRF = \frac{i(1+i)^N}{(1+i)^N - 1} \quad (3)$$

where  $N$  and  $i$  are the system lifetime and the annual real interest rate.

The total net present cost of each configuration can be calculated as follows [16]:

$$NPC(\$) = \frac{TAC}{CRF} \quad (4)$$

$$TAC = C_{acap} + \sum_{i=1}^n C_{OM,j} + C_f + \sum_{i=1}^n C_{R,i} \quad (5)$$

where  $n$  is the number of all the devices in the system,  $C_{OM,j}$  is the annual operation and maintenance (O&M) cost for the  $i$ th component of the system,  $C_f$  is total annual fuel cost, and  $C_{R,i}$  is the annualized replacement cost for the  $i$ th component of the system.

The LCOE is the ratio of the total annualized cost of the system to the annual electricity delivered by the system [17].

$$LCOE = \frac{TAC}{Q_t} \quad (6)$$

where  $Q_t$  is the electricity generated by the systems (kWh).

## 5 Result and Discussion

The optimal hybrid power generating system is the one which can supply power demand for the community at the lowest price or the systems which have the deepest total NPC, while supplying the electricity at the essential level of availability. Examining each feasible system configuration allows for economic and technical merit evaluation including the COE and renewable energy fraction. Other system functioning characteristics such as yearly electric power production, yearly electric load assisted, fuel feeding, extra electricity, capacity scarcity, unmet electric load, and emission can be also evaluated.

### Optimization Results

Looking at the overall and categorized simulation result illustrated in Table 2, the first, third, fourth, and fifth column cases are compared based on the total NPC, COE, operating cost over the life cycle of the system, and other functioning characteristics such as AEPP, capacity shortage, annual electric load served, surplus electricity, fuel feeding, unmet electric load, and emission.

#### 1. PV-generator hybrid system

From the replication result presented in Table 2, PV/diesel generator that excludes both wind turbine and battery is the most cost-effective hybrid power generation system for Deleta Village with total NPC of \$1,386,562, COE 0.34 \$/kWh (9.18 ETB/kWh). The quantity of diesel used yearly is 101,156 liters and the producer function for 8,732 h per year. The benefit of this result is that the total NPC and COE are the lowest, but renewable resource contributed is low 30%.

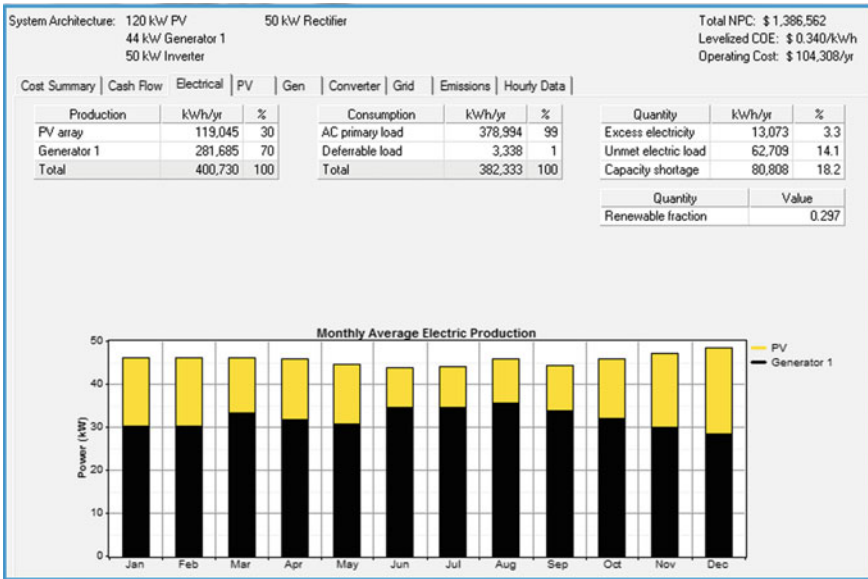


Fig. 5 Optimized PV/diesel generator system at 30% RF

Table 2 Summary of optimum hybrid system for 30% RF

System architecture		Annual electricity production (kWh/yr)		Annual electricity consumption (kWh/yr)		Emission (kg/yr)	
PV	120 kW	PV array	119,045	AC primary load	378,994	Carbon dioxide	266,380
Diesel generator	44 kW	Diesel generator	281,685	Deferrable load	3,338	Carbon monoxide	658
Converter	50 kW			<b>Cost summary</b>			
Dispatch strategy	CC	<b>Total</b>	400,730	capital cost	\$273,100	Particulate matter	49.6
		Excess electricity	13,073	Operating cost	104,308\$/yr		
		Unmet load	62,709	Total NPC	\$1,386,562	Sulfur dioxide	535
		Capacity shortage	80,808	LCOE	0.34 \$/kWh	Nitrogen oxides	5,867

The optimum hybrid power generation system architecture is shown in Fig. 5 with total annual energy creation of 30% PV array and 70% diesel generator. In this case, diesel generator activates at full yield power to assist the main load and any surplus electrical creation goes in the direction of the lower priority objectives. The excess annual electricity production, unmet electric load, and capacity shortage will stand at 3.3%, 14.1%, and 18.2%, respectively. The COE from these optimum hybrid power generation systems is more expensive than the national grid (0.273 \$/kWh) currently the consumer can pay. The detail of the optimized PV/diesel generator systems regarding the annual electricity production, yearly electricity ingesting, and emission from the system is obtainable in Table 2.

### 2. PV-generator-battery hybrid system

In view of the third simulation result, the most cost-effective system is the PV/generator/battery setup, For the optimum hybrid system architecture presented in Fig. 6, the total net present cost (NPC) is \$1,442,525, cost of energy (COE) is 0.351 \$/kWh, and the renewable resource contributed is 54%. The amount of diesel used annually is 74,857 L and the generators operate for 6,413 h per year. The power percentage share for the system is 54% PV array and 46% diesel generator.

Excess annual electricity production, unmet electric load, and capacity shortage will stand at 12.9%, 10.9%, and 14%, respectively. The COE from these optimum hybrid power generation systems is more expensive than the national grid (0.273

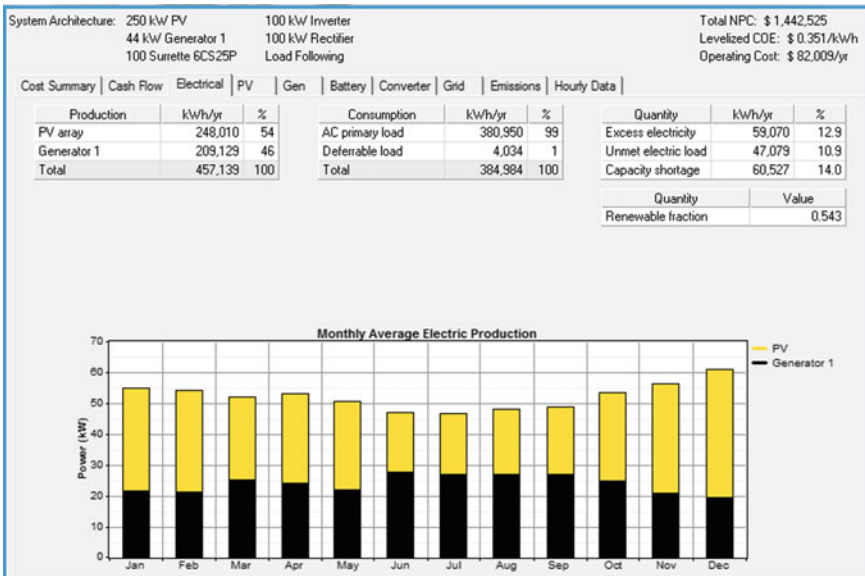


Fig. 6 Optimized PV/diesel generator/battery system at 54% RF

**Table 3** Summary of optimum hybrid system for 54% RF

System architecture		Annual electricity production (kWh/yr)		Annual electricity consumption (kWh/yr)		Emission (kg/yr)	
PV	250 kW	PV array	248,010	AC primary load	380,950	Carbon dioxide	197,124
Diesel generator	44 kW	Diesel generator	209,129	Deferrable load	4,034	Carbon monoxide	487
Battery	100 batteries			<b>Total</b>	<b>392,001</b>	Unburned hydrocarbons	53.9
				<b>Cost summary</b>			
Converter	100 kW	<b>Total</b>	457,139	capital cost (CI)	\$567,100	Particulate matter	36.7
Dispatch strategy	LF	Excess electricity	59,070	Operating cost	82,009 \$/yr		
		Unmet load	47,079	Total NPC	\$1,442,525	Sulfur dioxide	396
		Capacity shortage	60,527	LCOE	0.351 \$/kWh	Nitrogen oxides	4,342

\$/kWh) currently the consumer can pay. The detail of the optimized PV/diesel generator/battery systems regarding the annual electricity production, annual electricity consumption, and emission from the system is presented in Table 3.

### 3. PV–wind–generator hybrid system

As it is seen from the systems' setup, the fourth most cost-effective system is the PV/wind turbine/diesel generator setup, with the generator functions at complete yield power to assist the key load and any excess electrical creation goes in the direction of the lower priority objectives. For the optimum hybrid systems presented in Fig. 7, the total net present cost (NPC) is \$1,447,282, cost of energy (COE) is 0.348 \$/kWh, and renewable fraction contributed is 24%.

The amount of diesel used annually is 106,023 L and the generator operates for 8,753 h per year. The power percentage share for the system is 13% PV array, 12% wind, and 76% diesel generator. Excess annual electricity production, unmet electric load, and capacity shortage will stand at 1.2%, 10.5%, and 15.6%, respectively. The COE from these optimum HPGS is more expensive than the national grid (0.273 \$/kWh) currently the consumer can pay. The detail of the optimized PV/wind/diesel generator systems regarding the annual electricity production, annual electricity consumption, and emission from the system is presented in Table 4.

### 4. PV–wind–generator–battery hybrid system

The fifth optimal hybrid configuration system from the simulation result presented in Table 4 is the PV/wind/diesel generator/battery hybrid power generation with total net present cost (NPC) of \$1,506,689, COE of 0.36 \$/kWh, and renewable fraction of 60%. The amount of diesel used annually is 72,467 L and the generator operates for 6,673 h per year. The optimum hybrid power generation system architecture is shown



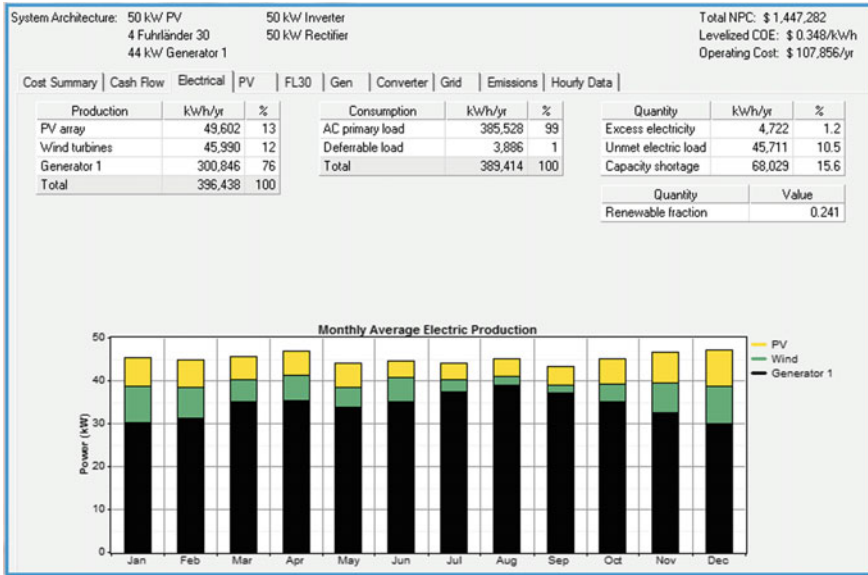


Fig. 7 Optimized PV/wind/diesel generator system at 24% RF

Table 4 Summary of optimum hybrid system for 24% RF

System architecture		Annual electricity production (kWh/yr)		Annual electricity consumption (kWh/yr)		Emission (kg/yr)	
PV	50 kW	PV array	49,602	AC primary load	385,528	Carbon dioxide	279,194
Wind Turbine	4(30 kW)	Wind turbine	45,990	Deferrable load	3,886	Carbon monoxide	689
				<b>Total</b>	<b>389,414</b>		
Diesel generator	44 kW	Diesel generator	300,846	<b>Cost summary</b>		Unburned hydrocarbons	76.3
Converter	50 kW	<b>Total</b>	<b>396,438</b>	capital cost	\$295,940	Particulate matter	52
Dispatch strategy	CC	Excess electricity	4,722	Operating cost	107,856\$/yr		
		Unmet load	45,711	Total NPC	\$1,447,282		
		Capacity shortage	68,029	LCOE	0.348 \$/kWh	Nitrogen oxides	6,149

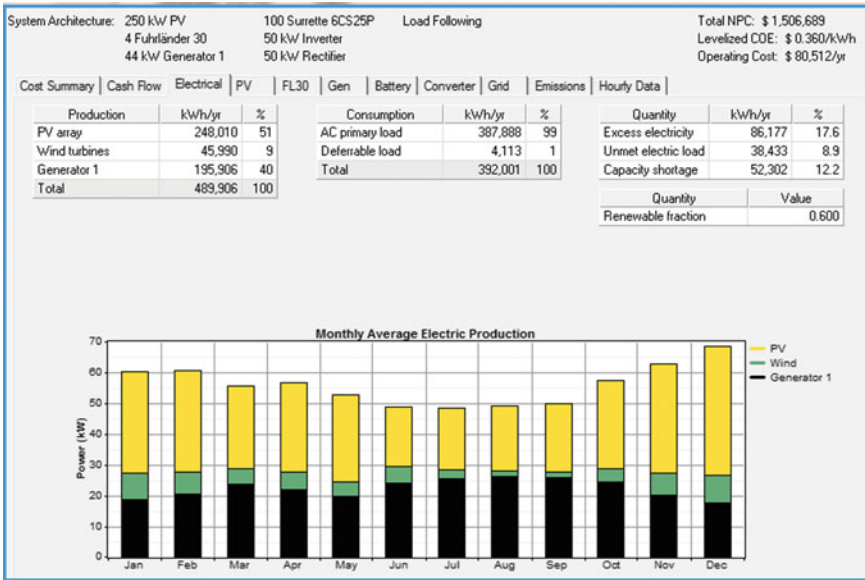


Fig. 8 Optimized PV/wind/diesel generator/battery system at 60% RF

in Fig. 8 with total annual energy production of 51% PV array, 9% wind turbine, and 40% diesel generator. In this case, a load following (LF) strategy is feasible (a dispatch strategy whereby the generator operates to produce only enough power to meet the primary load; lower priority objectives such as battery charging or serving the deferrable load is left to renewable power sources).

Excess annual electricity production, unmet electric load, and capacity shortage will stand at 17.6%, 8.9%, and 12.2%, respectively. The COE from these optimum hybrid power generation systems is also more expensive than the national grid (0.273 \$/kWh) currently the consumer can pay.

As it is seen from Fig. 8, the electrical power generated by hybrid system strongly depends on the nature of the energy sources. The power generated by solar photovoltaic depends on the time of the day and the strength of the solar radiation while the energy from the wind turbine depends on the availability of wind speed. Wind resource is intermittent in nature and it has a great impact on the output from the wind turbine. As it can be seen from the categorized optimization result illustrated in Table 6.2, there are renewable resources achieving renewable fraction of 100% and provide electric power excluding diesel generator. Renewable solar PV and wind are intermittent in nature; therefore, to supply continuous electric power, a diesel generator is mandatory.

## Conclusion

The grid comparison reveals that hybrid off-grid power generating system is feasible for electrification of rural community beyond the 3.66 km breakeven grid extension distance. The selected hybrid configuration system is an excellent solution to guarantee a reliable and affordable electric power supply without interruption of the load for the village of Deleta when compared with grid extension under certain conditions of the high capital cost of grid extension, sparsely populated, and low energy demand of the rural community. In this present case, the electric load is estimated and forecasted for the study community within 25 years of the project lifetime. The electrical load estimated for the study community is 1085kWh/day and the forecasted load demand is about 3674kWh/day. The optimization simulation result by HOMER shows that on the basis of lowest total NPC and cost of energy (COE), an optimal hybrid system configuration of PV–diesel generator system has been identified as the cheapest dependable solution with a NPC and COE. However, the optimal hybrid system cannot supply affordable and reliable power with required availability to meet the village load and it emits high GHG when compared with other feasible hybrid configuration systems.

## Recommendation

For further research and development relating to the electrification of countryside zones by using hybrid renewable PGS, the following points are recommended. To regulate the appropriate wind turbine siting and to determine the prevailing wind direction, wind data recorded for more than a year is very important for a specified wind command area. Therefore, the author of this thesis recommends that collecting wind speed data for the actual site at different locations using a wind mast equals to the hub altitude of the selected wind turbine for at least one complete year.

## References

1. Hadagu A (2006) Status and trends of Ethiopian rural electrification fund
2. Mengistie G (2011) Ethiopia: the case of small scale renewable energy for all financing access for the poor. Oslo Norway, 11 October 2011
3. Koteswararao B, Ranganath L, Ravi D, Babu KSK (2016) Designing of a coconut chopping machine and making fuel from tender coconut. *Indian J Sci Technol* 9:34
4. Barnes DF, Singh B, Shi X (2010) Modernizing Energy Services for the Poor: A World Bank Investment Review, Fiscal 2000–08
5. Ravi D, Somanath B, Rao KM, Ranganath L, Koteswararao B (2018) Experimental testing of thermal house for different weather conditions in Bale robe. *Mater Today: Proc* 5(9):18245–18250
6. Ravi D, Yohannes S, Feyissa HM, Koteswararao B (2017) Investigation on the performance of photovoltaic panel with various filters: (At rural areas of bale robe region in Africa continent). In: 2017 international conference on energy, communication, data analytics and soft computing (ICECDS) (pp 210–212). IEEE (August)
7. Rahmat AN et al (2018) Design of stand-alone hybrid power generation system at Brumbun beach Tulungagung, East Java. In: IOP conference series: materials science and engineering, vol 336, p 012003

8. Gabour A, Metatla A (2016) Optimal design and comparison between renewable energy, hybrid energy and non-renewable energy systems: case of Skikda, Algeria
9. Ibrahim H, Ghandour M, El-Jamal G (2018) Feasibility study of hybrid wind-diesel-battery power generating systems: parametric and sensitivity analysis. In: MATEC web of conferences, vol 171, p 01004. EDP Sciences
10. Furtado J (2012) Analysis of a biomass-based hybrid energy system for rural electrification—a case study in Uganda. Master of Science Thesis, Stockholm 2012
11. Nouni MR et al (2008) Providing electricity access to remote areas in India: an approach towards identifying potential areas for decentralized electricity supply. *Renew Sustain Energy Rev* 12:1187–1220
12. Gellings CW (1996) Demand forecasting for electric utilities. The Fairmont Press, Lilburn, GA
13. Maklad Y (2014) An introduction and costing of a biomass/wind/PV hybrid energy system for electricity microgeneration to domestic buildings in Armidale NSW, Australia. *Glob J Res Anal* 3(4):70–74
14. Mamaghani AH et al (2015) Exergetic, economic and environmental evaluations and multi-objective optimization of a combined molten carbonate fuel cell-gas turbine system. *Appl Therm Eng* 77:1–11
15. Koteswararao B, Radha Krishna K, Vijay P, Rajasurya N (2016) Experimental analysis of solar panel efficiency with different modes of cooling. 8(3), 1451–1456 (June–July)
16. Shirazi A et al (2016) Transient simulation and parametric study of solar-assisted heating and cooling absorption systems energetic, economic and environmental (3E) assessment. *Renew Energy* 86:955–971
17. Liu G et al (2012) Techno-economic simulation and optimization of residential grid-connected PV system for the Queensland climate. *Renew Energy* 45:146–155

# Assessment of Unconventional and Conventional Off-Grid Power Source for Rural Areas in Ethiopia



Yakkala M. K. Raghunadh, M. Chakrapani, Robera Daba Bededa, P. Vijay and G. Bheemanna

**Abstract** The Off-grid renewable power generation system cannot provide an efficient and continuous supply of electricity without a storage medium. Consequently, batteries are added to the hybrid system. In order to ensure the continuity of power supply without severe stress on the battery bank for a reduced overall cost, a conventional generator is also incorporated. After selecting the appropriate components and studying their characteristics, a hybrid system that consists of PV/wind/diesel generator/battery is demonstrated in HOMER using the estimated electrical load, renewable energy potential, and the costs of the hybrid system components. Then, the simulation is made to determine the best optimal hybrid configuration system that can supply the village load with the required level of availability.

**Keywords** Electric load · HOMER · Hybrid system · Renewable energy · Techno-Economic

---

Y. M. K. Raghunadh (✉) · M. Chakrapani · G. Bheemanna  
Department of Mechanical Engineering, Guru Nanak Institutions Technical Campus, Hyderabad, Telangana, India  
e-mail: [raghuy363@gmail.com](mailto:raghuy363@gmail.com)

M. Chakrapani  
e-mail: [sonuchakri09@gmail.com](mailto:sonuchakri09@gmail.com)

G. Bheemanna  
e-mail: [bheema7801@gmail.com](mailto:bheema7801@gmail.com)

R. D. Bededa  
Department of Mechanical Engineering, Maddawalabu University, Bale Robe, Ethiopia  
e-mail: [roberadaba@gmail.com](mailto:roberadaba@gmail.com)

P. Vijay  
Department of Mechanical Engineering, K.L.E.F, Vaddeswaram, Guntur, India  
e-mail: [Vijay.me250@kluniversity.in](mailto:Vijay.me250@kluniversity.in)

## 1 Introduction

The country Ethiopia is having plenty amount of natural resources but still there is no electric facility to the rural areas like Meta robe district and Bale robe rural. A recent study [1] says that the population growth in Ethiopia will be tremendous which means in future the people are going to face much electricity problems in future.

The problem not only affects electricity but it also affects technology development. There is no industrial and educational growth. The availability of sunlight is much more in Ethiopia which is suitable to generate power to serve to local community.

The research is also saying that [2] enough sun intensity is available in Ethiopia.

## 2 Literature Review

With the help of Homer, we have done the feasibility and sensitive analysis of homer. The research says that [3, 4] by the combination of wind, PV, and conventional generator, we can make the off-grid power supply system which will work stand alone. It is purely depending on off-grid system. In rural areas, there is power generation [5, 6] system based on municipal wastage.

The maximum utilization of solar panel is [7, 8] explained in the article clearly. So the use and utilization of nonconventional energy sources are explained clearly. The analysis [9] results are noted from the homer.

The load analysis is done for different conditions, the load varying from morning to midnight. At evening time peak load hours, we are making stand-alone conventional generator. The feasibility load analysis was done at each stage to check the economical output and unit cost of the power.

The various load parameters and calculations are shown in the sensitive analysis.

## 3 Sensitivity Results Analysis

### 3.1 Robustness of Optimization Results

Robustness or Sensitivity of the exaggeration can be examined by the reliability of the optimal system type as the sensitivity inputs change. The potential variations of wind cadence, PV capital cost, diesel prices, and electricity demand. In this study, the fuel price raised in a range from the current price 0.7 to 1\$/L and the load considered is the forecasted primary load of 3,674 kWh/day, wind speed resource considered is 2.9, 2, and 3.5 m/s, while the cost of PV capital considered is 0.4, 0.6, 0.8, 1, and 1.2. Diesel prices are predicted to rise and the current technological development would lead to decreased PV prices, as well as more utilization of new electrical devices would increase the future loads.

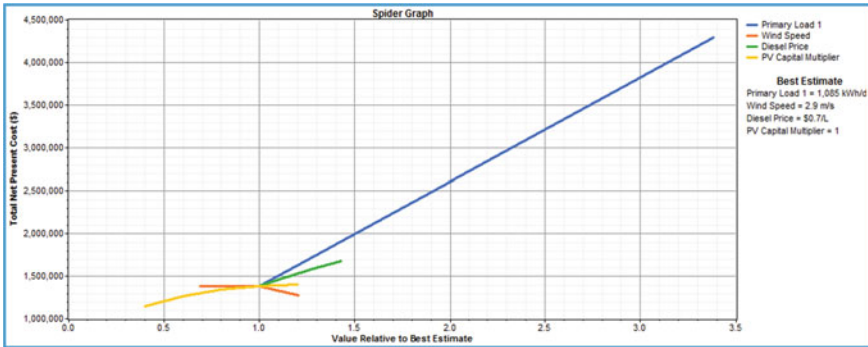


Fig. 1 Responsivity of NPC for the optimal PV/diesel/hybrid system

The responsiveness of NPC results for the optimal system with best estimate values of primary load = 1,085 kWh/day, diesel price = \$0.7/L, wind speed = 2.9 m/s, and PV capital cost multiplier = 1 is illustrated in Fig. 1. From Fig. 1., the origin of the graph lines is at the meeting point where the responsiveness inputs shown by the graph lines are equal to the best estimate values shown by the unity value relative to the best estimate on the horizontal axis. At this point, the total net present cost (NPC) \$1,375,000 on the vertical axis is equal to the predicted value shown on the categorized simulation result illustrated in Fig. 1.

Each of the graph lines shows how the NPC changes as the sensitivity input varies relative to its best estimate value by factors above unity to the right and below unity to the left.

The following observation can be made from the above Fig. 1:

- When the load increases by a factor of up to 3.4 relative to the baseline estimate of 1,085 kWh/day as shown by the sky blue line, the NPC of optimized system would change to \$4,375,000 (i.e., uncertainty of 33% in energy demand presents 68% uncertainty in NPC of the optimal hybrid system). With higher load, a larger system is required which increases the system life cycle costs.
- When PV capital cost would vary up to 1.2 (allowing a maximum uncertainty of 20% in the PV initial costs) relative to the best estimate of \$1340/kW as shown by the yellow line, the optimized NPC would increase to \$1,400,500 (i.e., a 20% uncertainty in PV capital cost would make the NPC increase by 2%).
- When diesel price would vary up to 1.4 relative to the best estimate of \$0.7/L as shown by green line (allowing up to 40% uncertainty in the diesel fuel price) the optimized NPC would increase up to \$1,700,000 (i.e., the diesel fuel uncertainty presents up to 19% uncertainty in the NPC of the optimal hybrid system).

The sensitivity of LCOE results for the optimal system with best estimate values of primary load = 1,085 kWh/day, diesel price = \$0.7/L, wind speed = 2.9 m/s, and PV capital cost multiplier = 1 is illustrated in Fig. 2.

From the above Fig. 2,

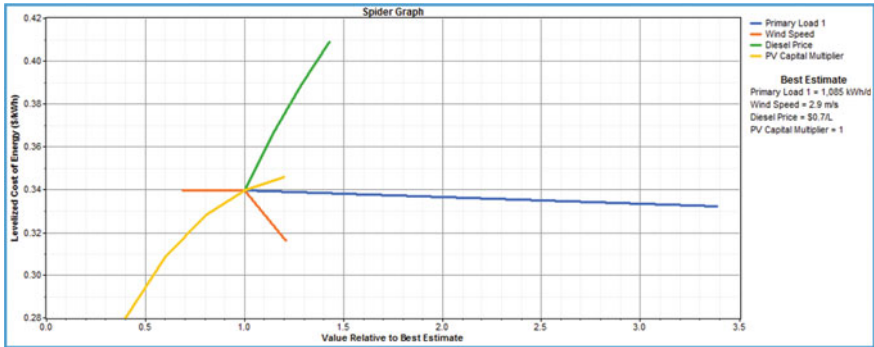


**Fig. 2** Sensitivity of LCOE for the optimal PV/diesel/hybrid system

- When the load would increase by a factor of up to 3.4 relative to the baseline estimate of 1,085 kWh/day as shown by the sky blue line, the optimized system would have a lower LCOE of \$0.33/kWh (i.e., a 33% uncertainty in load demand presents an uncertainty of 3% in the LCOE).
- When PV capital cost would vary up to 1.2 relative to the best estimate of \$1340/kW as shown by the yellow line, the LCOE of the optimized hybrid system would increase up to \$0.345/kWh (i.e., a 20% uncertainty in PV capital cost presents a 1.4% uncertainty in LCOE).
- When the wind speed would vary up to 1.2 relative to the best estimate of 2.9 m/s as shown by the red line, the LCOE of the optimized hybrid system would decrease up to \$0.315/kWh (i.e., a 20% uncertainty in wind speed presents a 7% uncertainty in LCOE).
- When diesel price would vary up to 1.4 relative to the best estimate of \$0.7/L as shown by green line, the LCOE of the optimized system would increase to \$0.41/kWh (i.e., a 40% uncertainty in diesel fuel price presents a 17% uncertainty in LCOE).

The results are shown in Fig. 3. It can be seen from the figure above that average wind speed of 2.9 m/s and PV capital cost multiplier one lead to LCOE of about \$0.34/kWh for a PV/generator hybrid configuration system. But when the wind speed increased to 3.4 m/s and the PV capital cost multiplier at 0.4, wind/PV/generator/battery hybrid configuration becomes the most cost-effective solution. LCOE varies from \$0.28/kWh to \$0.346/kWh when the wind speed is at 2 m/s with PV capital cost multiplier of 0.4 and varies to a favorable \$0.278/kWh for wind speed above 3.4 and PV capital cost multiplier 0.4.

The sensitivity analysis result for the 30% load demand increment with high diesel fuel price is illustrated in Fig. 4. In this case, the average wind speed at 2.9 m/s and PV capital cost multiplier 1.0 lead to levelized cost of energy (LCOE) increased load is still met but at high cost due to the multiple hybrid system, components need to meet the increased load demand. It is also evident from Fig. 4 that LCOE varies from a maximum of \$0.350/kWh when wind speed and PV capital cost multiplier are PV



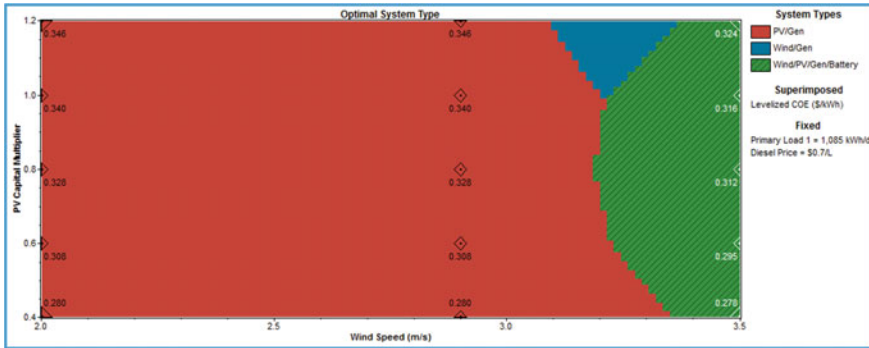


Fig. 3 Effects of PV capital multiplier and wind speed increment on operational system

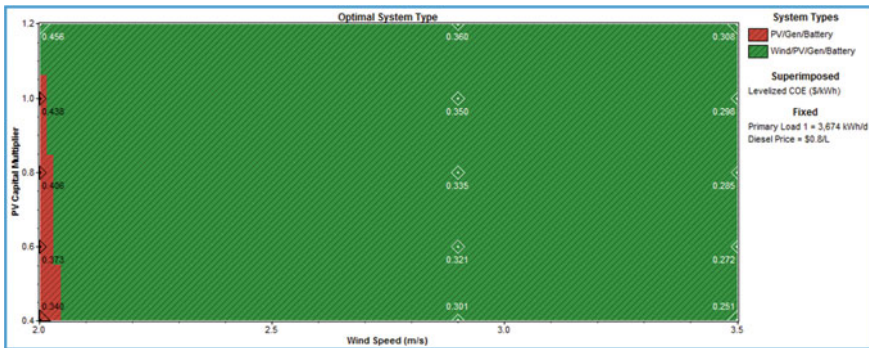


Fig. 4 Optimal system with 30% load increase

capital cost multiplier 0.4. In addition to this, beyond PV capital cost multiplier 1.0 with wind speed at 2.9 m/s, further the LCOE gets increased to \$0.360/kWh.

Net present cost and LCOE. The hybrid power generating total net present cost line comes out be a lower value than the breakeven distance for grid extension at a distance of 8.8 km, meaning that a decentralized hybrid power generating system is a better option than the grid extension for a community of the village which is at a distance greater than 8.8 km far from the national grid. At the cost of \$0.8/L, total net present cost of the system decreases (Fig. 5).

### 4 Grid Comparison Result

Breakeven grid extension distance (BGD) is the point at which the total NPC curve of grid extension and optimal hybrid off-grid power generating systems intersect each other. At this point, the optimal hybrid off-grid power generating system and

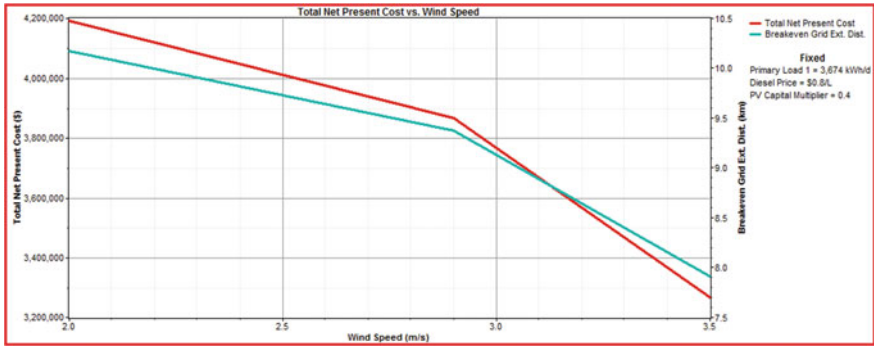


Fig. 5 Line graph for total NPC versus wind speed and breakeven grid extension distance

the extended grid to electrify the rural community load have equal total net present cost. In this case, the breakeven grid extension distance is 3.66 km, beyond this point, grid extension will not further be optimal. It is only feasible below the breakeven grid extension distance (i.e., 3.66 km). Hybrid off-grid power generating systems are feasible for electrification of rural community beyond the BGD.

The actual distance of the national grid from the location of the study community of Delta village is 27 km. Therefore from the simulation result given in Fig. 6, stand-alone hybrid system is feasible over grid extension to electrify the community.

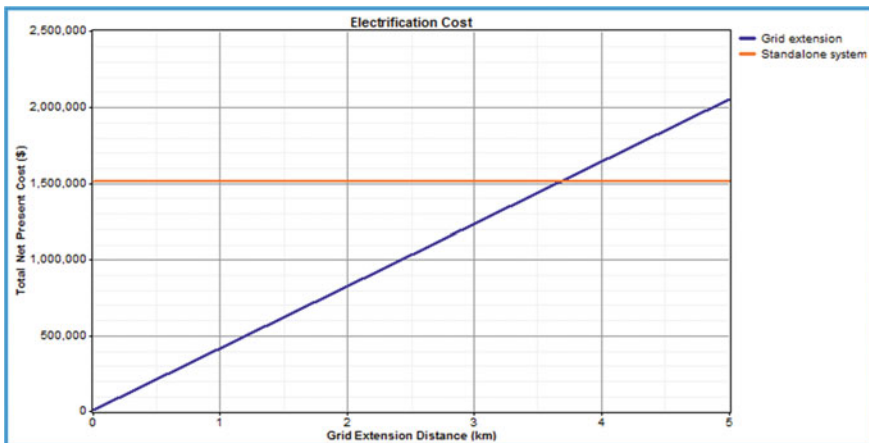


Fig. 6 Grid comparisons with stand-alone hybrid systems

#### **4.1 Post HOMER Analysis**

Evolution of rural electrification scheme based on hybrid power generation system in Delta village requires initial wherewithal of approximately \$647,240. This system can bestow power for 795 households including public service centers. Tariff issues will play a crucial role.

Generally, the basic rule in the electrification project is that the tariff structure must cover at least the capital and the lifetime O&M cost of the project. The LCOE is the indicator that presents the flat electricity tariff that can cover the capital and the O&M cost of the project during the lifetime. In contrast to the financial scheme, proper O&M scheme must be developed to ensure the sustainable operation of the rural electrification project. Local people can be trained for doing basic maintenance of the system and even for collecting the monthly fees from the consumer. O&M cost can be brought down by incorporating well-trained local people. However, the service of skilled technicians will be required for major maintenance activities especially in the diesel generator.

### **5 Conclusion**

The Responsivity analysis examines the consistency of the optimal system under different sensitivity inputs such as load, wind speed, diesel price, and PV capital cost multiplier and it reveals that the multiple hybrid systems (PV–wind–generator–battery) system is more favorable.

The Responsivity analysis result further reveals that due to varying wind speed and PV capital cost multiplier, COE varies from a minimum of \$0.298/kWh to a maximum of \$0.301/kWh and 30% load demand increased is also met by the hybrid configuration of (solar PV-wind-diesel-battery) system with a renewable fraction of 0.69.

The grid collation result revealed that both grid extension and stand-alone systems have equal total net present cost of \$1,500,000 at a breakeven distance of 3.66 km. Since grid extension is only feasible below this breakeven distance, hybrid off-grid power generation is suitable for electrification of study village. The study area is located 27 km away from the nearer substation; it means that the grid extension is much expensive and not recommended for the rural areas due to the high principal charge of grid extension, sparsely populated, and low energy demand of the rural community.

In summary, the replication outcome proves that the HPGS consisting of solar photovoltaic–wind–diesel generator–battery configuration is the greatest result to assurance the reliable and affordable electric power supply short of disruption of the load below the climatic statistics change.

### *Suggestion for Future Work*

1. The exact measurement of unconventional energy possessions such as solar energy also wind speed at different local times of the site.
2. Detailed electrical design and power quality analysis of hybrid system.
3. Addressing the possibility of replacing the convectional diesel generator in the hybrid power generating system by locally generated biofuels.

## **References**

1. Ravi D, Somanath B, Rao KM, Ranganath L, Koteswararao B (2018) Experimental testing of thermal house for different weather conditions in Bale robe. *Mater Today: Proc* 5(9):18245–18250
2. Ravi D, Yohannes S, Feyissa HM, Koteswararao B (2017) Investigation on the performance of photovoltaic panel with various filters: (At rural areas of bale robe region in Africa continent). In: 2017 international conference on energy, communication, data analytics and soft computing (ICECDS). IEEE, pp 210–212
3. Ibrahim H, Ghandour M, El-Jamal G (2018) Feasibility study of hybrid wind-diesel-battery power generating systems: parametric and sensitivity analysis. In *MATEC web of conferences*. EDP Sciences, vol 171, p 01004
4. Ravi D, Koteswararao B, Satish K (2018) Structural analysis of down the hole button bit with different materials. *Mater Today: Proc* 5(2):4711–4719
5. Koteswararao B, Ranganath L, Ravi D, Babu KSK (2016) Designing of a coconut chopping machine and making fuel from tender coconut. *Indian J Sci Technol* 9(34)
6. Shekar PC, Koteswararao B (2015) Investigation of machining parameters in electric discharge machining of high carbon steel. *Int J Res Eng Appl Sci* 5(4):17–30
7. Koteswararao B, Radha K, Vijay P, Raja N (2016) Experimental analysis of solar panel efficiency with different modes of cooling 8(3):1451–6
8. Koteswararao B, kishore Babu KS, Ravi D, Kumar KK (2017) Investigation of machining parameter in EDM of high carbon steel Alloy (EN31). *Mater Today: Proc* 4(2):1375–1384
9. Koteswararao B, Suresh Y, Ravi D (2017) Analysis of quality in solid state welding (copper-copper) by using NDT and DT by altering physical properties at constant time. *Mater Today: Proc* 4(8):7351–7356

# A Review on Advanced Optimization Algorithms in Multidisciplinary Applications



M. Sreedhar, S. Akshay Navaneeth Reddy, S. Abhay Chakra,  
T. Sandeep Kumar, S. Sreenatha Reddy and B. Vijaya Kumar

**Abstract** In various fields of engineering, optimization plays a key role in the development of new technology. In this wake, this paper discusses in detail, the concept of optimization, a few advanced methods and approaches most commonly used in different applications optimization process. The two most popular optimization procedures are also contrasted and discussed.

**Keywords** Optimization · Genetic algorithm · Particle swarm optimization · Heuristic · Algorithms

## 1 Introduction

Optimization is the process of finding the best result for any given problem. From stock market prediction to finding the best path for a drone, from animation mechanics to efficient operation of series robots, it is very important to engineers, scientists, economists, and researchers alike. In this process, many solutions are worked out for the given constraints and the solutions that best suit the problem are narrowed down. Since this is a heuristic process, accuracy is determined based on the number of iterations hence a computer is a perfect tool to perform optimization.

The solution of a typical optimization problem is determined by three key factors; design constraints, variables, and objective functions. If the problem is an experiment, then the design variables are physical inputs. Design constraints provide boundary conditions for the variables to operate within. Objective functions are determined based on the application for which the problem is being optimized for. The speed and accuracy with which a solution is found are dictated by the algorithm implemented.

---

M. Sreedhar (✉)

Research Scholar, Department of Mechanical Engineering, K L University, Guntur District, Andhra Pradesh, India

e-mail: [sreedhargnitmech@gmail.com](mailto:sreedhargnitmech@gmail.com)

S. A. N. Reddy · S. A. Chakra · T. S. Kumar · S. S. Reddy · B. V. Kumar

Department of Mechanical Engineering, Guru Nanak Institute of Technology, Hyderabad, India

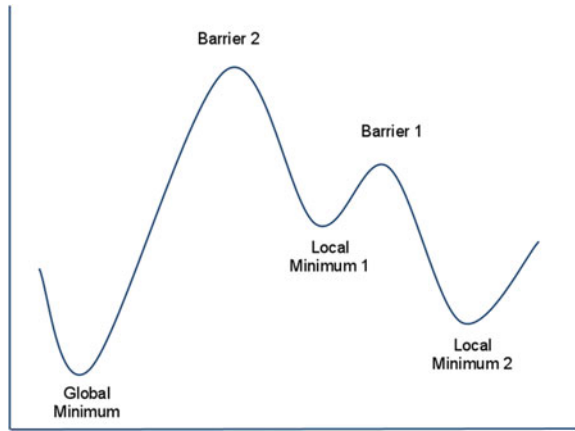
© Springer Nature Singapore Pte Ltd. 2020

G. S. V. L. Narasimham et al. (eds.), *Recent Trends in Mechanical Engineering*,

Lecture Notes in Mechanical Engineering,

[https://doi.org/10.1007/978-981-15-1124-0\\_66](https://doi.org/10.1007/978-981-15-1124-0_66)

**Fig. 1** Minimized objective function with local and global minima [3]



Since in engineering applications, we usually seek the minimum values such as minimum stress, weight, and cost, the output from the process or function defines as the cost function and it is something to be minimized. Now and then expanding a capacity bodes well. To maximize a function, just a negative sign is used in front of the output and minimize it.

The mathematical models of optimization are generally described as shown in

$$\begin{aligned} &\text{minimize } f(x) \\ &\text{Subjected to } g_i(x) \leq 0, i = 1, 2, 3 \dots\dots\dots, m \\ &\quad\quad\quad h_j(x) = 0, j = 1, 2, 3 \dots\dots\dots, n \end{aligned}$$

Mathematical equation for optimization problem

An example of mathematical model of an optimization problem is given. Here,

- $f(x)$  is the objective function,
- $g_i(x)$  is the inequality constraint, and
- $h_j(x)$  is the equality constraint (Fig. 1).

## 2 Types of Optimization

Depending upon the aspects of the minimization function, a minimization problem can be classified as

## ***2.1 Based on Continuity***

- (a) Continuous Optimization
- (b) Discrete Optimization

Some algorithms work efficiently only when the variables are from a discrete set, usually integers, while other algorithms can work with any variables: all real values. The advantage of using continuous optimization is that the curves obtained by the minimization function are smooth and the neighborhood values for any given objective function and constraint function can be easily found. Even though discontinuous, discrete optimization also creates a sequence of continuous subproblems [1].

## ***2.2 Based on Constraints***

- (c) Unconstrained Optimization
- (d) Constrained Optimization

Almost all the practical applications come under unconstrained optimization and because all constraints can't be defined, constraints are supplanted by a penalty term in the objective function. Constrained Optimization has well-defined constraints either by equalities or by inequalities [1].

## ***2.3 Based on Objective Function***

- (e) Single-Objective
- (f) Multi-Objective

Generally, optimization problems have only a single objective function. Engineering, economics, and logistics are some of the many fields where there are two or more objectives. For example, in logistics, the objectives might be to minimize time and maximize safety. However, multi-objective functions are converted to single-objective functions by altering the constraints involved [1].

## ***2.4 Based on Data Accuracy***

- (g) Deterministic Optimization
- (h) Stochastic Optimization

Deterministic optimization is used when the input data for a given question are defined accurately, which rarely happens in actual problems due to reasons like measurement error and miscalculations in predicting data for the problems. Stochastic optimization, however, accounts for these uncertainties in the problem [1].

### 3 Heuristic Algorithms

Earlier optimization studies implemented sophisticated mathematical methods to find exact solutions for optimization problems. But these exact solutions had only a limited scope of applications. This is when the heuristic algorithm gained prominence due to their simple mathematical background with basic formulations. The main benefit of the heuristic optimization algorithms is that they can be applied effectively on both constrained and unconstrained problems. When the constraints are not in the feasible region, in order to obtain minimized solutions satisfying the constraints, a penalty function is added to the objective function. The function formed by the conjunction of these two functions is called a fitness function. When the constraints are in the feasible region, the penalty function is taken zero.

Unlike the exact methods, heuristic algorithms find the solutions that are closer to the optimum solutions. Some heuristic optimization algorithms solve the subproblems separately and merge those independent solutions into a feasible solution for an overall problem. Karp explained the Traveling Salesman Problem (TSP) by partitioning the entire geographic region into small region and applying TSP independently for each subregion [2]. For problems like aggregate production planning or family scheduling, hierarchal planning is implemented [3]. Some algorithms solve the subproblems in scheduling problems iteratively as discussed by Morton and Pentico [4]. Few methods use the concept of analogy to generalize the behavior from smaller and simpler problems which can be observed in the location and scheduling problems done by Bilde and Vidal [5]. Some algorithms have an entirely different approach where they reduce the number of possible solutions by reducing the solution space by introducing extra constraints. Such methods are demonstrated in power optimizing for computing by Ehrhardt [6]. Some simplify the original question by replacing several variables by an aggregate value and after finding the solution, they reverse the process which gives the solution for the original problem. Geoffrion implemented this technique in optimizing logistics decision-making [7]. Some even modify the objective function by assuming a related simpler objective function as shown by Silver and Meal in selection of lot sizes under a time-varying demand situation [8]. Some methods rely on approximation of nonlinear constraint by a linear one or even completely ignore the constraints to check for solutions that satisfy the original constraints. This uses calculus to generate approximate extreme points as shown by Fisher and Jaikumar in vehicle routing problem [9]. This demonstrates that certain algorithms and approaches are inherently more efficient in solving certain problems. For example, nature-inspired algorithms prove to be faster and have less errors for predicting stock markets as shown by Hegazy, Soliman, and Mustafa [10]. With the success of natural algorithms over traditional algorithms, many new algorithms based on nature and societal behavior of animals are developed such as Ant Colony Optimization (ACO), Particle Swarm Optimization (PSO), Genetic Algorithm (GA), and Artificial Bee Colony (ABC). The most recent developments incorporate hybrid optimization in which combination of heuristic algorithms and exact methods are simultaneously implemented to give more desirable results as shown by Jourdan and Basseur [11].



Algorithms such as Genetic Algorithm and Particle Swarm Optimization are opted for the problems related to robotic manipulators and robotic grasps.

### 3.1 Genetic Algorithm

Genetic Algorithm (GA) is a nature-inspired heuristic algorithm used in artificial intelligence and computing introduced by John Holland in 1960 which was further extended by Goldberg in 1989. It mimics Darwin's theory of natural selection and evolutionary biology to find optimized solutions. This algorithm creates a group of individual solutions from a given population and these are evaluated with the evaluation constraints to eliminate the undesirable solutions. Solutions are further developed from the remaining individuals which follow the survival of the fittest principle of natural evolution.

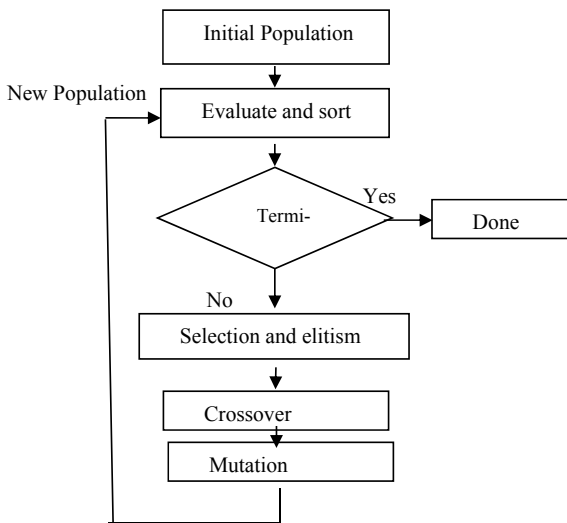
$$\begin{aligned}
 OF &= f_{obj}(x_1, x_2 \dots x_n) \\
 PF &= \sum_{i=1}^1 R_i (\max [0, g_i(x_1, x_2, \dots x_n, a)])^2 \\
 &+ \sum_{j=0}^m R_j (\max [0, h_j(x_1, x_2 \dots x_n, b) - tol])^2 \\
 FF &= OF + PF
 \end{aligned}$$

where  $a$  and  $b$  are constants,  $m$  is quality constraints number,  $h_j$ 's value is below the tolerance value and  $tol$  is the tolerance value,  $OF$  is the objective function,  $PF$  is the penalty function, and  $FF$  is the fitness function.

GA is one of the most favored algorithms due to its ability to satisfactorily solve wide range of problems and it has been successfully implemented in many disciplines like economics, material science, inverse kinematics optimization, computing, artificial intelligence, electronics, and networking. It is a discrete system that is likewise appropriate for combinatorial problems. GA was used by Satya Prasad, NagaRaju, and Kantam to develop a software dependability growth model to analyze software and detect software failures for efficiently debugging which proved to be more accurate than other comparable models [12]. Rashidifar and Abdolah used GA and Neural Networks jointly to optimize controller tuning in which minimization of tuning criteria is done by GA [13]. Micro Electric Discharge Machining process was optimized using GA to reduce the tool wear rate while drilling a micro-hole by Ashutosh, Kamlesh, and Abhay [14]. GA was used by Bilel and Fethi to tag parts of speech in Arabic language [15].

Genetic algorithm was used for generating efficient grasping patterns by Jaime J. Fernandez for Barret's hand in 1998 [26]. Pakize Erdogmus and Metin Toz solved the

inverse kinematics question for a PUMA robot using the same [25]. Emil Dale Bjoerlykhaug has concluded that using GA for optimizing closed-loop inverse kinematics solver proved to be much effective than using random values as it had much quicker convergence [27]. Z. Mohamed and G. Capi proposed the use of multi objective genetic algorithm for improvement of humanoid robot arm movement for obstacle avoidance [28]. GA based optimal regrasping was developed for the five-fingered robot hand, Anthrobot, by Aydan M. Erkmén, Mehmet Durna in Belgium in which they discussed that the GA based algorithm didn't seem to have much improvement until 700th generation due to low population diversity [24]. Zichen Zhang and Jason Gu produced a GA planner for generating pregrasp pattern of a dexterous hand for 3D spatial objects which proved GA parameters to have a crucial impact on the improved operation of the hand [23]. A GA based deep learning tuning for object identification and grasping has been performed by Delowar Hossain and Genci Capi who closed the multi-objective hereditary calculations to outflank the relegated errands when contrasted with customary techniques [21].



Flow chart describing the function of a Genetic Algorithm [21].

Inverse Kinematics is a standout among the most difficult issues in mechanical autonomy. The issue includes finding an ideal posture for a controller given the situation of the end-tip effector rather than forward kinematics, where the end-tip position is looked for a given posture or joint setup [29]. Typically, this position is communicated as a point in a facilitate framework [23] (e.g., in a Cartesian framework with  $x$ -,  $y$ -, and  $z$ -coordinates). In any case, the posture of the controller can likewise be communicated as the accumulation of joint factors that portray the angle of bending or twist (in revolute joints) or length of augmentation (in prismatic joints) [30].

Inverse Kinematics is especially troublesome because abundant arrangements can emerge. Naturally, one can imagine that an automated arm can have various methods for coming through a specific point. It is similar when you contact the table and move your arm without moving the fact of the matter you're contacting the table at [31].

Additionally, the estimation of these positions can be extremely difficult. Simple arrangements can be found for 3-DOF controllers yet attempting to take care of the issue for six or considerably more DOF can prompt testing algebraic issues.

The GA was used to put a robot at the objective position while constraining the greatest joint interpretation from the underlying position [12]. At present, GAs is appropriate for disconnected programming of an excess robot in point-to-point situating errands. Despite the fact that the last situating exactness isn't perfect, the straightforwardness and intensity of the GA make an intriguing commitment to the field of in-stanza kinematics. There are potentially a few additional tasks of GAs in redundant robot kinematics applications, where weighting factors are computed at different generations [24].

### 3.2 Particle Swarm Optimization

Particle Swarm Optimization (PSO) is a swarm propelled populace based heuristic improvement method created by Dr. Eberhart and Dr. Kennedy in 1995. It was enlivened by their perceptions of social rummaging conduct of a few creatures, for example, running of fowls and tutoring of fish. It impersonates the social conduct of a gathering where the individuals from the swarm fly through a domain to pursue the fitter individuals from the swarm on account of biasing toward the fitter individuals from the earth. In this algorithm, the estimations of the gathering factors are balanced toward the esteem nearest to the objective at some random minute. This fixing design proceeds until the point where the desired arrangement is accomplished. PSO has favorable position over GA in that it has no development administrators, for example, hybrid and change. In any case, PSO is a persistent procedure that is inadequately suited for combinatorial issues.

This algorithm initializes stochastic positions and locations to each of its particles and the dimension represents the number of particles. All particles start with random local and global best values. Every number moves along the global and local best values depending on the random weighed amount by the parameter system. Local best value is the best value a particle has found during that iteration and the global best value is the best value of all local best values found in that iteration. After every iteration, global and local best values are updated. Every next iteration is made along with the new updated local and global best values. After a number of iterations, all particles converge on to the global best value. Equations proposed for this optimization as given by Kennedy and Eberhart are [16]

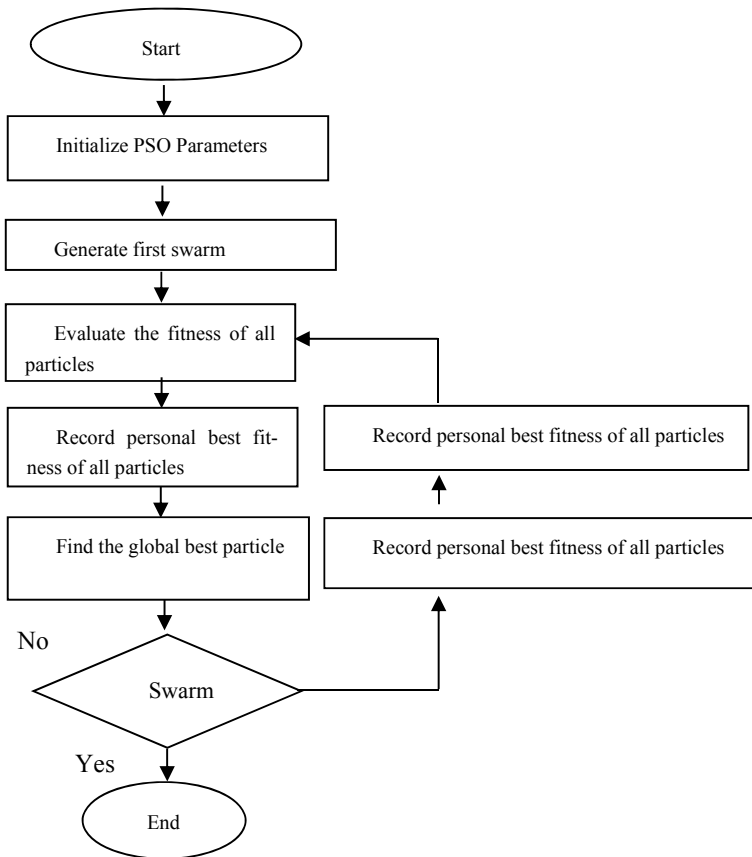
$$V_x[i] = V_x[i] + 2 * rand() * (pbestx[i] - presentx[i]) + 2 * rand() * (pbestx[gbest] - presentx[i])$$

where *rand* is a random number, *pbestx* is the local best value of a particle, *presentx* is the present value of that particle, and *gbest* is the global best of all particles. The

next position of a particle relies on the current position of the particle until they converge onto a global best position.

Hybrid Genetic Swarm Algorithm tackles the inverse kinematics issue by methods for naturally enlivened enhancement procedures and proposes a widespread agreement that can be applied on arbitrary joint chains [32].

There are a few intriguing perspectives for further investigations and enhancements which reach from completely computational to algorithmic and logical viewpoints. A productive parallel GPU or multicenter handling for wellness estimations may achieve a huge computational speedup. Upgrades can likewise be envisioned by adjusting the calculation to figure the issue for multiple end effectors simultaneously and to coordinate extra requirements into the plan of the target work [33]. Eventually, the algorithmic ideas are nonexclusive and may likewise be effectively material to different persistent and multimodal optimization problems.



Flow chart describing the function of a Particle Swarm Optimization [17].

Particle Swarm Optimization (PSO) is a relatively new algorithm and has many advantages such as simplicity and rapid convergence. A study by Rania, Babak, and Olivier to examine the effectiveness of both GA and PSO showed that PSO

required less computational effort to converge at the same desired solutions by GA [17]. Mohammad, Reza, Kwok, Sahaboddin, and Pezhman conducted a case study in which they found that PSO in conjunction with multilayer perceptron technique could accurately approximate the evaporation rates over a daily forecast horizon in northern Iran [18]. Support Vector Machines optimized with PSO proved to be more effective than those optimized with GA to automatically and accurately classify the MRI for the diagnosis of Dementia [19]. Hybrid PSO was found to be faster in solving multi area economic dispatch problem than other comparable methods in a test by Hyunh [20]. Nizar Rokbani, Adel. M Alimi used Particle swarm optimization for solving inverse kinematics which solves the issues of path planning, path optimization, and motion related problems in robotic arms and concluded the PSO-VG to be effective among all other types of PSO optimizations [22]. PSO when compared to GA seemed to have a much lower execution time for pathfinding operation and solving inverse kinematics for a PUMA robot [25].

## 4 Conclusion

This paper concentrates on two near-identical Evolutionary Algorithms: Genetic Algorithm (GA) and Particle Swarm Optimization (PSO). We observe that GA is more appropriate for discrete optimization whereas PSO is more widely used for continuous optimization. The solutions for GA are ranked based on fitness values where the traverse operation produces offspring with parts extracted from the parents where the solutions are more probable to be similar to that of parents. For PSO, it is observed that a new swarm of particles are generated through the velocity and position update equations. This confirms that all new particles can be much different than the old ones. Also, as it was discussed that the mechanism is relied on floating point arithmetic, it could generate any values within the solution set that may be much larger than those generated via GA. There are many academic journals that measure performances of these two evolutionary algorithms in solving some complicated optimization problems in various fields. The performance of algorithm is vague as many applied different solution representations along with various local searches. So, the comparison would be more exhaustive when benchmark problems are used with similar solution representation and similar number of function evaluations.

## References

1. <https://neos-guide.org/optimization-tree>
2. Karp RM (1977) Probabilistic analysis of partitioning algorithms for the traveling-salesman problem in the plane. *Math Oper Res* 2:209–224
3. Bitran GR, Tirupati D (1993) Hierarchical production planning. In: Graves SC, Rinnooy Kay AHG., Zipkin PH (eds) *Logistics of production and inventory*, vol 4. North Holland: Amsterdam, Chapter 10

4. Morton TE, Pentico DW (1993) Heuristic scheduling systems. Wiley—Interscience, New York
5. Bilde O, Vidal RVV (1973) On the connections between locations and scheduling problems. In: Johnson M and Ashour S (eds) SCI Proceedings for simulation in manufacturing industries, 3(2):30–42
6. Ehrhardt R (1979) The power approximation for computing (s, S) inventory policies. *Manage Sci* 25:777–786
7. Geoffrion AM (1977) A priori error bounds for procurement commodity aggregation in logistics planning models. *Nav Res Logist Q* 24:201–212
8. Silver EA, Meal HC (1973) A heuristic for selecting lot size quantities for the case of a deterministic time-varying demand rate and discrete opportunities for replenishment. *Prod Inven Manag J* 14:64–74
9. Fisher ML, Jaikumar R (1981) A generalized assignment heuristic for vehicle routing. *Networks* 11:109–124
10. Hegazy O, Soliman OS, Salam MA (2015) Comparative study between FPA, BA, MCS, ABC, and PSO algorithms in training and optimizing of LS-SVM for stock market prediction. *Int J Adv Comput Res* 5(18):35–45
11. Jourdan L, Basseur M, Talbi EG (2009) Hybridizing exact methods and metaheuristics: a taxonomy. *Eur J Oper Res* 199(3):620–629 (December, Elsevier)
12. SatyaPrasad R, NagaRaju O, Kantam RRL (2010) SRGM with imperfect debugging by genetic algorithms. *Int J Softw Eng Appl (IJSEA)* 1(2):66–79 (April)
13. Rashidifar MA, Abertavi A (2014) A novel technique for controller tuning. *Int J Appl Control, Electr Electron Eng (IJACEEE)* 2(2):1–12 (May)
14. Pandey AK, Tiwari K, Dubey AK (2014) Optimization of the process parameters in micro-electric discharge machining using response surface methodology and genetic algorithm. *Int J Sci Res Publ* 4(9):1–05 (September)
15. Ali BB, Jarray F (2013) Genetic approach for Arabic part of speech tagging. *Int J Nat Lang Comput (IJNLC)* 2(3):1–12 (June)
16. Kennedy J, Eberhart R (1995) Particle swarm optimization. *Proc IEEE Int Conf Neural Netw* 4:1942–1948
17. Hassan R, Cohanim B, De Weck O (2005) A comparison of particle swarm optimization and the genetic algorithm. In: Conference: proceedings of the 46th AIAA/ASME/ASCE/AHS/ASC structures, structural dynamics & material conference
18. Ali Ghorbani M, Kazempour R, Chau KW, Shamshirband S, Taherei Ghazvinei P (2018) Forecasting pan evaporation with an integrated artificial neural network quantum-behaved particle swarm optimization model: a case study in Talesh, Northern Iran. *Eng Appl Comput Fluid Mech* 12(1):724–737
19. Sivapriya TR (2011) An efficient wavelet based feature reduction and classification technique for the diagnosis of Dementia. *Int J Comput Sci, Eng Inf Technol (IJCSEIT)* 1(5):63–76 (December)
20. Binh HTT (2013) Hybrid particle swarm optimization for solving multi-area economic dispatch problem. *Int J Soft Comput (IJSC)* 4(2), 17–27 (May)
21. Hossain D, Capi G (2017) Genetic algorithm based deep learning parameters tuning for robot object recognition and grasping (March)
22. Rokbani N, Alimi AM (2013) Inverse kinematics using particle swarm optimization, a statistical analysis. *Procedia Eng* 64:1602–1611. <https://doi.org/10.1016/j.proeng.2013.09.242>
23. Zhang Z (2012) Vision-based grasp planning of 3d objects using Genetic Algorithms, Proceedings IEEE international conference on automation and logistics, pp 646–651
24. Erkmén AM, Durna M (1998) Genetic algorithm-based optimal regrasping with the Anthrobot 5-fingered robot hand, May
25. Erdogmus P, Toz M (2012) Heuristic optimization algorithms in robotics, serial and parallel robot manipulators. In: Kucuk MTE-S (ed) Rijeka: IntechOpen. pp 311–338 (Chapter 16)
26. Fernandez JJ, Walker ID (1998) Biologically inspired robot grasping using genetic programming. In: Proceedings. 1998 IEEE international conference on robotics and automation (Cat. No.98CH36146), 4 (May), pp 3032–3039. <https://doi.org/10.1109/ROBOT.1998.680891>

27. Bjoerlykhaug E (2018) A closed loop inverse kinematics solver intended for offline calculation optimized with GA. *Robotics* 7(1):7. <https://doi.org/10.3390/robotics7010007>
28. Mohamed Z, Capi G (2015) Multi objective optimization of humanoid robot arm motion for obstacle avoidance. In: 2015 IEEE international symposium on robotics and intelligent sensors (IRIS), Langkawi, pp 111–114. <https://doi.org/10.1109/iris.2015.7451596>
29. Parker JK, Khoogar AR, Goldberg DE (1989) Inverse kinematics of redundant robots using genetic algorithms. In: Proceedings, 1989 international conference on robotics and automation, pp 271–276
30. Collins TJ, Shen WM (2017) Particle swarm optimization for high-DOF inverse kinematics. In: 2017 3rd international conference on control, automation and robotics (ICCAR), pp 1–6. Polymorphic Robotics Laboratory, Department of Computer Science, University of Southern California, USA
31. Rokbani N, Alimi AM (2013) Inverse kinematics using particle swarm optimization, a statistical analysis. *Procedia Eng* 64:1602–1611 (Elsevier)
32. Starke S, Hendrich N, Magg S, Zhang J (2016) An efficient hybridization of genetic algorithms and particle swarm optimization for inverse kinematics. In: IEEE international conference on robotics and biomimetics (ROBIO), pp 1782–1789. Department of Informatics, University of Hamburg, Germany
33. Ayyıldız M, Çetinkaya, K (2016) Comparison of four different heuristic optimization algorithms for the inverse kinematics solution of a real 4-DOF serial robot manipulator. <https://doi.org/10.1007/s00521-015-1898-8>